ISSN 0288-4534
CODEN: KONAE7

KONA Powder and Particle Journal

No.30 (2013)

Published by Hosokawa Powder Technology Foundation

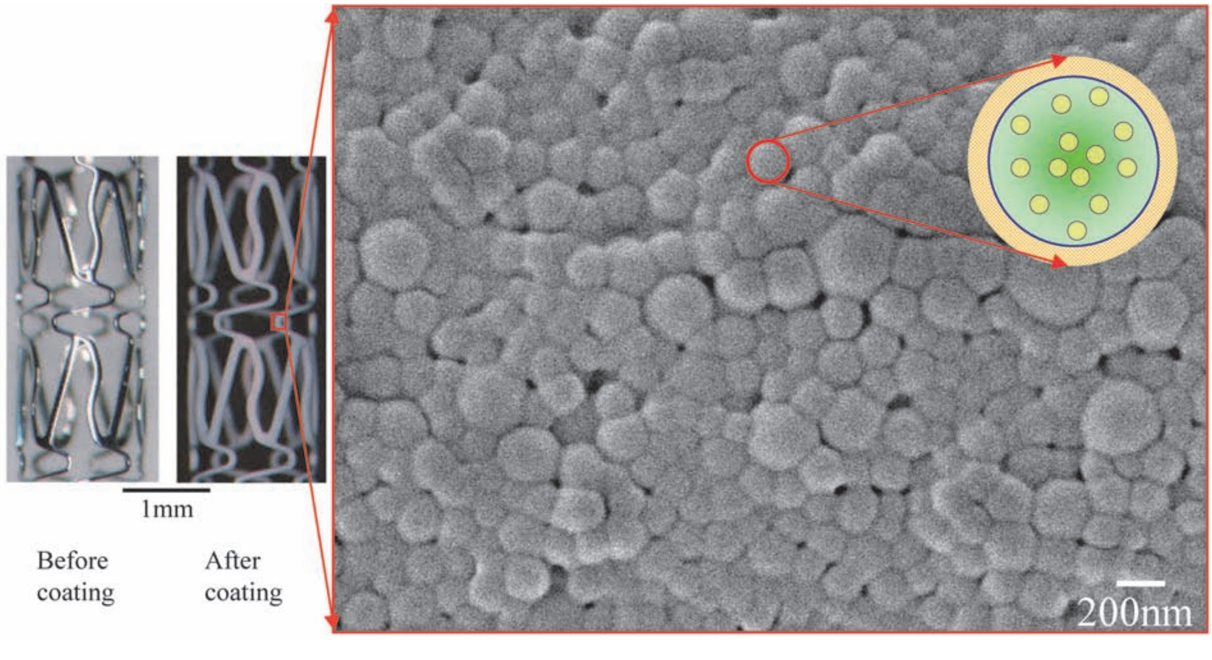

available online – www.kona.or.jp

KONA Powder and Particle Journal

http://www.kona.or.jp

KONA is a refereed scientific journal that publishes articles on powder and particle science and technology. KONA has been published annually since 1983 and is distributed to researchers, members of the scientific communities, universities and research libraries throughout the world.

About the Cover of Journal "KONA"

The Chinese character "粉" is pronounced "KONA" in Japanese, and means "Powder". The hand written "粉" is after the late Mr. Eiichi Hosokawa, founder of the Hosokawa Micron Corporation.

Headquarters of Hosokawa Micron Corporation

Editorial Board

J. Hidaka	Editor-in-Chief (Doshisha Univ., JAPAN)
Asia / Oceania Editorial Board	
Y. Fukumori	(Kobe Gakuin Univ., JAPAN)
K. Higashitani	(Kyoto Univ., JAPAN)
H. Kage	(Kyushu Institute of Technology, JAPAN)
Y. Kang	(Chungnam National Univ., KOREA)
J. Li	(Chinese Academy of Science, CHINA)
H. Masuda	(Professor Emeritus of Kyoto Univ., JAPAN)
M. Naito	(Osaka Univ., JAPAN)
K. Nogi	(Professor Emeritus of Osaka Univ., JAPAN)
K. Okuyama	(Hiroshima Univ., JAPAN)
Pradip	(Tata Research Development and Design Centre, INDIA)
M. Rhodes	(Monash Univ., AUSTRALIA)
M. Takahashi	(Nagoya Institute of Technology, JAPAN)
H. Takeuchi	(Gifu Pharmaceutical Univ., JAPAN)
W. Tanthapanichakoon	(Tokyo Institute of Technology, JAPAN)
Y. Tsuji	(Professor Emeritus of Osaka Univ., JAPAN)
Secretariat	
T. Yokoyama	(Hosokawa Powder Technology Foundation, JAPAN)
L. Cui	(Hosokawa Micron Corporation, JAPAN)
Europe / Africa Editorial Board	
M. Ghadiri	Chairman (Univ. of Leeds, UK)
B. Biscans	(Univ. de Toulouse, FRANCE)
N.Z. Lyakhov	(Institute of Solid State Chemistry, RUSSIA)
J. Marijnissen	(Univ. of Delft, NETHERLANDS)
W. Peukert	(Univ. Erlangen, GERMANY)
S.E. Pratsinis	(ETH Zürich, SWITZERLAND)
Secretariat	
J. Stein	(Hosokawa Alpine AG, GERMANY)
N. Winzer	(Hosokawa Alpine AG, GERMANY)
American Editorial Board	
B.M. Moudgil	Chairman (Univ. of Florida., USA)
D.W. Fuerstenau	Vice Chairman (Univ. of California, USA)
F. Concha	(Univ. of Concepció, CHILE)
R. Flagan	(California Institute of Technology, USA)
A.I. Hickey	(Univ. of North Carolina, USA)
R. Hogg	(Pennsylvania State Univ., USA)
V.A. Marple	(Univ. of Minnesota, USA)
S.B. Savage	(McGill Univ., CANADA)
Secretariat	
C.C. Huang	(Hosokawa Micron International INC., USA)

■Publication Office
Hosokawa Powder Technology Foundation
Shodai- Tajika 1-9, Hirakata, Osaka, 573-1132 Japan
e-mail : info@kona.or.jp

KONA Powder and Particle Journal　No. 30 (2013)

CONTENTS

＜Review Papers＞

＜Original Research Papers＞

＜ Information Articles ＞

The Letter from the Editor

Jusuke Hidaka
Editor-in-Chief

It is my great pleasure to announce Issue Number 30 of KONA. I recently took over as the editor-in-chief of KONA Powder and Particle Journal as well as the director of Hosokawa Powder Technology Foundation, which supports the publication of KONA.

This issue will be published as KONA 30 (2013) instead of KONA 30 (2012). The issuing year becomes 2013 because the date of issue has been revised from 10th December to 10th January in order to facilitate the count of the number of published papers in the year, which is to be used for the evaluation of the journal' s impact factor.

This issue marks the 30th anniversary of KONA as an international journal serving a global community on an annual basis. It was thirty years ago that KONA was first published, by the Council of Powder Technology, Japan, to disseminate the high-quality powder-based research done in Japan to the world. "KONA," the title of this journal, means *powder* in Japanese. Now, as we approach the 30th anniversary of the journal, the word KONA has become symbolic of powder technology. KONA has also been international in the sense that it is edited by three editorial boards-one each in Asia, North America and Europe. A number of excellent papers from researchers around the world are accepted by each of the editorial boards.

Although the trends of development in powder technology differ slightly from country to country because of the unique characteristics of powder technology in each country, this technology has mostly been developed as an engineering approach for designing the powder handling operations and the powder process systems.

One of the steps toward the advancement of the modern society to a more plentiful, healthy, comfortable, and safe society is to develop new powder technology that would yield highly functional materials having the high performance required to realize such a society. Such new powder technology should be developed as engineering approaches and should include not only powder process engineering but also the production engineering capable of designing the functional materials.

Powder technology is said to be a "global growth engine for tomorrow" , and about 70% of the final or intermediate products of materials processing industries are considered to be in particulate form. Research on powder technology is gaining ever-increasing importance in light of the ongoing innovations in the field of materials science and processing. In fact, it can generally be said that powder technology is one of the most important engineering fields for achieving progress and improvements in daily life.

I am certain that KONA will serve as an important platform for fruitful discussions on powder technology in the future as well. Finally, I truly hope to see KONA thrive and grow dynamically and continuously with support from both contributors and readers around the world.

J. Hidaka

Comment of the Cover Photograph

Development of drug-eluting stent coated with PLGA nanoparticles as drug carriers

Yusuke Tsukada and Hiroyuki Tsujimoto
[1] *Pharmaceutical & Beauty Science Research Center, Hosokawa Micron Corporation*

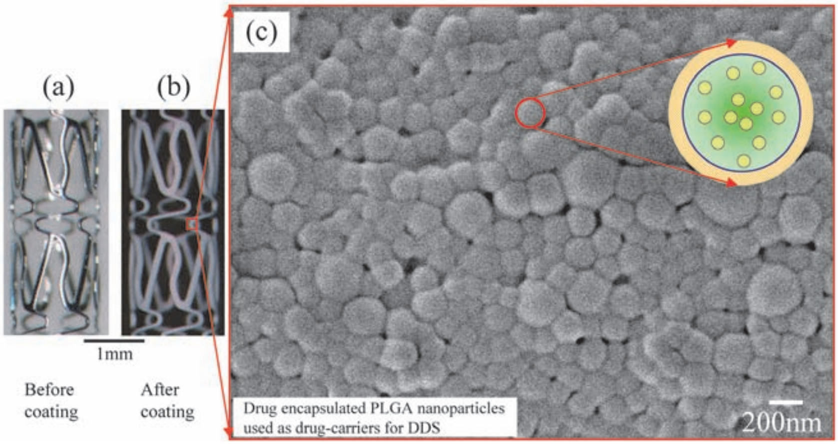

Fig. 1 Optical microscope photographs of a bare metal stent (a) and a drug-eluting stent coated with PLGA nanoparticles (b), SEM image of drug encapsulated PLGA nanoparticles coated onto the stent surface(c).

The photo shows the “stent” coated with “biocompatible and bioabsorbable poly (D, L-lactide-co-glycolide) (PLGA) nanoparticles (NPs)” which are known to have advanced DDS functions such as the sustained-release by its hydrolysis property and the intracellular delivery by its small size effect. “Stent” is a medical device formed of metallic meshed tube and used as a measure to treat the stenosis of the artery to improve the blood flow by eternal expanding and supporting of the blood vessels.

The use of a bare metal stent (BMS) as the 1st generation device is known to reduce the re-stenosis by 20~30%. The re-stenosis rate was reduced to <10% by drug-eluting stents (DES) developed as the 2nd generation, which gradually release a drug substance such as an anticancer or immunosuppressive agent from the polymer layer formed on the stent surface to the blood vessel. However, it became a new major concern1) that the late stent thrombosis (LST) resulted in higher rate of mortality or myocardial infarction by irritating properties of the polymer layer containing the drugs than BMS from the half year follow-up.

Under these circumstances, various kinds of the 3rd generation stent have been actively developed2). Authors also focus on the development of new stent using PLGA nanoparticles as the 3rd generation. The nonirritating drug loaded PLGA NPs coated stent can be expected to drastically restrain the re-stenosis rate by sustained-releasing the drug from the PLGA NPs delivered in inflammatory cells by the disembarrassment as nanoparticles from the surface of the expanded stent.

References

1) Nordmann A. J., Briel M. and Bucher H.C.(2006): Mortality in randomized controlled trials comparing drug-eluting vs. bare metal stents in coronary artery disease: a meta-analysis, Eur. Heart J., Vol.27, pp.2784-2814.
2) Iwata H. and Manabe I. (2011): Coronary stent update: current status and clinical problems, Biomaterial, Vol.29-3, pp.146-157.

---

[1] No.9, Shodai-Tajika 1-chome, Hirakata, Osaka 573-1132, JAPAN

Bridging Flocculation by Polymers[†]

Richard Hogg
[1] *Department of Energy and Mineral Engineering, The Pennsylvania State University*

Abstract

A comprehensive evaluation of flocculation processes is presented with emphasis on physical and engineering aspects. Flocculation by polymer bridging involves three basic sub-processes: mixing of the polymer with the particle suspension, adsorption of the polymer on particle surfaces and the formation and growth of flocs. Each of these is primarily controlled by agitation of the suspension. At the same time, agitation also promotes floc breakage. Since polymer adsorption tends to occur irreversibly, flocculation is a non-equilibrium process and the relative rates of the sub-processes play a critical role. The kinetics of these processes are reviewed and their implications with respect to process design are evaluated. Procedures for controlling the relative rates are shown to provide a basis for the design of efficient flocculation processes in batch systems. Some information on scale-up criteria is presented. Extension of the basic concepts to the design and operation of continuous processes is discussed.

Keywords: polymer adsorption kinetics, destabilization, floc formation and growth, mixing effects, batch flocculation scale-up, continuous flocculation in tanks and in-line mixers

Introduction

The use of polymers for flocculating fine particles is widely practiced in solid-liquid separations. The process can be highly effective, but the results are often quite variable even for very similar systems and conditions. Practical applications generally depend on adsorption of the polymer on the surfaces of suspended particles. The particular arrangement of the adsorbed molecules determines the performance of the process. Variations in performance can usually be attributed to differences in such arrangement, for example, uneven distribution among the particles due to poor mixing of polymer solution and particle suspension.

Polymer-induced flocculation typically proceeds through one or other of two basic mechanisms: charge-patch interaction1) or particle bridging2, 3). Charge-patch interaction results from the adsorption of, usually relatively low molecular weight, polyelectrolyte molecules on oppositely charged particle surfaces. These create a "patch" on the surface that is electrostatically attracted to regions of bare surface on other particles. Bridging flocculation occurs when high molecular weight polymer molecules adsorb simultaneously on more than one particle. Charge-patch flocculation is usually effective and performs consistently, but results only in relatively small flocs. Bridging flocculation, on the other hand, can produce very large flocs but performance can be erratic. This paper focuses on bridging flocculation and presents an evaluation of the causes and solutions to performance variability.

Polymer Adsorption

The polymers used in bridging flocculation are normally high molecular weight linear-chain compounds, commonly based on polyacrylamide. The molecules may be uncharged (nonionic) or partially hydrolyzed as an (anionic) poly-acrylamide/acrylate copolymer. Adsorption is generally considered to result primarily from hydrogen bonding between active groups (amide or hydroxyl) in the polymer chain and

---

[†] Accepted: January 16, 2012

[1] 232 Hosler Building, University Park, PA 16802, USA
E-mail: rxh19@psu.edu
TEL: +1-814-865-3802 FAX: +1-814-865-3248

© 2013 Hosokawa Powder Technology Foundation

hydroxylated sites on particle surfaces.

Typically, molecular weights exceed 10 million which corresponds to more than 100,000 individual segments each of which is capable of adsorbing on the surface. It follows that an adsorbed molecule can be expected to be attached through many such interactions. While each individual segment probably undergoes reversible adsorption/desorption steps, desorption of the molecule as a whole would require simultaneous desorption of all attached segments which is exceedingly unlikely. It follows that polymer adsorption is effectively irreversible[4]. Polymer adsorption generally occurs in two stages – initial attachment followed by conformational rearrangement on the surface. This rearrangement will normally involve spreading of individual molecules, increasing the area occupied by each. The process of rearrangement at the surface is considered to be much slower than the attachment step[5] and is unlikely to contribute to bridging flocculation.

Adsorption Kinetics

Adsorption rates are determined by particle/polymer molecule collisions. If particles and (coiled) molecules can be treated as spheres, classical expressions for collisions due to Brownian motion and/or shear can be used to estimate collision frequencies. For particles of diameter d_s and polymer molecules of effective hydrodynamic size d_p the collision frequency f_{sp} can be estimated from:

$$f_{sp} = K_{sp} n_s n_p \tag{1}$$

where n_s and n_p are the number concentrations of particles and polymer molecules respectively and K_{sp} is the collision frequency constant. Assuming that Brownian motion and shear act independently, the frequency constant, for a combination of the two processes, can be approximated by[6), 7)],

$$K_{sp} = \left[\frac{2k_B T}{3\mu} \left(2 + \frac{d_p}{d_s} + \frac{d_s}{d_p} \right) + \frac{\bar{G}}{6} \left(d_s + d_p \right)^3 \right] \tag{2}$$

where k_B is Boltzmann's constant, T is absolute temperature, μ is the liquid viscosity, d_s and d_p are, respectively, the solid particle and effective polymer molecule diameters and $\bar{G}$ is the mean shear rate due to agitation of the suspension.

For soluble polymers, adsorption will be limited by surface coverage as surface sites become blocked by adsorbed molecules. If each collision with bare particle surface results in the removal of one polymer molecule from suspension, the concentration remaining after time t can be obtained from,

$$\frac{dn_p}{dt} = -K_{sp} n_s n_p (1 - \theta) \tag{3}$$

where θ is the fractional surface coverage and is determined by the number and size of adsorbed molecules. Assuming, for simplification, that the size and shape of the adsorbed molecules are the same as in solution, θ can be estimated using

$$\theta = \frac{n_a}{4n_s} \left(\frac{d_p}{d_s} \right)^2 \tag{4}$$

where n_a is the number of adsorbed molecules per unit volume. The number of adsorbed molecules is simply

$$n_a = n_{p0} - n_p \tag{5}$$

where n_{po} is the total amount of polymer added. From Equations 3, 4 and 5

$$\frac{dn_p}{dt} = -K_{sp} n_s n_p \left[1 - \left(\frac{n_{po} - n_p}{4n_s} \right) \left(\frac{d_p}{d_s} \right)^2 \right] \tag{6}$$

or

$$\frac{dn_p}{dt} = -K_{sp} n_s n_p \left[1 - \theta_t \left(1 - \frac{n_p}{n_{p0}} \right) \right] \tag{7}$$

where θ_t is the fractional surface coverage that would exist if 100% of the added polymer were adsorbed, i.e.,

$$\theta_t = \frac{n_{p0}}{4n_s} \left(\frac{d_p}{d_s} \right)^2 \tag{8}$$

The solution to Equation 7, subject to the initial condition, $n_p = n_{po}$ at $t = 0$ is

$$\frac{n_p}{n_{p0}} = \left[1 - \theta_t \left(1 - \frac{n_p}{n_{p0}} \right) \right] E \tag{9}$$

where

$$E = \exp\left[-\left(1 - \theta_t\right) K_{sp} n_s t \right] \tag{10}$$

Solving for n_p/n_{po} leads to

$$\frac{n_p}{n_{p0}} = \frac{\left(1 - \theta_t\right) E}{\left(1 - \theta_t E\right)} \tag{11}$$

Surface Coverage

The fractional surface coverage θ can be obtained from Equations 4, 5, 8 and 11 giving,

$$\theta = \frac{\theta_t \left(1 - E\right)}{\left(1 - \theta_t E\right)} \tag{12}$$

Adsorption Time

A characteristic adsorption time t_{95} i.e., the time for 95% of the polymer to be adsorbed can be calculated by solving for t with n_p/n_{po} equal to 0.05. From Equation 9

$$E = \frac{n_p/n_{p0}}{[1-\theta_t(1-n_p/n_{p0})]} \tag{13}$$

When $t = t_{95}$, $E = E_{95}$ and, from Equation 13,

$$E_{95} = \frac{0.05}{1-0.95\theta_t} \tag{14}$$

Then, from Equation 12,

$$t_{95} = \frac{\ln\left[20(1-0.95\theta_t)\right]}{(1-\theta_t)K_{sp}n_s} \tag{15}$$

It is clear from the above that the adsorption time is determined by the solids concentration, particle size, polymer molecular weight and shear rate due to agitation. For a fixed ratio of polymer to solids concentration (constant θ_t), a simple inverse proportionality to solids content can be seen. The more complex effects of the other variables are illustrated in **Fig. 1** and **2**. Dependence on particle size and polymer molecular weight is shown in **Fig. 1**. The adsorption time is relatively insensitive to molecular weight but increases significantly with increasing particle size. Increased shear reduces adsorption time, especially for large particles, as seen in **Fig. 2** but has relatively minor effects on finer material for which particle/polymer collisions result mostly from Brownian motion.

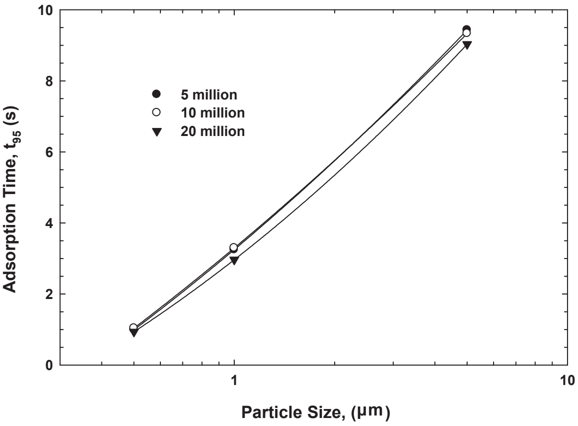

Fig. 1 The effect of particle size on theoretical adsorption times at a slurry concentration of 1% by volume and a mean shear rate of 100 s^{-1}.

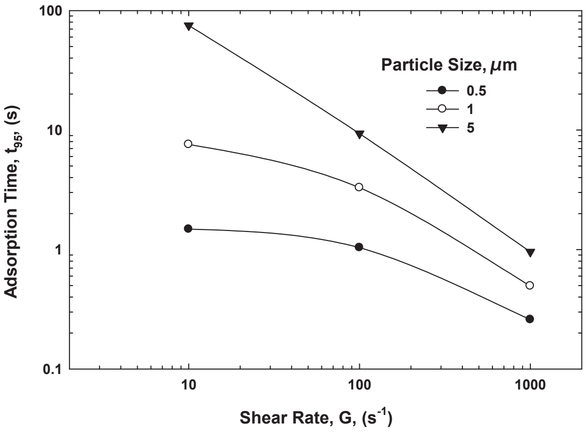

Fig. 2 The effect of shear rate on theoretical adsorption times for a 10 million molecular weight polymer at a slurry concentration of 1% by volume.

The calculations indicate that adsorption times can range from more than 2 hours for 0.01% suspensions of 5μm particles agitated at 10 s^{-1} to as little as 0.02 seconds for 10% suspensions of 0.5μm particles agitated at 1000 s^{-1}. Typical values for practical systems generally fall in the range of a few seconds or less.

Flocculation

Destabilization

The first step in the flocculation process is destabilization of the suspension by eliminating any repulsive interactions that prevent particles from coming into contact and adhering. Typically, such interactions involve electrical double layers at the surfaces of charged particles or steric effects due to solvation or the presence of protective coatings. Double-layer interactions can generally be suppressed by chemical treatments such as pH control or appropriate electrolyte addition. It has been clearly demonstrated[8, 9] that high molecular weight ($>10^6$) bridging polymers are inappropriate for destabilization in such applications – they can provide destabilization but only at excessively high dosage with correspondingly high cost. The real benefit of these flocculants is their effectiveness in promoting floc growth following destabilization, and the production of large, shear-resistant flocs appropriate for dewatering by sedimentation or filtration. The strong inter-particle linkages provided by the bridging polymer probably serve to promote growth by enhancing resistance to floc breakage under shear.

Lower molecular weight ($< 5.10^5$) polyelectrolytes, on the other hand, can be very effective in dispersion destabilization for both charge- and sterically-stabilized systems. In the case of charge stabilization, however, the simple chemical treatments noted above are usually equally effective and less costly. Unlike the high molecular weight polymers, the low molecular weight reagents do not generally promote the development of large strong flocs. Their use for destabilization is commonly followed by the addition

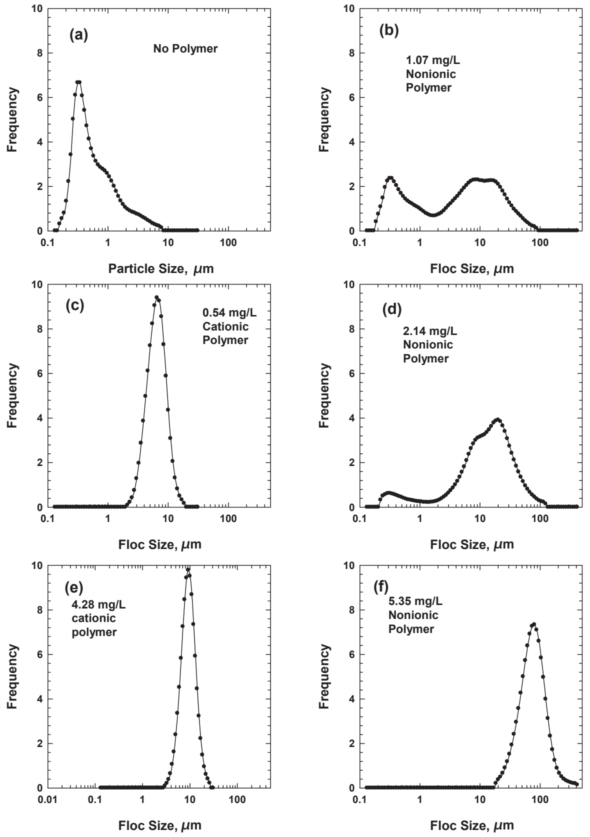

Fig. 3 Floc size distributions resulting from the application to an initially stable alumina suspension (plot a) of a 0.5 million molecular weight cationic polymer (plots c and e) and a 15 million molecular weight nonionic polymer (plots b, d and f). Data of Rattanakawin[10].

of higher polymer flocculants.

An example of the use of polymers for destabilization and floc growth in fine alumina suspensions is given in **Fig. 3**. It is clear from the figure that the low molecular weight (0.5 million) cationic polymer effectively destabilizes the suspension at low dosage (~0.5 mg/L) but provides only limited floc growth. In contrast, the high molecular weight (15 million) nonionic polymer requires much higher dosage (~5mg/L) to eliminate finer (submicron) particles but can promote growth to much larger sizes.

Floc Growth

Flocculation proceeds through the same basic mechanisms as polymer adsorption – particle/particle collisions due to Brownian motion and shear. The collision frequency between particles of size d_i and d_j can be expressed by a relationship analogous to Equation 2, i.e.,

$$K_{ij} = \left[\frac{2k_BT}{3\mu}\left(2+\frac{d_i}{d_j}+\frac{d_j}{d_i}\right)+\frac{\bar{G}}{6}\left(d_i+d_j\right)^3\right] \quad (16)$$

Smoluchowski[6] showed that the reduction due to aggregation in the total number of particles is determined by

$$\frac{dN}{dt} = -\frac{1}{2}\sum_{i=1}^{\infty}\sum_{j=1}^{\infty}K_{ij}n_in_j \quad (17)$$

If all collisions are assumed to lead to aggregation and the size distribution of the growing flocs approaches a "self-preserving" form[11, 12], the rate of decrease in the total number N of particles/flocs can be represented by[6, 13]:

$$\frac{dN}{dt} = -\left[K_BN^2+K_SN\right] \quad (18)$$

where K_B and K_S are effective rate constants for flocculation due to Brownian motion and shear respectively. The constants can be approximated by:

$$K_B = \frac{2k_BT}{3\mu}F_B \quad (19)$$

and

$$K_S = \frac{\bar{G}\phi}{\pi}F_S \quad (20)$$

The factors F_B and F_S are related to the moments of the self-preserving floc size distribution. Their values are estimated to be about 2 and 3 respectively[13].

The solution to Equation 18, subject to the initial condition that $N = N_o$ at $t = 0$, is

$$K_St = \ln\left[\frac{K_BN_0+K_S\left(N_0/N\right)}{K_BN_0+K_S}\right] \quad (21)$$

A characteristic time t_{95}, corresponding to a 95% reduction in the total number of particles, can be estimated by setting N_o/N equal to 20 in Equation 21. Examples of flocculation time estimates are shown

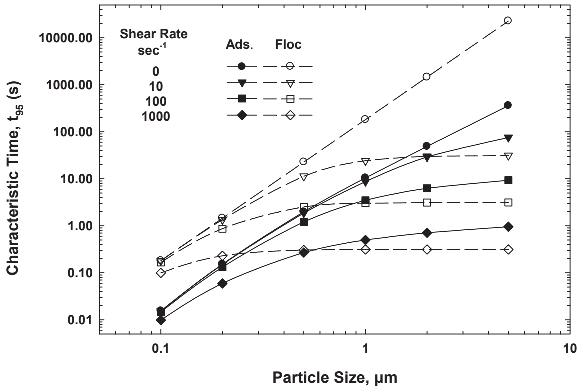

Fig. 4 Characteristic (theoretical) adsorption and flocculation times for suspensions at 1% by volume in the presence of a 10 million molecular weight polymer.

in **Fig. 4**. Adsorption times are included for comparison. It can be seen that predicted adsorption rates are higher than those for flocculation except for coarse particles for which the rates are similar. Adsorption times are more dependent on particle size than are flocculation times. It should be recognized, however, that while adsorption is almost complete at 95%, reduction by 95% of the total number of particles represents only an early stage in the flocculation process – for coalescing particles an average floc containing 20 primary particles would correspond to growth by factor of about 2.7 (i.e., $20^{1/3}$) only.

Batch Flocculation Process

In the above analysis, polymer adsorption and flocculation have been treated as independent processes. In practice, of course, they occur simultaneously and are mutually interdependent – collision efficiencies in flocculation depend on adsorption and adsorption depends on particle size which changes as a result of flocculation. However, the analysis can provide useful insight into the actual process. For example, if adsorption rates are significantly greater than flocculation rates, the polymer will be distributed over the entire surface area of the particles leading to high polymer consumption at relatively low coverage. Lower adsorption rates can actually control the rate of flocculation and reduce polymer consumption by restricting adsorption to the external surface of growing flocs.

Mixing

The analysis described so far also includes the implicit assumption that polymer is instantaneously distributed uniformly over the particle surfaces. This requires that the rate of mixing of the polymer solution with the particle suspension be much higher than the rate of adsorption. Otherwise, extensive local adsorption will occur at the point of initial contact between polymer and particle suspension. The effective irreversibility of polymer adsorption noted above precludes rapid redistribution of the adsorbed polymer resulting in a highly uneven coverage of the particle surfaces.

Experimental studies of the mixing of miscible liquids in agitated vessels can be used to estimate mixing times in flocculation systems. For turbine-agitated baffled tanks, Norwood and Metzner[14] presented a correlation of a mixing factor f_t with the Reynolds number for flow in the tank. The mixing factor can be expressed as[15]

$$f_t = nt_m\left(\frac{D_a}{D_t}\right)^2\left(\frac{D_t}{H}\right)^{1/2}\left(\frac{g}{n^2D_a}\right)^{1/6} \qquad (22)$$

where t_m is the mixing time, n is the agitator rotational speed (rps), D_a is the agitator diameter, D_t and H are the respective tank diameter and liquid depth and g is the acceleration due to gravity. The Norwood and Metzner correlation shows that f_t decreases with increased agitation and becomes approximately constant, at about 5, for Reynolds numbers greater than about 50,000. As a rough approximation for a six-bladed turbine in a baffled tank with $D_t/H = 1$ and $D_a/D_t = 1/3$, at high Reynolds number,

$$t_m \approx 45/n \qquad (33)$$

Theoretical adsorption times as determined from Equation 15 also depend on agitation, in this case through the shear rate G. For agitated tanks, the latter can be estimated from[16]

$$\bar{G} = \left(\frac{P}{\mu V}\right)^{1/2} \qquad (34)$$

where P is the power input, μ is the liquid viscosity and V is the liquid volume. The power input is given by

$$P = N_p\rho n^3D_a^5 \qquad (35)$$

ρ is the liquid density and N_p is the power number for which Reynolds number correlations for different tank configurations are available[17].

A comparison of polymer adsorption times and mixing times is shown in **Fig. 5**. It is clear that, for particles finer than a few micrometers at concentrations of 1% by volume, adsorption occurs much more rapidly than mixing of the polymer with the suspension. It follows that addition of polymer solution un-

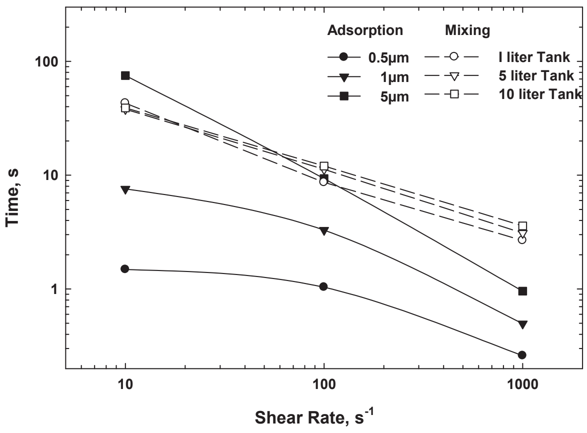

Fig. 5 Calculated adsorption and mixing times for suspensions at 1% solids by volume flocculated with a 10 million molecular weight polymer.

der such conditions, which are typical for chemical and mineral processing applications, inevitably leads to poor flocculation due to non-uniform polymer distribution. Because of the effective irreversibility of the adsorption, continued mixing following polymer addition can effect little if any improvement in the distribution. For the most part, continued mixing serves only to promote floc degradation. Because of the inverse relationship between adsorption time and solids concentration, the mixing problem is critical at high solids content but relatively insignificant for highly dilute systems.

Metered Polymer Addition

It has been observed[8, 18, 19] that the performance of batch flocculation processes can be significantly improved in terms of both floc size and liquid clarification by metered addition, either incremental or continuous, of the polymer to the particle suspension. In this way, rapid local adsorption is limited to each increment of added polymer and an fairly uniform overall dosage can be maintained. It follows that the effective rates of adsorption and subsequent flocculation are limited by the rate of polymer addition. An important consequence is that, with continuous polymer addition to concentrated suspensions in stirred tanks, the rates of adsorption and floc growth are determined by the rate of addition rather than by shear rate as suggested by Equations 2 and 16. The independence of initial growth on agitation speed (shear rate) is illustrated in **Fig. 6** using floc settling rate as a measure of floc size. The slight offset among the curves for different agitation speeds is probably due to variations in the initial floc size in the unstable suspension prior to polymer addition.

A direct correlation of initial growth rate with time normalized with respect to the rate of polymer addition, i.e., the accumulated polymer dosage, for different rates of addition can be seen in **Fig. 7**. At the lower addition rates, floc growth per unit of polymer dosage is independent of the rate, but falls off at the higher rates, as the rate approaches the instantaneous condition. At a rate of 35.2 mg/L.min., floc growth is complete at a dosage of 5 mg/L. which corresponds to a total addition time of about 8.5 seconds – not much longer than the estimated mixing time of about 5 seconds.

In contrast to its effects on floc growth and settling rate, increased rate of polymer addition has a somewhat detrimental effect on supernatant turbidity[8, 22). In all cases, turbidity decreases rapidly with time/polymer dosage eventually leveling off at a limiting value. This limiting turbidity appears to be increased at high rates of addition. The author has shown[23] that polymer adsorption rates in agitated systems favor preferential adsorption on larger particles/flocs partially starving the residual small flocs and primary particles that contribute to turbidity.

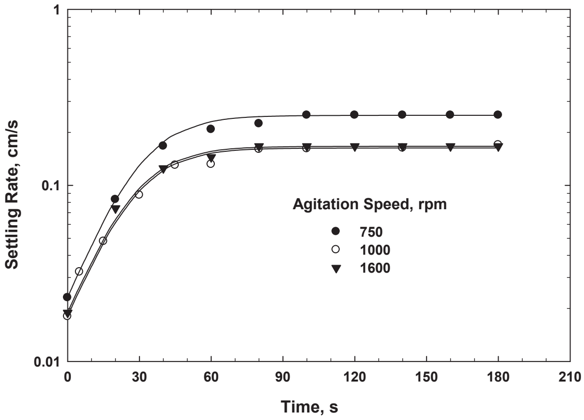

Fig. 6 The effect of agitation speed on floc growth (as represented by settling rate) for kaolin suspensions at 3% solids by weight flocculated by continuous nonionic polymer addition at 2 mg/L.min at pH 5. Data of Bunnaul[20].

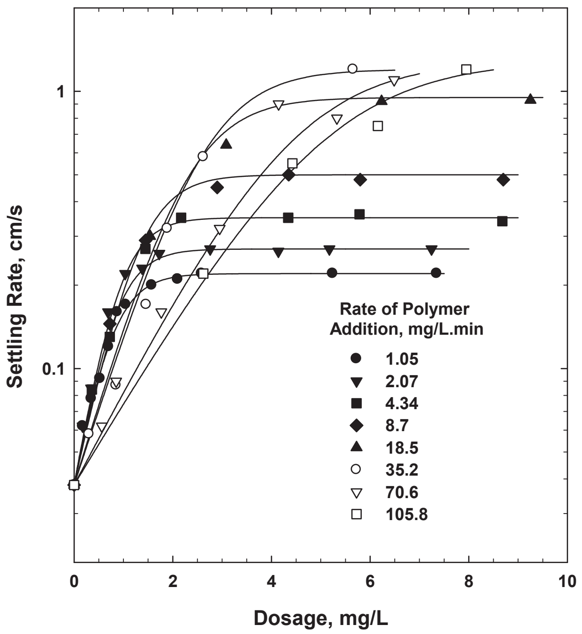

Fig. 7 Effect of the rate of continuous (nonionic) polymer addition on floc growth in 3% by weight kaolin suspensions. Data of Ray[19, 21].

Floc Breakage

Agitation of the suspension during polymer addition provides for mixing of the components and promotes the particle-particle collisions necessary

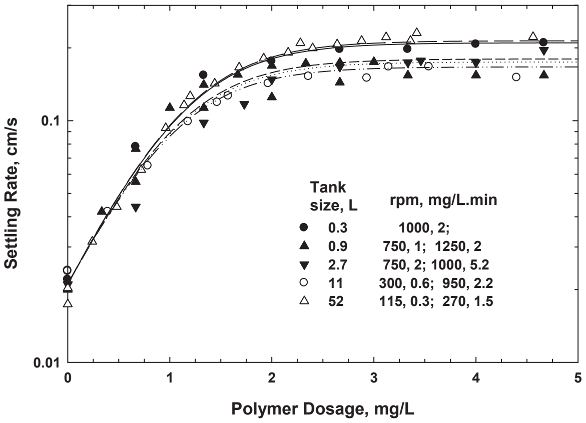

Fig. 8 Scale-up conditions for initial floc growth rate. Effect of tank size and agitation rate on settling rate for the flocculation of kaolin. Data of Maffei[34].

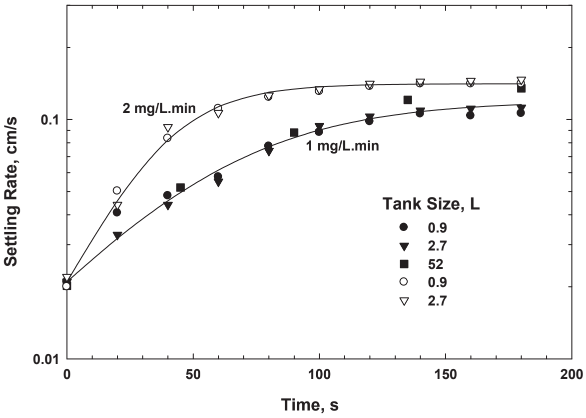

Fig. 9 Scale-up conditions for limiting floc size. Floc development at a fixed agitator tip speed of 270 cm/s and constant rate of polymer addition for different tank sizes. Data of Maffei[34].

for floc formation and growth. At the same time, however, it also causes floc breakage. Numerous investigations have demonstrated that growth rates generally decrease with increasing floc size[24-27], eventually leading to a limiting maximum size. The limitation is attributed to floc breakage. Analyses of the breakage of solid particles[28, 29] and the disruption of emulsion droplets[30] have clearly established that breakage rates increase with increasing size. It has been shown that similar analyses can be applied to floc breakage[31-33].

As flocs grow in an agitated suspension, breakage rates increase until a dynamic balance between growth and breakage is reached – at the limiting size. Enhanced breakage with increased agitation intensity leads to a reduction in the limiting size, as shown in **Fig. 6**, while increased rate of polymer addition increases growth rates with a consequent increase in the limiting size, as shown in **Fig. 7**.

Scale-up

The effects of tank size on batch flocculation have been investigated by Maffei[34]. His results, shown in **Fig. 8**, indicate that the initial floc growth rate, as measured by settling rate, is controlled by the rate of polymer addition per unit volume, essentially independent of tank size and agitation conditions. Variations in the limiting floc size are more complex, depending on agitation conditions as well as rate of polymer addition. Maffei's experiments suggest a correlation with impeller tip speed. Thus, systems operating with the same relative rate of polymer addition and impeller tip speed (providing similar mixing conditions) should show similar behavior. Some examples can be seen in **Fig. 9** and show reasonable agreement over a broad range of tank sizes.

Floc Structure

Aggregation of solid particles by flocculation does not involve coalescence into new solid particles. Rather, these processes yield porous entities (flocs) in which the original primary particles retain their identity. Numerous investigations, including both computer simulations[35-38] and experimental measurements[39-43] have shown that floc density decreases (porosity increases) as growth proceeds. Computer simulations have suggested that such aggregates have a fractal dimensionality D of about 1.75[42], indicating that the floc size d_s should vary with the number of included primary particles N according to:

$$d_s \propto N^{1/D} \tag{36}$$

The floc porosity would then vary according to:

$$1-\varepsilon \propto d_s^{D-3} \tag{37}$$

i.e.,

$$1-\varepsilon \propto d_s^{-1.25} \tag{38}$$

The results of experimental measurements generally agree with these relationships indicating fractal dimensions typically in the range of 1.7 to 2.1. There is some evidence that, for flocs produced using polymers under shear, densification of the finest "microflocs" can occur, leading to a shift in the size/density relationships to coarser sizes[41, 43]. The densification effect appears to be largely confined to primary particles in the 1 to 10 μm size range. Other variables, such as polymer type and solids concentration seem to have minimal effects on floc structure.

Continuous Flocculation Processes

While laboratory testing and some industrial operations are carried out in the batch mode, the majority of industrial applications, such as process water treatment, are performed on a continuous basis. Polymer may be added to a continuous stirred tank or directly into a pipe or launder prior to introduction into a separation system such as a thickener.

Stirred Tanks

Suharyono[22, 44] has investigated continuous flocculation in a stirred tank. His results indicate that while general trends in behavior are similar, performance seems to be significantly inferior to that observed in batch tests. Comparisons of batch and continuous test data are shown in **Fig. 10**. At similar polymer dosage and mixing/residence times, the batch process, with continuous polymer addition, gives much higher settling rates (about double) and much lower supernatant turbidities (less than one third) than those of the continuous system. The higher settling rates obtained in the batch process are attributed to the progressive polymer addition to a system of similar growing flocs, a condition not found in the steady-state continuous process where polymer dosage remains constant with time and the tank always contains a mixture of flocs at various stages of growth including fresh feed slurry. A possible enhancement of the process may be to use two or more tanks in series with polymer addition divided between them. This approach should provide an approximation to the continuous addition seen to be appropriate in the batch process.

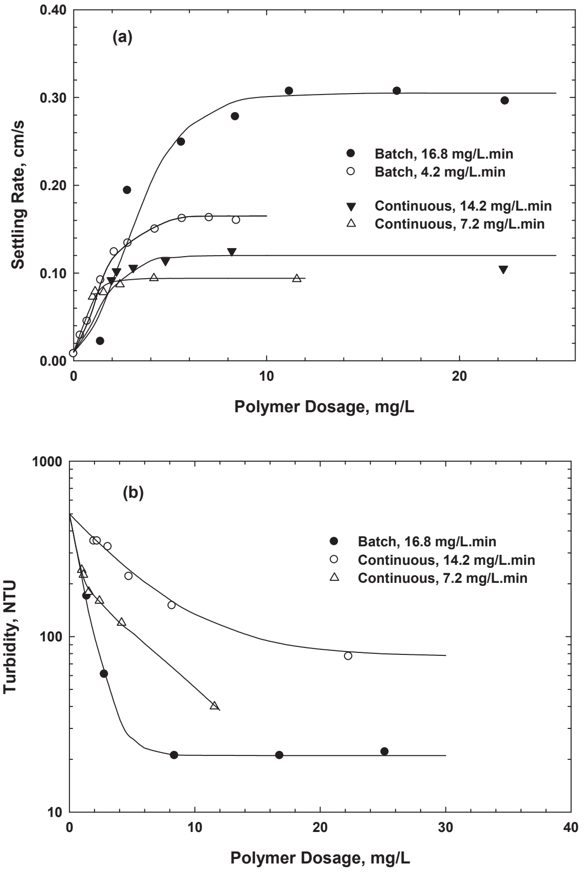

Fig. 10 Comparison of flocculation behavior in batch (with continuous polymer addition) and continuous systems: (a) settling rate, (b) supernatant turbidity. Data of Suharyono[22].

The increased turbidity at higher rates of polymer addition observed in batch processes is again evident in the continuous system. The factors responsible for reduced setting rates may contribute to further increase in turbidity for continuous processing. Mixing conditions could also play a role here. Under the agitation conditions used in the tests, the tank was shown to be essentially fully-mixed. This means that, particularly at high flow rates (short residence times), some fraction of the feed slurry could appear in the output stream without being subject to significant flocculation.

It seems reasonable to expect that the scale-up criteria suggested for the batch process – the same rate of polymer addition and impeller tip speed – should also apply to continuous flocculation.

Pipes and In-line Mixers

Flocculation by polymer injection into a pipe is quite common in industrial practice and potentially offers several advantages over addition to a stirred tank. Highly turbulent flow, which can be enhanced through the use of baffles or in-line mixer elements, provides very rapid mixing of feed slurry and polymer solution in the pipe. Fang and Lee[45] have indicated micromixing times of the order of nanoseconds in Kenics mixers at Reynolds numbers greater than about 1000. Sufficiently high turbulence to ensure high polymer-particle and particle-particle collision frequencies can readily be achieved while its role in floc degradation may be less severe than that of the impeller in a stirred tank.

Experimental studies of flocculation in turbulent pipe flow[46-48] have shown that rapid floc growth to a maximum size took place over a short time (less than 10 seconds, (corresponding to 50 – 100 pipe diameters, for the system investigated) and was followed by a continuous decrease in size with continued flow. The initial growth rate and the subsequent reduction in size were found to increase while the maximum floc size decreased with increasing Reynolds number. It was concluded that increased shear promoted initial growth through improved mixing and increased particle-polymer and particle-particle collision frequencies but also enhanced floc breakage rates as the free polymer in solution was depleted. Tests with two different pipe diameters gave similar behavior at similar shear rates suggesting a route to scale-up.

Experiments on pipes containing in-line, Kenics mixer elements gave generally similar results[44, 49], although the use of settling rates of the slurry after discharge from the pipe to assess performance rather than direct on-line size measurement precluded detection of the initial growth period in most cases. Again, relatively high short-time settling rates were found to decline with increased mixing time in the pipe. In this case, the maximum settling rate seemed to occur at less than 10 pipe diameters downstream from the injection point. Increased shear at high flow rates was again shown to reduce short-time settling rates.

These, somewhat limited, studies indicate that flocculation by direct polymer injection into a conduit is indeed a viable alternative to addition to a stirred tank. Important process design criteria appear to be that shear should be sufficient to ensure adequate mixing but limited to avoid excessive floc breakage. Additional mixing following polymer injection should be minimized. In general, the results of these investigations are consistent with those of batch tests with continuous or incremental addition to a stirred tank. In particular, tests where multistage polymer injection was used, i.e., incremental addition, showed enhanced performance both with[22, 49] and without[48] mixer elements.

Conclusions

In any flocculation process, it is important to distinguish between destabilization of the suspension, i.e., by suppressing or eliminating barriers to particle-particle contact, and the formation and growth of flocs. Destabilization can be accomplished by polymer bridging, but the process is rather inefficient due to the high polymer concentrations needed to link individual particles. Destabilization, e.g., by pH control, prior to the addition of high molecular weight polymers allows for the production of small aggregates, substantially reducing the number of linkages needed for significant floc growth by bridging.

The basic mechanism involved in the flocculation of fine-particle suspensions by molecular bridging with polymers is the simultaneous attachment of individual polymer molecules to more than one particle. Polymer adsorption rates are generally high – theoretically, in agitated suspensions at solids concentrations greater than about 0.1% by volume, 95% of the polymer can be expected to be adsorbed in a few seconds or less. Furthermore, multiple points of attachment to surfaces render polymer adsorption effectively irreversible. Consequently, mixing of the polymer with the suspension is a critical factor. In order to attain uniform polymer distribution among the particles and to avoid excessive local adsorption at the point of polymer addition, mixing times should be significantly less than adsorption times. Unfortunately, the reverse is typically the case in practice.

For the efficient promotion of floc growth by polymer bridging, it is desirable that growth rates be higher than adsorption rates. In this way, adsorption is mostly limited to the decreasing surface area of the growing flocs. Again, however, adsorption is typically faster than floc growth in practice. In batch processes, metered polymer addition, either incremental or continuous, offers a solution to the mixing problem while also encouraging floc growth. Controlling the rate of addition provides opportunities for optimizing floc growth and supernatant clarification.

Agitation promotes mixing and polymer adsorption and the particle-particle collisions necessary for floc formation and growth. It also causes floc breakage. Breakage rates increase with floc size so that, in batch systems with continuous polymer addition, growth reaches a limiting plateau when growth and breakage rate become equal. Continued agitation in the absence of further polymer addition leads to progressive degradation of the flocs. Increased rate of polymer addition tends to increase the limiting floc size due to increased growth rate while increased agitation intensity reduces the limiting size by increasing the breakage rate.

While laboratory testing and a few industrial processes are carried out in the batch mode, most applications employ continuous operation. These procedures typically involve polymer addition in a stirred tank or direct injection into a flow stream. Comparison of batch and continuous flocculation in a stirred tank reveal similar trends in performance but inferior results – lower settling rates and supernatant clarity – for the continuous systems. The differences are attributed to inability to circumvent mixing problems or to provide progressive polymer addition to growing flocs. A promising modification is the use of incremental polymer addition to two or more tanks in series.

Studies of flocculation in pipes with and without in-line mixer elements indicate that rapid floc growth occurs following polymer injection. It appears that there may be an optimum flow rate that provides the fully turbulent conditions, probably necessary to ensure adequate mixing, while keeping shear rate low enough to minimize floc breakage. Available experimental data indicate that floc size reaches a maximum after flow over around 100 pipe diameters beyond the injection point which may be reduced to as few as 10 diameters in the presence of static mixer elements. Continued flow leads to progressive floc degradation. Incremental polymer injection along the pipe has been shown to enhance floc growth for a given overall polymer dosage.

Nomenclature

d_k	agglomerate size in class k	[L]
d_p	polymer molecular size	[L]
d_s	solid particle size	[L]
D	fractal dimension	[–]
D_a	agitator diameter	[L]
D_t	tank diameter	[L]
E	exponential factor defined by Equation 10	[–]
E_{95}	E value corresponding to t_{95}	[–]
f_{sp}	particle/polymer molecule collision frequency	[$L^{-3}T^{-1}$]
F_B	distribution factor for Brownian flocculation	[–]
F_S	distribution factor for shear flocculation	[–]
g	acceleration due to gravity	[LT^{-2}]
$\bar{G}$	mean shear rate	[T^{-1}]
H	liquid depth in tank	[L]
k_B	Boltzmann's constant	[$ML^2T^{-2}K^{-1}$]
K_B	rate constant for Brownian flocculation	[$L^{-3}T^{-3}$]
K_S	rate constant for shear flocculation	[T^{-1}]
K_{sp}	rate constant for particle/polymer molecule collisions	[L^3T^{-1}]
K_{ij}	rate constant for i and j particle collisions	[L^3T^{-1}]
n	agitator rotational speed	[T^{-1}]
n_k	number concentration of k-size particles	[L^{-3}]
n_s	number concentration of solid particles	[L^{-3}]
n_p	number concentration of polymer molecules	[L^{-3}]
n_{po}	initial number concentration of polymer molecules	[L^{-3}]
N	overall number concentration of particles/flocs	[L^{-3}]
N_o	initial overall number concentration of particles	[L^{-3}]
N_p	power number for stirred tanks	[–]
P	power input to stirred tank	[ML^2T^{-3}]
t	time	[T]
t_{95}	time for 95% completion	[T]
t_m	mixing time	[T]
V	volume	[L^3]
ε	floc porosity	[–]
θ	fractional surface coverage	[–]
θ_t	fractional surface coverage for complete adsorption	[–]
μ	liquid viscosity	[$ML^{-1}T^{-1}$]
ρ	liquid density	[ML^{-3}]
ϕ	solids concentration by volume	[–]

References

1) Gregory, J. (1973): Rates of Flocculation of Latex Particles by Cationic Polymers, J. Coll. Interface. Sci., Vol.42, pp.448-456.

2) Smellie, R. H. and La Mer, V. K. (1958): Flocculation, Subsidence and Filtration of Phosphate Slimes, VI, Quantitative Theory of Filtration of Flocculated Suspensions, J. Colloid Sci., Vol.23, pp.589-599.

3) Healy, T. W. and La Mer, V. K. (1962): The adsorption-flocculation reactions of a polymer with an aqueous colloidal dispersion, J. Phys. Chem., Vol.66, pp.1835-1839.

4) Lyklema, J. (1985): "The Colloidal Background of Agglomeration", in Agglomeration '85, Proceedings, 4th International Symposium on Agglomeration, C. E. Capes, Editor, ISS/CSM. Toronto, pp.23-36.

5) Cohen Stuart, M. A. and Fleer, G. J. (1996): Adsorbed Polymer Layers in Non-Equilibrium Situations, Annu. Rev. Mater. Sci., Vol.26, pp.463-500.

6) Smoluchowski, M., (1916): Drei Vortäge über Diffusion, Brownische Molekularbewegung und Koagulation von Kolloidteilchen, Physik. Z., Vol.17, pp.557-571.

7) Overbeek, J. Th. G. (1952): "Kinetics of Flocculation, in Colloid Science I", H. R. Kruyt, Editor, Elsevier, Amsterdam, pp.278-301.

8) Hogg, R., Bunnaul, P. and Suharyono, H. (1993): Chemical and Physical Variables in Polymer-Induced Flocculation, Miner. Metall. Proc., Vol.10, pp.81-85.

9) Rattanakawin, C. and Hogg, R. (2001): Aggregate Size Distributions in Flocculation, Colloids & Surfaces, 177, pp.87-98.

10) Rattanakawin, C. (1998): "Aggregate Size Distributions in Flocculation", MS Thesis, The Pennsylvania State University.

11) Swift, D. L. and Friedlander, S. K. (1964): The Coagulation of Hydrosols by Brownian Motion and Laminar Shear Flow, J. Colloid Sci., Vol.1, pp.621-647.
12) Hidy, G. M. (1965): On the Theory of Coagulation of Noninteracting Particles in Brownian Motion, J. Colloid Sci., Vol.2, pp.123-144.
13) Hogg, R., Klimpel, R. C. and Ray, D. T. (1985): "Growth and Structure of Agglomerates in Flocculation Process", in Agglomeration '85, Proceedings, 4th International Symposium on Agglomeration, C.E.Capes, Editor, ISS/CSM. Toront, pp.581-588.
14) Norwood, K. W. and Wetzner, A. B. (1960): Flow Patterns and Mixing Rates in Agitated Vessels, AIChE Journal, , pp.432-437.
15) McCabe, W. L., Smith, J. C. and Harriott, P. (2005): "Chapter 9 in Unit Operations of Chemical Engineering", 7th Ed, pp.267.
16) Camp, T. R. and Stein, P. C. (1943): Velocity Gradients and Internal Work in Fluid Motion, J. Boston Soc. Civ. Engrs., Vol.3, pp.219-237.
17) Holland, F. A. and Chapman, F. S. (1966): "Liquid Mixing and Processing in Stirred Tanks", Reinhold, New York.
18) Keys, R. O. and Hogg, R. (1979): Mixing Problems in Polymer Flocculation, AIChE Symposium Series, Vol.75, pp.63-72.
19) Hogg, R., Klimpel, R. C. and Ray, D. T. (1987): Agglomerate Structure in Flocculated Suspensions and its Effects on Sedimentation and Dewatering, Miner. Metall. Proc., pp.108-113.
20) Bunnaul, P. (1993): "Clarification, Sedimentation and Consolidation of Flocculated Suspensions", PhD Thesis, The Pennsylvania State University.
21) Ray, D. T. (1988): "The Role of Polymers in Flocculation Processes and in the Binding of Compacted Powders", PhD Thesis, The Pennsylvania State University.
22) Suharyono, H. (1996): "Flocculation and Consolidation in Thickening Processes", PhD Thesis, The Pennsylvania State University.
23) Hogg, R. (1999): The Role of Polymer Adsorption Kinetics in Flocculation, Colloids and Surfaces, A: Physico-Chemical and Engineering Aspects, Vol.146, pp.253-263.
24) Parker, D. S., Kaufman, J. and Jenkins, D. (1972): Floc Break-up in Turbulent Flocculation Processes, J. Sanit. Eng. Div. Am. Soc. Civ. Eng., Vol.98, pp.79-99.
25) Smith, D. K. W. and Kitchener,J. A. (1978): The Strength of Aggregates Formed in Flocculation, Chem. Eng. Sci., Vol.33, pp.1631-1636.
26) Tomi, D. T. and Bagster, D. F. (1978): The Behaviour of Aggregates in Stirred Vessels, Part I – Theoretical Considerations on the Effects of Agitation, Trans. IChemE, Vol.56, pp.1-8.
27) Tomi, D. T. and Bagster, D. F. (1978): The Behaviour of Aggregates in Stirred Vessels, Part II – An Experimental Study of the Flocculation of Galena in a Stirred Tank, Trans. IChemE, Vol.56, pp.9-18.
28) Gardner, R. P. and Austin, L. G. (1962): "A Chemical Engineering Treatment of Batch Grinding", in Proceedings, 1st European Symposium on Size Reduction, H. Rumf and D. Behrens, Editors, Verlag Chemie, Weinheim, pp.217-247.
29) Herbst, J. A. and Fuerstenau, D. W. (1968): The Zero-Order Production of Fine Sizes in Comminution and its Implications in Simulation, Trans. AIME, Vol.252, pp.538-548.
30) Narsimhan, G., Ramkrishna, D. and Gupta, J. P. (1980): Analysis of Drop Size Distributions in Lean Liquid-Liquid Dispersions, AIChE Journal, Vol.26, pp.991-1000.
31) Pandya, J. D. and Spielman, L. A. (1982): Floc Breakage in Agitated Suspensions: Theory and Data Processing Strategy, J. Coll. Interface. Sci., Vol.90, pp.517-531.
32) Glasgow, L. A., Kim, Y. H. and Hsu, J-P, (1985): "Characterization of Turbulence-Induced Aggregate Breakage, in Flocculation, Sedimentation and Consolidation", Proceedings, Engineering Foundation Conference, B. M. Moudgil and P. Somasundaran, Editors, Engineering Foundation New York, pp.191-204.
33) Ray, D. T. and Hogg, R. (1987): Agglomerate Breakage in Polymer-Flocculated Suspensions, J. Coll. Interface. Sci., Vol.116, pp.256-268.
34) Maffei, A. C. (1989): "Scale-Up of Flocculation Processes", MS Thesis, The Pennssylvania State University.
35) Vold, M. J. (1963): Computer Simulation of Floc Formation in a Colloidal Suspension, J. Collod Sci., Vol.18, pp.684-695.
36) Sutherland, D. N. (1967): A Theoretical Model of Floc Structure, J. Coll. Interfac. Sci., Vol.25, pp.373-380.
37) Sutherland, D. N. and Goodarz-Nia, I. (1971): Chem. Eng. Sci., Vol.26, pp.2071-2085.
38) Meakin, P. (1984): Diffusion-Limited Aggregation in Three Dimensions: Results from a New Cluster-Cluster Aggregation Model, J. Coll. Interface. Sci., Vol.102, pp.491-512.
39) Medalia, A. I. (1967): Morphology of Aggregates, J. Coll. Interface. Sci., Vol.24, pp.393-404.
40) Klimpel, R. C., Dirican, C. and Hogg, R. (1986): Measurement of Agglomerate Density in Flocculated Fine Particle Suspensions, Particulate Science and Technology, Vol.4, pp.45-59.
41) Klimpel, R. C. and Hogg, R. (1986): Effects of Flocculation Conditions on Agglomerate Structure, J. Coll. Interface Sci., Vol.113, pp.121-131.
42) Weitz, D. A. and Huang, J. S. (1984): "Self-Similar Structures and the Kinetics of Aggregation of Gold Colloids", in Kinetics of Aggregation and Gelation, F. Family and D. P. Landau, Editors, North Holland, Amsterdam, pp.19-28.
43) Klimpel, R. C. and Hogg, R. (1991): Evaluation of Floc Structures, Colloids and Surfaces, Vol.55, pp.279-288.
44) Suharyono, H. and Hogg, R. (1994): Continuous Flocculation Processes, SME Preprint No. 94-231, Sosiety for Mining, Metallurgy and Exploration Inc., Littleton,

CO.
45) Fang, J. Z. and Lee, D. J. (2001): Micromixing Efficiency in Static Mixer, Chem. Eng. Sci., Vol.56, pp.3797-3802.
46) Heath, A. R., Bahri, P. A., Fawell, P. D. and Farrow, J. B. (2006): Polymer Flocculation of Calcite: Experimental Results from Turbulent Pipe Flow, AIChE Journal, Vol.52, pp.1284-1293.
47) Heath, A. R., Bahri, P. A., Fawell, P. D. and Farrow, J. B. (2006): Polymer Flocculation of Calcite: Population Balance Model, AIChE Journal, Vol.52, pp.1641-1653.
48) Owen, A. T., Fawell, P. D., Swift, J. D., Labbett, D. M., Benn, F.A. and Farrow, J.B. (2008): Using Turbulent Pipe Flow to Study the Factors Affecting Polymer Bridging-Flocculation of Mineral Systems, Int. J. Miner. Process, Vol.87, pp.90-99.
49) Suharyono, H. and Hogg, R. (1996): Flocculation in Flow through Pipes and In-Line Mixers, Miner. Metall. Proc., Vol.13, pp.501-505.

Author's short biography

Richard Hogg

Richard Hogg is Professor Emeritus of Mineral Processing and GeoEnvironmental Engineering at the Pennsylvania State University. He received a B.Sc. from the University of Leeds and the M.S. and PhD degrees from the University of California at Berkeley. Dr Hogg's research interests include fine particle processing, particle characterization, and colloid and surface chemistry.

A $PM_{1.0/2.5/10}$ Trichotomous Virtual Impactor Based Sampler: Design and Applied to Arid Southwest Aerosols
Part I: Design[†]

Virgil Marple[1]*, **Dale Lundgren**[2] **and Bernard Olson**[1]
[1] *Particle Calibration Laboratory, University of Minnesota*
[2] *University of Florida*

Abstract

A $PM_{1.0/2.5/10}$ Trichotomous sampler has been developed to determine if the particles in the saddle point between the coarse and fine particle modes (specifically the 1.0 μm to 2.5 μm size range) are primarily coarse or fine mode particles. The sampler consists of a standard high volume sampler with two high volume virtual impactors (one with a cut size of 2.5 μm and the other with a cut size of 1.0 μm) inserted between the PM_{10} inlet and the 8x10 inch (20x25 cm) after filter. By using nine 47 mm filters, at various locations within the trichotomous sampler, a technique has been developed for subtracting out the effects of particles smaller than the cutsize of a virtual impactor from the minor flow particle collection.

Keywords: atmospheric aerosols, virtual impactors, PM_{10}, $PM_{2.5}$, PM_1

Introduction

Many types of studies require measuring the aerodynamic diameter size distribution of air-borne (aerosol) particles, where the aerodynamic diameter of a particle is the diameter of a unit density sphere that has the same falling speed as the particle in question. One type of inertial classifier is the most common method for aerodynamic particle size classification, that being the air jet impacting on a solid plate inertial impactor(Marple, 1970). Since impactors were first developed in 1860, many single stage and cascade impactors have been designed, built, tested, and sometimes made commercially available (Marple, 2004)

One shortcoming of the inertial impactor is that particles can bounce off of the impaction plate (particle bounce), or can be blown off the plate after collection (particle blow-off). This will result in particles that are intended to be collected on a certain stage being collected on subsequent stages of the cascade impactor, giving an erroneous size distribution measurement.

A variation of the inertial impactor, which solves the particle bounce problem, is the virtual impactor (**Fig. 1a**), which replaces the impaction plate with an open ended tube, called a collection probe, a diameter of which is about 35% larger than the nozzle diameter (Xu, 1991) The entrance to the collection probe creates a condition that can be thought of as a virtual impaction surface (thus the name) through which particles pass into a void. Large particles penetrate far into the collection probe and are carried out the opposite end with a small percentage of the total flow, known as the minor flow. Smaller particles that do not penetrate as far into the probe, reverse direction and leave at the outer circumference of the probe with the remaining flow, known as the major flow. Performance of the virtual impactor stage is characterized by a collection efficiency curve, as shown in **Fig. 1b**. The size of particles that are collected with 50% efficiency is called the cutsize of the virtual impactor stage. Efficiency, defined as the percentage of particles passing through the virtual impactor nozzle and collected in the minor flow (Marple and Chein,

---

[†] Accepted: April 15, 2012
[1] 111 Church Street S. E Minnneapolis, MN 55455, USA
* Corresponding author:
E-mail: marple@me.umn.edu
TEL: +1-612-625-3441 FAX: +1-612-625-6069

ⓒ 2013 Hosokawa Powder Technology Foundation

1980), can have collection characteristics that are similar to inertial impactors.

Although the virtual impactor configuration solves the particle bounce problem of the inertial impactor, it does create another problem unique to virtual impactors. The problem is that the minor flow contains particles smaller than the cutsize in a concentration equal to that in the major flow. These small particles in the minor flow will be referred to as "background" particles in this paper and constitute a contamination of the large particle fraction with small background particles, and is the reason that the efficiency curve does not go to zero at small particles sizes in **Fig. 1b**.

A number of researchers have developed designs to eliminate these background particles by providing a clean particle free core of air in the central portion of the flow passing through the nozzle (Masuda et al., 1978; Chen et al.1986). This clean core of air will then be the air that passes through the collection probe, thus eliminating small background particles in the minor flow. This clean core of air does complicate the flow system of an otherwise simple classifier and is nearly impossible to incorporate into virtual impactors that have more than one nozzle/collection probe set in one stage, or in cascade designs.

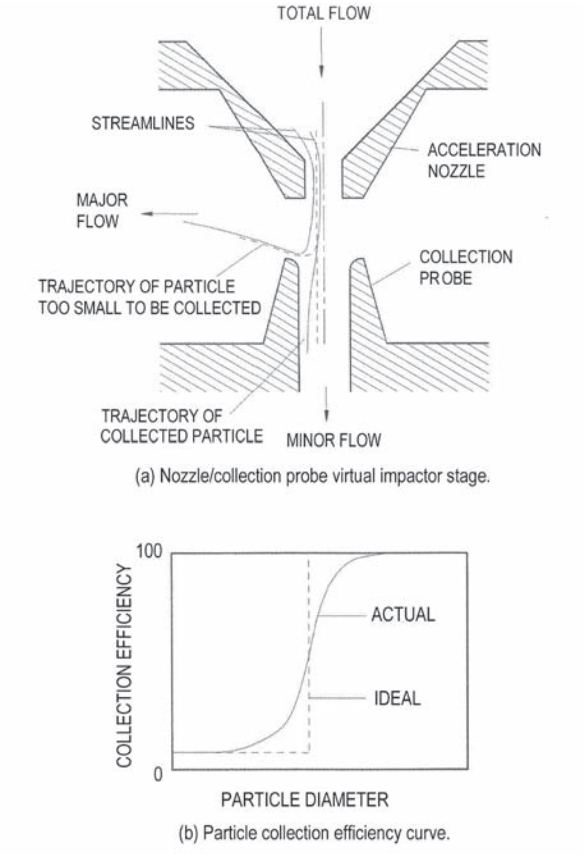

Fig. 1 Virtual Impactor Stage and Particle Collection Efficiency curve.
a) Nozzle/collection probe virtual impactor stage
b) Particle collection efficiency curve

In this paper we describe another solution to the background particle problem. The solution is to collect particles smaller than the virtual impactor cutsize on a filter that is identical in size, material, and flow rate to the filter collecting the particles larger than the cutsize (minor flow collection). Identical analysis of both filters will allow for the effects of the background particles to be subtracted from the particles larger than the cutsize. This technique is the one chosen in the design of the $PM_{1.0/2.5/10}$ Trichotomous sampler described in Part I of this paper. Part II, to be published in the 2013 issue of KONA, will describe the use of the $PM_{1.0/2.5/10}$ Trichotomous sampler in a study of atmospheric aerosol particles in the southwestern US, specifically in Phoenix, Arizona.

Design Criteria for the $PM_{1.0/2.5/10}$ Trichotomous Sampler

When the fine particle standard was established in the US in1997, there was much discussion among experts as to whether the standard should be set at 1.0 μm or 2.5 μm. The problem arose from the nature of the particle size distributions in atmospheric aerosols. Whitby (1978) discovered that atmospheric particle size distributions were trimodal in nature, with fresh combustion particles in the smallest mode, aged combustion particles in the intermediate mode (fine particle mode) and mechanically generated particles in the largest mode (coarse particle mode). An excellent discussion of this topic is presented by John (2011).

It was generally agreed that the particle size separating the fine and coarse particle modes was in the

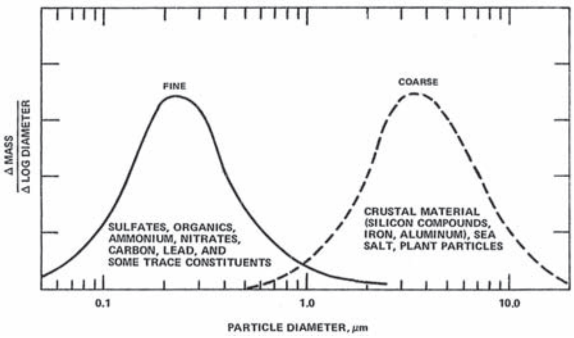

Fig. 2 Fine and Coarse Particle Modes. From U.S. Environmental Protection Agency (1982).

1 μm to 2.5 μm range. Particles in this size range consist of particles from the lower tail of the coarse particle mode and particles from the upper tail of the fine particle mode (see **Fig. 2**). The discussion centered on the question of whether the particles in the range of 1 μm to 2.5 μm were mostly fine or mostly coarse mode particles.

The $PM_{1.0/2.5/10}$ Trichotomous sampler was designed to answer this question by using two virtual impactors in series (cascade) with cut sizes of 2.5μm and 1.0 μm. It was decided to use the standard 40 cfm (1.13 m^3/min) 10 μm classifying inlet of the PM10 sampler as the sampler's first stage to avoid the need to develop a new sampling inlet.

$PM_{1.0/2.5/10}$ Trichotomous Sampler

Major Components

The superstructure of the trichotomous sampler is the standard high volume 40 cfm (1.13 m^3/min) flowrate PM10 sampler, which consists of a PM10 size selective inlet (McFarland et.al., 1984) and an 8 × 10 inch (20 × 25 cm) filter, but the heart of the $PM_{1.0/2.5/10}$ Trichotomous sampler is two high volume virtual impactors (HVVIs) (Marple and Olson, 1995) with cut sizes of 2.5 μm and 1.0 μm. The HVVIs, being of small size (8.25 in. × 6.75 in. × 2.75 in. high) (21cm × 17cm × 7cm) and yet having a flow rate of 40 cfm, were designed specifically to further size classify particles in the high volume PM_{10} sampler (Marple et.al., 1990). Two HVVIs are inserted in series between the PM10 inlet and the 8 × 10 filter. The 2.5 μm HVVI is located inside the lower cavity of the PM10 size selective inlet, with an additional chamber inserted between the inlet and the 8 × 10 filter to house the 1 μm HVVI, which is mounted directly above the 8 × 10 inch filter.

Figs. 3, 4 and **5** show schematics of the sampler and the two HVVIs and **Fig. 6** shows photos of the major components. The colored filter holders in these figures will be explained in the following section.

A schematic of the overall sampler is presented in **Fig. 3**. The flow path through the sampler is through: 1) the 10 um size selective inlet, 2) the 2.5 μm HVVI, 3) the 1.0 μm HVVI and then 4) the 8 × 10 inch after filter. Air is pulled through the sampler using two blowers in series rather than just one blower as in the standard high volume sampler. The blower system consists of a standard high volume blower with an auxiliary blower mounted at its exhaust. This modification to the standard high volume sampler is necessary due to the additional pressure drop of the HVVIs. Flow control is achieved with a mass flow controller supplied with the high volume sampler. This flow controller controls the speed of the second

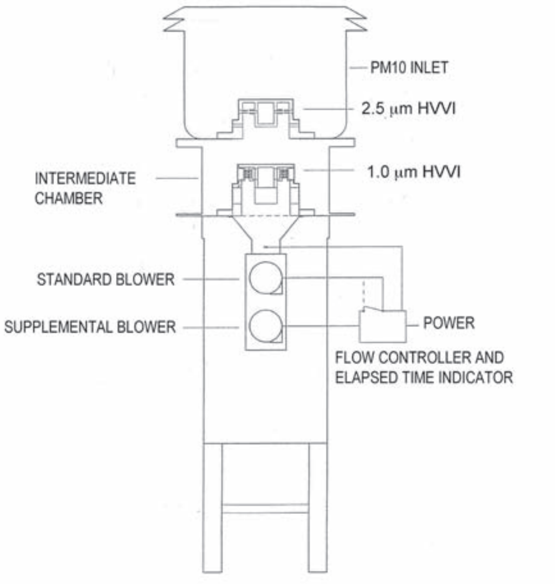

Fig. 3 Schematic of $PM_{1.0/2.5/10}$ Trichotomous Sampler.

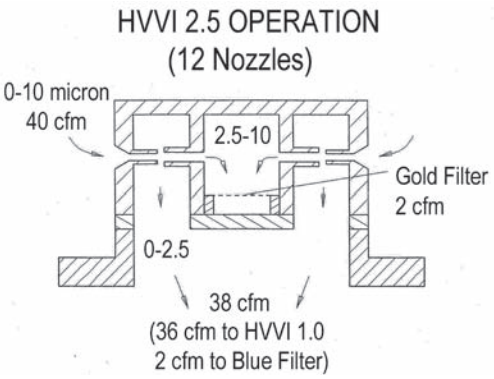

Fig. 4 Schematic of 2.5 μm HVVI.

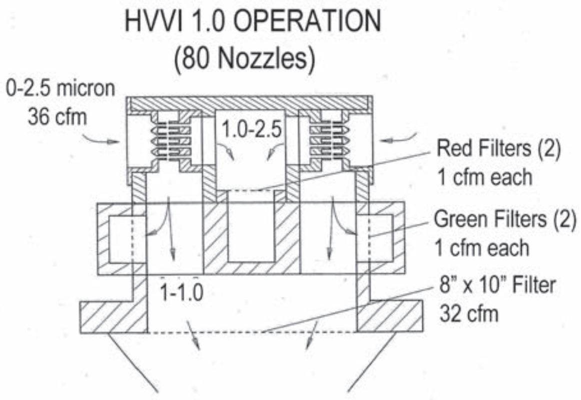

Fig. 5 Schematic of 1.0 μm HVVI.

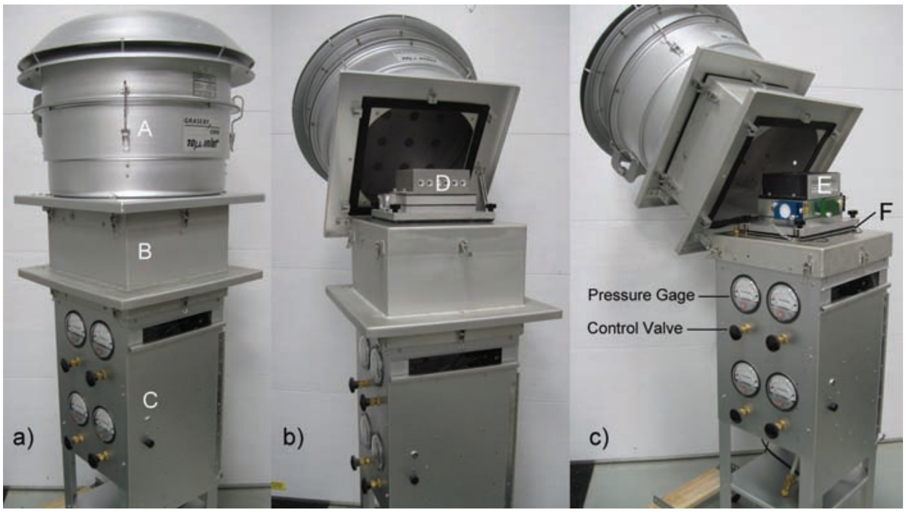

Fig. 6 Photos of $PM_{1.0/2.5/10}$ Trichotomous Sampler.
a) Assembled sampler; b) 2.5 μm HVVI; c) 1.0 μm HVVI
A-PM10 inlet; B-Intermediate chamber; C-Base; D-2.5 μm HVVI; E-1.0 μm HVVI; F-Afterfilter.

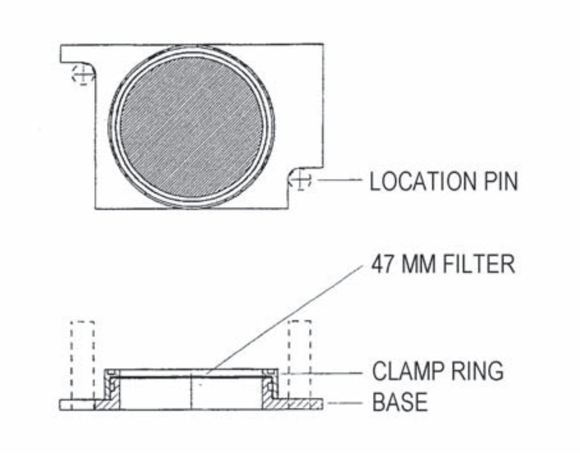

Fig. 7 47 mm filter holder.

blower only, thus, controlling the back pressure of the first blower, which operates at full speed.

Flow paths through the two HVVIs are similar and shown schematically in **Figs. 4** and **5**. Flow enters the HVVIs through nozzles (12 and 80 nozzles for the 2.5μm and 1.0μm HVVIs, respectively) on either side of the HVVI housings. Particles larger than the cutsize are collected with the minor flow in the center chamber, along with 5% of the particles smaller than the cutsize (the minor flow is 5% of the total flow for both HVVIs). Particles smaller than the cut size remain with the major flow and exit through the bottom of the HVVI housings.

Fig. 6 shows photos of major components of the sampler. **Fig. 6a** shows the assembled sampler with the PM10 high volume inlet, the intermediate chamber and the high volume sampler stand. Sets of pressure gages and control valves, located on both sides of the stand, are for controlling the flow through the various filters in the sampler. **Fig. 6b** shows the 2.5 μm HVVI located inside the PM_{10} inlet and on top of the intermediate chamber. **Fig. 6c** shows the 1.0 μm HVVI inside the intermediate section and on top of the standard 8 × 10 inch high volume filter. Both 2.5 μm and 1.0 μm HVVIs have bases specifically designed for the trichotomous sampler to accommodate the various 47 mm filters.

Filter Sample Locations

Nine 47 mm diameter filters are in various locations in the trichotomous sampler to collect particle samples of PM_{10}, $PM_{2.5}$, PM_1, $PM_{2.5\text{-}10}$ and $PM_{1\text{-}2.5}$. The filters are inserted into filter holders and the holders are clamped into manifolds within the trichotomous sampler. These filter holders are also used to transport the filters to and from the field test site. To ensure that the filter holders are inserted into the correct location in the sampler, filter holders, and manifolds, are color coded. In addition, the filter holders, shown in **Fig. 7**, are of special design so that they can only be inserted into the manifolds in one direction, insuring that the filter holders cannot be inserted backwards and the flow will always be in the correct direction through the filters. At some locations, two filters were used for the purpose of using two different particle analysis techniques.

Placement of the nine 47 mm filters in the trichotomous sampler are shown on the schematics in **Fig. 3**, and in the photos in **Figs. 8** and **9**, where **Figs. 8** and **9** shows the bases of the 2.5 µm and 1.0 µm HVVIs, respectively. The heads of the HVVIs have been removed in these photos.

Filters shown in **Figs. 8** and **9** are as follows:

Fig. 8

1. One 47mm PM_{10} filter (A, the grey holder) located after the PM_{10} inlet and before the 2.5 µm HVVI.
2. One 47mm $PM_{2.5\text{-}10}$ filter (B, the gold holder) samples particles from the minor flow of the 2.5 µm HVVI. Also shown is the 2 × 7 inch (5 × 17.5 cm) minor flow filter so that the total minor flow rate can be brought to 2 cfm.

Fig. 9

3. One 47mm $PM_{2.5}$ filter (D, the blue holder) samples the 2.5 µm HVVI major flow aerosol.
4. Two 47mm $PM_{1\text{-}2.5}$ filters (E, the red holders), which sample the 1.0 µm HVVI minor flow aerosol.
5. Two 47mm PM_1 filter (F, the green holders) which samples the 1.0 µm HVVI major flow aerosol.
6. Two 47mm background filters (G, the black holders) located above the 8 × 10 inch final filter. These filters have zero flow rate (are used as control filters).

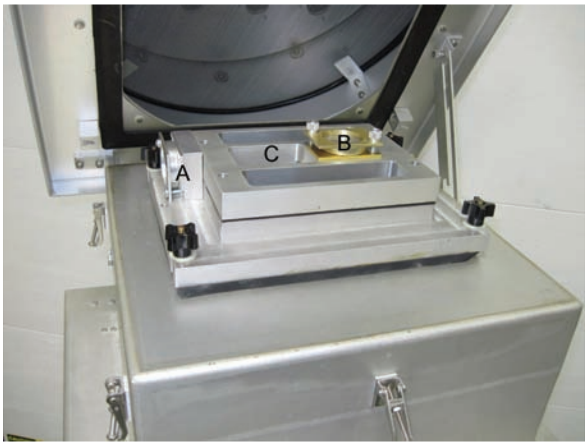

Fig. 8 Photo of 2.5 µm base showing 47 mm filter holder placements.
A-PM_{10} filter (grey filter holder); B-$PM_{2.5\text{-}10}$filter (gold filter holder); C-$PM_{2.5\text{-}10}$ 2 × 7 inch filter.

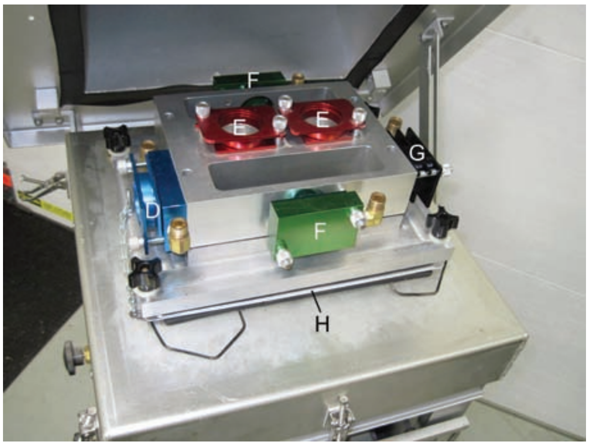

Fig. 9 Photo of 1.0 µm base showing 47 mm filter holder placements.
D-$PM_{2.5}$ filter (blue filter holder); E-$PM_{1\text{-}2.5}$ filter (red filter holders); F-PM_1 filter (green filter holders); G-background control filters (black filter holders); H-$PM_{<1}$ 8 × 10 inch filter.

The flow rate through each filter is controlled by a flow circuit consisting of an orifice flow meter, connected to a Magnehelic pressure gage, and followed by a manual flow control valve. Flow from each filter is routed back into the primary flow circuit downstream of the 8 × 10 inch filter, allowing the flow rate to be controlled, and remains constant at 40 cfm. Since a maximum of 2 cfm is passing through any 47 mm filter, normally the flow remains relatively constant over a 24 hour sampling period. Therefore, the control valve for each filter need only be set at the onset of sampling. However, for heavy particle loading conditions, an intermediate adjustment of flow rate can easily be made.

Collection Characterizes

There are three inertial classifiers in the trichotomous sampler: a PM10 high volume inlet, and two HVVIs virtual impactors. The PM_{10} inlet uses inertial impactor technology to remove particles larger than 10 µm, and has been the subject of many wind tunnel

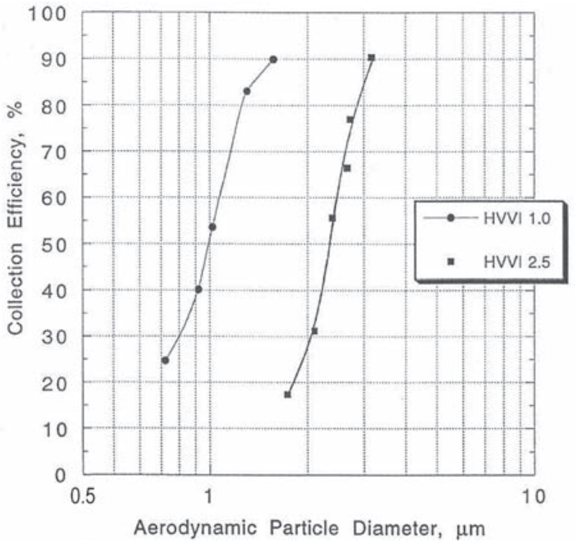

Fig. 10 Particle classification curves for 1.0 and 2.5 HVVIs.

evaluation and calibrations.

The 2.5 µm HVVI was designed specifically to further classify particles within the standard high volume PM10 sampler. Initial application was separation of coarse mechanically generated aerosol particles from smoke particles being emitted from wood burning fireplaces (Marple, et.al., 1990). Since these mechanically generated aerosols are solid, the 2.5 µm HVVI was calibrated with solid ammonium fluorescein particles generated using a vibrating orifice monodisperse aerosol generator (VOMAG) (Berglund and Liu, 1973). The collection efficiency curve of the 2.5 µm HVVI is shown in **Fig. 10**.

However, the 1.0 µm HVVI was designed specifically for use in the trichotomous sampler and had to be calibrated for this program. Since particles less than 1 µm in diameter are formed by condensation, liquid particles were used in its calibration. In a method commonly used in our laboratory, a VOMAG was used to generate oleic acid droplets tagged with uranine dye. By washing out various parts of the classifier with known amounts of wash solution and analyzing the wash solution with a fluorometer to determine the dye concentration, the collection efficiency of the HVVI was determined as a function of particle size. The resulting efficiency curve for the 1.0 µm HVVI is also shown in **Fig. 8**. Note in the efficiency curves for both 2.5 µm and 1.0 µm HVVIs that the lower efficiency asymptotically approaches the fraction of the minor flow (5%).

Analysis Techniques

The $PM_{1.0/2.5/10}$ Trichotomous sampler was developed to provide a means for determining if particles in the 1.0 to 2.5 µm size range are mostly coarse or mostly fine mode particles. Since coarse and fine mode particles originate from different sources, more than one analysis method had to be employed; one for coarse particles and one for fine particles. Therefore, two filters were used in some locations within the trichotomous sampler.

Part II of this paper, to be published in the 2013 issue of KONA, describes the use of $PM_{1.0/2.5/10}$ Trichotomous samplers in a study of atmospheric aerosol particles in the southwestern US, specifically in Phoenix, Arizona. Proton-induced X-ray emission (PIXE) and photon-induced x-ray fluorescence (XRF) methods were used to determine the concentration and composition of the coarse particle mode. Both of these methods are commonly used due to their non-destructive multi-element capabilities and relatively good sensitivities. A different analysis technique was used to analyze the filters for fine particles. The water-soluble portion of suspended particulate matter was quantified using ion chromatography (IC).

Filters in the grey, gold, blue, red and green filter holders were subjected to PIXI analysis and filters in the red and green filter holders were subjected to IC analysis.

Conclusion

An ambient high volume sampler has been specifically developed to answer the question of whether particulate matter in the saddle point between the coarse and fine particle modes (1.0 µm to 2.5 µm range) consist primarily of coarse or fine particles. The sampler consists of the standard 40 cfm high volume ambient air PM10 sampler with two high volume virtual impactors, one with a cut size of 2.5 µm and the other with a cut size of 1.0 µm, inserted between the PM_{10} inlet and the 8 × 10 inch after filter. Particles were collected on seven 47 mm filters at various locations within the sampler to enable analyses by different techniques to determine the fraction of the particles in the 1.0 µm to 2.5 µm range that was from the coarse mode aerosol or the fine mode aerosol.

Acknowledgements

Development and calibration of the $PM_{1.0/2.5/10}$ Trichotomous sampler has been supported by the National Mining Association.

References

Berglund, R. N. and Liu, B. Y. H. (1973): Generation of monodisperse aerosol standards, Environmental Science Technology, Vol.7, pp.147-153.

Chen, B. T., Yeh, H. C. and Cheng, Y. S. (1986): Performance of a modified virtual impactor, Aerosol Sci. Technol. Vol.5, pp.369-376.

John, W. (2011): “Size distribution characteristics of aerosols”, *Aerosol Measurement*, 3rd edition, eds: Kulkarni, Baron andWilleke, pp.41-54.

Marple, V. A. (1970): “A Fundamental Study of Inertial Impactors”, Ph.D. dissertation, University of Minnesota.

Marple, V. A. (2004): History of Impactors-The first 110 Years, Aerosol Science and Technology, Vol.38, pp.247-292.

Marple, V. A., and Chein, C. M. (1980): Virtual Impactors: A Theoretical Study, Environ. Sci. Technology, Vol.14, pp.976-985.

Marple, V. A., Liu, B. Y. H. and Burton, R. M. (1990): High-volume virtual impactor for sampling fine and coarse particles, J. Air Waste Management Assoc. Vol.40, pp.762-767.

Marple, V. A. and Olson, B. A. (1995): "A high volume PM10/2.5/1.0 trichotomous sampler", In Particulate Matter: Health and Regulatory Issues, VIP-49, Air and Waste Management Assoc. International Specialty Conference, Pittsburg, PA, pp.237-261.

Masuda, H., Hochrainer, D., and Stober, W. (1978): An improved virtual impactor for particle classification and generation of test aerosols with narrow size distributions, J. Aerosol Sci. Vol.10, pp275-287.

McFarland, A. R., Ortiz, C. A. and Bertch, Jr., R. W. (1984): A 10 μm Outpoint size selective inlet for Hi-Vol Samplers, J. Air Pollution Control Assoc. Vol.34, pp.544-547.

U.S. Environmental Protection Agency (1982): "Air quality criteria for particulate matter and sulfur", EPA-600/882-029b, December,1982.

Whitby,K. T. (1978): The physical characteristics of sulfur aerosols, Atmospheric Environment. Vol.12, pp.135-159.

Xu, X, (1991): "A Study of Virtual Impactors", Ph.D. dissertation, University of Minnesota.

Author's short biography

Virgil A. Marple

Virgil A. Marple is a Professor in the Mechanical Engineering Department at the University of Minnesota. He received his Ph.D. from the University of Minnesota in 1970. He is Director of the Particle Calibration Laboratory, and his research interest includes development of inertial classifiers, measurement of mining related aerosol in both the coal and taconite industries and measurement of pharmaceutical aerosols.

Dale A. Lundgren

Dale A Lundgren is Professor Emeritus - Environmental Engineering Department, University of Florida. He received his Ph.D. from the University of Minnesota in 1973. His recent research interest has been as a consultant to the National Resource Research Institute (University of Minnesota Duluth campus) studying particulate concentrations in cities and taconite mines on the Minnesota Iron range.

Bernard A. Olson

Bernard A. Olson is a Research Associate and Manager of the Particle Calibration Laboratory in the Mechanical Engineering Department at the University of Minnesota. He received his BSME, MSME, and Ph.D. from the University of Minnesota. For the past 22 years his research has been in the design, testing and numerical modeling of aerosol sampling instruments, characterization of mining aerosols related to the coal mine and taconite industries and effluents generated by cooking appliances in the commercial kitchen industry.

Processing, Characterization and Mechanical Properties of SiAlONs Produced from Low Cost β-Si_3N_4 Powder[†]

Hasan Mandal[1*] **and Nurcan Calis Acikbas**[2]
[1] *Materials Science and Engineering Programme, Sabancı University*
[2] *Department of Mechanical and Manufacturing Engineering, Engineering Faculty, Bilecik S.E. University*

Abstract

SiAlON ceramics have been known for many years as prime candidate materials in structural applications at ambient and high temperatures involving superior mechanical and/or chemical processes. In spite of their excellent properties, the utilization of SiAlONs has remained limited till today due to the high cost of raw materials and processing. In order to circumvent this problem, low cost refractory grade, coarse, impure, less sinter active β*-*Si_3N_4 *powder was used to produce SiAlON ceramics with satisfactory mechanical properties.*

In this article, the processing challenges in the production of SiAlON ceramics with β*-*Si_3N_4 *powder were discussed. The process parameters obviously affect the phase assemblage, densification, microstructural and mechanical properties of final SiAlON ceramics. Processed* β*-*Si_3N_4 *powder characteristics are majorly investigated by SEM-EDX, XRD, XRF, laser particle sizer and elemental analyser. The existence of undesirable impurities in the* β*-SiAlON crystal structure because of the use of impure* Si_3N_4 *powders has been shown to be tolerable by TEM microstructural analysis. Mechanical properties are in general evaluated by Vickers indentation method. Wear behaviour of the cost effective SiAlONs were compared with commercially available ceramic materials which are commonly being used in wear applications. Initially the use of such powders to produce materials for engineering applications proved challenging, however, satisfactory results have been obtained by the optimization of the initial chemical composition and process parameters.*

Keywords: powder processing, β-Si_3N_4 powder, particle size, sintering, characterization, wear

1. Introduction

SiAlON ceramic materials are very significant with their highly desirable, and proved potential, especially in industrial wear and high temperature applications[1-3)]. The final mechanical and chemical properties of these ceramics depend on microstructural evolution (grain size, grain aspect ratio, porosity, intergranular phase, impurities, etc.)[4-7)]. Powder processing stage has a strong effect on microstructural development, since ceramic parts are produced by the sintering of initial powder mixtures[8-12)]. Removal of impurities from the raw powders, initial particle size distribution, homogeneous dispersion of sintering additives, and grinding of starting non-oxide powders are the important parameters in the microstructural formation of SiAlON materials with superior mechanical properties[13-19)]. SiAlON production processes are based on homogenization of raw powders α or β-Si_3N_4 powder, Al_2O_3, AlN and sintering additives such as Y_2O_3, Sm_2O_3, Er_2O_3, Dy_2O_3, CaO, etc. in alcohol or water in order to achieve a predetermined composition ($\alpha:\beta$-SiAlON ratio ($\alpha':\beta'$), a determined intergranular phase chemistry),

---

[†] Accepted:August 10, 2012
[1] Orhanli, Tuzla/Istanbul, 34956 Turkey
[2] Bilecik, 11210, Turkey
[*] Corresponding author:
E-mail: hmandal@sabanciuniv.edu
TEL: +90-216-4839666 FAX: +90-216-4839118

ⓒ 2013 Hosokawa Powder Technology Foundation

followed by drying of slurry, shaping, and sintering.

Traditionally, high quality pure α-Si_3N_4 powder is used instead of β-Si_3N_4 powder due to its higher sinter activity. However, fine α-Si_3N_4 powders are very high in cost and this is a key determinant parameter for large scale applications. On the other hand, β-Si_3N_4 powders can be produced economically with combustion synthesis[20]. Free silicon and iron may originate from milling of the raw β-Si_3N_4 powder. Removal of these impurities and/or achieving desired final phases including these impurities in the sintered product is required. Besides milling and sintering process parameters have crucial effects on microstructural evolution. In this respect, SiAlON powder processing technology involves a number of know-how developments to produce materials with superior properties at low cost.

In this article, the manufacture low cost SiAlON ceramics with satisfactory mechanical properties by the use of low cost refractory grade, impure, less sinter active β-Si_3N_4 powder was described. Correlation between processed β-Si_3N_4 powder characteristics and process conditions with final phase assemblage, densification, microstructure and mechanical properties was determined.

2. Experimental Studies

In this study β-Si_3N_4 powder manufactured by combustion synthesis (Beijing Chanlian-Dacheng Trade Co. Ltd., China) was used as initial Si_3N_4 powder. Attrition milling in water with Si_3N_4 grinding media (3 mm in diameter) at 1400 rpm was performed to decrease the average particle size of β-Si_3N_4 starting powder. In order to completely understand correlation between processing-structure-property relationships, β-Si_3N_4 powder characteristics were investigated by using SEM-EDX, XRD, XRF, laser particle sizer and elemental analyser.

Since α' and β' phases are both stable thermodynamically, it is possible to produce hard and tough α-β-SiAlON composites. For this purpose $30\alpha:70\beta$-SiAlON composition was designed and Y-Sm-Ca multi cation doping system was chosen with the aim to produce self reinforcement microstructures. Y_2O_3 (>99.9%, H.C. Starck Berlin, Germany), Sm_2O_3 (>99.9%, Stanford Materials Corp., USA), $CaCO_3$ (>99.75%, Reidel-de Haen, Germany) were used as sintering additives. CaO was used to avoid α to β SiAlON transformation, Y_2O_3 and/or Re_2O_3 (where $Z_{Re} \geq 62$)) to increase the stability and hardness of α-SiAlON and Sm_2O_3 (where $Z_{Re} < 62$) to develop elongated β-SiAlON grains to increase fracture toughness). Si_3N_4 powders and sintering additives were mixed with high purity AlN powder (H Type, Tokuyama Corp. Japan, with 1.6wt% O content) and Al_2O_3 (Alcoa A16-SG Pittsburgh, USA). All of the prepared SiAlON compositions with β-Si_3N_4 powders were milled in water with 64wt% solid loadings. Tetramethylammonium hydroxide (TMAH) was used as a dispersant with 2.5 wt%. Milling was performed for a total duration of two hours. The slurry was sieved with 32 μm and homogenized together with 2 wt % plasticizer (Primal B60, Rhöm & Haas, Italy), 2 wt % binder (PEG 4000, Clariant Produkte GmbH, Germany) and 2 wt% lubricant (Zuzoplast Wem, ZSC Zimmer&Shwarz, Germany) in a mixer. The slurries were spray dried (Nubilosa LTC-2 model). The powders were uniaxially pressed at 25 MPa and subsequently cold isostatically pressed at 300 MPa to improve green density. Binder burn-out process was carried out at 550 ℃ for 30 minutes. The pellets were sintered both by gas pressure sintering (KCE, FPW 100/150-2200-25 type furnace), under 2.2 MPa nitrogen gas in a stan-

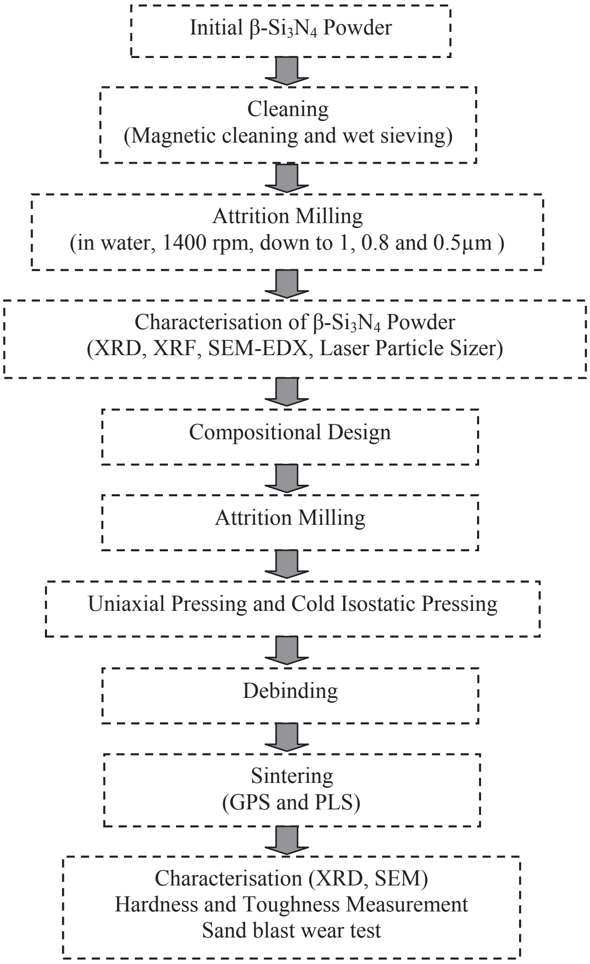

Fig. 1 Flow chart of the manufacturing process.

Table 1 Sand blast test conditions

Pressure	6 bar
Particle composition	Alumina
Particle size of alumina	0.5-1 mm
Alumina content	2 kg
Sample dimensions	24.5 × 7 mm
Test duration	10 min.
Distance to nozzle	10 mm
Impact angle	50°

dard manner and by pressureless sintering (Thermal Technology, 1000-4560-FP2000 model furnace). Post sintering heat treatment was performed at 1900℃ for 3 hours under 0.1 MPa nitrogen gas. Flow chart of the manufacturing process is given in **Fig. 1**.

$\alpha:\beta$ phase ratio and phase composition of the intergranular phase were determined by X-ray diffraction (Rigaku 2000 Rint, Japan). Polished surfaces of the sintered samples were gold coated prior to examination in a Zeiss VP50-Supra type scanning electron microscope (SEM) by using back-scattered electron imaging mode. Analytical TEM investigations were achieved by using 200 kV field emission TEM (JEOL JEM-2100F).

Hardness and fracture toughness measurements were carried out by Vickers indentation technique by applying 10 kg load for 10 seconds. At least 5 indentations were made for each sample. The sand blast wear tests were further performed at Röchling Leripa GmbH (Austria). The test conditions were given in **Table 1**. The erosion rates of the nozzles are defined as the nozzle mass loss divided by the nozzle density and so volume of the erodent abrasive particles (wear volume) is found.

3. Results and Discussion

3.1 Powder processing challenges and solutions

Widespread use of SiAlON parts is limited at present due to high cost of raw materials and of processing. In order to solve this problem, low cost refractory grade, coarse, impure and less sinter active β-Si_3N_4 powder was used. Utilization of this kind of powder brings about processing challenges to produce SiAlON ceramics with sufficient densification, phase assemblage and mechanical properties.

The first step was before milling, characterisation of as-received β-Si_3N_4 powder. XRD analysis was carried out to detect impurities in as-received β-Si_3N_4 powder (**Fig. 2**). According to **Fig. 2**, the powder contains Fe, Si, Fe_2Si and $FeSi_2$ as impurities. Iron contamination was believed to cause from the milling process of starting Si powder involving use of steel grinding media.

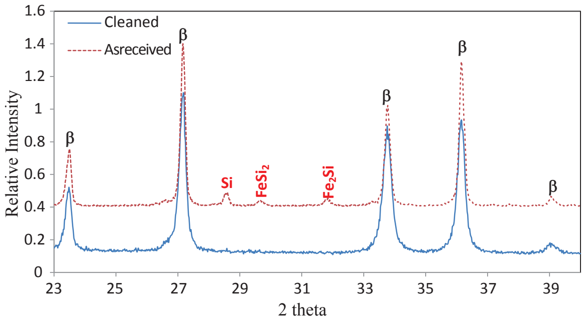

Fig. 2 An XRD analysis of cleaned and as-received β-Si_3N_4 powders.

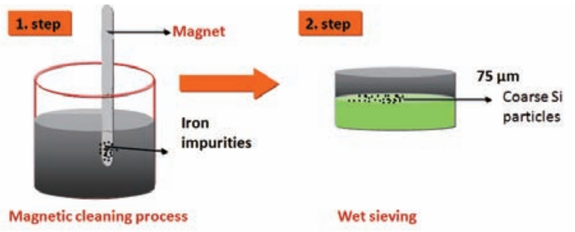

Fig. 3 Schematic illustration of iron and silicon removing processes.

In order to remove iron, magnetic cleaning process was applied as shown in **Fig. 3**. Initial β-Si_3N_4 powder was mixed in mixer with isopropyl alcohol and Fe impurities were collected with a magnet. This process was repeated until iron impurities were totally removed. To remove silicon impurities, obtained slurry after magnetic cleaning process were passed under 75 µm sieves to separate coarser silicon particles. Subsequently slurry was dried in rotary evaporator. A phase comprises of as-received and cleaned β-Si_3N_4 powder is given in **Fig. 2**. XRD analysis showed that this cleaning process is effective, since there were no silicon or iron/iron containing impurities detected.

3.2 Effect of milling on powder characteristics

Initial average particle size of β-Si_3N_4 powder was measured as 10 µm by laser diffractometer (**Fig. 4**). Attrition milling in water with Si_3N_4 balls (3 mm in diameter) at 1400 rpm was performed to decrease the average particle size of β-Si_3N_4 starting powder to 1µm, 0.8 µm and 0.5 µm. The related powders were designated as B1 (d50: 1 µm), B0.8 (d50: 0.8 µm) and B0.5 (d50: 0.5 µm). For the milling process,

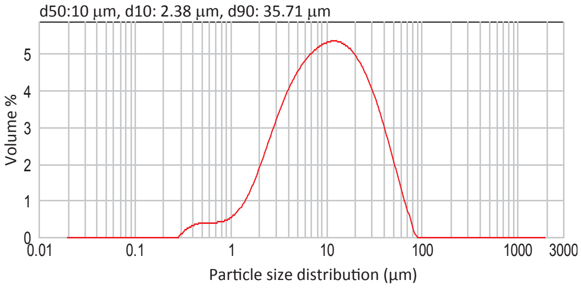

Fig. 4 Particle size distribution of as-received β-Si_3N_4 powder.

Table 2 Milling time versus particle sizes

Milling Time (h)	d50	d10	d90
0	10.05	2.38	35.71
1.5	3.58	0.89	9.34
2.5	2.59	0.84	5.79
4.5	1.40	0.55	3.22
7	1.19	0.56	2.43
9	**1.08**	0.55	2.07
11	0.98	0.46	1.97
13	**0.78**	0.30	1.69
15	0.67	0.19	1.64
17	0.62	0.20	1.50
19	0.59	0.19	1.48
21	**0.53**	0.18	1.40

Attrition milling at 1400 rpm in water

the ratio of powder to deionised water and dispersant was 800 g : 400 g : 16 g; the weight ratio of powder to Si_3N_4 milling balls was 1: 2.3. The vessel was cooled by water circulation throughout the process. The slurry temperature was systematically controlled every hour. If slurry temperature reaches 50℃, milling speed was decreased for the duration of the next 30 minutes. Milling efficiency was given in **Table 2**. In the first 1.5 hrs, particle size was down to 3.58 µm. After 7 hrs milling, particle size was down to 1.2 µm.

SEM analysis of as-received and milled β-Si_3N_4 powder was given elsewhere[21)]. As-received β-Si_3N_4 starting powder exhibited prismatic-elongated particle morphology, whereas the milled β-Si_3N_4 particles (B1, B0.8, and B0.5) showed an irregular morphology with sharp edges. The sum of initial Si_3N_4 powder characteristics were given in **Table 3**.

Total oxygen content of the powders was determined by the inert-gas-fusion method, using an elemental analyser. As-received β-Si_3N_4 powder contains 3 wt% oxygen. After 21 hours milling in water B0.5 powder has 7.8 wt% oxygen. This can be attributed to the hydrolysis of β-Si_3N_4 powder during milling in water after long hours. After 21 hours milling the slurry began to bubble with an ammonia odour. It was shown that the long term milling in isopropyl alcohol might have increased in the amount of Si-O-Si surface groups[10)].

Table 3 Starting Si_3N_4 powder characteristics

	B	B1	***B0.8***	B0.5
% α-Si_3N_4	0	0	0	0
% β-Si_3N_4	100	100	100	100
D50 (µm)	10	1.08	0.78	0.53
D10 (µm)	2.4	0.55	0.30	0.18
D90 (µm)	36	2.43	1.69	1.40
Milling time (h)	-	9	13	21
Particle shape	Prismatic	Irregular	Irregular	Irregular

Table 4 XRF analyses of B0.5 powder

	N	**Si**	**Al**	**Fe**	**Ca**	**Mn**	**P**	**Sr**	**Cu**	**Ni**	**Cr**
wt%	78.97	20.38	0.450	0.0898	0.0849	0.0077	0.0030	0.0022	0.0020	0.0020	0.0019

XRF analysis of B0.5 powder is given in **Table 4**. Fe, Ca, Mn, P, Sr, Cu, Ni and Cr are still present in very small quantities (less than 0.1 wt.%) in cleaned β-Si_3N_4 powder. XRF analyses verify the XRD analyses of cleaned β-Si_3N_4 powder. SEM-EDX elemental analyses of B0.5 powder showed the presence of Fe, Ca, Cu, Ba, S, Mn, Ti and Ni as impurities (**Fig. 5**).

3.3 Effect of milling time on SiAlON properties

3.3.1 Densification, phase assemblage and microstructure

Milling time is the most important variable that will effect final particle size, particle surface characteristics and hence densification, phase assemblage and microstructure. **Table 5** shows some characteristics of the powders (B1, B0.8 and B0.5), sintering conditions and some properties after sintering process. It was found that SiAlON obtained from B1 powder, milled for 9 h presents nearly full densification and designed α':β' phase ratio was achieved. Increase in milling time from 9 to 13h leads to increase in oxygen content of Si_3N_4 powder and this variation causes increase in β' content. During milling in water, following reaction may occur[22)].

$$Si_3N_4 + 6H_2O \rightarrow 3SiO_{2\ amorphous} + 4NH_3 \qquad (i)$$

SiO_2 formation due to this reaction shifts the composition to β' rich region. It is also expected that increased silica would preferentially react with α-SiAlON stabilizing additives and thus would reduce/prevent α-SiAlON formation.

Other important topic is sintering of coarse B0.8 powder by pressureless sintering route at 1800℃, for

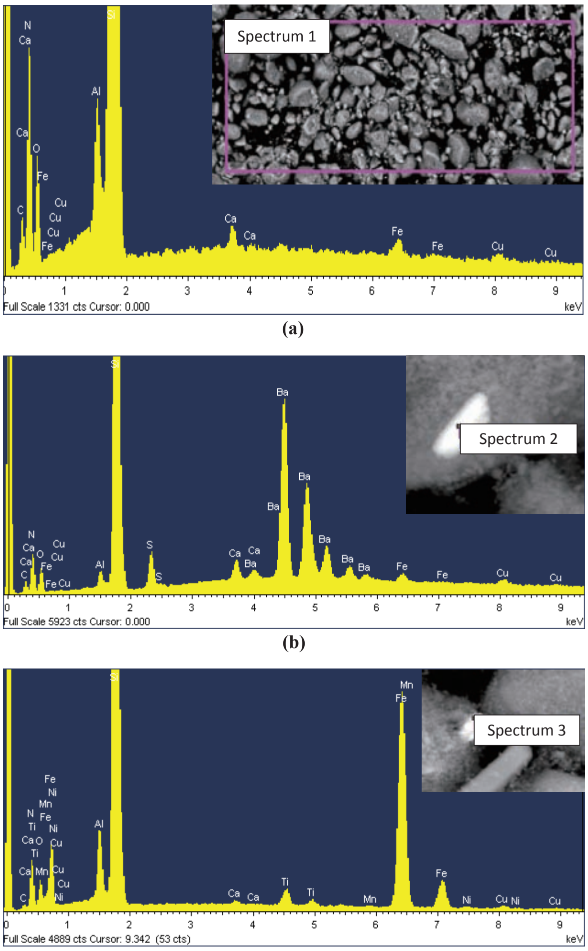

(a)

(b)

(c)

Fig. 5 SEM-EDX analyses of B0.5 powder.

1 h with almost full densification due to judiciously selection of dopant system[23]. One of the main aspects in designing SiAlONs with improved properties would be the chosen of additives that would provide a good liquid phase sintering behaviour. In this study Sm rich Y-Sm-Ca dopant system with cation molar ratio 30:64:6 was chosen because of the low eutectic temperature and high nitrogen solubility of the Sm-Si-Al-O-N system[24]. Moreover, the viscosity of Sm-Si-Al-ON liquids is less than the other lanthanide containing SiAlONs and this makes densification easier[24]. Further increase in milling time to 21 h results in further increase in oxygen content up to 7.8 wt.%. Higher oxygen content induces more liquid phase during sintering and leads to better densification even at 1850℃ but it has detrimental effect on high temperature properties due to higher liquid phase content.

Table 5 Characteristics of SiAlON ceramics

Powder	Milling Time (h)	O (wt. %)	Sintering Conditions	Phase Assemblage	Relative Density
B1	9	4	1940°C, 2 h, 2.2 MPa N_2	$73\beta':27\alpha'$	99.90
B0.8	13	4.7	1800°C, 1 h, 0.1MPa N_2 HT: 1900°C, 3 h, 0.1MPa N_2	$81\beta':19\alpha'$	99.90
B0.5	21	7.8	1850°C, 1 h, 2.2 MPa N_2	$100\beta'$	99.43

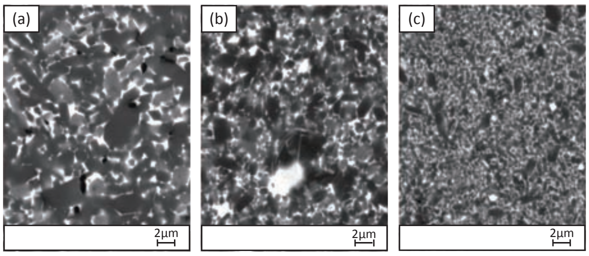

Fig. 6 BSE-SEM images of sintered SiAlONs prepared from (a) B1, (b) B0.8 and (c) B0.5 powders.

Fig. 6 shows BSE-SEM images of sintered SiAlONs prepared from β-Si_3N_4 powders which were subjected to different milling times. The differences in microstructure can be explained on the basis of differences in powder particle size and sintering conditions. The microstructure of B1 sample consisted of predominantly between 1-1.4 µm α' and β' grains diameter, the aspect ratio of grains changes between 2.5 to 7 (**Fig. 6a**). The diameter and length of grains were determined by the SEM micrographs of polished surfaces. Over 200 grains of each sample were measured. The apparent aspect ratio of the grains was calculated by dividing the length to diameter. A decrease in β-Si_3N_4 particle size to 0.8 µm (B0.8) resulted in decrease in α' and β' grains diameter to between 0.5-1.5 µm, but aspect ratio of grains almost similar (**Fig. 6b**). This sample was subjected to heat treatment at 1900℃ for 3 hrs under 0.1 MPa nitrogen gas pressure. However, substantial grain growth was not achieved due to coarse grain size of sintered samples. In order to obtain grain growth, grain size should be less than 0.5 µm. It was observed that in order to achieve grain growth and to develop self reinforced microstructure after heat treatment, the grain size of SiAlON after sintering should be rather fine, preferably less than 0.5 µm as in **Fig. 7** [21]. Otherwise, coarse grains, even around 1 µm, do not have enough driving force for grain growth. Similar observations were made on β-Si_3N_4 ceramics[25-28].

After 21 hrs milling, particle size was down to 0.5 µm and B0.5 specimen after sintering have fine elongated microstructure with grain size was around 0.2 µm and aspect ratio was about 7. It is evident that final grain size of β-Si_3N_4 derived SiAlON ceramics depends on the initial β-Si_3N_4 particle size (**Fig. 8**). During sintering, the solution of β-Si_3N_4 in the

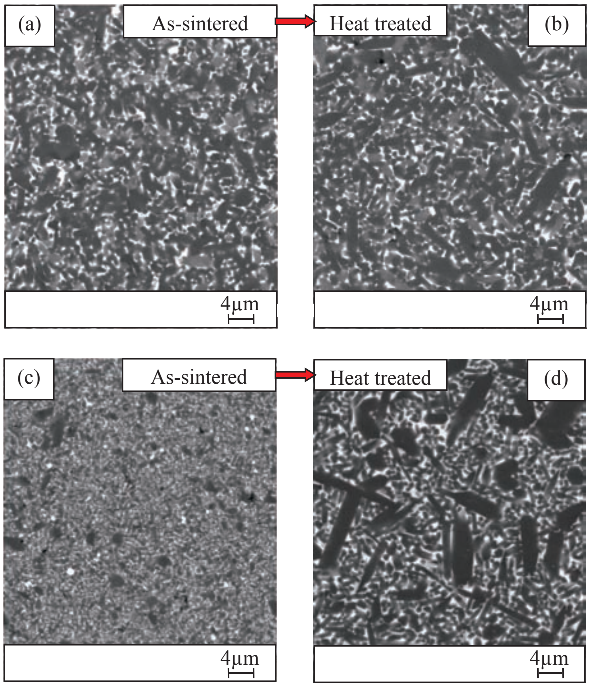

Fig. 7 BSE-SEM images representing the as-sintered and heat treated microstructure of (a, b) B1 and (c, d) B0.5.

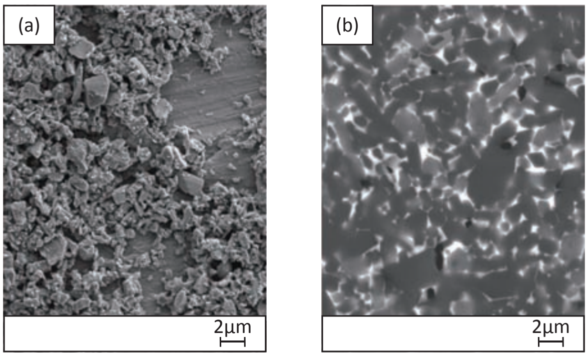

Fig. 8 (a) SEM-SE image of starting β-Si_3N_4 powder (d50:1 µm) and (b) SEM-BSE image of sintered B1 sample.

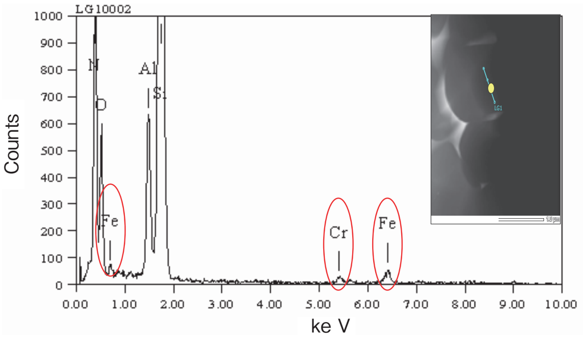

Fig. 9 TEM-EDX analyses of B1 sintered sample.

liquid phase and precipitation as $\alpha:\beta$-SiAlON might have caused the formation of $\alpha:\beta$-SiAlON from β-Si_3N_4 powder [18]. The nucleation can either be homogeneous from the liquid or heterogeneous on the existing β-Si_3N_4 grains. Given the fact that the initial particle size is an effective parameter on the final microstructure, the use of coarse or fine β-Si_3N_4 powders resulted in coarse or fine $\alpha:\beta$-SiAlON, respectively. It appears that nucleation of $\alpha:\beta$-SiAlON occurred heterogeneously on the pre-existing crystals in case of B0.8 and B1 powders.

Even if the starting β-Si_3N_4 powder was subjected to magnetic cleaning and sieving processes, some impurities may remain in powder. After a detailed TEM-EDX examination of the sintered SiAlON samples prepared from B1 powder, incorporation of undesirable Fe and Cr impurities into the β-SiAlON crystal structure was found (**Fig. 9**) [29]. As previously noted Be [30], Mg, Li [31] and Ga [32] may enter β-Si_3N_4 crystal structure. These results clearly showed that Fe and Cr can enter β-SiAlON crystal structure. As a conclusion it can be inferred that the use of Si_3N_4 powders with certain impurities can be used to produce a SiAlON phase microstructure.

3.3.2 Mechanical properties

The hardness and fracture toughness values of the SiAlON ceramics are summarized in **Table 6**. Increasing milling time resulted in a decrease in hardness. During milling in water, oxygen content of the composition increased. Therefore, the initial composition shifted to β' region. In addition, higher oxygen content led to a higher fraction of intergranular phase. This increment provided a decrease in hardness. B1 and B0.8 have similar hardness values. The difference in hardness between B1, B0.8 with that of B0.5 can be attributed to the presence of larger fraction of grain boundary phase in B0.5 due to prolonged milling time and also to the absence of harder α' phase. Although B1 and B0.8 specimens consisted of both α' and β' phases, hardness values were lower than expected. As mentioned before, incorporation of Fe and Cr impurities in β' crystal structure might have caused a decrease in hardness values.

Both indent diagonals and crack lengths around the indentations were measured from the SEM images and found that l/a ratio varies between 1.0 and 1.7 and such values indicated good crack growth resistance property of the investigated ceramics. The differences in microstructure and properties can be explained on the basis of differences in powder particle size. The development of more elongated grains

Table 6 Mechanical properties and developed phases of SiAlONs, prepared from different starting particle sizes 1 µm (B1), 0.8 µm (B0.8) and 0.5 µm (B0.5), when subjected to different sintering methods and heat treatment

Sample	Milling time (h)	HV (GPa)	K_{IC} (MPam$^{1/2}$)	Phases
B1	9	14.22 ± 0.03	5.30 ± 0.15	$73\beta':27\alpha'$
B0.8 (HT)	13	14.10 ± 0.07	5.20 ± 0.10	$81\beta':19\alpha'$
B0.5	21	13.00 ± 0.03	5.60 ± 0.20	$100\beta'$

in B0.5 resulted in relatively higher toughness than other sintered ceramics. B1 and B0.8 samples have similar aspect ratio (see **Fig. 6**) and thus fracture toughness values are similar. Post sintering heat treatment did not have any effect on grain growth for B0.8 sample (**Fig. 7**). It was concluded that to achieve grain growth and to develop self-reinforced microstructures by heat treatment, grain size of SiAlON microstructure after sintering should be less than µm (preferably ≤ 0.5 µm). Coarse grains would not have enough driving force for grain growth.

3.3.3 Wear resistance

Table 7 presents the hardness, flexural strength, fracture toughness, phase assemblage and wear volume of the samples. Sand blast wear tests were carried out on the developed SiAlON ceramics to simulate wear caused by severe particle impacts. In addition the wear volume of the developed cost effective SiAlON was compared with commercial ceramic materials were provided from CeramtecAG company (Germany) which are commonly used in wear applications.

The sand blast test results showed that SiAlON ceramic was much more durable than alumina ceramics which are widely used in wear applications. Although commercial Al_2O_3-ZrO_2 material is harder than B0.8 monolithic SiAlON, B0.8 monolithic SiAlON is 4.5 times more durable than commercial Al_2O_3-ZrO_2 material. SiAlON showed similar performance to silicon nitride ceramics although it was prepared from cost effective heterogeneous powders. When the hardness, toughness and strength values are compared, commercial Si_3N_4 proved advantageous over B0.8 sample. However, wear volume values are almost similar. In general, it can be concluded that SiAlON ceramics have better properties than Si_3N_4 ceramics for commercial applications.

Table 7 Properties and wear volumes of sand blast tested ceramics

Sample	HV (GPa)	K_{IC} (MPam$^{1/2}$)	Strength (MPa)	Phases	Wear Volume (mm^3)
B0.8	14.10	5.1	530	$81\beta':19\alpha'$	0.0360
Commercial Si_3N_4	16.00	5.5	850	β - Si_3N_4	0.0320
Commercial Al_2O_3-ZrO_2	17.00	4.4	450	Al_2O_3-ZrO_2	0.1600
Commercial Al_2O_3	17.00	4.0	380	Al_2O_3	0.4800

4. Conclusions

In this article, processing challenges of β-Si_3N_4 powder to produce SiAlON ceramics have been tried to clarify. It has been found that undesired iron and silicon impurities in starting silicon nitride powder can be significantly reduced by magnet and then wet sieving. On the other hand, incorporation of undesirable impurities into the β-SiAlON crystal structure and thus use of Si_3N_4 powders with certain impurities as characterized by TEM, are found to be possible.

The effect of powder processing conditions on phase assemblage, densification, microstructure and mechanical properties of SiAlON parts has been identified. The powder milling time was determined to see the effects on creating silica on silicon nitride powder. Silica content on silicon nitride powder governed the phase assemblage. If oxygen content is ~7.8 wt%, the designed $\alpha':\beta'$ ratio was not achieved and composition was shifted to β' rich region. It was observed that initial particle size have vital effects on microstructural evolution. If particle size is larger than 0.5 µm low aspect ratio grains developed. A combination of hardness of around 14 GPa and indentation toughness of 5.1 MPam1/2 could be obtained in ceramics sintered from coarse (0.8 µm) β-Si_3N_4 powders. This SiAlON ceramics prepared by with commercial Si_3N_4, showed similar wear resistance performance and proved more durable than commercial alumina ceramics which are widely used in wear applications.

Acknowledgement

The authors specially thank Prof.Dr. Ferhat Kara and Dr. Hilmi Yurdakul from Anadolu University for valuable discussion on the processing and TEM observations respectively. In addition, the financial support of the Scientific and Technological Research Council of Turkey (TUBITAK) (Ankara, Turkey) and the Ministry of Science, Industry and Technology under the framework of the San-Tez Programme have been gratefully acknowledged.

References

1) Ekström, T. and Nygren, M. (1992) : SiAlON ceramics, J. Am Ceram Soc, Vol.75, pp.259-276.
2) Mitomo, M. and Tayima, Y. (1991) : Sintering, properties and applications of silicon nitride and SiAlON ceramics, J. Jpn. Ceram. Soc., Vol.99, pp.1014.
3) Riley, F. (2000): Silicon nitride and related materials, J. Am. Ceram. Soc., No.83, pp.245-265.
4) Li, H. X., Sun, W. Y., Wang, P. L., Yan, D. S. and Tien, T. Y. (1997) : The effect of GPS parameters on mechanical properties of Y-α-SiAlON ceramics, Ceramics International, Vol.23, pp.449-56.
5) Hayama, S., Nasu, T., Ozawa, M. and Suzuki, S. (1997) :Mechanical properties and microstructure of reaction sintered β′-sialon ceramics prepared by a slip casting method, Journal of Materials Science, Vol.32, pp.4973-4977.
6) Salamon, D., Šajgalík, P., Liška, M. (2005) :Mechanical Properties and Microstructure of α-SiAlON Based Cutting Tools, Key Engineering Materials, Vol.290, pp.250-253.
7) Kumar, R., Acikbas Calis, N., Kara, F., Mandal, H., and Basu, B, (2009) : Microstructure - Mechanical Properties - Wear Resistance Relationship of SiAlON Ceramics, Metallurgical and Materials Transactions A, Vol.40, pp.2319-2332.
8) Rabe, T., and Linke’ D. (1992) : Attrition milling of silicon nitride powder under conditions for minimal impurity pickup, Ceramics International, Vol.18, pp.161-166.
9) Dai, J. Q., Huang, Y., and Ma, J. T. (2008) : Surface characteristics and aqueous dispersibility of commercial silicon nitride powders : Effects of acid leaching, surface hydrolysis and thermal oxidation, Ceramics International, Vol.34, pp.1835-1842.
10) Huang, Y., Dai, J. Q., Xie, Z. P., Ma, T., Yang, J. L., Ma, J. T. (2003) : Effects of liquid medium and ball milling on the surface group and aqueous dispersibility of Si_3N_4 powder, J. Euro. Ceram. Soc., Vol.23, pp.985-990.
11) Tapaszto, O. and Balazsi, C. (2010) :The efeect of milling time on the sintering kinetics of Si_3N_4 based nanocomposites, Ceramics International, Vol 36, pp.2247-2251.
12) Naito, M., Okumiya, M., Abe, H., Kondo, A., Huang, C.C. (2010) : Powder processing issues for high quality advanced ceramics, KONA Powder and Particle Journal, N0.28, pp.143-154.
13) Acikbas Calis, N., Kara, F., Mandal, H. (2009) :Development of α-β SiAlON Ceramics From Different Si_3N_4 Starting Powders, Key Engineering Materials, Vol.403, pp.107-108.
14) Herrmann, M., Höhn, S., Bales, A. (2011) : Kinetics of rare earth incorporation and its role in densification and microstructure formation of alpha-Sialon, J. Euro. Ceram. Soc., Vol.32, pp.1313-1319.
15) Rhee, S. H., Lee, J. D and Kim, D. Y. (2000): Effect of α-Si_3N_4 initial particle size on the microstructural evolution and phase transformation during sintering of Si_3N_4 ceramics, J. Euro. Ceram. Soc., Vol.20, pp.1787-1794.
16) Lee, C. J., Chae, J. I. and Kim, D. J., (2000): Effect of β-Si_3N_4 starting powder size on elongated grain growth in β-Si_3N_4 ceramics, J. Euro. Ceram. Soc., Vol.20, pp.2667-2671.
17) Mitomo, M. and Uenosono, S. (1992) : Microstructural development during gas-pressure sintering of α-silicon nitride, J. Am. Ceram. Soc., Vol.75, pp.103-107.
18) Ekström, T., Ingelström, N., Brage, R., Hatcher, M. and Johansson, T. (1988): α-β-SiAlON ceramics made from different silicon nitride powders, J. Am. Ceram. Soc., Vol.71, pp.1164-1170.
19) Li, Y. W., Wang, P. L., Chen, W. W., Cheng, Y.B. and Yan, D.S. (2000) : Phase formation and microstructural evolution of Ca α-SiAlON using different Si_3N_4 starting powders, J. Euro. Ceram. Soc., Vol.20, pp.1803-1808.
20) Irene G. Cano and Miguel A. Rodríguez (2004) : Synthesis of β-Silicon nitride by SHS: fiber growth, Scripta Materialia, Vol.50, pp.383-386.
21) Acikbas Calis, N., Kumar, R., Kara, F., Mandal, H., and Basu, B (2011): Influence of β-Si_3N_4 particle size and heat treatment on microstructural evolution of α : β-SiAlON Ceramics, J. Euro. Ceram. Soc., Vol.31, pp.629-635.
22) Boris, E. L., Zhmud, V. and Bergstrom, L. (2000) : Dissolution and Deagglomeration of Silicon Nitride in Aqueous Medium, J. Am. Ceram. Soc., Vol.83, pp.2394-2400.
23) Kara, F., Mandal, H., Turan, S., Kara, A. and Acikbas Calis, N.: Development Strategies for SiAlON Ceramics, Global Roadmap for Ceramics ICC2 Proceedings, pp.119-128, 2nd International Congress on Ceramics, June 29-July 4, Verona, Italy, 2008.
24) Mandal, H. (1992): “Heat treatment of sialon ceramics”, PhD. Thesis, University of Newcastle Upon Tyne, 149pp.
25) Mitomo, M., Tsutsumi, H., Tanaka, S., Uenosono, S. and Saito, F. (1990): Grain growth during gas-pressure sintering of β-silicon nitride, J. Am. Ceram. Soc., Vol.73, pp.2441-2445.
26) Lee, C. J., Chae, J. I. and Kim, D. J. (2000): Effect of beta-Si_3N_4 starting powder size on elongated grain growth in bet]-Si_3N_4 ceramics, J. Eur. Ceram. Soc., Vol.20, pp.2667-2671.
27) Mitomo, M., Hirotsuru, H., Suematsu, H. and Nishimura, T. (1995): Fine-grained silicon nitride ceramics prepared from β-powder, J. Am. Ceram. Soc., Vol.78, pp.211-214.
28) Hirosaki, N., Akimune, Y. and Mitomo, M. (1993): Effect of grain growth of β-silicon nitride on strength, Weibull modulus, and fracture toughness, J. Am. Ceram. Soc., Vol.76, pp.1892-1894.
29) Yurdakul, H., and Turan, S. (2011): Incorporation of the transition metals (Cr and Fe) into beta-SiAlON crystal structure, Ceramics International, Vol.37,

pp.1501-1505.

30) Huseby, I.C., Lukas, H.L. and Petzow, G., (1975) :Phase equilibria in the system Si_3N_4-SiO_2-BeO-Be_3N_2, J. Am. Ceram. Soc., Vol.58, pp.378-380.

31) Jack, K.H. (1973) :Nitrogen Ceramics, Trans, J. Br.Ceram. Soc., Vol.72, pp.376-384.

32) Oyama, Y. (1973) :Solid Solution in the System Si_3N_4-Ga_2O_3-Al_2O_3, Jpn. J. Appl., Phys., Vol.12, pp.500-508.

Author's short biography

Hasan Mandal

Hasan Mandal (Prof. Dr.) received his PhD in Ceramic Materials from University of Newcastle (UK) in 1992. In the period of 2007-2008, Dr. Mandal was at Karlsruhe University as Alexander von Humboldt Fellow. In 1996, he joined the Department of Ceramic Engineering at Anadolu University. He became the Head of Department (1999), Dean of the Faculty of Engineering (2004), Chairperson of Turkish Engineering Deans Council (2006), Chairperson of Global Engineering Deans Council (GEDC-2009), Vice Rector of Anadolu University (2010). He is currently is Vice President and also the Director of Research and Graduate Policies at Sabanci University/Istanbul. He has co-authored over a hundred publications, three patents about science and technologies on Si3N4 based ceramics including phase relationships, structure-property relations and applications. Because of these achievements, he was honoured by twenty awards including European Ceramic Society, Stuijts Award in 2005. He is a member of World Innovation Foundation and World Academy of Ceramics.

Nurcan Calis Acikbas

Nurcan Calis Acikbas received B.S., M.S. and PhD. Degrees in Ceramic Engineering from Anadolu University, Turkey in 2002, 2004 and 2009, respectively. She was with MDA Advanced Ceramics Ltd. from 2004 to 2010. She joined the Bilecik University, Mechanical and Manufacturing Engineering Department as assistant professor. She appointed as Deputy Director of Bilecik University Central Research Laboratory at 2011. She was honoured by award Turkey Technology Development Foundation (TTGV) the most successful thesis in university-industry collaboration. Her current research interest is structure-property relationship; tribology; Silicon Nitride based ceramics and its applications.

Assembly of Nanoparticles: Towards Multiscale Three-Dimensional Architecturing[†]

Hyangki Sung and Mansoo Choi*
[1] *Division of WCU Multiscale Mechanical Design, School of Mechanical and Aerospace Engineering, Seoul National University*

Abstract

Fundamental building block in nanotechnology is the nanoparticle and currently many excellent techniques are available to control its size, morphology and crystalline phase at mass quantity. However, the practical realization of novel nanodevices employing nanoparticles requires the construction of multiscale three-dimensional buildings consisting of the basic building block, nanoparticles, particularly as an ordered array, which remains challenging. In this review, we address various methodology developed for the assembly of nanoparticles by classifying them depending on manipulating force. Methods utilizing electric, capillary, and magnetic forces are discussed. Ion assisted aerosol lithography(IAAL) that utilizes ion induced focusing concept will be described in more detail since it provides an opportunity for multiscale multidimensional assembly of nanoparticles in a parallel fashion at atmosphere.

Keywords: nanoparticle assembly, nanoparticle patterning, multiscale architecturing, nanoparticle

Introduction

Significant advances have been made in synthesizing nanomaterials including organic molecules, nanoparticles and biological molecules. Especially, for nanoparticles, there has been great progress in developing methodologies for controlling their size, shape and crystalline phase in the past decade[1-16)]. Along with these advances, deposition of nanoparticles or molecules on desired position of a substrate with nanoscale resolution has received great attention in recent years, due to its promising potential to realize nanodevices for various applications in the fields of electronics, optics, chemistry, and biomedics[17-28)]. The realization of emerging convergence technology requires us to have control capability on multiscale phenomena including nano, micro, and macro scales. Bridging among different scales is a prerequisite for manufacturing practically various novel nanodevices exhibiting unprecedented performance, which include nano-bio sensors, nano-electric/optical/magnetic devices and nano-energy devices. Such ultimate integration among different scales in three dimensions can be called as multiscale three-dimensional architecturing which is challenging and demanding, but worthwhile to explore since it can become an important platform for convergence technology. A variety of techniques have been introduced to carry nanomaterials onto a surface in a serial or a parallel manner, consequently, to form patterns or arrays of the materials. We first review various methods of patterning nanomaterials (generally nanoparticles) according to the governing force employed to manipulate nanoparticles. In this review, we limit our discussion to the forces of electrostatic, capillary and magnetic forces, which are the three most frequently used forces in manipulating nanoparticles. Recently, methods for improving pattern resolution by producing a nanoparticle pattern with width smaller than the original pattern utilizing the focusing capability caused by electrostatic interactions have been reported such as electrodynamic focusing of charged aerosols, electrostatic funneling using surface treatment and p-n junction based electrostatic method. Among the electrodynamic focusing methods of

---

[†] Accepted: August 23, 2012
[1] Seoul, 151-744, Korea
* Corresponding author:
E-mail: mchoi@snu.ac.kr
TEL: +82-2-889-6669 FAX: +82-2-889-6671

ⓒ 2013 Hosokawa Powder Technology Foundation

charged aerosols, Ion Assisted Aerosol Lithography (IAAL) is a parallel atmospheric process for assembling nanoparticles in multiscale three dimensions with nanometer resolution thanks to the ion induced focusing capability. We will focus on this IAAL technique in the second part of this review. Finally, device applications based on nanoparticle assembly demonstrated by IAAL will be discussed.

1. Assembly Methods of Nanoparticles

1.1 Electrostatic force directed assembly

The use of electric fields is the most common approach to transport and assemble a large number of small particles in a parallel fashion because electrostatic interaction is long-range and non-material-specific[29)]. Micro- or nanosized particles can be trapped within the charged areas formed on the substrate surface leading to produce a particle pattern. Due to its effectiveness, there has been great interest in developing techniques to manipulate nanoparticles with high precision by means of electrostatic force on a large area. In this section, we will address on charge-writing method, nanoxerography, electric field induced aerosol method, biased p-n junction method, and electrostatic funneling method.

Charge-writing method

Localized charge patterns have been widely utilized to make patterns of nanoparticles because, just by exposing the substrate to a suspension of nanoparticles, the particles experience long-range Coulomb interactions and are selectively deposited on the charged area of the substrate[30-32)]. A stainless-steel needle was used to create lines of negative charges by contact charging on the surface of a oxidized silicon substrate[33)]. Charges maintained in the insulator for hours after the metal was removed[34)]. Then, charged aerosol particles were directly positioned along the patterns of surface charges on the insulating substrate. A conductive tip of an atomic force microscope (AFM) could be also used to deposit localized charge patterns on an electret followed by immersion of the substrate into a suspension of nanoparticles to form a pattern of the nanoparticles[35)]. Similar processes were conducted but the use of a focused ion beam (FIB), as shown in **Fig. 1(a)**, in forming patterns of surface charges and two-dimensional arrays were obtained as a result[36, 37)]. Although this method can provide fine structures of nanoparticles, the process to create surface charges with a conductive needle is a serial and time-consuming process and this method cannot be applied to conducting substrates.

Nanoxerography

Nanoxerography is a parallel method to fabricate nanoparticle arrys by utilizing a conductive flexible stamp with patterns that can transfer charge patterns on non-conducting surface in a single step[38-40)]. **Fig. 1(b)** shows a process of transferring charges on a poly(methylmethancrylate) (PMMA) thin film in parallel and depositing nanoparticles on the area of charge patterns. A poly(dimethylsiloxane) (PDMS), patterned in bas-relief, was made electrically conducting by forming 80-nm thick gold film with thermal evaporation on it. For the generation of charge patterns, a metal-coated PDMS stamp was placed on top of the 80-nm thick PMMA film supported on an n-doped silicon wafer and a voltage of 10 to 20-V

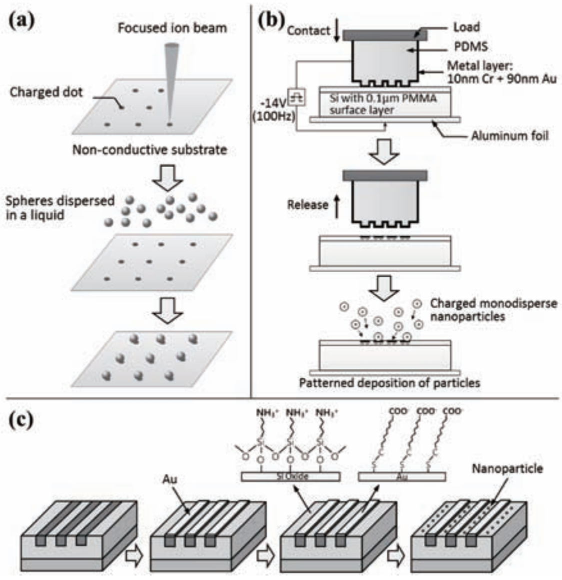

Fig. 1 (a) A schematic illustration of the steps to fabricate two-dimensional particle arrays using a charged pattern. A charged pattern is formed on an insulating substrate by scanning a charged beam in vacuum. Reprinted with permission from ref 36. Copyright 2002 Wiley-VCH. (b) A schematic illustration of the process of parallel charge patterning and nanoparticle deposition. A pulse voltage of -14V (100Hz) was applied between the PDMS stamp and the substrate for about 10s to generate charge patterns onto the substrate. Reprinted from ref 38, Copyright 2004, with permission from Elsevier. (c) A schematic illustration of the experimental process to place nanoparticles onto silicon oxide lines using electrostatic funneling scheme. Lines of nanoparticles appear as a result. Reprinted with permission from ref 48. Copyright 2007 American Chemical Society.

was applied between the gold on the PDMS and the back side of the silicon. With this method, Jacobs and Whitesides[29] showed that transfer of charge patterns ranging from 120-nm to 100-μm in size onto the PMMA was possible in less than 20s, and produced particle patterns by dipping the substrate into dry powders. During the process of coating the PDMS stamp with metal through thermal evaporation, buckling of the metal coating can appear due to thermal expansion and contraction of the PDMS stamp[41]. To prevent the buckling, a sputtering method[38] has been suggested. In addition, uniform contact between a stamp and a substrate in large area and fabrication of reliable stamps with nanoscale resolution are issues. It is also noted that nanoxerography cannot be utilized for conducting surface.

Electric field induced aerosol deposition method

Under a given electric field, Prost et al.[42] and Otten et al.[43] deposited singly charged lead sulfide (PbS) nanoparticles generated by aerosol techniques onto a GaAs substrate which is patterned with different resist structures having a minimum feature size of 600-nm. A lift-off process after particle deposition removed the resist while the patterns of deposited nanoparticles remained. It was observed that the size of deposited structures was smaller than the open area of the photoresist. This result was attributed that the resist was selectively charged by the deposition of charged particles and further deposition of the incoming particles on the resist are repelled by the predeposited particles with the same charge polarity. Similar approach utilizing the effect of electrostatic focusing caused by charged particle deposition was also reported by Jun et al.[44]. It is noted that charged particles should deposit everywhere randomly including on the photoresist surface and the exposed GaAs surface until sufficient amount of charged particles deposit on the photoresist surface to begin to show focusing phenomenon. Similar focusing phenomenon due to the deposition of charged particles was also observed when a Teflon mask was used during electrospraying[45]. On the other hand, the method utilizing ion induced focusing that our group developed enables electrodynamic focusing of charged aerosols[46] from the start without generating noise particle deposition. We call this method as “Ion Assisted Aerosol Lithography (IAAL)” since the ion injection is a crucial step to enable focused deposition of charged aerosols producing multiscale and three-dimensional architectures consisting of nanoparticles as basic building blocks for structures with nanoscale resolution. We will discuss this in full detail later.

Biased p-n junction method

Tsai et al.[47] developed a method of positioning metal nanoparticles delivered from a gas phase onto surfaces using electrostatic force generated by biased p-n junction patterned substrates. They prepared a p-n junction patterned substrate by fabricating 1-μm wide p-type lines on an n-type GaAs substrate using photolithography and charged nickel nanoparticles by aerosol technique. The negatively charged particles were repelled from the p-type regions and attracted to the n-type regions, particularly at the interface of p-n junctions, where the local field was the highest. If the polarity of the particle was changed to positive, the particles were attracted to the depletion zone of the p-type regions and were repelled from the n-type regions. As the reverse bias on the substrate increased, almost all the negatively charged nickel nanoparticles were deposited on the n-type regions. Although many noise particles existed on the resulting substrates, it is advantageous that this assembly method can be applied to commonly used substrate architectures and provide nanoparticle patterns quite easily on a large area.

Electrostatic funneling method

Electrostatic funneling was proposed by Ma et al[48] as a way to place nanoparticles onto predefined locations on a substrate in large area. As described in the **Fig. 1(c)**, the substrate was prepared to have alternating lines functionalized with positively and negatively charged molecules. When the substrate was dipped into a suspension of negatively charged gold nanoparticles, the particles were electrostatically guided onto the centers of the positively charged lines and deposited along the lines. Here, it was experimentally shown that the nanoparticles were funneled away from the boundary toward the center of the positively charged area when the electrostatic interaction energy gradient was strong while they were not when the gradient was weak. This method is simple and compatible with CMOS fabrication and packaging technology, but some treatments are needed to change the electrostatic interaction energy gradient as well as surface treatment.

1.2 Capillary force directed assembly

The phenomenon of capillarity has been given attention as another possible means to assemble particles[49-54]. It can be commonly observed that floating particles become clustered when liquid evaporates.

This is because, when two such particles are close to each other, the deformed interface around them is not symmetric as the interface height between them is lowered due to the interfacial tension, and the particles come to experience attractive capillary force between them[51, 53]. Based on this capillary phenomenon, deposition from a suspension of colloids has provided two- and three-dimensional arrays of crystal-like structures of particles[55-58], the mechanism of which usually involves aggregation initiated by capillary force, growth driven by a laminar flow, and evaporation of the solvent[59]. In this section, we will discuss some representative and interesting researches which have been carried out to manipulate particles by utilizing capillary force according to the following subjects: micromolding in capillaries, template-assisted assembly, and dip-pen nanolithography.

Micromolding in capillaries

Kim et al.[60] fabricated crystalline two- or three-dimensional arrays of microspheres using micromolding in capillaries[61]. **Fig. 2(a)** outlines the experimental process of micromolding in capillaries. An elastomeric mold with a relief pattern was made from PDMS and both ends of the channels in the mold were cut to allow the fluid to enter and escape. A network of channels was formed by placing the mold on a support. When a drop of a latex solution containing polystyrene microspheres was placed at one end, the fluid filled the channels by capillary action. As the liquid evaporates, the microspheres crystalized on the support within the confinement of the channels and, finally, lines of crystallized microspheres were obtained after the removal of the PDMS. They also fabricated more complex patterns of crystallized microspheres using this technique.

Template-assisted assembly

Similar but template-assisted fabrication methods using colloids have been demonstrated[62-67]. Xia et al. fabricated colloidal aggregates by dewetting aqueous dispersions of monodispersed spherical colloids across surfaces patterned with two-dimensional arrays of relief structures as shown in **Fig. 2(b)** and **(c)**. As the liquid was slowly de-wetted from the confined space, the spherical colloids were pushed into the templates which was influenced by the capillary force originated from the liquid meniscus, and consequently formed a densely packed structure. With this approach, they demonstrated not only homo-aggregates of silica beads, including circular rings, polygonal and polyhedral clusters, linear zigzag and spiral chains, but also hetero-aggregates containing spherical colloids of different sizes, compositions, densities, functions, or a combination of these features. However, the size of colloids they could successfully make use of was limited down to 50-nm due to the limitation of their ability to fabricate templates on such a small scale. Cui et al.[62] successfully assembled macromolecule-sized gold nanoparticles with diameters of less than 10-nm. Flat substrates patterned with hole and trench template were inserted vertically into a solution containing nanoparticles of interest. During the evaporation of the solvent, three-

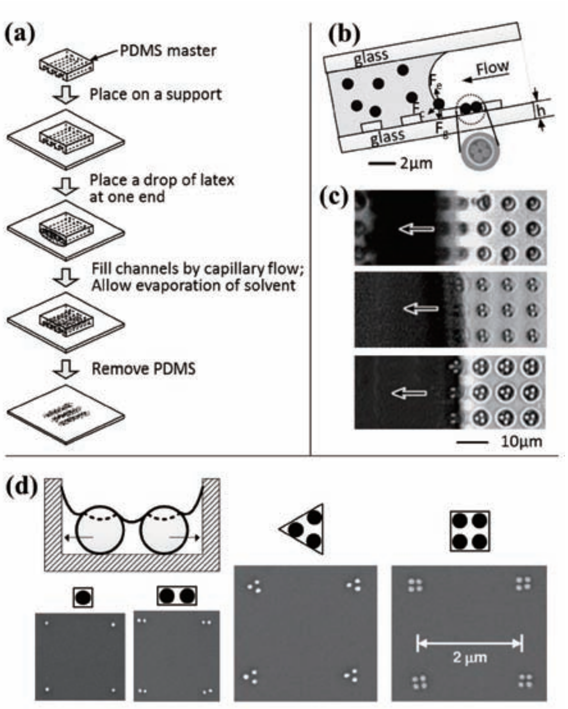

Fig. 2 (a) A schematic illustration for the process of micromolding in capillaries. Reprinted with permission from ref 60. Copyright 1996 VCH. (b) A schematic illustration of the process to generate aggregates of spherical colloids under the physical confinement of templates. A colloidal particle next to the rear edge of the liquid slug experiences three possible forces there: the capillary force (Fc), the gravitational force (Fg), and the electrostatic force (Fe). (c) Optical micrographs showing the assembly of polystyrene beads with different sizes into cylindrical holes with different sizes. (b) and (c) are reprinted with permission from ref 65. Copyright 2003 Willey-VCH. (d) A schematic illustration of the particle separation due to the probable free surface of the liquid in a pattern and the experimental results of the assembly of particles which are preferably positioned at the corner of each pattern. Reprinted with permission from ref 63. Copyright 2006 American Institute of Physics.

phase contact line moved slowly across the substrate, and the resulting capillary force pushed the particles into the denser parts of the solution when the evaporation zone passed over them. They also demonstrated to assemble anisotropic nanostructures such as tetrahedrally-shaped CdTe nano-tetrapods with 4-nm side and ~100-nm long arms. Gordon and Peyrade[63] presented arrays of one to four closely spaced nanoparticles, as shown in **Fig. 2(d)**, by controlling template shape and wettability. These arrays could be utilized as an etching mask for pattern transfer via reactive ion etching. Kraus et al.[64] developed a technique of printing nanoparticles with single-particle resolution. Here, sub-100-nm nanoparticles were individually placed by capillary force at the positions that were defined by the geometry of a template, and subsequently transferred to a second substrate having a higher level of particle adhesion than the printing plate.

Dip-pen nanolithography

Dip-pen nanolithography (DPN), a method for directly depositing molecules via capillary transport of molecules by an atomic force microscope (AFM) tip to the solid substrate, was originally designed to work on gold surfaces[68]. However, metal surfaces are not desirable for many of applications in electronics, photonics and sensing[69-74]. Therefore, there have been studies to deposit metal nanoparticles as dots or lines of clusters on various substrates using DPN or other AFM-based methods[74-80]. Ben Ali et al.[77] directly positioned gold nanoclusters on a silica surface by first depositing a small volume of solution of the clusters using DPN, then letting the solvent evaporate. Here, the size of deposited islands was strongly dependent on the contact force between the tip and the surface. In contrast, Tomas et al.[79] presented that pattern dimensions were independent on the applied contact force. The DPN experiments were carried out on mica substrates employing hydrosols containing chemically prepared lead nanocrystals and gold nanocrystals, and, notably, no lateral diffusion of the ink was observed. Garno et al.[78] also suggested a method to limit lateral diffusion of delivered patterns from a tip to a substrate by utilizing a covalent linkage between the gold nanoparticles and the substrate surface modified with a self-assembled monolayer (SAM). Further studies have been carried out to overcome low throughput of the DPN technique which is presumably caused by depletion of the ink. A microfluidic nanofountain probe has been developed for continuous feeding of the ink. With this approach, Wu et al.[80] fabricated arrays of 200-nm-diameter dots with gold nanoparticles and Taha et al.[74] did arrays of 100-nm-wide lines. However, unlike other small molecule-based inks, it is still relatively difficult to make AFM tips coated uniformly with metal nanoparticles because of their large size[81], and, consequently, it is difficult to obtain a uniform nanoparticle array with a controlled number of particles using DPN[82]. It is also noted that DPN is inherently a serial method.

1.3 Magnetic force directed assembly

Although there has not been much research on the manipulation of particles utilizing magnetic force in comparison to the cases of utilizing electrostatic and capillary force, there have been some efforts on assembling particles employing magnetic force[83-87]. Wolf and Birringer[85] demonstrated a two-dimensional carpetlike array of magnetic rods by depositing aerosol-grown magnetic iron nanoparticles onto a substrate in the presence of homogeneous magnetic field. The formation of regular patterns in the two-dimensional array of elastically deformable magnetic rods was attributed to the magnetic dipolar interaction between the bundles. Ennen et al.[83] presented a method to manipulate the assembly of magnetic nanoparticles by applying stray fields of magnetically patterned ferromagnetic layers which were pinned by the exchange bias interaction (EB)[84] to a neighboring antiferromagnetic layer. The magnetic patterning was generated by bombarding 10-keV He ions onto the areas to be patterned by nanoparticles in the presence of a magnetic field. On the other hand, Yellen et al.[87] introduced a method for assembling nonmagnetic colloidal particles with sizes ranging from several micrometers down to less than 100-nm into highly regular patterns by exploiting magnetic force. Here, magnetic force on nonmagnetic particles was transmitted through a fluid dispersion of magnetic nanoparticles, such as ferrofluid. The magnetization patterns as a template for producing reprogrammable magnetic field map were created by ferromagnetic thin film with discrete patches fabricated by lithographical patterning. With this technique, assembly of micrometer- and submicrometer-sized beads onto the magnetic traps of various shapes could be obtained.

2. Ion Assisted Aerosol Lithography (IAAL)

2.1 Mechanism of ion assisted aerosol lithography (IAAL)

In the IAAL process, both charged aerosols and ions having the same polarity are injected together into an electrostatic precipitator (ESP) chamber in which a conducting pre-patterned substrate with a dielectric material, generally a photoresist, is located[46]. Although charged aerosols and ions are fed into the ESP chamber together, ions, whose mobility is two orders of magnitude greater than charged aerosols, can reach the substrate first. The ions landing on the exposed surface of the conducting substrate are immediately neutralized while those on the photoresist surface become accumulated. These accumulated ions on the photoresist surface distort the initially flat equipotential planes into convex equipotential planes, which act as nanoscopic electrostatic lenses around the photoresist patterns as shown in **Fig. 3(a)**. Consequently, the charged aerosols following behind the ions are convergently guided into the center of the openings in the photoresist since charged particles should move in the direction perpendicular to the convex shaped equipotential planes. In addition, the ions accumulated on the photoresist surface form repelling fields, which serves to avoid generating deposition of noise particles on the photoresist surface and improve particle collection efficiency. As the deposition of nanoparticles proceeds, the focused deposits can develop to three-dimensional structures of multiple nanoparticles as shown in **Fig. 3(b)-(c)**. More details of the three-dimensional assembly will be discussed later. Following the removal of the photoresist, a micro- or nanoarray composed of nanoparticles is finally obtained. **Fig. 4** shows some examples of focused patterns fabricated using IAAL[46, 88]. **Fig. 4(a)** and **(b)** shows the arrays of deposited patterns consisting of multiple 10-nm silver nanoparticles on the silicon substrate with the prepatterned photoresist having 230-nm wide dots with 230-nm thickness on it. Here, the invisible electrostatic lenses formed by the accumulated ions on the photoresist surface lead the incoming silver nanoparticles onto the center regions of the exposed Si surface while hindering them from depositing on the photoresist surface. It is clearly shown that silver nanoparticles are assembled in 75-nm dots in **Fig. 4(a)**, which means that the focusing effect of IAAL reduced the

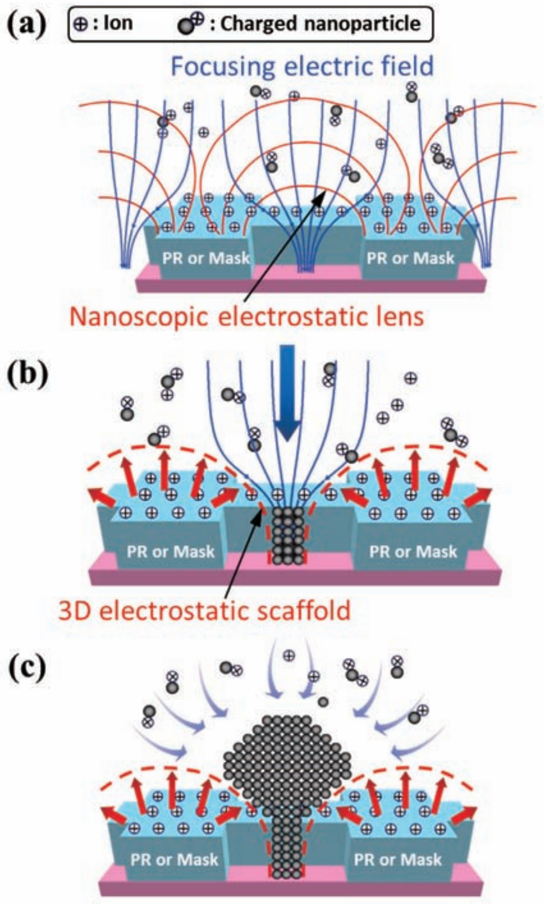

Fig. 3 A schematic illustration of the process to develop nanoparticle structures to three-dimensional structures using IAAL. The blue solid lines indicate the electric field and the red solid lines indicate the equipotential lines.

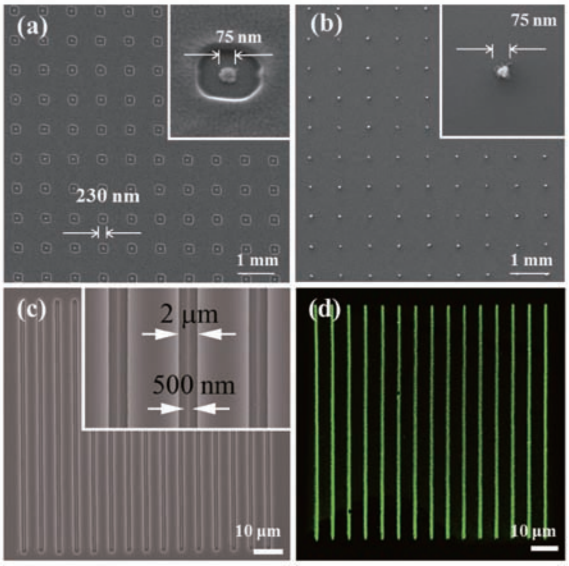

Fig. 4 (a) A SEM image of 75-nm dot arrays of 10-nm Ag particles formed within 230-nm PR square patterns. (b) A SEM image of 70-nm dot arrays of 10-nm Ag particles after the removal of the photoresist layer. (a) and (b) are reprinted with permission from ref 46. Copyright 2006 Nature Publishing Group. (c) A SEM image of patterned human IgG. (d) A fluorescence image of Alexa 488-tagged monoclonal goat anti-human IgG (absorption 495-nm, emission 519-nm) with CLSM. (c) and (d) are reprinted with permission from ref 89. Copyright 2010 Willey-VCH.

width of the particle patterns to about one-third of that of the original 230-nm photoresist prepatterns. An appropriate photoresist stripping process utilizing acetone and deionized water can remove the photoresist layer, which finally generates the focused patterns of silver nanoparticles as shown in **Fig. 4(b)**. It is noted that IAAL enables to fabricate a micro- or nanoarray of nanoparticle assembly whose feature size is much smaller than that of the original photoresist patterns by the ion-induced focusing effect in IAAL. It is also noted that any nanoparticles can be used to the IAAL mediated deposition once they are prepared in the form of charged aerosols. Kim et al.46) electrosprayed a suspension of monodisperse 20-nm gold nanoparticles which were commercially available to lead them to the IAAL system in the form of charged aerosols and fabricated focused assembly of the gold nanoparticles. Focused assembly of proteins were also demonstrated by Woo et al.88) by delivering electrosprayed protein nanoparticles to the IAAL system. **Fig. 4(c)** shows that human IgG was convergently deposited onto the center regions within 2-μm line patterns of SiO_2, which indicates the possibility of the selective immobilization of proteins onto the desired locus88, 89). The fluorescence image of Alexa 488 through confocal laser scanning microscope (CLSM) in **Fig. 4(d)** confirms the reaction of the Alexa Fluor 488-tagged anti-human IgG and the deposited human IgG, which verifies the protein activity after the deposition. Protein nanoarrays up to 50 nm scales were also produced via the same method in a parallel fashion.

The deposition configuration of the charged aerosols can be predicted by computing Lagrangian particle trajectories39). In IAAL, the motion of the nanosized charged aerosols in a gas flow under external electric field can be described by the following Langevin equation considering the fluid drag force (F_D), Brownian diffusion force (F_B), Coulomb force (F_C) and van der Waals force (F_{vdW}):

$$m_p \frac{dv_p}{dt} = F_D + F_B + F_C + F_{vdW}$$

where m_p is the mass of the particle in the aerosol form, t is the time and v_p is the particle velocity vector. Numerical simulations for the IAAL system can be done by solving this Langevin equation and the detailed simulation method and its results can be found in other studies89, 90).

2.2 Process parameters

As mentioned earlier, IAAL provides focused deposition of nanoparticles of interest with smaller size than the prepatterned openings on a substrate. The representative process parameters include surface charge density, applied voltage, the aspect ratio of photoresist patterns and the charges of particles. Details of each process parameters will be discussed below.

The magnitude of surface charge density can be easily controlled by changing the ion flow rates. **Fig. 5** shows the comparison of the configurations of particle depositions investigated with both experimental and computational methods according to different surface charge densities90). The particle depositions were carried out within 230×230-nm^2 square photoresist patterns (thickness ~135-nm) using IAAL. **Fig. 5[(a),(d)]**, **[(b),(e)]**, and **[(c),(f)]** are the cases of surface charge density of 3.6×10^{-5} C/m^2, 2.66×10^{-4} C/m^2, and 7.57×10^{-4} C/m^2, respectively. The cases of no ion injection, **Fig. 5[(a),(d)]**, of which surface charge density is arisen from the charged particles deposited on the photoresist, show that 10-nm silver particles are randomly deposited all over the surfaces including the photoresist surface and the exposed silicon surface. A little focusing of the particles near the exposed silicon surface even without ion injections is attributed to the charges of the deposited particles on the photoresist surface, which was previously observed42, 45). It is clearly shown that the deposited pattern under higher surface charge density forms a more focused feature. It also can be

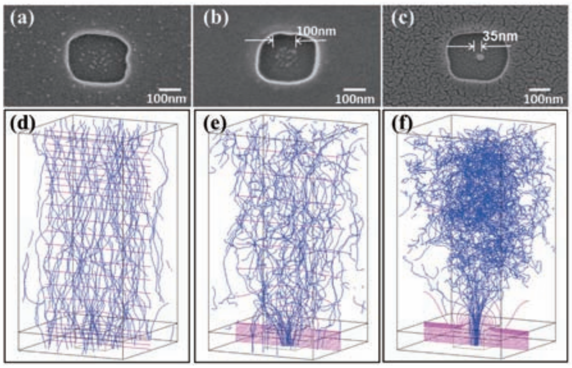

Fig. 5 The focusing effect dependent on the surface charge density of the substrate prepatterned with a 135-nm thick photoresist having 230-nm square openings. (a)-(c) Experimental results. Reprinted with permission from ref 46. Copyright 2006 Nature Publishing Group. (d)-(f) Simulation results of the trajectories of nanoparticles and the equipotential lines in three dimensions. Reprinted from ref 90. Copyright 2007, with permission from Elsevier. Surface charge densities are increased from 3.6×10^{-5}C/m^2[(a),(d)] to 2.66×10^{-4}C/m^2[(b),(e)] and 7.57×10^{-4}C/m^2[(c),(f)].

seen that the flat equipotential lines, indicated by the pink solid lines in the particle trajectory simulation, for the case of no ion injections are strongly modified into convex as the surface charge density increases, and, accordingly, a large number of particles are effectively guided into the center region of the opened Si surface. When the surface charge density increases to 7.57×10^{-4} C/m^2, about a 35-nm dot pattern consisting of multiple 10-nm Ag particles was formed within the 230-nm wide photoresist pattern, which indicates that the ion-induced focusing effect reduced the feature size of the particle assembly to about one-seventh of the original photoresist pattern. The higher surface charge density enables not only the greater focusing effect but also the stronger screening effect. As shown in the computational results in **Fig. 5**, particles are remarkably suppressed to land on the photoresist surface as the surface charge density increases, which reflects that Brownian motion of the particles approaching the substrate is suppressed near the electrostatic lens region, where their kinetic energy is much larger than the thermal energy (~k_BT).

The extent of focusing can be also controlled by modifying the curvature of the electric field lines by adjusting the applied potential on the substrate. Lee et al.[91)] showed that IAAL mediated circle patterns of charged polystyrene nanoparticles became narrower as the applied potential on the substrate decreased from -4 to -0.3 kV. In the simulation results, the curvature of the convex equipotential lines near the photoresist patterns gets increased as the applied potential on the substrate decreases from -4 to -0.3kV, and, accordingly, the electric field lines become more converged. Charged particles can follow the electric field lines with less deviation and form more focused deposition at lower applied potential since the electric field gradient near the substrate and the inertial effect on the particles are smaller at the lower applied potential.

The shape of photoresist patterns also influence on the shape of the electric field around the photoresist patterns, which consequently affect the focusing effect of IAAL. You and Choi[90)] computationally demonstrated the effect of the aspect ratio of a photoresist pattern on the trajectories of charged particles during the IAAL deposition process. In the simulation, photoresist patterns with different thickness of 105-nm, 135-nm and 165-nm but the same width of 230-nm were tested. The result indicated that more focused depositions could be formed when the aspect ratio of a photoresist pattern was smaller since the inertial effect that particles experienced was smaller, and, consequently, deviation of particle trajectories from the convergent electric fields was more suppressed.

Finally, control of the particle inertia is critical for highly focused and noise-free depositions of nanoparticles in IAAL, and, in this respect, it is important to avoid using highly charged nanoparticles to control the particle inertia. Lee et al.[91)] showed the influence of charges that nanoparticles possessed on the resolution of their deposited structures both experimentally and computationally. They electrosprayed 30-nm polystyrene nanoparticles on a silicon substrate on which 3-μm wide lines and 2-μm wide circles were prepatterned with a photoresist with thickness of 1.3-μm. Unexpectedly the particles were not focused at all but deposited everywhere even though the electrostatic lenses were established by injecting positive ions first. This non-focusing problem occurred because electrosprayed nanoparticles could get high charges which resulted in high velocity under the given electric field. Particles with high velocity tend to deviate from the converging electric field and move straight finally to deposit on the substrate surface without focusing. This inertial effect caused by high particle charge could be controlled by making the highly charged nanoparticles pass through a neutralizer and eventually neutralizing the particle charges. For example, depositions of polystyrene nanoparticles having passed a neutralizer, polonium-210, did not involve noise particles on the surface of the photoresist. The effect of nanoparticle charges on the extent of focusing in IAAL was also analyzed using numerical simulations by You and Choi[90)]. The numerical results indicated that the larger charges the particle had, the larger velocity the particle gained, and, consequently, the greater inertial effect it experienced and the more it deviated from the converging electric field leading to the broadening.

2.3 Nanoparticle focusing mask

IAAL can utilize a patterned dielectric mask instead of a prepatterned photoresist layer, which enables to simplify the fabrication process and increase the array density. You et al.[89)] introduced a way of using a patterned dielectric mask in the IAAL process that does not need any surface modifications to make prepatterns for a deposition. They replaced the patterned photoresist layer with a patterned dielectric mask such as silicon nitride or epoxy masks, which enabled to eliminate multiple steps of fabricating photoresist patterns and its removal process. The reason for using dielectric materials for the focusing mask is to form the electrostatic lenses around the patterns. To make use of a patterned mask in IAAL, one of the surfaces of the mask should be dielectric so that ions can be accumulated on it. Furthermore, the use of a patterned mask makes it possible to increase the array density with repeated depositions following sequential translation of the mask. **Fig. 6(a)** shows the sequential operation of a patterned dielectric mask. Here, 20-nm silver nanoparticles were deposited each time the mask was deliberately placed, and **Fig. 6(b)** clearly shows that the array density can be increased by the sequential translation of the mask and subsequent deposition. In addition, the use of the patterned mask enables to alternately deposit different materials on the same flat substrate without contamination from depositing different materials by translating the mask horizontally. Moreover, it also enables to deposit multilayer structures composed of different materials by translating the mask vertically and delivering different nanomaterials each time.

The use of the nanoparticle focusing mask also makes it possible for IAAL to be applicable to nonconducting substrates. Actually, Kim et al.[45] and You et al.[89] demonstrated that IAAL was effectively applicable to a substrate with a nonconducting surface as well as a conducting substrate. However, the focusing capability disappeared when the thickness of a SiO_2 layer on a silicon substrate became larger than a few micrometers according to the simulation results[89]. In order to produce focused patterns of nanoparticles on a thick nanoconducting substrate using IAAL, a thin conducting liquid film was introduced to the surface of the nonconducting substrate which was to be covered with a patterned dielectric mask only during the deposition. The conducting liquid film kept the surface of the nonconducting substrate conductive during the IAAL deposition process and could be removed by evaporation after the deposition process had completed. With this technique, You et al.[89] demonstrated focused depositions with IAAL on a thick glass as well as a thick flexible polymer film. They produced 420-nm wide line patterns of 30-nm polystyrene latex (PSL) particles using a silicon nitride mask with 2-μm-wide openings on a 0.7-mm-thick glass substrate. They also demonstrated 10-μm-wide line and 12-μm × 12-μmsquare patterns of 100-nm PSL particles using an epoxy mask with 50-μm-wide line and 50-μm × 50-μm square openings on a 0.1-mm-thick flexible poly(ethylene terephthalate) (PET) film.

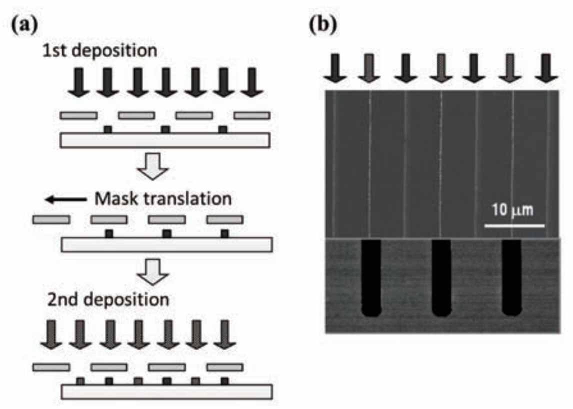

Fig. 6 Sequential operation of the ion-induced focusing mask. (a) A schematic illustration of the sequential patterning by translating the focusing mask. (b) A SEM image of line arrays of 20-nm silver nanoparticles after two sequential deposition. (a) and (b) are reprinted with permission from ref 89. Copyright 2010 Willey-VCH.

2.4 Three-dimensional assembly

Recently, Lee et al.[91] have extended IAAL up to the three-dimensional assembly by fabricating an array of multiscale and multidimensional micro-nanostructures consisting of nanoparticles. **Fig. 3** shows a schematic of the process to produce three-dimensional assembly of nanoparticles. As stated earlier, charged nanoparticles are guided into the center regions of the opened silicon substrate along the focusing electric field lines generated by the accumulated ions (**Fig. 3(a)**). Due to the antenna effect which refers to the enhanced field around the growing nanoparticle structure, the following nanoparticles are guided onto the being patterned structure and, consequently, the structure grows upward within the photoresist patterns (**Fig. 3(b)**). As the deposition of the nanoparticles continues, the structure grows beyond the photoresist height and then grows both in upward and lateral directions following the electric field lines. The strong repelling fields on the photoresist surface forms three-dimensional electrostatic fields in which charged particles could not penetrate. Therefore, deposits of charged particles could form specific three-dimensional shape depending on these three-dimensional electrostatic repelling fields which we call electrostatic scaffold that can be varied by changing photoresist patterns and ion accumulations (**Fig. 3(c)**). **Fig. 7** shows the arrays of the three-dimensional structures composed of 3-nm copper nanoparticles with various shapes formed on silicon substrates. The arrays of three-dimensional nanoparticle structures in **Fig. 7(a)** and **(b)** are formed within cross photoresist patterns with one side of 500-nm by depositing copper nanoparticles for (a) 90

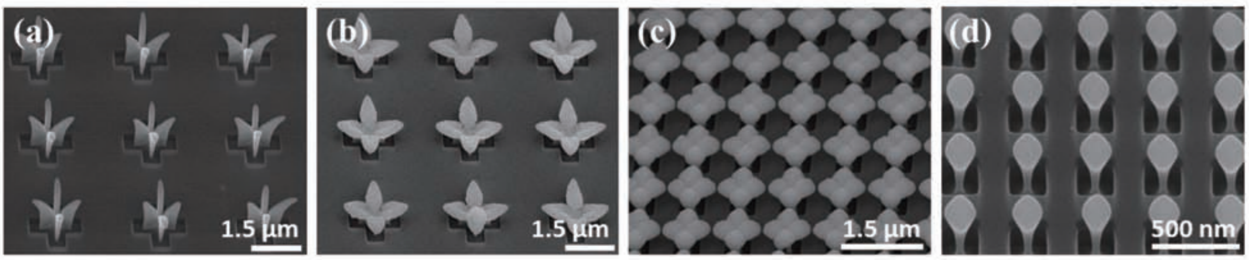

Fig. 7 (a)-(d) A variety of shapes of three-dimensional structures consisting of multiple 3-nm Copper nanoparticles. The combination of the ion-induced focusing and the three-dimensional electrostatic scaffold effects realizes selective formation of three-dimensional structures of nanoparticles on the photoresist patterns. (a)-(c) are reprinted with permission from ref 93. Copyright 2011 American Chemical Society.

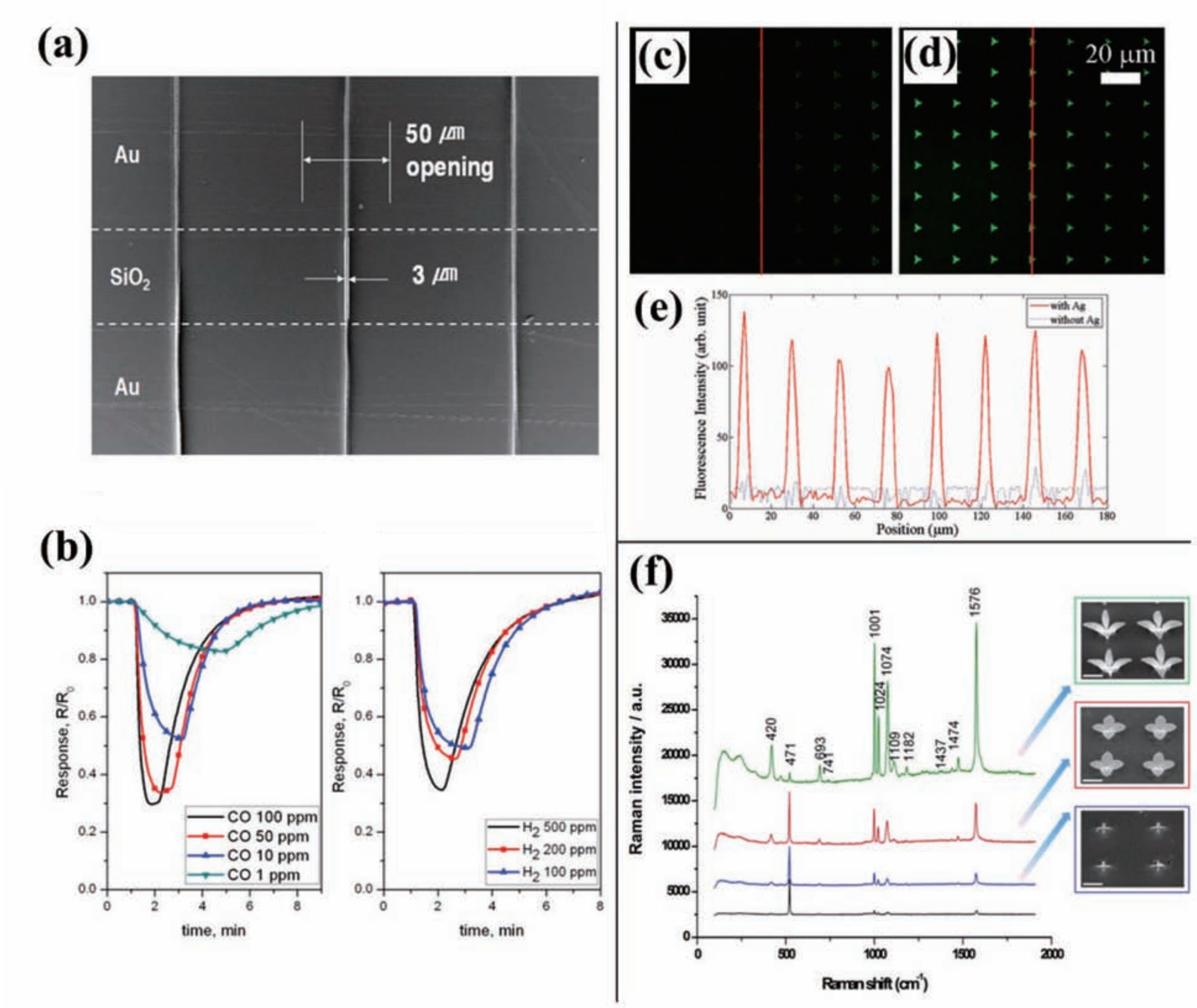

Fig. 8 (a)-(b) A gas sensor demonstrated by depositing patterns of ZnO nanoparticles on a silicon substrate coated by 200-nm-thick SiO_2 layer. (a) A SEM image of patterns of 3-µm-wide lines composed of 20-nm ZnO particles between two gold electrodes. (b) Sensor responses to CO and H2 gases, respectively. (a) and (b) are reprinted with permission from ref 89. Copyright 2010 Willey-VCH. (c)-(d) Fluorescence images of IgG-FITC (c) without silver particles and (d) with silver particles. (e) A profile of signal intensity observed following the red lines in (c) and (d). (c)-(e) are reprinted with permission from ref 89. Copyright 2010 Willey-VCH. (f) Raman spectra of thiophenol on three-dimensional structures of composite nanoparticles at different growth stages. Samples are composed of copper nanoparticles for the inner part and silver nanoparticles for the outer part. Reprinted with permission from ref 93. Copyright 2011 American Chemical Society.

minutes and (b) 120 minutes. Here, the structures of nanoparticles are quite distinguishable according to the deposition time and the fully-grown structures in **Fig. 7(b)** present flower-like shape. The arrays of three-dimensional structures in **Fig. 7(c)** are formed within square photoresist patterns with one side of 500-nm by depositing 3-nm copper nanoparticles for 90 minutes and the fully-grown shape is also flower-like but quite different from the shape of the nanostructures in **Fig. 7(b)**. It is noted that the shapes of the grown three-dimensional nanoparticle structures become quite different from their root shapes and, again, it is attributed to the repelling electric field from the photoresist surface as well as the electrostatic lenses formed by the accumulated ions on the photoresist surface. In this respect, the arrangement of openings in a prepatterned layer plays a very important role in determining the resulting shapes of three-dimensional nanoparticle structures. They also develop mushroom-like three-dimensional nanostructures within 200-nm wide square photoresist patterns by depositing for 40 minutes as shown in **Fig. 7(d)**. It is noted that arrays of nanoparticle structures with a variety of shapes can be obtained by designing photoresist or mask patterns on the substrates and controlling the deposition time in the IAAL process.

2.5 Applications

IAAL possesses potential to be widely applied to a variety of nanodevices, judging from its advantages that it can be applied to any kinds of particles if they are prepared in the form of charged aerosols, and to both conducting and nonconducting substrates without surface modification. In addition, IAAL can produce arrays of multidimensional, multiscale, and multimaterial structures with a simple parallel atmospheric process.

Using IAAL, You et al.[89] fabricated a gas sensing device which took advantage of the characteristics of ZnO nanoparticles that their electrical conductivity varied according to the concentration of surrounding gases. **Fig. 8(a)** shows a SEM image of the lines of 20-nm ZnO nanoparticles deposited on a 200-nm-thick SiO_2 film supported on a p-type silicon substrate by using an epoxy mask having 50-μm-wide line openings in the IAAL process. The gas-sensing sensitivity of this sensor was evaluated by examining its response to CO and H_2 and, as shown in **Fig. 8(b)**, it exhibits high sensitivity even to the low CO concentration of 1-ppm. Kim et al.[92] also demonstrated a gas sensing device by patterning lines of shell-shaped carbon nanoparticles (SCNP) with IAAL.

In addition, Metal enhanced fluorescence (MEF) was effectively observed by depositing silver nanoparticles into the triangular openings of SiO_2 followed by the selective deposition of fluorescence-tagged protein nanoparticles with IAAL on top of the silver nanoparticle patterns. From this process, one could avoid wasting proteins on the unwanted nonspecific adsorption[88]. **Fig. 8(c)-(e)** show the fluorescence images of IgG-FITC (fluorescein isothiocyanate) (c) without silver particles and (d) with silver particles. Here, the present design of human IgG-FITCs on top of sliver nanoparticles exhibits much strong fluorescent signals compared to the non-silver case.

Surface enhanced Raman scattering (SERS) device provided by IAAL was also demonstrated[93]. SERS substrates fabricated based on three-dimensional nanoparticle structures by utilizing IAAL showed much increased signals compared to two-dimensional cases. Three SERS substrates were prepared by depositing three-dimensional structures of copper nanoparticles for different deposition times, followed by deposition of silver nanoparticles on them since thiophenol did not chemically bind to copper nanoparticles but to silver. **Fig. 8(f)** shows the SEM images of the three SERS substrates and the corresponding Raman spectra of thiophenol on those samples. The Raman spectra clearly indicate that the Raman intensity of the full grown three-dimensional structures was noticeably stronger than the case of non-nanoparticles and the intensity increased as the two-dimensional structures grew to three-dimensional structures.

3. Summary

Development of technologies for highly precise assembling or patterning of nanoparticles over large areas is a prerequisite to realize nanodevices which are presently developed to take advantage of the unique properties of nanoparticles. In response to the demand, many research groups have demonstrated novel methods to manipulate nanoparticles. These methods can be classified according to the governing force which is exploited in manipulating nanoparticles. The three most employed forces are electrostatic, capillary and magnetic forces because they can simultaneously occur in a large area and make it possible to design a parallel process. Among them, electrostatic force, the mostly adopted force to manipulate nanoparticles, has brought out a variety of novel methods such as nanoxerography, electrodynamic focusing, biased p-n junction method, and so on. The methods utilizing capillary phenomenon such as micromolding in capillary, template-assisted assembly and dip-pen nanolithography have also presented well-defined arrays of nanoparticles. In addition, there have been some efforts to manipulate nonmagnetic nanoparticles utilizing magnetic force as well as magnetic nanoparticles. Among those patterning methods, IAAL is one of the effective electrodynamic focusing methods, which employs the ion induced focusing concept and, consequently, produces arrays of highly focused assembly made of nanoparticles in three dimensions. The resolution of the deposited assembly using IAAL is controllable with the following parameters: the surface charge density on the patterned mask, the applied voltage on the substrate, the aspect ratio of the photoresist patterns, and the particle charges. IAAL can be applicable to any kinds of nanoparticles prepared in the form of charged aerosols and does not need any surface modifications of a substrate by means of a nanoparticle patterning mask. It is also applicable to nonconducting substrates as well as conducting substrates. Moreover, three-dimensional assembly of nanoparticles can be easily fabricated with IAAL.

Acknowledgements

This work was supported by the Global Frontier Center for Multiscale Energy Systems funded by National Research Foundation under the Ministry of Education, Science and Technology (2011-0031561). Financial support from BK21 program and WCU (World Class University) multiscale mechanical design program (R31-2008-000-10083-0) through the Korea Research Foundation is gratefully acknowledged. Authors are also affiliated with the Institute of Advanced Machinery and Design, Seoul National University, Seoul 151-742, Republic of Korea.

References

1) Lu, X., Rycenga, M., Skrabalak, S. E., Wiley, B., and Xia, Y. (2009): Chemical Synthesis of Novel Plasmonic Nanoparticles, Annual Review of Physical Chemistry, Vol. 60, pp.167-192.
2) Laurent, S., Forge, D., Port, M., Roch, A., Robic, C., Vander Elst, L., and Muller, R. N. (2008): Magnetic Iron Oxide Nanoparticles: Synthesis, Stabilization, Vectorization, Physicochemical Characterizations, and Biological Applications, Chemical Reviews, Vol. 108, pp.2064-2110.
3) Lümmen, N. and Kraska, T. (2005): Molecular Dynamics Investigation of Homogeneous Nucleation and Dluster Growth of Platinum Clusters from Supersaturated Vapour, Nanotechnology, Vol. 16, pp.2870.
4) Erhart, P. and Albe, K. (2005): Molecular Dynamics Simulations of Gas Phase Condensation of Silicon Carbide Nanoparticles, Advanced Engineering Materials, Vol. 7, pp.937-945.
5) Gao, J., Gu, H., and Xu, B. (2009): Multifunctional Magnetic Nanoparticles: Design, Synthesis, and Biomedical Applications, Accounts of Chemical Research, Vol. 42, pp.1097-1107.
6) Amoruso, S., Ausanio, G., Barone, A. C., Bruzzese, R., Campana, C., and Wang, X. (2007): Nanoparticles Size Modifications during Femtosecond Laser Ablation of Nickel in Vacuum, Applied Surface Science, Vol. 254, pp.1012-1016.
7) Sau, T. K. and Rogach, A. L. (2010): Nonspherical Noble Metal Nanoparticles: Colloid-Chemical Synthesis and Morphology Control, Advanced Materials, Vol. 22, pp.1781-1804.
8) Matsushita, T., Iwamoto, T., Inokuchi, M., and Toshima, N. (2010): Novel Ferromagnetic Materials of $SmCo_5$ Nanoparticles in Single-Nanometer Size: Chemical Syntheses and Characterizations, Nanotechnology, Vol. 21, 095603, doi:10.1088/0957-4484/21/9/095603.
9) Choi, M., Altman, I. S., Kim, Y. J., Pikhitsa, P. V., Lee, S., Park, G. S., Jeong, T., and Yoo, J. B. (2004): Formation of Shell-Shaped Carbon Nanoparticles Above a Critical Laser Power in Irradiated Acetylene, Advanced Materials, Vol. 16, pp.1721-1725.
10) Lee, D. and Choi, M. (2002): Coalescence Enhanced Synthesis of Nanoparticles to Control Size, Morphology and Crystalline Phase at High Concentrations, Journal of Aerosol Science, Vol. 33, pp.1-16.
11) Lee, D., Yang, S., and Choi, M. (2001): Controlled Formation of Nanoparticles Utilizing Laser Irradiation in a Flame and Their Characteristics, Applied Physics Letters, Vol. 79, pp.2459-2461.
12) Sheen, S., Yang, S., Jun, K., and Choi, M. (2009): One-step Flame Method for the Synthesis of Coated Composite Nanoparticles, Journal of Nanoparticle Research, Vol. 11, pp.1767-1775.
13) Lee, D. and Choi, M. (2000): Control of Size and Morphology of Nano Particles Using CO2 Laser During Flame Synthesis, Journal of Aerosol Science, Vol. 31, pp.1145-1163.
14) Altman, I. S., Agranovski, I. E., and Choi, M. (2004): On Nanoparticle Surface Growth: MgO Nanoparticle Formation During a Mg Particle Combustion, Applied Physics Letters, Vol. 84, pp.5130-5132.
15) Han, K., Kim, W., Yu, J., Lee, J., Lee, H., Gyu Woo, C., and Choi, M. (2012): A Study of Pin-to-Plate Type Spark Discharge Generator for Producing Unagglomerated Nanoaerosols, Journal of Aerosol Science, Vol. 52, pp.80-88.
16) Sheen, S., Yang, S., Jun, K., Pikhitsa, P. V., and Choi, M. (2012): Crystallinity Control of Flame Generated

Composite Nanoparticles by Laser Irradiation, Powder Technology, Vol. 229, pp.246-252.

17) Joachim, C., Gimzewski, J. K., and Aviram, A. (2000): Electronics Using Hybrid-Molecular and Mono-Molecular Devices, Nature, Vol. 408, pp.541-548.

18) Alivisatos, A. P. (1996): Semiconductor Clusters, Nanocrystals, and Quantum Dots, Science, Vol. 271, pp.933-937.

19) Murray, C. B., Kagan, C. R., and Bawendi, M. G. (1995): Self-Organization of CdSe Nanocrystallites into Three-Dimensional Quantum Dot Superlattices, Science, Vol. 270, pp.1335-1338.

20) Sun, S., Murray, C. B., Weller, D., Folks, L., and Moser, A. (2000): Monodisperse FePt Nanoparticles and Ferromagnetic FePt Nanocrystal Superlattices, Science, Vol. 287, pp.1989-1992.

21) Daniel, M.-C. and Astruc, D. (2003): Gold Nanoparticles: Assembly, Supramolecular Chemistry, Quantum-Size-Related Properties, and Applications toward Biology, Catalysis, and Nanotechnology, Chemical Reviews, Vol. 104, pp.293-346.

22) Xia, Y., Rogers, J. A., Paul, K. E., and Whitesides, G. M. (1999): Unconventional Methods for Fabricating and Patterning Nanostructures, Chemical Reviews, Vol. 99, pp.1823-1848.

23) Firkowska, I., Giannona, S., Rojas-Chapana, J. A., Luecke, K., Brüstle, O., and Giersig, M. (2008): "Biocompatible Nanomaterials and Nanodevices Promising for Biomedical Applications Nanomaterials for Application in Medicine and Biology", 1st ed., Springer Netherlands.

24) Iwata, F., Kaji, M., Suzuki, A., Ito, S., and Nakao, H. (2009): Local Electrophoresis Deposition of Nanomaterials Assisted by a Laser Trapping Technique, Nanotechnology, Vol. 20, 235303 doi:10.1088/0957-4484/20/23/235303.

25) Seo, H. W., Han, C.-S., Jang, W. S., and Park, J. (2006): Manipulation of Carbon Nanotubes and Nanowires, Current Applied Physics, Vol. 6, pp.e216-e219.

26) Rao, C. N. R. and Cheetham, A. K. (2001): Science and Technology of Nanomaterials: Current Status and Future Prospects, Journal of Materials Chemistry, Vol. 11, pp.2887-2894.

27) Teo, B. K. and Sun, X. H. (2007): Silicon-Based Low-Dimensional Nanomaterials and Nanodevices, Chemical Reviews, Vol. 107, pp.1454-1532.

28) Park, W. I., Lee, C.-H., Chae, J. H., Lee, D. H., and Yi, G.-C. (2009): Ultrafine ZnO Nanowire Electronic Device Arrays Fabricated by Selective Metal–Organic Chemical Vapor Deposition, Small, Vol. 5, pp.181-184.

29) Jacobs, H. O. and Whitesides, G. M. (2001): Submicrometer Patterning of Charge in Thin-Film Electrets, Science, Vol. 291, pp.1763-1766.

30) Wright, W. M. D. and Chetwynd, D. G. (1998): Can Charge Writing Aid Nanotechnological Manipulation?, Nanotechnology, Vol. 9, pp.133-142.

31) Mesquida, P. and Stemmer, A. (2002): Maskless Nanofabrication Using the Electrostatic Attachment of Gold Particles to Electrically Patterned Surfaces, Microelectronic Engineering, Vol. 61-62, pp.671-674.

32) Li, Q., Zheng, J., and Liu, Z. (2002): Site-Selective Assemblies of Gold Nanoparticles on an AFM Tip-Defined Silicon Template, Langmuir, Vol. 19, pp.166-171.

33) Krinke, T. J., Fissan, H., Deppert, K., Magnusson, M. H., and Samuelson, L. (2001): Positioning of Nanometer-Sized Particles on Flat Surfaces by Direct Deposition from the Gas Phase, Applied Physics Letters, Vol. 78, pp.3708-3710.

34) Lowell, J. and Rose-Innes, A. C. (1980): Contact Electrification, Advances in Physics, Vol. 29, pp.947-1023.

35) Mesquida, P. and Stemmer, A. (2001): Attaching Silica Nanoparticles from Suspension onto Surface Charge Patterns Generated by a Conductive Atomic Force Microscope Tip, Advanced Materials, Vol. 13, pp.1395-1398.

36) Fudouzi, H., Kobayashi, M., and Shinya, N. (2002): Site-Controlled Deposition of Microsized Particles Using an Electrostatic Assembly, Advanced Materials, Vol. 14, pp.1649-1652.

37) Fudouzi, H., Kobayashi, M., and Shinya, N. (2002): Assembly of Microsized Colloidal Particles on Electrostatic Regions Patterned through Ion Beam Irradiation, Langmuir, Vol. 18, pp.7648-7652.

38) Kang, M., Kim, H., Han, B., Suh, J., Park, J., and Choi, M. (2004): Nanoparticle Pattern Deposition from Gas Phase onto Charged Flat Surface, Microelectronic Engineering, Vol. 71, pp.229-236.

39) Krinke, T. J., Deppert, K., Magnusson, M. H., and Fissan, H. (2002): Nanostructured Deposition of Nanoparticles from the Gas Phase, Particle & Particle Systems Characterization, Vol. 19, pp.321-326.

40) Lim, K., Lee, J.-R., Lee, H., Pikhitsa, P. V., You, S., Woo, C. G., Kim, P., Suh, K. Y., and Choi, M. (2012): Nanoxerography Utilizing Bipolar Charge Patterns, Submitted to Applied Physics Letters, Vol.

41) Bowden, N., Brittain, S., Evans, A. G., Hutchinson, J. W., and Whitesides, G. M. (1998): Spontaneous Formation of Ordered Structures in Thin Films of Metals Supported on an Elastomeric Polymer, Nature, Vol. 393, pp.146-149.

42) Prost, W., Kruis, F. E., Otten, F., Nielsch, K., Rellinghaus, B., Auer, U., Peled, A., Wassermann, E. F., Fissan, H., and Tegude, F. J. (1998): Monodisperse Aerosol Particle Deposition: Prospects for Nanoelectronics, Microelectronic Engineering, Vol. 41-42, pp.535-538.

43) Otten, F., Auer, U., Kruis, F. E., Prost, W., Tegude, F. J., and Fissan, H. (2002): Lithographic Tools for Producing Patterned Films Composed of Gas Pase Generated Nanocrystals, Materials Science and Technology, Vol. 18, pp.717-720.

44) Jun, T., Verrelli, E., and Tsoukalas, D. (2009): Assembly of Charged Nanoparticles Using Self-Electrodynamic Focusing, Nanotechnology, Vol. 20, pp.365605.

45) van der Eijk, W., Oldenof, W., and Zehner, W. (1973): Preparatio of Thin Sources, a Review, Nuclear Instru-

ments and Methods, Vol. 112, pp.343-351.

46) Kim, H., Kim, J., Yang, H., Suh, J., Kim, T., Han, B., Kim, S., Kim, D. S., Pikhitsa, P. V., and Choi, M. (2006): Parallel Patterning of Nanoparticles via Electrodynamic Focusing of Charged Aerosols, Nature nanotechnology, Vol. 1, pp.117-121.

47) Tsai, D. H., Kim, S. H., Corrigan, T. D., Phaneuf, R. J., and Zachariah, M. R. (2005): Electrostatic-Directed Deposition of Nanoparticles on a Rield Generating Substrate, Nanotechnology, Vol. 16, pp.1856.

48) Ma, L.-C., Subramanian, R., Huang, H.-W., Ray, V., Kim, C.-U., and Koh, S. J. (2007): Electrostatic Funneling for Precise Nanoparticle Placement: A Route to Wafer-Scale Integration, Nano Letters, Vol. 7, pp.439-445.

49) Bowden, N., Choi, I. S., Grzybowski, B. A., and Whitesides, G. M. (1999): Mesoscale Self-Assembly of Hexagonal Plates Using Lateral Capillary Forces: Synthesis Using the “Capillary Bond”, Journal of the American Chemical Society, Vol. 121, pp.5373-5391.

50) Bowden, N., Terfort, A., Carbeck, J., and Whitesides, G. M. (1997): Self-Assembly of Mesoscale Objects into Ordered Two-Dimensional Arrays, Science, Vol. 276, pp.233-235.

51) Chan, D. Y. C., Henry, J. D., and White, L. R. (1981): The Interaction of Colloidal Particles Collected at Fluid Interfaces, Journal of Colloid and Interface Science, Vol. 79, pp.410-418.

52) Grzybowski, B. A., Bowden, N., Arias, F., Yang, H., and Whitesides, G. M. (2000): Modeling of Menisci and Capillary Forces from the Millimeter to the Micrometer Size Range, The Journal of Physical Chemistry B, Vol. 105, pp.404-412.

53) Kralchevsky, P. A. and Nagayama, K. (2000): Capillary Interactions between Particles Bound to Interfaces, Liquid Films and Biomembranes, Advances in Colloid and Interface Science, Vol. 85, pp.145-192.

54) Ohara, P. C., Heath, J. R., and Gelbart, W. M. (1997): Self-Assembly of Submicrometer Rings of Particles from Solutions of Nanoparticles, Angewandte Chemie International Edition in English, Vol. 36, pp.1078-1080.

55) Wang, D. and Mohwald, H. (2004): Template-Directed Colloidal Self-Assembly - the Route to ‘Top-Down’ Nanochemical Engineering, Journal of Materials Chemistry, Vol. 14, pp.459-468.

56) Maury, P., Escalante, M., Reinhoudt, D. N., and Huskens, J. (2005): Directed Assembly of Nanoparticles onto Polymer-Imprinted or Chemically Patterned Templates Fabricated by Nanoimprint Lithography, Advanced Materials, Vol. 17, pp.2718-2723.

57) Malaquin, L., Kraus, T., Schmid, H., Delamarche, E., and Wolf, H. (2007): Controlled Particle Placement through Convective and Capillary Assembly, Langmuir, Vol. 23, pp.11513-11521.

58) Aubry, N., Singh, P., Janjua, M., and Nudurupati, S. (2008): Micro- and Nanoparticles Self-Assembly for Virtually Defect-Free, Adjustable Monolayers, Proceedings of the National Academy of Sciences, Vol. 105, pp.3711-3714.

59) Denkov, N., Velev, O., Kralchevski, P., Ivanov, I., Yoshimura, H., and Nagayama, K. (1992): Mechanism of Formation of Two-Dimensional Crystals from Latex Particles on Substrates, Langmuir, Vol. 8, pp.3183-3190.

60) Kim, E., Xia, Y., and Whitesides, G. M. (1996): Two- and Three-Dimensional Crystallization of Polymeric Microspheres by Micromolding in Capillaries, Advanced Materials, Vol. 8, pp.245-247.

61) Kim, E., Xia, Y., and Whitesides, G. M. (1995): Polymer Microstructures Formed by Moulding in Capillaries, Nature, Vol. 376, pp.581-584.

62) Cui, Y., Björk, M. T., Liddle, J. A., Sönnichsen, C., Boussert, B., and Alivisatos, A. P. (2004): Integration of Colloidal Nanocrystals into Lithographically Patterned Devices, Nano Letters, Vol. 4, pp.1093-1098.

63) Gordon, M. J. and Peyrade, D. (2006): Separation of Colloidal Nanoparticles Using Capillary Immersion Forces, Applied Physics Letters, Vol. 89, pp.053112.

64) Kraus, T., Malaquin, L., Schmid, H., Riess, W., Spencer, N. D., and Wolf, H. (2007): Nanoparticle Printing with Single-Particle Resolution, Nature nanotechnology, Vol. 2, pp.570-576.

65) Xia, Y., Yin, Y., Lu, Y., and McLellan, J. (2003): Template-Assisted Self-Assembly of Spherical Colloids into Complex and Controllable Structures, Advanced Functional Materials, Vol. 13, pp.907-918.

66) Varghese, B., Cheong, F. C., Sindhu, S., Yu, T., Lim, C.-T., Valiyaveettil, S., and Sow, C.-H. (2006): Size Selective Assembly of Colloidal Particles on a Template by Directed Self-Assembly Technique, Langmuir, Vol. 22, pp.8248-8252.

67) Peyrade, D., Gordon, M., Hyvert, G., Berton, K., and Tallal, J. (2006): Direct Observation and Localization of Colloidal Nanoparticles on Patterned Surface by Capillary Forces, Microelectronic Engineering, Vol. 83, pp.1521-1525.

68) Piner, R. D., Zhu, J., Xu, F., Hong, S., and Mirkin, C. A. (1999): “Dip-Pen” Nanolithography, Science, Vol. 283, pp.661-663.

69) Brust, M., Bethell, D., Kiely, C. J., and Schiffrin, D. J. (1998): Self-Assembled Gold Nanoparticle Thin Films with Nonmetallic Optical and Electronic Properties, Langmuir, Vol. 14, pp.5425-5429.

70) Fendler, J. H. (1996): Self-Assembled Nanostructured Materials, Chemistry of Materials, Vol. 8, pp.1616-1624.

71) Junno, T., Magnusson, M. H., Carlsson, S.-B., Deppert, K., Malm, J.-O., Montelius, L., and Samuelson, L. (1999): Single-Electron Devices via Controlled Assembly of Designed Nanoparticles, Microelectronic Engineering, Vol. 47, pp.179-183.

72) McConnell, W. P., Novak, J. P., Brousseau, L. C., Fuierer, R. R., Tenent, R. C., and Feldheim, D. L. (2000): Electronic and Optical Properties of Chemically Modified Metal Nanoparticles and Molecularly Bridged Nanoparticle Arrays, The Journal of Physical Chemis-

try B, Vol. 104, pp.8925-8930.
73) Shipway, A. N., Katz, E., and Willner, I. (2000): Nanoparticle Arrays on Surfaces for Electronic, Optical, and Sensor Applications, ChemPhysChem, Vol. 1, pp.18-52.
74) Taha, H., Lewis, A., and Sukenik, C. (2007): Controlled Deposition of Gold Nanowires on Semiconducting and Nonconducting Surfaces, Nano Letters, Vol. 7, pp.1883-1887.
75) Sung, M. G., Lee, T.-Y., Kim, B., Kim, T. H., and Hong, S. (2009): Uniform Patterning of Sub-50-nm-Scale Au Nanostructures on Insulating Solid Substrate via Dip-Pen Nanolithography, Langmuir, Vol. 26, pp.1507-1511.
76) Basnar, B. and Willner, I. (2009): Dip-Pen-Nanolithographic Patterning of Metallic, Semiconductor, and Metal Oxide Nanostructures on Surfaces, Small, Vol. 5, pp.28-44.
77) Ben Ali, M., Ondarçuhu, T., Brust, M., and Joachim, C. (2002): Atomic Force Microscope Tip Nanoprinting of Gold Nanoclusters, Langmuir, Vol. 18, pp.872-876.
78) Garno, J. C., Yang, Y., Amro, N. A., Cruchon-Dupeyrat, S., Chen, S., and Liu, G.-Y. (2003): Precise Positioning of Nanoparticles on Surfaces Using Scanning Probe Lithography, Nano Letters, Vol. 3, pp.389-395.
79) Thomas, P. J., Kulkarni, G. U., and Rao, C. N. R. (2004): Dip-Pen Lithography Using Aqueous Metal Nanocrystal Dispersions, Journal of Materials Chemistry, Vol. 14, pp.625-628.
80) Wu, B., Ho, A., Moldovan, N., and Espinosa, H. D. (2007): Direct Deposition and Assembly of Gold Colloidal Particles Using a Nanofountain Probe, Langmuir, Vol. 23, pp.9120-9123.
81) Wang, W. M., Stoltenberg, R. M., Liu, S., and Bao, Z. (2008): Direct Patterning of Gold Nanoparticles Using Dip-Pen Nanolithography, ACS Nano, Vol. 2, pp.2135-2142.
82) Li, B., Lu, G., Zhou, X., Cao, X., Boey, F., and Zhang, H. (2009): Controlled Assembly of Gold Nanoparticles and Graphene Oxide Sheets on Dip Pen Nanolithography-Generated Templates, Langmuir, Vol. 25, pp.10455-10458.
83) Ennen, I., Höink, V., Weddemann, A., Hütten, A., Schmalhorst, J., Reiss, G., Waltenberg, C., Jutzi, P., Weis, T., Engel, D., and Ehresmann, A. (2007): Manipulation of Magnetic Nanoparticles by the Strayfield of Magnetically Patterned Ferromagnetic Layers, Applied Physics Letters, Vol. 102, pp.013910.
84) Kiwi, M. (2001): Exchange Bias Theory, Journal of Magnetism and Magnetic Materials, Vol. 234, pp.584-595.
85) Wolf, H. and Birringer, R. (2005): Pattern Formation in an Array of Magnetic Nanoscale Rods Mimics Magnetic-Dipole Interaction-Driven Spinodal Decomposition, Applied Physics Letters, Vol. 98, pp.074303.
86) Yellen, B. B. and Friedman, G. (2004): Programmable Assembly of Heterogeneous Colloidal Particle Arrays, Advanced Materials, Vol. 16, pp.111-115.
87) Yellen, B. B., Hovorka, O., and Friedman, G. (2005): Arranging Matter by Magnetic Nanoparticle Assemblers, Proceedings of the National Academy of Sciences of the United States of America, Vol. 102, pp.8860-8864.
88) Woo, C. G., Shin, H., Jeong, C., Jun, K., Lee, J., Lee, J.-R., Lee, H., You, S., Son, Y., and Choi, M. (2011): Selective Nanopatterning of Protein via Ion-Induced Focusing and its Application to Metal-Enhanced Fluorescence, Small, Vol. 7, pp.1790-1794.
89) You, S., Han, K., Kim, H., Lee, H., Woo, C. G., Jeong, C., Nam, W., and Choi, M. (2010): High-Resolution, Parallel Patterning of Nanoparticles via an Ion-Induced Focusing Mask, Small, Vol. 6, pp.2146-2152.
90) You, S. and Choi, M. (2007): Numerical Simulation of Microscopic Motion and Deposition of Nanoparticles via Electrodynamic Focusing, Journal of Aerosol Science, Vol. 38, pp.1140-1149.
91) Lee, H., You, S., Woo, C. G., Lim, K., Jun, K., and Choi, M. (2009): Focused Patterning of Nanoparticles by Controlling Electric Field Induced Particle Motion, Applied Physics Letters, Vol. 94, pp.053104.
92) Kim, D., Pikhitsa, P. V., Yang, H., and Choi, M. (2011): Room temperature CO and H_2 sensing with carbon nanoparticles, Nanotechnology, Vol. 22, pp.485501.
93) Lee, H., You, S., Pikhitsa, P. V., Kim, J., Kwon, S., Woo, C. G., and Choi, M. (2011): Three-Dimensional Assembly of Nanoparticles from Charged Aerosols, Nano Letters, Vol. 11, pp.119-124.

Author’s short biography

Hyangki Sung

Hyangki Sung received her B.S. degree in Mechanical Engineering from Pohang University of Science and Technology (POSTECH), Korea, in 2010. She is currently working toward her Ph.D. degree in Mechanical and Aerospace Engineering at Seoul National University. Her research interests include assembly of nanoparticles, organic light emitting diodes and organic photovoltaics.

Mansoo Choi

Mansoo Choi received his B.S. (1980) and M.S. (1982) from Seoul National University and Ph.D. (1987) from University of California, Berkeley. After Ph.D., he moved to Chicago to work as an assistant mechanical engineer at Argonne National Laboratory from 1988 to 1991. In 1991, he returned home country, Korea to join in ME department of Seoul National University as an assistant professor and he is now a Professor of School of Mechanical and Aerospace Engineering. He was a Director of National CRI Center for Nano Particle Control from 1997 to 2011. Last year, he became a Director of Global Frontier Center for Multiscale Energy Systems that the Ministry of Education, Science and Technology is going to support up to 2020. As a societal service, he has been working as Co-Editor-in-Chief of the Journal of Aerosol Science from 2004. He served as a Chair for Thermal Engineering Division of KSME in 2009. His current research interests include aerosol synthesis and assembly of nanoparticles and nanodevices.

Synthesis and Applications of Hollow Particles[†]

Masayoshi Fuji[1*], **Yong Sheng Han**[2] **and Chika Takai**[1]
[1] *Advanced Ceramics Research Center, Nagoya Institute of Technology*
[2] *Institute of Process Engineering, Chinese Academy of Science*

Abstract

Hollow particle is a promising material with the special properties of low densities, thermal insulation and distinct optical activity. Due to their potential promising applications in the fields of drug delivery, catalysis and optics, a great effort has been devoted to develop new preparation methods which are collected and reviewed in this paper. All these methods are classified into three groups, namely sacrificed template method, in-situ template method and device-based method based on the characteristics of the methods. The advantage and disadvantage of each method are compared and the trends for preparation are pointed out. In light of the wide applications of hollow particles, the later part of this paper focuses on their potential applications in industry. Their applications are not limited in the fields of papermaking, rubber processing and plastic improvement, but also expanded to electronic, catalytic and biological areas.

Keywords: hollow particle, sacrificial template, core shell, porous

1. Introduction

Hollow particle is a kind of powder contained interior hollow structure. And the hollow structure is usually covered by a solid shell. Hollow particles with dimensions from nanometer to micrometer are becoming a focus in nanoscience and nanotechnology. In particular, hollow nanostructures made of metals are intriguing to be investigated due to their special plasmonic properties[1)] and catalytic activities[2)] totally different from their solid counterparts. For example, gold nanoshells have been synthesized for use as photothermal triggers for drug release and as a contrast-enhancing reagent in optical imaging[3-5)]. Owing to the special properties, such as low density, thermal insulation and prominent optical activities, hollow particles have been applied in many areas which include drug delivery[1,2)], bioencapsulation[6,7)], medical diagnostics[8)], catalysis[2)], plasmonics[1)] and composite electronic and structural materials[9,10)].

Various methods have been developed for preparation of hollow particles. A general route for the preparation of hollow particle is to coat /deposit desired materials on the surface of templates followed by the removal of template. The templates usually used include organic spheres[11-17)], inorganic particles[18)] and metal crystals[19)]. All these templates have to be removed after the coating process. The method involved these kinds of templates are called scarified template method[20,21)]. In addition, a great effort has been devoted to simply the preparation of hollow particles and developed in-situ template method which uses the reactant or product as template. The desired materials coat on the surface of reactants/product which are consumed in the later reaction, leading to the formation of hollow particles. The advantage of the new approaches is to save the process of template removal and to simplify the two-step process to one-step process. Besides, some device-based approaches are developed for the preparation of hollow particles, such as nozzle-based method. All these methods are reviewed in this paper and the comparison and analysis are elaborated.

[†] Accepted: August 24, 2012

[1] 3-101-1, Honmachi, Tajimi, Gifu 507-0033, JAPAN
[2] No. 1 Zhongguancun North Second Street, Beijing 100190, P.R. CHINA
[*] Corresponding author:
E-mail: fuji@nitech.ac.jp
TEL: +81-572-24-8110 FAX: +81-572-24-8109

ⓒ 2013 Hosokawa Powder Technology Foundation

2. Synthesis of Hollow Particles

In this paper, based on the different kinds of templates, the methods to prepare hollow particles were reviewed and classified into three groups, namely sacrificed template methods, in-situ template methods and device-based methods. Each group includes several methods with similar characteristics.

2.1 Sacrificed template method

This kind of methods were characterized with the preparation of hollow particles by coating a template (such as polymer bead, emulsion and inorganic colloids) with a thin layer of the precursor through sol-gel process or layer-by-layer (LBL) self-assembly technique[22] and subsequent removal of the template via a thermal decomposition or a chemical dissolution[23].

2.1.1 Organic bead template method

This method is designed to prepare hollow particles by using some organic beads (for example polystyrene spheres) as templates which are coated by desired materials (such as silica (SiO_2)[24], zirconia[25], zeolite[26], manganese oxide (MgO)[27], magnetite[28], zinc sulfide[29], cadmium sulphide (CdS)[30]) via deposition or electrostatic attraction[31]. After coating, the organic cores are removed by calcinations or decomposition to solvent, forming hollow particles. **Fig. 1** is the scheme illustration of this method.

F. Caruso and his colleagues have done many interesting works in this area[24,28,32]. They introduced a LBL self-assembly technique to this method. The LBL technique is a process to fabricate films on the surface of flat or spherical substance by alternating depositions of oppositely charged species based on electrostatic interaction or hydrogen bonding[33-39]. Caruso and co-workers have reported on the fabrication of hollow inorganic silica via the electrostatic LBL self-assembly of SiO_2 nanoparticle on the surface of PS latex particles. The PS particles with diameter of 640nm were firstly coated with polymer films to provide a smooth and positively charge surface. Then SiO_2 nanoparticles with negatively charged surface were coated on the surface of modified PS particles. For multi-coating, the polymer and silica were alternate adsorption on the PS template. The PS templates were removed by calcinations at 500℃. Then the hollow silica particles were prepared, as shown in **Fig. 2**. The advantage of this method is the readily permitted control of film thickness by variation of coating cycles.

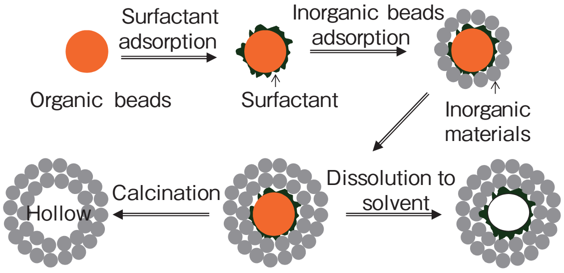

Fig. 1 Illustration for preparing inorganic hollow spheres with organic bead template[24].

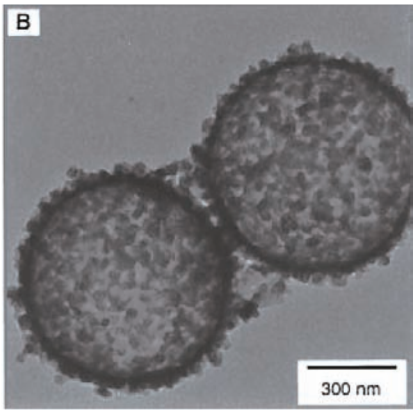

Fig. 2 TEM micrograph of hollow SiO_2 particles prepared by organic bead template[24].

Shell microstructures including shell thickness are important factors to realize functionalities of hollow particles. Fuji and his co-workers have prepared hollow silica nanoparticles through fabrication of core-shell particles whose shell was derived from sol-gel reaction of silicon alkoxide (tetraethoxysilane, TEOS). In this method, fine SiO_2 particles from hydrolysis and condensation of TEOS adsorb at the template surface to form a thin and dense SiO_2 layer. According to Iler, sol-gel reacting conditions such as pH, reaction time, and temperature strongly affect size and morphology of the formed fine SiO_2 particles[40]. Based on this theory, preparation technique to control shell microstructure was developed. They also proposed that the shell microstructure difference can be organized by apparent shell density which is defined by specific surface area and shell thickness. The apparent shell density of the obtained hollow SiO_2 nanoparticles has been controlled within the range between 1.14 and 2.2 g/cm^3 [41].

Beside hollow silica, hollow magnetite (Fe_3O_4) have been prepared by coating submicrometer-sized PS templates with magnetite (Fe_3O_4) layers alternately adsorbed with polyelectrolyte (PE)[28]. For the precursor sensitive to water and readily hydrolyzing and condensing upon direct contact with water, they proposed a new route that combines LBL colloid templating and *in-situ* sol-gel processes by exploiting polyelectrolyte multilayer-coated PS particles as templates. The use of PE-coated spheres as templates overcomes the common problem of particle aggregation by localizing the reactions within the thin PE coatings on the colloids[32].

Hollow calcium carbonate ($CaCO_3$) particles have also been fabricated by the organic bead template method. **Fig. 3** showed the hollow porous shells of crystalline $CaCO_3$ prepared by using micrometer-sized PS beads as the templates[42]. Monodisperse PS spheres with a uniform diameter of 1.09 μm were covered by a film of microemulsions which contained tetradecane and supersaturated aqueous calcium bicarbonate ($Ca(HCO_3)_2$) solution, and washed repeatedly in hot hexane. Loss of carbon dioxide (CO_2) at the air-water interface resulted in aragonite crystallization within the continuous aqueous layer surrounding the oil droplets. Removal of the surfactants and oil leaded to the formation of continuous cellular film of aragonite over the surface of polymer beads, followed by heat treatment of the mineral shell at 400℃, produced microshells of porous aragonite. The hollow shells were uniform in size with an external diameter and wall thickness of 1.35 μm and 125 nm, respectively. Kojima and Yasue[43] also synthesized hollow $CaCO_3$ via the organic template method.

Other hollow particles prepared by organic bead template method with the combination of LBL techniques include hollow MgO particles[44], hollow zeolite particle[45], hollow clay particles[46], hollow zinc oxide (ZnO)[47,48], hollow copper and copper compound particles[49].

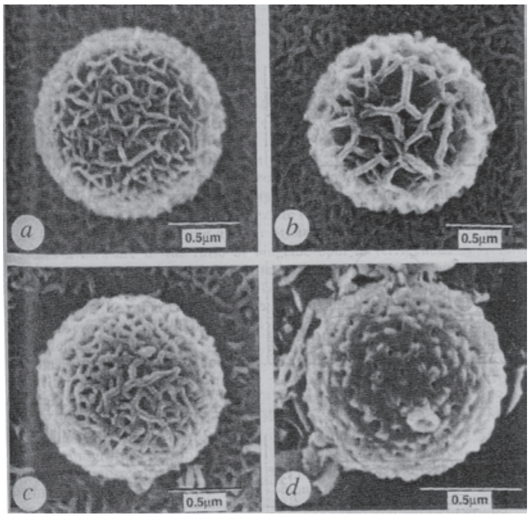

Fig. 3 SEM images of the synthetic aragonite shells[42].

One more interesting report is that X. Zhang and co-worker[50] have prepared cadmium selenide (CdSe) hollow spheres via an *in-situ* polymerization template under ultraviolet irradiation since the organic monomer have a tendency to rapid cross-link polymerization and form networks under high-energy irradiation. The obtained polymer from random coils restrains the appearance of special morphology and can provide the template to control the morphologies of CdSe. Based on the same idea, Y. Hu and co-workers[51] have prepared hollow nickel sulfide (NiS) sphere by using in-situ polymerization template.

2.1.2 Emulsion template method

An emulsion is defined as a heterogeneous system, consisting of at least two immiscible liquid or phase. Since emulsion is thermodynamically unstable, rearrangement from droplet into two bulks liquid is ready to occur with a net reduction of interfacial area, which is energetically favourable. So the surfactants or polymer, which can stabilize emulsion are necessary to use in the emulsion system. The emulsion template method is a process to fabricate hollow particles by localizing the reaction on the surface of emulsion and forming a solid shell. After removal of the emulsion template by calcination or solvent dissolution, hollow particles are obtained. The emulsion template is generally classified into two types. One is water-in-oil (w/o) templates which have oil continuous phase with water droplets. Another is oil-in-water (o/w) templates which have water continuous phase with oil droplets. The formation of these two kinds of emulsion is determined by the weight ratio of water and oil. High weight ratio of oil lead to the formation of w/o templates while high weight ratio of water result in the formation of o/w templates. The choice of which kinds of templates is determined by the reactants and reactions.

The emulsion template method has been successfully used to prepare hollow SiO_2 particle. J. H. Park and co-workers[52,53] have prepared hollow SiO_2 particles in the w/o emulsion with the presence of surfactants. Their preparation procedures can be briefly described as following: First, an external oil phase was prepared by dissolving hydroxyl propyl cellulose (HPC) in octanol. Here HPC is a stabilizer of emulsion structure. Second, polyvinylpyrrolidone (PVPC) which was used to control the viscosity of water droplet was dissolved into water. Third, the water phase was added to an external oil phase at a stirring rate of 12000 rpm to form a stable emulsion. Then, the reagent TEOS was added into w/o emulsions. TEOS is soluble in the continuous oil phase, but it because water-soluble after its hydrolysis. After hydrolysis, the samples were dried and calcined to form hollow structure. The hollow SiO_2 particles produced by this method are shown in **Fig. 4**.

M. Jafelicci Jr. and co-worker[54] also prepared hollow SiO_2 particles by the w/o emulsion template method. They added a fixed volume of aqueous phase (acid solution) to the heptane solution with surfactants, and then sodium silicate (Na_2SiO_3) diluted solution was added to the previously obtained microemulsion and sonicated. As hydrolysis and condensation of TEOS are pH sensitive reactions, they progress in acid medium, such as that of microemulsion interface region where is chemically adequate for a precipitation reaction to take place and form a SiO_2 inner shell, consuming Na_2SiO_3 and hydroxonium ion (H_3O^+). **Fig. 5** shows the model of microemulsion reactor.

The reports on preparation of hollow SiO_2 particles by emulsion template method also include reference[55] to reference [58].

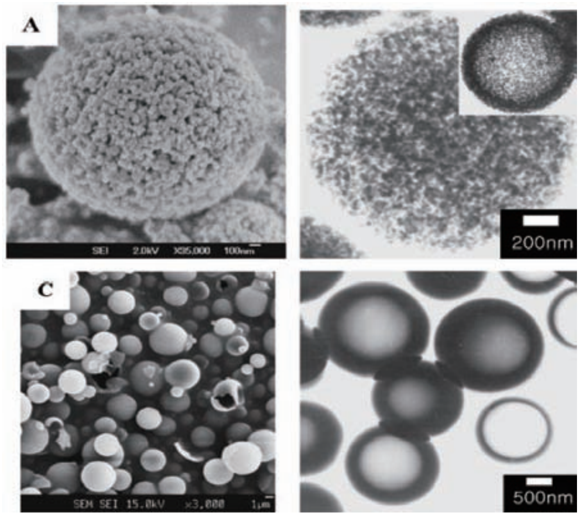

Fig. 4 SEM (A,C) and TEM (B,D) of hollow SiO_2 particles[53].

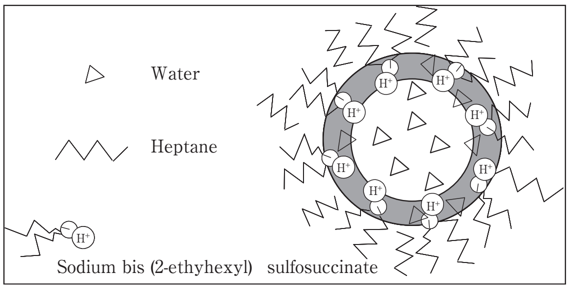

Fig. 5 Schematic representation of microemulsion model[54].

Except hollow SiO_2, hollow $CaCO_3$ particles have also been prepared by w/o emulsion template method. For example, D. Walsh and co-workers[59] reported a facile and high yield approach to produce spherical particles of crystalline $CaCO_3$ (vaterite) with an elaborate sponge-like micro architecture. J. A. Thomas and co-workers[60] also prepared $CaCO_3$ microcapsules for the encapsulation of organic and inorganic substrates using a liquid emulsion system. They prepared the emulsion by mixing a solution of 3.0 M sodium carbonate (Na_2CO_3) which contains the materials to be encapsulated within the oil membrane phase. The two phases were mixed together until a homogeneous macro-emulsion was formed. This w/o emulsion was then added to a solution of calcium chloride ($CaCl_2$) or calcium nitrate ($Ca(NO_3)_2$). Based on work by Nakahara[61], this method allows calcium ions (Ca^{2+}) to diffuse across the oil membrane into internal aqueous droplets that contains the materials to be encapsulated. Carbonate ions (CO_3^{2-}) in the internal aqueous phase react with the diffused Ca^{2+} at the o/w interface and solid $CaCO_3$ in the metastable vaterite form precipitates at the interface, encapsulating the materials dispersed in this phase. The vaterite spheres are prone to transformation to the more stable calcite polymorphy, which would destroy the capsules. In order to prevent this transformation and stabilize the vaterite, L-glutamic acid, a known inhibitor of calcite crystallization was added to the aqueous phase prior to precipitation. After decantation and centrifugation, hollow vaterite spheres inside with desired substance were obtained.

In addition to w/o emulsion template, the o/w template had also been applied to fabricate hollow particles. A. D. Dinsmone and co-worker[62] reported a flexible approach to produce hollow elastic capsules, with size ranging from micrometers to millimeters. Their fabrication process used controlled self-assembly in three steps. First, aqueous solution is added to oil containing colloid particles which were then adsorbed on the surface of emulsion droplets. Second, particles are adsorbed automatically onto the surface of the droplet to reduce the total surface area. After the droplet surface is completely covered by particles, these particles are subsequently locked together by addition of polycations. Third, if required, the capsules are transferred to water by centrifugation. The resultant structures, which are called “colloidosome” , are hollow, elastic shells whose permeability and elasticity can be precisely controlled.

M. M. Wu and co-workers[63] reported to prepare hollow bead titanate particles via an o/w emulsion template. The reactants titanium butoxide is just hydrolyzed at the o/w interface where the shells are formed through condensation. The morphology of lead titanate shells reflects the shape of oil spheres at the micrometer scale, indicating the reaction happening at the interface of emulsion. Hollow latex particles have also been prepared via o/w emulsion template by controlling the charged colloids adsorption around the emulsion droplets[64].

Besides, T. Nakashima and N. Kimizuka[65] have prepared hollow titania (TiO_2) particles in ionic liquids based on the limited miscibility of toluene with the ionic liquids. Microsized droplets are formed in the ionic liquid under vigorous stirring and the $Ti(OBt)_4$ molecules in the microdroplets are hydrolyzed selectively at the interface, resulting in the formation of smooth and hollow TiO_2 particles.

2.1.3 Surfactant vesicle template method

Amphiphilic block copolymers in water can self-assemble into various ordered mesospheres[66-70]. For example, low molecular weight macromolecular surfactants produced spheres which are readily dispersed in water at low concentration as spherical vesicles with the polar head group assemble together, creating a water core that is typically 10-100 nm in diameter[71,72]. F. Caruso and co-workers[73,74] have developed a technique for the preparation of monodisperse vesicles comprising asymmetric lipid bilayers supported on colloidal particles. The monodisperse asymmetric lipid-coated colloids were prepared by depositing two lipids which can form the inner and outer monolayers. Following formation of the lipid bilayer membranes, the core templates were removed by acid treatment to obtain vesicular particles.

The spherical vesicles can be used as template for preparation of hollow particles based on the hydrolysis and cross-linking of inorganic precursors at the surface of supramolecular surfactant assemblies. P. T. Tanev and T. J. Pinnavaia[75] have prepared hollow SiO_2 using surfactants vesicles as templates. Their approach is based on the hydrolysis of an inorganic alkoxide precursor in the interlayered regions of multilamellar vesiculars of surfactant that contains two polar head groups linked by a hydrophobic alkyl chain. The multilamellar regions of the vesicles are composed of closed packed layers of surfactant separated by water layers. The additions of TEOS penetrate the vesicle interface, diffuse into the multilamellar regions, and participate in hydrogen-bonding interactions with the lone electron pairs on the surfactant head groups. The simultaneous growth of the parallel SiO_2 layer leads to the formation of hollow particles.

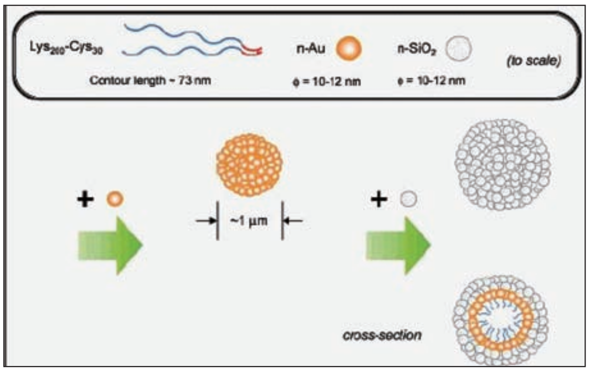

Fig. 6 Scheme of self-assembly of Au and SiO_2 nanoparticles[77].

T. Z. Ren and co-workers[76] prepared hollow TiO_2 microspheres with mesoporous crystalline shells with the assistance of non-ionic poly (alkylene oxide) surfactant molecules. The preparation of hollow TiO_2 microspheres was performed in a ethanol-surfactant system using decaoxyethylene cetyl ether ($C1_6(EO)_{10}$) surfactant as the template. M. S. Wong and co-worker[77] have reported a room temperature and wet chemical-based synthesis route in which SiO_2 and gold (Au) nanoparticles are cooperatively assembled with lysine-cysteine diblock copolypeptides into robust hollow spheres. Key determinants in the formation of the Au/SiO_2 hollow sphere (as shown in **Fig. 6**) are the ability of the sulfydryl group to form inter and intrachair disulfide bonds and the formation of the Au-thiolate bonds. Hollow sphere was formed only when the copolypetide was reacted with n-Au prior to reacting with n-SiO_2. The n-Au particles were thus found copolypeptide chains into the microsized aggregated around which n-SiO_2 attached. The scheme illustration of the assembly process is shown in **Fig. 6**.

Other hollow particles prepared by surfactants vesicles templates method include hollow $CaCO_3$[78], hollow zirconium oxide (ZrO_2)[79], hollow PS[80], and hollow aluminosilicate[81].

2.1.4 $CaCO_3$ template method

Recently, some researchers proposed to use nano-sized $CaCO_3$ as the sacrificed templates to prepare hollow particles[82-85]. M. Fuji and his colleagues firstly reported the preparation of nano-sized hollow SiO_2 particle using fine $CaCO_3$ particles as templates[18,87,88]. The hollow SiO_2 particles were prepared by coating SiO_2 layer on the surface of $CaCO_3$ particles via sol-gel process, followed by the removal of $CaCO_3$ template through acid etching. Then hollow particles with different morphologies (such as spherical, cubic and tube) were prepared by choosing the different crystal templates (vaterite, calcite and aragonite)[88]. They also showed that "skeletal" SiO_2 nanoparticles which consist of twelve SiO_2 nanoframe and six square windows using cubic-shaped calcite template whose surface was covered by organic acid. By control affinity between the organic acid and reaction solvent, skeletal SiO_2 nanoparticles can be obtained completely separately from hollow SiO_2 nanoparticles[89].

J. F. Chen and co-workers[90,91] have also done many interesting work in the area. They fabricated porous hollow SiO_2 particles by using $CaCO_3$ as templates. In their experiments, $CaCO_3$ nanoparticles were firstly modified by surfactants. Then the silica precursor ($NaSiO_3 \cdot 9H_2O$) was added into the solution. After the reaction, the core-shell composite with $CaCO_3$ as the core and SiO_2 as shell were prepared. The $CaCO_3$ cores were finally removed by acid etching (in HCl solution). The preparation procedure is illustrated as **Fig. 7**.

As further research, J. F. Chen developed a double-template method in which the $CaCO_3$ nanoparticles served as templates and the cetyltrimethylammonium bromide (CTAB) as shell structure directing agents. The prepared hollow particles have an average external diameter of about 85 nm with disordered mesopores shells[92].

Other carbonate templates include manganese carbonate ($MnCO_3$) which has been used to prepare hollow particles for encapsulation of deoxyribonucleic acid (DNA)[93]. $MnCO_3$ particles with diameter of 4 μm were used as template. The water insoluble DNA/sperimidine (Sp) complex was precipitated on the surface of $MnCO_3$ template. Further alternated LBL assembly of biocompatible poly[β-glucuronic acid-(1, 3)-N-acetyl-β-galactosamine-6-sulfate-(1, 4)] (PG)/poly(-L-arginine) (PA) shell was carried out. At the final step, $MnCO_3$ template particles were dissolved in HCl solution. As a result, biocompatible PG/PA capsules containing DNA/SP complex were obtained.

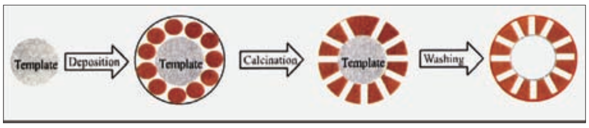

Fig. 7 Illustration on preparation of hollow porous SiO_2 particles prepared by $CaCO_3$ template method[91].

2.1.5 SiO_2 template method

SiO_2 particles with size ranging from nanometer to micrometer can be used as templates for preparation of hollow particles since they are easily decomposed into silyl tetrafluoride by a hydrofluoric acid (HF) solution. For example, Y. Itoh and co-workers[94] have prepared biodegradable hollow nanocapsules by an alternate LBL assembly of cationic chitosan (CT) and anionic dextran sulphate (Dex) on the surface of SiO_2 template. The assembly of the ultrathin polymer films on the SiO_2 nanoparticles was confirmed by microelectrophoresis. After coating, the SiO_2 templates were etched by HF solution, and hollow capsules were obtained. The particles size of prepared hollow capsules can be easily controlled from a nanometer to micrometer, depending on the size of the SiO_2 template.

F. Caruso and co-workers have reported to use mesoporous SiO_2 (MS) spheres as sacrificial template for both enzyme immobilization and PE multilayer capsule formation by PE coating on the surface of the catalase-adsorbed MS through LBL technique[95,96]. The MS templates were removed by exposure to HF. Their results indicated that the catalase encapsulated in biocompatible microcapsules can be released by pH- or salt- induced permeability changes.

S. B. Yoon and co-workers[97] have prepared hollow carbon particles by using SiO_2 spheres with solid core and mesoporous shell (SCMS) structures as templates. Phenol and formaldehyde were incorporated into the mesoporous shell, further carbonized to obtain carbon/aluminosilicate nanoparticles. The dissolution of the aluminosilicate template using either sodium hydroxide (NaOH) or HF solution generated hollow core and mesoporous shell carbon capsules. T. K. Mandal and co-workers[98] have prepared uniform hollow polymer microspheres by coating SiO_2 microsphere template with poly(benzyl methacrylate) using surface-initiated control radical polymerization and subsequently removing the core by HF etching. Shell thickness was controlled by varying the polymerization time. Y. Xia and co-workers[99] have synthesized polymer hollow spheres inside with a movable Au nanoparticle by using SiO_2 template. First, they coated the Au nanoparticle with uniform shells of amorphous SiO_2 derived from TEOS precursor. Second, uniform polymer shell with controllable thickness were formed on the SiO_2 surface. Finally, the SiO_2 shell sandwiched between Au core and the polymer shell was selectively dissolved using aqueous HF to generate hollow particles containing movable Au nanoparticle. The encapsulated u nanoparticle provides an optical probe for monitoring the diffusion of chemical reagents into and out of the polymer shells. Besides, hollow TiO_2[100] and hollow silicon carbide (SiC)[101] have also been prepared by using SiO_2 as template.

In this method, the choice of SiO_2 template is very important in producing efficient hollow particles because the properties of the templates, such as size, shape and ease of removal, govern the properties of the resultant hollow particles.

2.1.6 Hydroxyapatite (HAp) template method

HAp ($Ca_{10}(PO_4)_6(OH)_2$) is low cost materials that can be prepared in nanoparticles with high level of monodispersity and reproducibility. Synthetic HAp particles were prepared by the wet method in which molar ratio of Ca^{2+} and phosphate ions (PO_4^{3-}) was adjusted. The HAp surface possesses several kinds of P-OH group act as adsorption sites for various molecules, which are influenced by synthetic process like calcined temperature, additives, and so on. The number of surface P-OH groups determines various surface properties, for instance, acidity and basicity, affinity and reactivity to molecules and catalytic activity. Besides, HAp templates can be easily dissociated at mild acid concentrations and no special equipment is needed to recycle the dissolved HAp particles[102].

When using HAp as an inorganic template for hollow particle, such good affinity between HAp surface and shell species can be expected to form core-shell particle. The synthetic processes also provide various shapes to obtained HAp particles. Green and his coworkers synthesized hollow SiO_2 nanoparticles with HAp-replicated shapes such as rod-like and spherical[103]. Mesoporous SiO_2 shell can be obtained by using CTAB as a structure directing agent[103] while shell with micro-pores formed without any agent[104].

2.2 *In-situ* template method

Recently, some new and interesting results have been reported to fabricate hollow particles without using the additional template, which was called *in-situ* template method. The *in-situ* template method includes *in-situ* reactant template method and *in-situ* product template method. For *in-situ* reactant template method, hollow particles are formed by directly coating/precipitation nanocrystals on the surface of reactants that would be consumed in the following reactions. After reaction, the templates are consumed and hollow particles are directly obtained without the further treatment to remove the templates. For *in-situ* product templates method, hollow particles were formed on the surface of interim product which can be removed after reaction.

2.2.1 *In-situ* reactant template method

In such a process, one of reactants acts as the template for the formation of hollow particles. The advantage of utilizing such a template is that the template is automatically removed at the end of the reaction, which avoids the step of removing templates to obtain hollow products.

Y. Xia and his colleagues have done many interesting researches in this area. They have reported a procedure based on replacement reaction to generate nanoshells from various metals[19]. The mechanism of this process was illuminated with the Au/silver (Ag) combination as an example. Because the standard reaction potential of $AuCl_4^-$/Au redox pair (0.99V vs. the standard hydrogen electrode (SHE)) is higher than that of the Ag^+/Ag redox pair (0.80V vs. SHE), Ag nanoparticles are immediately oxidized to Ag+ when mixed with an aqueous chloroauric acid ($HAuCl_4$) solution[105] as shown in following chemical reaction (1).

$$3\,Ag\,(s) + AnCl_4^-\,(aq) = Au\,(s) + 3\,Ag^+\,(aq) + 4\,Cl^-\,(aq) \qquad (1)$$

The elemental Au should be mainly confined to the vicinity of the template surface. Once the concentration of Au atoms has reached a critical value, they will nucleate and grow into small clusters and eventually evolve into a shell-like structure around the Ag template.

The major steps involved in this process are shown in **Fig. 8**[106]. (A) Initiation of replacement reaction at a specific spot with relatively high surface energy; (B) Continuation of the replacement reaction between Ag and $HAuCl_4$ and the formation of a partially hollow nanostructure; (C) Formation of nanoboxes with a uniform, smooth, homogeneous wall composed of Au-Ag alloy; (D) Initiation of dealloying and morphological reconstruction of Au-Ag nanobox; (E, F) Continuation of dealloying, together with the formation of pores in the wall; and (G) Fragmentation of the porous Au nanobox. The cross-sectional views correspond to the plane along dashed lines.

Dr. Xia and other group have successfully prepared Ag nanostructures exhibiting a range of morphologies that include spheres, triangular plate, cubes, rods and wires[96-101]. By reaction these Ag nanostructures with aqueous $HAuCl_4$ solution, Dr. Xia have generated hollow structures of Au with various

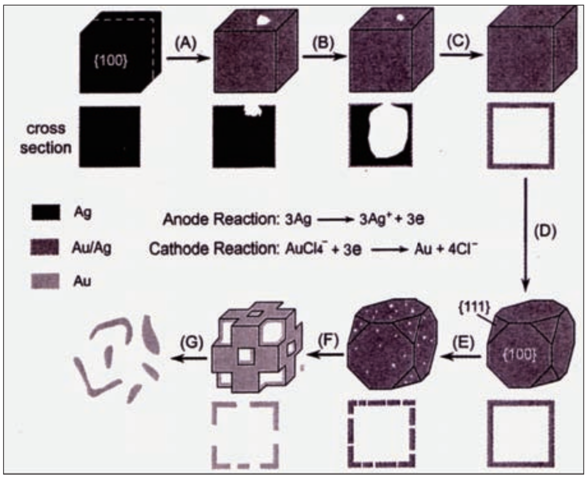

Fig. 8 Schematic illustrations on the preparation of porous Au nanoshell by templating again Ag nanoparticles106).

morphologies, similar those of the Ag templates. Besides, Dr. Xia and co-workers107) have prepared hollow platinum (Pt) with controllable dimensions using trigonal selenium (t-Se) as templates. A little difference is that the t-Se core are not fully consumed during the reduction of Pt^{2+} and the t-Se template were completely removed by soaking the sample in pure hydrazine monohydrate liquid after the formation of Pt shell. The galvanic displace reaction has also been exploited by other researchers108) to fabricate hollow cobalt-platinum (CoPt) nanostructures using Co nanoparticles as templates.

Y. Yin and co-worker109) also prepared hollow structure nanocrystals (such as cobalt sulphide (CoS)) by using cobalt nanocrystal as templates. The hollow CoS nanospheres were synthesized by immediate injection of a solution of sulphur (S) into hot Co nanocrystal dispersion. The reaction between Co and S results in the formation CoS shell at the surface of Co. After Co was consumed, hollow particles were obtained. But they attributed the formation of hollow particles to Kirkendall effect in which the mutual diffusion rates of vacancies and Co in a diffusion couple differ by a considerable amount, resulting in the void formation inside. As the reaction start, Co atoms diffuse out to the shell and the accompanying transport of vacancies leads to the formation of void inside. The authors have pointed out the formation of hollow particles by galvanic displace reactions may also involves this phenomenon.

Besides, Y. Qian and co-workers have also prepared some hollow particles by *in-situ* template method. For example, they prepared hollow bismuth telluride iodide (BiTeI) using bismuth telluride (Bi_2Te_3) as template110), hollow carbides using sodium as templates111) hollow CdS using carbon disulfide (CS_2) as template112). J. J. Zhu an co-workers113) prepared hollow CdSe using the reactant cadmium hydroxide ($Cd(OH)_2$) as templates with the assistance of sonochemistry. The use of sonication provided some active spots on the surface of $Cd(OH)_2$ for the formation of CdSe nuclei.

2.2.2 *In-situ* product template method

This method refers to the method to prepare hollow particles by using interim product or by product as template. After reaction, the templates are removed by selective etching or thermal decomposition, resulting in the formation of hollow particles. Y. Qian and co-workers114) have prepared hollow titanium carbide (TiC) spheres by using titanium tetrachloride ($TiCl_4$) nanotube and sodium as starting materials. They attributed the formation of hollow TiC particles to the small vesicles templates which were generated by gasification of $TiCl_4$ reactant. G. Hu and co-workers115) has prepared hollow carbon spheres using hexachlorobenzene (HCB) and sodium as starting materials. However, they ascribed the templates to sodium chloride (NaCl) particles generated in the start of reactions. In addition, Y. Xie116) also attributed the formation of their prepared hollow boron nitride (BN) particles to the templates of sodium bromide (NaBr) which is a by-product of the reaction. Even though their reaction and results are similar, their explanations on the formation of hollow particles are different. Further investigations are necessary to discover the truth of this mechanism.

Some researchers proposed to prepare hollow particles by using metal nanocrystals as templates which are generated in the reactions. The metal templates are removed by selective dissolution or sublimation after the formation of solid shell. For example, Z. Wang and co-workers117) have prepared ZnO cages and shells by using solidified zinc (Zn) nanocrystals as templates via a process comprised of solidification of liquid Zn droplets, surface oxidation, and sublimation. B. Liu and H. C. Zhang118) also fabricated hollow ZnO particles by using metallic Zn particles as templates via a modified Kirkendall process. While A. M. Herring119) prepared hollow carbon nanospheres from cellulose chars by using a reduction product of nickel (Ni) nanocrystals as templates. The Ni templates were removed by acid etching.

Besides, some researchers120-124) have reported that they have prepared hollow particles without using templates. Actually, even they did not add template at the start of reaction, the formation of hollow particles also involved the templates which were formed during reactions. For example, H. J. Hah and co-workers[120] have prepared hollow SiO_2 particles without using templates. Their preparation procedure included two steps. In the first step, the hydrolysis of phenyltrimethoxysilane (PTMS) was performed under acid conditions. In the second step, the condensation of the silane progressed under basic conditions. When PTMS was added to the acid solution in the first step, PTMS is immiscible with the aqueous solution and phase separation occurs in the mixed solution. Under stirring conditions, droplets of PTMS were formed and became smaller gradually due to miscibility of hydrolyzed PTMS with aqueous solution as the hydrolysis progresses. In the second step, after the addition of NaOH, the condensation is commenced immediately. The production of methanol caused by hydrolysis has an effect on the solubility of the underhydrolyzed PTMS, existent in the interior of droplets in the aqueous solution. The release of the unhydrolyzed PTMS with methanol from the droplets coincides with the formation of hollow SiO_2 particles.

2.2.3 Bubble template method

Bubble template method is novel process to prepare hollow particles by using bubbles as templates, proposed by M. Takahashi and his colleague[125] in Nagoya Institute of Technology, Japan. In this method, bubble is not only the template for hollow particles, but also one of reactants. Part of bubble dissolve into solution and reacted with the species in solution, forming nanocrystals. Owing to the high special surface areas, the newly-formed nanocrystals tend to assemble on the surface of left bubble and form a solid shell. After separation, the pure and clean hollow particles are obtained.

To test the feasibility of bubble template, a single bubble was used as a template with the purpose to observe a direct evidence of crystal nucleation on the surface of bubble[113]. A single ammonia (NH_3) bubble generated by a capillary tube was passed into a SiO_2 sol. After the bubble was passed into sol, the sol started to gel on the surface of bubble and bubble was completely coated by gel at last. This result indicated that it is possible for nanocrystals nucleated or coated on the surface of bubbles. It was shown that bubble surface in aqueous solution would maintain chemical compositions distinct from those of the bulk liquid. The presence of a chemical heterogeneity at the bubble liquid interface would lower the surface energy which would promote the assembling of crystals on the surface of bubbles.

In the following, hollow $CaCO_3$ particles have been successfully prepared by bubble template method via bubbling CO_2/nitrogen (N_2) mixed gas into $CaCl_2$ solution. When the mixed gases were passed into $CaCl_2$ solution, the CO_2 gas dissolve into solution and react with Ca^{2+}, forming $CaCO_3$ precipitates which are not stable and ready to attach on the surface of left bubbles to reach a minimum of total surface free energy. With the progress of reaction, the bubbles were completely coated by precipitates and formed a solid shell. After filtering and drying, the hollow $CaCO_3$ particles were obtained, as shown in **Fig. 9**[125,126].

The results of x-ray diffraction (XRD) measurements showed that the hollow particles were mainly composed of vaterite. In the case of calcium carbonate, three polymorphs, namely calcite, vaterite and aragonite are often found in crystallization from aqueous solution. The formation of specific form depends on the crystallization conditions (such as temperature, pH and supersaturation)[127-131]. Generally speaking, spherical vaterite is helpful to form stable hollow structures compared with other two polymorphs. Therefore, it is an important step to stabilize vaterite for the formation of hollow particles in this process. J. A. Thomas and co-workers have reported that stabilization of the vaterite by the addition of L-glutamic acid surfactant[60]. Besides, investigation of B. D. Chen and co-workers[132] indicated that the addition of surfactants leaded to the stability of bubbles and induced template nucleation on the surface of bubbles. This result inspired us to further improve the formation of hollow particles by using some surfactants. The surfactants are expected to have two functions. One is to stable the bubbles in solution. Second is to make the nanocrystals ready to assemble on the surface of bubble. Cationic, anionic and non-ionic surfactants have been tried in experiments. The results indicated that cationic surfactants play a positive effect on the

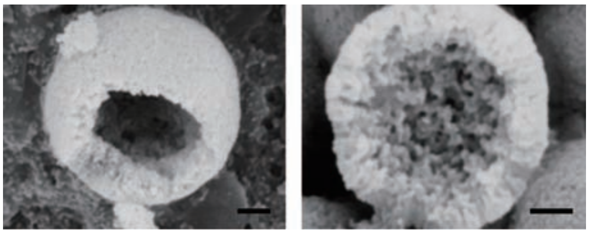
(a) (b)

Fig. 9 Hollow $CaCO_3$ particles of (a) broken and (b) cross-section areas which were prepared by bubble template method. Scale bars are 1 μm.

formation of hollow particles.

Recently, bubble template method has been used to prepare hollow ZnO by passing ammonia bubbles into zinc chloride ($ZnCl_2$) solution at 90℃. It was found that the prepared samples are ZnO tube with a diameter of 300-500 nm and average length of 5μm. The formation of ZnO nanotubes is attributed to the precipitation of ZnO on the surface of floating bubbles[133,134].

Detail mechanism of hollow structure formation using bubble is still on the way of investigation. Recently, Fuji and his co-workers reported how CO_2 gas bubbles affected formation of hollow calcium carbonate microspheres from stepwise microscopic analysis. When CO_2 gas dissolves in the starting solution, primary amorphous $CaCO_3$ particles firstly form and gather to be micro-sized secondary particles. With gradual decrease pH derived from further CO_2 dissolution, only primary particles which exist at outer shell of the secondary particle dissolve once and transfer to vaterite. Subsequently, amorphous $CaCO_3$ particles which just inside the outer shell start to transfer to vaterite crystal. During repeat of these dissolution and re-precipitation process, the outer $CaCO_3$ shell completes to form with columnar structure[135].

Even though the bubble template is a new process and still on the way of investigation, it was indicated that this method is a facile and promising process to prepare hollow particles with the characteristic of low cost and high production. One more advantage of this method is its universal property, which can be used in other system involved gas reactions.

2.3 Device-based methods

Device-based methods include the method to prepare hollow particles by using some equipment, such as spray pyrolysis, nozzle process and so on.

2.3.1 Spray pyrolysis

Spray pyrolysis is a powerful tool to synthesize a variety of materials in power form including metals, metal oxides, superconducting materials, fullerenes, and nanophase materials. G. L. Messing[136] has reviewed the formation of particles with different morphology using a variety of spray pyrolysis techniques. The report showed that the spray pyrolysis techniques allow to produce dense (solid), hollow, porous or fibrous particles and even to deposit thin film, but the formation of hollow spherical particle is the most typical.

Particles synthesis by spray pyrolysis involves the atomization of a precursor solution into discrete droplets. These droplets are subsequently transported through a furnace where the solvent is evaporated from particulate. Spray pyrolysis has a number of advantages including the followings: (1) the particles produced are spherical, (2) the distribution of their diameter is uniform and controllable from nanometer to micrometer, (3) the purity of the product is high, and (4) the process is continuous. **Fig. 10** showed the sample of hollow spherical particles prepared by K. T. Wojciechowski[137] using spray pyrolysis method. The microscopic observations have shown that the hollow particles have the diameter ranging from 100 to 300 nm with shell thickness of 8-50 nm. Some big hollow particles also prepared by spray pyrolysis, as shown in **Fig. 11**[138].

The most apparent theory for the formation of hollow particles in spray pyrolysis is the surface precipitation induced by rapid drying rate of droplet in

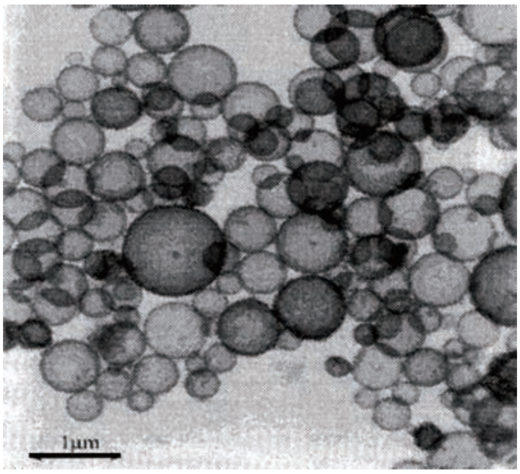

Fig. 10 TEM image of hollow particles prepared by spray pyrolysis[137]. Scale bar is 1 μm.

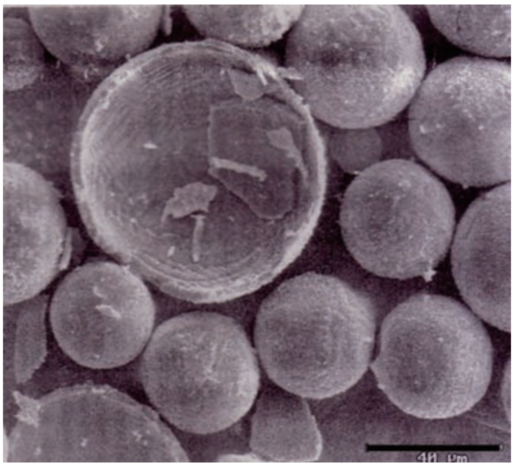

Fig. 11 SEM image of hollow Al_2O_3 particles prepared by spray pyrolysis[138]. Scale bar is 40 μm.

thermal condition. The formation of hollow particles can be controlled by changing aerosol decomposition parameters. For example, Lenggoro[139)] have demonstrated experimentally that hollow ZrO_2 particle is formed if the reactor temperature is high and initial solute concentration is low. Furthermore, the results of his simulation indicated that hollow particles are formed if the initial droplets are large and the droplet number concentration is low.

2.3.2 Nozzle process

Nozzle process is developed to prepare big hollow particles by using inert bubbles as templates, which involves a coaxial nozzle, as shown schematically in **Fig. 12**.

In nozzle process, a non-reactive gas is fed through the inner nozzle and a slurry, made up of dispersed solid particles (which can be metal, ceramic or a mixture), a binder and a continuous volatile liquid phase, is fed through the outer nozzle. The slurry exits the nozzle in the form of hollow cylinder that close at a constant diameter due to surface tension and hydrostatic forces, forming a hollow sphere. The monosized spheres are hardened in flight by the binder as the solvent evaporates. After forming, the spheres are sintered to dense and strength the walls. Due to the high rates of spherical production and low cost fabrication, nozzle process is economical. Torobin[140-144)] has done many interesting research in this area. R Meyer Jr.[145)] has prepared hollow lead zirconate titanate (PZT) particles by using nozzle process. These hollow particles have potential applications in medical ultrasound, non-destructive testing and low density transducer arrays. I. G. Loscertales et al.[146)] have combined nozzle process with electrohydrodynamically (EHD) process and generate a liquid-filled hollow fibre. The thickness and diameter of fibres are easily to be controlled by adjusting the applied voltage.

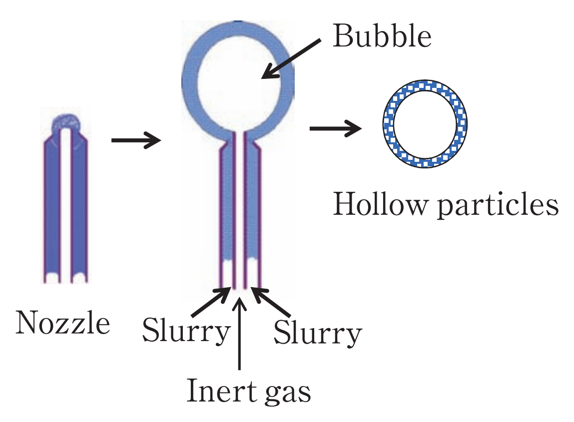

Fig. 12 Illustration of nozzle process to prepare hollow particles.

Besides, some researchers[147)] proposed to prepare hollow particles using the electrostatic atomization combined with alcohol solidification. The nozzle is composed of a stainless-steel hypodermic needle. The ground electrode is an aluminum plate with a hole at its center for the produced droplets to pass through. High voltage is applied between the nozzle and the ground electrode using a dc high voltage supply. The material in the sample vessel is pressurized by gas, and flows through the nozzle. The nozzle can control the particle size by adjusting voltage. The produced droplets immediately fall into an alcohol bath to dehydrate their surface. After filtered and dried, the hollow silica particles were produced.

3 Applications of Hollow Particle

3.1 Papermaking

One of the disadvantages of recycled paper when compared to paper from virgin pulp is difficult to gain high brightness. To improve brightness, papermakers make efforts to develop recycling process such as introducing a strong surfactant in flotation and intensive bleaching. But, these process demand more water and energy, causing adversity to environment. Another possible idea is to hide gray appearance with an efficient coating or internal loading for high opacity. Hollow spheres made of $CaCO_3$ could be suitable for this purpose because hollow structure scatters more light resulting in higher brightness and opacity.

T. Enomae and K. Tsujino[148)] have reported the preparation of spherical particles made of $CaCO_3$ by emulsion template method. Prepared spherical particles were tried to be applied to papermaking as a filler and were compared with some kinds of ground $CaCO_3$ that are all of the commercial grades and of a similar particles size. Spherical particles were observed to disperse evenly while there were, though rarely, large particles 10 μm in diameter for the commercial $CaCO_3$. The density of paper loaded with the spherical particles was lower than that of the unloaded paper. This is often the case with filler loading because of acting as obstruction to interfiber bonding. The spherical particles increased surface smoothness presumably because the spherical particle trended to align with a flat surface due to their shape and no irregularly large particles protruding above the surface. The specific light scattering coefficient also increased with the spherical particles due to their porous structure. This finding suggests that the spherical hollow particles are promising for coating use although attention must be paid to coating rheology. Besides, the possible thermal insulation due to the hollow structure is a unique feature to potentially enhance thermal wax-transfer printing. It was found that more addition of spherical hollow particles provided a larger area of wax ink transfer because efficient thermal insulation due to the porous structure maintained the temperature.

3.2 Foam

Spherical hollow particles can be used to fabricate foam by sintering or bonding the packing of hollow particles. The foams produced by hollow particles have high porosities, low density and can be net-shape. Besides, some researchers have fabricated porous foam by using 3D colloid array as templates. For example, B. T. Holland and co-workers[149] have prepared TiO_2, ZrO_2 and aluminum oxide (Al_2O_3) foam by permeating the monomeric alkoxide precursor into the arrays of bulk PS sphere and condense in air. The foams with open pore were obtained after calcinations of the inorganic component. J. E. G. J. Wijnhoven and W. L. Vos[150] also synthesized TiO_2 foam by filling the voids of artificial opals and subsequently removing the original opal materials by calcinations.

J. K. Cochran[9] has made a review on the application of ceramic foam. For example, hollow ceramic spheres have been incorporated into metal and polymeric matrices to create syntactic foam which can be used as energy absorbing parts for occupant protection in automotive interiors and function well when the crush distance is limited. The polymer syntactic foam produced lower crush force and a squarer wave stress-strain behavior compared to the unfilled polymer foam. This translates to higher energy absorption at lower applied stress which is desirable for passenger protection. Besides, foam diffuser base made from mullite were shown to have excellent thermal shock resistance for radiant burners, in that the radiant surface could be heated to 1200℃ in 10 seconds and cooled through more than 100 cycles without visible effects. Besides, Q. Gu and co-workers[151] have prepared low density porous tin oxide (SnO_2) foam with a potential application as target materials for laser induced extreme ultraviolet (EUV) emission.

3.3 Drug delivery

SiO_2 is an important drug delivery media owing to its non-toxic and biocompatible. The advantages of such materials have attracted many attentions for the controlled delivery of therapeutics[152, 153].

J. F. Chen and co-workers[84, 154] have prepared porous hollow SiO_2 nanoparticles by using $CaCO_3$ nano-particles as the inorganic template. The hollow particles were uniform spherical particles with a diameter of 60-70 nm, wall thickness of approximately 10 nm. The as-synthesized hollow particles were subsequently employed as drug carrier to investigate *in vitro* release behavior of brilliant blue F (BB) in simulated body fluid. The preparation of drug carrying is illustrated as **Fig. 13**. BB release behavior from dense SiO_2 particles and hollow particles were investigated in deionized water solution, as shown in **Fig. 14**. BB loaded on normal SiO_2 nanoparticles exhibited a rapid release of 100 % within 10 min. However, BB loaded into the hollow particles showed a different release style: 60 % of BB was released in the first 10 min, while the other 40 % followed a typical sustained release pattern and was dissolved out slowly and evenly for a time period of 1140 min. This is because that through the BB loaded on the surface of hollow SiO_2 is release quickly while the release rate of BB entrapped in the inner core of hollow particles is constrained. The above results suggested that the prepared porous hollow SiO_2 nanoparticles could be applied as promising drug vehicles for controlled release systems[92].

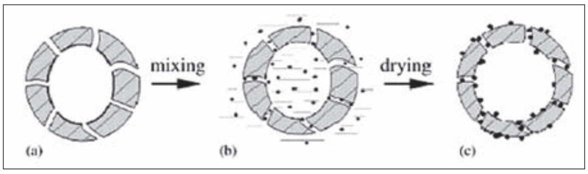

Fig. 13 Preparation of drug carrying for porous hollow SiO_2 particles. (a) hollow SiO_2 particles; (b) suspension of BB and hollow particles; (c) BB entrapped in hollow particles[154].

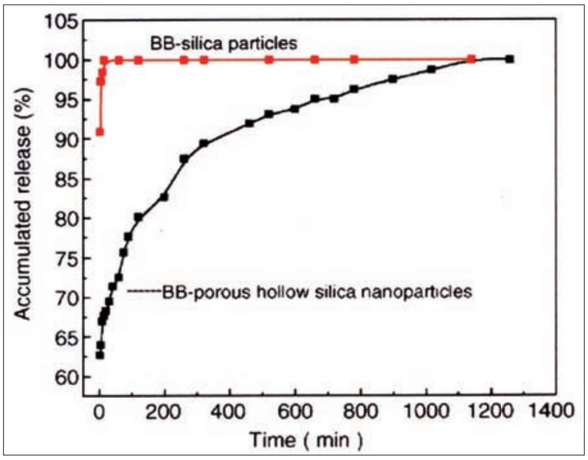

Fig. 14 Release profile of BB form hollow SiO_2[92].

Recently, the use of magnetic particle for the delivery of drugs or antibodies to the organs or tissues altered by disease has become an attractive field of research. The process of drug localization using magnetic delivery system is based on the competition between force exerted on the particles by flood compartment and magnetic force generated from the magnet, i.e. applied field. When the magnetic force exceeds the linear blood flow rates in arteries or capillaries, the magnetic particles are retained at the target site and maybe internalized by the endothelial cells of the target tissue. P. Tartaj and co-workers[155] have reported the preparation of SiO_2 coated Fe_2O_3 hollow spherical particles with an average size of 150 nm by aerosol pyrolysis of methanol solution containing iron ammonium citrate and TEOS at a total salt concentration of 0.25 M. It is worth mentioning that the small particles size of the composite renders these particles a potential candidate for their use in *in vitro* applications.

3.4 Nanoshell

N. J. Halas and co-workers[1,156,157] have fabricated a new type of composite nanoparticles called nanoshells, consist of a dielectric or semiconducting core coated with a nanometer scale metallic shell. These nanoparticles manifest a strong optical resonance that is dependent on the relative thickness of the nanoshell. This sensitive dependence of the optical resonance frequency on the structure of metal nanoshells is illustrated in **Fig. 15**. As the shell thickness decreases, the optical absorption is shifted to longer wavelengths. It is theoretically possible to shift the resonant absorption to beyond 10 μm in the infrared as shown in **Fig. 15b**. In **Fig. 15a**, as the core radius-shell thickness ratio is varied among 3 to 12, the predicted resonances of the nanoparticles span a range of 300 nm in wavelength. If the order of these layers were inverted, that is, a metallic core and a dielectric shell, less than 20 nm optical resonance shift would be expected.

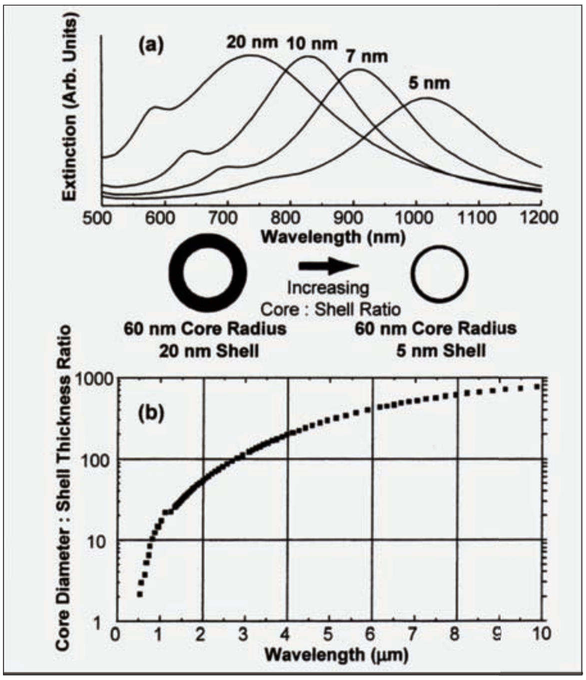

Fig. 15 (a) Theoretically calculated optical resonance of metal nanoshells over a range of core radius/shell thickenss ratios, (b) calculation of optical resonance wavelength versus core radius/shell thickness ratio for metal nanoshells (SiO_2 core, Au shell) [1].

SiO_2-Au nanoshells offer enormous flexibility to tune the resonance frequency by varying the relative dimensions of the SiO_2 core and Au shell. The resonance of SiO_2-Au nanoshell particles can easily be positioned in the “water windows” in the near-infrared (800-1300 nm) ranges, where absorption by organism is low. Together with the high degree of biocompatibility of Au nanoshells, these results open the door to a wide variety of biological applications. Halas and West showed nanoshells can be used to enable fast whole blood immunoassays. For conventional blood immunoassays performed at visible wavelengths, the whole procedures need several hours or days owing to a purification step needs to be carried out to separate out a variety of unwanted biomaterials that absorb visible lights. In the immunoassay procedure proposed by Halas and West, nanoshells are conjugated with antibodies, which manifest a strong plasmon related absorption feature with a fast absorption measurement in the water window, circumventing the time-intensive purification step. Halas and West also showed how nanoshells can be incorporated into temperature-sensitive hydrogels to synthesize a new type of composite materials that collapses on laser irradiation. Owing to the tunable absorption feature of nanoshells, SiO_2-Au nanoshells were designed to absorb light from laser irradiation and then transform the light to heat around nanoshell, which vaporized water and caused the collapse of hydrogel. Such a remotely addressable hydrogels may find applications in drug delivery and microfluidic values or pumps. F. Caruso and co-workers[158, 159] have reported the fabrication of optically addressable nanostructured capsules comprising a PE multilayer shell doped with light-absorbing Au nanoparticles. Their results indicated both enzyme lysozyme and macromolecules can be encapsulated within the PE/Au shell and the encapsulated samples can be released on demand without significant loss of bioactivity following irradiation with short pulse of near infrared (NIR) laser light.

The most exciting prospect is that nanoshells could play a role in future cancer treatments. These particles are small enough to find their way through human circulatory system on injection. Bioactive molecules can be attached to the nanoshells surface to cause selective binding or accumulation of these particles within a tumor. Using NIR laser, carcinoma tissue can then be destroyed by local thermal heating around nanoshells based on an efficient light-to-heat conversion.

Besides, C. Graf and A. V. Blaaderen160) have prepared hollow Au shells by dissolving the SiO_2 core in diluted HF. Their results indicated that removing the core would lead to a significant shift of the maximum of the extinction spectrum to shorter wavelengths, which is caused by change of the refractive index of the core from 1.45 (SiO_2) to 1.33 (water). This result demonstrated that the dissolution of the SiO_2 core allows a further adjustment of the optical properties of the Au nanoshell particles.

3.5 E-ink

Particle-based display systems are attractive for their optical and electronic properties. These beneficial properties result from the highly scattering and absorbing microparticles that contain pigments like TiO_2 and carbon black. The general representations of particle based display are an electrophoretic image display system161) and a rotating bichromal microspheres system162). Despite many attractive features, however, particle-based display systems suffer from some shortcomings, including difficulty to achieve perfect rotation and short lifetime due to coagulation and agglomeration caused by colloidal instability. To overcome these shortcomings, J. Jacobson and co-workers163) created E-ink, a new display system utilizing microencapsulation techniques with a fusion of chemistry, physics, electronics and other technologies. Each microcapsule with about the diameter of a human hair contains millions of tiny pigment microparticles that are well dispersed in an organic solution with a low dielectric constant. When an electric field is applied between microcapsules, the microparticles move in the low dielectric constant solution toward the oppositely charged electrode in the phenomenon of electrophoretic migration. If the top transparent electrode is positively charged, white microparticles with negatively charges should move toward the top electrode, making the surface appear white at that spot. At the same time, an opposite electric field pulls the black particles to the bottom of the microcapsules. By reversing this process, the black microparticles appear at the top of the microcapsules, which makes the surface become black at that spot. This is how microencapsulated ink (E-ink) forms letters and pictures on the display. The benefit of microencapsulation in this case is the isolation of electrophoretic dispersion in discrete compartments. In other words, agglomeration of electrophoretic dispersion in microcapsules has no influence on electrophoretic dispersion in neighboring microcapsules.

Japan is one of the leading countries in microencapsulation technology. The Japanese Ministry of Economy, Trade and Industry (METI) has created a nation project concerning paper-like display that employs microencapsulation, called the Full Color Rewritable Paper Using Functional Capsules Project164).

3.6 Catalysis

Palladium (Pd)-catalyzed cross-coupling reactions of aryl halides with arylboronic acid, often referred as Suzuki coupling reactions, are versatile method for synthesizing unsymmetrical biaryls. The Suzuki coupling reactions have been applied extensively in the synthesis of natural products, nucleoside analogues, and pharmaceuticals. Many Pd complexes have been used as homogeneous catalysis for these reactions. S. W. Kim and co-workers2) have reported the preparation of hollow Pd spheres by using the templates of uniform SiO_2 spheres. They have investigated the application of these hollow spheres to heterogeneous Suzuki coupling reactions. The results showed that the Pd hollow spheres are highly active for this reaction, in addition, the catalyst can be recycled and reused seven times without losing its catalytic activity. The high surface area of Pd spheres resulting from the nanoparticle nature of the shell is responsible for the high catalytic activity. Earlier studies by other research groups reported the Pd nanoparticles used in Suzuki coupling reactions were agglomerated after one cycle, resulting in a loss of catalytic activity. Heterogeneous catalysts often suffer extensive leaching of the active metal species during reactions and eventually lose their catalytic activities even after seven recycles. Elemental analysis of the filtrate after the reaction demonstrated to no leaching of Pd from the hollow spheres, which is very important when Pd catalysts are used for pharmaceutical production.

TiO_2 is a promising oxide that is able to degrade many kinds of organic pollutants in water with the

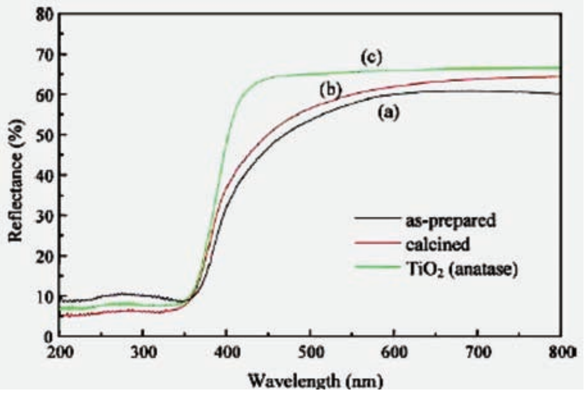

Fig. 16 UV-vis diffuse reflectance spectra of (a) as prepared, and (b) calcined hollow mesoporous TiO_2 microspheres, and (c) a well-crystalline TiO_2 sample of anatase phase[76].

production of hydrogen by photocatalysis. Although TiO_2 has been intensively investigated, its application in photocatalysis is limited because of its low efficiency in energy conversion. To enhance the efficiency, the absorption spectrum of TiO_2 is expected to extend to the visible range. Some researchers[73,165] found that the hollow TiO_2 particle has a smaller band gap and obvious absorption shift towards longer wavelength. **Fig. 16** is the diffuse reflectance spectra of hollow TiO_2 which was prepared by surfactant-assisted templating method. The onset wavelength (λ_{onset}) of the spectra recorded from anatase is about 420 nm, while the λ_{onset} of the hollow TiO_2 shift toward longer wavelength region. The band gaps estimated from the spectra in **Fig. 16** give an evident reduction of the band gap for hollow TiO_2 compared with anatase, since a red shift of λ_{onset} was observed for hollow TiO_2. This indicates that the present hollow TiO_2 microspheres should be efficient in photocatalysis applications[76].

However, some other researchers[166-168] have reported a different conclusion that hollow structures leaded to a blue shift of wavelength, which was explained as the result of quantum size effect. This confliction would inspire a further research to discover the truth of the properties of hollow particles. Even though the exact mechanism is still on the way of investigation, it might be speculated that the thickness and microstructure of shell should play an important on the optical properties of hollow particles.

3.7 Others

Fuji at Nagoya Institute of Technology, Japan, demonstrated superior thermal insulation of their synthesized hollow SiO_2 nanoparticles (HSNPs). The composite film where HSNPs were dispersed in polymer matrix exhibited ten-time higher thermal insulation than original polymer film and also high transparency in visible region. This excellent performance has been achieved by nano-sized hollow interior which can be as quasi-vacuum state[169].

Researchers at Pennsylvania State University, Led by Newnham[9,145], are developing miniature spherical transducers based on PZT hollow spheres. Tiny hollow spheres used as piezoelectric sensor and actuator manifested an improved resolution and high powder density. Hydrostatic coefficient for the hollow sphere transducer were 1-2 orders of magnitude larger than those for bulk PZT and the hydrophone figure of merit (FOM) was three orders of magnitude higher than that of bulk PZT. The hollow sphere of PZT have good dielectric and piezoelectric properties, which suggests a number of possible applications, such as flow noise sensor and sonar arrays with the advantage of low density. Besides, the geometry of spheres allows them to be used as sensors that are independent of receiving direction. The omnidirectional characteristic of the sphere also allow it to be used as a transducer in non-destructive testing and in monitoring flow noise in energizing system.

Another example for the application of hollow particles involves the improved magnetic property. J. Bao and co-workers[170] have prepared hollow Ni spheres with a typical coercivity of 32.3 Oe which is higher than that of the bulk Ni (around 0.7 Oe).

Besides, K. T. Lee and co-workers[171] have tried to improve the cycle performance of nanosized Tin (Sn) particles for anode material in lithium secondary batteries by encapsulating Sn particles with spherical hollow carbon. The spherical hollow carbon plays several important roles in this preparation. First, the hollow carbon acts as a barrio to provides a void space where Sn metal particles experience a volume charge without a collapse of carbon shell. Third, the hollow carbon itself is an active material for additional lithium (Li) ion storage. Finally, the carbon particles are spherical in shape, which provides a high packing density in practical Li cells to allow a high volumetric energy density.

4. Future Prospects

The development of hollow particles will continue focusing on the preparation of uniform products with controllable particles size and shell thickness. For virtually all the applications under consideration, properties will be enhanced by improvement in perfect of the particles geometry. The pore size and microstructure of solid shell are also significant when permeability of hollow particles is considered in their applications. Besides, new methods to prepare hollow particles with the characteristics of low cost and high production are warmly expected, especially in industrial production. In the applications of hollow particles, it is important to functionalize the interior of hollow particles to gain desired properties. And the applications of hollow particles in electronic and biologic areas promise us a golden and expecting future.

Acknowledgements

A part of this study was supported by Japan Society for the Promotion of Science (JSPS) Grant-in-Aid for Scientific Research (B) (22310066), Grant-in-Aid for challenging Exploratory Research (24655191), and Japan Science and Technology Agency (JST)-Advanced Low Carbon Technology Research and Development Program (ALCA).

References

1) Oldenburg, S. J., Averitt, R. D., Westcott, S. L. and Halas, N. J. (1998): Nanoengineering of optical resonances. Chemical Physics Letters, 288, pp.243-247.
2) Kim, S. W., Kim, M., Lee, W. Y. and Hyeon, T. (2002): Fabrication of hollow palladium spheres and their successful application to the recyclable heterogeneous catalyst for suzuki coupling reactions. Journal of the American Chemical Society, 124, pp.7642-7643.
3) Sershen, S. R., Westcott, S. L., Halas, N. J. and West, J. L. (2000): Temperature-sensitive polymer-nanoshell composites for photothermally modulated drug delivery. Journal of Biomedical Materials Research, 51, pp.293-298.
4) West, J. L. and Halas, N. J. (2000): Applications of nanotechnology to biotechnology: Commentary. Current Opinion in Biotechnology, 11, pp.215-217.
5) Oldenburg, S. J., Jackson, J. B., Westcott, S. L. and Halas, N. J. (1999): Infrared extinction properties of gold nanoshells. Applied Physics Letters, 75, pp.2897-2899.
6) Marinakos, S. M., Novak, J. P., Brousseau, L. C. Ⅲ , House, A. B., Edeki, E. M., Feldhaus, J. C. and Feldheim, D. L. (1999): Gold particles as templates for the synthesis of hollow polymer capsules. control of capsule dimensions and guest encapsulation. Journal of the American Chemical Society, 121, pp.8512-8518.
7) Marinakos, S. M., Anderson, M. F., Ryan, J. A., Martin, L. D. and Feldhein, D. L. (2001): Encapsulation, permeability, and cellular uptake characteristics of hollow nanometer-sized conductive polymer capsules, The Journal of Physical Chemistry B, 105, pp.8872-8876.
8) Tartaj, P., Morales, M. P., Veintemillas-Verdaguer, S., Gonalez-Carreno, T. and Serna, C. J. (2003): The preparation of magnetic nanoparticles for applications in biomedicine, Journal of Physics D: Applied Physics, 36, R182-R197.
9) Cochran, J. K. (1998): Ceramic hollow spheres and their applications. Current Opinion in Solid State and Materials Science, 3, pp.474-479.
10) Ohmori, M. and Matijevic, E. (1992): Preparation and properties of uniform coated colloidal particles. VII. Silica on hematite. Journal of Colloid and Interface Science, 150, pp.594-598.
11) Wang, L., Sasaki, T., Ebina, Y,. Kurashima, K. and Watanabe, M. (2002): Fabrication of controllable ultrathin hollow shells by layer-by-layer assembly of exfoliated titania nanosheets on polymer templates. Chemistry of Materials, 14, pp.4827-4832.
12) Caruso, F., Shi, X., Caruso, R. A. and Susha, A. (2001): Hollow titania spheres from layered precursor deposition on sacrificial colloidal core particles. Advanced Materials, 13, pp.740-744.
13) Braun, P. V. and Stupp, S. I. (1999): CdS mineralization of hexagonal, lamellar, and cubic lyotropic liquid crystals. Materials Research Bulltein, 34, pp.463-469.
14) Hubert, D. H. W., Jung, M. and German, A. L. (2000): Vesicle templating. Advanced Materials, 12, pp.1291-1294.
15) Schmidt, H. T. and Ostafin, A. E. (2002): Liposome directed growth of calcium phosphate nanoshells. Advanced Materials, 14, pp.532-535.
16) Brusinsma, P. J., Kim, A. Y., Liu, J. and Baskaran, S. (1997): Mesoporous silica synthesized by solvent evaporation: spun fibers and spray-dried hollow spheres. Chemistry of Materials, 9, pp.2507-2512.
17) Jafeliccit Jr., M., Pavalos, M. R., Jose de Santos, F. and Jose de Santos, A. (1999): Hollow silica particles from microemulsion. Journal of Non-Crystalline Solids, 247, pp.98-102.
18) Shin, T., Fuji, M., Takei, T., Chikazawa, M., Tanabe, K. and Mitsuhashi, K. (2002): Proceeding of the 105th Meeting of the Society of Inorganic Materials, Japan, November 14-15, pp.78-79.
19) Sun, Y., Mayers, B. T. and Xia, Y. (2002): Template-engaged replacement reaction:? a one-step approach to the large-scale synthesis of metal nanostructures with hollow interiors. Nano Letters 2, pp.481-485.
20) Yin, Y., Lu, Y., Gates, B. and Xia, Y. (2001): Synthesis and characterization of mesoscopic hollow spheres of ceramic materials with functionalized interior surfaces. Chemistry of Materials, 13, pp.1146-1148.
21) Ung, T., Liz-Marzan, L. M. and Mulvaney, P. (1998): Controlled method for silica coating of silver colloids. Influence of coating on the rate of chemical reactions. Langmuir, 14, pp.3740-3748.
22) Caruso, R. A., Susha A. and Caruso, F. (2001): Multilayered titania, silica, and laponite nanoparticle coatings on polystyrene colloidal templates and resulting inorganic hollow spheres. Chemistry of Materials, 13,

pp.400-409.
23) Mulvaney, P., Giersig, M., Ung, T. and Liz-Marzán, L. M. (1997): Direct observation of chemical reactions in silica-coated gold and silver nanoparticles. Advanced Materials, 9, pp.570-575.
24) Caruso, F., Caruso, R. A. and Möhwald, H. (1998): Nanoengineering of inorganic and hybrid hollow spheres by colloidal templating. Science, 282(6), pp.1111-1114.
25) Yin, J. Qian, X. Yin, J. Shi, M. Zhang, J. and Zhou, G. (2003): Preparation of polystyrene/zirconia core-shell microspheres and zirconia hollow shells. Inorganic Chemistry Communications, 6, pp.942-945.
26) Wang , X. D., Yang, W. L., Tang, Y., Wang, Y. J., Fu, S. K. and Gao, Z. (2000): Fabrication of hollow zeolite spheres. Chemical Communications, 21, pp.2161-2162.
27) Wang , L. Z., Ebina, Y., Takada, K. and Sasaki, T. (2004): Ultrathin hollow nanoshells of manganese oxide. Chemical Communications,9, pp.1074-1075.
28) Caruso, F., Spasova, M., Susha, A., Giersig, M. and Caruso, R. A. (2001): Magnetic nanocomposite particles and hollow spheres constructed by a sequential layering approach. Chemistry of Materials, 13, pp.109-116.
29) Yin, J., Qian, X., Yin, J., Shi, M. and Zhou, G. (2003): Preparation of ZnS/PS microspheres and ZnS hollow shells. Materials Letters, 57, pp.3859-3863.
30) Song, C. X., Gu, G. H., Lin, Y. S. and Wang, H. (2003): Preparation and characterization of CdS hollow spheres. Materials Research Bulltein 38, pp.917-924.
31) Decher, G. (1997): Fuzzy nanoassemblies: toward layered polymeric multicomposites. Science, 277, pp.1232-1237.
32) Wang, D. and Caruso, F. (2002): Polyelectrolyte-coated colloid spheres as templates for sol-gel reactions. Chemistry of Materials, 14, pp.1909-1913.
33) Caruso, F., Lichtenfeld, H., Giersig, M. and Möhwald, H. (1998): Electrostatic self-assembly of silica nanoparticle-polyelectrolyte multilayers on polystyrene latex particles. Journal of the American Chemical Society, 120, pp.8523-8524.
34) Caruso, F., Caruso, R. A. and Möhwald, H. (1999): Production of hollow microspheres from nanostructured composite particles. Chemistry of Materials, 11, pp.3309-3314.
35) Donath, E., Sukhorukov, G. B., Caruso, F., Davis, S. A. and Möhwald, H. (1998): Novel hollow polymer shells by colloid-templated assembly of polyelectrolytes. Angewandte Chemie International Edition, 37, pp.2201-2205.
36) Caruso, F., Schuler, C. and Kurch, D. G. (1999): Core-shell particles and hollow shells containing metallo-supramolecular components. Chemistry of Materials, 11, pp.3394-3399.
37) Caruso, F. Susha, A. S. Giersig, M. and Möhwald, H. (1999): Magnetic core-shell particles: preparation of magnetite multilayers on polymer latex microspheres. Advanced Materials, 11, pp.950-953.
38) Caruso, F. and Möhwald, H. (1999): Protein multilayer formation on colloids through a stepwise self-assembly technique. Journal of the American Chemical Society 121, pp.6039-6046.
39) Gittins, D. and I. Caruso, F. (2000): Multilayered polymer nanocapsules derived from gold nanoparticle templates. Advanced Materials, 12, pp.1947-1949.
40) Iler, R.K. (1979): “The Chemistry of Silica”, Wiley Interscience, New York.
41) Takai, C., Watanabe, H., Asai, T., Fuji, M. (2012): Determine apparent shell density for evaluation of hollow silica nanoparticles. Colloids and Surfaces A: Physicochemical and Engineering Aspects, 404, pp.101- 105.
42) Walsh, D. and Mann, S. (1995): Fabrication of hollow porous shells of calcium carbonate from self-organizing media. Nature 377, pp.320-323.
43) Kojima, Y. and Yasue, T. (2003): Synthesis of hollow calcium carbonate and its particle size control, Journal of the Society of Inorganic Materials, Japan 10, pp.78-85.
44) Wang, L. Z., Ebina, Y., Takada, K. and Sasaki, T. (2004): Ultrathin hollow nanoshells of manganese oxide. Chemical Communications, pp.1074-1075.
45) Wang, X. D., Yang, W. L., Tang, Y., Wang, Y. J., Fu, S. K. and Gao, Z. (2000): Fabrication of hollow zeolite spheres. Chemical Communications, pp.2161-2162.
46) Bour Cinos, A. B., Karakassidas, M. A. and Petridis, D. (2001): Synthesis and characterization of hollow clay microspheres through a resin template approach. Chemical Communications, 16, pp.1518-1519.
47) Neves, M. C. and Trindade, T. (2003): Preparation of hollow shells of zinc oxide/bismuth (III) vanadate. Materials Research Bulletin 38, pp.1013-1020.
48) Neves, M. C., Trindade, T., Timmons, A. M. B. and Jesus, J. D. P. de (2001): Synthetic hollow zinc oxide microparticles. Materials Research Bulletin, 36, pp.1099-1108.
49) Kawahashi, N. and Shiho, H. (2000): Copper and copper compounds as coatings on polystyrene particles and as hollow spheres. Journal of Materials Chemistry, 10, pp.2294-2297.
50) Zhang, X., Xie, Y., Xu, F., Xu, D. and Liu, X. H. (2004): In situ polymerization template route to CdSe hollow spheres under UV irradiation. Inorganic Chemistry Communications, 7, pp.417-419.
51) Hu, Y., Chen, J., Chen, W., Lin, X. and Li, X. (2003): Synthesis of novel nickel sulfide submicrometer hollow spheres. Advanced Materials,15, pp.726-729.
52) Park, J. H., Shin, C. O., Moon, S. K. and Oh, S. G. (2003): Preparation of hollow silica microspheres in W/O emulsions with polymers. Journal of Colloid Interface Science, 266, pp.107-114.
53) Park, J. H., Bae, S. Y. and Oh, S. G. (2003): Fabrication of hollow silica microspheres through the self-assembly behaviour of polymers in W/O emulsion. Chemistry Letters, 32, pp.598-599.
54) Jafelicci Jr, M., Davolos, M. R., Sartos, F. J. Dos and Andrade, S. J. de (1999): Hollow silica particles from microemulsion. Journal of Non-crystalline Solids, 247, pp.98-102.

55) Sun, Q. Y., Kooyman, P. J., Grossmann, J. G., Bomans, P. H. H. and Frederik, P. M. (2003): The formation of well-defined hollow silica spheres with multilamellar shell structure. Advanced Materials, 15, pp.1097-1100.
56) Li, W. J., Sha, X. X., Dong, W. J. and Wang, Z. C. (2002): Synthesis of stable hollow silica microspheres with mesoporous shell in nonionic W/O emulsion. Chemical Communications, pp.2434-2435.
57) Yu, C. Z., Tian, B. Z., Fan, J., Stucky, G. D. and Zhao, D. Y. (2002): Synthesis of siliceous hollow spheres with ultra large mesopore wall structures by reverse emulsion templating. Chemistry Letters, 31, pp.62-63.
58) Schacht, S., Huo, Q., Voigt-Martin, I. G. and Stucky, G. D. (1996): Oil-water interface templating of mesoporous macroscale structures. Science, 273, pp.768-771.
59) Walsh, D., Lebeau, B. and Mann, S. (1999): Morphosynthesis of calcium carbonate (vaterite) microsponges. Advanced Materials 11, pp.324-328.
60) Thomas, J. A., Seton, L., Davey, R. J. and Dewolf, C. E. (2002): Using a liquid emulsion membrane system for the encapsulation of organic and inorganic substrates within inorganic microcapsules. Chemical Communications pp.1072-1073.
61) Nakahara, Y., Mizuguchi, M. and Miyata, K. (1979): Effects of surfactants on $CaCO_3$ spheres prepared by interfacial reaction method. Journal of Colloid Interface Science 68, pp.401-407.
62) Dinsmone, A. D., Hsu, A. F., Nikolaids, M. G., Marquez, M., Bausch, A. R. and Weitz, D. A. (2002): Colloidosomes: selectively permeable capsules composed of colloidal particles. Science 298, pp.1006-1009.
63) Wu, M. M., Wang, G. G., Xu, H. F., Long, J. B., Shek, F. L. Y., Lo, S. M. F., Willians, I. D. Feng, S. H. and Xu, R. R. (2003): Hollow spheres based on mesostructured lead titanate with amorphous framework. Langmuir 19, pp.1362-1367.
64) Velev, O. D., Furusawa, K. and Nagayama, K. (1996): Assembly of latex particles by using emulsion droplets as templates. 1. microstructured hollow spheres. Largmuir 12, pp.2374-2384.
65) Nakashima, T. and Kimizuka, N. (2003): Interfacial synthesis of hollow TiO_2 microspheres in ionic liquids. Journal of the American Chemical Society 125, pp.6386-6387.
66) Won, Y. Y., Davis, H. T. and Bates, F. S. (1996): Giant wormlike rubber micelles. Science 283, pp.960-963.
67) Hajduk, D. A., Kossuth, M. B., Hillmyer, M. A. and Bates, F. S. (1998): Complex phase behavior in aqueous solutions of poly(ethylene oxide)-poly(ethylethylene) block copolymers. The Journal of Physical Chemistry B 102, pp.4269-4276.
68) Warriner, H. E., Idziak, S. H. J., Slack, N. L., Davidson, P. and Safinyn, C. R. (1996): Lamellar biogels: fluid-membrane-based hydrogels containing polymer lipids. Science 271, pp.969-973.
69) Yu, K. and Eisenberg, A. (1998): Bilayer morphologies of self-assembled crew-cut aggregates of amphiphilic PS-b-PEO diblock copolymers in solution. Macromolecules 31, pp.3509-3518.
70) Discher, B. M., Won, Y. Y., Ege, D. S., Lee, J. C. M., Bates, F. S., Discher, D. E. and Hammer, D. A. (1999): Polymersomes: tough vesicles made from diblock copolymers. Science 284, pp.1143-1146.
71) Jain, S. and Bates, F. S. (2003): On the origins of morphological complexity in block copolymer surfactants. Science 300, pp.460-464.
72) Jurg, H. M., Price, K. E. and Mcquade, D. T. (2003): Synthesis and characterization of cross-linked reverse micelles. Journal of the American Chemical Society 725, pp.5351-5355.
73) Katagiri, K. and Caruso, F. (2005): Monodisperse polyelectrolyte-supported asymmetric lipid-bilayer vesicles. Advanced Materials 17, pp.738-743.
74) Katagiri, K. and Caruso, F. (2004): Functionalization of colloids with robust inorganic-based lipid coatings. Macromolecules 37, pp.9947-9953.
75) Tanev, P. T. and Pinnavaia, T. J. (1996): Biomimetic templating of porous lamellar silicas by vesicular surfactant assemblies. Science 271, pp.1267-1269.
76) Ren, T. Z., Yuan, Z. Y. and Su, B. L. (2003): Surfactant-assisted preparation of hollow microspheres of mesoporous TiO_2. Chemical Physics Letters 374, pp.170-175.
77) Wong, M. S., Cha, J. N., Choi, K. S., Deming, T. J. and Stucky, G. D. (2002): Assembly of nanoparticles into hollow spheres using block copolypeptides. Nano Letters 6, pp.583-587
78) Qi, L. M., Li, J. and Ma, J. M. (2002): Biomimetic morphogenesis of calcium carbonate in mixed solutions of surfactants and double-hydrophilic block copolymers. Advanced Materials 14, pp.300-303.
79) Lyu, Y. Y., Yi, S. H., Shon, J. K., Chang, S., Pu, L. S., Lee, S. Y., Yie, J. E., Char, K., Stucky, G. O. and Kim, J. M. (2004): Highly stable mesoporous metal oxides using nano-propping hybrid gemini surfactants. Journal of the American Chemical Society 126, pp.2310-2311.
80) Jarg, J. and Lee, K. (2002): Facile fabrication of hollow polystyrene nanocapsules by microemulsion polymerization. Chemical Communications pp.1098-1099.
81) Lin, H. P., Mou, C. Y., Liu, S. B. and Tang, C. Y. (2001): Hollow spheres of MCM-41 aluminosilicate with pinholes. Chemical Communications, pp.1970-1971.
82) Virtudazo, R. V. R., Watanabe, H., Shirai, T. and Takahashi, M. (2011): Direct template approach for the formation of (anisotropic shape) hollow silicate micro particles. IOP Conference Series: Materials Science and Engineering 18, pp.062014.
83) Virtudazo, R. V. R., T., Fuji, Shirai, T. (2011): Fabrication of calcined hierarchical porous hollow silicate micro-size spheres via double emulsion process. Materials Letters 65, pp.3112-3115.
84) Wang, J.-X., Wen, L.-X., Liu, R.-J., Chen, J.-F. (2005): Needle-like calcium carbonate assisted self-assembly of mesostructured hollow silica nanotubes. Journal of Solid State Chemistry 178, pp.2383?2389.
85) Gao, L., Luo, L., Chen, J. and Shao, L. (2005): Synthe-

sis of hollow titania using nanosized calcium carbonate as a template. Chemistry Letters 34, pp.138-139.

86) Shin, T., Fuji, M., Takei, T., Chikazawa, M., Tanabe, K. and Mitsuhashi, K. (2003): Proceeding of 83rd Annual Meeting of the Chemical Society of Japan, March p. 366.

87) Fuji, M., Takai, C., Tarutani, Y., Takei T. and Takahashi, M. (2007): Surface properties of nanosize hollow silica particles on the molecular level, Advanced Powder Technology 18, pp.81-91.

88) Fuji, M., Shin, T., Watanabe, H. and Takei, T. (2011): Shape-controlled hollow silica nanoparticles synthesized by an inorganic particle template method, Advanced Powder Technology.

89) Takai, C., Fuji, M. and Fujimoto, K. (2011): Skeletal silica nanoparticles prepared by control of reaction polarity. Chemistry Letters 40, No.12, pp.1346-1348.

90) Yuan, L., Chen, J. F., Wang, J. X., Shao, L. and Wang, W. C. (2004): A novel pathway for synthesis of silica hollow spheres with mesostructured walls, Materials Letters 58, pp.2105-2108.

91) Li, Z. Z., Wen, L. X., Shao, L. and Chen, J. F. (2004): Fabrication of porous hollow silica nanoparticles and their applications in drug release control. Journal of Controlled Release 98, pp.245-254.

92) Yuan, L., Chen, J. F. and Wang, W. C. (2004): Study on the silica hollow spheres by experiment and molecular simulation. Applied Surface Science 230, pp.319-326.

93) Shchukin, D. G., Patel, A. A., Sukhorukov, G. B. and Lvov, Y. M. (2004): Nanoassembly of biodegradable microcapsules for DNA encasing. Journal of the American Chemical Society 126, pp.3374-3375.

94) Itoh, Y., Matsusaki, M., Kida, T. and Akashi, M. (2004): Preparation of biodegradable hollow nanocapsules by silica template method. Chemistry Letters 33, pp.1552-1553.

95) Wang, Y. Yu, A. and Caruso, F. (2005): Nanoporous polyelectrolyte spheres prepared by sequentially coating sacrificial mesoporous silica spheres. Angewandte Chemie International Edition 44, pp.2888-2892.

96) Yu, A., Wang, Y., Barlow, E. and Caruso, F. (2005): Mesoporous silica particles as templates for preparing enzyme-loaded biocompatible microcapsules. Advanced Materials 17, pp.1737-1741.

97) Yoon, S. B., Sohn, K., Kim, J. Y., Shin, C. H., Yu, J. S. and Hyeon, T. (2002): Fabrication of carbon capsules with hollow macroporous core/mesoporous shell structures. Advanced Materials 14, pp.19-21.

98) Mandal, T. K., Fleming, M. S. and Walt, D. R. (2000): Production of hollow polymeric microspheres by surface-confined living radical polymerization on silica templates. Chemistry of Materials 12, pp.3481-3487.

99) Kamata, K., Lu, Y. and Xia, Y. (2003): Synthesis and characterization of monodispersed core-shell spherical colloids with movable cores. Journal of the American Chemical Society 125, pp.2384-2385.

100) Jiang, P., Bertone, J. F. and Colvin, V. L. (2001): A Lost-wax approach to monodisperse colloids and their crystals. Science 291, pp.453-457.

101) Wang, H., Yu, J. S., Li, X. D. and Kim, D. P. (2004): Inorganic polymer-derived hollow SiC and filled SiCN sphere assemblies from a 3DOM carbon template. Chemical Communications pp.2352-2353.

102) Tanaka, H., Chikazawa, M., Kandori K. and Ishikawa, T. (2000): Influence of thermal treatment on the structure of calcium hydroxyapatite. Physical Chemistry Chemical Physics 2, pp.2647-2659.

103) Williamson, P. A., Blowera, P. J. and Green, M. A. (2011): Synthesis of porous hollow silica nanostructures using hydroxyapatite nanoparticle templates. Chemical Communications 47, pp.1568-1570.

104) Virtudazo, R. V. R., Tanaka, H., Watanabe, H., Fuji, M. and Shirai, T. (2012): Facile preparation in synthesizing nano-size hollow silicate particles by encapsulating colloidal-hydroxyapatite nanoparticles. Journal of Materials Chemistry 21, pp.18205-18207.

105) Sun, Y., Mayers, B. T. and Xia, Y. (2003): Metal nanostructures with hollow interior. Advanced Materials 15, pp.641-646.

106) Sun, Y. and Xia, Y. (2004): Mechanistic study on the replacement reaction between silver nanostructures and chloroauric acid in aqueous medium. Journal of the American Chemical Society 126, pp.3892-3901.

107) Mayers, B., Jiang, X., Sunderland, D., Cattle, B. and Xia, Y. (2003): Hollow nanostructures of platinum with controllable dimensions can be synthesized by templating against selenium nanowires and colloids, Journal of the American Chemical Society 125, pp.13364-13365.

108) Vasquez, Y., Sra, A. K. and Schaak, R. E. (2005): One-pot synthesis of hollow superparamagnetic CoPt nanospheres. Journal of the American Chemical Society 127, pp.12504-12505.

109) Yin, Y., Rioux, R. M., Erdonmez, C. K., Hughes, S., Somorjai, G. A. and Alivisatos, A. P. (2004): Formation of hollow nanocrystals through the nanoscale Kirkendall effect. Science 304, pp.711-714.

110) Wang, C. R., Tang, K., Yang, Q., Hu, J. and Qian, Y. (2002): Fabrication of BiTeI submicrometer hollow spheres. Journal of Materials Chemistry 12, pp.2426-2429.

111) Li, C., Yang, X., Yang, B., Yan, Y. and Qian, Y. (2003): A template-interface co-reduction synthesis of hollow sphere-like carbides. European Journal of Inorganic Chemistry, pp.3534-3537.

112) Huang, J., Xie, Y., Yin, B., Liu, Y., Qian, Y. and Zhang, S. (2000): In-situ source-template-interface reaction route to semiconductor CdS submicrometer hollow spheres. Advanced Materials 12, pp.808-811.

113) Zhu, J. J., Xu, S., Wang, H., Zhu, J. M. and Chen, H. Y. (2003): Sonochemical synthesis of CdSe hollow spherical assemblies via an in-situ template route. Advanced Materials 15, pp.156-159.

114) Gu, Y., Chen, L., Li, Z., Qian, Y. and Zhang, W. (2004): A simple protocol for bulk synthesis of TiC hollow spheres from carbon nanotubes. Carbon 42, pp.235-

238.
115) Hu, G., Ma, D., Cheng, M., Liu, L. and Bao, X. (2002): Direct synthesis of uniform hollow carbon spheres by a self-assembly template approach. Chemical Communications pp.1948-1949.
116) Wang, X., Xie, Y. and Guo, Q. (2003): Synthesis of high quality inorganic fullerene-like BN hollow spheres via a simple chemical route. Chemical Communications, pp.2688-2689.
117) Gao, P. X. and Wang, Z. L. (2003): Mesoporous polyhedral cages and shells formed by textured self-assembly of ZnO nanocrystals. Journal of the American Chemical Society 125, pp.11299-11305.
118) Liu, B. and Zhang, H. C. (2004): Fabrication of ZnO "dandelions" via a modified Kirkendall process. Journal of the American Chemical Society 126, pp.16744-16746.
119) Herring, A. M., Mckinnon, J. T., Kleebe, H. J. and Aldrich, D. J. (2003): A novel method for the templated synthesis of homogeneous samples of hollow carbon nanospheres from cellulose chars. Journal of the American Chemical Society 125, pp.9916-9917.
120) Hah, H. J., Kim, J. S., Jeon, B. J., Koo, S. M. and Lee, Y. E. (2003): Simple preparation of monodisperse hollow silica particles without using templates. Chemical Communications, pp.1712-1713.
121) Fowler, C. E., Khushalani, D. and Mann, S. (2001): Interfacial synthesis of hollow microspheres of mesostructured silica. Chemical Communications pp.2028-2029.
122) Guo, C. W., Cao, Y., Xie, S. H., Dai, W. L. and Fan, K. N. (2003): Fabrication of mesoporous core-shell structured titania microspheres with hollow interiors. Chemical Communications, pp.700-701.
123) Li, Z., Xie, Y., Xiong, Y. and Zhang, R. (2003): A novel non-template solution approach to fabricate ZnO hollow spheres with a coordination polymer as a reactant. New Journal of Chemistry 27, pp.1518-1521.
124) Peng, Q., Dong, Y. and Li, Y. (2003): ZnSe semiconductor hollow microspheres. Angewandte Chemie International Edition 42, pp.3027-3030.
125) 24 Han, Y. S., Hadiko, G., Fuji, M. and Takahashi, M. (2005): A novel approach to synthesize hollow calcium carbonate particles. Chemistry Letters, 34(2), pp.152-153.
126) Han, Y. S., Fuji, M., Shchukin, D., Möhwald, H. and Takahashi, M. (2009): A new model for the synthesis of hollow particles via the bubble templating method. Crystal Growth and Design 9, pp.3771-3775.
127) Han, Y. S., Tarutani, Y., Fuji, M. and Takahashi, M. (2006): Synthesis of hollow silica particle by combination of bubble templating method and sol-gel transformation. Advanced Materials Research 11-12, pp.673-676.
128) Han, Y. S., Hadiko, G. Fuji, M. and Takahashi, M. (2006): Factors affecting the phase and morphology of $CaCO_3$ prepared by a bubbling method. Journal of the European Ceramics Society 26, pp.843-847.
129) Han, Y. S., Hadiko, G. Fuji, M. and Takahashi, M. (2005): Effect of flow rate and CO_2 content on the phase and morphology of $CaCO_3$ prepared by bubbling method. Journal of Crystal Growth 276, pp.541-548.
130) Han, Y. S., Hadiko, G., Fuji, M. and Takahashi, M. (2006): Crystallization and transformation of vaterite at controlled pH. Journal of Crystal Growth 289, pp.269-274.
131) Han, Y. S., Hadiko, G. Fuji, M. and Takahashi, M. (2006): Influence of initial $CaCl_2$ concentration on the phase and morphology of $CaCO_3$ prepared by carbonation. Journal of Materials Science 41, pp.4663-4667.
132) Chen, B. D., Cilliers, J. J., Davey, R. J., Garside, J. and Woodburn, E. T. (1998): Templated nucleation in a dynamic environment: crystallization in foam lamellae. Journal of the American Chemical Society 120, pp.1625-1626.
133) Lin, L., Han, Y., Fuji, M., Endo, T. Endo, Watanabe, H. and Takahashi, M. (2007): A facile method to synthesize ZnO tubes by involving ammonia bubbles. Ceramic Transactions, 198, pp.269-274.
134) Han, Y., Lin, L., Fuji, M. and Takahashi, M. (2007): A novel one-step solution approach to synthesize tubular ZnO nanostructures. Chemistry Letters, 36, pp.1002-1003.
135) Tomioka, T., Fuji, M., Takahashi, M., Takai, C. and Utsuno, M. (2012): Hollow structure formation mechanism of calcium carbonate particles synthesized by the CO_2 bubbling method. Crystal Growth and Design 12 (2), pp. 771-776.
136) Messing, G. L., Zhang, S. C. and Jayanthi, G. V. (1993): Ceramic powder synthesis by spray pyrolysis. Journal of the American Ceramic Society 76, pp.2707-2726.
137) Wojciechowski, K. T. and Oblakowski, J. (2003): Preparation and characterization of nanostructured spherical powders for thermoelectric applications. Solid State Ionics 157, pp.341-347.
138) Karoly, Z. and Szepvolgyi, J. (2003): Hollow alumina microspheres prepared by RF thermal plasma. Powder Technology 132, pp.211-215.
139) Lenggoro, I. W., Hata, T. and Iskandar, F. (2000): An experimental and modeling investigation of particle production by spray pyrolysis using a laminar flow aerosol reactor. Journal of Materials Research 15, pp.733-743.
140) Torobin, L. B. (1987): Method for making hollow porous microspheres. US Patent 4671909.
141) Torobin, L. B. (1988): Hollow microspheres made from dispersed particle compositions and their production. US Patent 4,777,154.
142) Torobin, L. B. (1993): Hollow porous microspheres made from dispersed particle compositions. US Patent 5,212,143.
143) Torobin, L. B. (1993): Methods for producing hollow microspheres made from dispersed particle compositions. US Patent 5,225,123.
144) Torobin, L. B. (1995): Hollow porous microspheres

made from dispersed particle compositions. US Patent 5,397,759.

145) Meyer Jr., R., Weitzing, H., Xu, Q., Zhang, Q. and Newnham, R. E. (1994): Lead zirconate titanate hollow-sphere transducers. Journal of the American Ceramics Society, 77 (6), pp.1669-1672.

146) Loscertales, I. G., Barrero, A., Marquez, M., Spretz, R., Velarde-Drtiz, R. and Larsen, G. (2004): Electrically forced coaxial nanojets for one-step hollow nanofiber design. Journal of the American Chemical Society 126, pp.5376-5377.

147) Sato, M. (2000): Formation of hollow silica particles by electrostatic atomization in combination with alcohol solidification. Eight International Conference on Liquid Atomization and Spray System (ICLASS 2000), Pasadena, USA, pp.400-406.

148) Enomae, T. and Tsujino, K. (2002): Application of spherical hollow calcium carbonate particles as filler and coating pigment, TAPPI Journal online exclusives, Coating & Graphic Arts Conference and Trade Fair, Orlando, FL, United States, May 5-8, pp.357-377.

149) Holland, B. T., Blanford, C. F. and Stein, A. (1998): Synthesis of macroporous minerals with highly ordered three-dimensional arrays of spheroidal voids. Science 281 pp.538-541.

150) Wijnhoven, J. E. G. J. and Vos, W. L. (1998): Preparation of photonic crystals made of air spheres in titania. Science 281, pp.802-804.

151) Gu, Q., Norimatsu, T., Fujioka, S. and Nishimura, H. (2005): Preparation of low-density macrocellular tin dioxide foam with variable window size. Chemistry of Materials 17, pp.1115-1122.

152) Kortesuo, P., Ahola, M., Karlsson, S., Kangasniemi, I., Kiesvoara, A. and Yli-Urpo, J. (2000): Silica xerogel as an implantable carrier for controlled drug delivery evaluation of drug distribution and tissue effects after implantation. Biomaterials 21, pp.193-198.

153) Ahola, M. S., Sailynoja, E. S., Raitavue, M. H., Voahtie, M. M. and Salonen, J. I. (2001): In vitro release of heparin from silica xerogels. Biomaterials 22, pp.2163-2170.

154) Chen, J. F., Ding, H. M., Wang, L. X. and Shao, L. (2004): Preparation and characterization of porous hollow silica nanoparticles for drug delivery application. Biomaterials 25, pp.723-727.

155) Tartaj, P., Gonzalez, T. and Serna, C. J. (2001): Single-step nanoengineering of silica coated maghemite hollow spheres with tunable magnetic properties. Advanced Materials 13, pp.1620-1624.

156) Jackson, J. B., Wescott, S. L., Hirsch, L. R., West, J. L. and Halas, N. S. (2003): Controlling the surface enhanced Raman effect via the nanoshell geometry. Applied Physics Letters 82, pp.257-259.

157) Brongersina, M. L. (2003): Nanoscale photonics: Nanoshells: gifts in a gold wrapper. Nature Materials 2, pp.296-297.

158) Radt, B., Smith, T. A. and Caruso, F. (2004): Optically addressable nanostructured capsules. Advanced Materials 16, pp.2184-2189.

159) Angelatos, A. S., Radt, B. and Caruso, F. (2005): Light-responsive polyelectrolyte/gold nanoparticle microcapsules. The Journal of Physical Chemistry B 109, pp.3071-3076.

160) Graf, C. and Van Blaaderen, A. (2002): Metallodielectric colloidal core-shell particles for photonic applications. Langmuir 18, pp.524-534.

161) Fergason, J. L. (1985): Polymer encapsulated nematic liquid crystals for display and light control applications. Sessional Information Digest 85, pp.68-70.

162) Ota, I., Ohnishi, J. and Yoshiyama, M. (1973): Electrophoretic image display (EPID) panel. Proceedings of IEEE 61, pp.832-836.

163) Comiskey, B. Albert, J. D., Yoshizawa, H. and Jacobson, J. (1998): An electrophoretic ink for all-printed reflective electronic displays. Nature 394, pp.253-255.

164) Yoshizawa, H. (2004): Trends in Microencapsulation Research. Kona 22, pp.23-31.

165) Song, C. X., Wang, D. B., Gu, G. H. and Y. S. Lin (2004): Preparation and characterization of silver/TiO$_2$ composite hollow spheres. Journal of Colloids and Interface Science 272, pp.340-344.

166) Sun, Y., Yin, Y., Mayers, B. T., Herricks, T. and Xia, Y. (2002): Uniform silver nanowires synthesis by reducing AgNO$_3$ with ethylene glycol in the presence of seeds and poly(vinyl pyrrolidone). Chemistry of Materials14, pp.4736-4745.

167) Xia, Y., Yang, P., Sun, Y., Wa, Y., Mayers, B., Gates, B., Yin, Y., Kim, F. and Yan, H. (2003): One-dimensional nanostructures: synthesis, characterization, and applications. Advanced Materials 15, pp.353-389.

168) Jin, R., Cao, Y., Mirkin, C. A., Kelly, K. L., Schatz, G. C. and Zhang, J. G. (2001): Photoinduced conversion of silver nanospheres to nanoprisms. Science 294, pp.1901-1903.

169) Fuji, M. and Takai, C. (2012): Superior thermal insulation film with transparency achieved by hollow silica nanoparticles. Nanoparticle Technology Handbook, second edition, Elsevieir, pp.679-684.

170) Bao, J., Liang, Y., Xu, Z. and Si, L. (2003): Facile synthesis of hollow nickel submicrometer spheres. Advanced Materials 15, pp.1832-1835.

171) Lee, K. T., Jung, Y. S. and Oh, S. M. (2003): Synthesis of Tin-Encapsulated Spherical Hollow Carbon for Anode Material in Lithium Secondary Batteries. Journal of the American Chemical Society 125, pp.5652-5653.

Author's short biography

Masayoshi Fuji

Masayoshi Fuji is Professor of Advanced Ceramics Research Center, Nagoya Institute of Technology (NIT), Gifu, Japan. He received his Dr. Eng. from the Faculty of Engineering of Tokyo Metropolitan University in 1999. He joined the Dept. of Industrial Chemistry, Tokyo Metropolitan University, as a Research Associate in 1991. He was visiting Researcher at Engineering Research Center, University of Florida from 2000 to 2001. He joined NIT since 2002 and was promoted Professor in the Graduate School of Engineering in 2007. His research interests are surface chemistry, ceramic processing, and powder technology.

Yongsheng Han

Dr. Yongsheng Han got his bachelor degree from Changchun University and Science and Technology in 1997, master degree from Jilin University in 2000 and doctor degree from Tsinghua University in 2004 with the specialty of materials science and engineering. Immediately after his graduation, he went to Japan, Nagoya Institute of Technology and worked there as a postdoctoral researcher for more than 3 years. In 2007, he was awarded Alexander von Humboldt fellowship and went to Germany, Max Planck Institute of Colloids and Interfaces. In 2011, he succeeded in the application of Hundreds Talents Program and joined in the Institute of Process Engineering, Chinese Academy of Science. His current research interest is the controlled synthesis of catalysts and biomaterials.

Chika Takai

Chika Takai is a postdoctor of Advanced Ceramics Research Center, Nagoya Institute of Technology, Japan since 2010. She received B. S. from Department of Materials Engineering in 2001, M. S. from Graduate School of Engineering in 2003, and ph. D. from Graduate School of Engineering of Nagoya Institute of Technology in 2006. She joined Kurimoto Ltd. in 2007 which is cast-iron pipe company in Osaka and was involved in research and development. Her research interests are particle synthesis with structure control and control particle dispersion.

Some Recent Advances in Drying Technologies to Produce Particulate Solids[†]

Duu-Jong Lee[1,2], Sachin Jangam[3] and Arun S. Mujumdar[3,4*]
[1] *Department of Chemical Engineering, National Taiwan University of Science and Technology*
[2] *Department of Chemical Engineering, National Taiwan University*
[3] *Mechanical Engineering Department, National University of Singapore*
[4] *Institute of Chemical Technology, Mumbai, India*

Abstract

Thermal drying is a highly energy-consuming process found in almost all industries accounting for between 10-20% of national industrial energy consumption in the developed economies of the world. It is arguably the oldest unit operation and yet R&D in this area is only a few decades old. Over 50% of products consumed by humans are in particulate form so that drying of wet particulates as well as feedstock such as solutions, suspensions or pasty solids is of great industrial interest. Efficient drying technologies must produce engineered dry particulates of desired quality at minimum cost, low carbon footprint and little environmental impact. This article attempts to provide a global overview of recent advances in drying technologies most of which represent evolutionary innovations. In order to reduce investment costs one needs to enhance drying rates within limits imposed by the product properties and end product quality requirements. Several novel gas-particle contactors for example have been evaluated for drying. Combined modes of heating and hybrid dryers can improve drying performance in some cases. Recent interest in production of nanoparticles by wet processing also has stimulated interest in drying to produce nanoparticles. Drying of heat sensitive biotech and pharmaceutical products also pose new challenges. A capsule overview is presented of recent developments including enhancements in conventional drying technologies as well as more innovative new technologies.

Keywords: advances in drying, hybrid drying, innovative dryers, particulate matter, selection and classification

1. Introduction

Drying involves removal of a liquid- most of the time water- from diverse physical forms of feedstock at widely varying production rates (1 kg/h to 100t/h) subject to different quality constraints. In fact hundreds of variants are needed to meet the commercial requirements. Drying involves transient transport phenomena subject to rather severe constraints imposed by material science. Thus the same physical dryer will work differently for different materials and in fact may not work at all for some if there are some changes in properties such as stickiness or change in glass transition temperatures during drying[1)]. Minor changes in product formulations can affect drying kinetics such that the capacity of a given dryer may be altered substantially. Although recent R&D aims at injecting more science and engineering into the scale-up, design and operation of most dryers, industrial dryer design still depends heavily on empiricism and operating experience. Innovations therefore come slowly. Another reason for the slow rate of innovation in industrial drying may be the long shelf life of most dryers which may range from 25 to 50 years in some cases which makes it unattractive to change designs frequently[2, 3)]. Lack of fundamental knowledge makes scale-ups hard, unreliable and risky.

In this paper we will look at conventional dryers

[†] Accepted: September 1, 2012
[1] No.1, Sec. 4 Roosevelt Rd. Taipei, Taiwan 106
[2] 9 Engineering Drive 1, Singapore 117576
[*] Corresponding author:
E-mail: mpeasm@nus.edu.sg
TEL:+65-6516-4623 FAX:+65-6775-4710

© 2013 Hosokawa Powder Technology Foundation

which can be enhanced by simple modifications, combination with known drying technologies and modifying the way heat is input into the system. We shall also examine some newer gas-particle contactors which are or can be used as convective dryers due to their enhanced heat and mass transfer performance.

Note that when the feedstock is in liquid or sludge form some sort of pretreatment is often applied to speed drying or to reduce the drying duty. In the interest of space this aspect is not covered here. Readers may refer to Handbook of Industrial Drying1) for details. When selecting a dryer for a given application it is important to examine the whole drying system which may typically include mechanical dewatering before drying and some post-dryer operations such as cooling, coating, agglomeration etc. It is suggested that LCA should also be carried out before selecting the drying system as the concerns of global warming and resulting legislations may place severe limitations in emission of green house gases in not-too-distant future.

Selection of dryers is a major and most important task. It is necessary to look at conventional dryers as well as the newly developed ones although there is limited field experience with the latter. In the following section we will examine the classification and selection of dryers as it is central to further discussion on recent developments.

2. Some Conventional Dryers - Selection and Classification

Dryer selection has long been practiced as an art rather than science depending more on prior experience and vendors' recommendations. As drying technologies have evolved and become more diverse and complex, this has become an increasingly difficult and demanding task for the non-expert. For an optimal selection of process, one must examine the overall flowsheet as well as the "drying system" . A careful evaluation of as many of the possible factors affecting the selection helps to reduce the number of options. For a new application (new product or new process), it is important to follow a careful procedure leading to the right choice of the dryer.1) Characteristics of different dryer types should be recognized when selecting dryers. Changes in operating conditions of the same dryer can affect the quality of the product. So, aside from the dryer type, it is also important to choose the right operating conditions for optimal quality and cost of thermal dehydration. Each type of dryer has specific characteristics, which make it either suitable or unsuitable for a specific given application. The details can be found in Mujumdar (2006).1)

Baker5, 6) has suggested a "structural approach" for dryer selection, which is iterative. It includes following steps:

- List all key process specifications
- Carry out preliminary selection
- Carry out bench scale test including quality tests
- Make economic evaluation of alternatives
- Conduct pilot scale trials
- Select most appropriate dryer type

Sometimes the selection is based on the past experience rather than the technical approach. It has few limitations such as; the new choice will be less-than-optimal if the original selection is not optimal. Selection of a proper dryer is a crucial step, but best design of the wrong dryer is still a poor choice. Historically, dryer selection has been made by experts on the basis of their extensive knowledge. However, in recent years the computer based techniques have been developed, which have the potential of at least partially deskilling this process. Amongst these possibilities, fuzzy expert systems are the most promising. Before going for the selection of drying system proper classification of dryers based on various criteria is very necessary such as the one provided in **Fig. 1** based on mode of operation.

For illustrative purposes let us look at drying of foods. A wrong choice of a drying system and/or drying conditions can have adverse effects on both the physical and nutritional properties of the dried product. The selection of a dryer for a particular food product depends on the type of feed, the amount and type of moisture, drying kinetics, heat sensitivity, physical structure of the material to be dried, quality requirements of a dried food and many other factors 7-10). Dryers are commonly classified based on the mode of heat transfer (e.g. conduction, convection or radiation) and mode of operation (batch vs continuous). Long drying times and small throughputs favour batch drying.

Fig. 2 lists various conventional drying methods used for food applications. This is a very basic categorization of dryers based on physical nature of the wet material to be dried. For liquid feed, spray drying is still the most common way of drying although rotary drum dryers are also popular. Drying of liquids by spraying on beds of inert particles using some variants of the fluidized bed, spouted bed, moving bed, vibrated bed, agitated bed etc have also been proposed for drying pastes and slurries to produce

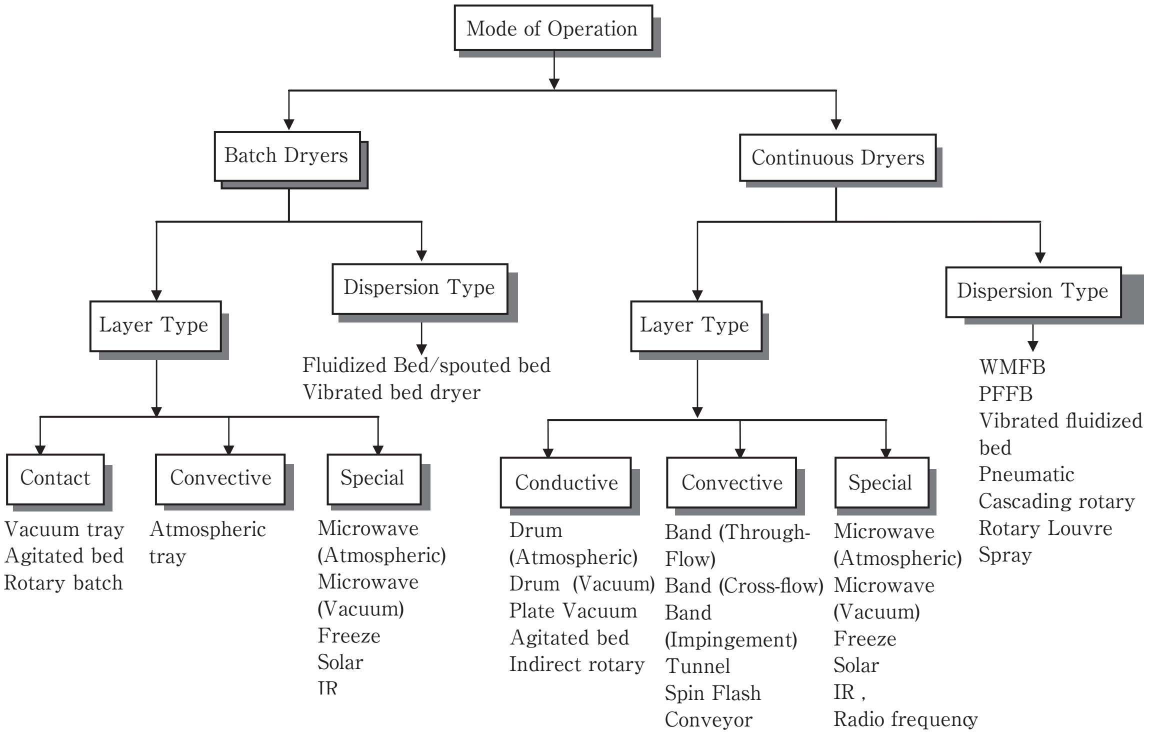

Fig. 1 Classification of dryers based on mode of operation.

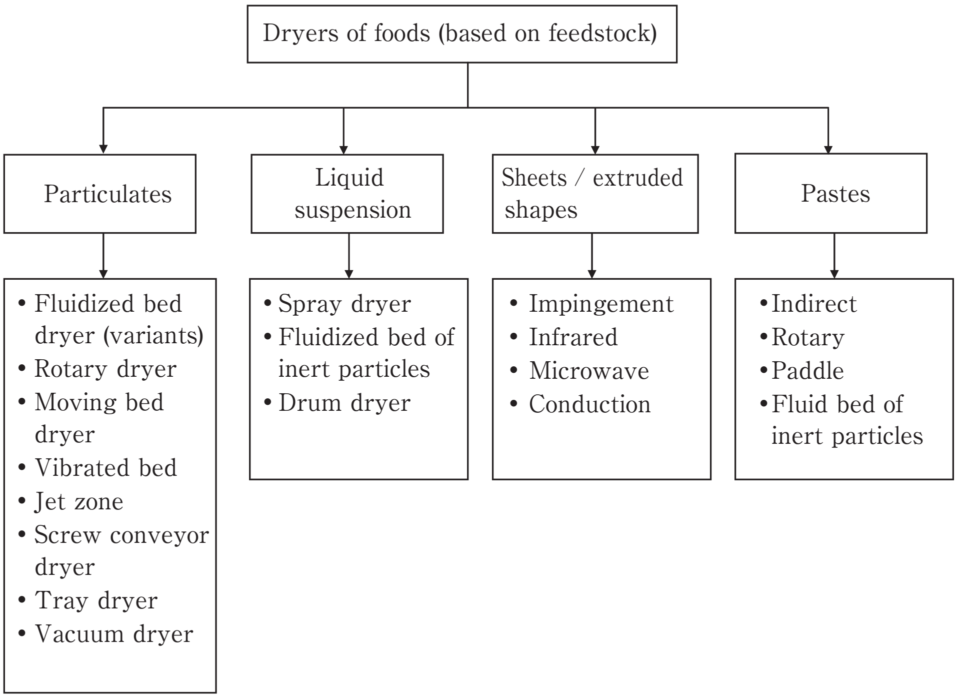

Fig. 2 Classification of dryers for food processing.

powders. Spray drying is an expensive technique to use for low value products, mainly because of its low thermal efficiency due to requirement of moving large quantity of drying air through a large chamber and then collecting the particles in a suitable gas cleaning system. Therefore a method such as inert bed drying has been proposed and recently much effort has been devoted to this technique[11-13]. However, the spray drying technique does offer the capability to produce high functional products through encapsulation processes and in controlling the particle size without milling or attrition which might damage the product. Also often only spray drying offers the physical characteristics needed for certain products.

For drying of particulates, there are a vast number of dryers available and the choice depends on the size, size distribution and shape of the wet feed material, stickiness, the feed moisture, drying kinetics etc. The commonly used dryers for particulate materials are listed in **Fig. 2**. Some of the variants of fluidized bed dryer are often preferred over the other drying systems for particulate drying because of the fact that fluidized beds provide very high heat and mass transport rates between gas and particles and have better thermal efficiency and lower maintenance costs and footprints than, say, rotary dryers which were very popular in the old days. However, a few constraints need to be addressed such as the physical nature of the feed (particle size and particle size distribution); this has resulted in several innovations in fluidized bed dryer technology for better gas-particle contact including use of mechanical agitation, vibration, pulsation of flow and more[1, 10].

For extruded products, drying can be achieved on a belt conveyor or in a batch process by use of either conductive or radiative heat transfer along with convection and application of vacuum. However, pasty materials are conventionally dried using indirect rotary, paddle or drum dryers and more recently but less commonly using beds of inert particles using some variants of the fluidized bed dryer as discussed previously for liquid suspensions. The more expensive techniques such as freeze drying are employed mainly to produce high quality dried products which are ultra-heat sensitive and have high market value. However, the cost of low temperature vacuum processing is many times higher than that of other convection dryers which makes it less attractive for most products. Heat pump drying is a technique which combines a heat pump with any convective dryer to accomplish drying at faster rate with very high energy efficiency, variable drying conditions and highly improved product quality compared to conventionally used convective dryers. Any convection dryer can be coupled to a heat pump as the dehumidification allows a larger potential for mass transfer even at lower operating temperatures.

There always exists scope for improvement in almost all conventional dryers in practice. Commonly this may involve mechanical design changes, choice of drying media, gas distribution systems, time cycles for drying, combining different heat transfer modes, multi-stage operation etc. **Table 1** identifies some key areas for enhancement of frequently used dryers. Often many of the enhancements are not available from commercial vendors. Note that it is just as important to select the operating conditions and control them effectively.

Table 1 Key areas for improvement in commonly used dryers

Dryer type	Scope for improvements
Tray	• Design of better air distribution system to achieve flow uniformity to achieve uniform moisture distribution • Use of intermittency; combined mode of heat transport • Use of heat pump to dehumidify drying air
Fluidized bed dryers	• Poor fluidization quality for Geldart's class 'C' and class 'D' particles; improve the quality by mechanical means such as agitation, vibration, pulsation etc • Improve gas distribution system • Use of internal heat exchangers for internal heat transfer • Combining fluidized beds with heat pump system • Superheated steam drying, low pressure drying, vacuum drying • Novel chamber designs • Variants of spouted bed dryers; spout-fluid beds
Spray dryers	• Improvements in drying chamber design for minimization of wall deposition • Improvements in atomization method for uniform particles size and size distribution, minimization of agglomeration • Use of ultrasonic atomizers • Use of superheated steam • Application of computational fluid dynamics for efficient design of spray dryer chambers • Injection of supplementary air to reduce wall deposits
Rotary dryers	• New designs of flights and use of internal heat exchangers • Precise control of final moisture content by controlling residence time distribution • Improvement in hot air injection system • Use of model-based control
Drum dryers	• Heat transfer enhancement by radiant heat or impinging streams • Increase the energy efficiency
Vacuum dryers	• Use of combined heating modes such as microwave • Use of radiative heating
Freeze dryers	• Use of magnetic and electric fields to control crystal size • Reduce the cycle time • Atmospheric pressure operation to reduce cost

3. Recent Advances in Drying Systems

Conventional dryers often have several limitations such as the development of non-uniform product quality due to over-drying or under-drying caused by either long, inadequate or non-uniform exposure of product to the drying medium; long drying times due to low contact efficiency between the drying medium and solids being dried and harder texture owing to case hardening of the product surface caused by over-drying etc. This gives rise to poor drying performance and higher operating costs. Several studies have been reported to overcome the operational difficulties encountered in conventional dryers and to improve the quality of the dried products. Most conventional dryers used in food processing are of direct or convection type and utilize fossil fuels as energy source. Typically such dryers have low thermal efficiency since it is typically not cost-effective to recover heat from the low temperature exhaust. In addition the combustion of fossil fuels leads to greenhouse gas (GHG) emissions. The long term effect of GHGs has been a major concern in recent years. Use of biomass and renewable energy may mitigate the problems but much remains to be done to ensure wide acceptance of better drying and preservation practices. The drying technique and operating conditions selected for a particular product affect the quality of the dried product as well as its cost. While selecting a dryer -whether conventional or innovative- one must evaluate both the energetic performance as well as quality attributes of the final product. It should be remembered that a dryer successfully used for one product can give a totally different performance for certain other product. Also, the choice of optimal dryer depends on the geographic location, cost of labor and energy source etc as well.

New developments in dryers and emerging drying technologies can be classified in different categories. These categories represent areas in drying technology that require improvement. However, all new developments and emerging drying technologies must be cost-effective. This is needed to ensure market acceptance as the industry will not accept a new dryer for its novelty[14-16]. New technologies are needed principally for one or more of more of the following reasons if the existing technology is deemed inadequate:

- Drying of new products and/or processes
- To improve thermal efficiency and production capacity than current technology permits
- Better quality and quality control than existing dryers
- Reduced fire, explosion, toxic hazards, safer operation
- Better overall cost
- Reduced environmental impact, use of renewable energy
- Minimizing the capital, operating and maintenance costs
- Shorter processing time while maintaining high product quality
- Better sustainability and lower carbon footprint from LCA
- Smaller footprint and ease of control

Some of the areas which need R&D have been addressed by researchers in recent years[2, 3]. **Fig. 3** summarizes briefly a number of possibilities for improvements in conventional dryers adopted for better performance. Significant advancement have been made over the past few years which have lead to new developments in drying that are briefly discussed in the following sections. Some general attributes of the recently developed dryers include[14-16].

- Multiple heat input concurrently or sequentially to match instantaneous (for batch) or local (for continuous) drying kinetics without adverse effect on product quality, e.g. convection followed by or simultaneously with conduction, radiation, or microwave heat input
- Time-dependent operating conditions (e.g. Temperature, pressure, humidity of drying gas, velocity of drying gas etc)
- Time-dependent operating pressure (e.g. the Swell Drying concept where vacuum and above atmospheric pressure are applied cyclically to enhance drying rate and also to make the dried product more porous)
- Superheated steam or inert gas as a drying medium at high, atmospheric or sub-atmospheric pressure
- Use of mechanical action to enhance drying rates
- Low temperature dehumidified air as drying medium at modified atmosphere which eliminates existence of oxygen
- Use of absorbents to remove water vapor as it is generated to maintain high driving force for mass transfer even at lower temperatures. Adsorbents must be edible for food applications for human as well as animal consumption
- Multi-stage drying and hybrid drying that combine different type of dryers or different types of heat input, e.g. MW-vacuum drying, spray drying followed by fluid bed/vibrated bed as second

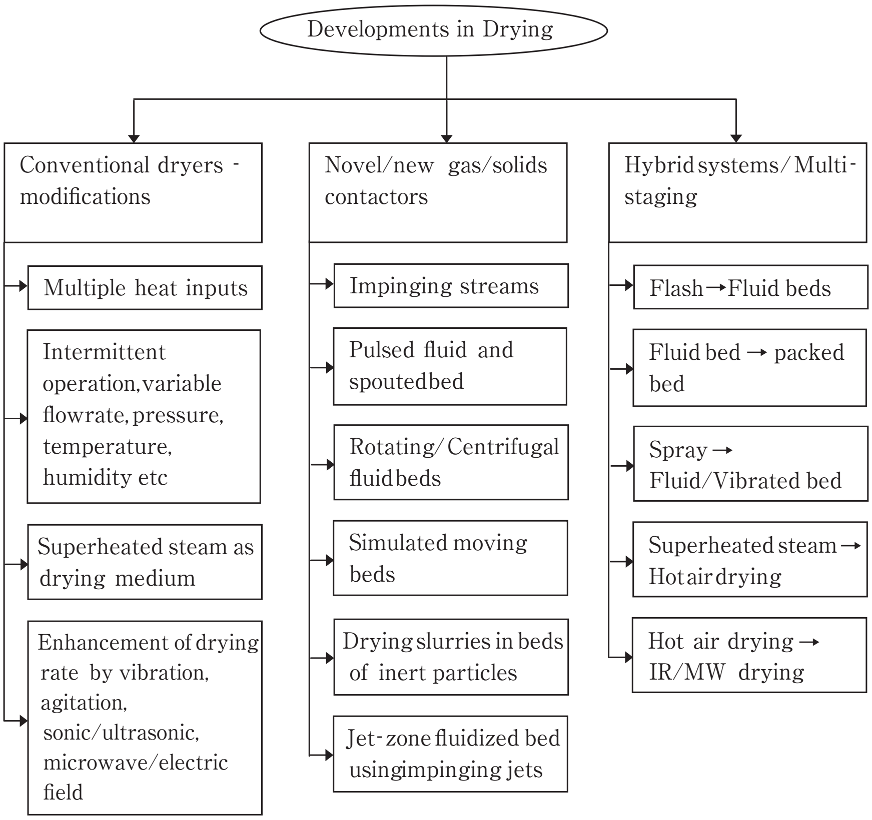

Fig. 3 Recent developments in drying.

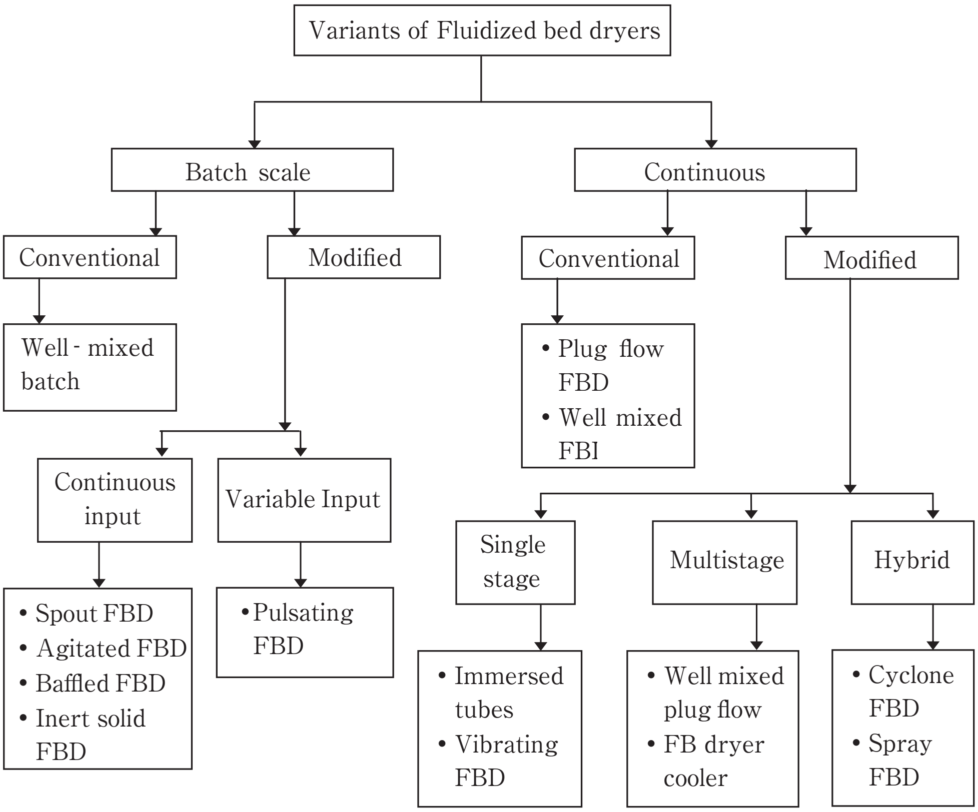

Fig. 4 Variants of fluidized bed dryers.

and/or third (some possibilities given in **Fig. 3**)

3.1 Fluidized Bed Drying (FBD)

There are various choices of fluidized bed dryers available for particulates[1, 17]. Some of the most commonly used FBDs are mentioned in **Fig. 4** along with modifications to cope up the limitations of conventional FBD. **Fig. 5** shows some schematics of some fluidized bed variants. Selecting a proper fluidized bed dryer for certain application itself is a big task. Particles/powders are classified into four major groups according to their characteristics when exposed to fluidizing gas stream, this is used as the main criteria for selection of FBD for a particular application. The details are provided elsewhere [1]. The quality of fluidization of Group C (Fine/ultrafine) and Group D (large particles) of Geldart classification is not very good leading to numerous problems such as channeling and poor contact efficiency. For most of the pharmaceutical and food applications batch fluid bed dryer is an obvious choice because of comparatively small quantity of wet material to be processed. On the other hand, batch fluid bed does not work well for drying of specialty chemicals and minerals where huge throughput is to be handled (sometimes as high as 200 tonnes per hour for coal processing). For such applications, vibrated bed or plug flow fluid bed are used. Recent developments in FBD include mechanically agitated FBD, use of pulsating flow, use of immersed tubes for efficient heat transfer, baffled FBD.

The quality of fluidization can be substantially improved either by mechanical vibrations, agitation or with a pulsating flow of fluidizing gas. Agitated fluid bed dryer is a modified version used for number of pharmaceutical applications to handle very fine/cohesive particles using lower fluidization velocity. By mechanically agitating the bed of particles, a homogeneous fluidizing bed of fine particles is formed without any channeling or big bubbles[17-19]. The other advantages are possibility of using a deeper bed depth without affecting the fluidization quality, reduction in agglomeration and increase in void fraction resulting in better fluidization quality[17]. In case of pulsating fluidized beds, the fluidization velocity pulsates with time in the form of regular or irregular patterns. Many studies have shown that pulsed fluidization can improve the fluidization quality as it eliminates the problem of channelling and slugging[20-22]. Li et al.[21] reported that the pulsating fluidized beds result into reduced bubble size and better gas-particle contact. Hence, some difficult-to-dry materials can

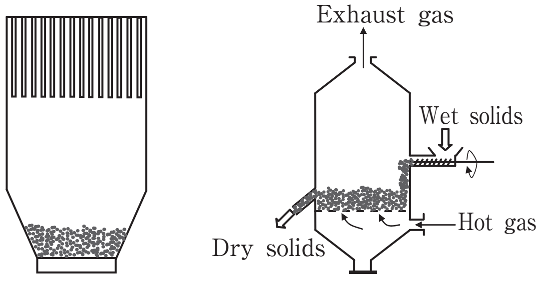

Batch fluidized bed dryer Well mixed fluidized bed dryer

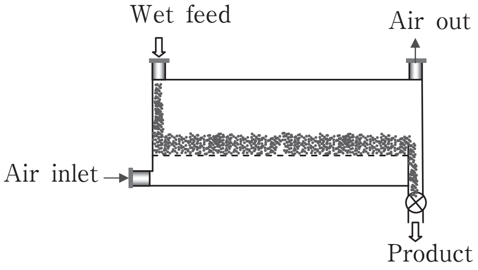

Plug flow fluid bed dryer

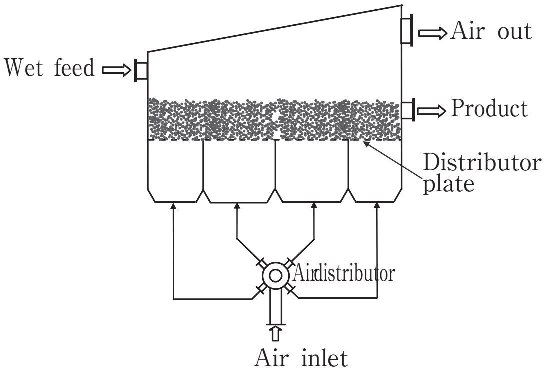

Pulsating flow fluid bed dryer

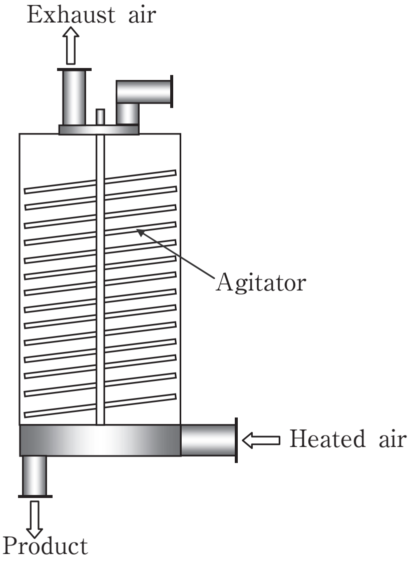

Agitated fluid fluidized dryer

Fig. 5 Schematics of selected fluid bed dryer variants.

be easily handled. Li et al.[21] have also carried out the theoretical study of the hydrodynamic behaviour of these dryers using two-fluid model for three pulsating frequencies of 0.4, 4 and 40Hz. It was concluded that 40Hz resulted in to normal fluidization. In addition, the bed expansion was more in pulsating fluidized bed dryer with low bed fluctuation rates which means improved fluidization quality. These types of fluidized bed dryers can replace traditional FBDs in for various applications and can be considered as better options to develop more efficient drying system. Variants of fluidized bed dryers have been successfully used for drying of suspensions and pastes in a bed of inert particles. Freire et al.[23] have reviewed drying of variety of pastes with inert particles using different fluidized beds. For heat sensitive materials a fluidized bed under reduced pressure can be used very effectively [24].

3.2 Spray Drying (SD)

Spray drying is one of the oldest and most commonly used technique for drying of liquid feedstock to particulate form in several industrial sectors. There are several designs of spray dryers available mainly categorized based on the flow directions of spray and drying gas, the type of atomizer and the number of stages. Selection of a proper atomizer is very important which decides the particles properties in addition to other operating parameters. For more details readers can refer to the recent review[25-27]. Spray drying for encapsulation and microencapsulation of valuable foods and neutraceutical ingredients is a one step and highly cost-effective technique compared to other methods of encapsulation. This is well-established technique used in several industrial sectors - mainly food and pharmaceutical.

As mentioned earlier, spray drying is very famous technique for liquid suspensions, but there are several limitations linked to it which include low energy efficiency, use of huge volumes of drying air, use of high temperature and wall deposition etc. There have been continual improvements in the design of spray dryers in order to overcome the aforementioned limitations. A notable work includes study on novel types of atomizers used to atomize highly viscous and non-Newtonian liquids which cannot be atomized using ordinary atomizers. The most recent development is sonic atomizer. In these types of atomizers the liquid breakdown occurs in the field of high-frequency sound created by a sonic resonance cup placed in front of the nozzle. However, this technique is still not well-developed a level of commercialization.

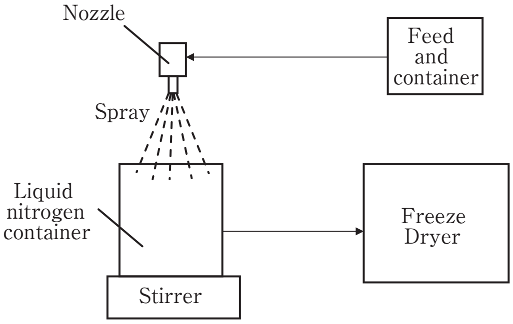

Fig. 6 Spray freeze drying.

A horizontal spray dryer was first suggested by Mujumdar in 1982 as an alternative to the conventional vertical types[28] to reduce difficulties in scale-up. Kwamya and Mujumdar[29] developed the first simple mathematical model to evaluate this novel concept. Recently, at least two US companies produce horizontal spray dryers, especially for heat-sensitive food and pharmaceutical materials. Low drying temperatures allow flavor retention, high solubility, controlled porosity and density and fine quality agglomerated products. They also claim substantial energy savings relative to the traditional vertical spray dryer with lower electrical load for given capacity. Commercial applications include dryers for egg, albumin, whole egg powder, cheese powder, skim milk, whey protein, etc.

Recently, a combination of spray drying and a well know Freeze drying is has been found to be very interesting. A spray freeze drying is a technique which gives extremely good quality dried (free flowing, ultrafine and uniform size) particles with very high surface area and porosity (**Fig. 6**). This technique mainly involves atomization of liquid feedstock in low temperature atmosphere and then dried using either atmospheric or vacuum freeze drying. The SFD is categorized based on the medium used to atomize the liquid solution. The SFD in liquid (also known as SFL) is the class in which the liquid feedstock is atomized in a cryogenic liquid (such as liquid nitrogen) to form the frozen droplets which are then separated and dried using either atmospheric or vacuum freeze dryer. This type of SFD provides nanoparticles with large surface area and hence can be used for several pharmaceutical applications. The SFD in gas (SFG) is the one in which the liquid feedstock is atomized in a refrigerated gas so that the droplets freeze immediately which are then dried using a freeze dryer. SFD over the gases in fluidized bed is the technique in which the particles frozen using gas are freeze dried in a fluidized bed chamber. Although the product quality is excellent the energy consumption and investment cost is very high for SFD. Hence this technique can be use for very special applications such as drugs, neutraceuticals, functional foods, and some high value products.

3.3 Drying to produce nano-particles

Nanomaterials represent today's cutting edge in the development of novel advanced materials, which promise tailor-made functionality for unique applications in all important industrial sectors, e.g., Automotive and aeronautics industries; Electronics and communications; Chemicals and materials, pharmaceuticals, healthcare, and life sciences; Manufacturing; Energy technologies; Space exploration and Environment etc.30). Preparation of nanomaterials can be classified into three main approaches according to the states of the reactants: liquid-phase, solid-phase and gas-phase method. One of the most popular methods in both laboratory and industry at present is the liquid-phase method. In the preparation of nanoparticles by the liquid-phase method, drying is an indispensable unit operation. Drying can be an essential step in a production cycle of the following groups: nanoparticles, nanostructured surfaces, and films and nanoporous materials.

Since spray drying is a well-mastered technology, easily controlled and one-step operation. Conventional spray dryers can be used to product nano-materials by some modification spraying technique that can produce much smaller droplets. This is also done by using very low initial concentration. There are several research articles which reports use of spray drying to produce nano-particles31-33). Arpagaus34) proposed a novel spray drying technique to produce nanoparticles. In their system, the liquid feed is atomized in to fine droplets using piezoelectric-driven vibrating mesh atomizer then subjected to drying in a drying chamber in order to yield solid particles and, finally, separated and collected by a suitable electrostatic dry powder collector. The technological novelty of this patented spray dryer lies in the gentle laminar drying flow, the vibrating mesh spray technology, and the highly efficient electrostatic particle collector. Chen and Wang35) have reviewed the role of freeze drying in nanotechnology and pointed out that freeze drying not only can remove solvent but also can produce desired nanoparticles. There are several papers on application of freeze drying to produce nanoparticles36, 37). Bulk drying methods like oven drying are sometimes used for drying nanoparticles at the laboratory scale. In order to avoid agglomeration, all ions and water have to be removed prior to drying38).

Supercritical drying is another method reported to produce nanoparticles38). Supercritical drying is a process to remove liquid in a precisely controlled way. When the pressure and temperature of the sample are raised above the critical point of moisture in an autoclave, surface tension disappears, and solvent can be evacuated slowly without affecting the structure. Supercritical drying goes beyond the critical point of the working fluid in order to avoid the direct liquid-gas transition seen in ordinary drying or the two phase changes in freeze drying. However, supercritical drying is very expensive process.

3.4 Superheated steam drying

In a superheated steam drying (SSD) (**Fig. 7**), the drying gas in a convective dryer is replaced with superheated steam. Superheated steam can be used in different types of convection dryers. Figure shows the simple concept of SSD. Superheated steam at certain pressure enters the drying chamber and takes out the moisture from the wet solids; the exhaust from the dryer is also superheated steam although at a lower specific enthalpy. A part of the steam can be recycled back after compression and the excess can be either used directly or purged out of the system. Superheated steam is an attractive drying medium for some products which give better product quality in the absence of oxygen. The net energy consumption of the SSD can be minimized only if the exhaust steam coming out of the dryer is either utilized elsewhere in the plant and not "charged" to the dryer1, 39, 40). In order to achieve efficient energy recovery from the exhaust steam it is necessary to have a leak-proof system to avoid air leakage. Use of superheated steam eliminates the risk of fire and explosion hazard as a result of absence of oxygen. Readers may refer to detailed discussion in Advanced Drying Technology by Kudra and Mujumdar41).

Typically superheated steam drying can also give

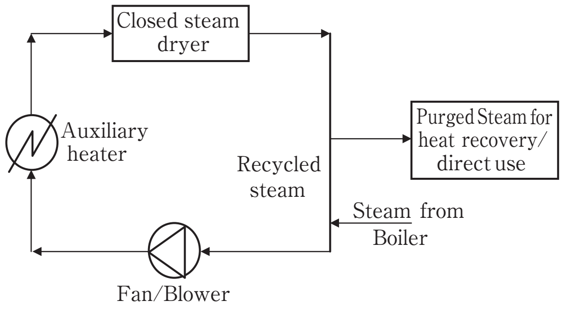

Fig. 7 Schematic of SSD.

higher drying rates in both constant and falling rate periods under certain conditions. The higher drying rates in constant rate period are possible only when the temperature used is above the inversion temperature. During the constant rate period using hot air and SS at the same operating temperature, the driving force (difference in the surface temperature and drying gas temperature) is higher in air drying. This is because the solid temperature is equal to the wet bulb temperature in case of air drying while in SSD it equals the saturation temperature of steam at the operating pressure. However the heat transfer coefficient in air drying is lower than that in SSD because of better thermal properties of steam. Hence there exists certain temperature called inversion temperature above which the drying rates in SSD are higher than air drying in constant rate period. However, the reason for higher drying rates in falling rate period is different. The surface temperature is higher in SSD hence the water mobility is higher in falling rate period which results in faster drying. This can of course affect product quality adversely. Pakowski and Adamski42) presented a method to determine the drying rate in falling rate period. They pointed out that surface temperature must be known accurately in order to predict the drying rates in falling rate period.

Superheated steam drying has been used to dry wide range of products including coal43, 44), wood45, 46), sludge47) and variety of food products, mainly at reduced pressure48-50). Mujumdar has discussed the principles, advantages and limitations as well as diverse applications of superheated steam drying technologies in a number of papers and books39, 40, 51), including the Handbook of Industrial Drying1). There have been several attempts to model heat and mass transfer during SSD process52, 53). However, SSD has several limitations such as complexity of the process, making the system leak-proof to avoid leakage of atmospheric air in the system which results in problems during condensation and compression if the steam is recycled. The SSD cannot handle the products which melt or undergo glass transition unless low pressures are employed. At low pressure the low density and thermal conductivity of superheated steam lowers the heat transfer coefficient and makes the process very slow.

3.5 Impinging Stream Drying (ISD)

Impinging stream dryers are novel alternatives to flash dryers for particulate materials with very high drying loads. Nevertheless, studies on ISD are still partial or limited to very few applications. In these type of dryers the intensive collision of opposed streams creates a zone that offers very huge heat, mass and momentum transfer54). Hence rapid removal of surface moisture is possible. Other advantages of impinging dryers are smaller foot prints and high robustness due to absence of any moving part. However, the design of such system is very important particularly the feeding arrangement and the design of the impinging pipes affect the value of volumetric heat transfer coefficient and in turn the water evaporation rate. Recently, Choicharoen et al.54) have carried out performance evaluation of impinging dryer with Okara as a ideal material and concluded that ISD gives very high volumetric heat transfer coefficient and the performance depends on the aforementioned parameters.

There are several possibilities of ISD based on geometries that require further study to enhance gas-solid mixing and heat transfer, both numerically as well as experimentally. It should be noted that impinging stream dryers can use a variety of drying media including air, flue gas and superheated steam. A hybrid technique which uses ISD combined with fluid bed, microwave or flash dryer can result in much better performance. All these possibilities and advantages of ISD allows one to consider it as a possible option for drying several particulate matter, however, throughput can be a major constraint. Another major limitation of these dryers is the scale of velocities used.

Kudra et al.55) have classified the wide assortment of ISDs although only a few have been studied so far. Most recently, Hosseinalipour and Mujumdar56) examined, via computational fluid dynamic modeling and Monte Carlo simulations, a novel two-dimensional ISD using superheated steam as the carrier medium. Effects of the degree of superheat, operating pressure and jets Reynolds number were examined numerically assuming a power law model for the falling rate drying kinetics. New criteria are formulated to characterize performance of dispersion dryers. Experimental validation is required although the computed results do appear physically plausible.

3.6 Contact-sorption drying

Contact-sorption drying is a combination of two drying techniques, contact drying in which a wet material is contacted with a heated surface and thereby the moisture is removed as a result of heat exchange and then sorption drying in which moisture is transferred from wet solids to the sorbent particles. The efficiency of drying can be enhanced by use of adsorbents such as zeolites which have strong attraction for water. A typical contact-sorption drying technique involves good mixing of wet solid particles with the sorbent particles to achieve good heat and mass transfer between the two and then separation of the two media. The sorbent particles are regenerated and returned to the dryer. The typical inert sorbent particles (also called as carrier) used for this purposes are molecular sieves, zeolites, activated carbon, silica gel. The most popular applications of contact-sorbent drying are the drying of various grains and pieces of fruits. The fruit pieces can also be dried in presence of sugar granules which will absorb moisture from the wet solids and will also result in sweeter taste. Kudra and Mujumdar[41] have discussed about this technique in more detail. For application to food products, adsorbents must be edible, stable and easy to regenerate. The overall system is rather complex and hence not commonly used in practice.

3.7 Pulse combustion dryer

The pulse combustion drying is another drying technology with good potential as the reported work suggests it offers very high heat transfer rates with reduced emission57-61). However, the notable limitations of this technique are noise and scale-up issues, which need to be worked out before any progress is made. The term Pulse combustion (PC) essentially mean an intermittent combustion of fuel. Such a periodic combustion generates intense pressure and velocity and to a certain extend temperature waves propagated from combustion chamber which can be used for different purposes such as drying. The mechanism of pulse combustion is very complex and the detail can be found elsewhere[59, 61].

In general pulse combustion drying can be achieved either within the gas jet coming out of the combustor or in a separate drying chamber. Pulse combustion drying technology can utilize one or multiple pulse combustors to produce high-temperature and high velocity pulsating jets. Short drying time, high energy efficiency, improved product quality, and environmentally friendly operation are noted as the key advantages of this drying[61]. The drying of liquid material within the gas jet from combustor is another way of achieving pulse combustion drying. Such a technique is especially useful for biomaterials. The technique mainly involves atomization of liquid using the sound energy generated by the combustor[62]. The liquid or pasty material is introduced in to a gas stream coming out of the combustor entering at the top of the drying chamber. The particle size achieved using such a system is very fine with a residence time of milliseconds in the high temperature zone. This allows drying of even highly temperature sensitive products. The pulse combustion spray dryers can handle corrosive products as there are no wear parts in the atomization system. This system has been used for number of food products such as yeast, spices, fibers, eggs etc.

Based on the published data on pulse dryer performance, Kudra and Mujumdar[61] have provided detailed information about the type of feedstock which can be handled using PC drying technique, which covers almost all forms of feedstock. They also have listed following observations based on the published literature.

- PC dryers can increase the drying rate by the factor of 2-3
- Reduce unit air consumption by 30-40%
- Improve the product quality
- Lower gas and product temperature during processing
- Handle sticky materials
- Disperse liquids, slurries and suspensions without the need of atomizer

Kudra and Mujumdar[61] have given a detailed comparison of conventional and pulse combustion spray drying based on various characteristics such as atomization, heat transfer rates, particle properties, overall efficiency. It should be noted that pulse-combustion drying is a promising, energy-efficient and environmentally friendly technology for various types of materials including minerals, chemicals, foods, as well as industrial/municipal wastes and by-products. This technology appears to be suitable for drying of heat-sensitive biomaterials, nutraceuticals and functional foods if direct contact with flue gases is permissible. Considerable R&D is essential at each scale in order to make this technique acceptable for wider range of products. PC drying is also proposed for drying waste sludge, nightsoil, pg manure etc since the high temperature of PC exhaust can be used to eliminate microbial contaminants in such materials for safe disposal.

3.8 Variable pressure drop (instantaneous/cyclic) method

As mentioned before a time varying cycle of operating conditions can be used to enhance the drying efficiency as well as product quality. A variation of operating pressure by controlled instantaneous means or in cyclic way can be used to achieve high quality of dried products[63, 64]. In a controlled instantaneous pressure drop (commonly referred to as DIC) method, the product is subjected to vacuum in a processing chamber and then exposed to steam pressure followed by an instantaneous drop in pressure toward a vacuum and finally a return to atmospheric pressure [65, 66]. By texturing by Instant controlled pressure drop DIC, raw materials (plants, medicinal herbs) could get higher porosity. Dehydration by successive decompression (DDS; de'shydratation par de'tentes successives) is a process particularly suited to thermo-sensitive products, in which the product undergoes a series of cycles, during which it is placed under pressure (<10 bar) for a defined time and is then subjected to an instantaneous decompression to a vacuum (5-90 kPa)[63-68] The product is maintained under a vacuum for a defined time before the following cycle begins. Each decompression step results in partial water removal by autovaporization. The amount of water removed depends on the water state in the system (free or linked) as well as the processing conditions. The DDS operation can be performed at room temperature, using desiccated air to create the pressure. The major advantage of this technique is considerable reduction in drying time compared to normal vacuum drying and hot air drying techniques used for food products. This technique is not only used for drying but also for various predrying processes such as steaming. Swell-drying involves coupling hot air drying to a DIC texturing operation. The use of low-temperature DIC in the Dehydration of biological natural products for pharmaceutical and cosmetic applications can result in shorter drying times with lower energy consumption[69].

4. Conclusions

A summary is provided on novel drying processes as well as trends in drying technologies to produce particulate matter. No pretence is made that the coverage is all-inclusive; it is only illustrative. Some of the common features of innovations are identified. There is need for further R&D and evaluation of new concepts. There will be fewer revolutionary innovations driven by technology-push because the market penetrability of such innovations is difficult and unpredictable. Since many of the conventional drying technologies have reached or are close to maturity further influx of R&D is unlikely to yield major dividends in several of these areas. While no mention was made here of the role of basic research to enhance the fundamental understanding of drying and dryers it is indeed a key factor in identifying and testing new drying concepts and dryer designs. Mathematical modelling can be used effectively as a tool to intensify innovation at reduced cost.

References

1) Mujumdar, A. S. (2006): "Handbook of industrial drying," 3rd Ed; CRC Press: Boca Raton, FL.
2) Mujumdar, A. S. (1996): Innovation in drying. Drying Technology, Vol.14, No.6, pp.1459-1475.
3) Mujumdar, A. S. (2004): Research and development in drying: Recent trends and future prospects. Drying Technology, Vol.22, No.1-2, pp.1-26.
4) Mujumdar, A. S. (2008): Classification and selection of industrial dryer. "Guide to Industrial Drying: Principles, Equipment and New Developments," Mujumdar, A.S., Ed.; Three S. Colors: Mumbai, India, pp.23-36.
5) Baker, C. G. J. (1997): Dryer Selection. "Industrial Drying of Foods," Baker, C.G.J., Ed.; Blackie Academic & Professional: London, pp.242-271.
6) Baker, C. G. J. and Lababidi, H. M. S. (2001): Developments in computer-aided dryer selection. Drying Technology, Vol.19, No.8, pp.1851-1873.
7) Perera, C. O. (2005): Selected quality attributes of dried foods. Drying Technology, Vol.23, No.4, pp.717-730.
8) Desai, K. G. H. and Park, H. J. (2005): Recent developments in microencapsulation of food ingredients. Drying Technology, Vol.23, No.7, pp.1361-1394.
9) Sablani, S. S. (2006): Drying of fruits and vegetables: Retention of nutritional/functional quality. Drying Technology, Vol.24, No.2, pp.123-135.
10) Jangam, S. V. (2011): An overview of recent developments and some r&d challenges related to drying of foods. Drying Technology, Vol.29, No.12, pp.1343-1357.
11) Pereira, N. R., Godoi, F. C. and Rocha, S. C. S. (2010): Drying of starch suspension in spouted bed with inert particles: Physical and thermal analysis of product. Drying Technology, Vol.28, No.11, pp.1288-1296.
12) Ciro-Vela'squez, H. J., Cunha, R. L. and Menegalli, F. C. (2010): Drying of xanthan gum using a two-dimensional spouted fluidized bed (2DSFB) with inert particles: Performance and rheological considerations. Drying Technology, Vol.28, No.3, pp.389-401.
13) Kutsakova, V. E. (2004): Drying of liquid and pasty products in a modified spouted bed of inert particles. Drying Technology, Vol.22, No.10, pp.2343-2350.
14) Mujumdar, A. S. (2006): Some recent developments in drying technologies appropriate for post-harvest processing. International Journal of Postharvest Technology and Innovation, Vol.1, pp.76-92.
15) Mujumdar, A. S. and Wu, Z. (2008): Thermal drying technologies?Cost-effective innovation aided by mathematical modeling approach. Drying Technology, Vol.26, No.1, pp.146-154.
16) Mujumdar, A. S. and Law, C. L. (2010): Drying technol-

ogy: Trends and applications in postharvest processing. Food and Bioprocess Technology, Vol.3, No.6, pp.843-852.

17) Daud, W. R. W. (2008): Fluidized Bed Dryers - Recent Advances. Advanced Powder Technology, Vol.19, No.5, pp.403-418.

18) Bait, R. G., Pawar, S. B., Banerjee, A. N., Mujumdar, A. S. and Thorat, B. N. (2011): Mechanically agitated fluidized bed drying of cohesive particles at low air velocity. Drying Technology, Vol.29, No.7, pp.808–818.

19) Reyes, A., Diaz, G. and Marquardt, F.-H. (2001): Analysis of mechanically agitated fluid-particle contact dryers. Drying Technology, Vol.19, No.9, pp.2235-2259.

20) Li, Z., Su, W., Wu, Z., Wang, R. and Mujumdar, A. S. (2010): Investigation of flow behaviors and bubble characteristics of a pulse fluidized bed via CFD modeling. Drying Technology, Vol.28, No.1-3, pp.78-93.

21) Godoi, F. C., Boin, E. A. S. F., Pereira, N. R. and Rocha, S. C. S. (2010): Fluid dynamics and drying of cohesive particles of a biodegradable polymer (poly-hydroxybutyrate) in a rotating pulsed fluidized bed, Drying Technology, Vol.28, No.11, pp.1297-1306.

22) Nitz, M. and Taranto, O. P. (2009): Drying of a porous material in a pulsed fluid bed dryer: The influences of temperature, frequency of pulsation, and air flow rate. Drying Technology, Vol.27, No.2, pp.212-219.

23) Freire, J. T., Ferreira, M. C., Freire, F. B. and Nascimento, B. S. (2012): A Review on Paste Drying with Inert Particles as Support Medium, Drying Technology, Vol.30, No.4, pp.330-341.

24) Tatemoto, Y. and Miyazawa, K. (2011): Drying of suspensions in a Fluidized Bed of inert particles Under Reduced Pressure, Drying Technology, Vol.29, No.10, pp.1204-1209.

25) Cal, K. and Sollohub, K. (2010): Spray drying technique. I: Hardware and process parameters. Journal of Pharmaceutical Sciences, Vol.99, pp.575–586.

26) Walzel, P. (2011): Influence of the spray method on product quality and morphology in spray drying. Chemical Engineering and Technology, Vol.34, No.7, pp.1039-1048.

27) Sollohub, K. and Cal, K. (2010): Spray drying technique: II. Current applications in pharmaceutical technology. Journal of Pharmaceutical Sciences, Vol.99, No.2, pp.587-597.

28) Mujumdar, A. S. (2000): Dryers for particulate solids, slurries and sheet-form materials, in “Mujumdar Practical Guide to Industrial Drying”, Ed. Devahastin, S., Exergex Corp., Montreal, Canada, pp.37-71.

29) Kwamya and Mujumdar, A. S. (1984): M. Eg. Project Report, Dept. Chem. Engg., McGill University, Canada.

30) Bourell, D. L. (1996): Synthesis and processing of nano-crystalline powder, Proceedings of annual meeting of the minerals, metals and materials society, Feb. 4-8, 1996, California, USA.

31) Kim, J., Wilhelm, O. and Pratsinis, S. E. (2002): Nanoparticle packaging. Advanced Engineering Materials, Vol.4, No. 7, pp.494-496.

32) Lo, M.-H., Cheng, F.-H. and Wei, W.-C. J. (1996): Preparation of Al2O3/Mo nanocomposite powder via chemical route and spray drying. Journal of Materials Research, Vol.11, No.8, pp.2020-2028.

33) Pilarska, A., Markiewicz, E., Ciesielczyk, F. and Jesionowski, T. (2011): The influence of Spray Drying on the dispersive and physicochemical properties of Magnesium Oxide. Drying Technology, Vol.29, No.10, pp.1210-1218.

34) Arpagaus, C. (2012): A Novel Laboratory-Scale Spray Dryer to Produce Nanoparticles. Drying Technology, Vol.30, No.10, pp.1113-1121.

35) Chen, G. and Wang, W. (2007): Role of freeze drying in nanotechnology. Drying Technology, Vol.25, No.1, pp.29-35.

36) Kim, D.-Y. and Im, H. (2012): Effects of freeze drying and silver staining on carbonization of cellulose: Carbon nano-materials, Journal of the Korean Physical Society, Vol.60, No.10, pp.1535-1538.

37) Patil, V. V., Dandekar, P. P., Patravale, V. B. and Thorat, B. N. (2010): Freeze drying: Potential for powdered nanoparticulate product. Drying Technology, Vol.28, No.5, pp.624-635.

38) Pakowski, Z. (2007): Modern methods of drying nanomaterials. Transp Porous Med, Vol. 66, pp.19–27.

39) Mujumdar, A.S. (1990): Superheated Steam Drying: Principles Practice and Potential for Use of Electricity; Canadian Electrical Association: Montreal, Quebec, Canada. Report No. 817, U 671.

40) Kumar, P. and Mujumdar, A. S. (1990): Superheated steam drying?A state of the art survey. In Drying of Solids; Mujumdar, A. S., Ed.; Sarita Prakashan: Meerut, India.

41) Kudra, T. and Mujumdar, A. S. (2009): Advanced Drying Technologies, 2nd Ed;CRC Press: Boca Raton, FL.

42) Pakowski, Z. and Adamski, R. (2011): On prediction of the drying rate in superheated steam drying process. Drying Technology, Vol.29, No.13, pp.1492-1498.

43) Fushimi, C., Kansha, Y., Aziz, M., Mochidzuki, K., Kaneko, S., Tsutsumi, A., Matsumoto, K., Yokohoma, K., Kosaka, K., Kawamoto N., Oura, K., Yamaguchi, Y. and Kinoshita, M. (2011): Novel Drying Process Based on Self-Heat Recuperation Technology. Drying Technology, Vol.29, No.1, pp.105-110.

44) Jangam, S. V. Karthikeyan, M. and Mujumdar, A. S. (2011): A critical assessment of industrial coal drying technologies: Role of energy, emissions, risk and sustainability. Drying Technology, Vol.29, No.4, pp.395-407.

45) Yamsaengsung, R. and Tabtiang, S. (2011): Hybrid drying of rubberwood using superheated steam and hot air in a pilot-scale. Drying Technology, Vol.29, No.10, pp.1170-1178.

46) Yamsaengsung, R. and Sattho, T. (2008): Superheated steam vacuum drying of rubberwood. Drying Technology, Vol.26, No.6, pp.798-805.

47) Tazaki, M., Tsuno, H., Takaoka, M. and Shimizu, K.

(2011): Modeling of sludge behavior in a steam dryer. Drying Technology, Vol.29, No.14, pp.1748-1757.

48) Kozanoglu, B., Flores, A., Guerrero-Beltrán, J.A. and Welti-Chanes, J. (2012): Drying of pepper seed particles in a superheated steam fluidized bed operating at reduced pressure. Drying Technology, Vol.30, No.8, pp.884-890.

49) Speckhahn, A., Srzednicki, G. and Desai, D. K. (2010): Drying of beef in superheated steam. Drying Technology, Vol.28, No.9, pp.1072-1082.

50) Suvarnakuta, P. Development and study of low-pressure superheated steam drying system for a heat-sensitive material, Ph D Theses, King Mongkut' s University of Technology Thonburi (KMUTT), Department of Food Engineering, Bangkok, Thailand 2007.

51) Mujumdar, A. S. (1992): Superheated Steam Drying of Paper: Principles, Status and Potential. In: Mujumdar, A. S. (Ed.). Drying of Solids. New York: International Science Publisher.

52) Yang, D., Wang, Z., Huang, X., Xiao, Z. and Liu, X. (2011): Numerical simulation on superheated steam fluidized bed drying: I. Model construction. Drying Technology, Vol.29, No.11, pp.1325-1331.

53) Shi, Y., Xiao, Z., Wang, Z., Liu, X. and Yang, D. (2011): Numerical simulation on superheated steam fluidized bed drying: II. Experiments and numerical simulation. Drying Technology, Vol.29, No.11, pp.1332-1342.

54) Choicharoen, K. Devahastin, S. and Soponronnarit, S. (2010): Performance and energy consumption of an impinge g stream dryer for high-moisture particulate materials. Drying Technology, Vol.28, pp.20-29.

55) Kudra, T., Mujumdar, A.S. and Meltser, V. (1995): Impinging Stream Dryers. In: Mujumdar, A.S. (Ed.). Handbook of Industrial Drying 2nd ed., Marcel Dekker Incl. New York, USA.

56) Hosseinalipour, S.M. and Mujumdar, A. S. (1995): Superheated steam drying of a single particle in an impinging stream dryer. Drying Technology, Vol.13, No.5-7, pp.1279-1303.

57) Zbicinski, I. (2002): Equipment, technology, perspectives and modeling of pulse combustion drying. Chemical Engineering Journal, Vol.86, No.1-2, pp.33-46.

58) Wu, Z. and Mujumdar, A. S. (2006): R&D Needs and Opportunities in Pulse Combustion and Pulse Combustion Drying. Drying Technology, Vol.24, No.11, pp.1521-1523.

59) Kudra, T. (2008): Pulse-Combustion Drying: Status and Potentials. Drying Technology, Vol.26, No.12, pp.1409-1420.

60) Zhonghua Dr., W., Long, W., Zhanyong, L. and Mujumdar, A. S. (2012): Atomization and Drying Characteristics of Sewage Sludge inside a Helmholtz Pulse Combustor. Drying Technology, Vol.30, No.10, pp.1105-1112.

61) Kudra, T. and Mujumdar, A. S. (2009): Advanced Drying Technologies, 2nd ed., CRC Press, Boca Raton, FL, USA.

62) Zbicinski, I., Smucerowicz, I., Strumillo, C. and Crowe, C. (2000): Application of pulse combustion technology in spray drying process. Brazilian Journal of Chemical Engineering, Vol.17, No.4, pp.441-450.

63) Maache-Rezzoug, Z., Rezzoug, S. A. and Allaf, K. (2002). Development of a new drying process—Dehydration by cyclical pressure drops (D.D.S.): Application to the collagen gel. Drying Technology, Vol.20, No.1, pp.109-129.

64) Cong, D. T., Al Haddad, M., Rezzoug, Z., Lefevre, L. and Allaf, K. (2008): Dehydration by successive pressure drops for drying paddy rice treated by instant controlled pressure drop. Drying Technology, Vol.26, No.4, pp.443-451.

65) Abdulla, G., Belghit, A. and Allaf, K. (2010): Impact of the instant controlled pressure drop treatment on hot air drying of cork granules. Drying Technology, Vol.28, No.2, pp.180-185.

66) Abdulla, G., Belghit, A. and Allaf, K. (2009): Impact of instant controlled pressure drop treatment on moisture adsorption isotherm of cork granules. Drying Technology, Vol.27, No.2, pp.237-247.

67) Albitar, N., Mounir, S., Besombes, C. and Allaf, K. (2011): Improving the drying of onion using the instant controlled pressure drop technology. Drying Technology, Vol.29, No.9, pp.993-1001.

68) Mounir, S., Besombes, C., Al-Bitar, N. and Allaf, K. (2011): Study of instant controlled pressure drop DIC treatment in manufacturing snack and expanded granule powder of Apple and Onion. Drying Technology, Vol.29, No.3, pp.331-341.

69) Rakotozafy, H., Louka, N., Thérisod, M., Therisod, H. and Allaf, K. (2000): Drying of baker's yeast by a new method: Dehydration by Successive Pressure Drops (DDS). Effect on cell survival and enzymatic activities. Drying Technology, Vol.18, No.10, pp.2253-2271.

Author's short biography

Duu-Jong Lee

Dr. Duu-Jong Lee received BS and PhD degrees in 1984 and 1989, respectively, both from Chemical Engineering Department, National Taiwan University. He is the Life-Time University Professor at National Taiwan Univerisity and Dean of College of National Taiwan University of Science and Technology. Dr Lee's expertise includes bioenergy recovery from waste, drinking water production using membrane, sludge treatment, and microscale heat and mass transport processes. He has served as an investigator for a number of industrial R&D projects funded by industrial collaborators and government agencies, and has been serving as a consultant to the industry in Taiwan in the area of wastewater treatment. Dr Lee is now the Vice President of Taiwan Institute of Chemical Engineers (TWIChE).

Sachin Vinayak Jangam

Dr. Sachin Vinayak Jangam is a Research Fellow in Minerals, Metals and Materials Technology Centre (M3TC) at National University of Singapore. He completed his Ph D in Chemical Engineering at the Institute of Chemical Technology, Mumbai, India. He is currently working on developing cost-effective drying techniques for minerals; however, he also has interest in dehydration of food and related products.

Arun S. Mujumdar

Dr. Arun S. Mujumdar is Director of Minerals, Metals and Materials Technology Centre and Professor of Mechanical Engineering. He is author of over 500 journal papers, author of three books, over 100 book chapters in heat-mass transfer and drying and editor of over 60 books. Founder of the International Drying Symposium (IDS) series, he is Editor-in-Chief of Drying Technology Journal.

Hydrostatic and Shear Behavior of Frictionless Granular Assemblies under Different Deformation Conditions[†]

Olukayode I. Imole, Nishant Kumar, Vanessa Magnanimo and Stefan Luding[*]
[1] *Multi-Scale Mechanics (MSM), Faculty of Engineering Technology, MESA+, University of Twente, Netherlands*

Abstract

Stress- and structure-anisotropy (bulk) responses to various deformation modes are studied for dense packings of linearly elastic, frictionless, polydisperse spheres in the (periodic) triaxial box element test configuration. The major goal is to formulate a guideline for the procedure of how to calibrate a theoretical model with discrete particle simulations of selected element tests and then to predict another element test with the calibrated model (parameters).

Only the simplest possible particulate model material is chosen as the basic reference example for all future studies that aim at the quantitative modeling of more realistic frictional, cohesive powders. Seemingly unrealistic materials are used to exclude effects that are due to contact non-linearity, friction, and/or non-sphericity. This allows us to unravel the peculiar interplay of stress, strain, and microstructure, i.e. fabric.

Different elementary modes of deformation are isotropic, deviatoric (volume-conserving), and their superposition, e.g. a uniaxial compression test. Other ring-shear or stress-controlled (e.g. isobaric) element tests are referred to, but are not studied here. The deformation modes used in this study are especially suited for the bi- and triaxial box element test set-up and provide the foundations for understanding and predicting powder flow in many other experimental devices. The qualitative phenomenology presented here is expected to be valid, even clearer and magnified, in the presence of non-linear contact models, friction, non-spherical particles and, possibly, even for strong attractive/adhesive forces.

The scalar (volumetric, isotropic) bulk properties, the coordination number and the hydrostatic pressure scale qualitatively differently with isotropic strain. Otherwise, they behave in a very similar fashion irrespective of the deformation path applied. The deviatoric stress response (i.e. stress-anisotropy), besides its proportionality to the deviatoric strain, is cross-coupled to the isotropic mode of deformation via the structural anisotropy; likewise, the evolution of pressure is coupled via the structural anisotropy to the deviatoric strain, leading to dilatancy/compactancy. Isotropic/uniaxial over-compression or pure shear respectively slightly increase or reduce the jamming volume fraction below which the packing loses mechanical stability. This observation suggests a necessary generalization of the concept of the jamming volume fraction from a single value to a "wide range" of values as a consequence of the deformation history of the granular material, as "stored/memorized" in the structural anisotropy.

The constitutive model with incremental evolution equations for stress and structural anisotropy takes this into account. Its material parameters are extracted from discrete element method (DEM) simulations of isotropic and deviatoric (pure shear) modes as volume fraction dependent quantities. Based on this calibration, the theory is able to predict qualitatively (and to some extent also quantitatively) both the stress and fabric evolution in another test, namely the uniaxial, mixed mode during compression. This work is in the spirit of the PARDEM project funded by the European Union.

Keywords: calibration, deformations, anisotropy, constitutive model, PARDEM

© 2013 Hosokawa Powder Technology Foundation

1. Introduction and Background

Dense granular materials are generally complex systems which show unique mechanical properties different from classic fluids or solids. Interesting phenomena such as dilatancy, shear-band formation, history dependence, jamming and yield stress - among others - have attracted significant scientific interest over the past decade. The bulk behavior of these materials depends on the behavior of their constituents (particles) interacting through contact forces. To gain an understanding of the deformation behavior, various laboratory element tests can be performed (GdR-MiDi, 2004; Samimi et al., 2005; Schwedes, 2003). Element tests are (ideally homogeneous) macroscopic tests in which the experimentalist can control the stress and/or strain path. Different element tests on packings of bulk solids have been realized in the biaxial box (see Morgeneyer and Schwedes, 2003, and references therein) while other deformation modes, namely uniaxial and volume-conserving shear, have been reported in Philippe et al., 2011 and Saadatfar et al., 2012. While such macroscopic experiments are pivotal to the development of constitutive relations, they provide little information on the microscopic origin of the bulk flow behavior of these complex packings.

The complexity of a granular assembly becomes evident when it is compressed isotropically. In this case, the only macroscopic control parameters are volume fraction and pressure (Göncü et al., 2010). At the microscopic level for isotropic samples, internal variables must be added to classify the microstructure (contact network), namely the coordination number (i.e. the average number of contacts per particle) and the fraction of rattlers (i.e. fraction of particles that do not contribute to the mechanical stability of the packing), see Göncü et al., 2010; Magnanimo et al., 2008. However, when the same material sample is subjected to shear deformation, not only does shear stress build up, but also the anisotropy of the contact network develops, as it relates to the creation and destruction of contacts and force chains (see Alonso-Marroquín et al., 2005; La Ragione and Magnanimo, 2012; Luding and Perdahcioğlu, 2011; Radjai et al., 1999; Walsh and Tordesillas, 2004; Yimsiri and Soga, 2010, among others). In this sense, anisotropy represents a history parameter for the granular assembly. For anisotropic samples, scalar quantities are not sufficient to fully represent the internal contact structure, but an extra tensorial quantity has to be introduced, namely the fabric tensor (Goddard, 1998; Oda, 1972). To gain more insight into the microstructure of granular materials, numerical studies and simulations on various deformation experiments can be performed, see Thornton, 2010; Thornton and Zhang, 2006, 2010; Yimsiri and Soga, 2010, and references therein.

In an attempt to classify different deformation modes, Luding and Perdahcioğlu, 2011, listed four different deformation modes: (0) isotropic (direction-independent), (1) uniaxial, (2) deviatoric (volume-conserving) and (3) bi-/triaxial deformations. The first two are purely strain-controlled, while the last (3) is mixed strain- and stress-controlled either with constant side stress (Luding and Perdahcioğlu, 2011) or constant pressure (Magnanimo and Luding, 2011). The isotropic and deviatoric modes 0 and 2 are pure modes which both take especially simple forms. The uniaxial deformation test derives from the superposition of an isotropic and a deviatoric test, and represents the simplest element test experiment (oedometer, uniaxial test or $\lambda-$meter as reported in Kwade et al., 1994) that activates both isotropic and shear deformation. Even though biaxial tests are more complex to realize and involve mixed stress- and strain-control instead of completely prescribed strain (Morgeneyer and Schwedes, 2003; Zetzener and Schwedes, 1998), they are assumed to better represent the deformation under realistic boundary conditions – namely the material can expand and form shear bands.

In this study, various deformation paths for assemblies of polydisperse packings of linearly elastic, nonfrictional cohesionless particles are modeled using the DEM simulation approach (Cundall and Strack, 1979). One goal is to study the evolution of pressure (isotropic stress) and deviatoric stress as functions of isotropic and deviatoric strain. Internal quantities such as the coordination number, the fraction of rattlers, and the fabric tensor are reported for improved microscopic understanding of the deformations. Furthermore, the extensive set of DEM simulations is used to calibrate the anisotropic constitutive model, as proposed by Luding and Perdahcioğlu, 2011; Magnanimo and Luding, 2011. After calibration through isotropic (Göncü et al., 2010) and volume-conserving pure shear simulations, the derived relations between the bulk material parameters and volume fraction are

---

† Accepted: September 3, 2012

[1] P.O. Box 217, 7500 AE Enschede, The Netherlands
* Corresponding author:
E-mail: s.luding@utwente.nl

used to predict uniaxial deformations, with the goal of improving the understanding of the macroscopic behavior of bulk particle systems and of guiding further developments of new theoretical models that properly and predictively describe it.

The focus on the seemingly unrealistic materials allows us to exclude effects that are due to friction, contact non-linearity and/or non-sphericity, with the goal of unraveling the interplay of microstructure (fabric), stress and strain. This is the basis for the present research – beyond the scope of this paper – that aims at the quantitative modeling of these phenomena and effects for realistic frictional, cohesive powders. The deformation modes used in this study are especially suited for the biaxial box experimental element test set-up and provide the fundamental basis for the prediction of many other experimental devices. The qualitative phenomenology presented here is expected to be valid, even clearer and magnified, in the presence of friction, non-spherical particles, and for strong attractive forces.

This paper is organized as follows: The simulation method and parameters used are presented in section 2 while the preparation and test procedures are introduced in section 3. Generalized averaging definitions for scalar and tensorial quantities are given in section 4 and the evolution of microscopic quantities is discussed in section 5. In section 6, the macroscopic quantities (isotropic and deviatoric) and their evolution are studied as functions of volume fraction and deviatoric (pure shear) strain for the different deformation modes. These results are then used to obtain/calibrate the macroscopic model parameters. Section 7 is devoted to theory, where we relate the evolution of the stress and structural anisotropy to strain, as proposed by Luding and Perdahcioğlu, 2011; Magnanimo and Luding, 2011, and confirm the predictive quality of the calibrated model.

2. Simulation Method

The Discrete Element Method (DEM) has been used extensively to perform simulations in bi- and triaxial geometries (Durán et al., 2010; Kruyt et al., 2010; Luding, 2005; Sun and Sundaresan, 2011; Yimsiri and Soga, 2010) involving advanced contact models for fine powders (Luding, 2008c) or more general deformation modes, (see Alonso-Marroquín et al., 2005; Thornton, 2010; Thornton and Zhang, 2010 and references therein).

However, since we restrict ourselves to the simplest deformation modes and the simplest contact model, and since DEM is otherwise a standard method, only the contact model parameters and a few relevant timescales are briefly discussed – as well as the basic system parameters.

2.1 Force model

For the sake of simplicity, the linear visco-elastic contact model for the normal component of the force has been used in this work and friction is set to zero (and hence neither tangential forces nor rotations are present). The simplest normal contact force model, which takes into account excluded volume and dissipation, involves a linear repulsive and a linear dissipative force, given as

$$\boldsymbol{f}^n = f^n \hat{\boldsymbol{n}} = \left(k\delta + \gamma\dot{\delta}\right)\hat{\boldsymbol{n}}, \qquad (1)$$

where k is the spring stiffness, γ is the contact viscosity parameter and δ or $\dot{\delta}$ are the overlap or the relative velocity in the normal direction $\hat{\boldsymbol{n}}$. An artificial viscous background dissipation force, $\boldsymbol{f}_\mathrm{b} = -\gamma_\mathrm{b}\boldsymbol{v}_i$, proportional to the velocity $\boldsymbol{v}_i$ of particle i is added, resembling the damping due to a background medium, as e.g. a fluid. The background dissipation only leads to shortened relaxation times, reduced dynamical effects and consequently lower computational costs without a significant effect on the underlying physics of the process – as long as quasi-static situations are considered.

The results presented in this study can be seen as a "lower-bound" reference case for more realistic material models, see e.g., Luding, 2008c, and references therein. The interesting, complex behavior and non-linearities of our most simple granular material *can not* be due to the contact model, but is related to the collective bulk behavior of many particles, as will be shown below.

2.2 Simulation parameters and timescales

Typical simulation parameters for the $N = 9261$ ($= 21^3$) particles with average radius $\langle r \rangle = 1$ [mm] are density $\rho = 2000$ [kg/m^3], elastic stiffness $k = 10^8$ [kg/s^2], and background dissipation $\gamma_b = 0.1$ [kg/s]. The polydispersity of the system is quantified by the width $w = r_\mathrm{max}/r_\mathrm{min}$ of a uniform distribution with a step function as defined in Göncü et al., 2010, where r_max 1.5 [mm] and r_min 0.5 [mm] are the radius of the biggest and smallest particles, respectively.

Note that the units are artificial; Luding, 2008c provides an explanation of how they can be consistently rescaled to quantitatively match the values obtained from experiments (thanks to dimensional analysis and the simplicity of the contact model used).

A typical response time is the collision duration t_c. For for a pair of particles with masses m_i and m_j, it is $t_c = \pi/\sqrt{k/m_{ij} - (\gamma/2m_{ij})^2}$, where $m_{ij} = m_i m_j/(m_i + m_j)$ is the reduced mass. The coefficient of restitution for the same pair of particles is expressed as $e = \exp(-\gamma t_c/2m_{ij})$ and quantifies dissipation. The contact duration t_c and the restitution coefficient e are dependent on the particle sizes and since our distribution is polydisperse, the fastest response timescale corresponding to the interaction between the smallest particle pair in the overall ensemble is $t_c = 0.228$ [μs] and $e = 0.804$. For two average particles, one has $t_c = 0.643$ [μs] and $e = 0.926$. Thus, the dissipation timescale for contacts between two average-sized particles, $t_d = 2m_{ij}/(\gamma)$= 8.37 [μs], is considerably larger than t_c and the background damping timescale $t_b = \langle m \rangle/\gamma_b$= 83.7 [μs] is much larger again, so that the particle- and contact-related timescales are well separated. The timescale set by the maximal strain-rate (defined below) of one of our typical simulations, is $t_s = 1/\dot{\epsilon}_{zz}^{\max} = 7.2\ 10^{-3}$ [s] and thus is much larger than the other timescales in the system. As usual in DEM, the integration time step was chosen to be about 50 times smaller than the shortest timescale, t_c (Luding, 2008c).

Our numerical “experiments” are performed in a three-dimensional triaxial box with periodic boundaries on all sides. One advantage of this configuration is the possibility of realizing different deformation modes with a single experimental set-up and a direct control of stress and/or strain (Durán et al., 2010; Luding and Perdahcioğlu, 2011). The systems are ideally homogeneous, which is assumed but not tested in this study.

The periodic walls can be strain-controlled to follow a co-sinusoidal law such that, for example, the position of the top wall as a function of time t is

$$z(t) = z_f + \frac{z_0 - z_f}{2}(1 + \cos 2\pi f t), \tag{2}$$

with strain in z-direction, $\epsilon_{zz}(t) = 1 - z(t)/z_0$, where z_0 is the initial box side length, z_f is the box length at maximum strain, and $f = T^{-1}$ is the frequency. The co-sinusoidal law allows for a smooth start-up and ending of the motion so that shocks and inertia effects are reduced. The maximum deformation is reached after half a period $t = T/2$, and the maximum strainrate applied during the deformation at $T/4$ and $3T/4$ is $\dot{\epsilon}_{zz}^{\max} = 2\pi f\,(z_0 - z_f)/(2z_0) = \pi f\,(z_0 - z_f)/z_0$.

Different strain-control modes are possible such as homogeneous strain-rate control for each time step (applied to all particles and the periodic walls, i.e. the system boundaries) or swelling instead of isotropic compression, as well as pressure control of the (virtual) walls. However, this is not discussed since it had no effect for the simple frictionless contact model used here and for the quasi-static deformations applied. For more realistic contact models (dating back to, e.g. Hertz, 1882; Mindlin and Deresiewicz, 1953), for friction and adhesion (Luding, 2008c and references therein) and for large strain rates, the modes of strain or stress control have to be revisited and carefully studied.

3. Preparation and Test Procedure

In this section, we describe first the sample preparation procedure and then the method for implementing the isotropic, uniaxial and deviatoric element test simulations. For convenience, the tensorial definitions of the different modes will be based on their respective strain-rate tensors. However, for presenting the numerical results, we will use the strain tensor as defined in section 4.2.1.

3.1 Initial isotropic preparation

Since careful, well-defined sample preparation is essential in any physical experiment to obtain reproducible results (Ezaoui and Di Benedetto, 2009), the preparation consists of three parts: (i) randomization, (ii) isotropic compression, and (iii) relaxation. All are equally important to achieve the initial configurations for the following analysis. (i) The initial configuration is such that spherical particles are randomly generated in a 3D box with a low volume fraction and rather large random velocities such that they have sufficient space and time to exchange places and to randomize themselves. (ii) This granular gas is isotropically compressed in order to approach a direction-independent configuration to a target volume fraction $\nu_0 = 0.640$, slightly below the jamming volume fraction $\nu_c \approx 0.665$, i.e. the transition point from fluid-like behavior to solid-like behavior (van Hecke, 2009; Majmudar et al., 2007; Makse et al., 2000; O‘Hern et al., 2002). (iii) This is followed by a relaxation period at a constant volume fraction to allow the particles to fully dissipate their energy and to achieve a static configuration.

Isotropic compression/decompression (negative/positive strain rate in our convention) can now be used to further prepare the system, with subsequent relaxation, so that we have a series of different initial isotropic configurations at volume fractions ν_c, achieved during loading and unloading, as displayed in **Fig. 1**. Furthermore, the isotropic compression can be considered as an element test itself (Göncü et al., 2010). It is realized by a simultaneous inward movement of all the periodic boundaries of the system, with strain-rate tensor

$$\dot{\mathbf{E}} = \dot{\epsilon_{\mathrm{v}}}\begin{pmatrix} -1 & 0 & 0 \\ 0 & -1 & 0 \\ 0 & 0 & -1 \end{pmatrix},$$

where $\dot{\epsilon_{\mathrm{v}}}(> 0)$ is the rate amplitude applied to the walls until the target volume fraction is achieved.

A general schematic representation of the procedure for implementing the isotropic and other deformation tests is shown in **Fig. 2**.

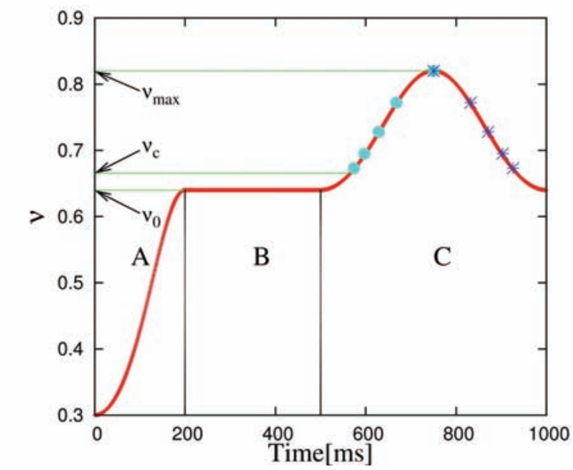

Fig. 1 Evolution of volume fraction as a function of time. Region A represents the initial isotropic compression up to the initial volume fraction ν_0. B represents relaxation of the system and C represents the subsequent isotropic compression up to $\nu_{\mathrm{max}} = 0.820$ and then decompression. Cyan dots represent some of the initial configurations, at different ν_{i}, during the loading cycle, and blue stars during the unloading cycle, both of which can be chosen for further study.

The compressed and relaxed configurations can now be used for other non-volume-conserving and/or stress-controlled modes (e.g. biaxial, triaxial and isobaric). One only has to use them as initial configurations and then decide which deformation mode to use, as shown in the figure under "other deformations". The corresponding schematic plots of deviatoric strain ϵ_{dev} as a function of volumetric strain ϵ_{v} are shown below the respective modes.

3.2 Uniaxial

Uniaxial compression is one of the element tests that can be initiated at the end of the "preparation", after sufficient relaxation indicated by the drop in potential energy to almost zero. The uniaxial compression mode in the triaxial box is achieved by a prescribed strain path in the z-direction, see Eq. (2), while the other boundaries x and y are non-mobile. During loading (compression), the volume fraction is increased as for isotropic compression from $\nu_0 =$ 0.640 to a maximum volume fraction of $\nu_{\mathrm{max}} =$0.820 (as shown in region C of **Fig. 1**), and reverses back to the original volume fraction ν_0 during unloading. Uniaxial compression is defined by the strain-rate tensor

$$\dot{\mathbf{E}} = \dot{\epsilon_{\mathrm{u}}}\begin{pmatrix} 0 & 0 & 0 \\ 0 & 0 & 0 \\ 0 & 0 & -1 \end{pmatrix},$$

where $\dot{\epsilon_{\mathrm{u}}}$ is the strain-rate (compression > 0 and decompression/tension < 0) amplitude applied in the uniaxial mode. The negative sign (convention) of the component $\dot{E}_{zz}$ corresponds to a reduction of length, so that tensile deformation is positive. Even though the strain is imposed only on the mobile "wall" in the z-direction, which leads to an increase of compressive stress on this wall during compression, the non-mobile walls also experience some stress increase due to the "push-back" stress transfer and rearrangement of the particles during loading, as discussed in more detail in the following sections. This is in agreement with theoretical expectations for materials with non-zero Poisson's ratio (Spencer, 1980). However, the stress on the passive walls is typically smaller than that of the mobile, active wall, as consistent with findings from laboratory element tests using the biaxial tester (Morgeneyer and Schwedes, 2003; Zetzener and Schwedes, 1998) or the so-called λ −meter.

3.3 Deviatoric

The preparation procedure as described in section 3.1 provides different initial configurations with volume fractions, ν_i. For the deviatoric deformation element test, unless stated otherwise, the configurations are from the unloading part (represented by blue stars in **Fig. 1**), to test the dependence of quantities of interest on the volume fraction during volume-conserving deviatoric (pure shear) deformations. The unloading branch is more reliable since it is much less sensitive to the protocol and rate of deformation during preparation (Göncü et al., 2010, Kumar et al., 2012b). Two different ways of deforming the system deviatorically with conserved volume are used here. The deviatoric mode D2 has the strain-rate tensor

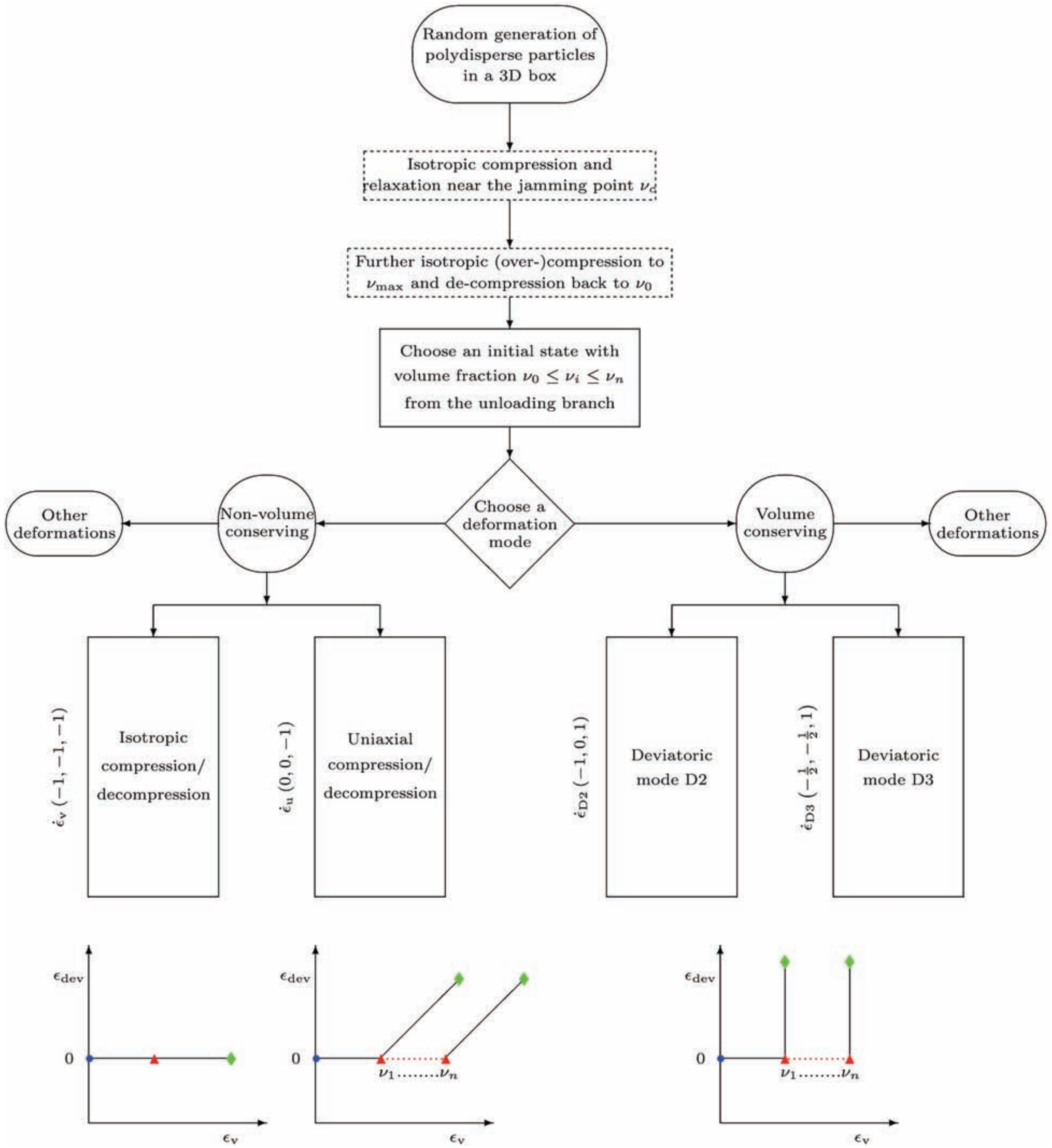

Fig. 2 Generic schematic representation of the procedure for implementing isotropic, uniaxial and deviatoric deformation element tests. The isotropic preparation stage is represented by the dashed box. The corresponding plots (not to scale) for the deviatoric strain against volumetric strain are shown below the respective modes. The solid square boxes in the flowchart represent the actual tests. The blue circles indicate the start of the preparation; the red triangles represent its end, i.e. the start of the test, while the green diamonds show the end of the respective test.

$$\dot{\mathrm{E}} = \dot{\epsilon}_{\mathrm{D2}} \begin{pmatrix} 1 & 0 & 0 \\ 0 & 0 & 0 \\ 0 & 0 & -1 \end{pmatrix},$$

where $\dot{\epsilon}_{\mathrm{D2}}$ is the strain-rate (compression in z-direction > 0) amplitude applied to the walls. We use the nomenclature D2 since two walls are moving while the third wall is stationary. The deviatoric mode D3 has the strain-rate tensor

Table 1 Summary of the deformation modes and the deviatoric strain rates $\dot{\epsilon}_{\mathrm{dev}}$, as well as shape factors, ζ, and Lode angles, α, (Thornton and Zhang, 2010) for the different modes in the respective tensor eigensystem, with sorted eigenvalues $\epsilon_{\mathrm{d}}^{(1)} \geq \epsilon_{\mathrm{d}}^{(2)}$, defined in section 4.2.1

Mode	Strain-rate tensor (main diagonal, sorted)	Deviatoric strain rate (magnitude)	$\zeta = \epsilon_{\mathrm{d}}^{(2)}/\epsilon_{\mathrm{d}}^{(1)}$	Lode angle $\alpha = \tan^{-1}\left[\frac{1}{\sqrt{3}}(1+2\zeta)\right]$
ISO (isotropic compression)	$\dot{\epsilon}_{\mathrm{v}}\ (-1,-1,-1)$	$\dot{\epsilon}_{\mathrm{dev}} = 0$	n.a.	n.a.
UNI (uniaxial compression)	$\dot{\epsilon}_{\mathrm{u}}\ (0,0,-1)$	$\dot{\epsilon}_{\mathrm{dev}} = \dot{\epsilon}_{\mathrm{u}} = \dot{\epsilon}_{zz}$	1	60°
D2 (pure shear – plane strain)	$\dot{\epsilon}_{\mathrm{D2}}\ (1,0,-1)$	$\dot{\epsilon}_{\mathrm{dev}} = \sqrt{3}\dot{\epsilon}_{\mathrm{D2}}$	0	30°
D3 (axisymmetric compression)	$\dot{\epsilon}_{\mathrm{D3}}\ (1/2,1/2,-1)$	$\dot{\epsilon}_{\mathrm{dev}} = (3/2)\dot{\epsilon}_{\mathrm{D3}}$	1	60°

$$\dot{\mathbf{E}} = \dot{\epsilon}_{\mathrm{D3}} \begin{pmatrix} 1/2 & 0 & 0 \\ 0 & 1/2 & 0 \\ 0 & 0 & -1 \end{pmatrix},$$

where $\dot{\epsilon}_{\mathrm{D3}}$ is the strain-rate (> 0 for compression in z-direction) amplitude applied. In this case, D3 signifies that all three walls are moving, with one wall twice as much (in the opposite direction) as the other two such that volume is conserved during deformation.

Note that the D3 mode is uniquely similar in "shape" to the uniaxial mode[1], see **Table 1**, since in both cases two walls are controlled similarly. Mode D2 is different in this respect and thus resembles more an independent mode (pure shear), so that unless differently stated, we plot by default the D2 results rather than the D3 ones (see section 2). The mode D2 with shape factor (as defined in **Table 1**) $\zeta = 0$ is on the one hand a plane strain deformation, and on the other hand allows for simulation of the biaxial experiment (with two walls static while four walls are moving, see Morgeneyer and Schwedes, 2003; Zetzener and Schwedes, 1998).

4. Averaged Quantities

In this section, we present the general definitions of averaged microscopic and macroscopic quantities. The latter are quantities that are readily accessible from laboratory experiments, whereas the former are often impossible to measure in experiments but are easily available from discrete element simulations.

4.1 Averaged microscopic quantities

Here, we define microscopic parameters including the coordination number, the fraction of rattlers, and the ratio of the kinetic and potential energy.

4.1.1 Coordination number and rattlers

In order to link the macroscopic load carried by the sample with the microscopic contact network, all particles that do not contribute to the force network – particles with exactly zero contacts – are excluded. In addition to these "rattlers" with zero contacts, there may be a few particles with a finite number of contacts for a short time which also do not contribute to the mechanical stability of the packing. These particles are called dynamic rattlers (Göncü et al., 2010), since their contacts are transient: The repulsive contact forces will push them away from the mechanically stable backbone. Frictionless particles with less than 4 contacts are thus rattlers, since they are mechanically unstable and hence do not contribute to the contact network. In this work, since tangential forces are neglected, rattlers can be identified by just counting their number of contacts. This leads to the following abbreviations and definitions for the coordination number (i.e. the average number of contacts per particle) and fraction of rattlers, which must be reconsidered for systems with tangential forces or

---

[1] The more general, objective definition of deviatoric deformations uses the orientation of the stresses (eigendirections) in the deviatoric plane from the eigenvalues, as explored elsewhere (Kumar et al., 2012a; Thornton and Zhang, 2006, 2010), since this is beyond the scope of this study.

torques:

N : Total number of particles
$N_4 := N_{c\geq=4}$: Number of particles with at least 4 contacts
M : Total number of contacts
$M_4 := M_{c\geq=4}$: Number of contacts of particles with at least 4 contacts
$\phi_r := \frac{N-N_4}{N}$: (Number) fraction of rattlers
$C^r := \frac{M}{N}$: Coordination number (simple definition)
$C = C^m := \frac{M_4}{N}$: Coordination number (modified definition)
$C^* := \frac{M_4}{N_4} = \frac{C}{1-\phi_r}$: Corrected coordination number
$\nu := \frac{1}{V}\sum_{p\in N} V^p$: Volume fraction of the particles, with V^p as particle volume.

Some simulation results for the coordination numbers and the fraction of rattlers will be presented below in subsection 5.1.

4.1.2 Energy ratio and quasi-static criterion

Above the jamming volume fraction ν_c, in mechanically stable static situations, there exist permanent contacts between particles; hence the potential energy (which is also an indicator of the overlap between particles) is considerably larger than the kinetic energy (which has to be seen as a perturbation).

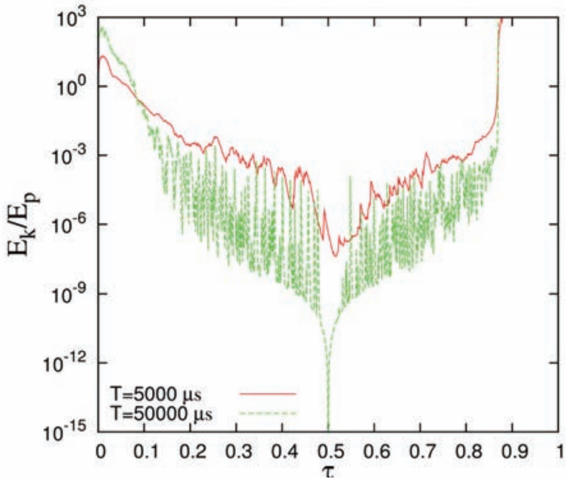

Fig. 3 Comparison of the ratio of kinetic and potential energy in scaled time $(\tau = t/T)$ for two simulations, with different period of one compression-decompression cycle T, as given in the inset.

The ratio of kinetic energy and potential energy is shown in **Fig. 3** for isotropic compression from ν_0 = 0.640 to $\nu_{\max}$ = 0.820 and back. The first simulation, represented by the solid red line, was run for a simulation time $T = 5000$ [μs] and the second (much slower) simulation, represented by the green dashed line was run for $T = 50000$ [μs]. For these simulations, the maximum strain rates are $\dot{\epsilon}_{zz}^{\max} =$ 138 $[\mathrm{s}^{-1}]$ and 13.8 $[\mathrm{s}^{-1}]$, respectively. During compression with increasing volume fraction, the energy ratio generally decreases and slower deformation by a factor of 10 leads to more than 100 times smaller energy ratios with stronger fluctuations. Most sharp increases of the energy ratio resemble reorganization events of several particles and are followed by an exponentially fast decrease (data not shown). The decrease is controlled by the interaction and dissipation timescales and not by the shear rate; in other words the timescale of energy dissipation $t_\mathrm{d} \approx 10^{-5}$ [s] is considerably smaller than the simulation timescale $t_s \approx 7.2\ 10^{-3}$ [s] or $7.2\ 10^{-2}$ [s], so that kinetic energy can be well relaxed before a considerable rearrangement of particles takes place; due only to the scaling of $\tau = t/T$, the decrease appears to be faster for the slower deformation. Explicitly, the rate of decay depends on material parameters only and is of the order of $1/t_\mathrm{e}$, however, it becomes larger the closer to jamming one gets. The large initial ratio of kinetic to potential energy $(E_\mathrm{k}/E_\mathrm{p} > 1)$ indicates that the system is in the unjammed regime, whereas after some compression it enters the quasi-static regime with much smaller energy ratios (Thornton and Anthony, 1998). In this way, dynamic effects are minimized and the system is as close as feasible to the quasi-static state. For many situations, it was tested that a slower deformation did not lead to large, considerably different results. For the majority of the data presented, we have $(E_\mathrm{k}/E_\mathrm{p} \leq 10^{-3})$. Lower energy ratios can be obtained by performing simulations at even slower rates, but the settings used are a compromise between computing time and reasonably slow deformations.

4.2 Averaged macroscopic quantities

Now the focus is on defining averaged macroscopic tensorial quantities – including strain, stress and fabric (structure) tensors – that reveal interesting bulk features and provide information about the state of the packing due to its deformation.

4.2.1 Strain

For any deformation, the isotropic part of the infinitesimal strain tensor ϵ_{v} is defined as:

$$\epsilon_{\mathrm{v}} = \dot{\epsilon}_{\mathrm{v}}\mathrm{dt} = \frac{\epsilon_{xx} + \epsilon_{yy} + \epsilon_{zz}}{3} = \frac{1}{3}\mathrm{tr}(\mathbf{E}) = \frac{1}{3}\mathrm{tr}(\dot{\mathbf{E}})\mathrm{dt}, \qquad (3)$$

where $\epsilon_{\alpha\alpha} = \dot{\epsilon}_{\alpha\alpha}$ dt with $\alpha\alpha = xx$, yy or zz are the diagonal elements of the strain tensor $\mathbf{E}$ in the Cartesian x, y, z reference system. The trace integral of $3\epsilon_{\mathrm{v}}$ denoted by ε_{v} is the true or logarithmic strain, i.e. the volume change of the system relative to the initial reference volume V_0 (Göncü et al., 2010).

Several definitions are available in literature (Imole et al., 2011; Thornton and Zhang, 2006, 2010; Zhao and Evans, 2011) to define the deviatoric magnitude of the strain. For the sake of simplicity, we use the following definition of the deviatoric strain to account for all active and inactive directions in a triaxial experiment, regardless of the deformation mode,

$$\epsilon_{\mathrm{dev}} = \sqrt{\frac{\left(\epsilon_{xx} - \epsilon_{yy}\right)^2 + \left(\epsilon_{yy} - \epsilon_{zz}\right)^2 + \left(\epsilon_{zz} - \epsilon_{xx}\right)^2}{2}}, \qquad (4)$$

Since, for our triaxial box, for all modes, the Cartesian coordinates resemble the fixed eigensystem, sorting the eigenvalues according to magnitude $\epsilon_d^{(1)} \geq \epsilon_d^{(2)} \geq \epsilon_d^{(3)}$ leaves the eigenvalue $\epsilon_d^{(1)}$ as the maximal tensile eigenvalue, with corresponding eigendirection, and $\epsilon_{\mathrm{dev}} \geq 0$ as the magnitude of the deviatoric strain[2]. The quantitative description of the tensor is completed by either its third invariant, the Lode angle α (Thornton and Zhang, 2010) or, equivalently, by the shape factor ζ, as given in **Table 1**. Note that the values for ζ are during uniaxial loading where compression is performed in the z-direction. The sorting will lead to different values, $\zeta = -1/2$, when the strain is reversed for both UNI and D3 modes.

4.2.2 Stress

From the simulations, one can determine the stress tensor (compressive stress is positive as convention) components:

$$\sigma_{\alpha\beta} = \frac{1}{V}\left(\sum_{p\in V} m^p v_\alpha^p v_\beta^p - \sum_{c\in V} f_\alpha^c l_\beta^c\right), \qquad (5)$$

with particle p, mass m^p, velocity v^p, contact c, force f^c and branch vector l^c, while Greek letters represent components x, y, and z (Luding, 2008a,b). The first sum is the kinetic energy tensor and the second involves the contact-force dyadic product with the branch vector. Averaging, smoothing or coarse graining (Weinhart et al., 2012) in the vicinity of the averaging volume, V, weighted according to the vicinity, is not applied in this study, since averages are taken over the total volume. Since the data in this study are quasi-static, the first sum can mostly be neglected.

The average isotropic stress (i.e. the hydrostatic pressure) is defined as:

$$P = \frac{\sigma_{xx} + \sigma_{yy} + \sigma_{zz}}{3} = \frac{1}{3}\mathrm{tr}(\boldsymbol{\sigma}), \qquad (6)$$

where σ_{xx}, σ_{yy} and σ_{zz} are the diagonal elements of the stress tensor $\boldsymbol{\sigma}$ in the x, y, and z box reference system and $\mathrm{tr}(\boldsymbol{\sigma})$ is its trace. The non-dimensional pressure (Göncü et al., 2010) is defined as:

$$p = \frac{2\langle r\rangle}{3k}\mathrm{tr}(\boldsymbol{\sigma}), \qquad (7)$$

where $\langle r\rangle$ is the mean radius of the spheres and k is the contact stiffness defined in section 2. We define the deviatoric magnitude of stress (similar to Eq. (4) for the deviatoric strain) as:

$$\sigma_{\mathrm{dev}} = \sqrt{\frac{\left(\sigma_{xx} - \sigma_{yy}\right)^2 + \left(\sigma_{yy} - \sigma_{zz}\right)^2 + \left(\sigma_{zz} - \sigma_{xx}\right)^2}{2}}, \qquad (8)$$

which is always positive by definition. The direction of the deviatoric stress is carried by its eigen-directions (in the present case coincident with the Cartesian reference system), where stress eigenvalues are sorted like strain eigenvalues, possibly with a different sign convention, according to their magnitude. Eqs. (4) and (8) can easily be generalized to account for shear reversal using a sign taken from the orientation of the corresponding eigenvectors and eigenvalues, or from the stress shape factor, however, this will not be detailed here for the sake of brevity.

It is noteworthy to add that the definitions of the deviatoric stress and strain tensors are proportional to the second invariants of these tensors, e.g. for stress: $J_2 = \left(1/\sqrt{3}\right)\sigma_{\mathrm{dev}}$, which makes our definition identical to the von Mises criterion (Fredlund, 1979; Hayhurst, 1972; Thornton and Zhang, 2006, 2010)[3].

---

[2] The objective definition of the deviatoric strain defines it in terms of the eigenvalues $\epsilon_{\mathrm{d}}^{(1)}$, $\epsilon_{\mathrm{d}}^{(2)}$ and $\epsilon_{\mathrm{d}}^{(3)}$, of the (deviatoric) strain tensor. However, since the global strain is given by the wall motion and the eigensystem stays practically unchanged during the deformation, the two definitions are equivalent for triaxial element tests.

4.2.3 Fabric (structure) tensor

Besides the stress of a static packing of powders and grains, the next most important quantity of interest is the fabric/structure tensor. For disordered media, the concept of the fabric tensor naturally occurs when the system consists of an elastic network or a packing of discrete particles. The expression for the components of the fabric tensor is:

$$F_{\alpha\beta} = \frac{1}{V}\sum_{p\in V} V^p \sum_{c=1}^{N} n_\alpha^c n_\beta^c, \tag{9}$$

where V^p is the particle volume which lies inside the averaging volume V and $\boldsymbol{n}^c$ is the normal unity vector pointing from the center of particle p to contact c. $F_{\alpha\beta}$ are thus the components of a symmetric rank-two 3 × 3 tensor, such as the stress tensor. The isotropic fabric $F_V = \mathrm{tr}(\boldsymbol{F})$ quantifies the contact number density as studied by Göncü et al., 2010. We assume that the structural anisotropy in the system is quantified (completely) by the anisotropy of fabric, i.e. the deviatoric fabric. To quantify it, we define a scalar similar to Eqs. (4) and (8) as:

$$F_{\mathrm{dev}} = \sqrt{\frac{\left(F_{xx}-F_{yy}\right)^2 + \left(F_{yy}-F_{zz}\right)^2 + \left(F_{zz}-F_{xx}\right)^2}{2}}, \tag{10}$$

where F_{xx}, F_{yy} and F_{zz} are the three diagonal components of the fabric tensor. The fabric tensor practically has only diagonal components with non-diagonal elements very close to zero, so that its eigensystem is close to the Cartesian reference system, as confirmed by eigenvalues analysis. Also for the fabric, a shape factor completes the picture.

4.2.4 Conclusion

Three macroscopic rank-two tensors were defined and will be related to microscopic quantities and each other in the following. The orientations of all the tensor eigenvectors show a tiny non-co-linearity of stress, strain and fabric, which we neglect in the next sections, since we attribute it to natural statistical fluctuations and consider a unique fixed eigensystem coincident with the Cartesian reference system for all our deformation modes. The shape factor, as defined for strain, can also be analyzed for stress and fabric, but this will be shown elsewhere.

5. Evolution of Micro-Quantities

In this section, we discuss the evolution of the microscopic quantities studied – including coordination number and fraction of rattlers – as a function of volume fraction and deviatoric strain, respectively, and compare these results for the different deformation modes.

5.1 Coordination number and rattlers

It has been observed by Göncü et al., 2010, that under isotropic deformation, the corrected coordination number C^* follows the power law

$$C^*(\nu) = C_0 + C_1\left(\frac{\nu}{\nu_c} - 1\right)^{\alpha}, \tag{11}$$

where $C_0 = 6$ is the isostatic value of C^* in the frictionless case. For the uniaxial unloading simulations, we obtain $C_1 \approx 8.370$, $\alpha \approx 0.5998$ and $\nu_c^{\mathrm{UNI}} \approx 0.6625$ as best-fit parameters.

In **Fig. 4**, the evolution of the simple, corrected and modified coordination numbers is compared as a function of the volume fraction during uniaxial de-

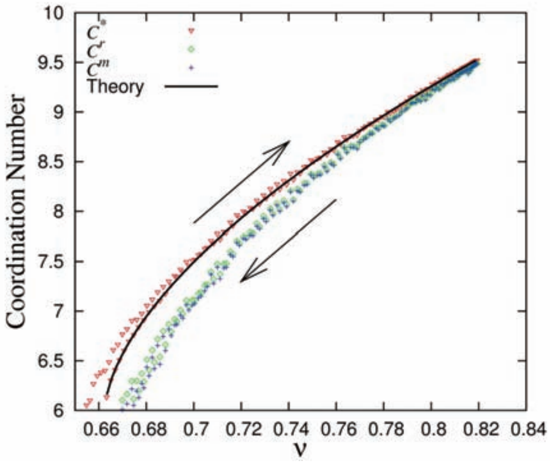

Fig. 4 Comparison between coordination numbers using the simple (‘+’, blue), modified (‘◇’, green) and corrected (‘∇’, red) definitions. Data are from a uniaxial compression-decompression simulation starting from $\nu_0 = 0.64 < \nu_c \approx 0.6625$. The solid black line represents Eq. (11) with parameters given in the text very similar to those measured in Göncü et al., 2010, see **Table 2**. The compression and decompression branches are indicated by arrows pointing right and left, respectively.

---

[3] Different factors in the denominator of Eqs. (4) and (8) have been proposed in literature (Imole et al., 2011; Zhao and Evans, 2011) but they only result in a change in the maximum deviatoric value obtained. For consistency, we use the same factor $\sqrt{1/2}$ for deviatoric stress and strain and a similar definition for the deviatoric fabric, see the next subsection.

formation (during one loading and unloading cycle). The contribution to the coordination number originating from particles with $C = 1$, 2 or 3 is small – as compared to those with $C = 0$ – since C^r and C^m are very similar, but always smaller than C^* due to the fraction of rattlers, as discussed below. The number of contacts per particle grows with increasing compression to a value of $C^* \approx 9.5$ at maximum compression. During decompression, the contacts begin to open and the coordination number decreases and approaches the theoretical value $C_0 = 6$ at the critical jamming volume fraction[4] after uniaxial decompression $\nu_c^{\mathrm{UNI}} \approx 0.662$. Note that the ν_c^{UNI} value is smaller than $\nu_c^{\mathrm{ISO}} \approx 0.665$ reached after purely isotropic over-compression to the same maximal volume fraction. The coordination numbers are typically slightly larger in the loading branch than in the unloading branch, due to the previous over-compression.

In **Fig. 5**, we plot the corrected coordination number for deformation mode D2 as a function of the deviatoric strain for five different volume fractions. Two sets of data are presented for each volume fraction starting from different initial configurations, either from the loading or the unloading branch of the isotropic preparation simulation (cyan dots and blue stars in **Fig. 1**). Given initial states with volume fractions above the jamming volume fraction, and due to the volume-conserving D2 mode, the value of the coordination number remains practically constant. It is only for the lowest volume fractions close to jamming, that a slight increase (decrease) in C^* can be seen for the initial states chosen from the unloading (loading) branch of the preparation step.

However, both reach similar steady-state values after large strain, as indicated by the solid lines. Hence, for further analysis and unless otherwise stated, we will only present the steady-state values of micro- and macro-quantities from deviatoric modes D2 and D3.

The rearrangement of the particles during shear thus does not lead to the creation (or destruction) of many contacts – on average. There is no evidence of the change of average contacts after 10 – 15 percent of strain. However, close to jamming, a clear dependence of C^* on the initial state exists, which vanishes in steady state when one gets saturated values in micro- and macro-quantities after large enough strain. For the same volume fraction, we evidence a range of $C^*_{\mathrm{oc}} \leq C^*_{\mathrm{s}} \approx C^*_{\mathrm{ic}}$, where the subscripts refer to over-compressed, steady, and initially compressed states, respectively. The coordination number, or alternatively the contact number density, as related to the trace of the fabric tensor (Göncü et al., 2010), is thus a control parameter closely linked to the volume fraction that contains more information about the structure than ν itself (above the jamming volume fraction), see Magnanimo et al., 2008 and references therein.

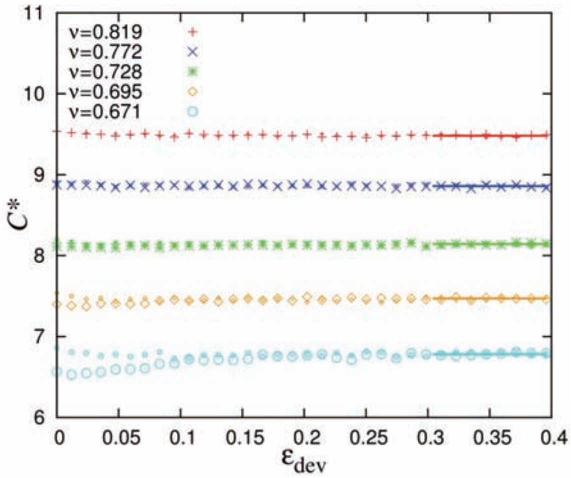

Fig. 5 Evolution of coordination numbers with deviatoric strain for the D2 mode. Smaller symbols represent data with initial configuration from the loading branch of an isotropic simulation, while the larger symbols start from an initial configuration with the same volume fraction, but from the isotropic unloading branch. The horizontal line at the large strain of the dataset indicates an average after saturation at steady state.

In **Fig. 6**, the corrected coordination number is shown as a function of volume fraction for the purely isotropic and for the uniaxial unloading data as well as for the large strain deviatoric deformation datasets. Different symbols show the values of C^* for the different deformation modes for various volume fractions. Interestingly, the power law for the coordination number derived from isotropic data describes well also the uniaxial and deviatoric datasets, with coefficients given in **Table 2**. This suggests that (for the cases considered, when particles are frictionless) the coordination number is almost independent of the deviatoric strain in steady state, and the limit values can be approximated by Eq. (11) as proposed for simple isotropic deformation. The distinction between the modes at the small (isotropic) strain region

---

[4] The value, $C_0 = 6$, is expected since it is the isostatic limit for frictionless systems in three dimensions (Göncü et al., 2010; Maxwell, 1864), for which the number of constraints (contacts) is twice the number of degrees of freedom (dimension) – in average, per particle – so that the number of unknown forces matches exactly the number of equations. (C_0 is different from the minimal number of contacts needed for a single mechanically stable frictionless sphere C^p_{min} in 3D).

is shown zoomed in the inset of **Fig. 6**. The mixed mode (uniaxial) is bordered on both sides by the pure modes, namely isotropic and deviatoric (D2 and D3 cannot be distinguished), indicating that the two pure modes are limit states or extrema for C^*. Alternatively, the range in C^* values can be seen as caused by a range in ν_c, with $\nu_c^{\mathrm{ISO}} > \nu_c^{\mathrm{UNI}} > \nu_c^{\mathrm{DEV}}$, which represent the maximal jamming volume fraction after previous (isotropic, strong) over-compression, the intermediate jamming volume fraction after (mixed mode) deformation, and the minimal jamming volume fraction after large deviatoric strain, respectively, with $\nu_c^{\mathrm{ISO}} \approx 0.6646$ and $\nu_c^{\mathrm{DEV}} \approx 0.6602$.

In other words, deviatoric deformations reduce the jamming volume fraction of the packing, i.e. can disturb and dilate a dense (over-compressed) packing so that it becomes less efficiently packed. This is opposite to isotropic over-compression, where after unloading, the jamming volume fraction is higher, i.e. the system is more efficiently packed/structured. This behavior is qualitatively expected for frictional particles, however, this is to our knowledge the first time that this small but systematic range in the jamming volume fractions is reported for frictionless packings – where the most relevant and only mechanism is structural reorganization, as will be discussed further in section 6.1.1.

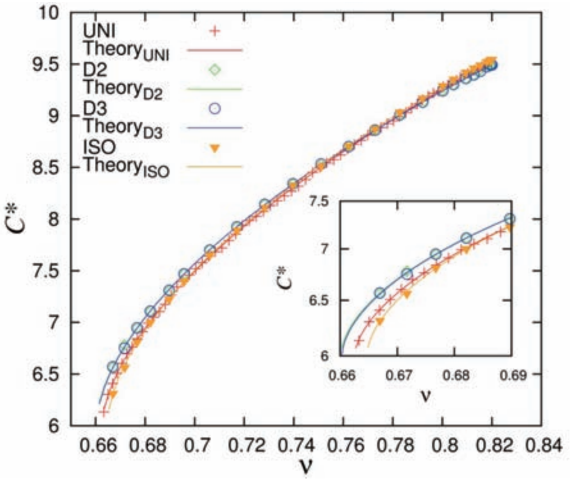

Fig. 6 Evolution of the corrected coordination number as a function of volume fraction during unloading for all modes. The symbols represent the respective simulation data while the solid lines represent the analytical equation according to Eq. (11) with the respective values of C_0, C_1, α and ν_c shown in **Table 2**. The inset shows the corrected coordination number at low volume fractions close to jamming.

Table 2 Fit parameters for the analytical predictions of coordination number, fraction of rattlers, and pressure in Eq. (11), with $C_0 = 6$ and Eqs. (12) and (15), respectively. ν_c is used from the fits of C^* to fit ϕ_r for the different deformation modes. The first rows of isotropic data ISOG are from Göncü et al., 2010, for various polydispersities and also during unloading, but for different over-compression density.

C^*	C_1	α	ν_c
ISO$_\mathrm{G}$	8.0 ± 0.5	0.58 ± 0.05	0.66 ± 0.01
ISO	8.2720	0.5814	0.6646
UNI	8.3700	0.5998	0.6625
D2	7.9219	0.5769	0.6601
D3	7.9289	0.5764	0.6603

ϕ_r	ϕ_c	ϕ_ν	
ISO$_\mathrm{G}$	0.13 ± 0.03	15 ± 2	
ISO	0.1216	15.8950	
UNI	0.1507	15.6835	
D2	0.1363	15.0010	
D3	0.1327	14.6813	

p^*	p_0	γ_p	ν_c
ISO$_\mathrm{G}$	0.04180	0.11000	0.6660
ISO	0.04172	0.06228	0.6649
UNI	0.04006	0.03270	0.6619
D2	0.03886	0.03219	0.6581
D3	0.03899	0.02819	0.6583

As a related interesting microscopic quantity, we recall the analytical expression for the fraction of rattlers proposed by Göncü et al., 2010:

$$\phi_r(\nu) = \phi_c \exp\left[-\phi_\nu\left(\frac{\nu}{\nu_c} - 1\right)\right], \qquad (12)$$

where the fit parameters for the different deformation modes are given in **Table 2**, and $\nu_c \approx 0.6646$ is obtained from extrapolation of C^* to the isostatic coordination number $C_0 = 6$. In **Fig. 7**, the evolution of the fraction of rattlers is plotted as a function of volume fraction for both isotropic and uniaxial unloading as well as for steady-state deviatoric mode simulations. We then compare these with the prediction/fit (solid lines) from the exponential decay equation, Eq. (12). Interestingly, in contrast to the coordination number, the fraction of rattlers displays stronger differences at the highest volume fraction ($\nu = 0.82$ in **Fig. 7**), and it is lower during isotropic unloading as compared to the steady-state deviatoric mode situations, and somewhat higher during uniaxial unloading. The difference between the modes is small close to jamming with largest ϕ_r for the UNI mode. For uniaxial simulations, at the end of unloading close to ν_c^{UNI}, a considerable fraction (almost 20 percent) of

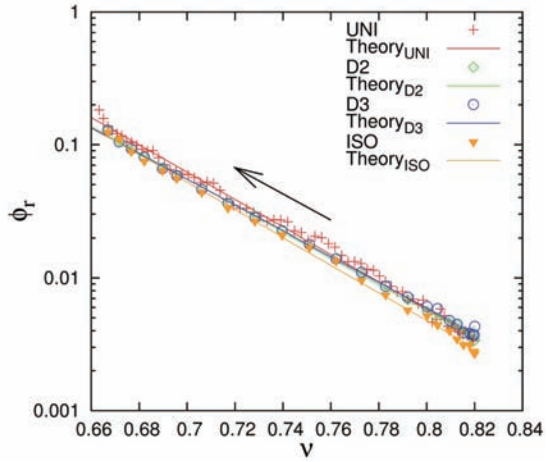

Fig. 7 Evolution of the fraction of rattlers as a function of volume fraction during unloading for all modes. The symbols represent the respective simulation data. The solid lines are the analytical fits of Eq. (12) for each mode with the values of fit parameters ϕ_c and ϕ_v for each mode shown in **Table 2**. The arrow indicates the unloading direction.

the total number of particles are rattlers that do not contribute to the stability of the network. For higher volume fractions, a strong exponential decay is evidenced[5].

To better understand the peculiar behavior of the jamming volume fraction under the different modes of deformation, some macroscopic quantities are studied next.

6. Evolution of Macro-Quantities

In the following, we discuss the evolution of the macroscopic tensors, stress and fabric, as defined in section 4.2. For clarity, we split them into isotropic and deviatoric parts in subsections 6.1 and 6.2, respectively.

6.1 Evolution of macro-quantities: isotropic

6.1.1 Isotropic pressure

In this section, the relation between pressure and volume fraction is studied. First, we consider the contact overlap/deformation δ_c, since the force is directly related to it and stress is proportional to the force. The infinitesimal change $\mathrm{d}\langle\Delta\rangle_c = 3Z\epsilon_v$ of the normalized average overlap $\Delta_c = \delta_c/\langle r\rangle$, can be related to the volumetric strain under the simplifying assumption of uniform, homogeneous deformation in the packing. As defined in subsection 4.2.1, $\epsilon_v = \epsilon_{ii}/3$ is the average of the diagonal elements of the infinitesimal strain tensor, and $Z \approx 0.425$ is a proportionality constant that depends on the size distribution and can be readily obtained from the average overlap and volume fraction (data not shown), see Eq. (13). The integral of $3\epsilon_v$ denoted by ε_v is the true or logarithmic volume change of the system relative to the reference volume V_{ref}. This is chosen without loss of generality at the critical jamming volume fraction $\nu_{\mathrm{ref}} = \nu_c$, so that the normalized average overlap is (Göncü et al., 2010):

$$\langle\Delta\rangle_c = -3Z\int_{V_0}^{V}\epsilon_v = -Z\varepsilon_v = Z\ln\left(\frac{\nu}{\nu_c}\right). \quad (13)$$

As in Eq. (7), see Refs. Göncü et al., 2010; Shaebani et al., 2012 for details, the non-dimensional pressure is:

$$p = \frac{2\langle r\rangle}{3k}\mathrm{tr}(\boldsymbol{\sigma}) = p_0\frac{\nu C}{\nu_c}(-\varepsilon_v)\left[1-\gamma_p(-\varepsilon_v)\right], \quad (14)$$

and the scaled pressure is:

$$p^* = \frac{p\nu_c}{\nu C} = p_0(-\varepsilon_v)\left[1-\gamma_p(-\varepsilon_v)\right], \quad (15)$$

where $p_0 \approx 0.040$, $\gamma_p \approx 0.033$, and the critical volume fraction $\nu_c \approx 0.6625$ are fit parameters to the pressure law for uniaxial unloading. Combining the quasi-static part of Eq. (5) with (14) leads to the proportionality relation $p \propto \nu C\langle\Delta\rangle_c$, which makes p a measure for the average overlap relative to the average particle diameter. On the other hand p^* in Eq. (15) scales various different pressures p for different deformation modes to their respective reference jamming volume fractions and is linear for small ε_v.

Note that the critical volume fraction $\nu_c \approx 0.6625$, as obtained from extrapolation of C^* to the isostatic coordination number $C_0 = 6$, is very close to that obtained from Eq. (14). When fitting all modes with pressure, one confirms again that ν_c^{UNI} falls in between the limits of the pure modes ν_c^{ISO} and ν_c^{DEV} (with values consistent within each mode) as summarized in **Table 2**.

In **Fig. 8**, we plot the total (non-dimensional) pressure p as a function of the deviatoric strain for different volume fractions in the deformation mode D2. Above the jamming volume fraction, the value of the pressure stays practically constant with increasing shear strain. A slight increase in p can be seen for

---

[5] The sharp jump observed in Göncü et al., 2010 at the jamming transition during unloading is not seen here because we keep the system above the jammed state. Interestingly, the simulation data for the uniaxial and deviatoric mode all collapse close to the (isotropic) exponential prediction.

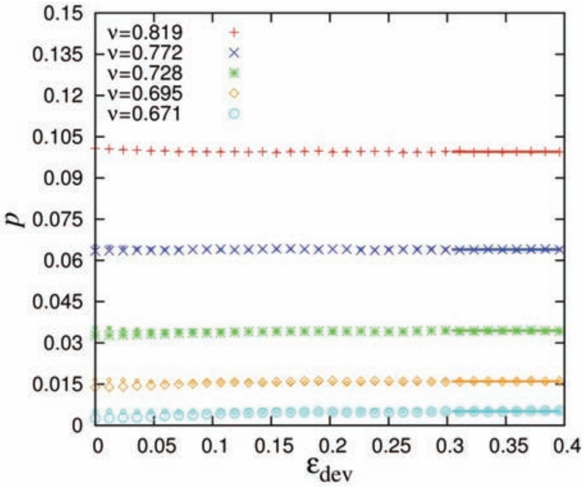

Fig. 8 Evolution of (non-dimensional) pressure, Eq. (7), with deviatoric strain for the D2 deformation mode, at different initial volume fractions ν_i. Small and large symbols represent simulations starting with initial isotropic configurations from the loading and unloading branch, respectively. The horizontal line at the large strain of the dataset indicates an average value of the pressure after saturation at steady state.

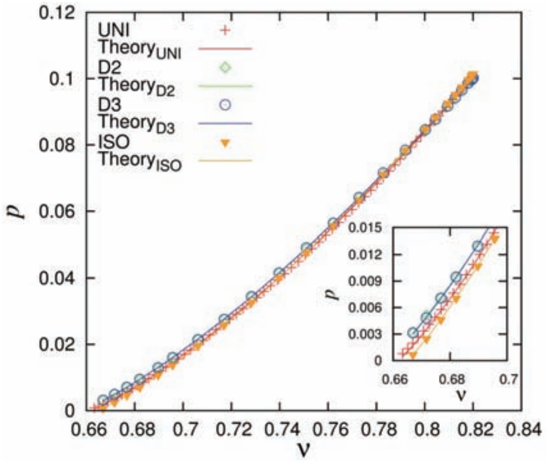

Fig. 9 Total (non-dimensional) pressure, Eq. (14), plotted as a function of volume fraction for the uniaxial and isotropic datasets during unloading, and for the D2/D3 deviatoric modes after large strain. The solid lines are the analytical fits of Eq. (14) for each mode, with parameters p_0, γ_p and ν_c shown in **Table 2**.

the lowest volume fractions when the initial states are chosen from the unloading branch of isotropic modes, whereas a slight decrease in p is observed for initial states chosen from the loading branch. Independently of the initial configuration, the pressure reaches a unique steady state at large strain, similarly to what is observed for the coordination number in **Fig. 6**.

In **Fig. 9**, the total pressure is plotted against volume fraction for isotropic, uniaxial and deviatoric (D2 and D3) modes, with data obtained from the unloading branch in the first two cases and after large deviatoric strain for the deviatoric modes (see **Fig. 8**). For these three modes, at large ν, the simulation data collapse on a unique curve with non-linear behavior. Due to the linear contact model, this feature can be directly related to the contact number density, i.e. the isotropic fabric, which quantifies the isotropic, direction-independent changes of structure due to rearrangements and closing/opening of contacts. When approaching the jamming transition, the pressure values diverge slightly (inset of **Fig. 9**) due to the difference in the critical volume fractions $\nu_c^{\mathrm{DEV}} < \nu_c^{\mathrm{UNI}} < \nu_c^{\mathrm{ISO}}$.

In **Fig. 10**, we plot the scaled pressure defined in Eq. (15) against the volumetric strain from the same data as in **Fig. 9**. The three datasets almost collapse for small strain. For increasing volume fractions (larger $-\varepsilon_{\mathrm{v}}$), the scaled pressure in the isotropic mode is considerably larger than the uniaxial and deviatoric modes, where again the uniaxial data fall in between isotropic and deviatoric values. This resembles the behavior of C^* and is consistent with the fact that the uniaxial mode is a superposition of the purely isotropic and deviatoric deformation modes.

The dependence of pressure on isotropic strain can be interpreted in relation to the sample history. The deviatoric modes (D2 or D3) lead to dilatancy and thus to higher steady-state pressure, with low ν_c^{DEV}; the isotropic mode is strictly compressive, with the lowest pressure after over-compression, during unloading and the highest ν_c^{ISO}; finally, the uniaxial mode is a mixed mode and thus interpolates between the two other modes.

The apparent collapse of all scaled p^* data at small strain, with similar pre-factors $p_0 \approx 0.040$ is interesting since, irrespective of the applied deformation mode – purely isotropic, uniaxial, and D2 or D3 deviatoric, it boils down to a linear relation between p^* and $-\varepsilon_{\mathrm{v}}$ with a small quadratic correction – different from the non-linear power laws proposed in previous studies, e.g. in Majmudar et al., 2007. The non-linearity due to $1 - \nu/\nu_c$ is hidden in νC, which is actually proportional to the isotropic fabric F_{v}.

6.1.2 Isotropic fabric

The random isotropic orientation of the contact directions in space was studied in detail in Refs. Göncü et al., 2010 and Shaebani et al., 2012, and is referred

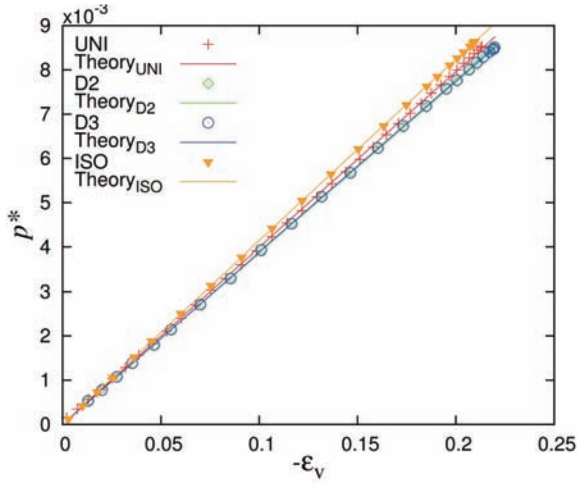

Fig. 10 The scaled pressure plotted against the (negative) volumetric strain for the same data as presented in **Fig. 9**. The solid lines are the predictions from Eq. (15) using the fits of p and C for each mode.

to as the contact number density with $\mathrm{tr}(\mathbf{F}) = g_3 \nu C$, where g_3 is of order unity and depends only on the size distribution (for our case with $w = 3$, one has $g_3 \approx 1.22$). Note that νC directly connects to the dimensionless pressure which, remarkably, hides the corrected coordination number and the fraction of rattlers in the relation $C = (1 - \phi_r)C^*$, which fully determines $\mathrm{tr}(\mathbf{F})$.

6.2 Evolution of macro-quantities: deviatoric

In the following, we will show the evolution of the deviatoric stress ratio (which can be seen as a measure of stress anisotropy) and the structural anisotropy, both as a function of the deviatoric strain. In particular, we present the raw data from deviatoric and uniaxial simulations and their phenomenology. The D2 volume-conserving simulations are used to calibrate the constitutive model, as presented in Refs. Luding and Perdahcioğlu, 2011, Magnanimo and Luding, 2011 and described in section 7. We further use the fitting parameters inferred from deviatoric data to predict the evolution of stress and fabric during uniaxial deformation.

6.2.1 Deviatoric stress

The behavior of the deviatoric stress ratio, $s_{\text{dev}} = \sigma_{\text{dev}}/P$ during deformation mode D2, is shown in **Fig. 11** as a function of the deviatoric strain for various different volume fractions. The stress ratio initially grows with applied strain until an asymptote (the maximum stress anisotropy) is reached where it remains fairly constant. The asymptote $s_{\text{dev}}^{\max} = (\sigma_{\text{dev}}/P)^{\max}$ is referred to as the deviatoric steady state or the macroscopic friction, where s_{dev} represents the mobilized friction at each step along the loading path. For lower volume fractions, higher maximum s_{dev} are reached and the deviatoric stress ratio increases faster, meaning a higher G^{oct}/P ratio, where G^{oct} is the octahedral shear modulus as defined by Barreto and O'Sullivan, 2012. This is opposite to what is expected for the shear modulus G^{oct} itself, being proportional to the volume fraction. Interestingly, the stress response observed for mode D3 (not shown) follows a very similar path as for mode D2, resembling independency of the results with respect to the particular deviatoric path, as will be discussed in more detail in section 7.

We use the deviatoric simulations to fit the exponential relation proposed in Luding and Perdahcioğlu, 2011; Magnanimo and Luding, 2011, for the biaxial box and report the theoretical curves in the same **Fig. 11**. Both the initial growth rate coefficient and the asymptotic values are inferred from the volume-conserving deviatoric data, following the procedure described in Section 7. We point out here that the softening behavior after maximal s_{dev} is ignored in the fitting procedure for the theoretical model, since we do not want this feature of the material to be plugged into the model as an additional element.

The stress-strain behavior in the case of uniaxial compression is shown in **Fig. 12** starting from initial volume fractions $\nu = 0.671$, 0.695, 0.728, to a common maximum value $\nu_{\max} = 0.820$. Unlike the volume-conserving deviatoric simulations discussed previously, the evolution of the deviatoric stress ratio during uniaxial compression leads to large fluctuations that do not allow the clear observation of a possible softening/hardening regime. This difference is because the uniaxial deformation mode has a continuously increasing density and pressure in contrast, for example, to mode D3 where σ_{zz} is increasing and $\sigma_{yy} \approx \sigma_{xx}$ are decreasing such that the pressure remains (almost) constant. The solid lines superimposed on the data in the plot represent the predictions of the constitutive relation in Eq. (17), with the parameters obtained from the deviatoric modes D2 and D3, as explained in detail in section 7.

Moreover, as the deviatoric strain increases during uniaxial deformation, the deviatoric stress ratio s_{dev} also increases with values that depend on the initial volume fraction. For lower volume fractions we observe a higher stress ratio, similar to what is observed in **Fig. 11**. Interestingly, uniaxial deformations for different initial volume fractions lead to

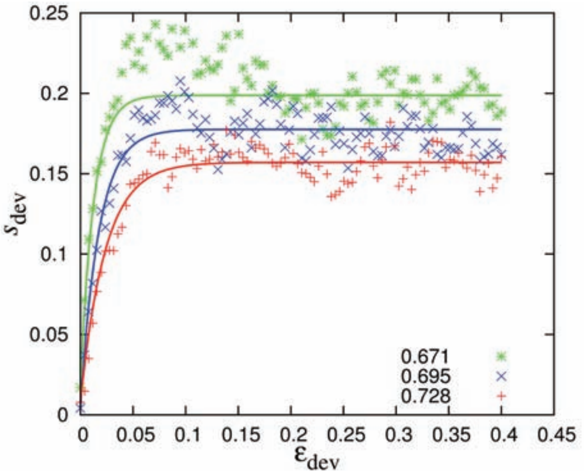

Fig. 11 Deviatoric stress ratio ($s_{\mathrm{dev}} = \sigma_{\mathrm{dev}}/P$) plotted against deviatoric strain from the D2 deformation mode for initial volume fractions ν_i during unloading, from which the simulations were performed, as given in the inset. The symbols ('*', '×' and '+') are the simulation data while the solid lines through them represent a fit to the data using Eq. (17).

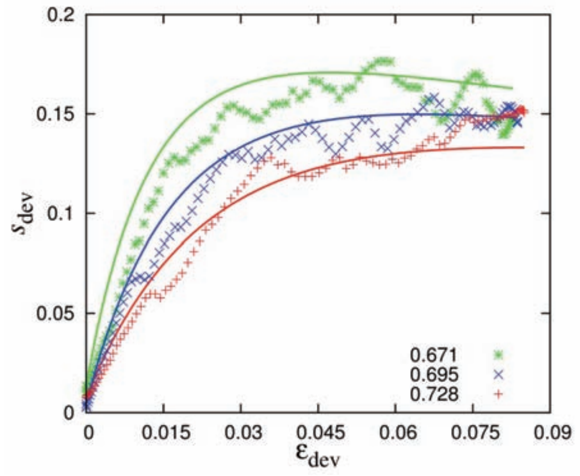

Fig. 12 Deviatoric stress ratio plotted against deviatoric strain from the uniaxial compression mode data for different initial volume fractions ν_i during unloading, from which the uniaxial deformations were initiated, as given in the inset. The symbols ('*' , '×' and '+') are the simulation data while the solid lines represent the prediction using Eq. (17).

convergence (and almost collapse) after about 7.5 percent deviatoric strain. This feature of the uniaxial simulations is also well captured by the anisotropy model in section 7.3.

6.2.2 Deviatoric fabric

The evolution of the deviatoric fabric F_{dev} as a function of the deviatoric strain is shown in **Fig. 13** for mode D2 simulations and three different volume fractions. It builds up from different random, small initial values and reaches different maximum saturation values $F_{\mathrm{dev}}^{\max}$. The deviatoric fabric increases faster at lower volume fractions in a very similar fashion to what was observed for the stress ratio in **Fig. 11**. Both the growth rate and the maximum deviatoric fabric are well defined and shown in **Fig. 13** together with the fitting curves used to deduce the theoretical values β_F and $F_{\mathrm{dev}}^{\max}$ for different volume fractions (see details in section 7.2).

The evolution of the deviatoric fabric for the D3 mode is not shown since it resembles the behavior of the D2 mode, implying that the fabric evolution is pretty much insensitive to the deviatoric deformation protocol employed, as was observed before also for the stress ratio. A more detailed study of the (small) differences among deformation modes with different shape factors, as predicted by Thornton and Zhang, 2010, will be reported elsewhere.

Fig. 14 shows the evolution of the deviatoric fabric during uniaxial compression as presented in section 6.2.1. The deviatoric fabric builds up as the deviatoric strain (and the volume fraction) increases. It begins to saturate at $\varepsilon_{\mathrm{dev}} \approx 0.06$ and a slight decreasing (softening) trend is seen towards the end of the loading path. The convergence of the deviatoric stress after large strain, for different volume fractions, as seen in **Fig. 12**, does not appear so clearly for the deviatoric fabric. The theoretical prediction of the constitutive relations from section 7 is in good qualitative agreement with the numerical data, but over-predicts the deviatoric fabric for larger strains. Their analytical form and the parameters involved will be discussed next.

7. Theory: Macroscopic Evolution Equations

Constitutive models are manifold and most standard models with wide application fields such as elasticity, elasto-plasticity, or fluid-/gas-models of various kinds were applied also to granular flows – sometimes with success, but typically only in a very limited range of parameters and flow conditions; for overviews see, e.g. GdR-MiDi, 2004; Luding and Alonso-Marroquín, 2011. The framework of kinetic theory is an established tool with quantitative predictive value for rapid granular flows only – but it is hardly applicable in dense, quasi-static and static situations (Luding, 2009). Further models, such as hyper- or hypo-elasticity, are complemented by hypo-

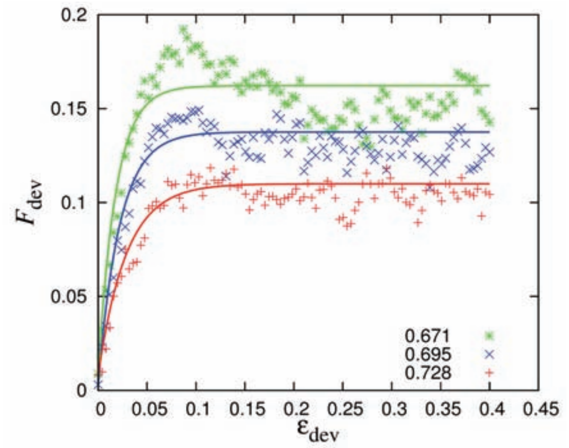

Fig. 13 Deviatoric fabric plotted against deviatoric strain from the D2 deformation simulations of **Fig. 11** The symbols (‘*’, ‘×’ and ‘+’) are the simulation data while the solid lines through them represent a fit to the data using Eq. (18).

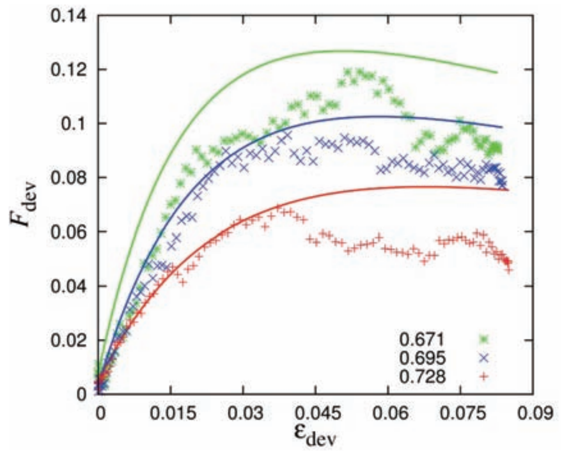

Fig. 14 Deviatoric fabric plotted against deviatoric strain from the uniaxial deformation simulations in **Fig. 12** The symbols (‘*’, ‘×’ and ‘+’) are the simulation data while the solid lines through them represent the prediction of the data using Eq. (18).

plasticity (Kolymbas, 1991) and the so-called granular solid hydrodynamics (Jiang and Liu, 2009), where the latter provides incremental evolution equations for the evolution of stress with strain, and involve limit states (Mašín, 2012) instead of a plastic yield surface as in plasticity theory. A strict split between elastic and plastic behavior seems invalid in granular materials, see, e.g. Alonso-Marroquín et al, 2005. More advanced models involve so-called non-associated / non-coaxial flow rules, where some assumptions on relations between different tensors are proposed, see Thornton and Zhang, 2006, 2010. While most of these theories can be or have been extended to accommodate anisotropy of the microstructure, only very few models account for an independent evolution of strain, stress and microstructure (see, for example, Thornton and Zhang, 2010; Sun and Sundaresan, 2011; Luding and Perdahcioğlu, 2011; Goddard, 2010) as found to be important in this study and many others.

In the following, we use the anisotropy constitutive model as proposed in Kumar et al., 2012a; Luding and Perdahcioğlu, 2011; Magnanimo and Luding, 2011, generalized for a $\mathcal{D}$ −dimensional system:

$$\delta P = \mathcal{D} B \delta\epsilon_{\mathrm{v}} + A S \delta\epsilon_{\mathrm{dev}},$$
$$\delta\sigma_{\mathrm{dev}} = A\delta\epsilon_{\mathrm{v}} + \mathcal{D} G^{\mathrm{oct}} S \delta\epsilon_{\mathrm{dev}},$$
$$\delta A = \beta_A \mathrm{sign}\,(\delta\epsilon_{\mathrm{dev}})(A^{\max} - A)\delta\epsilon_{\mathrm{dev}}. \tag{16}$$

In its simplest form, the model involves only three moduli: the classic bulk modulus B (Göncü et al., 2010), the octahedral shear modulus G^{oct}, and the new variable “anisotropy modulus” A, evolving independently of stress with deviatoric strain. Due to A, the model provides a cross-coupling between the two types of stress and strain in the model, namely the hydrostatic and the shear (deviatoric) stresses react to both isotropic and deviatoric strains. $S = (1 - s_{\mathrm{dev}}/s_{\mathrm{dev}}^{\max})$ is an abbreviation for the stress isotropy with $s_{\mathrm{dev}} = \sigma_{\mathrm{dev}}/P$. The parameter $s_{\mathrm{dev}}^{\max}$ resembles the macroscopic friction and β_s is the growth rate of s_{dev} with deviatoric strain ϵ_{dev}. The parameter $A^{\max}$ in the evolution equation of A represents the maximum anisotropy that can be reached at saturation, and β_A determines how fast the asymptote is reached (growth rate). Both $A^{\max}$ and β_A are model parameters for the anisotropy modulus and can be extracted from fits to the macroscopic, average simulation results. Note that the evolution of A is assumed to be kinematic, i.e. not explicitly dependent on pressure, but there is a possible volume fraction dependence of β_A and $A^{\max}$, as detailed below.

In the following, we test the proposed model by extracting the model parameters as functions of volume fraction ν from various volume-conserving deviatoric simulations. The calibrated model is then used to predict the uniaxial deformation behavior (see the previous section). The theory will be discussed elsewhere in more detail (Kumar et al., 2012a; Magnanimo and Luding, 2012). In short, it is based on the basic postulate that the independent evolution of stress and structure is possible. It comes together with some simplifying assumptions such as:

(i) the new macroscopic field A is proportional to the microscopic rank-two deviatoric fabric F_{dev} so that they have the same non-dimensional growth rates $\beta_F = \beta_A$;

- (ii) both A and $s_{\rm dev}$ – to lowest order, i.e. neglecting additional (missing) terms in Eqs. (16) – approach their limit states exponentially fast;
- (iii) only one anisotropy modulus A is sufficient (valid in 2D, questionable in 3D, possibly two moduli A_1 and A_2 are needed);

that lead to Eqs. (17) and (18) below. We use these two equations as empirical fit functions, since they are special cases of the complete constitutive model with anisotropy, and then use the fit result to predict another solution of the (simplified) theory for another deformation mode.

7.1 Reduced theoretical model

The reduced model consists of two evolution equations for the deviatoric stress ratio $s_{\rm dev}$ related to the mobilized macroscopic friction, and the deviatoric fabric $F_{\rm dev}$ based on DEM observations in 2D, see Luding, 2004, 2005. For volume-conserving pure shear, Figs. 11 and 13 show that $s_{\rm dev}$ and $F_{\rm dev}$ grow non-linearly until they approach exponentially a constant value at steady state, with fluctuations where the material can be indefinitely sheared without further change. As discussed by Luding and Perdahcioğlu, 2011, the coupled evolution equations (16) are (with above assumptions) consistent with $s_{\rm dev}$ approximated by:

$$s_{\rm dev} = s_{\rm dev}^{\rm max} - \left(s_{\rm dev}^{\rm max} - s_{\rm dev}^{0}\right) e^{-\beta_s \epsilon_{\rm dev}}, \qquad (17)$$

where $s_{\rm dev}^{0}$ and $s_{\rm dev}^{\rm max}$ represent the initial and maximum values of $s_{\rm dev}$ and β_s is its growth rate. Similarly, the deviatoric fabric is approximated by:

$$F_{\rm dev} = F_{\rm dev}^{\rm max} - \left(F_{\rm dev}^{\rm max} - F_{\rm dev}^{0}\right) e^{-\beta_F \epsilon_{\rm dev}}, \qquad (18)$$

where $F_{\rm dev}^{0}$ and $F_{\rm dev}^{\rm max}$ represent the initial and maximum (saturation) values of the deviatoric fabric and β_F is its rate of change. To study the variation of the parameters $s_{\rm dev}^{\rm max}$, β_s, $F_{\rm dev}^{0}$ and $F_{\rm dev}^{\rm max}$ with volume fraction ν, during deviatoric deformation, we perform several isochoric simulations at different volume fractions ν_i, and obtain the coefficients as shown in **Figs. 15** and **16** from fits to Eqs. (17) and (18).

As a final step, but not shown in this paper, in order to relate the macroscopic anisotropy (modulus) A to the evolution of the deviatoric fabric $F_{\rm dev}$, one can measure the elastic modulus A directly. For this, the sample is subjected to incremental deformations (either isotropic or purely deviatoric) at various different stages along the (large strain) deviatoric paths for D2 and D3 deformations. Details of the procedure and the results will be reported elsewhere (Kumar et al., 2012a). Here, we only note that a linear relation is found such that:

$$A \approx a_0^* F_{\rm dev} \frac{P \nu_c^2}{(\nu - \nu_c)} \approx \frac{a_0 k}{2\langle r \rangle} F_{\nu} F_{\rm dev} \qquad (19)$$

where $a_0 = 0.137$ is a combination of numerical constants including g_3, p_0.

7.2 Fitting of deviatoric deformations: calibration of the anisotropy model

From the analysis of various deviatoric D2 and D3 simulations with different volume fractions, using Eq. (17) we obtain the variation of $s_{\rm dev}^{\rm max}$ and β_s with ν,

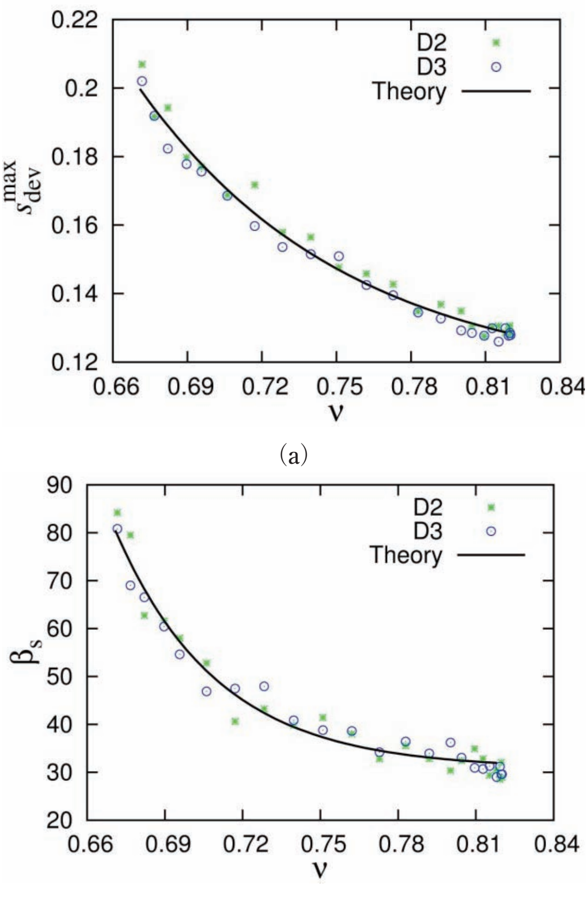

(a)

(b)

Fig. 15 Comparison of evolution parameters from Eq. (17): the maximum normalized deviatoric stress $s_{\rm dev}^{\rm max}$ and the growth rate β_s plotted against volume fraction ν for the D2 and D3 deviatoric modes. Each point represents a unique simulation; the green ' * ' s represent the D2 mode while the blue '⊙' s represent the D3 mode. The solid black line is the proposed analytical form in Eq. (20), with parameters given in **Table 3**.

see **Fig. 15**. The factor $s_{\mathrm{dev}}^{\max}$ decreases with increasing volume fraction ν and a similar trend is observed for β_s with some larger scatter. Both $s_{\mathrm{dev}}^{\max}$ and β_s seem to saturate towards a finite limit for large volume fractions, and these values can be extrapolated by the fitting procedure described later in this section. The fit procedure applied to the deformation modes D2 and D3 leads to very similar results for $s_{\mathrm{dev}}^{\max}$ and β_s. This is not surprising: the same net deviatoric strain applied in the two modes leads to (almost) the same net deviatoric stress ratio response, even though the shapes of deformations are different.

Table 3 Fitting coefficients for the parameters in Eqs. (17) and (18) with ν_c =0.6653

Evolution Parameters	$Q_{\max}$	Q_{v}	α
$s_{\mathrm{dev}}^{\max}$	0.1137	0.09166	7.916
β_s	30.76	57.00	16.86
$F_{\mathrm{dev}}^{\max}$	0	0.1694	4.562
β_F	0	57.89	5.366

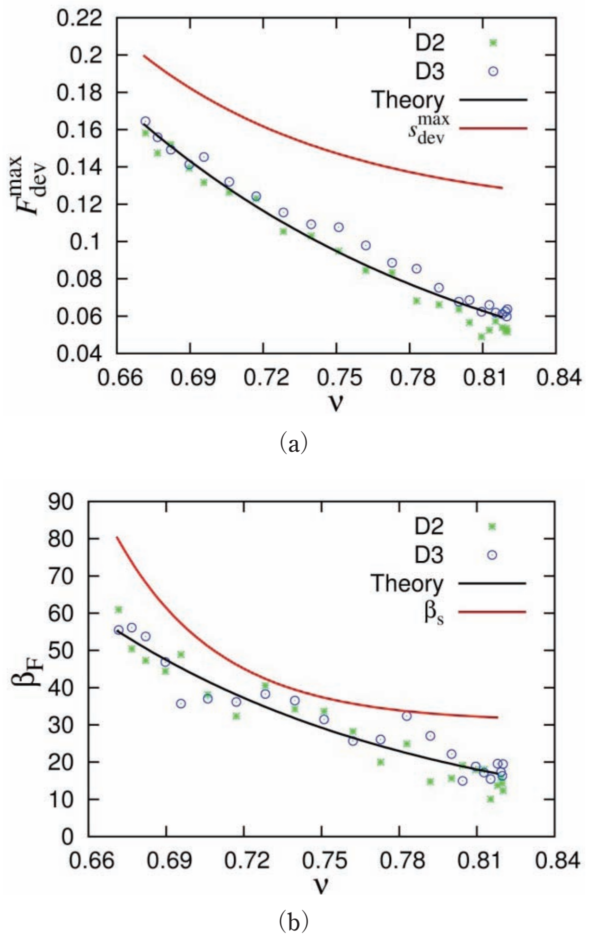

(a)

(b)

Fig. 16 Comparison of evolution parameters from Eq. (18): the maximum anisotropy $F_{\mathrm{dev}}^{\max}$ and the growth rate β_F plotted against volume fraction ν for the D2 and D3 deviatoric modes. The solid black line is the proposed theory, Eq. (20), for $F_{\mathrm{dev}}^{\max}$ and β_F, respectively, while the red lines are the corresponding parameters $s_{\mathrm{dev}}^{\max}$ and β_s in **Fig. 15**.

Fig. 16(a) shows the variation of $F_{\mathrm{dev}}^{\max}$ with volume fraction for the same simulations as in **Fig. 15**, where the two deviatoric deformation modes D2 and D3 almost collapse on each other. $F_{\mathrm{dev}}^{\max}$ decreases strongly with volume fraction ν for the two modes. For higher volume fractions, the motion of spheres is more constrained by more contacts and hence the contact anisotropy developed in the system is smaller. **Fig. 16**(b) shows a similar decreasing behavior of β_F with volume fraction ν, where stronger scatter is seen. The analytical fits of the normalized stress parameters ($s_{\mathrm{dev}}^{\max}$ and β_s) are shown for comparison.

A different behavior of the normalized stress and the deviatoric fabric with respect to both parameters (maximum saturation value and the evolution rate) proves that stress and fabric evolve independently of deviatoric strain (La Ragione and Magnanimo, 2012), as is the basic postulate for the anisotropic constitutive model.

For the fit, we propose a generalized analytical relation for both the stress parameters $s_{\mathrm{dev}}^{\max}$, β_s and the fabric parameters $F_{\mathrm{dev}}^{\max}$, β_F. The dependence of the parameters on the volume fraction ν is well described by the general relation:

$$Q = Q_{\max} + Q_{\mathrm{v}} \mathrm{e}^{\left(-\alpha\left(\frac{\nu}{\nu_c}-1\right)\right)}, \tag{20}$$

where $Q_{\max}$, Q_{v} and α are the fitting parameters with values presented in **Table 3**, and $\nu_c \approx 0.6653$ is chosen as the jamming volume fraction, see **Table 2**. For all four parameters, the $Q_{\max}$ values are the limit for large volume fractions, while $Q_c = Q_{\max} + Q_{\mathrm{v}}$ represents the limit at $\nu \to \nu_c$ and α is the rate of variation (decay) with the volume fraction increasing above ν_c. We assume, as is consistent with the data, that the structural anisotropy parameters $F_{\mathrm{dev}}^{\max}$ and β_F tend towards zero as the volume fraction increases, therefore we keep $Q_{\max} = 0$ in the fitting functions. Eq. (20) represents the solid black lines shown in **Figs. 15** and **16**, with coefficients given in **Table 3**.

7.3 Prediction of uniaxial deformation

We use the parameters determined from the deviatoric simulations presented in **Table 3** to predict the behavior of uniaxial simulations in subsection 6.2, where the volume fraction is changing with deviatoric strain and hence dependence on ν is needed to properly describe the deformation path.

Fig. 12 above shows the normalized deviatoric stress s_{dev} against the deviatoric strain ϵ_{dev} for uniaxial deformations starting from three different volume fractions ($\nu = 0.671$, 0.695 and 0.728), compared with the predictions of Eq. (17) with coefficients $s_{\mathrm{dev}}^{\max}(\nu)$ and $\beta_s(\nu)$ taken from Eq. (20) and coefficients from **Table 3**. The proposed model, although in its simplified version, is able to properly capture the behavior of the material qualitatively, approaching exponentially a maximum value and then decreasing due to the volume fraction dependence of the parameters. Note that the softening present in some of the deviatoric DEM data is on purpose not plugged into the model as a constraint, which renders the softening present in the uniaxial theoretical curves in **Fig. 12** as a valuable prediction of the model. Furthermore, the convergence of s_{dev} for uniaxial loading simulations with different initial volume fraction at large strains, as discussed in section 6.2.1, is also well captured by the theoretical model with calibrated parameters from the deviatoric simulations (where this does not happen).

Fig. 14 shows the evolution of the deviatoric fabric F_{dev} with deviatoric strain ϵ_{dev} for uniaxial deformations – as above – together with the predictions of Eqs. (18) and (20). The model is still able to qualitatively describe the behavior of the deviatoric fabric, but with up to 30 percent over-prediction. For better quantitative agreement, the complete coupled model needs to be used and possibly improved as will be presented elsewhere (Kumar et al., 2012a).

8. Conclusions and Outlook

The discrete element method has been used to investigate the bulk response of periodic, polydisperse, frictionless sphere packings in 3D, subjected to various deformation modes, in terms of both their micro- and macroscopic responses. The main goal was to present a procedure to calibrate a constitutive model with the DEM data and then to use the same to predict another independent simulation (mode). The (overly) simple linear material (model) allows us to focus on the collective/bulk response of the material to *different* types of strain, excluding complex effects due to normal or tangential non-linearities. Therefore, the present study has to be seen as a reference “lower limit”, and the procedure rather than the material is the main subject.

We focused on the strain-controlled loading and unloading of isotropic, uniaxial and two deviatoric (pure shear) type deformation modes (D2 and D3). Experimentally most difficult to realize is the isotropic deformation, while both uniaxial and deviatoric modes can be realized in various element tests where, however, often mixed strain- and stress-control procedures are applied. Both micro-mechanical and coarse-grained macroscopic properties of the assemblies are discussed and related to each other. The study covers a very wide range of isotropic, uniaxial and deviatoric deformation amplitudes and thus practically all volume fractions with mechanically stable packings – except for those very close to the jamming transition and higher than about 10 percent contact deformation, above which DEM pair contact models become questionable.

8.1 Microscopic quantities

The microscopic coordination number C, defined as the ratio of the total number of contacts to the total number of particles, has been analyzed as a function of volume fraction and deviatoric strain. By disregarding particles with less than four contacts (called rattlers), the corrected coordination number C^* is well described by Eq. (11) for all deformation modes (since the particles are frictionless). For the uniform size distribution used here, the fraction of rattlers shows an exponentially decaying trend towards higher volume fractions, very similar for all modes, see Eq. (12) and **Table 2**. These analytical relations provide *a prediction for the coordination number* $C = (1 - \phi_r)C^*$ that notably shows up in the macroscopic relations for both pressure and isotropic fabric, in combination with volume fraction ν, instead of C^*. Note that C^* is better accessible to theory, while νC is related to the wave-propagation speed, which is experimentally accessible, while both are linked by the fraction of rattlers, which was already identified as a control parameter of utmost importance (Bi et al., 2011).

A small but systematic difference in C^* and Φ_r parameters appears for the different deformation modes. Most important, *the jamming volume fraction* ν_c *is not a single, particular volume fraction,* but we observe a range of jamming volume fractions dependent on the deformation modes, i.e. the “history” of the sample. Over-compression leads to an increase of ν_c, i.e. to a better, more efficient packing. Subsequent deviatoric (pure shear) deformations slightly reduce the jamming volume fraction of such a previously over-compressed packing, causing it to become less efficiently packed. Thus more/less efficient packing is reflected by a large/small jamming volume fraction and, inversely, small/large coordination numbers. The observed differences are more pronounced as the volume fraction becomes lower. A slight increase in the fraction of rattlers due to deviatoric deformations is also reported, as consistent with the decrease in coordination number.

8.2 Macroscopic quantities

When focusing on macroscopic quantities, an important result from this study is that at small strains, the uniaxial, deviatoric and isotropic modes can be described by the same analytical pressure evolution, Eq. (15), with parameters given in **Table 2**, evidenced by the collapse of the data from these deformation modes when the scaled pressure is plotted as a (linear) function of the volumetric strain.

This linearity is due to the scaling with the nonlinear terms $p^* \propto p/(\nu C)$ in particular. Thanks to the linear contact model used, it allows the conclusion that the non-linear (quadratic) corrections are due to the structural rearrangements and non-affine deformations. The scaled deviatoric and uniaxial results deviate from the isotropic pressure data. This appears at larger strains due to the build-up of anisotropy in the system, caused by deviatoric strain, obviously not present in the isotropic deformation mode. The good match of the data suggests an advantage of the "cheaper" uniaxial (and deviatoric) deformation modes over the experimentally difficult to realize isotropic deformation mode (three walls have to be moved simultaneously in the isotropic case, while a less complicated set-up is required for the other modes).

The deviatoric stress ratio (the deviatoric stress scaled with the isotropic pressure) as a function of the deviatoric strain develops almost independently of the volume fraction when the deviatoric magnitude is defined in a similar fashion to the second deviatoric invariant (Thornton and Zhang, 2006) for all quantities studied. The deviatoric stress builds up with increasing deviatoric strain until a steady state is reached (where we do not focus on peak and softening behavior, which becomes more pronounced when the jamming volume fraction is approached). Starting from isotropic initial configurations, we also show that the slope G^{oct}/P of the normalized deviatoric stress as a function of deviatoric strain decreases with increasing volume fraction, unlike the shear modulus G^{oct}, which increases with volume fraction. This indicates that the pressure (and bulk modulus B) has a "stronger" dependence on the volume fraction than the shear modulus.

From the macroscopic data, one observes that deviatoric and isotropic stresses and strains are cross-coupled by the structural anisotropy. The latter is quantified by the deviatoric fabric, which is proportional to the bulk anisotropy modulus/moduli A, as relevant for the constitutive model. Cross-coupling means that in the presence of structural anisotropy, isotropic strain can cause deviatoric stress responses and deviatoric strain can cause isotropic stress responses (dilatancy or compactancy). The structural anisotropy response to deviatoric strain is very similar to that of the deviatoric stress ratio. The response rates of both stress and structure anisotropies with deviatoric strain are functions of volume fraction and, most important, are different from each other.

8.3 Constitutive model calibration

As a first step, the parameters of a simple constitutive model that involves anisotropy as proposed for 2D by Luding and Perdahcioğlu, 2011, Magnanimo and Luding, 2011 have been calibrated from DEM data. From the isotropic deformation mode, one can extract the bulk modulus B, as was done by Göncü et al., 2010. From the volume-conserving D2 and D3 modes, by fitting the idealized evolution equations for shear stress in Eq. (17), the macroscopic friction $s_{\mathrm{dev}}^{\max}$ and the deviatoric stress rate β_s can be inferred as functions of the volume fraction, entering the shear modulus G^{oct}. Similarly, the fit of Eq. (18) provides a relation for the maximum fabric anisotropy at steady state $F_{\mathrm{dev}}^{\max}$ and the fabric rate β_F as functions of volume fraction. A relation between the deviatoric fabric and the anisotropy modulus/moduli A in the model is finally needed to close the system and allow integration of the coupled evolution equations for stress and structure.

As a second step and major result, the constitutive model calibrated on deviatoric data has been used to predict qualitatively (and to some extent also quantitatively) both stress and fabric evolution under uniaxial deformation. This is very promising, since the basic qualitative features are caught by the model, even though it was used in a very idealized and short form, with the single anisotropy modulus $A \propto F_{\mathrm{dev}}$ the only main new ingredient. Several additional terms of assumed minor impact are ignored and have to be added to complete the model, see Kumar et al., 2012a; Magnanimo and Luding, 2011; Sun and Sundaresan, 2011; Thornton and Zhang, 2010, and references therein, as postponed to future studies. (For example, an objective tensorial description of stress, strain and fabric involves also the third tensor invariants. Alternatively/equivalently, these deviatoric tensors can be completely classified by the shape factors in their respective eigen-systems, which allow us to distinguish all possible deformation and response modes in 3D.)

8.4 Outlook

In this paper, we have reviewed and presented new results for frictionless particles undergoing isotropic, uniaxial, and (pure) shear deformation. Since the particles are too idealized here, the results cannot be applied to practical systems where shape, friction, and other non-linearities are relevant. However, they form the basic reference study with details given on the calibration procedure that yields a constitutive model with satisfactory predictive quality. Therefore, the next steps in our research will involve more realistic contact models with friction, cohesion, and other physically meaningful material parameters. Only then can the validity of the analytical expressions be tested for realistic systems, to predict well the phenomenology for pressure as well as the scaling arguments for the deviatoric stress and fabric.

Laboratory element test experiments should also be performed with the biaxial box to validate the simulation results with realistic material properties. Macroscopic quantities that can be readily obtained experimentally – for example, the pressure-volume fraction relation and the shear stress evolution with deviatoric (pure shear) strain – can then be compared with simulation data. Moreover, the work underlines the predictive power of constitutive models with anisotropy (as in Luding and Perdahcioğlu, 2011; Magnanimo and Luding, 2011; Sun and Sundaresan, 2011) that can be further tested, validated and extended with more advanced physical and numerical experiments.

Given the detailed insights from DEM, the (missing) terms and the parameters for the constitutive models can now be further analyzed to perform the rigorous micro-macro transition.

Open questions concern, among others:

(i) the validity of the 2D model in 3D, related to missing terms and parameters,

(ii) the validity of global versus local coarse-graining, i.e. the scale of the micro-macro transition (Kuhn and Bagi, 2009),

(iii) the microscopic (restructuring) and macroscopic (non-affine motions) origin of the peak and softening phenomenology at low volume fractions, possibly related to the (in)homogeneity of the packings,

(iv) the validity of the model predictions for strain-reversal and cyclic deformations, and

(v) the possible dependence of the moduli in the constitutive relations on other quantities (e.g. pressure) than the volume fraction, as focused on in this study.

For future application, the present calibration procedure should be checked also for other materials and applied to different element tests, among which there are (cylindrical) triaxial tests, ring-shear tests and also avalanche flow experiments like in chutes or rotating drums, all of which are more widely available than the “academic” biaxial box. In the end, the material properties and parameters should not depend on the element test chosen and the predictive value of the model(s) should be proven for more than only one validation test, be it another element test or a real-size or lab-scale process such as, e.g. granular flow in a silo or during a landslide.

Acknowledgements

Helpful discussions with F. Göncü, J. Ooi, M. B. Wojtkowski and M. Ramaioli are gratefully acknowledged. This work is financially supported by the European-Union-funded Marie Curie Initial Training Network, FP7 (ITN-238577), see http://www.pardem.eu/ for more information.

References

Alonso-Marroquín, F.; Luding, S.; Herrmann H. J. and Vardoulakis, I. (2005): “Role of anisotropy in the elastoplastic response of a polygonal packing.” Phyical Review E., 71:051304:1-18.

Barreto, D. and O’Sullivan, C. (2012): “The influence of inter-particle friction and the intermediate stress ratio on soil response under generalised stress conditions.” Granular Matter, 14(4):505-521.

Bi, D.; Zhang, J; Chakraborty, B. and Behringer, R. P. (2011): “Jamming by shear.” Nature, 480(7377):355-358.

Cundall, P. A. and Strack, O. D. L. (1979): “A discrete numerical model for granular assemblies.” Géotechnique, 29(1):47-65.

Durán, O.; Kruyt, N. P. and Luding, S. (2010): “Micromechanical analysis of deformation characteristics of three-dimensional granular materials.” International Journal of Solids and Structures, 47(17):2234-2245.

Ezaoui, A. and Di Benedetto, H. (2009): “Experimental measurements of the global anisotropic elastic behaviour of dry Hostun sand during triaxial tests, and effect of sample preparation." Géotechnique, 59(7):621-635.

Fredlund, D. G. (1979): "Second Canadian Geotechnical Colloquium: Appropriate concepts and technology for unsaturated soils." Canadian Geotechnical Journal, 16(1):121-139.

GdR-MiDi. (2004): "On dense granular flows." The European Physical Journal E: Soft Matter and Biological Physics, 14(4):341-365.

Goddard, J. D. (1998): "Continuum Modeling of Granular Assemblies." In Herrmann, H. J.; Hovi, J. P., and Luding, S. editors, Physics of dry granular media - NATO ASI Series E 350, pages 1-24, Dordrecht, Kluwer Academic Publishers.

Goddard, J. D. (2010): "Parametric hypoplasticity as continuum model for granular media: from Stokesium to Mohr-Coulombium and beyond." Granular Matter, 12:145-150.

Göncü, F.; Duran, O. and Luding, S. (2010): "Constitutive relations for the isotropic deformation of frictionless packings of polydisperse spheres." C. R. Mécanique, 338(10-11):570-586.

Hayhurst, D. R. (1972): "Creep rupture under multi-axial states of stress." Journal of the Mechanics and Physics of Solids, 20(6):381-382.

Hertz, H. (1881): "Über die Berührung fester elastischer Körper." Journal für die Reinen und Angewandte Mathematik, 92:156-171.

Imole, O. I.; Kumar, N. and Luding, S. (2011): "Deformation modes of packings of frictionless polydisperse spheres." Particulate Systems Analysis Conference Proceedings, pages 1-6.

Jiang, Y and Liu, M. (2009): "Granular solid hydrodynamics." Granular Matter, 11:139–156.

Kolymbas, D. (1991): "An outline of hypoplasticity." Archive of Applied Mechanics, 61:143-151.

Kruyt, N. P.; Agnolin, I.; Luding, S. and Rothenburg, L. (2010): "Micromechanical study of elastic moduli of loose granular materials." Journal of the Mechanics and Physics of Solids, 58(9):1286-1301.

Kuhn, M. R. and Bagi, K. (2009): "Specimen Size Effect in Discrete Element Simulations of Granular Assemblies." Journal of Engineering Mechanics, 135(6):485-492.

Kumar, N.; Imole, O. I.; Magnanimo, V. and Luding, S. (2012a): "Predictive methods for deformation modes using constitutive modeling for frictionless spheres: Micro-macro transition to an Anisotropy model." In preparation.

Kumar, N.; Imole, O. I.; Magnanimo, V. and Luding, S. (2012b): "Deformation Modes for Assemblies of Frictionless Polydisperse Spheres." Advanced Materials Research, 508:160-165.

Kwade, A.; Schulze, D. and Schwedes, J. (1994): "Determination of the stress ratio in uniaxial compression tests - Part 2." Powder Handling & Processing, 6(2):199-203.

La Ragione, L. and Magnanimo, V. (2012): "Contact anisotropy and coordination number for a granular assembly: A comparison of distinct element method simulations and theory." Phyical Review E., 85:031304:1-8.

Luding, S. (2004): "Micro-Macro Models for Anisotropic Granular Media." In Vermeer, P. A.; Ehlers, W.; Herrmann, H. J. and Ramm, E. editors, Modelling of Cohesive-Frictional Materials, pages 195-206, Leiden, Netherlands, Balkema.

Luding, S. (2005): "Anisotropy in cohesive, frictional granular media." Journal of Physics: Condensed Matter, 17(24):S2623-S2640.

Luding, S. (2008a): "Constitutive relations for the shear band evolution in granular matter under large strain." Particuology, 6(6):501-505.

Luding, S. (2008b): "The effect of friction on wide shear bands." Particulate Science and Technology, 26(1):33-42.

Luding, S. (2008c): "Cohesive, frictional powders: contact models for tension." Granular Matter, 10(4):235-246.

Luding, S. (2009): "Towards dense, realistic granular media in 2D." Nonlinearity, 22(12):R101-R146.

Luding, S. and Alonso-Marroquín, F. (2011): "The critical-state yield stress (termination locus) of adhesive powders from a single numerical experiment." Granular Matter, 13(2):109-119.

Luding, S. and Perdahcioğlu, E. S. (2011): "A Local Constitutive Model with Anisotropy for Various Homogeneous 2D Biaxial Deformation Modes." Chemie Ingenieur Technik, 83(5):672-688.

Magnanimo, V.; La Ragione, L.; Jenkins, J. T.; Wang, P. and Makse, H. A. (2008): Characterizing the shear and bulk moduli of an idealized granular material. Europhysics Letters 81(3): 34006:1-6.

Magnanimo, V. and Luding, S. (2011): "A local constitutive model with anisotropy for ratcheting under 2D axial-symmetric isobaric deformation." Granular Matter, 13(3):225-232.

Magnanimo, V. and Luding, S. (2012): "A 2D non-linear constitutive model with anisotropy for granular materials." Philosophical Magazine, (Under review).

Majmudar, T. S.; Sperl, M.; Luding, S. and Behringer, R. P. (2007): "Jamming Transition in Granular Systems." Phyical Review Letters, 98(5):058001:1-4.

Makse, H. A.; Johnson, D. L. and Schwartz, L. M. (2000): "Packing of compressible granular materials." Phyical Review Letters, 84(18):4160-4163.

Mašín, D. (2012): "Asymptotic behaviour of granular materials." Granular Matter, 14: 759-774

Maxwell, J. C. (1864): "On the calculation of the equilibrium and stiffness of frames." Philosophical Magazine, 27 (182):598-604.

Mindlin, R. D. and Deresiewicz, H. (1953): "Elastic spheres in contact under varying oblique forces." Journal of Applied Mechanics, 75:327-344.

Morgeneyer, M. and Schwedes, J. (2003): "Investigation of powder properties using alternating strain paths." Task Quarterly, 7(4):571-578.

Oda M. (1972): "Initial fabrics and their relations to mechanical properties of granular material." Soil and foundations, 12(1):17-36.

O'Hern, C. S.; Langer, S. A.; Liu, A. J. and Nagel, S. R. (2002): "Random packings of frictionless particles." Phyical Review Letters, 88(7):075507:1-4.

Philippe, P.; Bonnet, F. and Nicot, F. (2011): "Settlement of a granular material: boundary versus volume loading." Granular Matter, 13(5):585-598.

Radjai, F.; Roux, S. and Moreau, J. J. (1999): "Contact forces in a granular packing." Chaos, 9(3):544-550.

Saadatfar, M.; Sheppard, A. P.; Senden, T. J. and Kabla, A. J. (2012): "Mapping forces in a 3D elastic assembly of grains." Journal of the Mechanics and Physics of Solids, 60(1):55-66.

Samimi, A.; Hassanpour, A. and Ghadiri, M. (2005): "Single and bulk compressions of soft granules: Experimental study and DEM evaluation." Chemical Engineering Science, 60(14):3993-4004.

Schwedes, J. (2003): "Review on testers for measuring flow properties of bulk solids." Granular Matter, 5(1):1-43.

Shaebani, M. R.; Madadi, M.; Luding, S. and Wolf, D. E. (2012): "Influence of polydispersity on micromechanics of granular materials." Phyical Review E., 85(1):011301:1-12.

Spencer, A. J. M. (1980): Continuum mechanics. Dover Publishers, USA.

Sun, J. and Sundaresan, S. (2011): "A constitutive model with microstructure evolution for ow of rate independent granular materials." Journal of Fluid Mechanics, 682:590-616.

Thornton, C. (2010): "Quasi-static simulations of compact polydisperse particle systems." Particuology, 8(2):119-126.

Thornton, C. and Anthony, S. J. (1998): "Quasistatic deformation of particulate media." Philosophical Transactions of the Royal Society of London. Series A: Mathematical, Physical and Engineering Sciences, 356(1747): 2763-2782.

Thornton, C. and Zhang, L. (2006): "A numerical examination of shear banding and simple shear non-coaxial flow rules." Philosophical Magazine, 86(21-22):3425-3452.

Thornton, C. and Zhang, L. (2010): "On the evolution of stress and microstructure during general 3D deviatoric straining of granular media." Géotechnique, 60(5):333-341.

van Hecke, M. (2009): "Jamming of soft particles: geometry, mechanics, scaling and isostaticity." Journal of Physics: Condensed Matter, 22(3):033101:1-24.

Walsh, S. D. C. and Tordesillas, A. (2004): "A thermomechanical approach to the development of micropolar constitutive models of granular media." Acta Mechanica, 167(3):145-169.

Yimsiri, S. and Soga, K. (2010): "DEM analysis of soil fabric effects on behaviour of sand." Géotechnique, 60(6): 483-495.

Weinhart, T.; Thornton, A. R.; Luding, S. and Bokhove, O. (2012): "From discrete particles to continuum fields near a boundary." Granular Matter, 14(2):289-294.

Zetzener, H. and Schwedes, J. (1998): "Deformation behaviour and relaxation of bulk solids at different deformation rates." In proceedings of the 6th International Conference on Handling and Transportation, Australia. pages 51-55.

Zhao, X. and Evans, T. M. (2011): "Numerical analysis of critical state behaviors of granular soils under different loading conditions." Granular Matter, 13(6):751-674.

Author's short biography

Olukayode I. Imole

Olukayode I. Imole completed his BEng degree in mechanical engineering at the University of Ado-Ekiti, Nigeria. He received the DAAD scholarship to study for a MSc degree in quality, safety and environment at the Otto-von-Guericke University, Magdeburg, Germany, where he worked with the mechanical process engineering group chaired by Prof. Jürgen Tomas. His master's thesis was titled "Investigation of the kinetics of disintegration processes during titania nanoparticle synthesis" . He is presently on a Marie Curie fellowship for his PhD in the multi-scale mechanics group, Faculty of Engineering Technology (CTW), chaired by Prof. Stefan Luding at the University of Twente, Netherlands. His research interests include experimental work on element tests with focus on cohesive powders, discrete element simulations of frictionless, frictional and cohesive granular assemblies and other industry-relevant research. He collaborates with other researchers in various institutions and industries including TU Braunschweig, Germany, UT Compiegne, France, and Nestle Research, Switzerland.

Author’s short biography

Nishant Kumar

Nishant Kumar is a PhD student in the multi-scale mechanics (MSM) group at the faculty of Engineering Technology, CTW, University of Twente, Netherlands. He finished his B.Tech. degree in Chemical engineering at the Indian Institute of Technology (IIT), Kanpur, in 2008. He received his MS with honors in Mechanical engineering from the University of California, San Diego (UCSD), in 2008. Later, he joined the MSM group in 2010. His research interests include the constitutive modeling of materials with an internal micro-structure such as soils and cohesive powders and his focus is on anisotropy models. He is also working on shear jamming in granular materials.

Vanessa Magnanimo

Vanessa Magnanimo is assistant professor in the multi-scale mechanics (MSM) group at the faculty of Engineering Technology, CTW, University of Twente, Netherlands. She received a MSc degree in construction engineering from the Politecnico of Bari, Italy, with subsequent graduate studies on the elasticity of discrete materials. In 2007 she received her PhD in continuum mechanics from the same university. She was a visiting scientist at the Levich Institute - CCNY (2005) and at T&AM - Cornell University (2008). Her research interests concern theoretical analysis and modern simulation techniques applied to sound propagation and the constitutive modeling of materials with an internal micro-structure such as soils, asphalt, powders and bio-materials.

Stefan Luding

Stefan Luding studied physics at the University of Bayreuth, Germany, focusing on reactions on complex and fractal geometries. He continued his research in Freiburg for his PhD on simulations of dry granular materials in the group of Prof. A. Blumen. He spent his post-doctorate time in Paris IV, Jussieu, with E. Clement and J. Duran before he joined the computational physics group with Prof. Herrmann for his habilitation. In 2001, he moved to DelftChemTech at the TU Delft in Netherlands as associate professor for particle technology. Since 2007 he has held the chair on multi-scale mechanics (MSM) at the Faculty of Engineering Technology, CTW, at the University of Twente, Netherlands, with ongoing research on fluids, solids, particle interactions, granular materials, powders, asphalt, composites, bio- and micro-fluid systems and self-healing materials. Stefan Luding has been managing editor in chief of the journal Granular Matter since 1998. He has written more than 200 publications and is a member of several international working parties, including presidentship of AEMMG that organizes the Powders and Grains Conference in 2009 and 2013.

Mechanical Resistance due to Shearing of Partially Wet Granular Media[†]

Driss Oulahna[*], **Romain Collet and Alain de Ryck**
[1] *Université de Toulouse, Mines Albi, CNRS, Centre RAPSODEE*

Abstract

Mixing granular media with a given amount of liquid is an operation conducted and used intensively for the preparation of concrete. The power and time required to obtain good homogeneity of the granular paste are known to have a complex relationship with the physical properties of the particles, with the liquid and with the mixer design. In this paper some of these issues are addressed by evaluating the shear resistance of a granular paste. Using model spherical materials (glass beads) and ground and sieved minerals (calcite $CaCO_3$*), we investigate experimentally the impact of the particle size, liquid amount and morphology of the particles.*

From quasi-static experiments in shear cells, different regimes of shear resistance are revealed. In dry conditions, van der Waals' forces dominate. In wet conditions, a capillary or consolidation regime where shear resistance is dominated by capillary forces is strongly impacted by the morphology of the particles and by the formation of texture. These regimes are qualitatively observed in a bowl mixer for which the variation of the current intensity correlates with the shear resistance observed in quasi-static experiments.

Keywords: wet granular mixing, shearing, quasi-static system, powder mechanics

1. Introduction

In order to understand why the mixing of a composition requires more or less energy than another composition, we need to classify the different factors (powders and liquid properties, process parameters) and the different forces (capillary, van der Waals, gravitational, frictional and viscous forces) that have an effect on the shear resistance[1-3]. Usually, power or intensity consumption measurements are taken during mixing to evaluate the different wetting states[4-8]. The use of progressive addition, with a controlled flow, makes it possible to differentiate the various wetting regimes. The consumption intensity profile, represented as a function of mixing time or of the amount of liquid added, may be related to different states of liquid saturation (**Fig. 1a**, **1b**): *dry state*, *pendular state* when particles are held together by a liquid bridge at their contact points, *capillary state*, occurring when all the voids are filled with the liquid and the surface liquid is drawn back into the pores under capillary action, and *funicular state* as a transition state between the pendular and capillary state where the voids are not fully saturated with liquid.

In a recent work[9-11], we showed that the behaviour

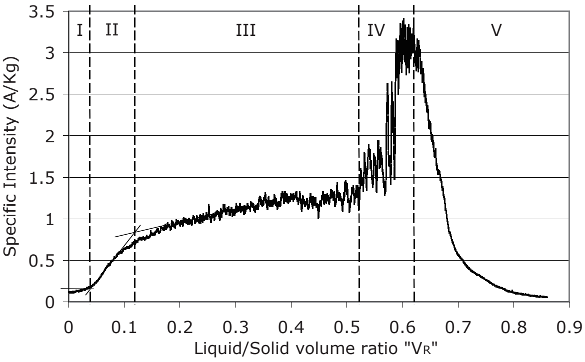

Fig. 1a Intensity consumption of the calcite 1 mixed with a progressive water addition (40 ml/min; 120 rpm) and schematic wetting regime states (*pendular II*, *funicular III*, *capillary IV*)

[†] Accepted: September 7, 2012

[1] Campus Jarlard, 81013 Albi, France
[*] Corresponding author:
E-mail: oulahna@mines-albi.fr
TEL: +33-5-63-49-30-00 FAX: +33-5-63-49-30-25

ⓒ 2013 Hosokawa Powder Technology Foundation

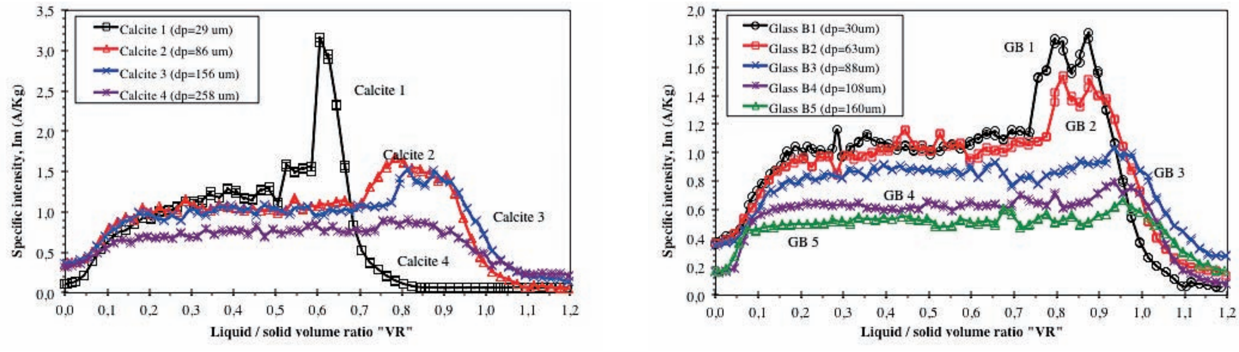

Fig. 1b Intensity consumption of the calcite (left) or glass beads (right) mixed with a progressive water addition (40 ml/min; 120 rpm) in a planetary mixer CAD.

of the granular medium during mixing (planetary mixer) is greatly affected by the granular properties, by the mixer process parameters and by the liquid addition method. We also studied the interparticulate porosity of granular samples removed during mixing, and the effects of particle size. Measurements of calcite granular porosities during mixing (with water) showed that the porosity is not constant from the dry to the capillary state[9-11], the capillary state being denser then the funicular state.

The mixing energy consumption depends on the particle interaction forces, their density and how the shear deformation occurs in the mixer. To distinguish these contributions, an alternative method is to study particulate interactions in a quasi-static shear tester, for which the shear deformation is well controlled.

Generally, quasi-static tests are used with dry powders to study cohesive flow behaviour. The flow data obtained can then be used to design silos and hoppers that provide gravitational flow[12, 18]. We used such a device to obtain information about cohesive (capillary or van der Waals' forces) and frictional forces acting in wet granular media. The low velocity used leads to negligible viscous forces when compared to capillary forces. The second advantage of using a shear cell is that it simplifies definition of the shearing zone, which is reduced to a known surface plane. The simplicity of the shear area allows the shear stress to be calculated.

Section II of this paper presents the shear test, a short description of the Schulze annular shear cell and the materials used. Section III summarises the results obtained for the quasi-static shear cell experiments, taking into account the influence of the consolidated normal load, the amount of liquid, the mean diameter, and the shape of the particles. Finally, the last section presents a comparative evaluation between quasi-static and shear mixing experiments.

Table 1 Solids properties

	d_V10 (μm)	d_V50 (μm)	d_V90 (μm)	$\frac{d_{v90}-d_{v10}}{d_{v50}}$	True density ρ_S (g/cm^3)	Bulk density ρ (g/cm^3)	Porosity ε (%) (dry state)	Contact angle (water) θ	i_V10	Sphericity index i_V50	i_V90
Glass beads 1	18	30	48	1.00	2.48	1.44	42	0	0.45	0.91	0.95
Glass beads 2	45	63	88	0.68	2.51	1.43	43	0	-	-	-
Glass beads 3	64	88	122	0.66	2.51	1.49	41	0	0.47	0.96	0.98
Glass beads 4	78	108	149	0.66	-	-	-	0	-	-	-
Glass beads 5	117	160	219	0.64	2.52	1.49	41	0	0.68	0.96	0.99
Glass beads 6	164	218	295	0.60	-	-	-	0	-	-	-
Glass beads 7	194	261	353	0.61	2.52	1.46	42	0	0.60	0.94	0.99
Glass beads 8	244	332	455	0.64	2.49	1.49	40	0	-	-	-
Calcites 1	3	29	68	2.24	2.73	1.32	51	51	0.35	0.71	0.90
Calcites 2	55	86	142	1.01	0.73	1.31	52	51	0.49	0.77	0.92
Calcites 3	102	156	225	0.79	0.73	1.36	50	51	0.51	0.73	0.89
Calcites 4	181	258	354	0.67	0.73	1.38	49	51	0.45	0.71	0.88

2. Materials, Experimental Set-up and Methods

The materials used (**Table 1**) were spherical glass beads supplied by SOVITEC® and calcites supplied by OMYA®. The volume size distributions were obtained by a MALVERN® Mastersizer 2000. The wetting angles with water θ were obtained from capillary rise experiments, using the methodology of Galet[13]. The average volume roundness index i_V50 (ratio of the smaller and higher diameters of the particle) came from a volumetric roundness distribution obtained with the MALVERN® PharmaVision 830 (PVS) automated optical device (2D). The true density of the solids ρ_S was obtained using a helium pycnometer (Accupyc 1330-MICROMERITIC®), and the dry porosities ε (or the compacity C) by using the values of the true ρ_S and bulk ρ densities:

$$\varepsilon = 1 - \frac{\rho}{\rho_s} = 1 - C \tag{1}$$

The liquid used for all the tests was water.

Every quasi-static shear test was carried out with a dry or wet granular medium previously mixed in a planetary mixer from the CAD® Company (Mlx60)[9-11]. This mixer can be used to make a paste, and it allows the power consumption to be recorded at a frequency of 10 points per second. The available rotation velocity is between 0 and 300 rpm and the volume of the bowl is 4 litres. A preliminary study allowed the process parameters to be set at the following values: an impeller speed of 120 rpm, a droplet-by-droplet liquid flow rate of 40 ml/min, and an initial bulk volume of 1250 cm^3, corresponding to a 32% filling rate of the bowl mixer.

To study the interaction forces that take place during the shearing, we used an annular shear cell allowing a sheared interface of known constant area. The shear velocity was given by the rotational speed (ω = 3.5 10^{-3} rad/s, ranges from 100 to 200 μm/s from the inner (6 cm) to the outer (12 cm) diameter of the cell). These velocities give very low capillary numbers (of the order 10^{-5}), allowing the viscous forces to be neglected in these quasi-static experiments.

An experimental standard method developed by Jenike[14, 18] was used. This method consists of measuring a yield locus, i.e. the tangential stress necessary to shear a granular medium for a given normal stress and a powder sample previously prepared by a consolidation process. It is a two-step measurement. During the first step, the shear under a normal stress σ_c consolidates the granular sample to a critical state where there are no further variations in volume. The resulting consolidated shearing stress τ_c is constant. The sample is then sheared under a normal load σ, which is lower than σ_c. This second step allows the yield shear stress τ_y to be obtained at the peak, and the steady-state shear stress τ_D to be measured when a plateau is reached again in the shear stress versus deformation curve or time. These two stages are repeated several times with a constant consolidated normal stress σ_c and an increasing normal stress[15-16] (see **Fig. 2**).

The curves representing the yield and the steady-state shear stress (τ_S or τ_D) versus the normal stress σ are called the yield[17-19] and the dynamic locus, respectively. In the present study, they are both well fitted by a linear Coulombic law:

$$\tau_x = \mu_x \sigma + c_x \tag{2}$$

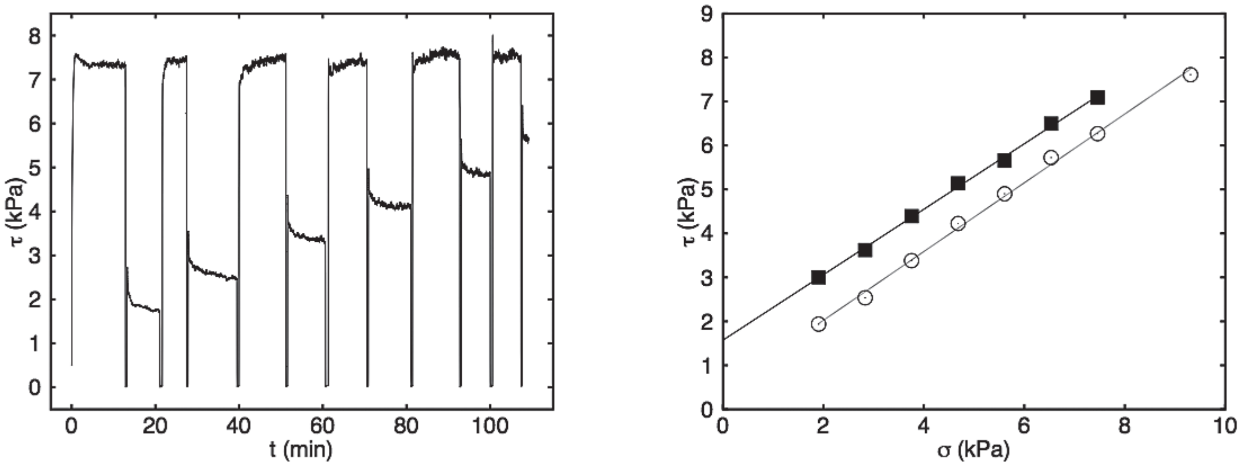

Fig. 2 Shear test (left) and corresponding yield (squares) and dynamic (circles) locii for the 50-125 μm sieved calcite with a liquid to solid ratio of 0.5. The consolidation normal stress here is σ_c = 9.3 kPa.

It was observed experimentally that the dynamic cohesion is close to zero and the dynamic behaviour is only characterised by the dynamic friction coefficient (μ_D) linked to the frictional forces between particles. The cohesion c ($= c_y$), coming from the yield locus built with peak stresses is directly linked to the cohesive forces (capillary and van der Waals' forces).

Since the cohesion appears to increase with the consolidation, this procedure is repeated for at least three normal consolidation stresses. Finally, following the Jenike methodology, rather than using the pair (c, σ_c), we compute the unconfined yield stress f_c and the maximal principal stress σ_I. These quantities are obtained from the yield locus using the Mohr circles representative of the stress state of an unconfined material at failure, and the maximal stress state for this consolidation (the left and right circles in **Fig. 3**, respectively). f_c is the minimal stress necessary to shear an unconfined consolidated material and σ_I the maximal stress that this consolidated material has experienced previously. It is observed that the greater the consolidation, the greater the unconfined yield stress. The one-point Flow Function as defined by Schultze[18] is the ratio (σ_I/f_c). In this paper, we investigate the evolution of the ratio (f_c/σ_I): inverse ratio of the definition of Schulze. Changes in the ratio is an increasing function whose slope is limited. Indeed, the yield stress τ_y remains lower than the shear stress at consolidation ($\tau_C = \mu_D\ \sigma_C$), which gives the yield locus in **Fig. 3** a positive slope. As a consequence, the diameter of the left Mohr circle is, at most, equal to the diameter of the right Mohr circle, giving the following:

$$\frac{f_C}{\sigma_I} \leqslant \frac{2\mu_D}{1+\mu_D} \tag{3}$$

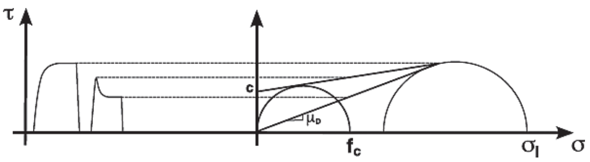

Fig. 3 Yield locus construction from shear experiment data. Mohr circles for the determination of f_c and σ_I.

3. Quasi-Static Results and Discussion

3.1 Consolidation and liquid amount effect

The effects of consolidation and liquid amount on cohesive and frictional interactions were studied with both glass beads and calcites at different particle size distributions (**Table 1**). They were sheared in dry conditions and wet states with a volume-liquid ratio (V_R: ratio of liquid volume by solid volume) up to 0.6. From each yield locus, the cohesion is linearly extrapolated and **Fig. 4**-left gives the results obtained for the calcite sieved between 50 and 125 µm. The cohesion, which has a non-zero value at the dry state due to the van der Waals' forces, increases when adding the liquid to reach a plateau value when the liquid amount attains 10% in volume. This plateau is maintained until 60% in volume.

Three consolidation normal stresses were used (0.25, 0.5 and 1 kPa). It was observed that the cohesion increases proportionally to the consolidation normal stress. As a consequence, for reasons of clarity, the results will be presented using the ratio f_c/σ_I. This ratio is independent of the consolidation, in the range of liquid content between 10 to 60%. The Flow Function (the relationship between the unconfined yield stress f_c and the maximal principal stress σ_I) is therefore fully characterised by their ratio.

To conclude this section, the cohesion for wetted

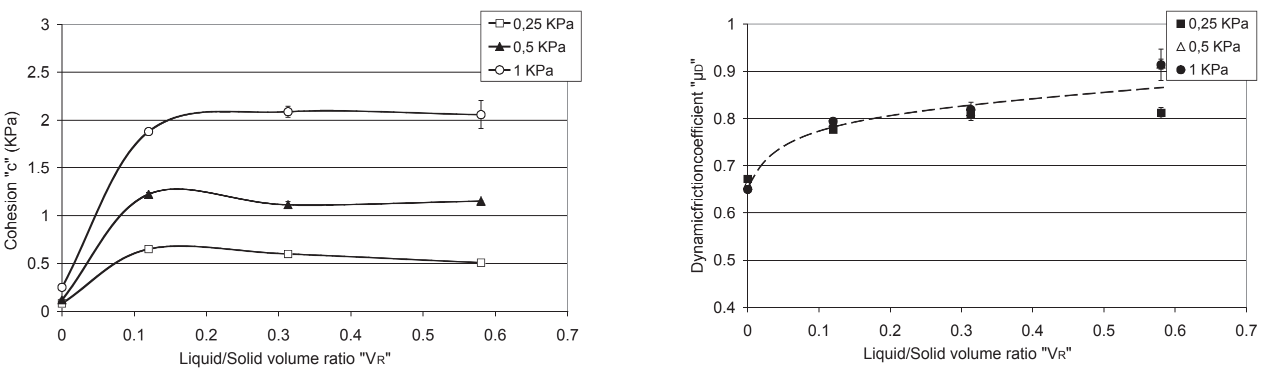

Fig. 4 Cohesion (left) and dynamic friction coefficient (right) of the calcite 50-125 µm as a function of liquid amount, for 3 consolidation normal stresses (0.25, 0.5 and 1 kPa).

granular media is linked both to the liquid and to the compacity (caused by the consolidation procedure in a shearing test). Strengthening by the addition of liquid is considerable from the dry state to a liquid/solid volume ratio equal to 0.1. For higher liquid amounts, the cohesion remains constant, and the strength is only dependent on the consolidation. These results are in accordance with the fact that the capillary force does not vary very much with the volume of the liquid bridge[20, 21]. As a consequence, in the following section, we shall restrict discussion to only two cases: the dry state and the funicular state. The latter is chosen at a mean value for a liquid ratio between 30 to 40%, for which the quasi-static results and energy consumption for mixing presented in section IV are mainly independent of the liquid ratio. Finally, the presence of liquid also modifies the dynamic friction behaviour of the granular medium.

3. 2 Particle size effect

For both glass beads and calcites, the evolutions of the dynamic coefficient of friction μ_D and the ratio (f_c/σ_I) were studied while varying the mean size of the quasi-monodisperse granular materials.

Glass beads and calcites with different sizes (between 30 and 330 μm) were used to perform shear experiments in the dry and funicular wet state. The ratio (f_c/σ_I) and dynamic friction coefficient data from yield and dynamic loci are displayed as a function of the inverse of particle diameter in **Fig. 5**.

For the unconfined yield stress normalised by the principal maximal consolidation stress, **Fig. 5**-left displays the behaviour at dry and funicular conditions.

Dry case, calcites and glass beads: The evolution of (f_c/σ_I) for the dry case is close to being inversely proportional to the particle size, as may be inferred by the Rumpf relation[22]. Rumpf writes the tensional resistance T of a cohesive granular material as:

$$T = \frac{2}{\pi}\frac{f}{d^2}(1-\varepsilon)\kappa\,, \tag{4}$$

where f is the interparticulate force, d the particle diameter, ε the porosity and κ the coordination number. For dry particles, the interparticulate forces are van der Waals' forces, which for spheres are given by:

$$f_{vdW} \approx \frac{A\,d}{h^2}\,, \tag{5}$$

where A is the Hamaker constant and h the interdistance between particles. They are proportional to the particle size and therefore the tensional or shear resistance of the dry powder is expected and observed in **Fig. 5**-left to be proportional to the inverse of the particle size (Eq. 5 in Eq. 4).

It is possible to obtain the constant of proportionality between the Flow Function and the particle size for the calcites and the glass beads by measuring the slopes s_1 and s_2 in **Fig. 5**-left. Their difference when changing the material is due to several factors: the Hamaker constant A is different, the roughness and sphericity of both materials are different and finally, the texture of the particle assembly, i.e. the porosity and coordination number may be different. For ε and κ, which are geometric numbers, we expect equivalent values for both materials since they are close to monodispersity.

We find that the ratio of the slopes of the linear fits of (f_c/σ_I) versus (d^{-1}) in the dry conditions for the

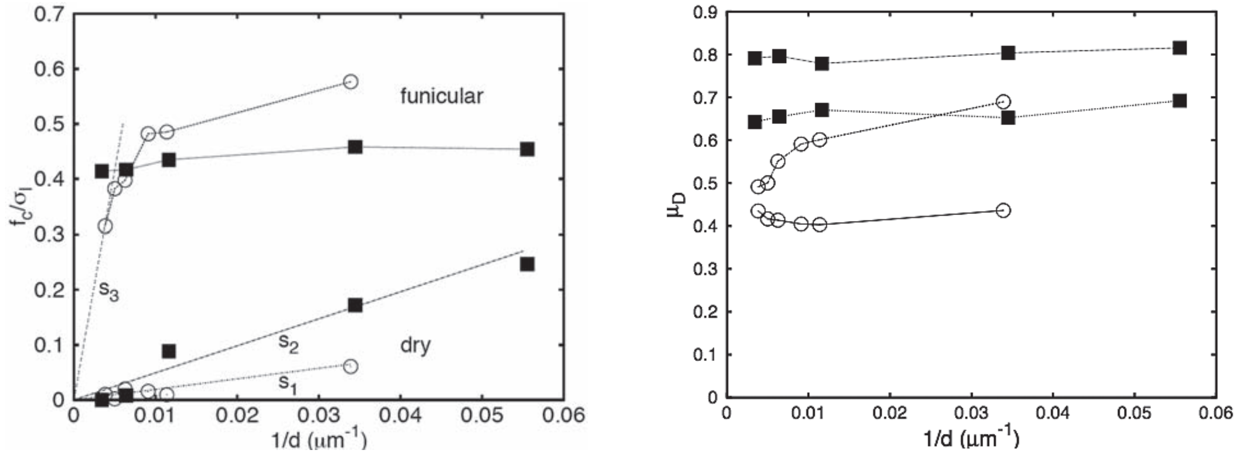

Fig. 5 Inverse of the one-point Flow Function of calcites and glass beads (left) or coefficient of dynamic friction (right) as a function of the inverse of the mean diameter for dry and funicular states. Squares: calcites, circles: glass beads.

calcite and glass beads gives a factor of 2.4, which is similar to the ratio of the Hamaker constants of the two materials ($A_{glass} = 6.5\ 10^{-20}$ J, $A_{calcite} = 10.1\ 10^{-20}$ J). This result is quite satisfying and indicates that the particle roughness and the morphology of the calcite, compared to the glass beads, have a low impact on the magnitude of the van der Waals' forces.

Wet case, glass beads: In the funicular state, the dominant interparticulate force is the capillary force, which can be written as:

$$f_{capillary} \approx \gamma d\,, \tag{6}$$

in the case of wetted spheres (**Fig. 6**-left) where γ is the surface tension of the liquid employed. Here again, the interparticulate force is proportional to the particle size, and we therefore expected shear resistance to increase proportionally with d^{-1}, with a constant of proportionality greater than in the dry case. However, this is not what was observed. Although we noticed an increase in the shear resistance when decreasing the size (**Fig. 5**-left, upper data points), the proportionality with d^{-1} was only perceptible for the glass beads at particle sizes greater than 100 μm. The linear fit between (f_c/σ_I) and (d^{-1}) in this range gives a slope s3 (**Fig. 5**-left) 500 times greater than the slope in the dry case (slope s1 in **Fig. 5**-left). The ratio of capillary and van der Waals' forces is then of the order $(f_{capillary}/f_{VdW}) \sim \frac{\gamma h^2}{A} \sim 500$, leading to a van der Waals' interdistance (roughness) $h_{glass\text{-}beads} \approx 20$ nm, a reasonable value giving some confidence in the interpretation of the quasi-static shear resistance for glass beads of a size greater than 100 μm.

For the smaller sizes of glass beads, the shear strength becomes lower than that extrapolated from the behaviour of (d^{-1}). This is due to the fact that the ratio f_c/σ_I is bound to a value around 0.8 for the glass beads (Eq. 3). We then observe the transition between a capillary regime for large particles (larger than 100 μm) where the shear resistance decreases as the inverse of the particle size when increasing the size, and a consolidation regime for the small sizes (smaller than 100 μm) where the shear resistance cannot increase proportionally with the inverse of the particle size, but is limited by the consolidation.

In this small size regime, the Rumpf relation (Eq. 4) suggests that a formation of texture takes place and that the porosity and/or coordination number decreases when the particle size decreases. This observation is corroborated by the observation of the dynamic coefficient of friction (**Fig. 5**-right).

Fig. 6 Liquid bridge of wetted spheres and (left) radius r of curvature of the meniscii for particle with some flatness (right).

For glass beads at high particle sizes, the difference in behaviour for the funicular and dry states tends towards zero, which is expected if the capillary interparticle forces become negligible compared to the particle weight, together with a similar texturation of the powder bed.

Wet case, calcites: For the wet calcites, in the range of sizes used (30 to 250 μm), the shear strength is quasi-constant ($f_c/\sigma_I \approx 0.42 \pm 0.2$). In particular, we do not observe the regime at high particle size approaching the dry case, as for the glass beads. This difference of behaviour between the glass beads and the calcites is interpreted as follows: the tensional or shear resistance is scaled by $f_{capillary}/d^2$, where the capillary force scales like the product of the Laplace pressure multiplied by the area of the meniscii. For wetted particles, the area of the meniscii scales like d^2 and therefore we have:

$$f_{capillary} \approx \frac{\gamma}{r} d^2\,, \tag{7}$$

where r is the radius of curvature of the meniscii. If the particles are smooth spheres like the glass beads, $r \sim d$ and $T \sim \gamma / d$. If the particles are rough with some flatness, r is close to the roughness, and then $T \sim \gamma / r$ is independent of the particle size (see **Fig. 6**-right). The independency of the strength and the particle size for the calcites suggests that this morphology effect takes place. For grains of irregular shapes with flattened surface areas, the curvature of the meniscii is then controlled by the local roughness of these areas, leading to a constant shear resistance. Nevertheless, this argument supposes that the local roughness is independent of the particle size for the range of particle sizes studied here. This point merits further investigation.

This size independency is also observed in dynamic conditions for the corresponding μ_D in dry and funicular conditions (**Fig. 5**-right). In particular, there is no convergence of the wet dynamic coefficient of friction towards the dry one when the particle size is increased, indicating that the capillary forces remain greater than the weight of the particles for all the sizes of calcites used.

Conclusion on the particle size effect in quasi-static experiments: The use of a shear cell allowed us to measure quantitatively the Flow Function of spherical and non-spherical particles in dry and wet conditions. From the results obtained, we extracted different shear resistance mechanisms. When the particles are dry, the shear resistance is induced by van der Waals' interparticle forces (Eq. 4), which leads to a shear resistance inversely proportional to the mean size of the particles. This shear resistance remains weak enough to remain below the saturation due to consolidation, and we observe only this van der Waals-dominated regime for all the range of particle sizes for both calcites and glass beads.

When they are wetted by 10 to 60% v/v by water, the shear resistance is induced by the capillary forces, which are of higher magnitude than the van der Waals' forces. Depending on the morphology of the particles, this capillary force is given by Eqs. (5) or (6), leading to a shear resistance inversely proportional to the mean particle size for the glass beads and a constant shear resistance for the non-spherical calcites. This capillary regime may be dominated by a consolidation regime where the shear resistance is limited by the consolidation (Eq. 3).

These quantitative measurements allow us to discriminate between different regimes of shear resistance. We shall now investigate whether these different regimes can be qualitatively observed in a planetary mixer, for which neither the surface of the sheared area nor the stresses acting upon it can be obtained, and only the torque on the impeller is measurable.

4. Comparison Between Quasi-Static and Shear-Mixing Experiments

In order to compare the quasi-static shear experiments with the shear-mixing experiments, we recorded the current intensity required to mix at constant velocity in dry and funicular conditions obtained by reading the actual current intensity minus the current intensity when the bowl is empty. The rotational velocity of the impeller was also recorded in order to check that it remained constant and thus provided a proportionality between this current intensity and the torque on the impeller or the power consumed. For these experiments, the mass was adjusted to obtain the same bulk volume in the mixer (leading to $M_{glass} = 1830 \pm 30$ g and $M_{calcite} = 1650 \pm 150$ g). We should then expect that the surface sheared remained approximately the same for all the experiments. **Fig. 7** reports the ratio $I_m = I/M$ obtained for the calcites and glass beads.

This mixing intensity was expected to be proportional to a mean force acting on the bowl, which may be heuristically written as:

$$I \propto S\left(c + \mu_D \sigma\right), \tag{8}$$

where S is the mean sheared surface in the mixer, which is not properly defined, as in the quasi-static experiments of section III.c, and σ the mean cohesion and normal stress exerted by the powder on this shear plane. The normal stress was again not measured, but for a half-filled bowl, we expected that the main contribution would be the weight of the particles themselves. σ is then expected to be proportional to the mass M, introduced as: ($\sigma = \beta M$), where β is a geometrical proportionality constant. The powder in the mixer to be consolidated by this normal stress, and therefore the cohesion, writes

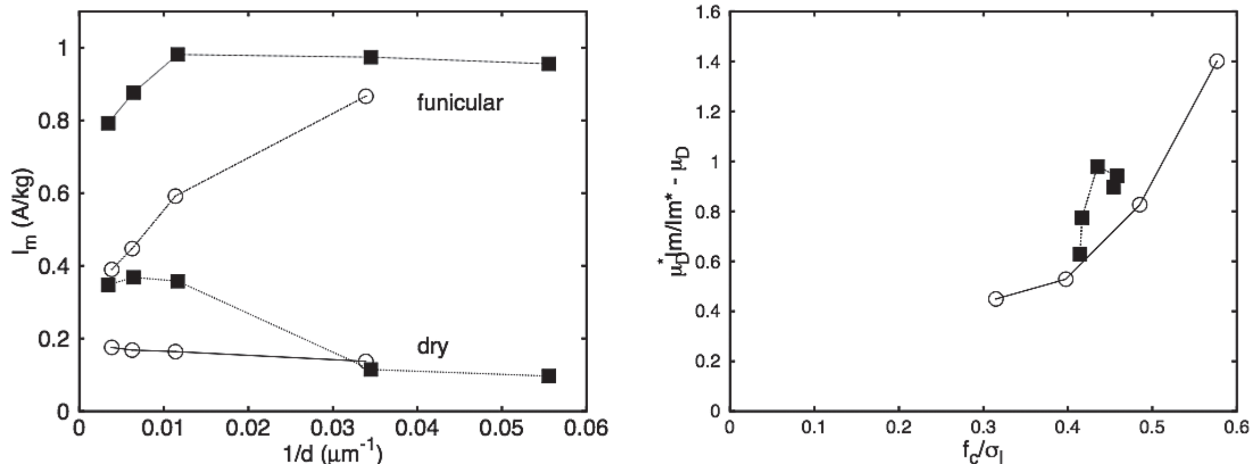

Fig. 7 Left: specific intensity at dry or funicular state versus the inverse of the mean diameter. Right: scaled specific intensity at funicular state (Eq. 6) versus the inverse of the one-point Flow Function. Squares: calcites, circles: glass beads.

as: $c = \lambda (f_c/\sigma_I)\, \sigma$, where λ is a coefficient of order unity. We then have:

$$I_m = S\beta(\lambda \frac{f_c}{\sigma_I} + \mu_D) \tag{9}$$

In the latter expression, $(S\beta)$ is unknown. In order to eliminate this unknown parameter, we can only compare two experiments with the same geometry. In dry conditions and for particle sizes greater than 100 μm, the mechanical behaviour of the powders used are those of a non-cohesive powder. As a consequence, we have:

$$I_m^* = S\beta\mu_D^*, \tag{10}$$

where the asterisk indicates the dry non-cohesive conditions. From Eqs. (9) and (10), we can now relate the measured intensities and quasi-static characterizations of the powders with the following expression:

$$\mu_D^* \frac{I_m}{I_m^*} - \mu_D \propto \frac{f_c}{\sigma_I}, \tag{11}$$

where the coefficients of order unity are taken to unity. This relation was checked by plotting the left member of Eq. (11) versus the right member in **Fig. 7**-right.

We observe in this figure that the calcites present a weak variation in both coordinates: in quasi-static and dynamic experiments, the mechanical resistance is mainly constant. The data points representing the calcite collapse, along with those obtained for the glass beads. For the glass beads, the variations for both coordinates are in correct linear correlation. These correlations remain qualitative and although it would be of interest to add more experimental data for different materials and equipments, they nevertheless give some credence to the assertion that the shear resistance in the mixer at funicular state may be described by the quasi-static resistance of a powder consolidated and submitted to its own weight.

The correlations indicate that the variation of the shear resistance with the mean size of the particles is similar in both quasi-static shear cell and mixer for dry and funicular conditions as directly observed in **Fig. 8**, where the results of **Fig. 7** are plotted versus d^{-1} for direct comparison with **Fig. 5**-left (two upper curves).

Finally, for the glass beads of 100 μm mean diameter, we checked that the viscous forces remain negligible in the mixer under the operating conditions or the rotational velocity used. To do this we performed a series of experiments with water-glycerol mixtures of different viscosities. The results obtained are displayed in **Fig. 9**, which shows the intensity versus the viscosity, both scaled with the values obtained for pure water. It is particularly noticeable that the experiments with water are on a plateau: I does not depend on the viscosity, indicating that the viscous forces are negligible compared to friction and capillary forces in our experiments with water.

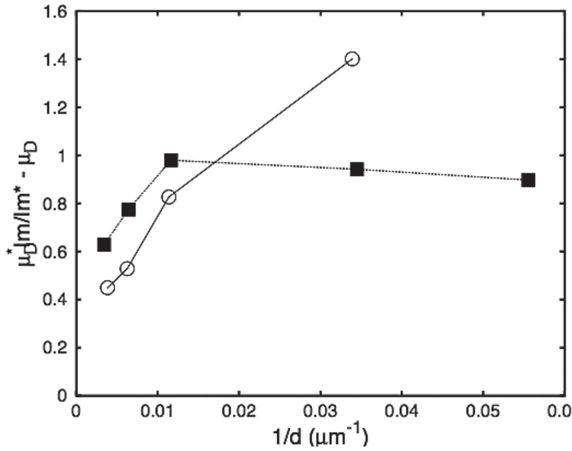

Fig. 8 Results of **Fig. 7**-right versus the inverse of the mean diameter. Squares: calcites, circles: glass beads.

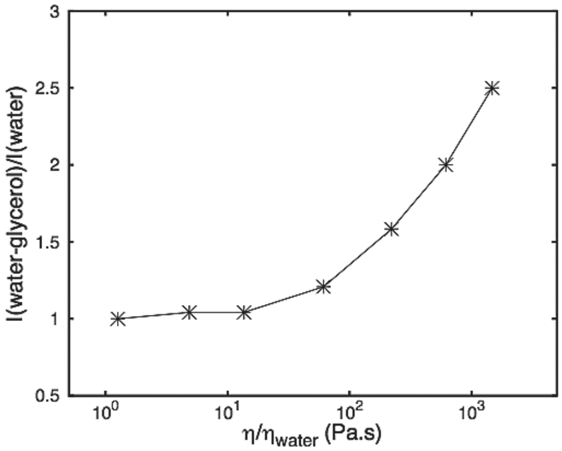

Fig. 9 Intensity consumption at funicular state for water-glycerol, scaled by the intensity using water, versus the corresponding scaled viscosity for 100 μm glass beads.

5. Concluding Remarks

A quasi-static system was used to obtain the cohesion (due to capillary or van der Waals' forces) and frictional forces acting in sheared granular media. They present a rich phenomenology, depending on the dominant forces in action and on the texturation taken by the paste.

This quasi-static behaviour is shown to explain qualitatively the behaviour of the same granular media sheared in a planetary mixer at the funicular state. The agreement between the two types of experiments suggests that the consolidation process in the bowl mixer is identical for all the samples explored and close to a consolidation due to the weight of the particles themselves.

This correlation between quasi-static experiments and planetary mixer experiments indicates that the strengthening of the granular material is similar in the funicular state in both cases. The shear resistance regimes investigated quantitatively in the quasi-static shear cell (van der Waals, capillary particle morphology and texturation regimes) all apply.

Acknowledgements

It is a pleasure to thank M. Martin and P.-H. Jézéquel from Société Lafarge for their support and contribution to this research field, and the referee for the remarks that led to improvements in the article.

List of symbols

A	Hamaker constant
C	Compacity (%)
c	Cohesion (Pa)
$d=dv_{50}$	Mean particle diameter (μm)=dp
f_C	Unconfined yield stress (Pa), (another common designation is σ_C)
$f_{capillary}$	Capillary force
f_{vdW}	van der Waals force
h	Interdistance between solid paticles
iv_{50}	Mean volume roundness index (-), sphericity index
I	Intensity (A)
Im	Specific intensity (A/Kg), = I/M_S
k	Coordination number
m_s	Solid mass (g)
M_s	Solid mass (kg)
r	Radius of curvature of meniscii.
S	Mean sheared surface
T	Tensional resistance of a cohesive granular materials
t	Time (s)
(σ_I/f_c)	One-point Flow Function (-)
V_P	Porous volume (cm^3)
Vs	Volume of dry solid (cm^3)
V_L	Volume of liquid (cm^3)
V_R	Ratio of liquid volume by solid volume (-)
V_T	Total volume (cm^3) = ($V_P + V_S$)

Greek symbols

ε	Interparticulate porosity of dry granular medium
$\gamma = \gamma_L$	Liquid surface tension ($mN.m^{-1}$)
θ	Liquid-solid contact angle (°), by capillary rise experiments
ρ_S	Solid true density ($g.cm^{-3}$)
ρ	Solid bulk density ($g.cm^{-3}$)
ω	Angular shear velocity ($rad.s^{-1}$)
σ	Normal stress (Pa)
σ_C	Consolidation normal stress (Pa)
τ_S	Yield shear stress (Pa)
τ_D	Steady-state shear stress (Pa)
τ_C	Consolidation shear stress (Pa)
μ_D	Dynamic friction coefficient (-)
σ_I	Major principal stress (Pa),
η_{water}	Water viscosity (Pa.s)
$\eta_{W\text{-}G}$	Water-glycerol viscosity (Pa.s)
β	Coefficient: geometrical proportionality constant (Eq.9)
λ	Coefficient of order unity (Eq.9)

References

1) Feng, J. Q., Hays, D. A. (2003): Relative importance of electrostatic forces on powder particles, Powder Technology, Vol.135, pp.65-75.
2) Iveson, S. M., Beathe, J. A. and Page, N.W. (2002): The dynamic strength of partially saturated powder compacts: The effect of liquid properties, Powder Technology, Vol.127, pp.149-161
3) Seville, J. P. K., Willett, C. D. and Knight, P. C. (2000): Inter-particle forces in fluidisation: A review, Powder Technology, Vol.113, pp.261-268.
4) Betz, G., Bürgin, P. J. and Leuenberger, H.,(2003): Power consumption profile analysis and tensile strength measurements during moist agglomeration, International Journal of Pharmaceutics, Vol.252, pp.11-25.
5) Betz, G., Bürgin, P. J., and Leuenberger, H. (2004): Power consumption measurement and temperature recording during granulation, International Journal of Pharmaceutics, Vol.272, pp.137-149.
6) Cazacliu, B., and Legrand J, (2008): Characterization of the granular-to-fluid state process during mixing by power evolution in a planetary concrete mixer, Chemical Engineering Science, Vol.63, pp.4617-4630.
7) Goldszal, A., and Bousquet, J. (2001): Wet agglomeration of powders: From physics toward process optimization, Powder Technology, Vol.117, pp.221-231.
8) Newitt, D. M., Conway-Jones, J. M. (1958): A contribution to the theory and practice of granulation, Transac-

tions of the Institution of chemical Engineers, Vol.36, pp.422-442.
9) Collet, R., Oulahna, D., De Ryck, A., Jézéquel, P. H. and Martin, M. (2010): Mixing of a wet granular medium: Effect of the Particle size, the liquid and the granular compacity on the intensity consumption, Chemical Engineering Journal, Vol.164, pp.299-304.
10) Collet, R., Oulahna, D., De Ryck, A., Jezequel, P. H. and Martin, M. (2011): Mixing of a wet granular medium: Influence of the liquid addition method, Powder Technology, Vol.208, pp.367-371.
11) Collet, R. (2010): "Critères de malaxabilité des mélanges granulaires humides", Ph.D. Thesis, Université de Toulouse, France.
12) Rhodes, M. (1990): "Principles of powder technology", John Wiley & Sons.
13) Galet, L., Patry, S. and Dodds, J. (2010): Determination of the wetability of powders by the Washburn capillary rise method with bed preparation by a centrifugal packing technique, Journal of Colloid and Interface Science, Vol.346, pp.470-475.
14) The institution of chemical engineers (1989), Standard shear testing techniquefor particulate solids using the shear cell, IchemE.
15) Carson, J. W., Wilms, H. (2006): Development of an international standard for shear testing, Powder Technology, Vol.167, pp.1-9.
16) Schwedes, J. (1996): Measurement of flow properties of bulk solids, Powder Technology, Vol.88, pp.285-290.
17) Johanson, K., Rabinovich, Y., Moudgil, B., Breece, K.and Taylor, H. (2003): Relationship between particle scale capillary forces and bulk unconfined yield strength, Powder Technology, Vol.138, pp.13-17.
18) Schulze, D. (2008): "Behaviour, characterization, storage and flow", Powders and bulk solids, Springer.
19) Bocquet, L., Charlaix, E. and Restagno, F. (2002): Physics of humid granular media, Comptes Rendus Physique, Vol.3, pp.207-215.
20) Pierrat, P. and Caram, H. S. (1997): Tensile strength of wet granular materials, Powder Technology, Vol.91, pp.83-93.
21) Pietsch, W. (1991): "Size enlargement by agglomeration", John Willey & Sons, New Jersey.
22) Rumpf, H. (1962): "The strength of granules and agglomerates", In William A. Knepper, editor, Agglomeration, Interscience publishers, New York.

Author's short biography

Driss Oulahna

Driss Oulahna received his chemical engineering degree in 1988 and his PhD in chemical and process engineering in 1992 from École des Mines de Saint-Etienne, France. After a post-doctoral position, he joined the Process Engineering Laboratory of Rapsodee Center-CNRS 5302, École des Mines d'Albi (France) as assistant professor in 1996. His research is in the field of powder technology (agglomeration, granulation, compaction) and particle characterisation methods such as solids-liquids interactions and their role in chemical engineering processes.

Romain Collet

Romain Collet obtained a master's degree in "Applied physico-chemistry of Materials" in 2006 from Montpellier II university. After a PhD at École des Mines d'Albi where he studied "Criteria of blending wet granular mixtures", he joined Parex-Group (R&D center, Saint Quentin Fallavier, France). He is currently an R&D engineer and works on the formulation of ready-to-use mortars for floors (tile adhesive, grout and floor covering).

Alain De Ryck

Alain de Ryck is a graduate of the École polytechnique (1990), has a MSc in solid physics (Université Paris-Sud) and a PhD in physics (UPMC, Paris 1994). After a post-doctoral position in fluid mechanics at the Instituto Pluridisciplinar-Universidad Complutense, Madrid, he joined the Rapsodee Center-CNRS 5302, Ecole des Mines d'Albi in 1996. Professor and former director, he currently works on granular friction and flows of cohesive bulk materials, gas-solid interactions.

Characterization of Nanocrystalline ZnO Flakes Synthesized by a Simple Reaction Process[†]

Amor Sayari

[1] *Department of Physics, Faculty of Science, King Abdulaziz University (North Jeddah Branch)*

[2] *Equipe de Spectroscopie Raman, Département de Physique, Faculté des Sciences de Tunis, Campus Universitaire*

Abstract

In this research, nanocrystalline ZnO flakes were synthesized via a simple reaction process by using zinc acetate dihydrate, diethyl amine and sodium hydroxide. It is confirmed by scanning electron microscopy analysis that nanocrystalline ZnO flakes are flat, irregular in shape, have a high thickness and their average dimension is about 300 nm. The X-ray diffraction (XRD) and FT-IR results indicated that the synthesized ZnO product has the pure wurtzite structure with lattice parameters a and c of 3.253 and 5.210 Å, respectively. The average crystallite size of the ZnO nanostructures deduced from the Scherrer formula is ~31 nm. Raman scattering exhibits a sharp and strong E_2^H *mode at 438* cm^{-1} *which further confirms the good crystallinity and wurtzite hexagonal phase of the prepared ZnO nanostructures. The synthesized powder exhibited the UV absorption at around 370 nm with the estimated direct band gap energy of 3.278 eV. The particle size was also deduced by using the Brus equation and the estimated band gap energy of the ZnO nanopowder sample. The obtained value is in agreement with the calculated one from the Scherrer formula. The strain in the ZnO nanoparticles was also calculated.*

Keywords: ZnO, nanoflake, chemical synthesis, X-ray diffraction, Raman scattering, optical properties

1. Introduction

Recently, nanostructured ZnO materials have attracted a great deal of attention due to their potential applications in ultraviolet (UV) lasers, solar cells, sensors and photocatalysts, etc.[1-4]. Nano-scale ZnO structures with a high surface area have been produced to enhance the physicochemical and electrochemical properties of the above applications. In fact, when the size of a nanostructure approaches the Bohr radius of excitation, optical, electronic and structural properties are greatly affected by the quantum confinement effect. Therefore, nanosized materials are very different from their bulks[5-7]. As a consequence, semiconductor nanoparticles are viewed as promising candidates for many important future technological applications.

The properties of ZnO nanostructures depend greatly on their size, orientation, morphology, respect ratio, and density of crystal[8-10]. The size and morphology control of ZnO nanoparticles is necessary to study their size-dependent properties and explore their applications in the diverse areas of nanotechnology. ZnO is readily produced in a large variety of one-dimensional and two-dimensional forms such as nanorods, nanoneedles, nanosheets, and nanoflakes[11-14]. ZnO nanoflake structures possess lots of interesting unique properties such as porous structures and large surface areas. It is reported that sensors based on ZnO nanoflake structures have an improved performance and a higher sensitivity compared to ZnO nanorods/nanowires[15]. To synthesize uniform nanosized ZnO particles and control their sizes and morphology, a variety of techniques have

---

[†] Accepted: September 14, 2012

[1] Jeddah, P.O. Box 80203, Jeddah 21589, Kingdom of Saudi Arabia

[2] El-manar, 2092 Tunis, Tunisia
E-mail: amor.sayari@laposte.net
TEL: +966-2-6952287 FAX: +966-2-6952278

ⓒ 2013 Hosokawa Powder Technology Foundation

been used such as thermal oxidation of metallic zinc, hydrothermal methods, plasma chemical synthesis, laser ablation and vapor condensation[16-18]. Among these various fabrication techniques, the wet chemical route promises to be simpler, less energy intensive, less expensive – which is more profitable for large-scale production[19].

In this research, we investigated nanocrystalline ZnO flakes prepared by a simple solution process using zinc acetate and diethylamine under refluxing at 85℃ for 4 h. The structural, morphological, vibrational and optical properties of the as-synthesized ZnO nanoparticles are characterized by various techniques.

2. Experimental Details

Nanocrystalline ZnO flakes were synthesized at low temperature by a simple solution process. The starting materials for the synthesis of ZnO flakes were zinc acetate dihydrate, diethyl amine and sodium hydroxide. All the reagents were purchased from Sigma-Aldrich and were used as received without further purification.

For the synthesis of nanocrystalline ZnO flakes in a typical reaction process, 0.1 M zinc acetate dihydrate, made in 50 ml of deionized water was mixed with an aqueous solution of 0.1 M diethyl amine (50 ml) under vigorous stirring at room temperature. To maintain the pH = 13 of the reaction mixture, several drops of NaOH was added under continuous stirring. The obtained solution was then refluxed at 85℃ for 3 h. During refluxing, the solution temperature was controlled by manually inserting an adjustable thermocouple in the refluxing pot. After refluxing, white-colored precipitate was obtained which was washed with methanol and acetone several times and dried at room temperature. The synthesized ZnO flakes were characterized in terms of their structural, morphological and optical properties. The characterization techniques used in this work are field emission scanning electron microscopy (FE-SEM) equipped with energy dispersive spectroscopy (EDS), X-ray diffraction (XRD), FT-IR, UV-Visible and Raman scattering. The Raman spectrum was performed at room temperature with a Labram system equipped with a microscope in back-scattering configuration. The excitation line was at 514.5 nm from an Ar$^+$ laser.

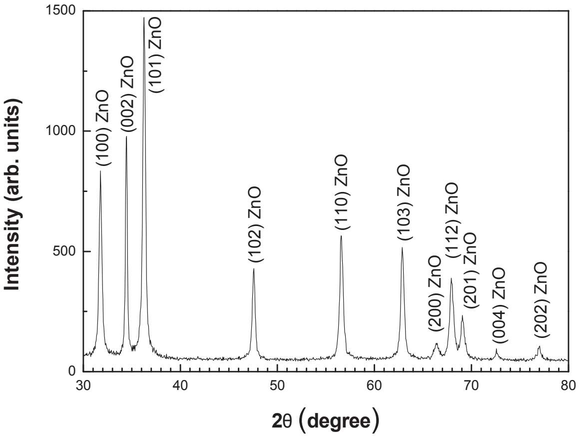

Fig. 1 XRD data of the nanocrystalline ZnO flakes synthesized via a solution process using zinc acetate and diethylamine under refluxing at 85℃ for 4 h.

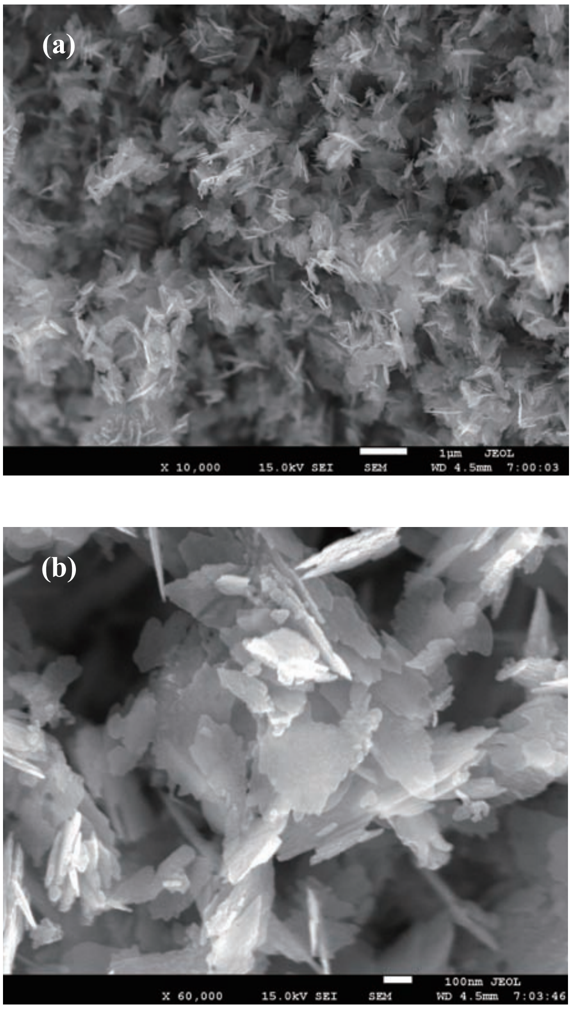

Fig. 2 FE-SEM images showing the morphology of the nanosized ZnO powdered sample. (a) low resolution and (b) high resolution.

3. Results and Discussions

3.1 Structure and morphology of ZnO nanoparticles

The XRD patterns of the ZnO nanocrystals measured with Cu-Kα radiations (λ = 1.54178 Å) in the range of 20 - 80° with 6°/min scanning speed are shown in **Fig. 1**. The XRD spectrum indicates that these nanosized ZnO particles are highly crystallized in structure and the entire diffraction peaks match well with Bragg reflections of the standard wurtzite-type ZnO structure[20, 21]. Diffraction peaks related to the impurities were not observed in the XRD spectrum, confirming the high purity of the synthesized nanocrystals with cell constants of a = 3.253 Å and c = 5.210 Å. Furthermore, it could be seen that the diffraction peaks shown in **Fig. 1** were more intensive and narrower, implying a good crystalline nature of the synthesized ZnO product. The average crystallite size of the ZnO nanoparticles (d) calculated from the widths of the major diffraction peaks observed in **Fig. 1** through the Scherrer formula are given in **Table 1** [22]. The average crystallite size is ~31 nm and is consistent with the value of nanosized ZnO particles reported in literature[23]. **Fig. 2** shows FE-SEM images of the ZnO nanopowder sample synthesized by a simple solution process. The ZnO nanoparticles look like flakes in shape and are synthesized in a very large quantity as confirmed by the low resolution image (**Fig. 2(a)**). The nanocrystalline ZnO flakes are flat and irregular in shape (**Fig. 2(b)**). They have a high thickness (~30 ± 10 nm) and an average dimension of 300 ± 100 nm.

3.2 Raman scattering

The room-temperature Raman spectrum of nanocrystalline ZnO flakes synthesized by a simple solution process is reported in **Fig. 3**. At the region of low frequency, the peaks at ~332, 384 and 409 cm^{-1} are attributed to 2E$_2$(M), transverse optical (TO) A$_1$ and E$_1$ modes[24], respectively. The phonons in a nanocrystal are confined in space and all the phonons over the entire Brillouin zone will contribute to the first-order Raman spectrum. The intense peak at ~438 cm^{-1} is the E$_2$(high) (E$_2^H$) mode, characteristic of the ZnO crystallinity[25]. Observation of these modes indicates that the ZnO product has the wurtzite structure as confirmed by XRD analysis. The Raman mode at around 583 cm^{-1}, which falls just between the A$_1$(LO) (574 cm^{-1}) and E$_1$(LO) (590 cm^{-1}) modes[26] of a single crystal of ZnO, may be interpreted as an LO quasi-mode with mixed A$_1$ and E$_1$ symmetry due to relaxation of symmetry properties in nanoparticles. Recent reports related the appearance of this mode to lattice defects, being either oxygen vacancies or zinc interstitials or their combination[27, 28]. The weak peak at ~539 cm^{-1} can be attributed to 2B$_1$(low) second-order mode[26]. At high frequency, the broad and relatively intense peak at 1153 cm^{-1}, which is found between the doubled frequencies measured for the A$_1$(LO) and E$_1$(LO) modes, contains contributions of 2A$_1$(LO) and 2E$_1$(LO) modes at the Γ point of the Brillouin zone[26].

Table 1 The estimated average crystallite size from XRD data along the major reflection planes

(101)		(002)		(100)		Average crystallite size
FWHM (degree)	crystallite size d(nm)	FWHM (degree)	crystallite size d(nm)	FWHM (degree)	crystallite size d(nm)	d_{av}(nm)
0.302	27.40	0.206	39.80	0.318	25.64	30.94

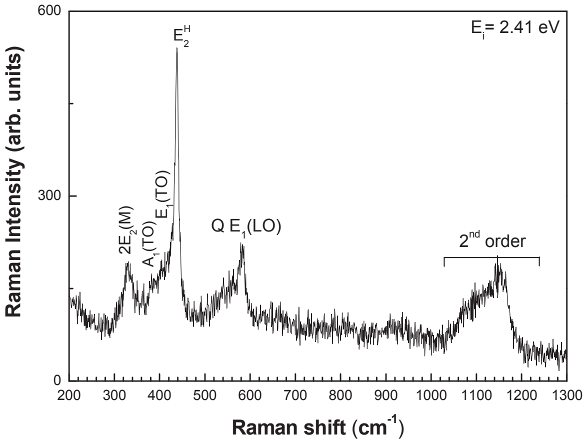

Fig. 3 Room-temperature Raman backscattering spectrum of the nanocrystalline ZnO flakes.

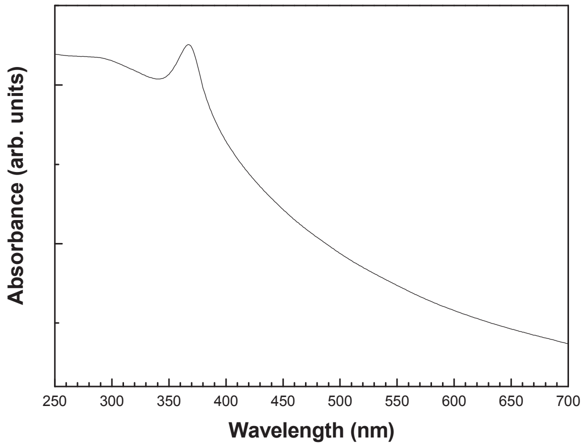

Fig. 4 Room-temperature UV-Vis optical absorbance spectrum of the nanocrystalline ZnO sample.

3.3 UV-Visible absorption spectroscopy

The room-temperature optical absorption spectrum for the ZnO powdered sample is shown in **Fig. 4**. This spectrum reveals that nanoparticles have low absorbance in the visible region, which is a characteristic of ZnO. The absorbance spectrum exhibits an excitonic absorption feature peaked at 367 nm. No other peaks were observed in the absorbance spectrum, which confirms the purity of the synthesized ZnO product. The absorption peak of the ZnO nanoparticles has a blue shift compared to that of the ZnO bulk (375 nm). It was demonstrated that this blue shift depends on the nanocrystal size[29]. Moreover, the local stain in the ZnO nanoparticles (3.941×10^{-3}), estimated from the Stokes-Wilson equation, can contribute to the blue shift of the absorption peak.

In order to extract the band gap energy (E_g) from the absorption spectrum, we use the point of inflection obtained from the first derivative of absorbance with respect to photon energy and find the maximum in the derivative spectrum[30]. The E_g is associated to the maximum in the spectrum, i.e. where the absorbance has a maximum increase with respect to photon energy. A derivative spectrum of the nanopowder sample is presented in **Fig. 5** and the obtained band gap energy is 3.278 eV.

The band gap energy including the quantum confinement as a function of the average particle size is obtained from the effective mass model given by the following equation[31]:

$$E_g = E_g^b + \frac{h^2}{8R^2\mu} - \frac{1.8e^2}{4\pi\varepsilon_r\varepsilon_0 R} - \frac{0.124e^4\mu}{(2h\varepsilon_r\varepsilon_0)^2}$$

where E_g^b (3.35 eV) is the bulk band gap energy, h is Plank's constant, R is the particle radius, μ (1.4257×10^{-31} Kg) the reduced mass of electron and hole, e is the charge on the electron, ε_r (3.7) is the relative permittivity, and ε_0 is the permittivity of free space. The different parameters of ZnO bulk used in the Brus equation were taken from Ref. 32. The E_g value (3.278 eV) injected in the Brus equation yields a nanoparticle size of 33.28 nm. The comparison of the average crystallite size obtained from XRD analysis and that calculated from the Brus equation shows a good agreement. We note that no quantum confinement effect is observed in the synthesized powders because the crystallite size is larger than 10 nm.

3.4 FT-IR and EDS measurements

Fig. 6 illustrates the FT-IR spectrum of the nanosized ZnO powder in the range 500-4000 cm^{-1}. In the FT-IR spectrum there is a significant spectroscopic band at around 521 cm^{-1}. This is the characteristic band of ZnO[33]. The peak at 885 cm^{-1} is probably due to the carbonate moieties which are generally observed when FT-IR samples are measured in air. Also, the characteristic absorption bands at about 3425, 1632 cm^{-1} are observed and correspond to the O-H stretching and bending modes of water absorbed on the surface of nanocrystals[34], respectively. The EDS analysis confirms that the synthesized ZnO flakes are composed only of zinc and oxygen with a weight percentage of 41.08 and 58.92, respectively. It may be noted that the slightly higher oxygen content in the powdered sample is due to the ambient air where the ZnO powder reacts with atmospheric oxygen. This result is confirmed by FT-IR measurements where an O-H group is detected.

4. Summary

In summary, ZnO nanoparticles with an average crystallite size of 31 nm and synthesized via a simple solution process using zinc acetate and diethylamine under refluxing at 85℃ for 4 h were investigated by a variety of techniques. The XRD data indicate the high crystallinity of the ZnO nanoparticles in the hexagonal lattice with parameters a and c of 3.253 and 5.210 Å, respectively. The average size of the nanocrystalline ZnO flakes, estimated from FE-SEM, is about 300 nm. The nanocrystalline ZnO powder exhibited

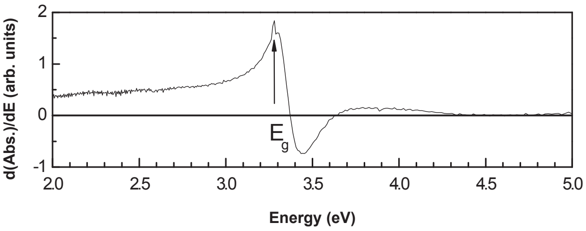

Fig. 5 First derivative absorption spectrum of the nanocrystalline ZnO flakes.

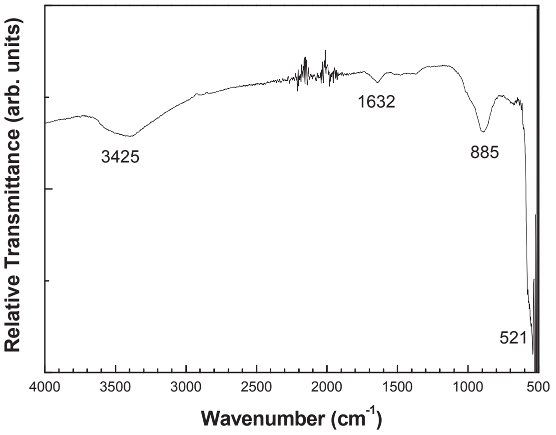

Fig. 6 Room-temperature FT-IR spectrum of the nanosized ZnO powdered sample.

the direct optical band gap energy of 3.278 eV. The grain size deduced from XRD and the one calculated from the Brus equation show a good agreement. Raman scattering, EDS and FT-IR analysis confirmed the high purity of the nanocrystalline ZnO flakes prepared by the simple reaction process which is a low-cost method.

Acknowledgments

The author is grateful to Professor A. A. Al-Ghamdi for his support and constant interest in the present work, for help with the UV-Vis, FT-IR and FE-SEM measurements and for discussions.

References

1) Fan, X., Fang, G., Guo, S., Liu, N., Gao, H., Qin, P., Li, S., Long, H., Zheng, Q. and Zhao, X. (2011): Controllable synthesis of flake-like Al-doped ZnO nanostructures and its application in inverted organic solar cells, Nanoscale Research Letters, 6:546.
2) Zeng, Y., Zhang, T., Yuan, M., Kang, M., Lu, G., Wang, R., Fan, H., He, Y., and Yang, H. (2009): Growth and selective acetone detection based on ZnO nanorod arrays, Sens. Actuators B, Vol.143, pp.93-98.
3) Ali, S. M. U., Ibupoto, Z. H., Kashif, M., Hashim, U. and Willander, M. (2012): A Potentiometric Indirect Uric Acid Sensor Based on ZnO Nanoflakes and Immobilized Uricase, Sensors, Vol.12, pp.2787-2797.
4) Hsu, C. L., Hsueh T. J. and Chang, S. P. (2008): Preparation of ZnO Nanoflakes and a Nanowire-Based Photodetector by Localized Oxidation at Low Temperature, J. Electrochem. Soc., Vol.155, pp. K59-K62.
5) Peng, Z., Dai, G., Chen, P., Zhang, Q., Wan, Q., Zou, B. (2010): Synthesis, characterization and optical properties of star-like ZnO nanostructures, Materials Lett., Vol.64, pp.898-900.
6) Kadam, P., Agashe, C., and Mahamuni, S. (2008): Al-doped ZnO nanocrystals, J. Appl. Phys., Vol.104, pp.103501-103504.
7) Umar, A., Hajry, A. Al., Al-Heniti, S. and Hahn, Y. B. (2008): Hierarchical ZnO nanostructures: growth and optical properties, J. of Nanosc. and Nanotech., Vol.8, pp.6355-6360.
8) Zhang, J., Sun, L., Yin, J., Su, H., Liao, C. and Yan, C. (2002): Control of ZnO morphology via a simple solution route, Chem. Mater., Vol.14, pp.4172-4177.
9) Wang, Z. L. (2004): Zinc oxide nanostructures: growth, properties and applications, Phys-Condens. Mat. Vol.16, pp.R829-R858.
10) Zhao, Q., Zhang, H., Zhu, Y., Feng, S., Sun, X., Xu, J. and Yu, D. (2005): Morphological effects on the field emission of ZnO nanorod arrays, Appl. Phys. Lett. Vol.86, pp.203115-203117.
11) Manekkathodi, A., Lu, M.-Y., Wang, C. W. and Chen, L.-J. (2010): Direct Growth of Aligned Zinc Oxide Nanorods on Paper Substrates for Low-Cost Flexible Electronics, Adv. Mater., Vol.22, pp.4059-4063.
12) Cho, S. and Lee, K.-H. (2010): Solution-Based Epitaxial Growth of ZnO Nanoneedles on Single-Crystalline Zn Plates, Cryst. Growth Des. No.10, pp.1289-1295.
13) Kashif, M., Ali, S. M. U., Foo, K. L., Hashim, U. and Willander, M. (2010): Enabling Science and Nanotechnology (ESciNano), International Conference, Kuala Lumpur, Malaysia, (AIP Conf. Proc.) 1341, pp.92-95.
14) Kashif, M., Ali, U., Syed M., Ali, M. E., Abdulgafour, H. I., Hashim, U., Willander, M. and Hassan, Z. (2012): Morphological, optical, and Raman characteristics of ZnO nanoflakes prepared via a sol–gel method, Phys. Status Solidi A, Vol.209, pp.143-147.
15) Fulati, A., Usman Ali, S. M., Asif, M. H., Alvi, N.H., Willander, M., Brännmark, C., Strålfors, P., Börjesson, S.I., Elinder, F. and Danielsson, B. (2010): An intracellular glucose biosensor based on nano-flake ZnO. Sens. Actuators B, Vol.150, pp.673–680.
16) Jang, J., Kim, C., Ryu, H., Razeghi, M., Jung, W. (2008): ZnO 3D flower-like nanostructure synthesized on GaN epitaxial layer by simple route hydrothermal process, J. Alloy. Comp. Vol.463, pp.503-510.
17) Huang, M. H., Mao, S., Feick, H., Yan, H. Q., Wu, Y. Y., Kind, H., Weber, E., Russo, R. and Yang, P. (2001): Room-Temperature Ultraviolet Nanowire Nanolasers, Science No.292, pp.1897-1899.
18) Fan, H. J., Scholz, R., Kolb, F. M. and Zacharias, M. (2004): Two-dimensional dendritic ZnO nanowires from oxidation of Zn microcrystals, Appl. Phys. Lett., Vol.85, pp.4142-4144.
19) Vayssieres, L. (2003): Growth of Arrayed Nanorods and Nanowires of ZnO from Aqueous Solutions, Adv. Mater., Vol.15, pp.464-466.
20) Liu, B. and Zeng, H. C. (2003): Hydrothermal synthesis of ZnO nanorods in the diameter regime of 50 nm, J. Am. Chem. Soc., Vol.125, pp.4430-4431.
21) Shen, G. Z., Cho, J. H., Yoo, J. K., Yi, G. C. and Lee, C. J. (2005): Synthesis and optical properties of S-doped nanostructures: Nanonails and nanowires, J. Phys. Chem. B, Vol.109, pp.5491-5496.
22) Cullity, B. D. and Stock, S. R. (2001): “Elements of X-ray Diffraction” , Prentice Hall, New York.
23) Hosseini-Sarvari, M. (2011): Synthesis of Quinolines Using Nano-Flake ZnO as a New Catalyst under Solvent-Free Conditions, J. Iran. Chem. Soc., Vol.8, pp.S119-S128.
24) Calleja J. M. and Cardona, M. (1977): Resonant Raman scattering in ZnO, Phys. Rev. B, Vol.16, pp.3753-3761.
25) Damen, T. C., Porto, S. P. S. and Tell, B. (1966): Raman Effect in Zinc Oxide, Phys. Rev., Vol.142, pp.570-574.
26) Cusco, R., Alarcon-Llado, E., Ibanez, J., Artus, L., Jimenez, J., Wang, B. and Callahan, M. J. (2007): Temperature dependence of Raman scattring in ZnO, Phys. Rev. B, Vol.75, pp.165202-165212.
27) Chen, Z. Q., Kawasuso, A., Xu, Y., Naramoto, H., Yuan, X. L., Sekiguchi, T., Suzuki, R. and Ohdaira, T. (2005):

Microvoid formation in hydrogen-implanted ZnO probed by a slow positron beam, Phys. Rev. B, Vol.71, pp.115213-115220.

28) Kaschner, A., Haboeck, U., Strassburg, M., Kaczmarczyk, G., Hoffmann, A., Thomsen, C., Zeuner, A., Alves, H. R., Hofmann, D. M. and Meyer, B. K. (2002): Nitrogen-related local vibrational modes in ZnO:N, Appl. Phys. Lett., Vol.80, pp.1909-1911.

29) Ashtaputre, S. S., Deshpande, A., Marathe, S., Wankhede, M. E., Chimanpure, J., Pasricha, R., Urban, J., Haram, S. K., Gosavi S. W. and Kulkarni, S. K. (2005): Synthesis and analysis of ZnO and CdSe nanoparticles, Pramana J. Phys., Vol.65, pp.615-620.

30) Becerril, M., Silva-López, H. and Zelaya-Angel, O. (2004): Band gap energy in Zn-rich $Zn_{1-x}Cd_xTe$ thin films grown by r.f. sputtering, Rev. Mex. Fís. Vol.50, pp.588-593.

31) Brus, L. E. (1984): Electron-electron and electron hole interactions in small semiconductor crystallites: The size dependence of the lowest excited electronic state, J. Chem. Phys., Vol.80, pp.4403-4409.

32) Studenikin, S. A., Golego, N. and Cocivera, M. (1998): Fabrication of green and orange photoluminescent, undoped ZnO films using spray pyrolysis, J. Appl. Phys., Vol.84, pp.2287-2294.

33) Gupta, T. K. (1992): Microstructural engineering through donor and acceptor doping in the grain and grain boundary of a polycrystalline semiconducting ceramic, J. Mater. Res., Vol.7, pp.3280-3295.

34) Goswami, N. and Sen, P. (2004): Water-induced stabilization of ZnS nanoparticles, Solid State Commun., Vol.132, pp.791-794.

Author's short biography

Amor Sayari

Amor Sayari, born in 1964, received a bachelor's degree in physics in 1989 from the University of Tunis, a master of science, and a PhD graduate degree in solid-state physics in 1991 and 1998, respectively, from the University of Tunis, Tunisia. He obtained the habilitation qualification in physics at the University of Tunis in July 2012. Dr. Sayari worked as an assistant at the University of Sfax from 1992 to 1998. After his PhD on "study of folding, confinement and interface effects in GaAs/AlAs superlattices and quantum wells by Raman spectroscopy" , Dr. Sayari became an assistant professor at the University of Tunis where he combined teaching activities with experimental research in the field of solid-state physics. He is a member of the Raman Group, Faculty of Science Tunis.

His research interest is vibrational, optical and structural properties, especially for III/V and II/VI semiconductor heterostructures.

In 2006, he joined the King Abdulaziz University, Saudi Arabia, where he became interested in ZnO nanoparticles and their applications in nanotechnology.

Powder Technology and Pharmaceutical Development: Particle Size and Particle Adhesion[†]

Frank M. Etzler* **and Mohammad Nasir Uddin**
[1] *School of Pharmacy, Lake Erie College of Osteopathic Medicine*

Abstract

Both the FDA (U.S. Food and Drug Administration) and ICH (International Conference on Harmonisation) have urged the incorporation of Quality by Design (QbD)1) into the manufacture of pharmaceutical products2).

The performance of many pharmaceutical manufacturing processes and the performance of some pharmaceutical products requires a knowledge of powder properties. Under the principles of QbD it is possible to adjust processes to account for variations in powder properties. These adjustments, in turn , require knowledge of the relation between powder properties and manufacturing performance. This relation between powder properties and performance is often not well understood; thus, the required information is not collected.

In this paper, particle-particle and particle-surface interactions are considered to be a source of product variability. As particle size effects are intertwined with particle adhesion effects this topic is also considered. From the discussion below, it can be seen that the surface chemistry of particles can vary due to mechanical treatment, crystallization solvent, and surface contamination. Variations in surface chemistry affect interparticle adhesion and thus may lead to process or product performance changes. Issues concerning the role of interparticle adhesion that are related to tableting and dry powder inhalers are discussed in some detail.

It is clear that a deeper understanding of the powder state and the establishment of appropriate analytical tools will be required to fully implement QbD. Improvements in particle sizing technologies, improvements powder sampling procedures and measurements of particle surface properties will be required. It is hoped that this paper will stimulate thought on this issue.

Keywords: particle adhesion, particle size analysis, quality by design, surface chemistry, AFM, powder characterization, dry powder inhalers, lactose, tableting, surface free energy

1. Introduction

Many pharmaceutical products use powders in their manufacture. Tablets, capsules and dry powder inhalation formulations, for example, require knowledge of powder properties in order to optimize their pharmaceutical performance and manufacture. The optimal design of dry powder inhalers is, in particular, challenging.

Both the FDA (U.S. Food and Drug Administration) and ICH (International Conference on Harmonisation) have urged the incorporation of Quality by Design (QbD)1) into the manufacture of pharmaceutical products2).

The use of QbD principles offers additional flexibility in the manufacture of products but requires a rather detailed knowledge of material and process properties and their impact on product performance. Traditionally manufacture of drugs has assumed material properties are constant (or held to exacting specifications). Manufacturing processes are similarly held to specific specifications. It is assumed if process and material properties are held constant then product quality will be the same. Traditional manufacturing is performed in batches with the quality of

---

[†] Accepted: May 28, 2012

[1] 1858 W. Grandview Blvd., Erie, PA 16509, USA
* Corresponding author:
E-mail: fetzler@lecom.edu
TEL: +1-814-860-5184

ⓒ 2013 Hosokawa Powder Technology Foundation

each batch assessed at the end of the manufacturing process. Traditional manufacturing has focused greatly on the chemical purity of materials. Certainly, chemical purity is essential to pharmaceutical production but does not, in itself, assure adequate product performance. Quality by design offers additional flexibility by allowing for variable material properties, variable processing conditions and continuous manufacture. Quality by design does, however, require a detailed scientific knowledge of the important quantities affecting material properties and their impact on manufacturing conditions. Some factors which limit the full implementation of quality by design in industry include limitations in current analytical technology and a detailed understanding of the powder state.

In this paper, current limitations in analytical technologies that affect understanding of pharmaceutical product performance are discussed. Some particle properties which may affect product or process performance are also discussed.

2. The Powder State

Physical chemistry generally classifies materials as being solids, liquids or gases. Traditional analytical methods are usually adequate to provide characterization of the intrinsic properties of such materials (purity, density, crystalline state, etc.). Pharmaceutical materials are generally well characterized with regards to such properties as various compendial tests address such issues (e.g. chemical purity, etc.). From a theoretical perspective, statistical mechanics, at least in principle, can account for the intrinsic properties of solids, liquids and gases based on fundamental knowledge of intermolecular forces and molecular size and shape.

Powders are composed of solid particles with spaces between the particles that contain a gas (most often air). Materials are generally considered to be powders when particles are less than 40μm. If the particles are of greater size then the material is usually considered to be granular.

The fundamental forces acting on particles in a powder are adhesion, friction and gravitational forces. For granular materials, gravitational forces dominate whereas for powders adhesion and frictional forces dominate. Adhesion and frictional forces are of great importance for fine powders and less so for granular materials. These forces depend on particle surface chemistry and particle mechanical properties.

Typical powders are composed of particles that vary in shape and size. Unlike solids and liquids powders are not characterized by a single density (at fixed T and P). The powder bulk density can be modified by various processes acting on the powders and can be affected by past history. Powders, in contrast to liquids and gases, are nonergodic. Following a single particle over a long period of time will not allow one to assess the overall behavior of the powder as it would for a molecule in a liquid or gas. Simulation of non-ergodic systems is clearly more difficult and may be beyond current computer capabilities. An "accurate" description of particle size is part of the description of a powder.

As the physics of various shaped and sized particles interacting in a gaseous medium is very complex, a detailed fundamental knowledge of powder behavior lags considerably behind that for ordinary matter.

Because, full implementation of quality by design for many pharmaceuticals depends to a substantial degree on a fundamental knowledge of properties of powders, the full implementation of quality by design has not yet been achieved. Full implementation would enhance the ability to trouble shoot problems that occur during development or manufacture.

In this paper, several areas that limit a more complete understanding of powder behavior are identified and discussed. The properties discussed here are generally related to interparticle interactions. It is hoped that this paper will inspire others to make advances in at least some of the identified areas. It is also important to recognize the current limits of current science and technology when addressing product development challenges.

3. Particle Size and Shape

3.1 Importance of particle size and shape to pharmaceutical manufacture

Particle size affects the behavior of powders in a number of ways. Some of these ways are discussed below.

The mixing of materials is an important operation[3]. Mixtures containing particles of significantly different sizes segregate by size during transport. The ability to obtain uniform mixtures of materials is thus affected by the relative sizes of the components. Hence, it is generally desirable to have the sizes of the component materials be similar. Particle size and interparticle adhesion affect mixing performance.

The flowability of powders is affected by particle size[3-5]. In the case of small particle sizes, where the friction and adhesion forces between particles are important, flow decreases with decreasing particle size. The opposite is true when gravitational forces dominate. Jallo and co-workers, in particular, have considered the relation between interparticle adhesion and a measure of flowability[5].

Low dosage tablets require that drug material be distributed amongst a significant number of particles. If the average number of particles per unit dose is too small then content uniformity problems will result. The normal rules of statistical selection are responsible for the variation in content. The frequent use of volume weighted distributions in the pharmaceutical industry deemphasizes the importance of particle numbers in sampling.

Granulation times and the amount of liquid used for granulation are affected by surface area and hence the particle size[6]. The packing density of powders is affected by the particle size and particle size distribution[7]. The tabletting properties of the powder are governed, in part, by the ability of the powder to densify under pressure. Both packing density and particle size thus influence the tabletting process. Granulation may affect the nature of the particle surfaces by promoting contamination of surfaces thus changing the strength of interparticle adhesion.

Products for pulmonary delivery require aerosolized particles in the 2-5µm range. Interparticle adhesion and adhesion to container walls is also influenced, in part, by particle size[8]. The choice of formulation materials affects the ability to deliver particles of the desired respirable size.

The dissolution rate of materials[9] depends on surface area. Powders consisting of small particles have greater specific surface areas. Control of particle size may be of particular importance to those developing formulations from poorly soluble compounds. Processing times for the dissolution of materials incorporated into liquid formulations may also be important.

Particle shape also affects powder behavior in the above listed areas. The effects of particle shape are less well studied are not considered in detail in this paper.

3.2 Particle size analysis

The measurement of particle size and shape is difficult for both technical and philosophical reasons. Allen[10] and Etzler[11] have previously provided more complete discussions of particle size analysis. Iococca[12], Rawle[13] and Moschwitzer[14] have more recently discussed particle size analysis.

For spherical particles the particle size can be unambiguously be assigned as the particle diameter or radius. It is also possible to assign unambiguous sizes to other regularly shaped particles such as cubes but it is not usual to do so. In the case of cubes, edge length could be used as a measure of size.

For particles of irregular shape it is not possible to assign sizes unambiguously. In this instance, it is typical to express particle size as equivalent spherical diameters. Any measurement of length, area, volume or mass may be used to specify the equivalent diameter. Equivalent spherical diameters for irregularly shaped particles determined in different ways are not numerically equal. For particles that are compact but nonetheless not spherical (e.g. icosahedra) the various measures may give results that do not differ greatly from each other. Needles, disks and flakes are, however, particularly problematic. In this instance, various measurements of size may greatly differ. For this reason it is necessary to be clear with regard to the method used for particle size analysis. It is also necessary to consider the appropriateness of a particular particle size method to the problem at hand.

Particle size data can be presented in a number of ways[10]. Data can be presented as either a cumulative, differential, or as a histogram distribution. A histogram plot displays the fraction in a given size interval. A cumulative plot shows the fraction of particles having a size less than a certain value. This plot often has a characteristic sigmoid shape. A differential plot is the first derivative of the cumulative plot. The differential and histogram plots may look similar and should be not confused with one another. When data are presented the type of plot used should be made clear.

Particle size distributions may be based on number, volume or surface area. Only the number distribution represents a census of the particles in the system. The volume or mass distribution reflects the fraction of mass which is composed of particles of a specified size. Similarly, the surface area distribution reflects the fraction of surface area composed of particles of a specified size. Each type of plot is useful. For a given population of particles the various plots may look very different from one another. It is, thus, important to make clear which type of distribution is presented. Many publications in the pharmaceutical literature do not make this distinction clear. It is infrequent that investigators make clear the type of distribution being presented as well as the limitations of the method used. It is even more infrequent that the results of several methods are compared to provide a more complete understanding of the material at hand.

Materials composed of particles of different size will segregate by size during transport and handling. Care must be taken to ensure that size segregation does not occur during the process of providing samples to the laboratory. Laboratories receiving improperly sampled materials will report incorrect results10),15-16).

Instruments used to determine particle size distributions usually have quite high precision. If identical samples are presented to the instrument, then nearly identical particle size distributions will result. It is reasonable for the analyst to conclude that sampling errors in the laboratory have occurred if the particle size distributions of replicate samples significantly differ. It is possible to remove quite small and still representative samples from very large containers, if proper procedures are followed. The spinning riffler is considered to be the gold standard for sampling devices17).

The authors have not found that good sampling practices are consistently applied in the pharmaceutical industry. Conclusions based on poor sampling may delay product development or prevent the proper identification of problems that are, in fact, not related to particle size. For instance, two samples apparently exhibiting different particle sizes may do so because poor sampling practices have been employed. Manufacturing problems thus are mistakenly attributed to particle size when another variable is indeed causing the problem. Sampling issues can be particularly problematic when volume distributions are measured for polydisperse powders. The particles representing the greatest mass (or volume) may, indeed, be rather few in number a thus may be quite sensitive to sampling. The variable numbers of large particles may sometimes lead to variations is dissolution rates. It should be recognized that the rigor to which sampling procedures must be held depends on the nature of the powder and its use in the manufacturing process or its effect on product performance. The authors have encountered powders which are nearly impossible properly sample.

A list of the most common instrument types employed in the pharmaceutical industry is given below.

- Optical and Scanning Electron Microscopy. (Both manual and automated image analysis)
- Laser Diffraction -Mie and Fraunhoffer Diffraction.
- (Instruments from various manufacturers are used.)
- Sieves (various types).
- Light Obscuration (HIAC and PSS Accusizer).
- Malvern Zetasizer.
- PCS / Dynamic Light Scattering for nanoparticles. New technologies offered by Nanosight18-19) and Izon 20-21) may advance nanoparticle sizing.
- Aerosizer -time of flight. The Aerosizer was replaced by the TSI Particle Size Distribution Analyzer. Both instruments are now obsolete despite their rather good performance.
- Anderson Cascade Impactor.

Microscopy and Laser Diffraction instruments are the industry workhorses. Sieving is probably the third most used particle sizing method but is not suitable for fine pharmaceutical powders. The above list indicates, however, that a variety of particle sizing instruments are used in the pharmaceutical industry. Because a variety of equipment is used it is important to achieve an understanding of the relative performance of various instruments. More detailed discussions of the various techniques have been published in the literature10,15,22). At the present time, light microscopy is often used in conjunction with image analysis and automatic scanning to allow large numbers of particles to be measured. Several commercial instruments combine image analysis and light microscopy for particle size analysis.

The various particle sizing techniques can be generally divided into two classes - ensemble methods and particle counting methods. Particle counting methods assess the size of individual particles. The size data is then pooled into size classes in order to construct a histogram. Microscopy, Light Obscuration, Aerosizer, Nanosight and Malvern Zetasizer are examples of particle counting instruments. Ensemble methods, in contrast, do not assess the size of individual particles but rather assess the nature of the entire or a large portion of the population. Light scattering, Sieving and the Anderson Cascade Impactor are examples of ensemble methods.

The nearly procrustean use of light scattering methods (PCS and Mie-Fraunhoffer) for particle sizing by the pharmaceutical industry, while understandable in a number of regards, is unfortunate. Particle size distributions calculated from light scattering data are the result of rather complex calculations and numerical approximations. These calculations impose restrictions on the form of the calculated distribution which may not correspond to the form of the real distribution. These restrictions are most severe in the case of PCS. Commercial implementations of Mie-Fraunhoffer assumes that particles are spherical. When particles are spherical, no azimuthal dependence of the scattering pattern is observed. In contrast, if particles are not spherical a marked azimuthal dependence may be observed23-25). Appli-

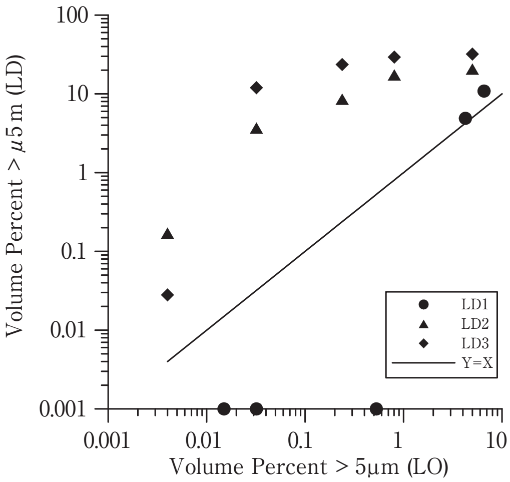

Zero plotted as 10^{-3} for purposes of plotting.

Fig. 1 Percentage of Particles greater than 5 μm as determined by Laser Diffraction versus that determined by Light Obscuration for unstable Lipid Emulsions[26]. Laser diffraction shows non linear response to particle population. Note various laser diffraction instruments give different results. Light Obscuration has been shown to be accurate.

cation of a model intended for spherical particles to non-spherical particles may result in the reporting of ghost particles. Ghost particles are not present in the real population and are an artifact of the calculation. Each equipment manufacturer, necessarily, makes numerical assumptions in the calculation of particle size from the scattering intensities. Unfortunately, these assumptions do not appear to be the same between manufacturers. Results from Mie-Fraunhoffer instruments from different manufactures can differ significantly[26]. (See **Fig. 1**) Conclusions made using results from such instruments may be in error due to the presence of ghost particle or numerical artifacts. Number counting devices fair much better.

Problems associated with the use of light scattering methods have been discussed by a number of authors[4,11,18-21,26-28]. The reader is directed to these resources for a more detailed discussion.

3.3 Particle sizing summary

Particle size (and the particle size distribution) is a fundamental characteristic of a powder that influences the behavior of the powder in various applications. The determination of particle size is difficult for both philosophical and technical reasons. The method chosen to assess particle size affects the result as particle size for irregularly shaped particles is represented by the equivalent spherical diameter. As any measure of length, volume (mass) or surface area spherical diameters determined using different measures may differ. Particle size can be represented as a number, volume (mass) or surface area distribution. Not all authors make clear which type of distribution is reported or make clear that the chosen type of distribution is appropriate to the problem at hand. Particle size distributions determined by light scattering methods (PCS and Mie-Fraunhoffer) may at least partially reflect artifacts caused by fitting inappropriate optical models to the scattering data or resulting from numerical artifacts.

In order for QbD to be fully realized it will be necessary to develop and use new particle sizing tools. Limitations of currently available particle sizing equipment and the impact of these limitations on product development must also be recognized. Comparison of particle size distributions obtained using different methods may be the best way, at present, to assess the nature of a powder.

4. Particle Adhesion

The adhesion between particles is also important to the behavior of powders. Zimon[29] has published and extensive and important review concerning the physics of the adhesion of particles and particles to surfaces. The principal forces acting on powders are gravity and interparticle adhesion forces. Frictional forces are also important.

4.1 The role of surface free energy – adhesion fundamentals

The adhesion between materials is determined by the area of intimate contact and the strength of the interaction between bodies. Factors such a particle shape and size as well as the degree of compression, in the case of tablets, control the quantity of interaction. Surface chemistry and surface free energy control the quality of this interaction.

The thermodynamics of the surface free energy, γ, of solids has been reviewed by Etzler[30]. The ideal work of adhesion, W_A, between materials A and B is defined by the following relation.

$$W_A = \gamma_A + \gamma_B - \gamma_{AB} \tag{1}$$

where the subscripts A and B on the surface free energy terms refer to materials A and B. Similarly, if materials A and B are identical the work of cohesion, W_c, can be defined as:

$$W_c = 2\gamma_{A,B} \tag{2}$$

Fowkes[31-32] suggested that surface free energy and thus the work of adhesion could be considered as a sum of components resulting from various types of intermolecular interactions. At present, it is conventional to express the work of adhesion as a sum consisting of a term for Lifshitz-van der Waals interactions and second term resulting from Lewis acid-base interactions[30]. Frequently, Lifshitz-van der Waals interactions are dominant.

Intermolecular forces between molecules result from interactions between their corresponding electron orbitals. The principal non-bonding interactions result from induced dipole–induced dipole (London), dipole–induced dipole (Debye) and dipole–dipole (Keesom) interactions. The intermolecular potential energy function, *U*, for each of these three types of interactions is of the same form. Here, *r* is the separation distance between bodies.

$$U = \frac{-\beta_{12}}{r^6} \tag{3}$$

If only London dispersion forces are considered the constant in Eqn. (3), β_{12}, can be expressed as follows:

$$\beta_{12}^d = \left(\frac{2\sqrt{I_1 I_2}}{I_1 + I_2}\right)\left(\beta_{11}^d \beta_{22}^d\right)^{1/2} \tag{4}$$

Here the subscripts 11, 22 and 12 refer to interactions between like molecules (11, 22) and dissimilar molecules (12). β ,again, is the coefficient in Eqn. (3). I is the ionization potential. If $I_1 \approx I_2$ then

$$\beta_{12}^d = \left(\beta_{11}^d \beta_{22}^d\right)^{1/2} \tag{5}$$

Eqn. 5 forms the basis of the Berthelot principle [33-34] which states that dispersion interactions between dissimilar molecules can be estimated as the geometric mean of the interactions between like molecules.

The interaction potentials between molecules have been used to determine the interactions between macroscopic bodies. In this instance, the Hamaker constants, *A*, derived from β , also follow the geometric mean rule[30,34-35]. Thus,

$$A_{12} = \left(A_{11} A_{22}\right)^{1/2} \tag{6}$$

and assuming further that intermolecular distances, *d*, also follow the geometric mean rule[30]. Continuing the argument, the work of adhesion due to London dispersion forces may be expressed as follows.

$$W_{12}^d \approx \frac{\left(A_{11} A_{22}\right)^{1/2}}{12\pi d_{11} d_{22}} = \left(W_{11}^d W_{22}^d\right)^{1/2} = 2\left(\gamma_{11}^d \gamma_{22}^d\right)^{1/2} \tag{7}$$

It has been further generalized that all of the Lifshitz-van der Waals components follow the same rule thus

$$W_A^{LW} = 2\left(\gamma_1^{LW} \gamma_2^{LW}\right)^{1/2} \tag{8}$$

Berthelot's rule (Eqn. (8)) is widely accepted and is part of most models used to explain adhesion and contact angle phenomena.

The Lewis acid-base component of the surface free energy has been modeled in a number of ways. Etzler[30] has discussed the various models in detail. Here we highlight the use of two models, one by van Oss, Chaudhury and Good and the other by Fowkes, that are frequently discussed in the literature.

According to the van Oss, Chaudhury and Good model [36-37] the Lewis acid-base component is modeled as follows

$$\gamma_i^{AB} = 2\left(\gamma_i^+ \gamma_i^-\right)^{1/2} \tag{9}$$

where γ^+ is the Lewis acid parameter and γ^- is the Lewis base parameter. van Oss, Chaudhury and Good further choose

$$\gamma_i^+ = \gamma_i^- \equiv 0 \tag{10}$$

for alkanes, methylene iodide and α-bromonaphthalene which presumably interact only through Lifshitz-van der Waals interactions. For water

$$\gamma_{H_2O}^+ = \gamma_{H_2O}^- \equiv 25.5 \text{ mJ / m}^2 \tag{11}$$

Based on these above numerical choices γ^+ and γ^- have been experimentally determined for a variety of liquids. van Oss[37] has compiled and reviewed the determination of these values (also see Etzler[30]) Della Volpe[38] has suggested that assumption expressed in Eqn. (11) is not the best choice and has offered another choice for the assignment of γ^+ and γ^- .

Earlier Owens and Wendt[39] described surface free energy in terms of two components which were called dispersive γ^d and polar γ^p. Thus

$$\gamma = \gamma^d + \gamma^p \tag{12}$$

While it is generally recognized that $\gamma^d \approx \gamma^{LW}$ the meaning of γ^p is perhaps hopelessly confused in the literature. According to Fowkes[31-32], γ^p should refer to dipole-dipole (Debye) interactions. In the van Oss, Chaudhury and Good model such interactions are, however, incorporated into γ^{LW}. Good[40] no longer recommends the use of γ^p. See Etzler[30] for a more complete discussion.

Recalling Eqns. (1), (8) and (9) together with the relation

$$\gamma = \gamma^{LW} + \gamma^{AB}, \tag{13}$$

it follows that

$$W_a = \gamma_l\left[1+\cos\left(\theta\right)\right] = 2(\gamma_l^{LW}\gamma_s^{LW})^{1/2} + 2(\gamma_l^{+}\gamma_s^{-})^{1/2} + 2(\gamma_l^{-}\gamma_s^{+})^{1/2} \tag{14}$$

If the van Oss, Chaudhury and Good parameters are known for at least three liquids and the contact angles of these liquids on a solid are measured, then Eqn. (14) can be used to determine the van Oss, Chaudhury and Good parameters for the surface free energy of the solid. van Oss[37)], for instance, has reviewed the numerous publications which have reported the determination of the van Oss, Chaudhury and Good parameters for various liquids.

As discussed above, Fowkes[31-32)] first suggested that surface free energy could be considered as a sum of components resulting from different classes of intermolecular interactions. The van Oss, Chaudhury and Good model draws upon the idea of Fowkes and as discussed above uses the geometric mean approximation to model Lifshitz-van der Waals interactions. Fowkes [31,41-42)] however, has suggested a different approach to evaluating the acid base character of surfaces (also see[43)]). Fowkes has criticized the use of contact angles for measurement of interfacial properties[44)]. Fowkes' approach is, for experimental reasons, more applicable to powdered samples. As stated previously,

$$W_a = W_a^{LW} + W_a^{AB} \tag{15}$$

W^{AB} is then, according to Fowkes, expressed by the following relation

$$W_a^{AB} = -f \cdot N \cdot \Delta H_a^{AB} \tag{16}$$

where N is the number of sites per unit area and

$$f = \left[1 - \frac{\partial \ln W_a^{AB}}{\partial \ln T}\right]^{-1} \tag{17}$$

where

$$f \approx 0.2 \ldots 1.0 \tag{18}$$

When using the Fowkes approach some authors have taken *f* as unity although this does not seem to be a good approximation[43)]. Because *f* and N are generally not known, direct calculations of the work of adhesion are often not made. Determination of ΔH^{AB} for multiple probe liquids on a given solid together with models by Drago[45)] or Gutmann[46-47)] can be used to assess the acid-base nature of the surface (also see[48)]). Here we only elaborate further on Gutmann's acid-base scale.

Gutmann[46-47)] introduced the notion of electron donor numbers (DN) and electron acceptor numbers (AN)[48)]. These parameters are similar to the van Oss, Chaudhury and Good surface free energy parameters as they both describe the same molecular parameters but from different points of view. In 1966 Gutmann[46)] introduced the donor number based on the interaction with $SbCl_5$. DN has units corresponding to enthalpy (e.g. kJ/mole). In 1975, Mayer et al[49)]. introduced the acceptor number based on the relative ^{31}P shift induced by triethylphosphine oxide. AN has arbitrary units. In 1990 Riddle and Fowkes[48)] removed the dispersive component from AN. The corrected AN^* values have the usual units of enthalpy. According to Gutmann's theory

$$\Delta H^{AB} = K_a DN + K_d AN^* \tag{19}$$

Where K_a and K_d reflect the acceptor and donor characteristics of a solid. Gutmann's model works best with hard (low polarizability) atoms. Gutmann's approach is suitable for use with inverse gas chromatography. It should be noted that Gutmann's scale is based on enthalpies while the van Oss scale is based on free energies.

Inverse gas chromatography is an excellent method used to determine γ^{LW} and ΔH^{AB}. Etzler[30)] has discussed, in detail, the use of inverse gas chromatography (IGC) for determination of surface free energy components.

4.2 Adhesion and atomic force microscopy

The atomic force microscope has, in recent years, become an important tool to investigate the nature of surfaces. AFM can be used to both acquire fundamental information on particle-particle and particle-surface interactions. It can furthermore be used to investigate surface heterogeneity. Each of these factors can contribute significantly to the understanding of product or process performance. Here, an overview of the AFM and its application to the contamination surfaces and the assessment of particle properties is presented. General reviews of AFM have been published by Leitte and Herrmann[50)] and by zur Muhlen and Niehus[51)].

The atomic force microscope[52)] does not use the transmission of electromagnetic radiation or electron beams to form images. Instead, a probe is scanned over the surface in a raster fashion similar to that employed in television. Typically (but not exclusively) a sharp probe is located at the tip of a diving board shaped or V shaped cantilever composed of silicon. A piezoelectric scanner moves the sample with subnanometer displacement with applied voltage. The

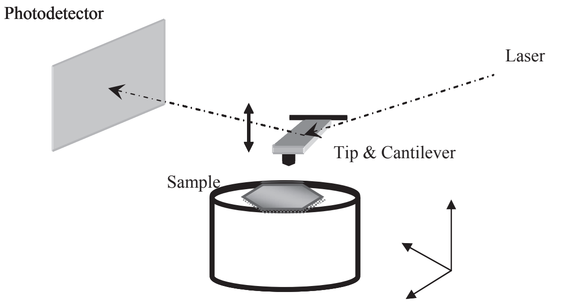

Fig. 2 Schematic drawing of atomic force microscope[53]. Scanner moves in three directions and deflection of cantilever is detected by a photodetector.

piezoelectric scanner is capable of three dimensional movements with respect to the probe tip. In order to create an image the probe tip is brought in close proximity to the surface or in contact to the surface. The piezoelectric system is then employed to scan the probe over the sample in raster fashion. Forces between the sample and probe caused either by sample topography or the nature of forces between the sample and probe result in cantilever deflection. An image is thus constructed on a line by line basis from the deflection of the cantilever. A photodiode detector is used to detect the deflection of the cantilever using a laser light reflection of the surface of the cantilever. See Liette and Herrmann for further details regarding the operation of an AFM[50]. **Fig. 2** is a cartoon illustrating the configuration of an AFM.

AFM is a high resolution form of microscopy that can be used to investigate the nature of surfaces. It is able to produce images at much higher resolution than optical microscopy and sometimes can achieve atomic resolution. Gan has recently discussed the resolution of AFM images[54]. The sample preparation and apparatus is much simpler for AFM than it is for electron microscopy. Samples may be studied in either gaseous or liquid media. The nature interaction of the probe with the surface can, furthermore, be varied; thus several AFM modes are available to the investigator. These different modes allow for the study many aspects of a surface beyond simple topography. In the present context, it will be particularly, important to consider modes that allow measurement of adhesion of particles to other particles and surfaces.

4.3 Measurement of forces using AFM

Commercially available cantilevers can be used to measure forces down to about 10pN[55]. The AFM is thus particularly suitable for making force measurements. The displacement control of the instrument is on the order of 0.01 nm and the sample tip contact area is typically near 10 nm^2. **Fig. 3** shows a hypothetical force curve for tip sample interaction. Looking at the advancing curve in **Fig. 3** beginning with large distance and moving to shorter distances, it is noted that once the attractive force exceeds the cantilever stiffness the cantilever jumps into contact with the surface (distance C in the figure). Moving the cantilever closer to the surface causes repulsive forces into increase. Again, repulsion is caused by the overlapping of electron orbitals. Upon withdrawal, the tip remains in contact with the surface beyond the initial contact point (distance C in the figure). Eventually the force exceeds the adhesion force or pull off force between the sample and the probe causing the cantilever to snap off the surface (point A in the figure). If the receding and advancing curves are not parallel then plastic deformation of the surface has occurred[56-57].

Displacement of the cantilever is translated into force, F, using Hooke's Law.

$$F = k\delta_c \tag{20}$$

Here k is the spring constant and δ_c the cantilever displacement. It is usually necessary to determine spring constants experimentally. Calculation of the

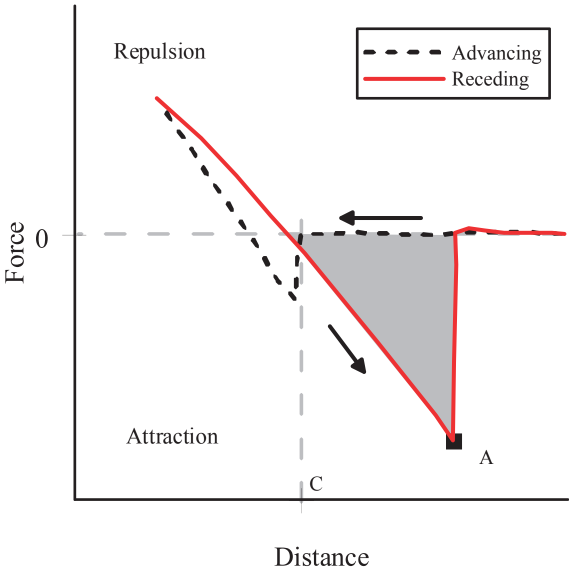

Fig. 3 Hypothetical force curve for probe surface interaction[53]. Dashed curve represents probe advancing toward surface. Solid curve represents probe receding from surface. A is the probe snap off force representing the force of adhesion between probe and surface. C is the probe surface contact position with advancing motion. The shaded area has sometimes been used as a method for determining the adhesion strength[62].

spring constant involves determining the resonant frequency of the cantilever before and after adding a small mass to the tip[58], determining the resonant frequency knowing the dimensions and density of the cantilever[59] or measuring thermal fluctuation of the cantilever[60-61].

Force-distance curves similar to the example in **Fig.3** can be collected for an array of points on a surface. For each pixel of the surface a force-distance curve has been, thus, collected. Extraction of various quantities from the force-distance curve allows for the construction of various images representing the surface.

The adhesion force may, for example, be extracted from each the force-volume curve to construct an adhesion map that would be capable, for instance, of identifying the presence of surface contamination. Other types of maps constructed from force-distance curves might include measurements of hardness or deformability of surfaces. Any quantity that may be extracted from a force-distance curve may be utilized as basis to form and image[62-65].

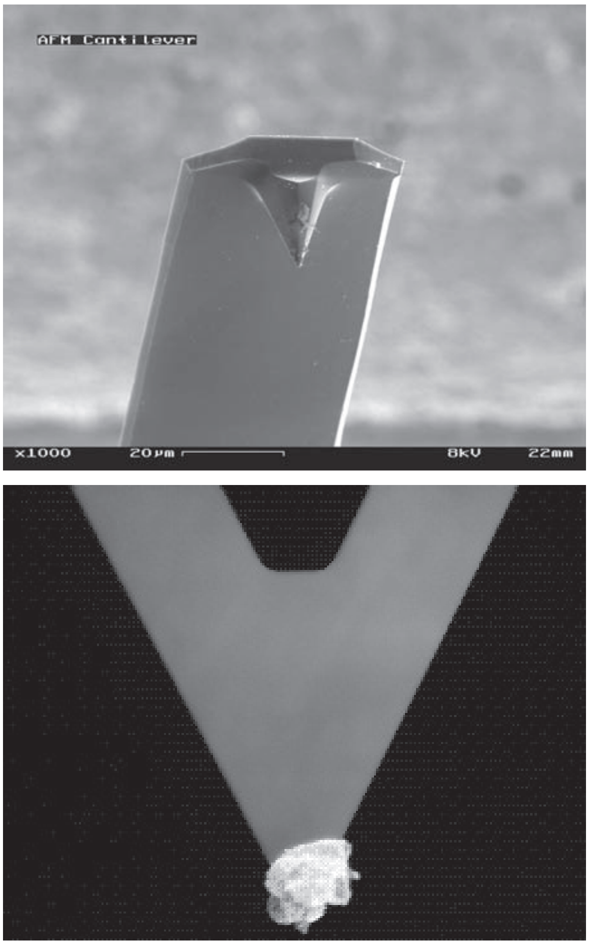

Fig. 4 Up : AFM cantilever tip. Down : AFM Cantilever with lactose particle mounted as colloidal probe.

A particle to be studied can be substituted for the normally sharp tip mounted to the cantilever. (See **Fig. 4**) The attached particle usually has a diameter between 1-20 μm. In this configuration the AFM may be used to investigate the adhesion of the probe particle with other particles or surfaces. The measured adhesion force depends on the intrinsic adhesion between the materials and the contact topography of the particular site. It is not unusual to average the results of many adhesion measurements to understand the nature of the surface. The colloidal probe method had been used by several authors[62,66-71].

4.4 Adhesion forces

The adhesion of particles to surfaces and between particles has been investigated by several authors. A rather comprehensive discussion of particle adhesion has been given by Zimon[29]. The measured adhesion force between bodies is the summation of forces resulting from different types of interactions. These forces may include van der Waals forces, capillary forces, electrostatic forces and chemically specific forces (acid-base).

The adhesion force between particles and surfaces is usually dominated by London dispersion forces in a dry atmosphere. The adhesion mechanics of spheres to planar surfaces has been described by Johnson, Kendall and Roberts (JKR)[72] and by Derjaguin, Muller and Toporov (DMT)[73].

According to the DMT theory the adhesion force, F_{ad}^{DMT} is given by the following relation

$$F_{ad}^{DMT} = 2\pi R w_{ijk} \tag{21}$$

Where R is the particle radius and w_{ijk} is the work of adhesion between i and j in medium k. According the JKR model the adhesion force is alternately expressed as:

$$F_{ad}^{JKR} = \frac{3}{2}\pi R w_{ijk} \tag{22}$$

For smooth surfaces, the DMT prediction and JKR prediction represent the upper and lower bounds of the experimentally observed adhesion force with $\frac{3}{2}\pi$ being the coefficient for soft spheres and 2π the coefficient for hard spheres. An empirical expression based the DMT and JKR expressions is thus

$$F_{ad} = \alpha\pi R w_{ijk} \tag{23}$$

From this expression the reduced load, $\overline{F}$, may also be defined

$$\overline{F} = \frac{F_{ad}}{\pi R w_{ijk}} \tag{24}$$

In AFM applications $\alpha \approx 1.6 \cdots 1.9$. A more complete discussion of this material has been given by Leitte and Herrmann[50].

The work of adhesion is determined by the surface chemistry of the materials in contact is given models such as that suggested by van Oss, Chaudhury and Good. (See above discussion concerning measurement of surface free energies.) For real particles with rough surfaces and irregular geometry proper estimation of the correct contact area is difficult or impossible. The correct contact area is necessary for the calculation of the proper adhesion force. The ability of predicting the adhesion force does not, however, preclude the constriction of useful adhesion maps based of observed adhesion forces or cantilever deflections.

4.4.1 Friction force mode

In addition to measuring the normal force exerted on the probe the lateral force may be measured from the torsion of the cantilever. The behavior of the cantilever has been found to be consistent with the classical theories of friction but is additionally influenced by adsorbed layers of water when surfaces are studied in air[74-75].

4.4.2 Tapping or intermittent contact mode[76-78]

In tapping mode the cantilever is excited into oscillations near the resonance frequency of the cantilever with amplitude of up to 100 nm. These oscillations cause the cantilever to tap along the surface in a manner not to dissimilar to a blind man's cane. The tapping mode image is constructed from the contacts of the tip with the surface. Tapping mode is more gentle to the surface and is thus more suitable for use on soft materials such as those used in, for instance, the pharmaceutical industry.

In tapping mode, the phase of the driver oscillation can be compared to that of the cantilever oscillation. Interaction of the probe with the surface will cause a phase difference between the two oscillations. The observed phase shift appears to reflect various properties of the surface including the viscoelastic properties of the surfaces. Tapping mode height images and phase images are collected at the same time. The phase image is particularly useful for identifying the presence of surface contaminants. The phase image is often able to identify surface features that cannot be identified in the height or topographic image.

4.5 Particle adhesion and particle size

The adhesion between particles within powders is a complex topic. Zimon, in particular, has reviewed the subject of adhesion of dusts and powders[29]. In the absence of triboelectric charging or capillary condensation (which is the usual case at moderate humidity) van der Waals and Lewis acid-base interactions contribute to the adhesion between particles. It would be typical to find that van der Waals interactions dominate.

Both the JKR and DMT models indicate that the force of adhesion, F_{ad} , proportional to the particle radius or diameter. The drag force, F_{dr}, on the particle resulting from fluid flow would be proportional to the radius squared and the mass of the particle proportional to radius cubed.

For small particle diameters

$$\frac{F_{ad}}{F_{dr}} \propto \frac{1}{r} \tag{25}$$

thus the adhesion force causes small particles to be very difficult to remove. If particles are sufficiently small then it may be impossible to remove particles from a surface by hydrodynamic means. Because small particles are nearly impossible to remove from surfaces some manufacturing processes are performed in clean rooms.

For large particles the gravitational force presents the greatest obstacle for removal of particles. In this instance

$$\frac{w}{F_{dr}} \propto r \tag{26}$$

Thus particles with the greatest mass are the most difficult to separate from surfaces.

From the above discussion it can be seen that both particle size and particle adhesion are interrelated. The relation between particle size and particle adhesion is not often well considered when thinking about pharmaceutical development problems.

4.6 Particle adhesion and crystalline state

Particle adhesion depends, in part, on the surface free energy of particles. The surface free energy depends on the precise chemical details of the surface. Heng, Williams and co-workers[79-81] have investigated the surfaces of crystalline materials used in pharmaceuticals. **Table 1** and **2** show advancing contact angles of water on individual crystal faces a few pharmaceutical substances and the surface free energy components (Owens and Wendt model) for Paracetamol polymorphs. These crystals were of macroscopic size. From the tables, it is clear that each crystal face has its own surface chemical char-

Table 1 Advancing contact angles (Deg.) of water on facets of macroscopic single crystals[81)]

Facet	Paracetamol Form I	Paracetamol Form II	Aspirin	Racemic Ibuprofen	S(+) Ibuprofen
(201)	38.1 (4.6)				
(001)	15.9(3.1)	64.5(3.5)	60.7(3.5)	68.5(4.8)	64.5(3.9)
(011)	29.8(5.7)		42.9(4.8)	46.9 (5.5)	
(110)	50.8(4.9)	16.6(1.4)			48.4(4.0)
(010)	67.7 (2.5)	17.9 (2.5)			
(100)			52.9(2.5)	77.2(4.0)	70.7(3.1)

Table 2 Surface Free Energy Analysis (Owens and Wendt) of Paracetamol Form I and Form II[81)]. (mJ/m^2)

	Form I			Form II		
Facet	γ^{LW}	γ^{AB}	γ^{AB}/γ	γ^{LW}	γ^{AB}	γ^{AB}/γ
(201)	34.9	27.5	0.44			
(001)	34.4	38.0	0.53	42.3	9.5	0.18
(011)	33.9	32.7	0.49	33.4	38.5	0.55
(110)	34.2	20.2	0.37			
(010)	45.1	7.0	0.13	32.2	38.9	0.54

acteristics. The area fraction of each crystal face is affected by the composition of the solvent from which the crystals are grown and the subsequent treatment of the crystals. The 010 face of paracetamol form I has the highest water contact angle and lowest acid-base contribution surface free energy. Crystal planes such as this are likely fracture planes and are less water wettable. The wettability and adhesion of materials thus can be affected by milling by altering the area fraction of each crystal plane.

As the surface chemistry of particles affects the adhesion between particles, the studies by Heng and co-workers suggest that the choice of crystallization solvent and milling may affect interparticle adhesion by altering the exposed fraction of individual crystal planes. At present, it is not usual to consider surface variability in the formulation of pharmaceuticals despite the fact that surface chemical variations may cause product and process variations.

4.7 Particle adhesion and surface contamination

In most discussions of material characteristics of formulation components it is usual to assume that the surfaces of materials reflect the inherent nature of the studied substance. Above it is has been shown that the surface characteristics of a material can be altered by exposing different crystal planes. Alternatively, contamination of surfaces with foreign materials or intentional surface modification may alter the surface characteristics. One of us (Etzler) has investigated the surface contamination of materials used in the formulation of dry powder inhalers. A general discussion concerning dry powder inhalers has be given by Alagusundaram and co-workers[82)]. Particle size of the component materials as well as interparticle adhesion and adhesion of particles to the delivery device affect the performance of such products.

Water is a surface contaminant the affects adhesion between particles. Beach and Drelich[83)] have investigated the adhesion of insulin particles to acrylonitrile-butadiene-styrene (ABS) and polypropylene (PP) surfaces as a function of relative humidity. These polymers could be used as a lining for a blister to be used in association with a dry powder inhalation device. The results are summarized in **Fig. 5**. From this figure it can be seen that the pull off force of insulin particles on PP is greater than that of ABS. Estimation of the pull-off forces using the JKR model (Eqn. (4)) combined with estimates of the works of adhesion are unable account for the magnitude of the observed adhesion forces. The RMS roughness determined from height images for the ABS and PP surface are 57.0 ± 6.3 nm and 386 ± 21.4 nm respectively. Presumably, the surface roughness contributes to the magnitude of the observed adhesion force and accounts at least in part for the greater adhesion to PP. **Fig. 5** also shows that adhesion is a dependent on humidity and that this dependence occurs is step

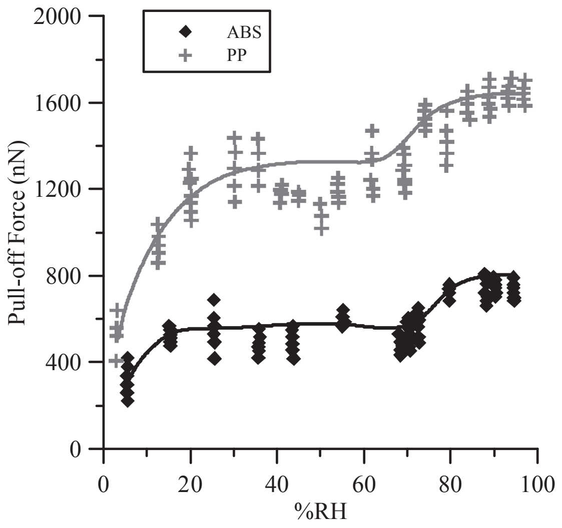

Fig. 5 Pull-off force of insulin particles on PP and ABS surfaces versus relative humidity. Figure redrawn from data by Beach and Drelich[83)]. Results indicate that surface roughness and capillary forces contribute significantly to the adhesion force. See text and original work[83)] for details.

like manner so that three distinct adhesion ranges can be observed. It appears that in the 1st region (low humidity) the adhesion force is dominated by van der Waals forces, in the 2nd region the force results from a combination of capillary forces and van der Waals forces and in the 3rd (high humidity) region capillary forces dominate.

Lactose surface chemistry has also been has also been investigated and related to adhesion to gelatin capsule surfaces[84]. **Fig. 6** shows the variation of surface free energy parameters for various lots of lactose. The figure suggests that both the Lifshitz-van der Waals and acid-base components vary between lots. The variation of surface acidity has been correlated with retention in (adhesion to) capsules used for dry powder inhalation (**Fig. 7**). Furthermore, evidence for the surface contamination, of lactose, can be directly observed using AFM. (**Fig. 8**). It appears that lactose surfaces are variably contaminated with protein and or lipid materials from milk. Lactose is isolated from milk.

5. Interparticle Adhesion and Pharmaceutical Product Performance.

From the above discussion, it can be seen that the properties of a powder can be influenced by particle size and by the nature of the interaction between particles. While many processes and products performance are influenced by power properties, this paper will briefly address two aspects – tableting and the performance of dry powder inhalers.

5.1 Tableting

Tablets are formed by placing a powder under pressure. In order to achieve sufficient tablet tensile strength particles must have sufficient deformability under pressure (quantity of interaction) to increase the area of intimate contact. Fracture of particles may also increase the area of contact. Tablet tensile strength is sometimes referred to as tablet hardness but this type of hardness is not hardness in the traditional sense. (It is not indentation hardness.)

Cao[85] and co-workers have measured the indentation hardness of several pharmaceutical materials including ibuprofen, phenacetin, sucrose, etc. using AFM nanointentation[86-88] to determine the hardness of single particles. AFM nanoindentention is similar to more usual indentation hardness tests except for the fact that an AFM tip is used to make the indentation. The use of an AFM tip allows for hardness to be determined on single particles rather than macroscopic surfaces.

The measurements of particle hardness by Cao and co-workers indicates that materials with either high or low hardness show poor tableting characteristics. Recall that adhesion requires both quality of interaction (surface chemistry) and quantity of interaction (surface area of intimate contact). Hard particles

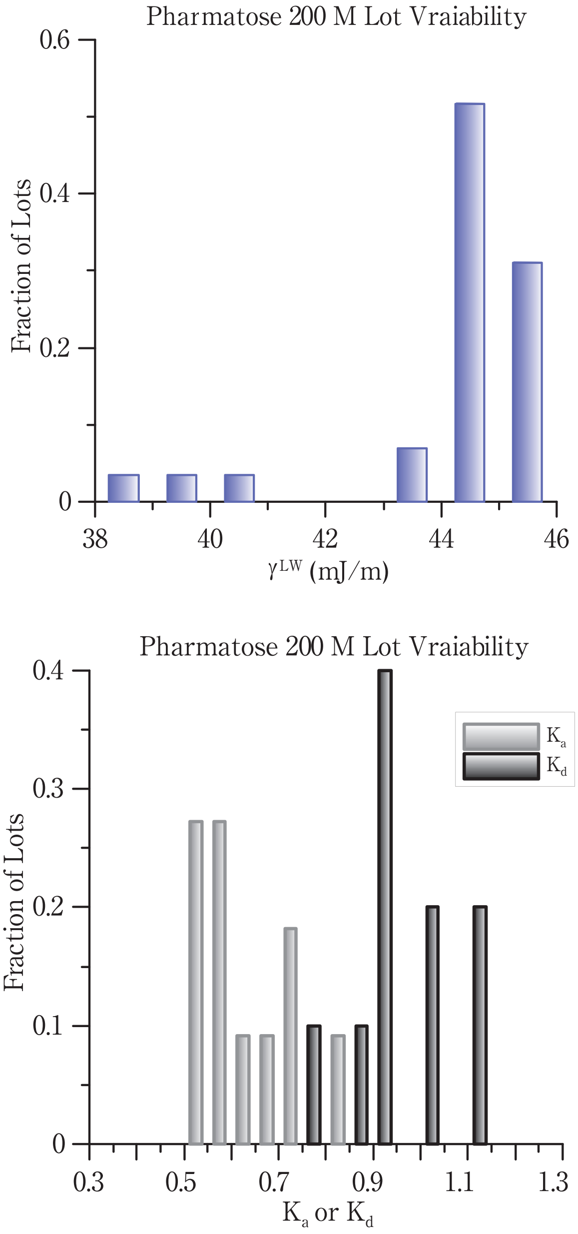

Fig. 6 Surface free energy parameters for various lots of Lactose as determined using IGC[84]. γ^{LW} is the Lifshitz –van der Waals component of the surface free energy. K_a and K_d are the acid and base parameters describing the lactose surface using Gutmann's acid-base model (See Etzler[30] for an explanation of acid-base models). The figure suggests that the surface chemistry of lots of lactose is variable.

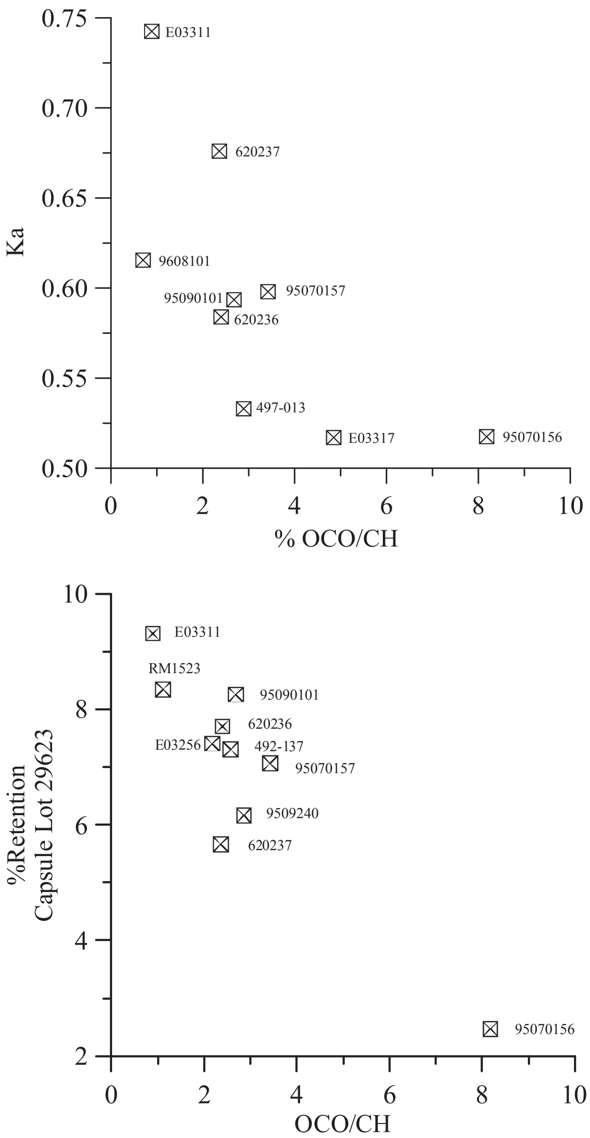

Fig. 7 Surface acidity (K_a) for various lots of lactose and retention in capsule for various lots of lactose versus ratio of OCO carbons to aliphatic (CH) carbons on lactose surfaces[84]. CH carbons represent surface contamination. The oxidation states of surface carbons were determined using XPS (ESCA). Adhesion to capsule walls is affected by surface chemistry.

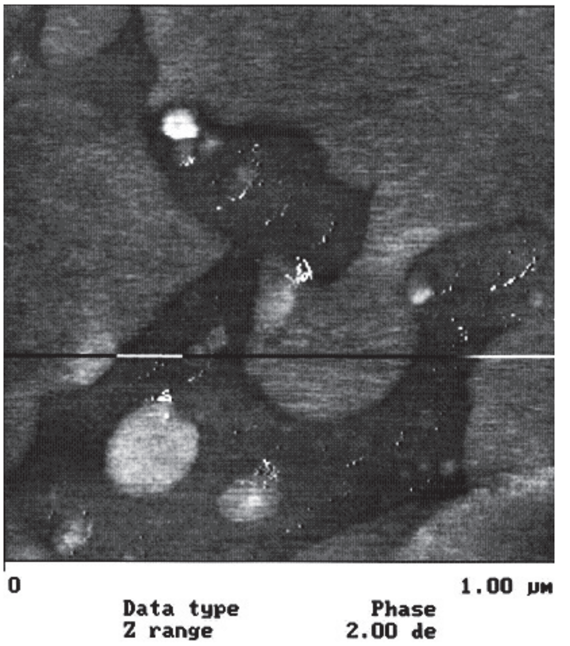

Fig. 8 SPM phase image obtained using Tapping Mode (1 × 1 µm) of a Pharmatose 200M surface. Dark areas and white specks represent surface contaminates. XPS analysis suggests contamination with lipids and proteins from milk[84].

may not sufficiently deform under compaction pressure and thus not allow for intimate contact between surfaces. The lack of intimate contact reduces adhesion strength. Soft particles, in contrast, may have low cohesive strength and low surface free energies reducing adhesion strength as a result of poor quality of interaction.

Etzler and co- workers[89] have recently investigated tablet tensile strength from an adhesion science perspective. Earlier, Ryshkewitch[90] and Duckworth[91] proposed an empirical equation to relate tablet tensile strength, τ, to porosity of the tablet, ε. Thus,

$$\tau = \tau_0 e^{-k\varepsilon} \tag{27}$$

Here τ_0 is the tensile strength of the material at zero porosity ($D = 1$) and k a characteristic constant.

Over the past several decades the Ryshkewitch-Duckworth equation has been discussed a number of times. Recently, the Ryshkewitch-Duckworth equation has been discussed by Doelker[92], Barraleta *et al.*[93], Nyongesa and Aduda[94] as well as by Tye *et al.*[95]. The literature suggests that the Ryshkewitch-Duckworth equation has been successfully applied to a variety of systems that have applications both to pharmaceutical science and to other disciplines.

The importance of the Ryshkewitch-Duckworth equation is that it suggests that porosity is a measure of the outcome of the tableting process. Tablets of the same porosity have the same mechanical properties even though they might have been made on vastly different tablet presses operating at different speeds.

In an earlier paper, Wu *et al.*[96] proposed a model to calculate the radial tensile strength of tablets from the Ryshkewitch-Duckworth parameters of the individual components of the powder being compressed. Tye *et al.*[95] and Sun[97] have also commented further on this approach. In particular, Tye *et al.*[95] have extended the application to quaternary mixtures. These studies establish the importance of the Ryshkewitch-Duckworth equation for understanding tensile strength of tablets composed of multiple components. Furthermore, they reiterate the importance of porosity as a measure of the outcome of the tableting process. Tablets even though produced by vastly different tablet presses operating at different speeds can be expected to have the same mechanical properties if they have the same porosity. The compaction force or compaction pressure may, however, not be the same if different tablet presses are employed.

Etzler and co-workers[89)] have proposed a model which is similar to that proposed by Wu *et al.*[96)] but which differs from that of the earlier authors by drawing more strongly from the principles of adhesion science. The form of the final equation also differs. According to this model the following relation relating tablet sensile strength to the Ryshkewitch-Duckworth parameters of the component materials is proposed.

$$\tau = \prod_i \left(\tau_{0_i} e^{-k_i \varepsilon}\right)^{\varphi_{vi}} \rightarrow \ln(\tau) = \sum_i \varphi_{vi}\left[\ln\left(\tau_{0_i}\right) - k_i \varepsilon\right] = \ln(\tau_{0m}) - k_m \varepsilon \qquad (28)$$

Eqn. (28) indicates that the Ryshkewitch-Duckworth parameters for a powder composed of several components may be calculated from the Ryshkewitch-Duckworth parameters of the individual components using the following relations.

$$\ln(\tau_{0m}) = \sum_i \varphi_{vi} \ln\left(\tau_{0_i}\right) \qquad (29)$$

$$k_m = \sum_i \varphi_{vi} k_i \qquad (30)$$

Here ϕ_v is the volume fraction of the ith component. The subscript m refers to the mixture. The following shows an example confirming the above two equations.

Further investigations have shown that wet granulation of individual components has no effect on the observed Ryshkewitch-Duckworth parameters. The wet granulation of mixtures containing sodium dodecyl sulfate, in contrast, are found to have lower than expected tensile strength when wet granulated. This result supports the argument that tablet tensile strength results from the adhesion between particles. Recall, that adhesion depends on the properties of the surfaces. Contamination of these surfaces by, for instance, sodium dodecyl sulfate would have the effect of reducing tensile strength. The role of surface chemistry in determining the values of the Ryshkewitch-Duckworth parameters deserves further consideration.

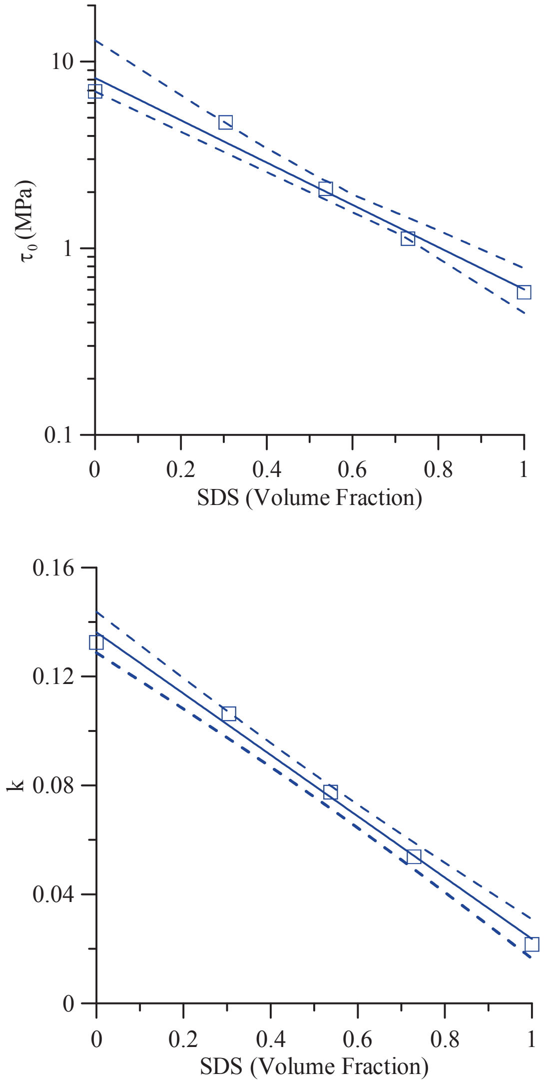

Fig. 9 Ryshkewitch-Duckworth parameters for dicalcium phosphate and sodium dodecyl sulfate mixtures. Results conform to the proposed model and Eqns. (29) and (30). The 90% confidence interval of the fit is indicated the dashed lines. The solid is a least squares fit to the data points.

6. Dry Powder Inhalers

A brief overview concerning dry powder inhalers has been given by Alagusundaram[82)] and Xu and coworkers[98)]. Dry powder inhalers must deliver drugs of respirable size (2-5 μm) to the lung. The adhesion between particles is extremely important to the performance of such inhalers as particle must be seperated and aerosolized. While the design of dry powder inhalers varies, it is typical to have a formulation containing lactose and drug contained in a foil blister or gelatin capsule. Adhesion of particles to the blister walls or variable adhesion between particles is significantly responsible for performance variations in these products. From the data presented above we have learned that the surface chemistry of lactose varies due to the presence of different levels of surface contaminants. The presence of different levels of surface contaminants, furthermore, affects the adhesion of lactose to capsule walls which in turn alters the performance of product. The role of surface contamination in dry powder inhaler performance has been discussed in more detail by Etzler[84]. **Fig. 7** illustrates the role of surface chemistry to adhesion of powder to gelatin capsule walls. Adhesion to capsule walls is a major factor that affects the performance of dry power inhalers.

7. Summary

Both the FDA (U.S. Food and Drug Administration) and ICH (International Conference on Harmonisation) have urged the incorporation of Quality by Design (QbD)[1] into the manufacture of pharmaceutical products[2].

The performance of many pharmaceutical products and processes used for manufacturing pharmaceuticals depends on knowledge of powder properties. The behavior of powders, in turn, depends on the particle shape and size as well as the adhesion and friction between particles. Full implementation of QbD thus requires knowledge of, at least, the above discussed properties and methods to assess these relevant properties.

The relevant properties addressed in this work include:

- particle size,
- particle surface chemistry
- and particle hardness.

Particle sizing is difficult for both philosophical and technical reasons. The pharmaceutical industry employs many methods for particle size analysis but light scattering methods (Mie-Fraunhoffer and PCS) are common. The reported particle size distributions determined by these methods often contain instrumental artifacts. It is important to consider alternate methods, that are less prone to artifacts for particle size analysis. In the pharmaceutical industry it is not common to find rigorous powder sampling protocols in place. Both poor sampling and instrumental artifacts (or limitations) may lead an investigator to improperly assign development or manufacturing problems to particle size.

The adhesion between particles also affects powder properties and the performance of processes and products. The adhesion between particles is affected by both the mechanical and surface chemical properties. The surface chemistry of particles is affected by the area fractions of individual crystal planes. The area fraction of a particular crystal plane can be affected by the choice of solvent used for crystallization or milling. Weakest planes are the most likely to fracture. In addition to the area fraction of various crystal planes, surface contamination affects interparticle adhesion. One of us (Etzler) has found that variable surface contamination of formulation components significantly affects the performance of dry powder inhalers.

It is clear that full implementation of QbD will require further understanding of the role of interparticle interactions in the performance of powders. It will furthermore be necessary to routinely employ appropriate analytical methods to that establish particle size and particle surface chemistry. Routine use of good sampling methods will also required. A considerable amount of work will be required to achieve the level of understanding required for implementation of QbD.

References

1) Juran, J. M. (1992): "Juran on Quality by Design: The new steps for planning quaility in goods and services", 1st ed., New York: The Free Press: A Division of of Simon and Schuster, New York.
2) ICH (2009): "Pharmaceutical Development Q8(R2): Current Step 4 version", ICH Expert Working, Geneva, Switzerland.
3) Kaye, B. H. (1997): "Powder Mixing", New York: Chapman and Hall.
4) Kaye, B. H. (1994): "A Random Walk through Fractal Dimensions". 2 ed., New York:VCH.
5) Jallo, L. J., Chen, Y., Bowen, J., Etzler, F., Dave, R. (2011): Prediction of inter-particle adhesion force from surface energy and surface roughness, J. Adhesion Sci. and Tech., 25, pp.367-384.
6) Sekiguchi, M. (1997): "Adhesion and mechanical strength of a powder bed", Powder Technology Handbook, 2nd ed., eds: Gotoh, Masuda, Higashitani, New York:Marcel Dekker, pp.351-360.
7) Suzuki, M. (1997). "Description of particulate assemblies" Powder Technology Handbook, 2nd ed., eds: Gotoh, Masuda, Higashitani, New York: Marcel Dekker, pp.305-320.

8) Etzler, F. M., Ibraham, T., Burk, T. R., Neuman, R. D. (2002): "Direct adhesion measurements between pharmaceutical materials" , Particles On Surfaces, Vol.7, ed: Mittal VSP, Utrecht, The Netherlands, pp.235-252.

9) Kawashima, Y. (1997): "Solubility and dissolution rate" Powder Technology Handbook, eds: Gotoh, Masuda, Higashitani, New York:Marcel Dekker, pp.217-230.

10) Allen, T. (1990): "Particle Size Measurement", London:Chapman Hall.

11) Etzler, F. M. (2006): "Particle size analysis", Solid State Characterization of Pharmaceuticals, eds: M &A. Zakrzewski, Danbury, CT: ASSA, Inc.. p 493-536.

12) Iococca, R. (2007): Particle size analysis in the pharmaceutical industry, Amer. Pharm. Rev., Vol.10, pp.20-23.

13) Rawle, A. F. (2010): "Analytical tools for suspension characterization" Pharmaceutical Suspenstions: From Formulation Development to Manufacturing, eds: Kuldshreshtha, Singh, Wall, New York: Springer Scence and Business Media, LLC, pp.177-230.

14) Moschwitzer, J. (2010): The role of particle size analysis in the development process of nanosized drug products Amer. Pharm. Rev., Vol.13, pp.98-101.

15) Allen, T. (2003): "Powder Sampling and Particle Size Determination" New York: Elsevier.

16) Etzler, F. M., Deanne, R. (2007): Particle size Analysis: importance of sampling, Amer. Pharm. Rev., Vol.10, p.132.

17) Allen, T. and Khan, A. A. (1970) Critical evaluation of powder sampling procedures, The Chemical Engineer, Vol.238, pp.108-112.

18) Montes-Burgos, A., Walczyk, D., Hole, P., Smith, J., Lynch, I. and Dawson, K. (2010): Characterisation of nanoparticle size and state prior to nanotoxicological studies, J. Nanopart. Res., Vol.12, pp.437-475.

19) Filipe, V., Hawe, A., Jiskoot, W. (2010): Critical evaluation of nanoparticle tracking analysis (NTA) by nanoSight for the measurement of nanoparticles and protein aggregates, Pharm. Res., Vol.27, pp.796-810.

20) Henriquez, R. R., Ito, T., Sun, L., Crooks, R. M. (2004): The Resurgence of coulter counting for analyzing nanoscale objects, The Analyst, Vol.129, pp.478-482.

21) Ito, T., Sun, L., Bevan, M. A., Crooks, R. M. (2004): Comparison of nanoparticle size and electrophoretic mobility measurements using a carbon nanotube-based coulter counter, dynamic light scattering, transmission electron microscopy, and phase analysis light scattering Langmuir, Vol.20, pp.6940-6945.

22) Jillavenkatesa, A., Dapkunas, S. J., Lum, L.H. (2001): "Particle Size Characterization, NIST Recommended Practice Guide, Special Pub, 960-1" Washington,DC: US GOVT Printing Office.

23) Leblanc, J. (1986): "The Shape and Size Characterization of Respirable Dusts", M. Sc. Thesis, Laurentian University.

24) Murphy, R. (1972). "Optical Information Processing Procedures for Determining the Essential Features of Particle Shape", M. Sc. Thesis, Laurentian University.

25) Kaye, B. H. (1986). "Fractal dimension and signature waveform characterization of fineparticle shape", American Laboratory April, p.55.

26) Driscoll, D. F., Etzler, F. M., Barber, T. A., Nehne, J., Neimann, W., Bistrain, B. R. (2001): Physicochemical assessment of parental lipid emulsions: light obscuration versus laser diffraction Intl. J. Pharmaceutics, Vol.219, pp.21-37.

27) Etzler, F. M., Sanderson, M. S. (1995): Particle size analysis: a comparative study of various methods, Part. Part. Syst. Characterization, Vol.12, pp.217-224.

28) Etzler, F. M., Deanne, R. (1997): Particle size analysis: a comparison of various methods II., Part. Part. Syst. Charact., Vol.14, pp.278-282.

29) Zimon, A. (1982): "Adhesion of Dust and Powder", 2nd Ed., New York: Consultants Bureau.

30) Etzler F. M. (2003): "Characterization of surface free energies and surface chemistry of Solids" Contact Angle Wettability and Adhesion, Vol. 3, ed. Mittal, Utrecht, The Netherlands: VSP. pp.219-264.

31) Fowkes, F. M. (1968): Calculation of work of adhesion by pair potential summation, J. Colloid Interf. Sci., Vol.28, pp.493-505.

32) Fowkes, F. M. (1962): Determination of interfacial tensions, contact angles and dispersion forces by assuming additivity of intermolecular interactions in surfaces, J. Phys. Chem., Vol.66, p. 382.

33) Berthelot, D. (1898): Sur le melange des gaz Compt. Rend. Vol.126, p.1857.

34) Chang W. V., Qin X. (2000): "Repulsive acid-base interactions: fantasy or reality", Acid-Base Interactions: Relevance to Adhesion Science and Technology, Vol. 2, ed: Mittal New York: VSP, pp.3-54.

35) Adamson, A. W. (1990): "Physical Chemistry of Surfaces", 4th ed., New York: J.Wiley.

36) Good, R. J. (1993): "Contact angle, wetting and adhesion: a critical review" Contact Angle, Wettability and Adhesion, Utrecht, The Netherlands: VSP. pp.3-36.

37) van Oss, C. J. (1994): "Interfacial Forces in Aqueous Media", New York: Marcel Dekker.

38) Della Volpe, C., Siboni, S. (1997): Some reflections on acid–base solid surface free energy theories, J. Colloid Interf. Sci., Vol.195, pp.121-136.

39) Owens, D. K., Wendt, R. C. (1969): Estimation of the Surface Free Energy of Polymers, J. Appl. Polym. Sci., Vol.13, pp.1741-1747.

40) Good, R. J. (2000): "On the acid/base theory of contact angles" , Acid-Base Interactions: Relevance to Adhesion Science and Technology, Vol 2, ed: Mittal, Utrecht, The Netherlands: VSP. pp.167-171.

41) Fowkes, F. M., Mostafa, M. A. (1978): Acid-base interactions in polymer adsorption, Ind. Eng. Chem. Prod. Res. Dev., Vol.17, pp.3-7.

42) Fowkes, F. M. (1972): Donor-acceptor interactions at interfaces, J. Adhesion, Vol.4, pp.155-159.

43) Vrbanac, M.,D., Berg, J. C. (1991): "The use of wetting measurements in assessment of acid-base interactions at solid-liquid interfaces", Acid-Base Interactions:

Relevance to Adhesion Science and Technology, eds: Mittal, Anderson, Utrecht, The Netherlands: VSP., p. 67.
44) Fowkes, F.M. (1987): role of acid-base interfacial bonding in adhesion, J. Adhesion Sci. Technol., Vol.1, pp.7-27.
45) Drago, R. S., Vogel, G. C., Needham, T. E. (1971): Four-parameter equation for predicting enthalpies of adduct formation, J. Amer. Chem. Soc., Vol.93, pp.6014-6026.
46) Gutmann, V., Steininger, A., Wychera, E. (1966): Donorstarken in 1,2-Dichlorathan Montash Chem., Vol.97, pp.460-467.
47) Gutmann, V. (1978): "The Donor-Acceptor Approach to Molecular Interaction", New York: Plenum.
48) Riddle, F. L., Fowkes, F. M. (1990): Spectral shifts in acid-base chemistry. 1. van der Waals contributions to acceptor numbers, J. Amer. Chem. Soc., Vol.112, pp.3259-3264.
49) Mayer, U., Gutmann, V., Wychera, E. (1975): The acceptor number-a quantitative empirical parameter for the electrophilic properties of solvents, Montash. Chem., Vol.106, pp.1235-1257.
50) Leitte, F. L., Herrmann, P. S. P. (2005): "Application of atomic force spectroscopy (AFS) to studies of adhesion phenomenon: a review", Atomic Force Microscopy in Adhesion Studies, eds: Drelich, Mittal, Leiden: VSP, pp.3-43.
51) Muhlen, E., Nieus, H. (1997): Introduction to atomic force microscopy and its application to the study of lipid nanoparticles. Particle and Surface Characterisation Methods, eds: Muller, Mehnert, Stuttgart: Medpharm Scientific Publishers.
52) Binnig, G., Quate, C.F., Gerber, C. (1986): Atomic Force Microscope, Phys. Rev. Lett., Vol.56, pp.930-933.
53) Etzler, F. M., Drelich, J. (2012): "Atomic force microscopy for characterization of surfaces, particles, and their interactions" Developments in Surface Contamination and Cleaning, eds. Kohli, Mittal, New York: Elsevier, pp.307-332.
54) Gan, Y. (2009): Atomic and subnanometer resolution in ambient conditions by atomic force microscopy, Surface Science Reports, Vol.64, pp.99-121.
55) Viani, M. B., Schaffler, T.S., Chand, A., Reif, M., Gaub, H. E., Hasma, P.K. (1999): Small cantilevers for force spectroscopy of single molecules, J. Applied Phys., Vol.86, pp.2258-2262.
56) Meyer, E. (1992): Atomic force microscopy, Prog. Sur. Sci., Vol.41, pp.3-49.
57) Grasias, D. H., Somorja, G. A. (1998): Continuum force microscopy study of elastic modulus, hardness and friction of polyethylene and polypropylene surfaces, Macromolecules, Vol.31, pp.1269-1276.
58) Cleveland, J. P., Manne, S., Brock, D., Hansma, P. K. (1993): A nondestructive method for determining the spring constant of cantilevers for scanning force microscopy, Rev. Sci. Instrum., Vol.64, pp.403-405.
59) Sader, J. E., Larson, I., Mulvaney, P., White, L. R. (1995): method for the calibration of atomic force microscope cantilevers, Rev. Sci. Instrum., Vol.66, pp.789-3798.
60) Hutter, J. L., Bechhiefer, J. (1993): Calibration of atomic-Force microscope tips, Rev. Sci. Instrum, Vol.64, pp.1868-1873.
61) Levy, R., Maaloum, M. (2002): Measuring the spring constant of atomic microscope cantilevers: thermal fluctuations and other methods, Nanotechnology, Vol.13, pp.33-37.
62) Willing, G.A ., Ibrahim, T. H., Etzler, F. M., Neuman, R. D. (2000): New approach to the study of particle-surface adhesion using atomic force microscopy, J. Colloid Interf. Sci., Vol.226, pp.185-188.
63) Rotsch, C., Radmacher, M. (1997): Mapping local electrostatic forces with the atomic force microscope, Langmuir, Vol.13, pp.2825-2832.
64) Sugisaki, K., Nakagiri, N. (1999): Data processing in force curve mapping, Appl. Surf. Sci., Vol.145, pp.613-617.
65) Mizes, H. A., Loh, K. G., Miller, R. J. D., Ahuja, S. K., Grabowski, E. (1991): Submicron probe of polymer adhesion with atomic force microscopy: dependence on topography and material inhomogeneities, Appl. Phys. Lett., Vol.59, pp.2901-2903.
66) Drucker, W. A., Senden, T. J., Pashley, R. M. (1992): Measurement of forces in liquids using a force microscope, Langmuir, Vol.8, pp.1831-1836.
67) Giebers, M., Kleijn, J. M., Coehn-Stuart, M. A. (2002): The electrical double layer on gold probed by electrokinetic and surface force, J. Colloid Interf. Sci., Vol.248, pp.88-95.
68) Bowen, W.R., Hilal, N., Lovitt, R.W., Wright, C.J. (1999): An atomic force microscopy of the adhesion of a silica sphere to a silica surface - effects of surface cleaning, Colloid Surf. A, Vol.157, pp.117-125.
69) Ibraham, T. H., Burk, T. R., Etzler, F. M., Neuman, R. D. (2000): Direct adhesion measurements of pharmaceutical particles to gelatin capsule surfaces, J. Adhesion Sci. Technol., Vol.14, pp.1225-1242.
70) Drucker, W. A., Senden, T. J., Pashley, R. M. (1991): Direct measurement of colloidal forces using an atomic force microscope, Nature, Vol.353, pp.239-241.
71) Stewart, M. D. (2001): Characterisation of adhesional properties of lactose carriers using atomic force microscopy, J. Pharm. Biomed. Anal., Vol.25, pp.559-567.
72) Johnson, K. L., Kendall, K., Roberts, A. D. (1971): Surface energy and the contact of elastic solids, Proc. R. Soc. London A, Vol.324, pp.301-313.
73) Derjaguin, B. V., Muller, V. M., Toporov, Y. P. (1975): Effect of contact deformations on the adhesion of particles, J. Colloid Interf. Sci., Vol.53, pp.314-326.
74) Yuan, Y., Lenhoff, A. M. (2003): Measurement of mobility of adsorbed colloids by lateral force microscopy, J. Colloid Interf. Sci., Vol.267, pp.352-359.
75) Zamora, R. R. R., Sanchez, C. M., Freire, F. L., Prioli, R. (2004): Influence of capillary condensation of water in nanoscale friction, Phys. Stat. Solid A, Vol.201, pp.850-856.

76) Putman, C. A. J., van der Werf, K. O., de Grooth, B. G., Hulst N. F., Greeve, J. (1999): Tapping mode force microscopy in liquid, Appl. Phys. Lett., Vol.64, pp.2454-2456.
77) Zhong, Q., Innes, D., Kjoller, K., Ellings, V. B. (1993): Fractured polymer/silica fiber surface studied by tapping mode atomic force microscopy, Surf. Sci. Letters, Vol.290, pp.L688-L692.
78) Garcia, R., Perez, R. (2002): Dynamic atomic force microscopy methods, Surf. Sci. Rep., Vol.47, pp.197-301.
79) Heng, J. Y. Y., Bismark, A., Lee, A. F., Wilson, K., Williams, D. R. (2007): Anisotropic Surface Chemistry of Aspirin Tablets, J. Pharm. Sci., Vol.96, pp.2134-2144.
80) Ho, R., Hinder, S. J., Watts, J. F., Dilworth, S. E., Williams, D. R., Heng, J. Y. Y. (2010): Determination of surface heterogeneaty of D-mannitol by sessile drop contact angle and finite concentration inverse gas chromatography, Intl. J. Pharmaceutics, Vol.387, pp.79-86.
81) Heng, J. Y. Y., Bismark, A., Williams, D. R. (2006): Anisotropic surface chemistry of crystalline pharmaceutical solids, AAPS PharmSciTech, Vol.7, pp.E1-E9.
82) Alagusundaram, M., Deepthi, N., Ramkanth, S., Angalaparameswari, S., Mohamed-Saleem, T. S., Gnanaprakash, K., Thiruvengadarajan, V. S., Madhusudhana-Chetty, C. (2010): Dry powder inhalers - an overview, Intl. J. Res. Pharm. Sci., Vol.1, pp.34-42.
83) Beach, E. R., Drelich, J. (2011): Atomic force microscope pull-off force measurements for insulin in contact with acrylonitrile–butadiene–styrene and polypropylene surfaces at various humidities, J. Adhesion Sci. Technol., Vol.25, pp.435-449.
84) Etzler, F. M., Ibrahim, T. H., Burk, T. R., Wiulling, G. A., Neuman, R. D. (2002): “The effect of the acid-base chemistry of lactose on its adhesion to gelatin capsules: conclusions from contact angles and other surface chemical techniques”, Contact Angle, Wettability and Adhesion, Vol. 2, ed: Mittal, Zeist, The Netherlands: VSP, pp.13-44.
85) Cao, X., Morganti, M., Hancock, B. C., Materson, V. M. (2010): Correlating particle hardness with powder compaction performance, J. Pharm. Sci., Vol.99, pp.4307-4316.
86) Cao, X., Materson, V. M. (2008): Evaluating particle hardness of pharmaceutical solids using AFM nanoindentation, Intl. J. Pharmaceutics, Vol.362, pp.163-171.
87) Lao, X., Wiedmann, T. S. (2005): Measurment of process-dependant material properties of pharmaceutical solids by nano indentation, J. Pharm. Sci., Vol.94, pp.79-92.
88) Ramos, K. J., Bahr, D. F. (2007): Mechanical behavior assessment of sucrose using nanoindentation, J. Mater. Res., Vol.22, pp.2037-2045.
89) Etzler, F. M., Bramante, T., Deanne, R., Sienkiewicz, S., Chen, F. J. (2011): Tablet tensile strength: an adhesion science perspective, J. Adhesion Sci. and Tech., Vol.25, pp.501-519.
90) Ryshkewitch, E. (1953): Compression strength of porous sintered alumina and zirconia, 9th Communication to Ceramography. J. Am. Ceram. Soc., Vol.36, pp.65-68.
91) Duckworth, W. (1953): Discussions of Ryshkewitch paper by Winston Duckworth, J. Am. Ceram. Soc., Vol.36, p.68.
92) Doelker, E. (1994): “Assessment of powder compaction” Powder Technology and Pharmaceutical Processes, eds: Chulia, Deleul, Pourcelot, New York: Elsevier, p 403.
93) Barraleta, J. E., Grovera, L., Gaunta, T., Wright, A. J., Gibsonc, I. R. (2002): Preparation of macroporous calcium phosphate cement tissue engineering scaffold, Biomaterials, Vol.23, pp.3063-3072.
94) Nyongesa, F. W., Aduda, B. O. (2004): Fracture strength of porous ceramics: stress concentration vs. minimum solid area models, AJST, Vol.5, pp.19-27.
95) Tye, C. K., Sun, C., Amidon, G. E. (2005): Evaluation of the effects of tableting speed on the relationships between compaction pressure, tablet strength and tablet solid fraction, J. Pharm. Sci., Vol.94, pp.465-472.
96) Wu, C.-Y., Best, S. M., Bentham, A. C., Hancock, B. C., Bonfield, W. (2005): A simple predictive model for the tensile strength of binary tablets, European Journal of Pharmaceutical Sciences, Vol.25, pp.331-336.
97) Sun, C. (2005): Critical roles of porosity in tableting properties characterization and solids formulation development, Amer. Pharm. Rev., Vol.8, pp.105-108.
98) Xu, Z., Mansour, H. M., Hickey, A. J. (2011): Particle interactions in dry powder inhaler unit processes:a review, J. Adhesion Sci. and Tech., Vol.25, pp.451-482.

Author’s short biography

Frank M. Etzler

Dr. Etzler earned a Ph.D. in physical chemistry from the University of Miami. He is currently an Associate Professor of Pharmaceutics in the School of Pharmacy at the Lake Erie College of Osteopathic Medicine (LECOM). Prior to coming to LECOM in 2011, he was the leader of the Material Science Laboratory at Boehringer-Ingelheim Pharmaceuticals for nearly 20 years. This laboratory was responsible for the physical characterization of powders.

Prior to this, Dr. Etzler was a faculty member in pharmaceutics at the University of Kentucky and a faculty member in surface and colloid science at the former Institute of Paper Chemistry.

Mohammad Nasir Uddin

Mohammad Nasir Uddin is an Assistant Professor in School of Pharmacy at Lake Erie College of Osteopathic Medicine, LECOM. He received his M. Sc. in Chemistry from Emory University in 2006 and his Ph.D in Pharmaceutics from Mercer University in 2011. Both institutions are located in Atlanta, GA. He also worked on nano-particle based vaccine development for Human Papillomavirus (HPV) as scientist at CDC in 2010 and 2011. His research interests include particles used in formulation development of vaccines. He is also interested in adhesion of nanoparticulates. His research has lead to 12 peer reviewed papers and 26 scientific presentations.

100 Years of Vitamins: The Science of Formulation is the Key to Functionality[†]

Alexandra Teleki[*], **Andrea Hitzfeld and Manfred Eggersdorfer**
[1] *DSM Nutritional Products Ltd., Nutrition R&D Center Forms and Application*

Abstract

Micronutrients and nutraceuticals such as vitamins, carotenoids, polyunsaturated fatty acids and polyphenols are classes of food ingredients that are essential for human health and well-being. These compounds are rarely added purely to the targeted food application but rather in encapsulated, solid, dry product forms with added functionalities such as improved stability, bioavailability or handling. This review presents some of the industrially most relevant particle technologies, as well as emerging ones, for synthesis and formulation of micronutrients and nutraceuticals. The influence of technological process parameters on product particle physicochemical properties such as size, morphology and structure are highlighted as well as their importance for end-use applications.

Keywords: microencapsulation, vitamin, nutraceutical, micronutrient, formulation

1. The History of Vitamins

In 1912, the Polish biochemist Casimir Funk (1884-1967) coined the term vitamins. The discovery of vitamins as essential factors in the diet was a scientific breakthrough that changed the world! Already in 1906, Frederick Gowland Hopkins indicated that "no animal can live on a mixture of pure protein, fat and carbohydrate" – this started the search for "growth factors" in food. The Dutch physician Christian Eijkman found that a constituent of rice bran can prevent a beriberi-like disease in chickens and Gerret Gryns was the first scientist to adopt the deficiency theory for the etiology of this disease. He stated that the disease breaks out when a substance necessary for the metabolism is lacking in the food.

In 1912, Casimir Funk isolated a bioactive substance from rice bran which was at first given the name "vita-amine". Funk realized that this substance could cure chickens and human patients from beriberi. He published a landmark paper "The etiology of the deficiency diseases" and stated that all "deficiency diseases can be prevented and cured by the addition of certain preventive substances, the deficient substances", for which he proposed the name "vitamines"[1)]. Two years later in 1916, the American biochemist Elmer V. McCollum introduced capital letters to differentiate between vitamin A, vitamin B, vitamin C and vitamin D. Later, vitamin E and vitamin K were added and it was realized that a food containing vitamin B can contain more than one factor and a further differentiation into vitamin B_1, vitamin B_2 and so on was applied.

These observations and findings facilitated the experimental research in the following years enormously. The next three decades were full of scientific breakthroughs in the understanding of the role of vitamins and by 1941, all 13 vitamins had been discovered and characterized. These are now classified as either water- (e.g. vitamin C) or fat-soluble (e.g. vitamin A), as listed in **Table 1**. The scientific breakthroughs were honored with twelve Nobel Awards to 20 Nobel Prize winners. The Nobel Award in Chemistry 1928 was given to Adolf Windaus for his studies on the constitutions of the sterols and their connection with the vitamins. This was followed by the Nobel Prize in Medicine and Physiology in 1929 jointly to Christiaan Eijkman for the discovery of the anti-neuritic vitamin and to Sir Frederick Gowland Hopkins for the discovery of the growth-stimulating vitamins.

[†] Accepted: August 20, 2012

[1] P.O. Box 2676, CH-4002 Basel, Switzerland.
[*] Corresponding author:
E-mail: alexandra.teleki@dsm.com
TEL: +41-61-815-80-49

ⓒ 2013 Hosokawa Powder Technology Foundation

Table 1 Main groups of micronutrients and nutraceuticals

Micronutrients & Nutraceuticals	Major formulation challenge
Water-soluble vitamins Vitamin B_1 (thiamine), vitamin B_2 (riboflavin), vitamin B_3 (niacin), vitamin B_5 (pantothenic acid), vitamin B_6 (pyridoxine), vitamin B_7 (biotin), vitamin B_9 (folate), vitamin B_{12} (cyanocobalamin), vitamin C (ascorbic acid)	*chemical stability (oxidation, hydrolysis, light, temperature, pH), sensory (taste), discoloration*
Fat-soluble vitamins[2] Vitamin A (retinol, retinyl esters, retinal, retinoic acid), carotenoids, vitamin D (ergocalciferol, cholecalciferol), vitamin E (α-tocopherol, tocotrienol), vitamin K (phylloquinone, menaquinone)	*chemical stability (oxidation, hydrolysis, light, temperature, pH), solubility in water, bioavailability*
Polyunsaturated fatty acids (PUFAs) e.g. omega-3 fatty acids such as docosahexaenoic acid (DHA)	*chemical stability (oxidation), sensory (smell, taste)*
Polyphenols[3, 4] e.g. epigallocatechin gallate (EGCG), resveratrol	*chemical stability (temperature, oxygen, light, pH), bioavailability, sensory (taste)*
Minerals e.g. Fe, Zn, Ca, Mg	*sensory (taste)*
Plant extracts[5, 6]	*chemical stability, sensory*

Already in the 1940s, authorities had started to establish dietary standards and nutrient requirements (recommended daily allowance) for the optimal intake of vitamins depending on age, gender and risk groups. In order to secure a sufficient intake of vitamins for the full population, a number of countries implemented fortification programs of staple food; today food fortification is established in more than 60 countries. Examples are the fortification of flour or sugar with vitamin A especially in low-income countries, the fortification of flour with folic acid in the US, Canada and Latin American countries, the fortification of margarine with vitamin A and D or the fortification of milk and juices with vitamin D. The World Bank's assessment of fortification was: “probably no other technology available today offers as large an opportunity to improve lives and accelerate development at such low cost and in such a short time” . Today, there is a wide consensus amongst scientists about adequate vitamin intake and the relation to health and healthy aging. Science continues to provide new approaches and insights on the role of vitamins and to demonstrate that “the identification of the role of vitamins was one of the most important contributions of science to mankind”.

2. Micronutrients and Nutraceuticals: A Formulation Challenge

The understanding that micronutrients are essential for human and animal growth and health[7] and that they have to be part of the diet was a major stimulus for nutrition science. Research was extended also to nutraceuticals and health ingredients such as polyunsaturated fatty acids, oily plant extracts and fruit powders that provide certain health benefits (but are not essential)[8]. Subsequent to the recognition of the vitamins and the discovery of their function it became clear that breakthroughs in the production, formulation and application would have to be achieved in order to allow them to be used by humans and animals. This inspired scientists in pharmaceutical companies in Europe and the US to develop synthetic routes and formulation technologies. The first production of a vitamin on a technical scale was achieved by Hoffmann-La Roche in 1934 for vitamin C based on a combined fermentation and chemical process developed by Tadeus Reichstein. In the following years all vitamins became available via chemical synthesis, fermentation or extraction from natural materials. Industrial production was not the complete solution yet, and new challenges arose with the incorporation of micronutrient and nutraceuticals in end-user applications such as tablets, vitamin waters, beverages, yoghurts and other foodstuffs.

Especially lipids and fat-soluble vitamins[2] are difficult to add to food products (e.g. to a hydrophilic environment such as a beverage), and are often chemically unstable to, e.g. oxidation, hydrolysis, light and heat[9, 10]. New technologies had to be explored and again know-how and formulation competencies of pharmaceutical companies gave the basis for the development of vitamin forms. This offered opportunities to provide vitamins for humans and animals for optimal growth and health. Therefore, micronutrients and nutraceuticals are nowadays rarely sold in pure form and are mostly delivered in microencapsulated product forms to protect the active ingredient from the surrounding environment[11-14]. Thereby the stability and shelf-life of the compounds are prolonged and they can be released in a controlled and tailored manner. Further benefits of microencapsulation processes include easier handling, improved sensory properties with respect to appearance and taste and uniform dispersion of low-concentrated actives[15]. Innovation in colloid and nanosciences facilitates the development of product forms for different applications. Progress in formulation results from close

Table 2 Commercially most relevant materials for microencapsulation in the food industry[16, 23]

	Animal	Plant	Marine	Microbial
Carbohydrate 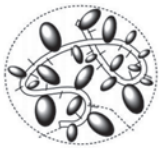	chitosan	*tree exudates:* gum arabic, gum karaya, gum ghatti, gum tragacanth *plants:* starch, cellulose *extracts:* guar gum, pectin, galactomannans *polysaccharides:* soluble soy polysaccharide, maltodextrins	carrageenan agar alginate	xanthan gellan dextran curdlan pullulan
Protein 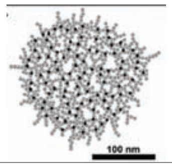	gelatin casein whey egg white lactoglobulin	gluten soy pea rice sorghum lupine zein		
Lipid 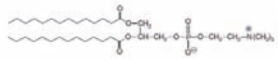	fatty acids glycerides / waxes phospholipids Shellac	fatty acids glycerides waxes phospholipids		

Structural schemes of gum arabic[23] (carbohydrate), casein micelle[24] (protein) and phosphatidylcholine[16] (lipid).

cooperation between basic science carried out at universities and applied science in industry. However, the knowledge of formulation is often a special expertise of companies, protected by patents and not available in textbooks.

Particle properties in these dry product forms are of the utmost importance to achieve the desired performance in target applications and have to be carefully controlled during their synthesis. For example, particle size can govern the optical appearance and sensory perception of the product as well as the dissolution rate and bioavailability of the active. Particle morphology and shape influence flowability, ease of handling and processing of the powders. For example, during the preparation of multivitamin-multimineral tablets, several nutraceutical components and excipients are blended. The mixture must be uniform (no segregation) and free-flowing for accurate dosing in the tabletting equipment. Encapsulates are traditionally classified as reservoir (core-shell) or matrix-type spherical particles[16], however, other shapes and morphologies such as rods or irregular shapes as well as aggregates and agglomerates also have to be considered. The internal structure and composition such as porosity, crystallinity and glass transition temperature would affect the stability and shelf-life of the products. Controlled release and stability of encapsulated active compounds can be achieved by the proper selection of the matrix material and its concentration[17-20]. Common encapsulation materials in the food industry are listed in **Table 2**. One of the central issues in the design of an optimal encapsulation material is the molecular mobility through the matrix as this affects the stability of the active ingredient. It has been shown that small quantities of low-molecular-weight compounds such as glycerol, sucrose or maltodextrin, in combination with high-molecular-weight carbohydrates improve storage stability[21]. The molecular mobility can be understood with the concepts of glass transition of amorphous biopolymers as well as the molecular free volume present in their disordered matrix. The oxygen diffusivity in a glassy carbohydrate matrix depends exponentially on the radius of the free volume element[22]. Therefore, already small differences in free volume can have a substantial impact on degradation of the encapsulated bioactive substance via chemical reactions, e.g. fish-oil lipid oxidation.

Here, the synthesis and formulation technologies (not solely limited to microencapsulation) of micronutrients and nutraceuticals are reviewed that result in solid physical morphology. Emphasis is placed on resulting particle properties such as size and shape and their influence on performance in target applications. Industrially most relevant microencapsulation technologies such as spray drying and extrusion will be covered. Novel technologies that are not yet applied on an industrial scale and mostly yield nanoscale particles will also be highlighted. Although the application of nano-sized delivery systems in foods is still under some debate, the worldwide sales of nanofood products has grown and nanotechnologies are applied by several major food companies[25]. Emulsion technologies that are often part of encapsulation processes in the liquid state especially of lipophilic compounds will not be described here, and the reader is kindly referred to recent reviews focused on this topic[26-29]. However, emulsions are often converted from the liquid state to dry powders[3] by technologies such as spray- or freeze-drying that are covered in the following text. Encapsulation technologies such as inclusion complexation[30, 31] and liposomes[32-34] will also not be discussed as their use in foods is limited due to regulatory, cost or performance issues[16]. Finally, a focus is placed on recent advances, and therefore primarily literature published within the past 5 years is reviewed.

3. Particle Technologies from Nano to Macro Sizes

Particle technologies applied for the synthesis and formulation of nutraceuticals in industry or academia span several length scales from nano to macro sizes (**Table 3**). Product properties are to a large extent governed by the particle size. Therefore, performance in the final application can be modulated by the proper choice of particle synthesis and formulation technology (**Table 3**), which are typically classified as either 'top-down' or 'bottom-up' approaches[8]. The former involves the break-up of larger particles or droplets to smaller ones using mechanical energy in classic processes such as milling[35] or emulsification[26-28]. In the case of emulsions, the smaller droplets formed are then typically stabilized by surface-active compounds, so-called emulsifiers, such as low-molecular-weight surfactants, proteins or polysaccharides. These emulsifiers adsorb at the droplet surface thereby reducing the interfacial energy and facilitate droplet disruption during processing and/or prevent droplet coalescence[28]. The final microencapsulated product particle is then formed during the drying step, e.g. by spray drying[36], or by directly cooling the emulsion to form solid lipid nanoparticles[26]. In the 'bottom-up' approach, individual components such as molecules, monomers or ions are assembled into larger structures or particles using a physical or chemical process[8] such as flame spray pyrolysis or precipitation/crystallization. These processes mostly yield particles of the pure compounds in the nanometer size range. On the other hand, e.g. extrusion technology can produce macro-sized particles with incorporated nutraceuticals that can be directly applied in the final food application.

Industrially most relevant as well as emerging novel technologies for the synthesis and formulation of nutraceuticals will be described in the order of the resulting particle sizes from nano to macro, though a certain overlap between the various technologies exists (**Table 3**).

3.1 Flame spray pyrolysis

Flame spray pyrolysis (FSP) is a bottom-up approach for the synthesis of nanostructured materials[37]. Traditionally and on an industrial scale, vapor-fed flame reactors have been utilized for the synthesis of metal oxide nanoparticles such as SiO_2 or TiO_2. The emergence of FSP technology, where a liquid precursor solution, emulsion or slurry is sprayed and ignited, enabled the development of functional nanostructured materials with a first break-through in the synthesis of highly active supported noble metal catalysts[38]. In recent years, this has been followed up by research on bio-related compounds for dental, orthopedic and even nutritional applications.

Rohner *et al.*[39] produced amorphous $FePO_4$ by FSP with closely controlled particle characteristics (**Fig. 1**). Water-soluble, highly bioavailable Fe compounds such as $FeSO_4$ often cause unacceptable changes in the color or taste of foods, whereas poorly water-soluble Fe compounds such as $FePO_4$, although more stable in foods, tend to have a low bioavailability. The absorption of the latter in the human body can be improved by decreasing their size to the nanoscale[40], e.g. by a bottom-up approach such as FSP. An organic Fe-containing precursor solution is atomized through conventional air-assist or ultrasonic nozzles during FSP synthesis[37]. The thus formed spray is ignited by rather small pilot flames and the organic solution is combusted. Particles are formed by nucleation from the gas phase and grow by surface reaction and/or coagulation and subsequent coalescence into larger particles[37]. The size of the as-produced $FePO_4$ nanoparticles (**Fig. 1**) can be precisely controlled by FSP process parameters such as precursor composition or precursor feed rate to the reactor. The chemical composition of FSP-made particles can also be tailored to produce multicomponent compounds[37]. Combined Fe/Zn-containing nanoparticles[41] as well as Mg- or Ca-doped Fe_2O_3[42] have been produced by FSP for iron food fortification in foodstuffs such as rice, flour or dairy products. The nano-sized particles have high specific surface areas (SSA; up to 200 m^2/g)[41] that ensure their high solubility and bioavailability[41, 43]. Each primary, single, constituent particle is dense and spherical[39]. However, during synthesis, multiple particles can assemble into larger

Table 3 Common synthesis and formulation technologies for nutraceuticals

Technology	Particle Morphology	Size (μm)	Active	Processing aids Raw materials	Solubility
FSP		0.01 – 0.1	minerals	organic solvents	hydrophilic
SLN **NLC**	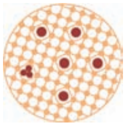	0.1 – 100	carotenoids lipophilic vitamins	triglycerides fatty acids waxes	lipophilic
Precipitation		0.1 – 100	carotenoids polyphenols	supercritical fluids	hydrophilic lipophilic
Spray Drying	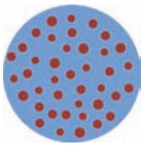	10 – 100	PUFA oily extracts	maltodextrin starch gum arabic	hydrophilic
Spray Chilling	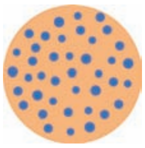	10 - 1000	hydrophilic vitamins minerals	waxes	lipophilic
Complex Coacervation	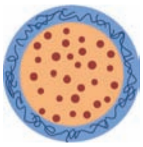	10 – 1000	carotenoids lipophilic actives	gelatin & gum arabic	(hydrophilic)
Microbeads	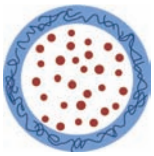 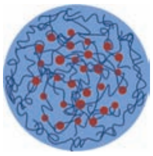	10 – 5000	polyphenols lipophilic actives	alginates	hydrophilic
Extrusion	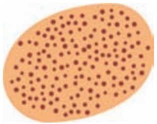 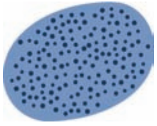	500 - 5000	minerals, hydro- & lipophilic actives	maltodextrin starch waxes	hydrophilic lipophilic

● lipophilic active ● hydrophilic active

● hydrophilic matrix ● hydrophilic gel ● lipophilic matrix

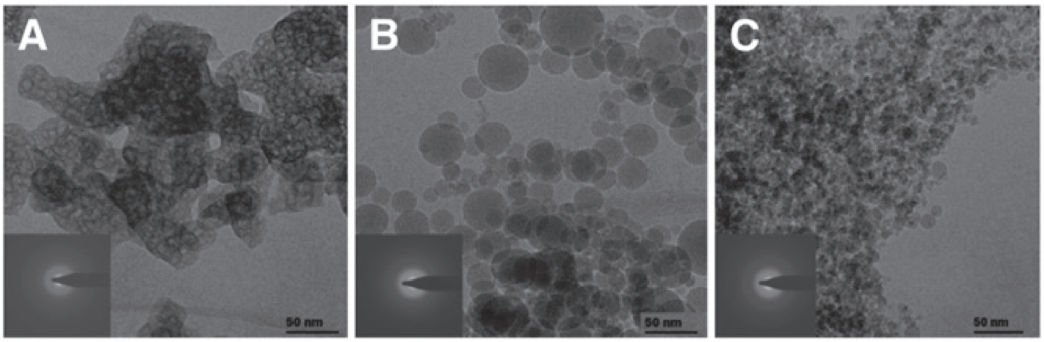

Fig. 1 Transmission electron microscope (TEM) images of commercial (a: SSA = 33 m^2/g) and FSP-made (b,c: 69 and 195 m^2/g, respectively) $FePO_4$ particles. The FSP-made $FePO_4$ particles were dense and spherical, while the commercial ones exhibited an irregular and highly porous structure. The particle size calculated from specific surface area measurements corresponds to 11 nm for the small, FSP-made particles (c). The SAED (selected area electron diffraction) patterns in the insets are characteristic of an amorphous substance for all three compounds39).

fractal-like structures, so-called aggregates or agglomerates held together by chemical or physical bonds, respectively37). The presence of agglomerates can actually facilitate the powder handling and they can also easily be broken up to their constituent aggregates and/or primary particles, e.g. by ultrasonication or high-pressure dispersion44).

The *in vivo* bioavailability of these FSP-made Fe and Fe/Zn compounds in rats was comparable to the golden standard $FeSO_4$, and no tissue accumulation could be detected43). Thus the nanosizing of such poorly water-soluble Fe compounds is a promising approach to increase their absorption in the human body and their nutritional value, though further toxicological studies also in humans are required before this technology can be applied industrially40). From a technological point of view, the scale-up of FSP reactors from laboratory to pilot scale is feasible and has already been realized in industrial-oriented settings45).

3.2 Solid lipid nanoparticles (SLN) and nanostructured lipid carriers (NLC)

An emerging type of encapsulation system are lipid nanoparticles. The first and second generations are termed solid lipid nanoparticles (SLN) and nanostructured lipid carriers (NLC), respectively46-50). Lipid nanoparticles have been widely studied for pharmaceutical and cosmetic applications where nanotechnologies can be implemented more readily. Their potential in food and agricultural industries has recently also been highlighted51, 52). In general, lipid nanoparticles can be compared with conventional liquid emulsions in the sense that lipid droplets stabilized by a surfactant are dispersed in an aqueous continuous phase. However, in the case of SLN or NLC, the lipid phase is either fully or partially solidified26, 50). The lipids used to prepare both SLN and NLC are typically triglycerides, fatty acids, waxes and partial glycerides50). Some of the main advantages associated with SLN are high encapsulation efficiencies, good physical stability, no organic solvents required during synthesis, easy large-scale production with cheap raw materials and a controlled release profile of the active substance due to the solid matrix50, 52). SLN typcially crystallize with imperfections in their crystal lattice after preparation, which also allows the incorporation of active substances. However, during storage, a polymorphic transition to lower-energy crystal lattice arrangements can occur resulting in the expulsion of the incorporated active substance. In order to overcome this drawback of SLN, NLC were developed that exhibit a less ordered crystal lattice arrangement by blending solid and liquid lipids. The imperfections in NLC also allow for a higher loading of active substances compared to SLN50, 53).

Lipid nanoparticles are commonly prepared by forming an oil-in-water emulsion (at a temperature above the melting point of the lipid phase) and then cooling the emulsion so that the dispersed lipid phase completely or partially solidifies50). The preparation of a fine emulsion is crucial in order to obtain particle sizes in the nano range with preferably narrow polydispersity for the product SLN or NLC. Production techniques include, e.g. melt homogenization, melt microencapsulation and cold homogenization, which have all been reviewed elsewhere51).

Mainly lipophilic nutraceuticals have been incor-

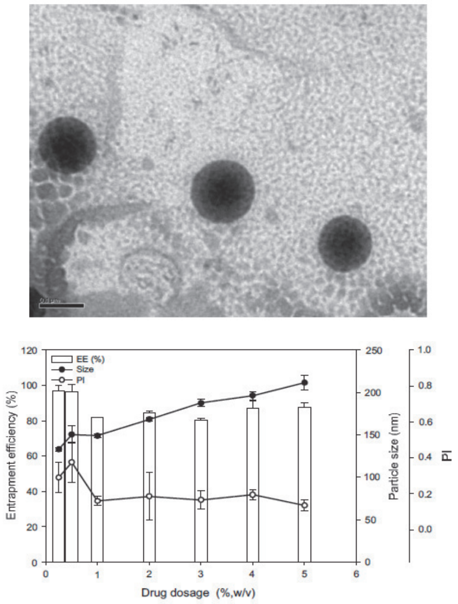

Fig. 2 TEM image (scale bar: 100 nm) of vitamin-K_1-loaded SLN (left) and the effect of the vitamin K1load on the particle size, entrapment efficiency (EE) and polydispersity index (PI) (right). The incorporation of more vitamin K_1 into the SLN increased the particle size due to incorporation of the vitamin into the matrix of the lipid nanoparticles[58].

porated into lipid nanoparticles, as they can enhance the chemical stability of these active substances that are sensitive to light, oxidation and hydrolysis[50]. Several studies have demonstrated the incorporation of carotenoids such as lutein[53, 54] or β-carotene[55-57] into NLC. Liu *et al.*[53] developed lutein-loaded NLC by optimizing the concentration of lipophilic and hydrophilic surfactants during their preparation. The lutein-loaded NLC had an imperfect crystalline lattice and a spherical morphology with particle sizes as small as 130 nm. However, the particle size increased with increasing lutein load due to entrapment of the active substance in the matrix of the nanoparticles. The encapsulated lutein was effectively protected in the presence of a simulated gastric fluid, and slowly released lutein *in vitro* into simulated intestinal fluid[53]. The particle sizes of NLC loaded with β-carotene were stable and did not exhibit polymorphic transitions after 7 months of storage at 4-8℃ , which could make them feasible in beverage applications[57]. Thrandur *et al.*[56] emphasized the proper choice of surfactants during NLC manufacture to improve the protection of β-carotene against chemical degradation. The role of the surfactant is dual, as it controls the formation of the crystal lattice structure during synthesis and stabilizes it during storage.

Lipophilic α-tocopherol[55], vitamins K_1[58] and A[59-61] have also been incorporated into NLC. The reported concentration of encapsulated active substance is typically quite low, e.g. 2% for vitamin A palmitate[59] and <5% for vitamin K_1[58]. Similarly to lutein-loaded NLC[53], the SLN size increased with increasing vitamin K_1 content (132 and 212 nm for 0.25 and 5.0% vitamin K_1, respectively) and furthermore the entrapment efficiency decreased (**Fig. 2**)[58]. Vitamin-K_1-loaded SLN were stable after 4 months with respect to particle size and vitamin content if stored at temperatures < 25℃. The stability of NLC loaded with vitamin A palmitate was improved by freeze-drying[61]. Cryoprotectants such as glucose or mannitol were added during freeze-drying in order to prevent particle aggregation resulting in the sizes 200 – 250 nm in the dry product form[61].

3.3 Precipitation

Precipitation or crystallization is a bottom-up approach for the synthesis of nano- to micron-sized particles. It was mainly developed in the pharmaceutical industries to increase the aqueous solubility and oral bioavailability of poorly water-soluble drugs[62, 63]. Product properties such as particle size, morphology and surface properties can be more closely controlled by precipitation methods compared to classic top-down approaches such as milling[64]. The nucleation and growth kinetics dictate the final particle size and are controlled via supersaturation[63]. However, the precipitation process is more challenging compared to a relatively simple milling method. The high surface area formed by precipitation needs to be rapidly stabilized to avoid aggregation/agglomeration, recrystallization and Ostwald ripening[62, 63]. For example, the Ostwald ripening of β-carotene nanoparticles has been investigated both numerically and experimentally[65]. It was shown that the particle dispersions are more stable the narrower the initial size distribution, as the difference in solubility between small and large particles decreases[65].

Precipitation approaches have mainly been applied to carotenoids[66-73] and polyphenols[3] amongst the micronutrient and nutraceutical compounds, and are mostly carried out with supercritical fluid technologies. In the supercritical gas phase, carbon dioxide is most commonly used as it is inert, non-toxic and has a low supercritical temperature ideal for heat-sensitive materials[64]. Carotenoids have a low solubility in supercritical CO_2 and therefore the CO_2 is used as an antisolvent in such precipitation processes[70]. Particle size and morphology can be controlled by

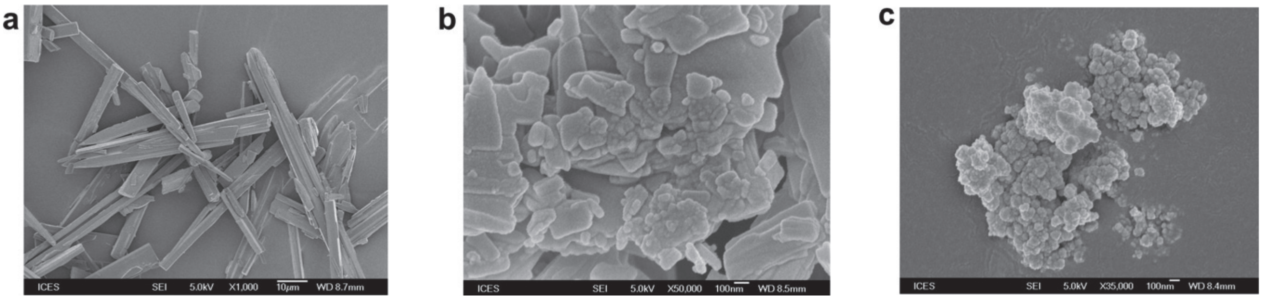

Fig. 3 Scanning electron microscopy (SEM) images of commercial *trans*-resveratrol particles (a) as well as after precipitation without (b) and with (c) HPMC[74].

antisolvent precipitation process parameters such as temperature and pressure, generally resulting in mean sizes between 1 and 200 µm or even smaller[70]. For example, the mean particle size of *trans*-resveratrol was reduced from 560 to 230 nm by decreasing the precipitation temperature from 25 to 5℃[74]. The *trans*-resveratrol particles were stabilized by adsorption of hydroxypropyl methylcellulose (HPMC) on the particle surface (**Fig. 3**). The commercial *trans*-resveratrol particles were needle-shaped and had particle sizes ranging between 20 and 100 µm (**Fig. 3a**). Precipitation without HPMC resulted in irregularly shaped particles several microns in size (**Fig. 3b**), while aggregates of almost spherical particles ~240 nm in size were formed in the presence of HPMC (**Fig. 3c**)[74]. The saturation solubility and dissolution rate of precipitate *trans*-resveratrol nanoparticles were significantly higher compared to the commercial starting material and could be attributed both to the decrease in particle size as well as to crystallinity[74].

Active compounds can also be directly encapsulated by co-precipitating them simultaneously with a second component such as a biopolymer or a sugar, forming either a polymer coating around the active compound, polymer particles with the active compound incorporated or co-crystals with the individual components connected by non-covalent interactions[3, 69, 70, 73, 75]. For example, the solubility of pterostilbene can be dramatically increased by forming co-crystals with compounds of a significant aqueous solubility[75, 76]. The concentration ratio between the active compound and the biopolymer during co-precipitation has a great influence on the final particle morphology, encapsulation efficiency and yield[69, 70]. Green-tea polyphenols have been co-precipitated and encapsulated with a biodegradable polymer poly-ε-caprolactone[77]. The product particles were rather spherical, 3 – 5 µm in size with a narrow particle size distribution but a high degree of agglomeration. A high fraction of the polyphenols was entrapped in the crystalline domains of the polymer and can thus only be released by matrix degradation, a process that may take months[77].

3.4 Spray drying

Spray drying as an encapsulation process was introduced in the 1930s[9, 10] and is still the most frequently used technology in the food industry[4]. The process is relatively cheap, straightforward and flexible, and produces stable particles of high quality[9, 18, 36, 78]. It has been used to encapsulate and protect a range of lipophilic micronutrient and nutraceutical compounds such as fish oil, vitamins and polyphenols[15, 19, 79-82]. For many years, the spray drying of heat-sensitive active compounds was a challenge due to high process inlet temperatures. However, process optimization and control of the temperature has now also enabled the spray drying of sensitive active compounds such as lycopene, anthocyanins and β-carotene[36, 81, 83, 84].

In a spray drying process, a liquid product is atomized in a hot gas current to instantaneously evaporate water and obtain a dry powder. The initial liquid feed can be a solution, an emulsion or a suspension[3, 15]. The three main steps of microencapsulation by spray drying are preparation of the dispersion or emulsion, homogenization, and finally atomization of the

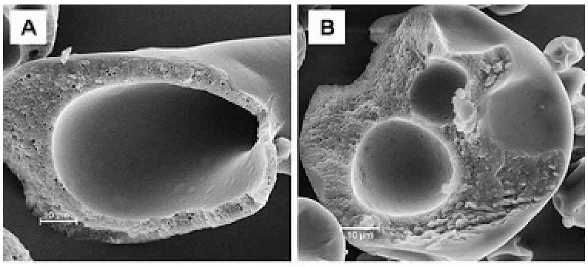

Fig. 4 Scanning electron micrographs of spray-dried fish oil microcapsules. A higher inlet/outlet temperature results in lower-density powders as the particles are elongated with large volumes of included air (a: 210/90℃; b: 160/60℃)[78].

mass into the drying chamber[9]. The particle size and shape of spray-dried products depend to a large extent on the initial feed properties (e.g. solution viscosity, matrix materials and their concentration in the solution) as well as on the process parameters (e.g. nozzle geometry, tower height, inlet temperature). Typically, spray-dried products are rather fine powders of spherical particles 10 - 100 μm in size. However, with an adequate set of process parameters available, large-sized particles (2 – 3 mm) can also be obtained[3, 9]. Wide size distributions are not uncommon due to the droplet size distribution in the liquid spray.

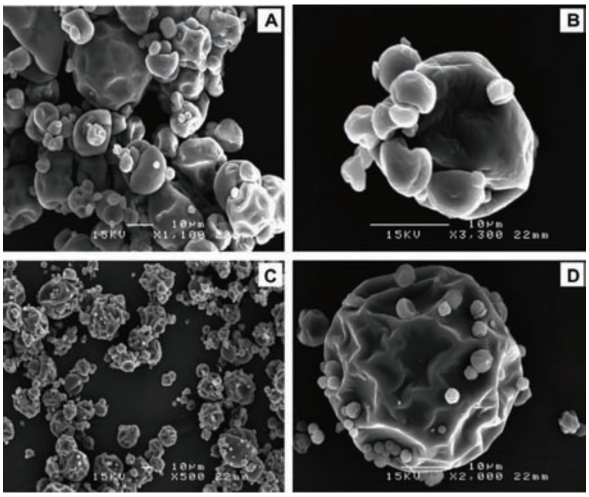

Fig. 5 Scanning electron microscope images of fish oil microcapsules spray-dried with WPC (a,b) or modified food starch (c,d)[87].

The influence of process parameters on product particle properties has been investigated in several studies[9, 78, 85, 86]. The oil droplet size in the emulsion should be rather small and the viscosity should be low enough to prevent air inclusion and the formation of elongated, large particles[78]. Furthermore, a low emulsion droplet size results in a lower amount of unprotected (fish) oil on the surface of the particles that is essential for the shelf-life of the product[87]. A low inlet temperature facilitates the formation of dense particles with a spherical shape (**Fig. 4**), smooth surfaces and a uniform particle size distribution[78, 86]. At higher temperatures, the water evaporation rates increase and yield irregular particle shapes due to cycles of rapid wall solidification, inflation and collapse[78]. However, the choice of too low an inlet temperature results in inefficient drying and powder agglomeration[78, 86, 88].

Matrix materials used for spray drying must be soluble in water at an acceptable level and available for food applications, this narrows down the available choices[15]. Maltodextrins were the most widely applied matrix materials for spray drying in the past[3]. Nowadays, research focuses on combinations of mainly plant-based materials to obtain particles with improved protective barriers. Jafari *et al.*[87] spray-dried fish oil with either whey protein concentrate (WPC) or modified food starch as surface-active biopolymers. The particles produced with modified food starch had more surface dents and shrinkage compared to WPC (**Fig. 5**) that could be attributed to a slower skin formation during drying[87]. Therefore,

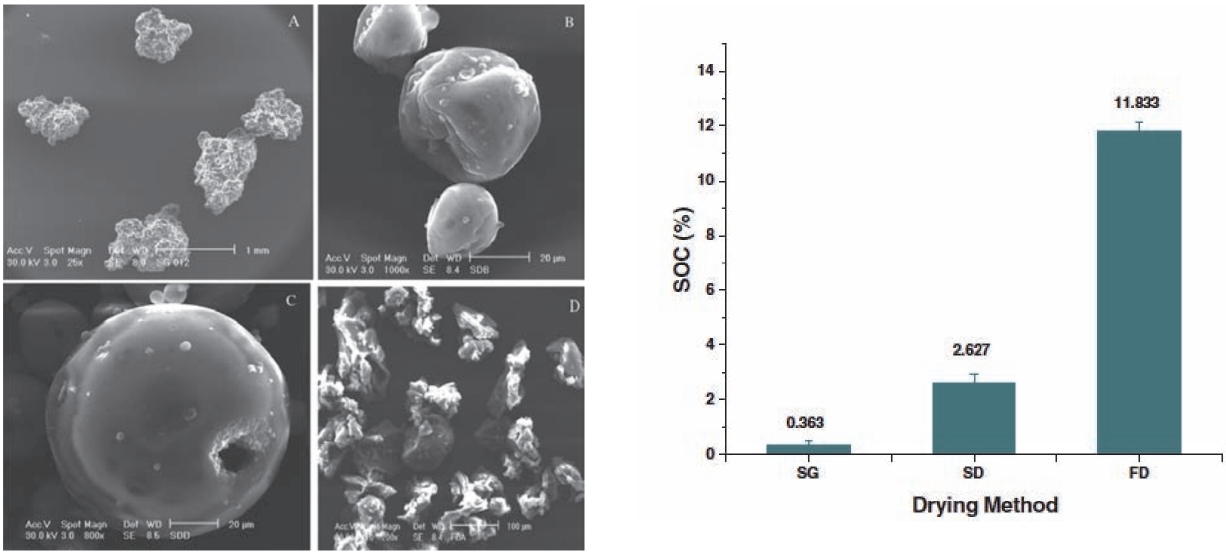

Fig. 6 Scanning electron micrographs of fish oil microcapsules produced by spray granulation (SG; a), spray drying (SD; b,c) or freeze drying (FD; d). The lowest surface oil content (SOC) was found for the spray-granulated product[93].

the fish oil was better entrapped in the modified food starch formulation. Similarly, Drusch *et al.*[89] found that a higher protein (caseinate) content in fish oil microcapsules leads to an increase of lipid oxidation during storage. Furthermore, an excess of protein increased the free volume which could negatively affect oxygen diffusion into the capsules[89]. Alginate, a marine carbohydrate, has been combined with starch as wall materials for the spray drying of fish oil microcapsules[90]. The addition of alginate resulted in a higher oil load capacity and in quite spherical particles with a high protection of the fish oil against oxidation. Microcapsules with up to 50% fish oil loading and > 90% encapsulation efficiency have been produced with sugar beet pectin[17, 88]. Nevertheless, residual metal ions in sugar beet pectin accelerate the fish oil oxidation, resulting in poor storage stability. Blends of maltodextrin and apple pectin have also been investigated as encapsulation materials for polyphenols[91]. The combination of pectin with maltodextrin improved the storage stability and sensory properties of the product microcapsules compared to maltodextrin alone.

3.5 Freeze drying

Freeze drying is considered an alternative technology to encapsulate heat-sensitive compounds, as the active compound does not experience high temperatures during processing[92]. Although spray drying is considered an energy-intensive process due to its poor heat utilization, freeze drying remains a considerably more expensive technology[9]. Therefore, at least on an industrial level, freeze drying cannot yet be considered an alternative to spray drying and requires further research. Anwar *et al.*[93] made a comparative study of spray drying, spray granulation and freeze drying for the encapsulation of fish oil (**Fig. 6**). The microcapsule product stability decreased in the order spray granulation > spray drying > freeze drying. This could be attributed to the process drying temperature: a longer residence time at a lower temperature was found favorable for a lower oxidation of the fish oil. Although the temperature during freeze drying is very low, the resulting particle morphology is porous, irregular and flake-like, which allows oxygen diffusion[93].

3.6 Spray chilling

A similar process to spray drying is spray chilling or spray cooling where a molten liquid is atomized into cooled or chilled air. The resulting droplets solidify and form prills or powders that are solid at room temperature. The same processing equipment as for spray drying can be used[94]. Common spray-chilled carriers for encapsulation are fats, waxes, polyethylene glycols, fatty acids and fatty alcohols (**Table 2**)[16]. Unlike spray drying, spray chilling does not involve the evaporation of water around the core[15]. However, the resulting products are not water-soluble and therefore their application should not require this function. An advantage of spray cooling is the possibility to produce different particle sizes, ranging from about 10 to 1000 µm (**Table 3**)[11]. Wegmüller *et al.*[95] investigated the triple fortification of salt by spray cooling a mixture of vitamin A, iron and iodine in a hydrogenated palm fat matrix. The active compounds were quite stable during storage but high losses were found during processing. This process is nevertheless not as common for the microencapsulation of nutraceuticals as spray drying.

3.7 Complex coacervation

Coacervation is a liquid-liquid phase separation of an initial solution of one or more hydrocolloids into two aqueous phases: a hydrocolloid-rich phase (coacervate) and a hydrocolloid-lean phase[16, 96]. It is one of the oldest techniques of encapsulation and only a few studies have been published on this technology in the past years for micronutrients and nutraceuticals. Nevertheless, the production cost of particles by complex coacervation is still very high, and this technology is therefore only suitable for the microencapsulation of high-value active or for unstable compounds, e.g. polyphenols[4]. Fish oil coacervates are added to a number of food products including bread, yoghurt, milk and infant formulae, and it has been shown that they are as bioavailable and bioequivalent as standard fish oil soft-gel capsules[97]. Complex coacervates are typically made from an oil-in-water emulsion with oppositely charged proteins and polysaccharides, e.g. gelatin and gum arabic[98], and the process is carried out in five steps involving polymer dissolution and hydration, emulsification (formation of the core), coacervation (formation of the shell), hardening and washing/separation[96]. Coacervate particles are often not perfectly spherical but have rather an oval shape[4, 16]. The slurry containing the coacervates can also be spray-dried or fluid-bed-dried to convert it into a dry powder, however, this might result in a loss of the initial structure[16, 97, 98]. Important process parameters include pH, ionic strength, temperature, molecular weight and concentration of the polymers that also determine the solubility of the resulting coacervates[4, 96, 98, 99]. Gum arabic can be replaced by

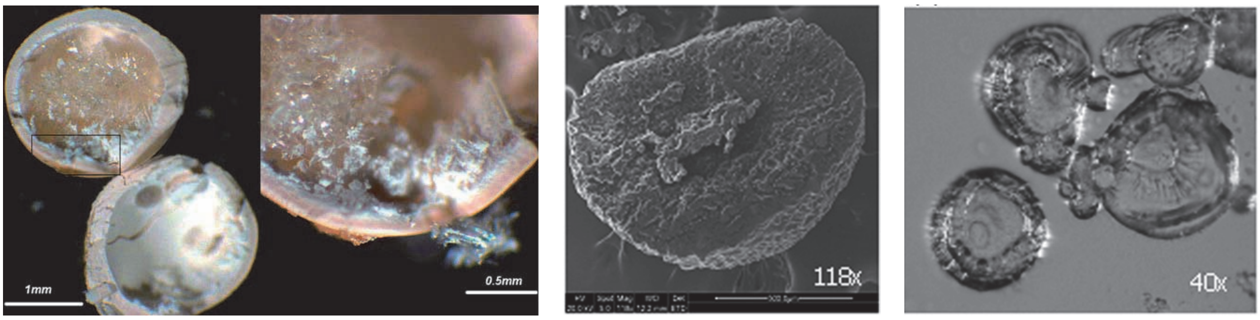

Fig. 7 Cross-section of hollow core-shell beads synthesized from MCE and EGCG solutions (left)[107] and chitosan beads with vitamin A palmitate embedded in the core matrix and surrounded by double chitosan-alginate and calcium-alginate shells[104].

other negatively charged molecules such as pectin, carrageenan or alginate and gelatin by whey proteins[16, 100-102]. Recently, hydrophobic nutraceuticals such as vitamin D_2 or fish oil have been entrapped in electrostatically stable nanoparticles < 100 nm in size. The small nanocomplexes yield transparent solutions and can be used in clear acid beverages[101, 103].

3.8 Gel-particle technologies

Gel-particle technologies produce microparticles (or microbeads) composed of a biopolymer network that entraps the active compound[16]. The particle morphology can be either a homogeneous matrix or a core-shell structure (**Table 3**). The gel microparticles are typically produced in the presence of the active compound, but post-loading especially of core-shell structures is also possible. Sodium alginate – $CaCl_2$ is the most commonly used gelling system (ionic gelation), and has been applied to a range of nutraceuticals, e.g. vitamin A palmitate[104] or β-carotene[66]. Gel particles are typically produced by either so-called extrusion (dropping) or emulsion processes[105]. In the extrusion process, the size of the particles can be controlled by the droplet generation tool, e.g. vibrating nozzles or piezo effects, as well as by the viscoelasticity of the polymer solution. The generated droplets fall into a gelling bath containing, e.g. a $CaCl_2$ solution and react into gel particles. This process has the advantage of producing rather spherical and monodisperse particles. The use of concentric nozzles (co-extrusion) allows the synthesis of core-shell microcapsules. In the emulsion process, particle formation occurs by the addition of either $CaCl_2$ or an acid to an emulsion of alginate solution and the active compound in an oil, although several variations of the process exist[16, 105]. Smaller microparticles can be produced by this method compared to the extrusion process and the particle size can be adjusted by common emulsification process parameters.

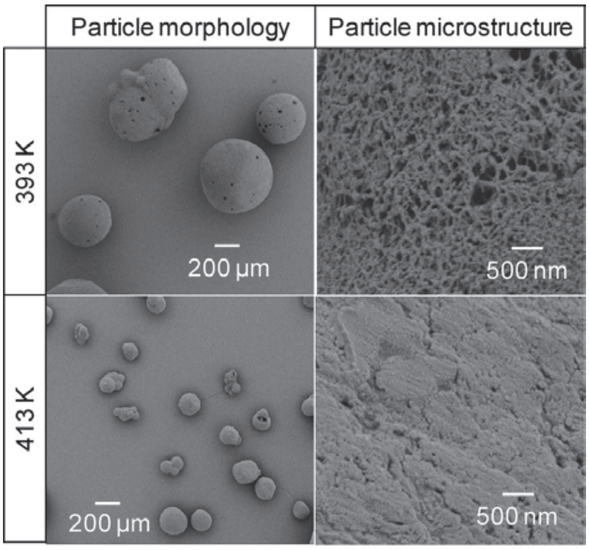

Fig. 8 Effect of gelatinization temperature on the particle morphology and microstructure of starch aerogels[109].

Novel material systems have been exploited for the generation of microbeads. Ca-pectinate beads have been investigated for the site-specific and sustained-release delivery of resveratrol[106]. Dropping solutions of water-soluble cellulose ethers such as methyl cellulose (MCE) or hydroxyl propyl methylcellulose (HPMC) into an aqueous solution of polyphenol (EGCG) results in the formation of spherical milky white beads with average diameters 600 – 2500 µm (**Fig. 7**)[107]. The beads have a core-shell structure with a porous shell (thickness 200 – 350 µm) and a hollow core with some unreacted polymer, and is formed due to the strong interactions of polymer and EGCG on the bead surface. The shell actually consists of a network of colloidal aggregates 200 – 500 nm in size[107].

Additional coating layers are often applied to particles in order to improve the stability of the active compound. Vitamin A palmitate has been formulated into double-layer capsules: the vitamin A palmitate/chitosan core was surrounded by a chitosan-alginate membrane and an additional calcium-alginate outer shell (**Fig. 7**)[104]. The resulting capsules were 1000 – 1200 μm in size and exhibited a high vitamin A palmitate encapsulation efficiency (>90%) and loading (42.5%). This resulted in a significantly improved long-term stability of vitamin A palmitate at both refrigerator and ambient conditions[104]. EGCG-loaded gelatin nanoparticles about 200 – 300 nm in size have been coated layer by layer with shells of polyelectrolytes 5 – 20 nm thick[108]. This resulted in the sustained release of EGCG from the coated nanoparticles with a maximum EGCG concentration in solution after 8 h compared to 15 min from uncoated gelatin nanoparticles[108].

A novel class of gel-like materials is constituted by the so-called aerogels that are highly porous (ε = 90 - 99%), lightweight (ρ = 0.07–0.46 g/cm^3) and with a high surface area (S_a = 70 – 680 m^2/g) resulting in enhanced active bioavailability and loading capacity[109]. Aerogels are obtained from wet gels (e.g. hydrogels) by using a suitable drying technology, usually a supercritical drying process, in order to preserve the porous texture. However, a drawback in the processing is the replacement of water present in the gel structure by a solvent (solvent exchange), forming an alcogel prior to the drying step.

Traditionally, this method focused on the synthesis of silica and carbon aerogels, however, recent research has led to the development of biodegradable and biocompatible polysaccharide-based aerogels that could also be of interest for food applications[109-111]. Aerogels have been produced from polysaccharides such as starch, pectin, alginate, κ-carrageenan, agar, chitosan and cellulose[109]. Alginate aerogel microspherical particles possess a high surface area of up to 680 m^2/g, a pore volume of up to 4.0 cm^3/g and mean particle diameters ranging from 25 μm to few hundred microns[112]. The structural properties of polysaccharide aerogels depend on their preparation method and the chemical nature of the gel phase[109, 111]. For example, an increase in temperature during gelation leads to densification of the nanoporous structure in starch aerogels (**Fig. 8**)[109, 111]. The loading of such aerogel structures still has to be demonstrated with micronutrients or nutraceuticals as research has so far focused on pharmaceutical actives.

3.9 Extrusion

The extrusion process has mostly been used to encapsulate active compounds in a carbohydrate melt (melt extrusion)[16]. Most commonly, the carbohydrate melts are processed and mixed with active compounds in twin-screw extruders and are pressed downstream through a die to shape the product particles. Cutters can be mounted directly at the die to obtain pellets, or post-processing shaping equipment such as mills or spheronizers can be used[12, 16]. The particles produced by extrusion techniques are typically dense, spherical and 0.5 to 2 mm in size[12]. Most studies on melt extrusion have focused on the encapsulation of flavor or pharmaceutical compounds rather than micronutrients or nutraceuticals. Chang *et al.* encapsulated ascorbic acid in an amorphous maltodextrin matrix by extrusion[113]. Control of the water content was the most important process parameter to assure that the product extrudates had glass transition temperatures above room temperature[113]. Vitamin K_1 and vitamin D_3 have been encapsulated in matrices consisting of mannitol, sorbitol, gluconolactone and maltodextrin by melt extrusion[114]. The encapsulation of oil in a starch matrix in the presence of low-molecular-weight emulsifiers by extrusion has also been demonstrated[115]. Li *et al.* developed a cold-forming extrusion process for the agglomeration and microencapsulation of ferrous fumarate in dough matrices[116]. The extruded particles were 300 – 700 μm in size and had a higher density, lower porosity and smoother surface texture compared to particles made by fluidized-bed agglomeration. It was possible to apply a coating to the extruded particles and they were then suitable for fortification of iodized salt[117].

4. Performance in Application: Influence of Particle Properties

In the preceding sections, particle technologies for the synthesis and formulation of micronutrients and nutraceuticals have been briefly presented. A thorough characterization of the as-obtained micronutrient- or nutraceutical-loaded particles is essential, including physicochemical properties such as particle size, size distribution, morphology, density, porosity, surface charge, shell thickness, mechanical strength, glass transition temperature, degree of crystallinity, flowability and compressibility[16]. Luykx *et al.* recently published a comprehensive review on analytical methods including separation (e.g. chromatography), imaging (e.g. TEM, SEM, atomic force microscopy) and characterization (e.g. photo correlation spectroscopy, NMR spectroscopy, X-ray diffraction, small-angle X-ray scattering) techniques for nano delivery

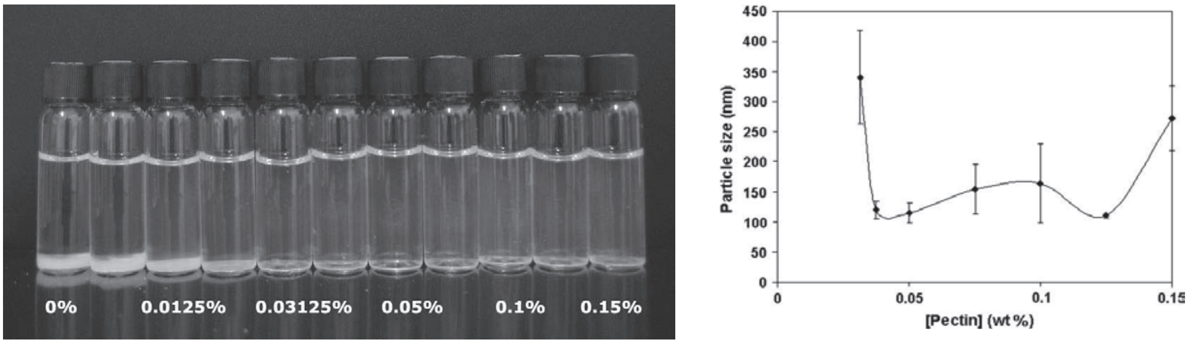

Fig. 9 Colloidally stable nanocomplexes of DHA-loaded β-lactoglobulin and increasing concentration of low methoxyl pectin. A precipitate is visible in the first four vials while the dispersions in the other vials are transparent. The visual observation correlates well with the mean particle size of the complexes as a function of the pectin concentration. Transparent, stable solutions had average particle sizes of ~100 nm[103].

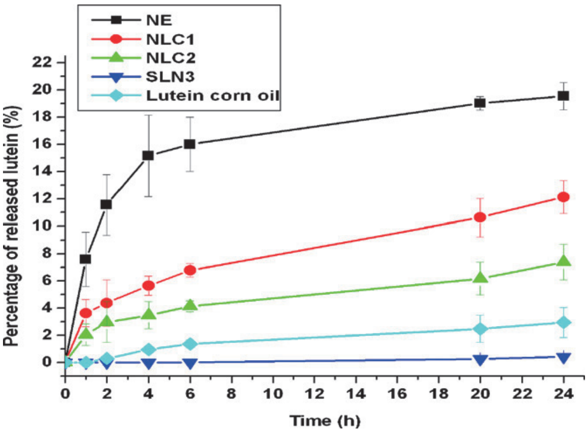

Fig. 10 Release profiles of lutein at pH 5.5 from lipid nano delivery systems. NE: nanoemulsion, NLC: nanostructured lipid carriers 1 with glyceryl tripalmitate and 2 with carnauba wax, SLN3: solid lipid nanoparticles with carnauba wax. The release profiles depend on the lipid matrix compositions, active load and mode of incorporation in the matrix and surfactant type[54].

systems in food[118]. The particle's physicochemical characteristics will in turn govern its interaction with other molecular species and determine the bulk physicochemical properties of the overall food system (e.g. appearance, texture and stability)[119]. The choice of technology, control and understanding of the resulting particle properties is therefore crucial to achieve the desired performance in target end-use applications; several examples have already been cited in the preceding paragraphs. Readers are also kindly referred to the reviews on colloidal delivery systems for micronutrients and nutraceuticals by Velikov and Pelan[8] as well as on properties of biopolymer particles by McClements and coworkers[119, 120].

Particle size is probably the most important property in the design of micronutrient or nutraceutical delivery systems. The recent trend has been a 'down-sizing' from micro- to nano-sized delivery systems[25]. Nanoparticles provide a greater surface area compared to micro-sized particles and can therefore increase solubility and bioavailability[3, 8]. This has been demonstrated, e.g. for flame-made Fe and Fe/Zn compounds[43] and precipitated resveratrol[74]. However, although the primary particle size might be small, aggregation during post-processing steps such as freeze drying can reduce the effective surface area exposed to the dissolution medium and thereby reduce the dissolution rate[74]. The particle crystal structure also has an influence on solubility[42, 74]. It has been demonstrated that the surface area has a limited influence on the solubility of amorphous compounds (as it is mostly high already), while a high specific surface area is required to ensure a high solubility of crystalline compounds[41].

Particle size also has a pronounced effect on optical properties. This is exploited in the development of carotenoids as natural colorants turning from yellow through orange to red by changing the particle size[121]. Particles ideally < 50 nm that do not scatter light are required in transparent, low-turbidity beverages enriched with nutraceuticals (**Fig. 9**)[101, 103, 119]. In contrast, large particles (> 500 nm) are used in opaque products. Alternatively, the particle refractive index or the concentration can also be modulated to alter the optical properties[119]. The particle composition itself can play a role as for example iron, which can be delivered in different molecular forms to avoid color and sensory changes when used to fortify food[41]. Small particle sizes (< 400 nm) are also favorable for product stability to avoid creaming or sedimentation in food applications[8, 57]. Particle shape and morphology affects flowability, miscibility with other food ingredients, appearance, rheology, mouth feel and release characteristics[120].

Probably one of the most challenging tasks in the formulation of micronutrients and nutraceuticals is to control the release rate while still assuring protection of the active compound during processing, transport and storage. In general, the release of an entrapped compound from a dense particle is slower than from a highly porous structure which also inversely impacts the stability of the active compound[78, 120]. Release of active ingredients from particles dispersed in a liquid medium is often measured to determine the release kinetics and effective diffusion coefficients. These will depend on, e.g. diffusion of the active compound through the matrix, the size and morphology of the particles, composition, transfer from the matrix to the environment and degradation or dissolution of the matrix material[16]. Four release mechanisms are typically distinguished for the dissolution of a particle: diffusion, erosion, fragmentation and swelling/shrinking[119]. The difference in lutein release profiles shown for SLN and NLC in **Fig. 10** can be related to the particle matrix composition and internal structure. This on the other hand can also be used as means to improve the stability of active compounds, e.g. as in the case of compounds entrapped in extruded hydrophilic glassy matrices that provide an almost impermeable barrier against oxygen[11, 113, 122] .

5. Concluding Remarks

One hundred years of vitamins – the “history of vitamins” has still not come to an end! Triggered by new technologies and building on new science, a renaissance in vitamin research started. We see a constantly increasing number of publications and studies which open up new and improved applications. We learn about nutrient-gene interactions and with the discovery of polymorphism, specific requirements for vitamins are identified. In addition we still have to assure that everyone all over the globe has access to vitamins according to recommendations. This can only be achieved by industrial production providing vitamins in the desired quality and bioavailability delivered via product forms tailored to the targeted application (e.g. acceptable sensory characteristics, storage stability, ease of handling).

Table 3 summarizes the synthesis and formulation technologies for the dry powder delivery systems of micronutrients and nutraceuticals described in this review. A broad choice of technologies exist covering particles from nano- through micro- to macro-sizes with morphologies ranging from core-shell to matrix-type. The industrially most relevant particle formation technology is spray drying. The influence of process parameters on the resulting particle characteristics such as size and morphology is quite well understood. Nevertheless, only a few studies discuss the importance of particle shape for processing in the food industry, e.g. the influence of surface irregularities and particle morphology on flowability and coating[123]. Novel techniques can quantify and classify the particle shape (e.g. elongation, circularity, compactness and convexity) with advanced image analysis techniques and software algorithms[124]. Novel developments are mostly made in the field of nanotechnology, as the nanostructures can provide unprecedented properties. However, the scalability of these upcoming nanotechnologies still has to be proven in many cases. Another challenge is the compatibility of some technologies with legislatively approved, food-grade raw materials without the use of solvents during processing. Furthermore, technologies developed in other industries, e.g. the pharmaceutical industry, might be too costly for processing food ingredients and need to be adapted to reduce cost.

The thorough characterization of particulate delivery systems described in this review is of great importance to understand and design their behavior in end-use applications. Physical, mechanical, structural and mass transfer properties need to be considered[16]. Often a compromise has to be made to ensure the protection of the active compound during processing and storage while still controlling the release at the desired location and time. Analysis of the systems is often complicated by their multicomponent nature including bio-polymers whose properties might even vary from batch to batch. A range of powerful characterization techniques are nowadays available for the delivery systems of micronutrients and nutraceuticals. For example, the mechanical stability of microcapsules can be studied with a combination of fluorescence and atomic force microscopy to help understand the release behavior and deformation properties[125, 126]. The observed mechanical properties have to be explained by and related to the structural properties on a molecular level inside the microcapsules. Current research therefore tries to identify the complex relationship between these properties by advanced analysis methods often combining several techniques and modeling. Innovative methods that are in development include, e.g. moisture sorption isotherms[127], positron annihilation lifetime spectroscopy to determine free volume[21, 128], coupled with exact measurements of the glass transition temperature of the product as a function of water activity and composition.

Consumer awareness towards a healthy and well-balanced diet and therefore the demand for functional, high-quality food products and nutritional supplements steadily increases. Formulation scientists in industry and academia will therefore continue to enhance the delivery systems of micronutrients and nutraceuticals to provide the best performance and quality for the costumers’ needs.

References

1) Funk, C. (1912): The Etiology of the Deficiency Diseases. Beri-Beri, Polyneuritis in Birds, Epidemic Deopsy, Scurvy, Experimental Scurvy in Animals, Infantile Scurvy, Ship Beri-Beri, Pellagra, The Journal of State Medicine, Vol.20, pp.341-368.
2) Gonnet, M., Lethuaut, L. and Boury, F. (2010): New Trends in Encapsulation of Liposoluble Vitamins, Journal of Controlled Release, Vol.146, pp.276-290.
3) Fang, Z. and Bhandari, B. (2010): Encapsulation of Polyphenols - A Review, Trends in Food Science and Technology, Vol.21, pp.510-523.
4) Munin, A. and Edwards-Lévy, F. (2011): Encapsulation of Natural Polyphenolic Compounds; a Review, Pharmaceutics, Vol.3, pp.793-829.
5) Nobili, S., Lippi, D., Witort, E., Donnini, M., Bausi, L., Mini, E. and Capaccioli, S. (2009): Natural Compounds for Cancer Treatment and Prevention, Pharmacological Research, Vol.59, pp.365-378.
6) Pandey, N., Meena, R. P., Rai, S. K. and Pandey-Rai, S. (2011): Medicinal Plants Derived Nutraceuticals: A Re-Emerging Health Aid, International Journal of Pharma and Bio Sciences, Vol.2, pp.419-441.
7) www.nutri-facts.org (2012): Nutri-Facts: Understanding Vitamins & More.
8) Velikov, K. P. and Pelan, E. (2008): Colloidal Delivery Systems for Micronutrients and Nutraceuticals, Soft Matter, Vol.4, pp.1964-1980.
9) Gharsallaoui, A., Roudaut, G., Chambin, O., Voilley, A. and Saurel, R. (2007): Applications of Spray-Drying in Microencapsulation of Food Ingredients: An Overview, Food Research International, Vol.40, pp.1107-1121.
10) Shahidi, F. and Han, X. Q. (1993): Encapsulation of Food Ingredients, Critical Reviews in Food Science and Nutrition, Vol.33, pp.501-547.
11) Gouin, S. (2004): Microencapsulation: Industrial Appraisal of Existing Technologies and Trends, Trends in Food Science & Technology, Vol.15, pp.330-347.
12) Kuang, S. S., Oliveira, J. C. and Crean, A. M. (2010): Microencapsulation as a Tool for Incorporating Bioactive Ingredients into Food, Critical Reviews in Food Science and Nutrition, Vol.50, pp.951 - 968.
13) Madene, A., Jacquot, M., Joël, S. and Desobry, S. (2006): Flavour Encapsulation and Controlled Release - a Review, International Journal of Food Science and Technology, Vol.41, pp.1-21.
14) Augustin, M. A. and Hemar, Y. (2009): Nano- and Micro-Structured Assemblies for Encapsulation of Food Ingredients, Chemical Society Reviews, Vol.38, pp.902-912.
15) Desai, K. G. H. and Park, H. J. (2005): Recent Developments in Microencapsulation of Food Ingredients, Drying Technology, Vol.23, pp.1361-1394.
16) Zuidam, N. J. and Nedović, V. (2010), “Encapsulation Technologies for Active Food Ingredients and Food Processing” , 1st ed., Springer Science+Business Media, New York, USA.
17) Polavarapu, S., Oliver, C. M., Ajlouni, S. and Augustin, M. A. (2011): Physicochemical Characterisation and Oxidative Stability of Fish Oil and Fish Oil-Extra Virgin Olive Oil Microencapsulated by Sugar Beet Pectin, Food Chemistry, Vol.127, pp.1694-1705.
18) Chiou, D. and Langrish, T. A. G. (2007): Development and Characterisation of Novel Nutraceuticals with Spray Drying Technology, Journal of Food Engineering, Vol.82, pp.84-91.
19) Xie, Y. L., Zhou, H. M., Liang, X. H., He, B. S. and Han, X. X. (2010): Study on the Morphology, Particle Size and Thermal Properties of Vitamin A Microencapsulated by Starch Octenylsuccinate, Agricultural Sciences in China, Vol.9, pp.1058-1064.
20) Teixeira, M. I., Andrade, L. R., Farina, M. and Rocha-Leao, M. H. M. (2004): Characterization of Short Chain Fatty Acid Microcapsules Produced by Spray Drying, Materials Science and Engineering C, Vol.24, pp.653-658.
21) Roussenova, M., Murith, M., Alam, A. and Ubbink, J. (2010): Plasticization, Antiplasticization, and Molecular Packing in Amorphous Carbohydrate-Glycerol Matrices, Biomacromolecules, Vol.11, pp.3237-3247.
22) Drusch, S., Rätzke, K., Shaikh, M., Serfert, Y., Steckel, H., Scampicchio, M., Voigt, I., Schwarz, K. and Mannino, S. (2009): Differences in Free Volume Elements of the Carrier Matrix Affect the Stability of Microencapsulated Lipophilic Food Ingredients, Food Biophysics, Vol.4, pp.42-48.
23) Philips, G. O. and Williams, P. A. (2009), “Handbook of Hydrocolloids”, 2nd ed., Woodhead Publishing Limited, Cambridge, UK.
24) McMahon, D. J. and Oommen, B. S. (2008): Supramolecular Structure of the Casein Micelle, Journal of Dairy Science, Vol.91, pp.1709-1721.
25) Kaya-Celiker, H. and Mallikarjunan, K. (2012): Better Nutrients and Therapeutics Delivery in Food through Nanotechnology, Food Engineering Reviews, pp.1-10.
26) McClements, D. J., Decker, E. A. and Weiss, J. (2007): Emulsion-Based Delivery Systems for Lipophilic Bioactive Components, Journal of Food Science, Vol.72, pp.R109-R124.

27) McClements, D. J. and Li, Y. (2010): Structured Emulsion-Based Delivery Systems: Controlling the Digestion and Release of Lipophilic Food Components, Advances in Colloid and Interface Science, Vol.159, pp.213-228.

28) McClements, D. J. and Rao, J. (2011): Food-Grade Nanoemulsions: Formulation, Fabrication, Properties, Performance, Biological Fate, and Potential Toxicity, Critical Reviews in Food Science and Nutrition, Vol.51, pp.285-330.

29) Mason, T. G., Wilking, J. N., Meleson, K., Chang, C. B. and Graves, S. M. (2006): Nanoemulsions: Formation, Structure, and Physical Properties, Journal of Physics Condensed Matter, Vol.18, pp.R635-R666.

30) Del Valle, E. M. M. (2004): Cyclodextrins and Their Uses: A Review, Process Biochemistry, Vol.39, pp.1033-1046.

31) Marques, H. M. C. (2010): A Review on Cyclodextrin Encapsulation of Essential Oils and Volatiles, Flavour and Fragrance Journal, Vol.25, pp.313-326.

32) Jesorka, A. and Orwar, O. (2008): Liposomes: Technologies and Analytical Applications, Annual Review of Analytical Chemistry, Vol.1, pp. 801-832.

33) Mozafari, M. R., Johnson, C., Hatziantoniou, S. and Demetzos, C. (2008): Nanoliposomes and Their Applications in Food Nanotechnology, Journal of Liposome Research, Vol.18, pp.309-327.

34) Taylor, T. M., Davidson, P. M., Bruce, B. D. and Weiss, J. (2005): Liposomal Nanocapsules in Food Science and Agriculture, Critical Reviews in Food Science and Nutrition, Vol.45, pp.587-605.

35) Merisko-Liversidge, E., Liversidge, G. G. and Cooper, E. R. (2003): Nanosizing: A Formulation Approach for Poorly-Water-Soluble Compounds, European Journal of Pharmaceutical Sciences, Vol.18, pp.113-120.

36) Murugesan, R. and Orsat, V. (2012): Spray Drying for the Production of Nutraceutical Ingredients - a Review, Food and Bioprocess Technology, Vol.5, pp.3-14.

37) Strobel, R. and Pratsinis, S. E. (2007): Flame Aerosol Synthesis of Smart Nanostructured Materials, Journal of Materials Chemistry, Vol.17, pp.4743-4756.

38) Strobel, R., Baiker, A. and Pratsinis, S.E. (2006): Aerosol Flame Synthesis of Catalysts, Advanced Powder Technology, Vol.17, pp.457-480.

39) Rohner, F., Ernst, F. O., Arnold, M., Hilbe, M., Biebinger, R., Ehrensperger, F., Pratsinis, S. E., Langhans, W., Hurrell, R. F. and Zimmermann, M. B. (2007): Synthesis, Characterization, and Bioavailability in Rats of Ferric Phosphate Nanoparticles, Journal of Nutrition, Vol.137, pp.614-619.

40) Zimmermann, M. B. and Hilty, F. M. (2011): Nanocompounds of Iron and Zinc: Their Potential in Nutrition, Nanoscale, Vol.3, pp.2390-2398.

41) Hilty, F. M., Teleki, A., Krumeich, F., Büchel, R., Hurrell, R. F., Pratsinis, S. E. and Zimmermann, M. B. (2009): Development and Optimization of Iron-and Zinc-Containing Nanostructured Powders for Nutritional Applications, Nanotechnology, Vol.20, Article Vol.475101.

42) Hilty, F. M., Knijnenburg, J. T., Teleki, A., Krumeich, F., Hurrell, R. F., Pratsinis, S. E. and Zimmermann, M. B. (2011): Incorporation of Mg and Ca into Nanostructured Fe_2O_3 Improves Fe Solubility in Dilute Acid and Sensory Characteristics in Foods, Journal of Food Science, Vol.76, pp.N2-N10.

43) Hilty, F. M., Arnold, M., Hilbe, M., Teleki, A., Knijnenburg, J. T. N., Ehrensperger, F., Hurrell, R. F., Pratsinis, S. E., Langhans, W. and Zimmermann, M. B. (2010): Iron from Nanocompounds Containing Iron and Zinc Is Highly Bioavailable in Rats without Tissue Accumulation, Nature Nanotechnology, Vol.5, pp.374-380.

44) Teleki, A., Wengeler, R., Wengeler, L., Nirschl, H. and Pratsinis, S. E. (2008): Distinguishing between Aggregates and Agglomerates of Flame-Made TiO_2 by High-Pressure Dispersion, Powder Technology, Vol.181, pp.292-300.

45) Wegner, K., Schimmoeller, B., Thiebaut, B., Fernandez, C. and Rao, T. N. (2011): Pilot Plants for Industrial Nanoparticle Production by Flame Spray Pyrolysis, KONA Powder and Particle Journal, No.29, pp.251-265.

46) Mehnert, W. and Mäder, K. (2001): Solid Lipid Nanoparticles: Production, Characterization and Applications, Advanced Drug Delivery Reviews, Vol.47, pp.165-196.

47) Müller, R. H., Radtke, M. and Wissing, S. A. (2002): Solid Lipid Nanoparticles (SLN) and Nanostructured Lipid Carriers (NLC) in Cosmetic and Dermatological Preparations, Advanced Drug Delivery Reviews, Vol.54, pp.S131-S155.

48) Wissing, S. A., Kayser, O. and Müller, R. H. (2004): Solid Lipid Nanoparticles for Parenteral Drug Delivery, Advanced Drug Delivery Reviews, Vol.56, pp.1257-1272.

49) Bunjes, H. (2011): Structural Properties of Solid Lipid Based Colloidal Drug Delivery Systems, Current Opinion in Colloid and Interface Science, Vol.16, pp.405-411.

50) Puglia, C. and Bonina, F. (2012): Lipid Nanoparticles as Novel Delivery Systems for Cosmetics and Dermal Pharmaceuticals, Expert Opinion on Drug Delivery, Vol.9, pp.429-441.

51) Weiss, J., Decker, E. A., McClements, D. J., Kristbergsson, K., Helgason, T. and Awad, T. (2008): Solid Lipid Nanoparticles as Delivery Systems for Bioactive Food Components, Food Biophysics, Vol.3, pp.146-154.

52) Fathi, M., Mozafari, M. R. and Mohebbi, M. (2012): Nanoencapsulation of Food Ingredients Using Lipid Based Delivery Systems, Trends in Food Science and Technology, Vol.23, pp.13-27.

53) Liu, C. H. and Wu, C. T. (2010): Optimization of Nanostructured Lipid Carriers for Lutein Delivery, Colloids and Surfaces A: Physicochemical and Engineering Aspects, Vol.353, pp.149-156.

54) Mitri, K., Shegokar, R., Gohla, S., Anselmi, C. and Müller, R. H. (2011): Lipid Nanocarriers for Dermal Delivery of Lutein: Preparation, Characterization, Stability and Performance, International Journal of Pharmaceutics, Vol.414, pp.267-275.

55) Trombino, S., Cassano, R., Muzzalupo, R., Pingitore, A., Cione, E. and Picci, N. (2009): Stearyl Ferulate-Based Solid Lipid Nanoparticles for the Encapsulation and Stabilization of β-Carotene and α-Tocopherol, Colloids and Surfaces B: Biointerfaces, Vol.72, pp.181-187.

56) Thrandur, H., Awad, T. S., Kristberg, K., Eric, A. D., David, J. M. A. and Jochen, W. (2009): Impact of Surfactant Properties on Oxidative Stability of β-Carotene Encapsulated within Solid Lipid Nanoparticles, Journal of Agricultural and Food Chemistry, Vol.57, pp.8033-8040.

57) Hentschel, A., Gramdorf, S., Müller, R. H. and Kurz, T. (2008): β-Carotene-Loaded Nanostructured Lipid Carriers, Journal of Food Science, Vol.73, pp.N1-N6.

58) Liu, C. H., Wu, C. T. and Fang, J. Y. (2010): Characterization and Formulation Optimization of Solid Lipid Nanoparticles in Vitamin K_1 Delivery, Drug Development and Industrial Pharmacy, Vol.36, pp.751-761.

59) Kong, R., Xia, Q. and Liu, G. Y. (2011): Preparation and Characterization of Vitamin A Palmitate-Loaded Nanostructured Lipid Carriers as Delivery Systems for Food Products, Advanced Materials Research, Vol.236-238, pp.1818-1823.

60) Jee, J.-P., Lim, S.-J., Park, J.-S. and Kim, C.-K. (2006): Stabilization of All-Trans Retinol by Loading Lipophilic Antioxidants in Solid Lipid Nanoparticles, European Journal of Pharmaceutics and Biopharmaceutics, Vol.63, pp.134-139.

61) Xia, Q. and Kong, R. (2011): Freeze-Drying and Characterization of Vitamin A Palmitate-Loaded Nanostructured Lipid Carriers (NLC), Materials Science Forum, Vol.694, pp.365-369.

62) Hu, J., Ng, W. K., Dong, Y., Shen, S. and Tan, R. B. H. (2011): Continuous and Scalable Process for Water-Redispersible Nanoformulation of Poorly Aqueous Soluble APIs by Antisolvent Precipitation and Spray-Drying, International Journal of Pharmaceutics, Vol.404, pp.198-204.

63) D'Addio, S. M. and Prud'homme, R. K. (2011): Controlling Drug Nanoparticle Formation by Rapid Precipitation, Advanced Drug Delivery Reviews, Vol.63, pp.417-426.

64) Rasenack, N. and Müller, B. W. (2004): Micron-Size Drug Particles: Common and Novel Micronization Techniques, Pharmaceutical Development and Technology, Vol.9, pp.1-13.

65) Liu, Y., Kathan, K., Saad, W. and Prud'homme, R. K. (2007): Ostwald Ripening of β-Carotene Nanoparticles, Physical Review Letters, Vol.98, pp.036102.

66) Astete, C. E., Sabliov, C. M., Watanabe, F. and Alexandru, B. (2009): Ca^{2+} Cross-Linked Alginic Acid Nanoparticles for Solubilization of Lipophilic Natural Colorants, Journal of Agricultural and Food Chemistry, Vol.57, pp.7505-7512.

67) de Paz, E., Martín, T., Estrella, A., Rodríguez-Rojo, S., Matias, A. A., Duarte, C. M. M. and Cocero, M. J. (2012): Formulation of β-Carotene by Precipitation from Pressurized Ethyl Acetate-on-Water Emulsions for Application as Natural Colorant, Food Hydrocolloids, Vol.26, pp.17-27.

68) Franceschi, E., De Cesaro, A. M., Ferreira, S. R. S. and Vladimir Oliveira, J. (2009): Precipitation of β-Carotene Microparticles from SEDS Technique Using Supercritical CO_2, Journal of Food Engineering, Vol.95, pp.656-663.

69) Franceschi, E., de Cezaro, A., Ferreira, S. R. S., Kunita, M. H., Muniz, E. C., Rubira, A. F. and Vladimir Oliveira, J. (2010): Co-Precipitation of beta-Carotene and Bio-Polymer Using Supercritical Carbon Dioxide as Antisolvent, Open Chemical Engineering Journal, Vol.4, pp.11-20.

70) Mattea, F., Martín, A. and Cocero, M. J. (2009): Carotenoid Processing with Supercritical Fluids, Journal of Food Engineering, Vol.93, pp.255-265.

71) Mattea, F., Martín, A., Matías-Gago, A. and Cocero, M. J. (2009): Supercritical Antisolvent Precipitation from an Emulsion: β-Carotene Nanoparticle Formation, Journal of Supercritical Fluids, Vol.51, pp.238-247.

72) Zhu, Z., Margulis-Goshen, K., Magdassi, S., Talmon, Y. and Macosko, C. W. (2010): Polyelectrolyte Stabilized Drug Nanoparticles Via Flash Nanoprecipitation: A Model Study with β-Carotene, Journal of Pharmaceutical Sciences, Vol.99, pp.4295-4306.

73) Santos, D.T. and Meireles, M.A.A. (2012): Micronization and Encapsulation of Functional Pigments Using Supercritical Carbon Dioxide, Journal of Food Process Engineering, doi:10.1111/j.1745-4530.2011.00651.x.

74) Kim, S., Ng, W. K., Dong, Y., Das, S. and Tan, R. B. H. (2012): Preparation and Physicochemical Characterization of Trans-Resveratrol Nanoparticles by Temperature-Controlled Antisolvent Precipitation, Journal of Food Engineering, Vol.108, pp.37-42.

75) Bethune, S. J., Schultheiss, N. and Henck, J. O. (2011): Improving the Poor Aqueous Solubility of Nutraceutical Compound Pterostilbene through Cocrystal Formation, Crystal Growth and Design, Vol.11, pp.2817-2823.

76) Schultheiss, N., Bethune, S. and Henck, J. O. (2010): Nutraceutical Cocrystals: Utilizing Pterostilbene as a Cocrystal Former, CrystEngComm, Vol.12, pp.2436-2442.

77) Sosa, M. V., Rodríguez-Rojo, S., Mattea, F., Cismondi, M. and Cocero, M. J. (2011): Green Tea Encapsulation by Means of High Pressure Antisolvent Coprecipitation, Journal of Supercritical Fluids, Vol.56, pp.304-311.

78) Drusch, S. and Schwarz, K. (2006): Microencapsulation Properties of Two Different Types of n-Octenylsuccinate-Derivatised Starch, European Food Research and Technology, Vol.222, pp.155-164.

79) Rocha, G. A., Fávaro-Trindade, C. S. and Grosso, C. R. F. (2012): Microencapsulation of Lycopene by Spray Drying: Characterization, Stability and Application of Microcapsules, Food and Bioproducts Processing, Vol.90, pp.37-42.
80) Goula, A. M. and Adamopoulos, K. G. (2012): A New Technique for Spray-Dried Encapsulation of Lycopene, Drying Technology, Vol.30, pp.641-652.
81) Shu, B., Yu, W., Zhao, Y. and Liu, X. (2006): Study on Microencapsulation of Lycopene by Spray-Drying, Journal of Food Engineering, Vol.76, pp.664-669.
82) Loksuwan, J. (2007): Characteristics of Microencapsulated β-Carotene Formed by Spray Drying with Modified Tapioca Starch, Native Tapioca Starch and Maltodextrin, Food Hydrocolloids, Vol.21, pp.928-935.
83) Ersus, S. and Yurdagel, U. (2007): Microencapsulation of Anthocyanin Pigments of Black Carrot (Daucus Carota L.) by Spray Drier, Journal of Food Engineering, Vol.80, pp.805-812.
84) Quek, S. Y., Chok, N. K. and Swedlund, P. (2007): The Physicochemical Properties of Spray-Dried Watermelon Powders, Chemical Engineering and Processing: Process Intensification, Vol.46, pp.386-392.
85) Rosenberg, M., Kopelman, I. J. and Talmon, Y. (1990): Factors Affecting Retention in Spray-Drying Microencapsulation of Volatile Materials, Journal of Agricultural and Food Chemistry, Vol.38, pp.1288-1294.
86) Wang, R., Tian, Z. and Chen, L. (2011): A Novel Process for Microencapsulation of Fish Oil with Barley Protein, Food Research International, Vol.44, pp.2735-2741.
87) Jafari, S. M., Assadpoor, E., Bhandari, B. and He, Y. (2008): Nano-Particle Encapsulation of Fish Oil by Spray Drying, Food Research International, Vol.41, pp.172-183.
88) Drusch, S. (2007): Sugar Beet Pectin: A Novel Emulsifying Wall Component for Microencapsulation of Lipophilic Food Ingredients by Spray-Drying, Food Hydrocolloids, Vol.21, pp.1223-1228.
89) Drusch, S., Serfert, Y., Berger, A., Shaikh, M. Q., Rätzke, K., Zaporojtchenko, V. and Schwarz, K. (2012): New Insights into the Microencapsulation Properties of Sodium Caseinate and Hydrolyzed Casein, Food Hydrocolloids, Vol.27, pp.332-338.
90) Tan, L. H., Chan, L. W. and Heng, P. W. S. (2009): Alginate/Starch Composites as Wall Material to Achieve Microencapsulation with High Oil Loading, Journal of Microencapsulation, Vol.26, pp.263-271.
91) Sansone, F., Mencherini, T., Picerno, P., D'Amore, M., Aquino, R. P. and Lauro, M. R. (2011): Maltodextrin/Pectin Microparticles by Spray Drying as Carrier for Nutraceutical Extracts, Journal of Food Engineering, Vol.105, pp.468-476.
92) Bejrapha, P., Min, S.-G., Surassmo, S. and Choi, M.-J. (2010): Physicothermal Properties of Freeze-Dried Fish Oil Nanocapsules Frozen under Different Conditions, Drying Technology, Vol.28, pp.481-489.
93) Anwar, S. H. and Kunz, B. (2011): The Influence of Drying Methods on the Stabilization of Fish Oil Microcapsules: Comparison of Spray Granulation, Spray Drying, and Freeze Drying, Journal of Food Engineering, Vol.105, pp.367-378.
94) Jyothi, N. V. N., Prasanna, P. M., Sakarkar, S. N., Prabha, K. S., Ramaiah, P. S. and Srawan, G. Y. (2010): Microencapsulation Techniques, Factors Influencing Encapsulation Efficiency, Journal of Microencapsulation, Vol.27, pp.187-197.
95) Wegmüller, R., Zimmermann, M.B., Bühr, V. G., Windhab, E. J. and Hurrell, R. F. (2006): Development, Stability, and Sensory Testing of Microcapsules Containing Iron, Iodine, and Vitamin A for Use in Food Fortification, Journal of Food Science, Vol.71, pp.S181-S187.
96) Lemetter, C. Y. G., Meeuse, F. M. and Zuidam, N. J. (2009): Control of the Morphology and the Size of Complex Coacervate Microcapsules During Scale-Up, AIChE Journal, Vol.55, pp.1487-1496.
97) Barrow, C. J., Nolan, C. and Holub, B. J. (2009): Bioequivalence of Encapsulated and Microencapsulated Fish-Oil Supplementation, Journal of Functional Foods, Vol.1, pp.38-43.
98) Junyaprasert, V. B., Mitrevej, A., Sinchaipanid, N., Boonme, P. and Wurster, D. E. (2001): Effect of Process Variables on the Microencapsulation of Vitamin A Palmitate by Gelatin-Acacia Coacervation, Drug Development and Industrial Pharmacy, Vol.27, pp.561-566.
99) Zhang, K., Zhang, H., Hu, X., Bao, S. and Huang, H. (2012): Synthesis and Release Studies of Microalgal Oil-Containing Microcapsules Prepared by Complex Coacervation, Colloids and Surfaces B: Biointerfaces, Vol.89, pp.61-66.
100) Bédié, G. K., Turgeon, S. L. and Makhlouf, J. (2008): Formation of Native Whey Protein Isolate–Low Methoxyl Pectin Complexes as a Matrix for Hydro-Soluble Food Ingredient Entrapment in Acidic Foods, Food Hydrocolloids, Vol.22, pp.836-844.
101) Ron, N., Zimet, P., Bargarum, J. and Livney, Y. D. (2010): Beta-Lactoglobulin–Polysaccharide Complexes as Nanovehicles for Hydrophobic Nutraceuticals in Non-Fat Foods and Clear Beverages, International Dairy Journal, Vol.20, pp.686-693.
102) Silva, D. F., Favaro-Trindade, C. S., Rocha, G. A. and Thomazini, M. (2012): Microencapsulation of Lycopene by Gelatin-Pectin Complex Coacervation, Journal of Food Processing and Preservation, Vol.36, pp.185-190.
103) Zimet, P. and Livney, Y. D. (2009): Beta-Lactoglobulin and Its Nanocomplexes with Pectin as Vehicles for ω-3 Polyunsaturated Fatty Acids, Food Hydrocolloids, Vol.23, pp.1120-1126.
104) Albertini, B., Di Sabatino, M., Calogerà, G., Passerini, N. and Rodriguez, L. (2010): Encapsulation of Vitamin A Palmitate for Animal Supplementation: Formulation, Manufacturing and Stability Implications, Journal of Microencapsulation, Vol.27, pp.150-161.

105) Champagne, C. P. and Fustier, P. (2007): Microencapsulation for the Improved Delivery of Bioactive Compounds into Foods, Current Opinion in Biotechnology, Vol.18, pp.184-190.
106) Das, S. and Ng, K.-Y. (2010): Resveratrol-Loaded Calcium-Pectinate Beads: Effects of Formulation Parameters on Drug Release and Bead Characteristics, Journal of Pharmaceutical Sciences, Vol.99, pp.840-860.
107) Patel, A. R., Nijsse, J. and Velikov, K. P. (2011): Novel Polymer-Polyphenol Beads for Encapsulation and Microreactor Applications, Soft Matter, Vol.7, pp.4294-4301.
108) Shutava, T. G., Balkundi, S. S., Vangala, P., Steffan, J. J., Bigelow, R. L., Cardelli, J.A., O'Neal, D. P. and Lvov, Y. M. (2009): Layer-by-Layer-Coated Gelatin Nanoparticles as a Vehicle for Delivery of Natural Polyphenols, ACS Nano, Vol.3, pp.1877-1885.
109) García-González, C. A., Alnaief, M. and Smirnova, I. (2011): Polysaccharide-Based Aerogels - Promising Biodegradable Carriers for Drug Delivery Systems, Carbohydrate Polymers, Vol.86, pp.1425-1438.
110) García-González, C. A., Uy, J. J., Alnaief, M. and Smirnova, I. (2012): Preparation of Tailor-Made Starch-Based Aerogel Microspheres by the Emulsion-Gelation Method, Carbohydrate Polymers, Vol.88, pp.1378-1386.
111) Mehling, T., Smirnova, I., Guenther, U. and Neubert, R. H. H. (2009): Polysaccharide-Based Aerogels as Drug Carriers, Journal of Non-Crystalline Solids, Vol.355, pp.2472-2479.
112) Alnaief, M., Alzaitoun, M. A., García-González, C. A. and Smirnova, I. (2011): Preparation of Biodegradable Nanoporous Microspherical Aerogel Based on Alginate, Carbohydrate Polymers, Vol.84, pp.1011-1018.
113) Chang, D., Abbas, S., Hayat, K., Xia, S., Zhang, X., Xie, M. and Kim, J. M. (2010): Encapsulation of Ascorbic Acid in Amorphous Maltodextrin Employing Extrusion as Affected by Matrix/Core Ratio and Water Content, International Journal of Food Science & Technology, Vol.45, pp.1895-1901.
114) Petritz, E., Tritthart, T. and Wintersteiger, R. (2006): Determination of Phylloquinone and Cholecalciferol Encapsulated in Granulates Formed by Melt Extrusion, Journal of Biochemical and Biophysical Methods, Vol.69, pp.101-112.
115) Yilmaz, G., Jongboom, R. O. J., Feil, H. and Hennink, W. E. (2001): Encapsulation of Sunflower Oil in Starch Matrices Via Extrusion: Effect of the Interfacial Properties and Processing Conditions on the Formation of Dispersed Phase Morphologies, Carbohydrate Polymers, Vol.45, pp.403-410.
116) Li, Y. O., Yadava, D., Lo, K. L., Diosady, L. L. and Wesley, A. S. (2011): Feasibility and Optimization Study of Using Cold-Forming Extrusion Process for Agglomerating and Microencapsulating Ferrous Fumarate for Salt Double Fortification with Iodine and Iron, Journal of Microencapsulation, Vol.28, pp.639-649.
117) Li, Y. O., Diosady, L. L. and Wesley, A. S. (2010): Iodine Stability in Iodized Salt Dual Fortified with Microencapsulated Ferrous Fumarate Made by an Extrusion-Based Encapsulation Process, Journal of Food Engineering, Vol.99, pp.232-238.
118) Luykx, D. M. A. M., Peters, R. J. B., Van Ruth, S. M. and Bouwmeester, H. (2008): A Review of Analytical Methods for the Identification and Characterization of Nano Delivery Systems in Food, Journal of Agricultural and Food Chemistry, Vol.56, pp.8231-8247.
119) Jones, O. G. and McClements, D. J. (2010): Functional Biopolymer Particles: Design, Fabrication, and Applications, Comprehensive Reviews in Food Science and Food Safety, Vol.9, pp.374-397.
120) Matalanis, A., Jones, O. G. and McClements, D. J. (2011): Structured Biopolymer-Based Delivery Systems for Encapsulation, Protection, and Release of Lipophilic Compounds, Food Hydrocolloids, Vol.25, pp.1865-1880.
121) Horn, D. and Rieger, J. (2001): Organic Nanoparticles in the Aqueous Phase - Theory, Experiment, and Use, Angewandte Chemie International Edition, Vol.40, pp.4330-4361.
122) Van Sleeuwen, R. M. T., Zhang, S. and Normand, V. (2012): Spatial Glass Transition Temperature Variations in Polymer Glass: Application to a Maltodextrin-Water System, Biomacromolecules, Vol.13, pp.787-797.
123) Saad, M., Sadoudi, A., Rondet, E. and Cuq, B. (2011): Morphological Characterization of Wheat Powders, How to Characterize the Shape of Particles?, Journal of Food Engineering, Vol.102, pp.293-301.
124) Almeida-Prieto, S., Blanco-Méndez, J. and Otero-Espinar, F. J. (2007): Microscopic Image Analysis Techniques for the Morphological Characterization of Pharmaceutical Particles: Influence of the Software, and the Factor Algorithms Used in the Shape Factor Estimation, European Journal of Pharmaceutics and Biopharmaceutics, Vol.67, pp.766-776.
125) Delcea, M., Schmidt, S., Palankar, R., Fernandes, P. A. L., Fery, A., Möhwald, H. and Skirtach, A. G. (2010): Mechanobiology: Correlation between Mechanical Stability of Microcapsules Studied by AFM and Impact of Cell-Induced Stresses, Small, Vol.6, pp.2858-2862.
126) Fernandes, P. A. L., Delcea, M., Skirtach, A. G., Möhwald, H. and Fery, A. (2010): Quantification of Release from Microcapsules Upon Mechanical Deformation with AFM, Soft Matter, Vol.6, pp.1879-1883.
127) Carter, B. P. and Schmidt, S. J. (2012): Developments in Glass Transition Determination in Foods Using Moisture Sorption Isotherms, Food Chemistry, Vol.132, pp.1693-1698.
128) Liu, H., Chaudhary, D., Roberts, J., Weed, R., Sullivan, J. and Buckman, S. (2012): The Interaction in Sorbitol-Plasticized Starch Bionanocomposites Via Positron Annihilation Lifetime Spectroscopy and Small Angle X-Ray Scattering, Carbohydrate Polymers, Vol.88, pp.1172-1176.

Author's short biography

Alexandra Teleki

Alexandra Teleki received her Master of Science in chemical engineering from the Royal Institute of Technology, Stockholm (Sweden) in 2003 and her Ph.D. from the Department of Mechanical and Process Engineering at ETH Zurich (Switzerland) in 2008. She worked as a lecturer and research associate at the particle technology laboratory at ETH before she took up her current position as a scientist at DSM Nutritional Products in Basel (Switzerland). Her research interests are formulation and microencapsulation technologies of micronutrients and nutraceuticals for application in foods or nutritional supplements.

Andrea Hitzfeld

Andrea Hitzfeld received her diploma degree (Dipl. Ing.) in food technology from the Technical University of Munich (Germany) in 2005. She is currently working at the research and development center of DSM Nutritional Products in Basel (Switzerland) as an associate scientist in the research area of vitamin formulation.

Manfred Eggersdorfer

Manfred Eggersdorfer studied chemistry at the Technical University Munich and did his PhD in organic chemistry in the field of the synthesis and characterization of unusual amino acids. He was post-doc at Stanford University, California, working with Carl Djerassi on the isolation and characterization of sterols of marine origin. He joined Roche in 1999 as head of R+D Vitamins and Fine Chemicals which was acquired by DSM. Prior to Roche, Manfred Eggersdorfer was working for BASF, Ludwigshafen, in different positions including head of research and development fine chemicals. Manfred Eggersdorfer is active as a member of the advisory board of the John Hopkins Bloomberg School of Public Health, of the strategy board of the Institute of Food Science University Hamburg, and has published many papers in the field of nutrition.

A Review of Inverse Gas Chromatography and its Development as a Tool to Characterize Anisotropic Surface Properties of Pharmaceutical Solids[†]

Raimundo Ho[1]* **and Jerry Y.Y. Heng**[2]
[1] *Solid State Chemistry, Global Pharmaceutical Research & Development, Abbott Laboratories*
[2] *Surfaces and Particle Engineering Laboratory, Department of Chemical Engineering, Imperial College London*

Abstract

Surface properties can profoundly impact the bulk and interfacial behavior of pharmaceutical solids, and also their manufacturability, processability in drug product processes, dissolution kinetics and mechanism in drug delivery. Variation in the inter- and intra-molecular interactions gives rise to anisotropic surface properties of crystalline solids which display direction-dependent characteristics relative to the orientation of the crystal unit structure. Despite its establishment since the 1950s, inverse gas chromatography (IGC) is still an evolving technology in the field of pharmaceutical R&D. In this review, the principles behind IGC as a physicochemical technique to measure the surface properties of solids are presented. The introduction is followed by an overview of its utility in pharmaceutical R&D, spanning a variety of applications including batch-to-batch variability, solid-solid transitions, physical stability, interfacial behavior in powder processing, and more. For anisotropic materials, IGC has been utilized to characterize the heterogeneity of materials using adsorption and energy distribution functions. Recent development and applications of IGC at finite concentration (IGC-FC) to determine the surface heterogeneity distribution of solids are presented. This methodology overcomes a number of limitations associated with traditional experiments.

Keywords: inverse gas chromatography, surface energy, heterogeneity, anisotropy, crystal, energy distribution

1. Introduction

Many organic pharmaceutical crystalline solids exist in different solid-state forms in relation to their internal molecular conformations, resulting in differences in lattice energy and entropy. Anisotropic substances, as a result, exhibit different physical and chemical properties along different index crystal planes. For pharmaceutical solids, the properties that are of greatest interest are physical, thermodynamic, kinetic, surface, spectroscopic, optical, and electrical properties[1], which to a different extent, display anisotropy at the molecular level. Due to the anisotropic nature of crystalline solids, it is a subject of considerable interest for researchers.

A careful understanding of the anisotropic material properties plays a critical role in pharmaceutical development, formulation and manufacturing. During crystallization of the active ingredient, the crystal morphology is controlled by the solute-solvent interactions at the nuclei solid-liquid interface and the internal crystal structure anisoptropy[2]. Particle size and morphological control in mechanical size reduction processes are impacted by mechanical anisotropy which plays a fundamental role in the underlying breakage mechanism[3]. The dissolution rate of a solid form is dictated by the dissolution kinetics

---

[†] Accepted: August 21, 2012

[1] 1401 Sheridan Road, North Chicago, IL 60064, U.S.A.
[2] South Kensington Campus, London SW7 2AZ, United Kingdom
* Corresponding author:
E-mail: raimundo.ho@abbott.com
TEL: +1-847-937-3324 FAX: +1-847-938-5932

ⓒ 2013 Hosokawa Powder Technology Foundation

of individual crystal planes, therefore the crystal morphology of the drug[4]. Owing to their anisotropic optical properties, crystalline solids exhibit birefringence under polarized light microscopes - a common method to detect residual crystallinity[5]. The surface properties of a drug are influenced by its localized, facet-dependent surface chemistry, which ultimately dictates the strength and polarity of interactions at the interface[6].

For anisotropic materials, it is not uncommon to assume the dominant crystal plane to dictate its overall properties. However, with the technological improvement of physical characterization techniques and molecular modeling tools in combination with knowledge advancements, the anisotropy of the crystalline solids can now be more readily studied and predicted. The modern paradigm of materials science is gradually shifting away from old-school approaches based on simplified assumptions that particles are spherical and isotropic. This is evident in the growing number of research publications relating to anisotropic material properties, for instance, in the subjects of indentation hardness anisotropy[7], impact of crystal morphology on processing[8, 9], and physical simulation modeling of crystal shape using polygonal meshing and spherical composites[10].

The surface properties, the focus of this review, are known to profoundly impact material properties including dissolution[11], flowability[12], cohesion and adhesion[13], and a variety of processing behaviors including crystallization[14], wet granulation[15], milling[16], drug-excipient compatibility and mixing[17], coating, tableting[18] and aerolization performance of dry powder inhaler (DPI) formulations[19]. The experimental validation of the surface anisotropy of crystalline solids was reported by Heng *et al.* who conducted sessile drop contact angle measurements and X-ray photoelectron spectroscopy (XPS) analyses on indexed surfaces of macroscopic crystals and showed, for the first time, the facet-dependent surface chemistry of crystalline pharmaceutical solids[20]. Although the anisotropic surface properties of a crystalline solid may be dominantly attributed to individual crystal planes, the unique combination of impurities, growth steps, crystal edges, surface pores, surface disorders, and local degree of crystallinity can be important, particularly for imperfect crystalline systems. The anisotropic surface properties of crystalline solids are also referred to as 'heterogeneous' surface properties, owing to the fact that the material exhibits a *continuous* distribution of surface characteristics.

In this review, the principles behind inverse gas chromatography (IGC) as a tool to measure surface properties of solids are presented. This is followed by an overview of its applications in pharmaceutical research and development, and its utilization to measure the anisotropy and heterogeneity of compounds using adsorption and energy distribution functions. Finally, recent development and applications of IGC at finite concentration (IGC-FC) as a tool to determine the surface heterogeneity distribution of solids are presented.

2. Theoretical Aspects of IGC

2.1 Partition coefficient

The discovery of chromatography was made by the American petroleum chemist David T. Day and the Russian botanist Mikhail S. Tswett between 1903 and 1906. Tswett, however, was the first to recognize the sequential sorption-desorption interactions of chromatographic processes in his original experiments in which plant pigments were classified into colored bands by elution with petroleum ether through a bed of powdered calcium carbonate[21]. Since then, a highly sophisticated family of chromatographic techniques has evolved for physicochemical and analytical studies, involving gas-liquid, gas-solid, liquid-liquid and liquid-solid chromatography.

IGC, the inverse use of gas chromatography (GC) or gas-solid chromatography (GSC), was developed in the 1950s when the focus of physicochemical studies was directed towards the derivation of kinetic information and determination of thermodynamic quantities from sorption equilibria[22]. Much effort of this earlier work was focused on the characterization of catalytic materials such as activated carbon, alumina and silica. To date, IGC has become a well-established source of physicochemical data for various uses including polymers[23], inorganic compounds and catalysts[24, 25], food substances[26], carbon nanotubes[27], wood composites[28], and pharmaceuticals[29]. Its applications cover a wide spectrum including characterization of surface energetics, surface acid-base properties, solid-solid phase transitions, adsorption isotherm, energy distribution, solubility parameters[30], Flory-Huggins interaction parameters[23], diffusion kinetics, and polymer cross-link density.

IGC is a vapor probe technique applicable to powders and fibrous materials, and is compatible with sample porosity, irregular surface topographies, and surface heterogeneity, making it an attractive way of characterizing particulate pharmaceutical solids. In IGC, probe molecules in the vapor phase (adsorbate or solute) are passed over a sample solid (stationary phase adsorbent) which is packed in a column of inert surface via a carrier gas (mobile phase). The distribution of the solute between the stationary phase and the mobile phase at a particular temperature and pressure corresponds to an equilibrium when the solute-free energy is at a minimum. The partition coefficient (unit: unit length), K_R, is related to the concentration of adsorbate in the mobile phase (unit: mass/mole per unit area), c_M, and that in the stationary phase (unit: mass/mole per unit volume), c_S, via:

$$K_R = \frac{c_S}{c_M} = \frac{V_N}{\sigma \cdot m_S} \tag{1}$$

The partition coefficient is also directly related to the mass of the solid, m_S, the specific surface area of the solid, σ, and the net retention volume, V_N, which is defined as the volume of carrier gas required to elute the injected adsorbate through the column. Both K_R and V_N are indications of the interaction strength between the adsorbate and the solid sample of interest. Together, they form the fundamental basis for the derivations of equilibrium sorption thermodynamic parameters.

2.2 Pulse experiments at different surface coverage values

IGC experiments at infinite dilution are conducted via pulse injection of the probe vapors using very small amounts of adsorbate (<3% partial pressure typically). The use of low probe molecule concentrations results in very low surface coverage on the adsorbent and is therefore commonly referred to as 'adsorption at zero surface coverage'. Adsorption under these conditions follows Henry's Law, where the amount of probe molecules adsorbed is linearly dependent on the injection concentration. Chromatograms obtained under this regime are symmetrical and Gaussian in shape, and the retention time, t_R, is independent of the injection size (**Fig. 1a**). Due to high sensitivity, this regime is most ideal for measurements of thermodynamic parameters.

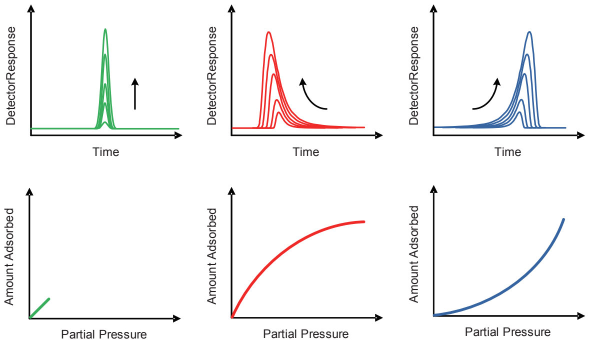

a) b) c)

Fig. 1 IGC chromatograms at a) infinite dilution b) finite concentration with 'tailing' and c) finite concentration with 'fronting'.

Experiments where the probe injection concentrations are increased beyond the Henry's Law region are referred to as finite concentration (IGC-FC) experiments. Chromatographic peaks under the finite concentration regime can show either 'tailing' (**Fig. 1b**) or 'fronting' (**Fig. 1c**). In 'tailing', the rate of change in the amount adsorbed decreases as a function of partial pressure. This adsorption is characterized by a Type I, II, or IV mechanism (IUPAC classification) with the formation of a monolayer of adsorbate on the adsorbent. In 'fronting', the rate of change in the adsorbed amount increases as a function of partial pressure. This adsorption is characterized by a Type III or IV mechanism, in which the binding affinity between adsorbate and adsorbent is weaker than the affinity between adsorbate molecules.

Two commonly employed detectors in gas chromatography are the thermal conductivity detector (TCD) and the flame ionization detector (FID), although the latter is probably more frequently used. The TCD measures the reduction in thermal conductivity of the carrier gas in the presence of the analyte and is therefore universally suitable for the detection of both organic and inorganic vapors. Thermal conductivity is established by measuring the heating resistance of a heating filament, and the measured current is compared to a reference current in a bridge circuit. However, since the thermal conductivity difference between the carrier gas and the analyte is important to the sensitivity of this type of detector, carrier gases other than hydrogen and helium (thermal conductivities are 6-10 times higher than those of organic vapors) are in principle not suitable because the drop in thermal conductivity in the presence of the analyte can be too small (detection limit: 10^{-8} g ml^{-1})[31]. The FID, on the other hand, is particularly sensitive to all compounds containing C-C and C-H bonds, and measures the change in electrical conductivity of a hydrogen flame in an electric field when feeding organic compounds.

The solute gross retention time, t_R, is the time required for the center of gravity of the solute band to pass completely through the column. In the infinite dilution regime where the chromatogram peak is symmetrical with a Gaussian profile, the centre of gravity is at the point of maxima of the chromato-

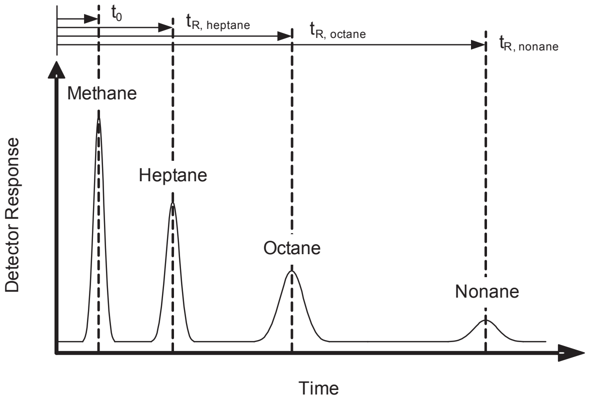

Fig. 2 The increase in retention time for increasing n-alkane chain lengths at infinite dilution concentration.

gram and therefore t_R corresponds to the time taken between injection and the peak maximum (**Fig. 2**). In the finite concentration regime, the elution time at peak maximum may be substantially different to the elution time computed from the center of gravity of the chromatogram.

The retention time is a measure of the strength of molecular interactions between the probe and the solid surface of sample packing in the column, and is the key measurement parameter in IGC analysis. The dead time, t_0, is the time required for a non-interacting, non-adsorbed ($K_R = 0$) solute to pass through the column. It is typically determined by methane, but argon, nitrogen and hydrogen are sometimes used. Experiments are possible with the frontal technique, in which case the breakthrough point of the breakthrough curve corresponds to the retention time. Due to its rarity in the literature, experiments in the frontal mode are not elaborated in this review.

With the column dead-time and gross solute retention time, the net retention volume, V_N, is determined via:

$$V_N = j \cdot F_c \cdot (t_R - t_0) \tag{2}$$

where F_c is the carrier gas flow rate in the column, and j is the James-Martin correction factor which corrects the net retention time for the pressure drop and variation in packing density of the solids within the column bed. The James-Martin correction factor, j, is defined as:

$$j = \frac{3}{2}\left[\frac{(P_{in}/P_{out})^2 - 1}{(P_{in}/P_{out})^3 - 1}\right] \tag{3}$$

where P_{in} and P_{out} are the inlet and outlet pressures, respectively.

Since V_N is dependent on the amount of the stationary phase and the experimental temperature, T, the specific retention volume referenced to 0° C, V_g^0, is sometimes used in place of the net retention volume, where:

$$V_g^0 = \left(\frac{V_N}{m_S}\right) \cdot \left(\frac{273.15}{T}\right) \tag{4}$$

Combining equation 2 and 4 yields:

$$V_g^0 = \frac{j}{m_S} \cdot F_c \cdot (t_R - t_0) \cdot \frac{273.15}{T} \tag{5}$$

2.3 Thermodynamic relationships

The standard Gibbs free energy change associated with the isothermal adsorption and desorption per mole of molecules, expressed respectively as ΔG_{ad}^0 and ΔG_{de}^0, is related to the net retention volume and partition coefficient via:

$$\Delta G_{de}^0 = -\Delta G_{ad}^0 = RT \ln V_N + C_1. \tag{6}$$

$$\Delta G_{de}^0 = -\Delta G_{ad}^0 = RT \ln K_R + C_2. \tag{7}$$

where C_1 and C_2 are constants depending on the chosen reference state[32]. Adsorption is considered as an exothermic event, whereas desorption is an endothermic event – the reason for the opposite directionality between the two ΔG^0.

Using van't Hoff's relationship, the standard enthalpy change of adsorption, ΔH_{ad}^0, can be obtained by measuring V_N at a range of experimental temperatures:

$$\Delta H_{ad}^0 = -R \cdot \frac{d \ln K_R}{d\left(\frac{1}{T}\right)} = -R \cdot \frac{d \ln\left(\frac{V_N}{\sigma \cdot m_S}\right)}{d\left(\frac{1}{T}\right)} \tag{8}$$

And the standard entropy change of adsorption, ΔS_{ad}^0, is related to the enthalpy and free energy terms by:

$$\Delta G_{ad}^0 = \Delta H_{ad}^0 - T \Delta S_{ad}^0 \tag{9}$$

The net retention volume of each alkane injection is related to the standard Gibbs free energy change of adsorption, ΔG_{ad}^0, and the work of adhesion by:

$$-\Delta G_{ad}^0 = RT \ln V_N + C_1 = N_A \cdot a_m \cdot W_A \tag{10}$$

where N_A is the Avogadro number and a_m is the molecular cross-sectional area of the adsorbed probe molecule. Applying Fowkes' principle for Lifshitz van der Waals interaction[33], Eq. 10 leads to:

$$RT \ln V_N = N_A \cdot a_m \cdot 2\sqrt{\gamma_{SV}^d \gamma_{LV}^d} + const. \tag{11}$$

Schultz *et al.* identified that the dispersive surface energy of solids can be obtained using a series of

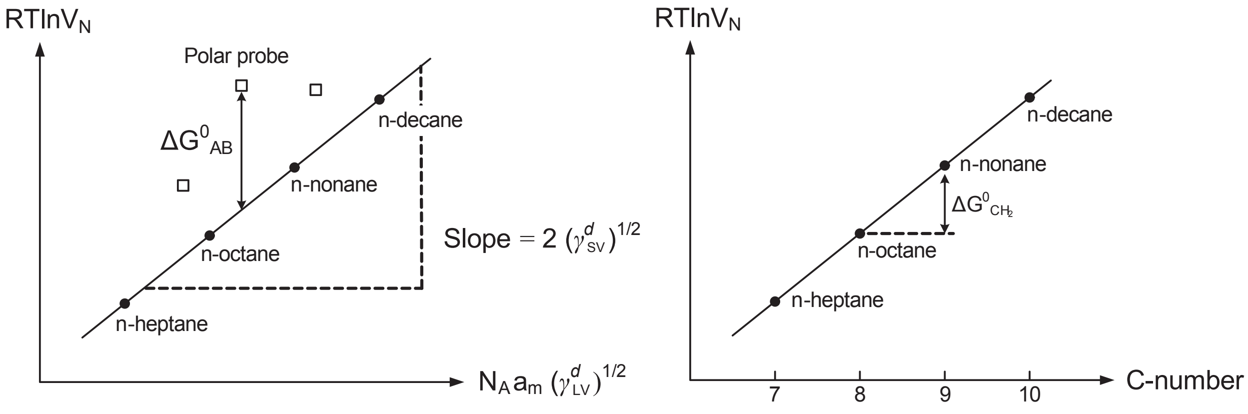

a)

b)

Fig. 3 Determination of solid-vapor surface free energy and acid/base free energy change of adsorption from a) the Schultz approach and b) the Dorris-Gray approach.

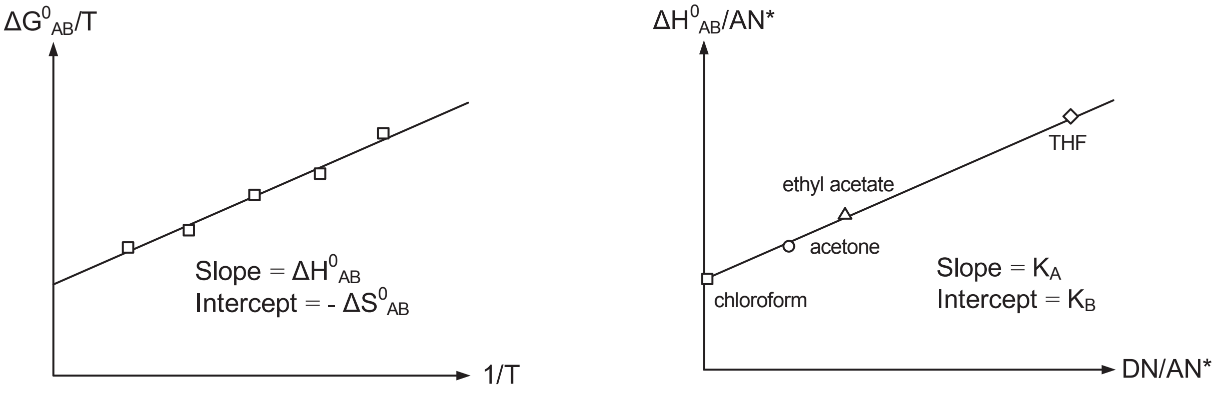

a)

b)

Fig. 4 Determination of a) acid-base enthalpy and entropy of adsorption from the acid/base free energy of adsorption via temperature variation, and b) the Gutmann's acid and base constants.

n-alkanes from a plot of $RT\ln V_N$ versus $N_A a_m \sqrt{\gamma^d_{LV}}$[32]. The γ^d_{SV} of the solid is calculated from the slope of a linear regression of the *n*-alkane line (**Fig. 3a**). Alternatively, γ^d_{SV} can be determined by considering the contribution of a methylene group (CH_2) in the normal alkane series to the free energy of adsorption, $\Delta G^0_{CH_2}$ (**Fig. 3b**) according to the Dorris and Gray approach[34]:

$$-\Delta G^0_{CH_2} = N_A \cdot a_{CH_2} \cdot 2\sqrt{\gamma_{CH_2}\gamma^d_{SV}} + const. \qquad (12)$$

where a_{CH_2} is the surface area occupied by a methylene group (6 Å^2) and γ_{CH_2} is the surface energy of a methylene group. Both methods are reported to give similar results for polycarbonates[35].

With the use of polar solute molecules, the Gibbs free energy change of adsorption now comprises an acid-base (polar) adsorption component, ΔG^0_{AB} , in addition to the dispersive component, ΔG^0_D :

$$\Delta G^0_{ad} = \Delta G^0_D + \Delta G^0_{AB} \qquad (13)$$

As such, the retention volumes measured with a polar probe will consist of a dispersive and acid-base (polar) component leading to higher absolute V_N values when compared with the occurrence of dispersive interactions alone using alkanes. The difference between the alkane regression line and the polar probe equates to ΔG^0_{AB} (**Fig. 3a**).

By measuring the absorbent with polar probes at different temperatures following Eq. 8, the acid-base (polar) component of ΔH^0_{ad} and ΔS^0_{ad} can be determined (**Fig. 4a**). The values of ΔH^0_{AB} obtained using various polar probes can then be used to evaluate the acid-base characteristics of the solid adsorbent via the modified Gutmann's equation[36, 37]:

$$-\Delta H^0_{AB} = K_A DN + K_B AN^* \tag{14}$$

where DN is the electron donor number of the adsorbate and AN^* is the corrected electron acceptor number of the adsorbate, and K_A and K_B are the acid and base numbers of the solid reflecting its surface electron accepting and donating characteristics, respectively. The acid and base numbers, K_A and K_B, are obtained from the slope and intercept, respectively, of a plot of $\Delta H^0_{AB}/AN^*$ versus DN/AN^* (**Fig. 4b**).

3. Applications of IGC at Infinite Dilution for Pharmaceutical Solids

3.1 Batch-to-batch variability, polymorphs and optical forms

With the suitability for particulate solid materials, it is not surprising that the interest in IGC in the pharmaceutical industry is growing. Despite the history of IGC in the studies of inorganic materials and polymers, it was not until the late 1980s that the first application of IGC on pharmaceutical solids was reported. The technique was first applied to study the bulk property of pharmaceutical solids by Phuoc *et al.*, who determined the Hansen partial and total solubility parameters of lactose, caffeine, theophylline, methyl-*p*-hydroxybenzoate and microcrystalline cellulose[38, 39]. The use of solubility parameters in the design of the pharmaceutical dosage form was reviewed by Hancock[30]. In 1994 and 1996, IGC was first applied to study the surface properties of pharmaceutical solids by Ticehurst *et al.*, who differentiated chemically and structurally equivalent batches of salbutamol sulphate[40] and α-lactose monohydrate[41], which exhibited variable processing performance.

In the subject of polymorphism, Tong *et al.* examined the thermodynamic properties of two polymorphs of salmeterol xinafoate prepared from supercritical fluids in which the metastable polymorph was shown to exhibit a higher surface energy, surface entropy and surface polarity than the stable form[42].

The strength of dispersive and acid-base (polar) interactions of solid surfaces can be explained based on the localized surface chemical environment. In a study of DL-mannitol and the β polymorph of D-mannitol by Grimsey *et al.*, differences in the surface properties were attributed to the surface densities of the dispersive and acidic sites from inspection of the crystallographic structure[43]. Sexena *et al.* combined IGC with dynamic molecular modeling to study the impact on surface energy due to factors such as surface pore, surface cavity size, functional groups and the presence of surface water molecules[44]. The modeled kinetic, structural and thermodynamic factors at the molecular level were responsible for the measured surface energetics.

3.2 Amorphous solids and glass transition

IGC has been used to study amorphous solids, including the determination of glass transition temperature (T_g), localized disorder, and structural relaxation of the amorphous glass. This capability stems from the unique sensitivity of IGC at infinite dilution in detecting subtle localized surface disorders, where alternative solid-state characterization techniques, such as conventional powder X-ray diffraction (PXRD), differential scanning calorimetry (DSC), thermal gravimetric analysis (TGA), Raman or FTIR spectroscopy, may fail.

Ohta and Buckton observed a direct correlation between the Gutmann basicity ratio (K_B/K_A) and the percentage crystallinity of cefditoren pivoxil from IGC measurements[45]. The dependence of γ^d_{SV} and basicity as a function of % RH was attributed to the exposure of basic carbonyl groups on the surface as crystallinity decreased. Hasegawa *et al.* applied IGC to examine the surface structural relaxation of an IMC-PVP dispersion below the T_g by monitoring the retention volume of decane over time[46]. The decrease in V_N was attributed to the surface structural relaxation of the solid dispersion. The kinetics of relaxation was modeled based on the rate of decrease in V_N to yield the relaxation parameter, τ^β, of the Kohlraush-Williams-Watts equation. The smaller τ^β from IGC than those obtained from DSC was attributed to a faster rate of structural relaxation at the surface compared to the bulk.

The physicochemical stability of granules of amorphous cefditoren pivoxil, with and without polymers, prepared from spray-drying and wet granulation was compared by Yokoi *et al.* using a variety of techniques including IGC[47]. The addition of polymers increased the physical stability of both spray-dried and wet-granulated cefditoren pivoxil. However, while the increase in physicochemical stability could be attributed to a decrease in molecular mobility (as determined by T_g shift) for the spray-dried materials, the granulated materials did not exhibit any difference in T_g by DSC. IGC and diffuse reflection IR revealed that for the granulated materials, the physicochemical stability was determined by molecular interactions between the drug and polymer at the surface, resulting in granules displaying a similar stability to that obtained from spray-drying.

The glass transition temperature of amorphous solids can be determined from retention volume measurements using IGC. The methodology is based on the principle that amorphous materials exhibit very different sorption mechanisms above and below the T_g, leading to changes in the molecular retention mechanism. As an amorphous solid is heated through the glass transition region, the glassy and rubbery states can co-exist, resulting in a retention mechanism combining surface adsorption and bulk absorption. Below the glass transition region where the glassy state dominates, surface adsorption is the dominating retention mechanism. In the rubbery state above T_g, the retention mechanism is via a combination of both surface and bulk sorption. The variation in V_g^0 as a function of temperature can therefore be used to determine the onset of T_g. Following this approach, Surana *et al.* investigated the T_g of amorphous sucrose and co-lyophilized sucrose-PVP mixtures using IGC, and compared the results with results obtained from DSC48). T_g values at 0% RH obtained by IGC were in good agreement with those determined using DSC49). As the relative humidity increased, a progressive decrease in T_g was measured as a result of the plasticizing effect of water. The predicted T_g values of the plasticized materials were in very good agreement with those determined experimentally using IGC.

Otte and Caravajal employed a combination of particle size, surface area, IGC, DSC and PXRD to examine the surface disorder and bulk properties of ketoconazole and griseofulvin as a function of cryomilling time50). A reduction in surface crystallinity and an increase in γ_{SV}^d and ΔG_{AB}^0 were observed for both compounds upon cryomilling. Ketoconazole underwent a change in surface structure, whilst a phase transition event which occurred at much lower temperature than the T_g was detected by IGC for griseofulvin. The authors concluded that the mechanofusion of surface fines and the existence of an intermediate metastable phase are the consequences of cryomilling for the two compounds, respectively.

Brum and Burnett utilized IGC to quantify the amorphous content in both a model drug substance and lactose by a linear summation of the individual work of adhesion components due to the amorphous phase and crystalline phase based on their respective surface area fractions51). Using physical mixtures of known quantities and known amorphous surface area fraction, a calibration curve can be established from the measurements of surface area normalized dispersive surface energies. By characterizing the dispersive surface energy, the fraction of amorphous content in lactose and in the model drug substance was quantified successfully from the calibration curves.

3.3 Crystal morphologies

The recrystallization of crystalline materials from solution can result in various forms of crystal morphologies or shapes. Storey investigated the surface properties of ibuprofen recrystallized from methanol, acetonitrile and hexane by IGC52). Both the γ_{SV}^d and acid-base surface properties were found to be dependent on the crystal shape, and could be explained based on the difference in the percentage area of polar and apolar crystal facets as a consequence of the solvent used during crystallization. Heng *et al.* studied the surface properties of paracetamol crystals grown from methanol and acetone, which resulted in crystals exhibiting prismatic and planar morphology, respectively. Although the γ_{SV}^d values were found to be similar, the two morphological entities possessed different K_A and K_B 53). It is expected that crystals with the planar morphology are dominant in facet (201), and hence will exhibit a higher degree of basicity due to the presence of carbonyl functionality.

3.4 Surface properties and powder processing

Infinite dilution IGC has also been used to measure process-related changes in surface properties and to assess the performance of drug delivery systems and powder processes. The effects of milling on the surface properties of paracetamol were investigated by Heng *et al.* 54). Crystals may cleave across their cleavage planes upon milling with increasing tendency as the particle size is reduced. Surface property measurements were performed on unmilled and milled samples of paracetamol crystals of various size fractions. An increase of γ_{SV}^d with decreasing particle size was measured, revealing an increased dominance of the weakest attachment energy facet. On the other hand, the γ_{SV}^d for the unmilled fractions was independent of particle size and was reflective of the surface energies of the external facet. The effects of micronization on the γ_{SV}^d and relative basicity of salbutamol sulphate and DL-propranolol hydrochloride were investigated by Feeley *et al.* 55) and York *et al.* 56), respectively. Both micronized materials were found to possess a higher γ_{SV}^d than the unmicronized substances, whereas the acid-base properties were slightly different. It was concluded that the change in surface properties was due to preferential cleavage along the weakly attached facet. Davies *et al.* compared surface energetics of unmilled and micronized budesonide determined from atomic force microscopy (AFM) and IGC. In AFM, a small fraction of the total surface area is measured, and the surface energies are therefore related to the location and local topography, whereas IGC at infinite dilution would overestimate the average surface energy of a material. However, because of their abilities to characterize materials at different scales (particulate level or bulk level), it was concluded that both AFM and IGC are useful complimentary tools to assess, in a quantitative manner, particulate interactions and intrinsic material properties.

The performance of dry powder inhalation formulations was examined by Tong *et al.,* who investigated the relative influence of drug-drug cohesion and drug-carrier adhesion on the *in vitro* performance of salmeterol xinafoate (drug) with lactose (carrier) by measuring the surface energies and solubility parameters of the components using IGC at infinite dilution[57]. The inhaler performance of salmeterol xinafoate was found to improve significantly if the drug-carrier adhesion was stronger than drug-drug cohesion. Cline and Dalby similarly observed that increasing surface interaction between drug and carrier, as measured by IGC, resulted in an improved fine particle fraction of the drug[58]. Das *et al.* found a negative correlation between the total surface energy and dispersiblity of a DPI formulation of salmeterol xinafoate and lactose[59]. The fine particle fraction of the mixture decreased significantly after storage at 75%RH. The decrease was primarily attributed to the presence of surface-adsorbed moisture after storage at 75%RH, resulting in an increase of surface energy due to the introduction of new polar sites on the surfaces of the particles.

In a separate study on the suspension stability of pressurized metered dose inhalers (pMDIs), Triani *et al.* investigated the surface properties of salbutamol sulphate, budensonite and formoterol fumarate dihydrate in a model propellant, using both AFM and IGC[60]. The authors suggested that polar contributions to surface energy may be crucial in determining the stability of these suspensions.

The effect of primary particle surface energy in fluidized bed wet granulation was studied by Thielmann *et al.*, in which the hydrophobic particles agglomerated to become larger particles compared to the hydrophilic species[61]. Dispersive and non-dispersive surface energies of the particles, measured by IGC pre- and post-granulation, revealed that a thin binder coating layer was present on the surface of the hydrophilic particles after granulation. It was suggested that the relatively thin binder layer was not able to dissipate the kinetic energy of granules during impact, resulting in a certain critical granule size.

Fichtner *et al.* studied the effect of surface energy on the compactability of amorphous spray-dried lactose, with or without a low proportion of surfactant, by measuring γ_{SV}^{d}, K_A and K_B using IGC[18]. The compactability and γ_{SV}^{d} was found to be dependent on the composition of powders. At constant tablet porosities, the decrease of tablet strength was due to the decrease in powder surface energy. The authors concluded that the strength of bonding forces between particle contacts is controlled by surface energy which in turn can be altered by the presence of surfactants.

4. Existing Approaches for Characterizing Energy Distributions

Despite the sensitivity of IGC at infinite dilution, experiments at this concentration range may be criticized for their tendency to characterize higher energy sites of the solid surface. Small concentrations of adsorbates that are used in infinite dilution studies are thought to preferentially interact with the higher energy sites on the surface, and therefore the interaction with lower energy sites of the adsorbent would be limited, if not excluded[62]. As a result, this measured upper limit estimate may not be representative of the whole surface and may yet be incomparable to the surface energetics measured by alternative characterization techniques, such as sessile drop contact angle when the energy is expressed as an average of the probed area.

The possibility to characterize the surface energy distribution of a surface by IGC was recognized in the 1970s. These approaches to characterize energy heterogeneity can be categorized into pressure- or temperature-dependent adsorption and desorption methods[63]. The former method results in either an adsorption energy distribution[64] or adsorption potential distribution[63, 65], whereas the latter leads to a desorption energy distribution. More elaborated reviews on the determination of surface heterogeneity from adsorption measurements can be found elsewhere[66, 67].

4.1 Adsorption energy distribution

All approaches on the adsorption energy distribution described in the literature are based on a physical model which assume that an energetically heterogeneous surface consists of a continuous distribution of adsorption energies and may be described as a superposition of a series of homogenous adsorption patches. In this model, the surface coverage, n/n_m, is given by the integral equation:

$$n/n_m(P) = \int_{\in_{\min}}^{\in_{\max}} \theta_L(\in, P)\cdot\chi(\in)d\in \text{ For constant } T \quad (15)$$

where θ_L is the local adsorption isotherm, $\in$ is the adsorption energy of a site and χ is the continuous adsorption energy distribution function. As the equation has no general solution, approaches towards its solution are not trivial and typically rely on extensive computer simulations. The task of solving the equation is additionally magnified by its 'ill-posed' nature, which is related to the large variation in energy distribution function with just a small variation in the experimental data[64]. Since the distribution function $\chi(\in)$ is a quantitative description of energetic heterogeneity characterizing the solid surface, extensive efforts have been made in solving Eq. 15 with respect to $\chi(\in)$.

In Eq. 15, only the experimental (global) isotherm is known, the choice of the local isotherm $\theta_L(\in, P, T)$ has to be chosen according to the physical hypothesis describing the interactions between probe and adsorbent molecules, and the interactions between neighboring probe molecules. The energy distribution function $\chi(\in)$ is therefore strongly dependent on the choice of this local isotherm. A number of methods have been proposed to describe the energy distribution function[64]. The first category of methods ascribes a given analytical form to $\chi(\in)$, but many authors who tried to develop solution methods failed to consider the shape of the distribution function. The second category of methods assumes a discrete distribution of monoenergetic sites. With an increasing number of monoenergetic sites, the inversion of the matrix containing a large number of linear equations is not a simple task, leading to instability of the solution. The third category of methods is by solving Eq. 15 using local isotherm approximations such as condensation approximation. The final category of methods relies on the application of Plancherel's theorem to correlate the Fourier transform of the distribution function directly to the ratio of the Fourier transforms of the experimental isotherm and the Fourier transform of the local isotherm.

Although considerable developments have been made in trying to solve the integral equation, it is conceded that the method will not allow the attainment of the *absolute* surface energy distribution of the solids. Sacchetti reported the use of the discretization approach in the analysis of the surface heterogeneity of α-lactose monohydrate which displays regions of higher energy and ultrahigh energy 'hotspots'[68]. To the best of our knowledge, this is the only application of the adsorption energy distribution on an organic pharmaceutical solid.

4.2 Adsorption potential distribution

From the adsorption isotherm, the adsorption potential, A, can be related to the equilibrium partial pressure, P, the saturation pressure, P_0, and the column temperature, T, via[69]:

$$\mathrm{A} = RT\ln\left(\frac{P_0}{P}\right) \quad (16)$$

The adsorption potential distribution, X_n, is obtained from the first derivative of the characteristic adsorption curve which is a plot of the amount adsorbed n against the adsorption potential A.

$$\mathrm{X}_n = -\frac{dn}{d\mathrm{A}} \quad (17)$$

The adsorption potential distribution can be normalized by dividing Eq. 16 by the monolayer capacity. The approach of adsorption potential distribution was reported to be less affected by experimental variations, to produce more reliable results, and to be much simpler[25]. Nevertheless, the validity of the adsorption potential distribution relies on the assumption of a physisorption interaction between the probe and the surface site[25]. Molecules such as some polar probes adsorb via a reversible or irreversible chemisorption, leading to a slow desorption or non-desorption of the probes.

4.3 Desorption energy distribution

In the case of reversible chemisorption, the surface heterogeneity can be determined by combining IGC with thermal desorption methods in the temperature-programmed desorption (TPD) technique. In this approach, a sample is heated at a defined heating rate and the partial pressure and amount of the desorbed molecules are measured. Although one can obtain the surface heterogeneity of the sample from the desorption profile (or TPD spectrum), in reality the quantitative interpretation of the desorption profiles is difficult due to diffusion and re-adsorption effects on the overall rate of desorption[70].

Characterization of the desorption energy distribution is based on the first linear Fredholm equation, similar in structure to Eq. 15, and the desorption distribution function is calculated as a kernel by inversion of the integral equation[71]. The solution of this 'ill-posed' problem again requires an extensive computing algorithm which has been mainly applied in the studies of catalysts[71-73].

In comparison between the temperature and pressure method in the characterization of surface heterogeneity, the former is more suitable for highly energetic surfaces, while the latter method is more appropriate for less energetic surfaces and also more sensitive to surfaces with smaller differences between energy levels. Though these methods can lead to a distribution of surface heterogeneity, the interactions of the adsorbing molecules with surface sites depend on the chemical nature of the probes. These methods therefore only provide information concerning the 'relative' heterogeneity and can only be used as fingerprints for comparisons between different materials. Until recently, there has been a lack of emphasis on the understanding of the surface energy heterogeneity of pharmaceutical materials, despite the apparent anisotropic properties displayed by many crystalline materials.

5. Recent Development in Characterizing Surface Energy Heterogeneity Distribution

5.1 Theoretical aspects

We recently reported a new methodology to measure the surface energy heterogeneity of particulate solids based on IGC-FC[6, 74, 75]. The advantage of this new approach not only stems from the fact that it contains fewer drawbacks compared to methodologies described in the previous section, this approach also permits attainment of an *explicit* γ_{SV}^{d} distribution from adsorption data using IGC.

The measurement of dispersive and acid-base (polar) surface energy distribution relies on a series of finite concentration IGC experiments using a series of *n*-alkanes and polar solvents. The first step is to determine the adsorption isotherms of all probe molecules with IGC at finite concentrations. A detailed description of the determination of adsorption isotherms by IGC-FC is given by Cremer and Huber[76]. Generally, two methods can be distinguished for adsorption isotherm calculations from IGC elution chromatograms: the peak maximum method (PM) and the elution of a characteristic point (ECP) method (**Fig. 5**). In the PM method, an increasing concentration of probe vapor is injected into the column, and the equilibrium partial pressure for each single concentration is measured from the peak maximum of each chromatogram (**Fig. 6** – Step 1). In the ECP method, it is assumed that the maxima of each individual peak from the single injections coincide with the rear of the chromatogram produced by the highest injection concentration. The ECP method is experimentally faster because the isotherm is calculated from the chromatogram of only the greatest injection concentration. The ECP method, however, relies on the adsorption mechanism being physisorption of Type II, IV or V, and that the rear of the chromatogram is entirely due to sorption effects which neglect the gas phase diffusion and which may deviate the ECP calculations from those resulting from the PM method.

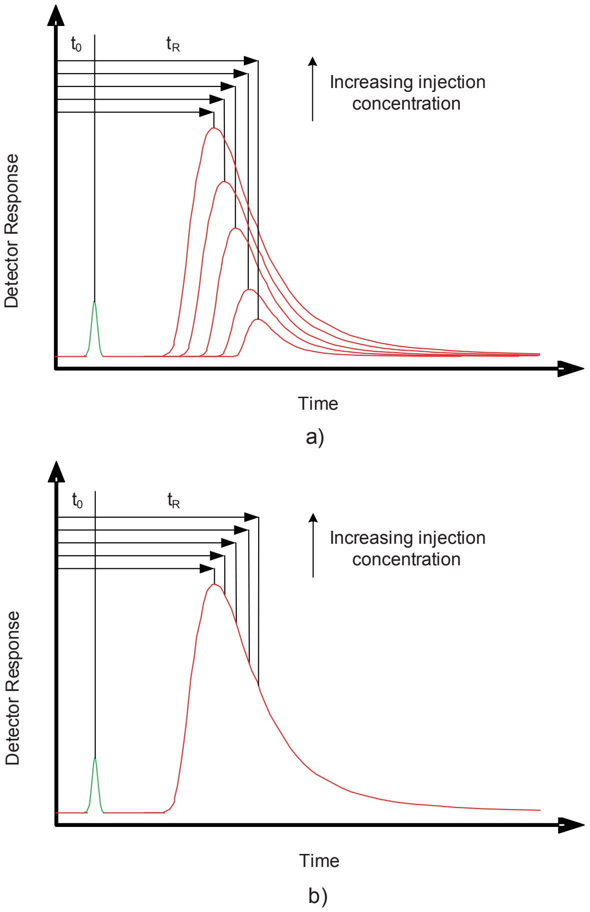

Fig. 5 Schematic of a) the PM method and b) the ECP method.

In the PM method which in the experience of the authors, provides more accurate adsorption isotherms, the equilibrium partial pressure, P, for each concentration of vapor in the column can be calculated from the chromatogram shape via (**Fig. 6** – Step 2):

$$P = \frac{h_c}{F_c \cdot A_c} \cdot V_{Loop} \cdot \frac{273.15}{T_{Loop}} \cdot P_{inj} \tag{18}$$

where h_c is the chromatogram peak height, A_c is the chromatogram peak area, V_{Loop} is the injection loop

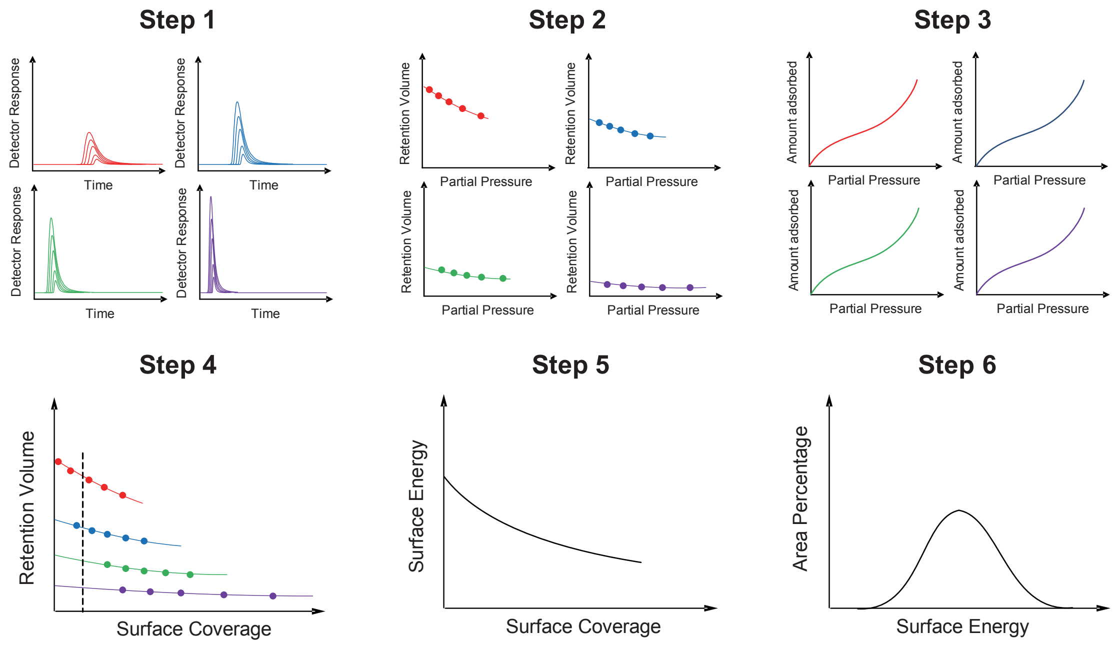

Fig. 6 Determination of surface energy distribution by IGC-FC.

volume, T_{Loop} is the injection loop temperature and P_{inj} is the partial pressure of the solute inside the injection loop. The corresponding retention volume, V_N, for each injection concentration can be determined as usual via Eq. 2. The adsorbed amount, n, and therefore the adsorption isotherm for each probe vapor can then be obtained by integration of V_N versus P (**Fig. 6** – Step 3):

$$n = \frac{1}{m_S}\int \frac{V_N}{RT}dP \qquad (19)$$

In order to determine the surface energy distribution, the retention volumes must be corrected to their corresponding surface coverage, n/n_m. This is due to the fact that injections with different concentrations of adsorbate will result in different extents of surface coverage of the probe over the solid surface (**Fig. 6** – Step 4). By assuming that the alkanes or weakly polar probes are absorbed in a Type II or IV adsorption mechanism, the BET model can be applied to determine the monolayer capacity, n^m, from Eq. 20 provided that the specific surface area of the sample, σ, is known:

$$\sigma = a_m \cdot N_A \cdot n_m \qquad (20)$$

The BET specific surface area of the sample can be calculated from one of the alkane isotherms or determined separately by another technique, for instance by nitrogen adsorption at 77K. Although the adsorption mechanisms of pharmaceutical solids are predominantly Type II or IV, the measurement of a complete adsorption and desorption profile will provide added assurance on the applicability of the BET model. The corresponding surface coverage, n/n_m, at each injection concentration can now be calculated from the amount adsorbed n from the monolayer capacity. The process is repeated on other n-alkanes and polar probes being tested such that the net retention volumes are provided as a function of probe surface coverage values.

The next step in the methodology is to determine γ_{SV}^d and ΔG_{AB}^0 (for polar probes) at constant isosteres, i.e. constant probe surface coverage values. The solid-vapor surface energy can be determined at a number of isosteres by applying the Schultz or Dorris-Gray approach to calculate the γ_{SV}^d values, thereby resulting in a profile of γ_{SV}^d as a function of surface coverage (**Fig. 6** – Step 5). Similarly for a polar probe, the profile of the acid-base (polar) Gibbs free energy change of adsorption, ΔG_{AB}^0, can be calculated. The regression coefficient, R^2, for the linearity of fit of the alkane retention data was proposed as a criterion for predicting the robustness of the γ_{SV}^d profiles obtained[77]. It was proposed that the relative error in γ_{SV}^d values determined from the alkane regression line is a function of the R^2 coefficient, with an R^2 of 0.9999 providing γ_{SV}^d profiles of least error.

Applying the van Oss, Chaudhury and Good (vOCG) approach, the acid-base surface energy profile, γ_{SV}^{ab}, of the solid can be obtained by using a pair of monopolar acidic and monopolar basic probes from their respective ΔG_{AB}^0 values[78]. However, the accuracy of this approach to obtain γ_{SV}^{ab} is sensitive to the acid, γ^+, and base, γ^-, parameters of the probes. van Oss *et al.* utilized water as a reference with γ^+: γ^- equal to unity, which is assumed to be the cause of the "basicity catastrophe"[79]. Della Volpe and Siboni, however, proposed a different ratio suggesting that water is acidic rather than amphoteric[80]. In addition to the debate surrounding the scale of acidity to basicity, the monopolarity of the probes is a critical requirement for this approach. Hence in its current state, this reported approach to the calculation of acid-base surface energy profiles may only be applicable on relative terms to compare the relative magnitude of acid-base properties between batches.

The surface energy profile can be further processed mathematically to obtain a surface energy distribution by numerical integration of the profile across the entire range of surface coverages (0-100%) (**Fig. 6** – Step 6). A surface energy distribution is analogous in principle to a particle size distribution wherein particle size is replaced by surface energy and frequency density is replaced by area increment or surface area percentage. However, to enable an integration across the full surface coverage range, the experimentally determined functions of V_N versus n/n_m may need to be extrapolated with best-fit curves to full surface coverage. This need is primarily driven by the fact that traditional IGC instrumentation is designed and constructed to perform small injections in the Henry region. Therefore a full coverage, especially with large molecular probes with low saturation vapor pressures, may not be achievable due to hardware limitations.

5.2 Recent applications for pharmaceutical characterization and process understanding

Applying this methodology using IGC-FC, the surface energy heterogeneity due to the anisotropy of crystalline pharmaceutical solids was investigated using a pharmaceutical excipient, D-mannitol, as a model material[6]. To test the robustness of this methodology, the measured surface energetic heterogeneity profile was compared to the facet-dependent surface energetics measured by the sessile drop contact angle technique on macroscopic single crystals. The γ_{SV}^d determined from both IGC-FC and contact angle showed extremely good agreement: the lowest γ_{SV}^d measured with IGC-FC corresponds to the lowest γ_{SV}^d measured on single crystals, i.e. facet (011), and γ_{SV}^d of facet (120) and (010) both fall within the range of the measured surface energy profile.

In a separate study, the sensitivity of the technique in probing subtle anisotropic variations of the crystals due to morphological changes was examined[74]. As the aspect ratio of D-mannitol decreased (longer crystals), the surface energy profile revealed a decrease in the overall contribution of the lower dispersive surface energy regions, which could be attributed to the decrease in the proportion of the lowest energy crystal facet (011). With these validational experiments, it is clear that the surface energy heterogeneity/anisotropy by IGC-FC correlates well with complimentary techniques such as sessile drop contact angle. Due to the practicality and suitability for studying particulate materials, it is logical that IGC-FC will become a more useful tool to determine the surface heterogeneity of solids.

In addition to applications for heterogeneous/anisotropic materials, this methodology was also employed to examine surface homogeneous/isotropic solids prepared from surface modification via functionalization of methyl groups[6]. Upon surface modification, surface energy profiles of D-mannitol exhibited remarkable changes: untreated D-mannitol showed a high level of surface heterogeneity in both dispersive and polar interactions, whereas upon surface methylation, the surface energy profiles of γ_{SV}^d and ΔG_{AB}^0 became energetically homogeneous. These studies revealed that the new approach using IGC-FC is not only sensitive to surface energetic and chemical anisotropy, but also to surface homogeneity and subtle surface chemical changes.

For drug delivery systems and in the processing of crystalline solids, the utilization of surface energy heterogeneity may play an important role in understanding the underlying fundamental behavior. One such example is demonstrated by the performance of carrier-based DPI drug delivery systems which is determined to a significant degree by the preparation of the formulation[19]. It is known that the relative strength of drug-carrier adhesion and drug-drug cohesion is critical to provide an adequate fine particle dose (FPD) of the drug[81]. In this respect, the study of surface energy distributions may provide further understanding of the intrinsic material properties, in addition to the aerodynamic particle size distributions, shape distributions, bulk and true densities, surface roughness (rugosity) and electrostatic propensity which can also impact the aerolization performance of the formulation[82]. Considered from a purely surface energetic perspective, if the loaded drug dose is increased beyond a state in which the high energy sites of the carrier are fully 'saturated', the overall drug-excipient interaction would be weak enough to provide adequate drug detachment upon aerosolization. However, if the cohesion between drug-drug particles or excipient-excipient particles is stronger than drug-excipient adhesion, a robust formulation would be difficult to achieve.

Thielmann *et al.* employed IGC-FC to examine differences in γ_{SV}^{d} profiles of α-lactose monohydrate as a function of processing routes, in which untreated, recrystallized and amorphous lactose, prepared by spray-drying, was investigated[83]. Recrystallized lactose was energetically more homogeneous than milled and untreated lactose. The broader and more heterogeneous surface energy distribution displayed by milled and untreated lactose was due to surface amorphous regions and anomeric compositions, respectively. Their findings are particularly interesting, especially from a formulation development perspective, because the trend of γ_{SV}^{d} at low surface coverages (infinite dilution region) compared to that at high surface coverages is reversed. This study provided important insights into various aspects of the anisotropic/heterogeneous properties in drug delivery systems, e.g. What are the relative contributions to the overall behavior? What is the dominant contribution? Which is the contribution that is dictating the process? To answer these questions, it is clear that attention should be paid to the utilization of characterization approaches, not limited to IGC, which would provide a thorough understanding of the material's physical and chemical properties.

In DPI formulation, the use of a ternary formulation to optimize drug delivery of the active ingredient has been reported, whereby a small amount of fine excipient particles is added to the coarse carrier and the drug blend[84, 85]. Despite the evidence that the use of such methods shows an improved FPD of the active agent, the mechanism by which the fine particles alter the performance of the formulation has remained elusive[86]. A hypothetical mechanism is the passivation of high energy sites by the addition of fine excipient particles such that the drug particles are forced to bind to surfaces with lower energies during subsequent blending of the drug into the binary carrier-fine particle mixture[86]. To provide practical understanding behind the mechanism, the surface energetic profiles of different processed coarse lactose and the subsequent changes to the surface energy profiles by the blending of fine lactose particles were characterized using IGC-FC[75]. The unmilled coarse lactose sample (LH100) showed less heterogeneity than the milled sample (LH250), whilst the fine particles (LH210) exhibited a higher surface energy than both the coarse and milled lactose. Upon loading different quantities of fine fraction (LH210) to milled lactose (LH250), the surface energy heterogeneity of the blend decreased with increasing fines content. It is postulated that homogenizing the surface properties of the carrier by the addition of fine excipient particles may create more consistent drug-carrier interactions, therefore increasing the stability of the formulation.

In a recent study, IGC-FC was employed to study the impact of crystal morphology on the milling mechanism of crystalline solids using D-mannitol as a model compound[87]. Upon milling D-mannitol with a needle morphology, the crystals preferentially fractured along their shortest axis, exposing the (011) plane to create particles with greater hydrophilicity and a lower aspect ratio. The results are in contrast to attachment energy modeling which predicts a fracture mechanism across the (010) plane with increased hydrophobicity and a small change in particle shape. This study is the first in literature to show that the surface energy, γ_{SV}^{d}, can be reduced by milling, which typically results in a higher surface energy and entropy due to surface disorders induced as a result of high-energy processing. The reduction in surface energy was caused by a geometrically driven fracture mechanism along the axis of least distance as opposed to a thermodynamic fracture process based on intrinsic crystal lattice energy. The study revealed that the surface properties are directly dictated by the mechanism of milling, leading to substantial changes in the surface chemistry – increase or decrease in surface polarity are both equally viable. This work also provides a fundamental scientific basis on how to investigate the anisotropic behavior of pharmaceutical solids, and its impact on processing behavior.

Besides size reduction processes, IGC-FC has also been applied to study agglomeration processes in the example of high-shear wet granulation[15]. The initial phase in wet granulation is driven by successful nucleation of agglomerates from primary particles in the granulator by the liquid binder. These nuclei granules are initiated by energetically favorable wetting of the solid particles by the liquid binder, which is governed by interfacial thermodynamics. In a study on the wet granulation of an energetically heterogeneous model excipient and an energetically homogeneous excipient, clear distinctions between the cumulative granule size distributions can be observed by changing the ratio of the two components in the mixture. The study revealed that increasing the mass of low-energy energetically homogeneous content resulted in a reduction of the granule particle size. This was explained by the lack of viscous contacts between particles of poorly wettable surfaces resulting in a low probability of particle coalescence, because the collision kinetic energy cannot be dissipated sufficiently without the presence of a liquid boundary layer. Furthermore, the microstructure of the granules was revealed to differ significantly, with granules of lower mechanical integrity generated from an increase of the low surface energy component in the mixture.

6. Conclusions

The anisotropic properties of pharmaceutical solids pose difficult challenges to API and drug product process development. A lack of understanding in the relationship between bulk powder behavior and its anisotropic properties can lead to difficulties in assessing the effects of material properties on process performance without significant experimental effort, which is inefficient and resource-consuming. To aid the prediction of process and formulation performance from material properties, traditional approaches have been based on idealized assumptions of particles. Nevertheless, rapid advancement in the field of materials science for pharmaceutical solids together with technological improvements in characterization, processing and modeling tools are attracting growing research efforts in the field of particle engineering.

As discussed in this review, the surface properties of materials are important to help predict a wide variety of material behavior, processing and product performances in pharmaceutical development and manufacturing. Although IGC has been applied widely in the study of inorganic materials and polymers for over 50 years, it is still an evolving technology in pharmaceutical R&D. As reviewed in this work, IGC is a *complimentary* tool to provide additional information on the solid state properties, in particular the surface properties, of materials to aid the understanding of material changes under various conditions, as well as their behavior during processing. Experiments with IGC are often conducted at infinite dilution conditions, often probing the higher energetic sites. When the surface properties of crystalline solids are anisotropic, conventional approaches for the determination of surface energetics that yield a single value can be of limited use. Recently, a novel methodology using IGC at finite concentrations has been developed for the measurement of particulate surface energetic distributions.This methodology, extensively reviewed here, allows the surface energy of particulates to be determined at different surface coverage, overcoming drawbacks and limitations to the conventional approach of measuring surface heterogeneity using energy or potential distribution functions. Its applications have been demonstrated in a number of different case studies in this review. For a pharmaceutical crystalline material, it is the relationship between its crystallographic structure, solid state properties, and bulk and interfacial behavior that will determine its performance as a drug substance or drug product.

References

1) Byrn, S. R. et al. (1999): "Solid-State Chemistry of Drugs”. 2nd ed., SSCI, Inc., West Lafayette.
2) Lahav, M. and Leiserowitz, L. (2001): The effect of solvent on crystal growth and morphology, Chemical Engineering Science, vol.56, pp.2245-2253.
3) Olusanmi, D. et al. (2011): The breakage behaviour of Aspirin under quasi-static indentation and single particle impact loading: Effect of crystallographic anisotropy, International Journal of Pharmaceutics, vol.411, pp.49-63.
4) Snyder, R. C. et al. (2008): The evolution of crystal shape during dissolution: Predictions and experiments, Crystal Growth & Design, vol.8, pp.1100-1101.
5) Sugano, K. et al. (2006): High throughput solubility measurement with automated polarized light microscopy analysis, Journal of Pharmaceutical Sciences, vol.95, pp.2115-2122.
6) Ho, R. et al. (2010): Determination of surface heterogeneity of D-mannitol by sessile drop contact angle and finite concentration inverse gas chromatography, International Journal of Pharmaceutics, vol.387, pp.79-86.
7) Duncan-Hewitt, W. C. et al. (1994): Hardness anisotropy of acetaminophen crystals, Pharmaceutical Research, vol.11, pp.616-623.
8) Chikhalia, V. et al. (2006): The effect of crystal morphology and mill type on milling induced crystal disorder, European Journal of Pharmaceutical Sciences, vol.27, pp.19-26.
9) Rasenack, N. and Muller, B. W. (2002): Crystal habit and tableting behaviour, International Journal of Pharmaceutics, vol.244, pp.45-57.
10) Jia, X. and Williams, R. A. (2001): A packing algorithm for particles of arbitrary shapes, Powder Technology, vol.120, pp.175-186.
11) Lippold, B. C. and Ohm, A. (1986): Correlation between wettability and dissolution rate of pharmaceutical powders, International Journal of Pharmaceutics, vol.28, pp.67-74.
12) Han, X. et al. (2011): Simultaneous micronization and surface modification for improvement of flow and

dissolution of drug particles, International Journal of Pharmaceutics, vol.415, pp.185-195.

13) Clint, J. H. (2001): Adhesion and components of solid surface energies, Current Opinion in Colloid & Interface Science, vol.6, pp.28-33.

14) Lovette, M. A. et al. (2008): Crystal shape engineering, Industrial & Engineering Chemistry Research, vol.47, pp.9812-9833.

15) Ho, R. et al. (2011): Role of surface chemistry and energetics in high shear wet granulation, Industrial & Engineering Chemistry Research, vol.50, pp.9642-9649.

16) Newell, H. E. et al. (2001): The use of inverse phase gas chromatography to measure the surface energy of crystalline, amorphous, and recently milled lactose, Pharmaceutical Research, vol.18, pp.662-666.

17) Rumondor, A. C. F. et al. (2009): Phase behavior of poly(vinylpyrrolidone) containing amorphous solid dispersions in the presence of moisture, Molecular Pharmaceutics, vol.6, pp.1492-1505.

18) Fichtner, F. et al. (2008): Effect of surface energy on powder compactibility, Pharmaceutical Research, vol.25, pp.2750-2759.

19) Chow, A. H. L. et al. (2007): Particle engineering for pulmonary drug delivery, Pharmaceutical Research, vol.24, pp.411-437.

20) Heng, J. Y. Y. et al. (2006): Anisotropic surface energetics and wettability of macroscopic form I paracetamol crystals, Langmuir, vol.22, pp.2760-2769.

21) Tswett, M. S. (1906): Physical chemical studies on chlorophyll adsorptions, Berichte der Deutschen botanischen Gesellschaft, vol.24, pp.316-323.

22) Laub, R. J. and Pecsok, R. L., (1978): "Physicochemical Applications of Gas Chromatography". 99 ed., John Wiley & Sons, New York.

23) Voelkel, A., et al. (2009): Inverse gas chromatography as a source of physiochemical data, Journal of Chromatography A, vol.1216, pp.1551-1566.

24) Tisserand, C., et al. (2009): Comparison of two techniques for the surface analysis of alumina (Al_2O_3): Inverse Gas Chromatography at Finite Concentration (IGC-FC) and Dynamic Vapor Sorption (DVS), Powder Technology, vol.190, pp.53-58.

25) Thielmann, F. (2004): Introduction into the characterisation of porous materials by inverse gas chromatography, Journal of Chromatography A, vol.1037, pp.115-123.

26) Zhou, Q. and Cadwallader, K. R. (2004): Inverse gas chromatographic method for measurement of interactions between soy protein isolate and selected flavor compounds under controlled relative humidity, Journal of Agricultural and Food Chemistry, vol.52, pp.6271-6277.

27) Menzel, R., et al. (2009): Inverse gas chromatography of as-received and modified carbon nanotubes, Langmuir, vol.25, pp.8340-8348.

28) Heng, J. Y. Y., et al. (2007): Methods to determine surface energies of natural fibres: a review, Composite Interfaces, vol.14, pp.581-604.

29) Grimsey, I. M., et al. (2002): Analysis of the surface energy of pharmaceutical powders by inverse gas chromatography, Journal of Pharmaceutical Sciences, vol.91, pp.571-583.

30) Hancock, B. C., et al. (1997): The use of solubility parameters in pharmaceutical dosage form design, International Journal of Pharmaceutics, vol.148, pp.1-21.

31) Mermet, J.-M., et al., (2004): "Analytical Chemistry: A Modern Approach to Analytical Science". 2nd ed., Wiley-VCH Verlag GmbH, Weinheim.

32) Schultz, J., et al. (1987): The role of the interface in carbon fibre-epoxy composites Journal of Adhesion, vol.23, pp.45-60.

33) Fowkes, F. M. (1964): Attractive forces at interfaces, Industrial and Engineering Chemistry, vol.56, pp.40-52.

34) Dorris, G. M. and Gray, D. G. (1980): Adsorption of normal-alkanes at zero surface coverage on cellulose paper and wood fibers, Journal of Colloid and Interface Science, vol.77, pp.353-362.

35) Panzer, U. and Schreiber, H. P. (1992): On the evaluation of surface interactions by inverse gas chromatography, Macromolecules, vol.25, pp.3633-3637.

36) Gutmann, V. (1966): Coordination chemistry of certain transition-metal ions. The role of solvent, Coordination Chemistry Reviews, vol.2, pp.239-256.

37) Riddle, F. L. and Fowkes, F. M. (1990): Spectral shifts in acid-base chemistry .1. van der Waals contributions to acceptor numbers, Journal of the American Chemical Society, vol.112, pp.3259-3264.

38) Phuoc, N. H. et al. (1986): Determination of partial solubility parameters of lactose by gas-solid chromatography, Journal of Pharmaceutical Sciences, vol.75, pp.68-72.

39) Huu-Phuoc, N. et al. (1987): Determination of partial and total cohesion parameters of caffeine, theophylline, and methyl p-hydroxybenzoate by gas-solid chromatography, Journal of Pharmaceutical Sciences, vol.76, pp.406-410.

40) Ticehurst, M. D. et al. (1994): Determination of the surface-properties of 2 batches of salbutamol sulfate by inverse gas-chromatography, International Journal of Pharmaceutics, vol.111, pp.241-249.

41) Ticehurst, M. D. et al. (1996): Characterisation of the surface properties of alpha-lactose monohydrate with inverse gas chromatography, used to detect batch variation, International Journal of Pharmaceutics, vol.141, pp.93-99.

42) Tong, H. H. Y. et al. (2002): Influence of polymorphism on the surface energetics of salmeterol xinafoate crystallized from supercritical fluids, Pharmaceutical Research, vol.19, pp.640-648.

43) Grimsey, I. M. et al. (1999): Interpretation of the differences in the surface energetics of two optical forms of mannitol by inverse gas chromatography and molecular modelling, International Journal of Pharmaceutics,

vol.191, pp.43-50.
44) Saxena, A. et al. (2010): A combined modelling and experimental study of the surface energetics of α-lactose monohydrate, Journal of Pharmaceutical Sciences, vol.99, pp.741-752.
45) Ohta, M. and Buckton, G. (2004): Determination of the changes in surface energetics of cefditoren pivoxil as a consequence of processing induced disorder and equilibration to different relative humidities, International Journal of Pharmaceutics, vol.269, pp.81-88.
46) Hasegawa, S. et al. (2009): Determination of the structural relaxation at the surface of amorphous solid dispersion using inverse gas chromatography, Journal of Pharmaceutical Sciences, vol.98, pp.2133-2139.
47) Yokoi, Y. et al. (2004): Changes in surface properties by granulation and physicochemical stability of granulated amorphous cefditoren pivoxil with additives, International Journal of Pharmaceutics, vol.280, pp.67-75.
48) Surana, R. et al. (2003): Determination of glass transition temperature and in situ study of the plasticising effect of water by inverse gas chromatography, Pharmaceutical Research, vol.20, pp.1647-1654.
49) Surana, R. et al. (2003): Determination of glass transition temperature and in situ study of the plasticizing effect of water by inverse gas chromatography, Pharmaceutical Research, vol.20, pp.1647-1654.
50) Otte, A. and Carvajal, M. T. (2011): Assessment of milling-induced disorder of two pharmaceutical compounds, Journal of Pharmaceutical Sciences, vol.100, pp.1793-1804.
51) Brum, J. and Burnett, D. (2011): Quantification of surface amorphous content using dispersive surface energy: the concept of effective amorphous surface area, AAPS PharmSciTech, vol.12, pp.887-892.
52) Storey, R. A. (1997): “The nucleation, growth and solid state properties of particulate pharmaceuticals,” Ph.D. Dissertation, University of Bradford.
53) Heng, J. Y. Y. (2006): “Anisotropic Surface Properties of Crystalline Pharmaceutical Solids,” Ph.D. Dissertation, University of London.
54) Heng, J. Y. Y. et al. (2006): The effects of milling on the surface properties of form I paracetamol crystals, Pharmaceutical Research, vol.23, pp.1918-1927.
55) Feeley, J. C. et al. (1998): Determination of surface properties and flow characteristics of salbutamol sulphate, before and after micronisation, International Journal of Pharmaceutics, vol.172, pp.89-96.
56) York, P. et al. (1998): Characterisation of the surface energetics of milled DL-propranolol hydrochloride using inverse gas chromatography and molecular modelling, International Journal of Pharmaceutics, vol.174, pp.179-186.
57) Tong, H. H. Y. et al. (2006): Predicting the aerosol performance of dry powder inhalation formulations by interparticulate interaction analysis using inverse gas chromatography, Journal of Pharmaceutical Sciences, vol.95, pp.228-233.
58) Cline, D. and Dalby, R. (2002): Predicting the quality of powders for inhalation from surface energy and area, Pharmaceutical Research, vol.19, pp.1274-1277.
59) Das, S. et al. (2009): Surface energy changes and their relationship with the dispersibility of salmeterol xinafoate powders for inhalation after storage at high RH, European Journal of Pharmaceutical Sciences, vol.38, pp.347-354.
60) Traini, D. et al. (2005): Surface energy and interparticle forces correlations in model pMDI formulations, Pharmaceutical Research, vol.22, pp.816-825.
61) Thielmann, F. et al. (2008): The effect of primary particle surface energy on agglomeration rate in fluidised bed wet granulation, Powder Technology, vol.181, pp.160-168.
62) Newell, H. E. and Buckton, G. (2004): Inverse gas chromatography: Investigating whether the technique preferentially probes high energy sites for mixtures of crystalline and amorphous lactose, Pharmaceutical Research, vol.21, pp.1440-1444.
63) Thielmann, F. and Pearse, D. (2002): Determination of surface heterogeneity profiles on graphite by finite concentration inverse gas chromatography, Journal of Chromatography A, vol.969, pp.323-327.
64) Balard, H. (1997): Estimation of the surface energetic heterogeneity of a solid by inverse gas chromatography, Langmuir, vol.13, pp.1260-1269.
65) Jaroniec, M. et al. (1996): Relation between adsorption potential distribution and pore volume distribution for microporous carbons, Colloids and Surfaces A: Physicochemical and Engineering Aspects, vol.118, pp.203-210.
66) Rudzinski, W. and Everett, D. H., (1992): “Adsorption of Gases on Heterogeneous Surfaces”. Academic Press, San Diego, CA, USA.
67) Jaroniec, M. and Madey, R., (1988): “Physical Adsorption on Heterogeneous Solids”. Elsevier, Amsterdam.
68) Sacchetti, M. (2006): The nitrogen adsorption isotherm of alpha-lactose monohydrate, Pharmaceutical Development and Technology, vol.11, pp.351-358.
69) Jaroniec, M. and Choma, J. (1987): Characterization of activated carbons by distribution functions of adsorption potential and micropore dimension, Materials Chemistry and Physics, vol.18, pp.103-117.
70) Kowalczyk, P. (2005): New approach to determination of surface heterogeneity of adsorbents and catalysts from the temperature programmed desorption (TPD) technique: One step beyond the condensation approximation (CA) method, Journal of Colloid and Interface Science, vol.291, pp.334-344.
71) Koch, K. et al. (1997): A new method of analysing temperature-programmed desorption (TPD) profiles using an extended integral equation, Journal of Catalysis, vol.172, pp.187-193.
72) Beta, I. A. et al. (2001): Characterisation of extraframework cations in zeolites. A temperature-programmed desorption (TPD) study, Journal of Thermal Analysis and Calorimetry, vol.64, pp.1191-1199.

73) Choudhary, V. R. and Sansare, S. D. (1980): Gas-chromatographic technique for temperature-programmed desorption of reversibly and irreversibly adsorbed species, Journal of Chromatography, vol.192, pp.420-424.
74) Ho, R. et al. (2009): Crystal habits and the variation in surface energy heterogeneity, Crystal growth & design, vol.9, pp.4907-4911.
75) Ho, R. et al. (2010): Influence of fines on the surface energy heterogeneity of lactose for pulmonary drug delivery, International Journal of Pharmaceutics, vol.388, pp.88-94.
76) Cremer, E. and Huber, H. (1962): Measurement of adsorption isotherms by means of high temperature elution gas chromatography, Proceedings of the International Symposium on Gas Chromatography, vol.3, pp.169.
77) Yla-Maihaniemi, P. P. et al. (2008): Inverse gas chromatographic method for measuring the dispersive surface energy distribution for particulates, Langmuir, vol.24, pp.9551-9557.
78) Das, S. C. et al. (2011): Determination of the polar and total surface energy distributions of particulates by inverse gas chromatography, Langmuir, vol.27, pp.521-523.
79) Volpe, C. D. et al. (2003): Recent theoretical and experimental advancements in the application of van Oss–Chaudury–Good acid–base theory to the analysis of polymer surfaces I. General aspects, Journal of Adhesion Science Technology, vol.17, pp.1477-1505.
80) Della Volpe, C. and Siboni, S. (1997): Some reflections on acid-base solid surface free energy theories, Journal of Colloid and Interface Science, vol.195, pp.121-136.
81) Begat, P. et al. (2004): The cohesive-adhesive balances in dry powder inhaler formulations I: Direct quantification by atomic force microscopy, Pharmaceutical Research, vol.21, pp.1591-1597.
82) Raula, J. et al. (2010): Investigations on particle surface characteristics vs. dispersion behaviour of l-leucine coated carrier-free inhalable powders, International Journal of Pharmaceutics, vol.385, pp.79-85.
83) Thielmann, F. et al. (2007): Determination of the surface energy distributions of different processed lactose, Drug Development and Industrial Pharmacy, vol.33, pp.1240-1253.
84) Shur, J. et al. (2008): The role of fines in the modification of the fluidisation and dispersion mechanism within dry powder inhaler formulations, Pharmaceutical Research, vol.25, pp.1931-1940.
85) Louey, M. D. and Stewart, P. J. (2002): Particle interactions involved in aerosol dispersion of ternary interactive mixtures, Pharmaceutical Research, vol.19, pp.1524-1531.
86) Jones, M. D. and Price, R. (2006): The influence of fine excipient particles on the performance of carrier-based dry powder inhalation formulations, Pharmaceutical Research, vol.23, pp.1665-1674.
87) Ho, R. et al. (2012): Effect of milling on particle shape and surface energy heterogeneity of needle-shaped crystals, Pharmaceutical Research, vol.29, pp.2806-2816.

Author's short biography

Raimundo Ho

Dr Raimundo Ho received his Masters in chemical engineering (2005) and Ph.D. in chemical engineering (2009) from the Imperial College London. His Ph.D. research, in collaboration with AstraZeneca, focused on the development of inverse gas chromatography (IGC) to characterize the energetic heterogeneity of surfaces, and the role of surface chemistry on pharmaceutical powder processing. In 2010, he joined Surface Measurement Systems as an application scientist specializing in IGC and vapor sorption techniques. He is currently a senior scientist in solid state chemistry at the Abbott Laboratories headquarters in Lake County, Illinois. His current research interests are characterizing bulk powders and surface properties, applying the derived knowledge of materials and combining modeling approaches and X-ray crystallography to predict and enhance drug substance and drug product processing and manufacturing.

Jerry Heng

Dr Jerry Heng (JH) currently heads the Surfaces and Particle Engineering Laboratory (www.imperial.ac.uk/spel) at the Department of Chemical Engineering in the Imperial College London, UK. JH graduated from Universiti Teknologi Malaysia (UTM) with a B.Eng in chemical engineering (1st Class) in 2002 and a Ph.D. from the Imperial College London in 2006, joining the faculty at the Imperial College London in 2007. JH's research interest is in the area of material characterization and particle engineering, specifically in the area of crystallization. JH's approach is based on fundamental understanding of the role of particle surface properties, relating these to their impact on processing, the effects of processing and formulation or product performance.

Trend of Nanoparticle Technology in ASEAN with Emphasis on Thailand[†]

Wiwut Tanthapanichakoon[1*], Tawatchai Charinpanitkul[2], Suracha Udomsak[3], Butra Boonliang[3] and Kajornsak Faungnawakij[4]

[1] *Graduate School of Science and Engineering, Tokyo Institute of Technology*
[2] *Center of Excellence in Particle Technology, Chulalongkorn University, Thailand*
[3] *SCG Chemicals Co., Ltd., Thailand*
[4] *National Nanotechnology Center, National Science and Technology Development Agency, Thailand*

Abstract

First we survey the scope and level of research activities in nanoparticle technology (NPT) in ASEAN by looking at relevant international journal publications (2006–2012) in terms of absolute numbers (AN), numbers of publications per million population (PMP) and per billion USD GDP (PBG). Obviously, the statistics show that, within ASEAN, the strength of Singapore covers a wide range of nanotechnology fields and applications, including carbon materials, biosensors, bioelectronics, and pharmaceutics. Malaysia places emphasis on alloys & compounds, carbon materials, and separation technology. Thailand's emphasis is on molecular modeling, carbon materials, and biosensors. When classification is made on the morphology of nanoparticles mentioned in the titles, the topmost are nanotubes (including CNT, SWCNT, MWCNT) at 392 out of 612 (64.1%), followed by generic nanoparticle/ nanopowder and nanofiber (including nanowire, nanorods). Next we look closer at 2 nanoparticle R&D organizations in Thailand, namely, CEPT (CU) and NANOTEC together with their alliances. The interest in nanotechnology of SCG (Siam Cement Group), a leading Thai industrial conglomerate, will also be briefly introduced. .

Keywords: nanoparticle, nanomaterial, nanostructure, CNT, ASEAN

1. Introduction

Being a subset of nanomaterials, nanoparticles or nanopowders here include nanospheres, nanotubes, nanofibers, nanorods, nanohorns, nano-onions, nanocapsules, nanoclusters, nanocrystals, and the like. Ultrafine particles or nanoparticles are generally sized between 1 and 100 nanometers. Nanoclusters have at least one dimension between 1 and 10 nanometers and a narrow size distribution. Nanopowders are agglomerates of nanoparticles or nanoclusters. Nanoparticles can be produced either by the top-down or bottom-up method. The former employs size reduction technique such as ball mill, planetary ball mill, etc. The latter employs laser ablation, CVD, arc discharge, plasma, sol-gel, spray pyrolysis, etc. Nanoparticle research is currently an area of intense scientific interest due to a wide variety of potential applications in nearly all industrial fields, including biomedical, optical and electronic.

ASAEN is currently composed of ten members (in alphabetical order): Brunei (B), Cambodia (C), Indonesia (I), Laos (L), Malaysia (M), Myanmar (MY), Philippines (P), Singapore (S), Thailand (T), and Vietnam (V). The top 3 most populous are Indonesia (233 million), Philippines (93.6M), and Vietnam (88.4M) whilst the 3 least populous are Brunei (0.41M), Singapore (5.14M), and Laos (6.44M). In terms of GDP per capita, the top 3 are Singapore (USD 43.3K), Brunei (USD 26.4K) and Malaysia (USD 8.52K) whilst the bottom 3 are Myanmar (USD 0.50K), Cambodia (0.80K) and Laos (USD 1.16K).

[†] Accepted: August 30, 2012

[1] 2-12-1, S1-420, Ookayama, Meguro-ku, Tokyo 152-8550, Japan

* Corresponding author:
E-mail: wiwutt@chemeng.titech.ac.jp
TEL: +81-3- 5734-2117 FAX: +81-3- 5734-2117

ⓒ 2013 Hosokawa Powder Technology Foundation

Table 1 Relevant Statistics of Publications on Nanoparticle Technology

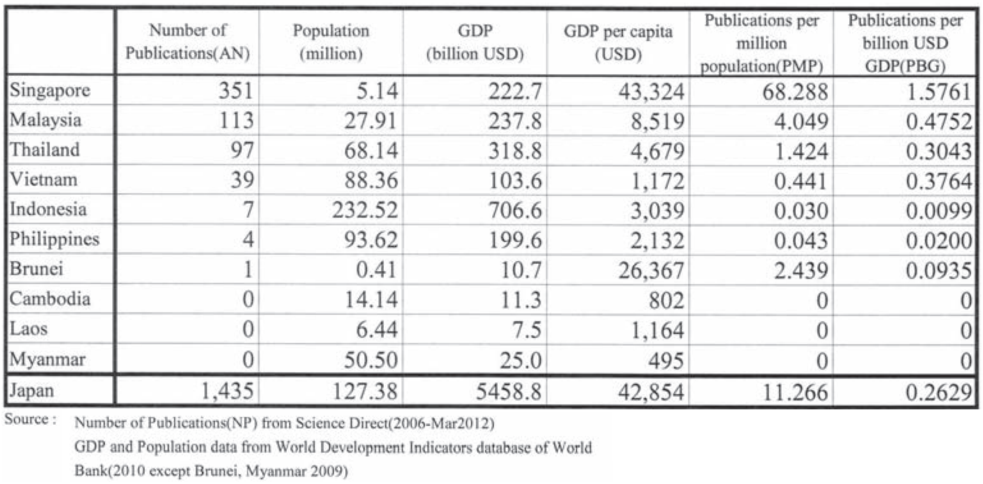

	Number of Publications(AN)	Population (million)	GDP (billion USD)	GDP per capita (USD)	Publications per million population(PMP)	Publications per billion USD GDP(PBG)
Singapore	351	5.14	222.7	43,324	68.288	1.5761
Malaysia	113	27.91	237.8	8,519	4.049	0.4752
Thailand	97	68.14	318.8	4,679	1.424	0.3043
Vietnam	39	88.36	103.6	1,172	0.441	0.3764
Indonesia	7	232.52	706.6	3,039	0.030	0.0099
Philippines	4	93.62	199.6	2,132	0.043	0.0200
Brunei	1	0.41	10.7	26,367	2.439	0.0935
Cambodia	0	14.14	11.3	802	0	0
Laos	0	6.44	7.5	1,164	0	0
Myanmar	0	50.50	25.0	495	0	0
Japan	1,435	127.38	5458.8	42,854	11.266	0.2629

Source : Number of Publications(NP) from Science Direct(2006-Mar2012)
GDP and Population data from World Development Indicators database of World Bank(2010 except Brunei, Myanmar 2009)

Table 1 lists the cumulative number of international journal publications (in decreasing order), 2010 GDP, Population, GDP per capita and relevant publication statistics of each ASEAN country.

The present article first surveys the scope and level of research activities in nanoparticle technology (NPT) in ASEAN and the major fields of national focuses. Next it looks closer at NPT R&D activities in Thailand as well as the interest in nanotechnology of a leading Thai industrial conglomerate, the Siam Cement Group. Specific reviews are given on recent researches carried out in the Center of Excellence in Particle Technology (CEPT) of Chulalongkorn Univ. (CU), the National Nanotechnology Center (NANOTEC), and their alliances.

2. Scope and Level of R&D Activities in Nanoparticle Technology in ASEAN

A comprehensive literature search was carried out in March 2012 to look for international journal articles with the keyword *Nanoparticle or Nanopowder* in their titles and with one of the authors' affiliations located in an ASEAN country from Year 2006 onward using the ScienceDirect database. As expected, Singapore shows the highest number of articles (351) followed by Malaysia at 113, Thailand 97, Vietnam 39, Indonesia 7, Philippines 4, Brunei 1, Cambodia = Laos = Myanmar = 0, respectively. Since the ASEAN total is 612, Singapore alone is associated with 57.4% of the total with Malaysia's and Thailand's shares being 18.5% and 15.8%, respectively. Thus the top three countries are associated with nearly 92% of the whole ASEAN. Admittedly, the above search statistics could have a few double or triple counts when the authors' affiliations of a single article belong to more than one ASEAN country. In any case, the statistics here reflect only the quantity, and not quality or citation impact, of the publications. In the meantime, nanostructural materials (including nanoporous) and ultrathin films (nanofilms, nanocoat) generally are not counted. As shown in **Table 1**, in terms of absolute publication numbers (AN), the numbers of publications per one-million population (PMP) and per 1-billion-USD GDP (PBG), the statistics show Singapore to be on top of all 3 categories, whilst Malaysia ranks 2nd in all 3 categories. Thailand, Brunei and Vietnam, respectively, rank 3rd in terms of AN, PMP, and PMG. For comparison, **Table 1** shows that, having 1,435 publications, Japan is ahead of Singapore only in terms of AN but ranks 2nd after Singapore in term of PMP and 5th after Thailand in term of PBG.

The top 10 journals in terms of number of publications in the entire ASEAN are:

#1: *Carbon = 48* (including S 34, M 7, T 5, V 1 and I 1)

#2: *Biosensors & Bioelectronics = 30* (including S 25, T 4 and I 1)

#3: *J of Alloys and Compounds = 22* (including M 13, S 8 and T 1)

#4: *Applied Surface Science = 21* (including S 8, M 6, V 4 and T 3)

#5: *Electrochimica Acta = 18* (including S 13, T 3, and M 2)

#6: *Sensors and Actuators B: Chemical = 15* (S 11, V 3, and T 1)

#6: *Thin Solid Films = 15* (including S 8, T 3, M 2, V 1 and P 1)

#6: *J of Power Sources = 15* (including S 14 and T 1)

#9: *Chemical Physics Letter = 14* (including S 8, T 4, M 1 and V 1)

#9: *Inter J of Hydrogen Energy = 14* (including S 10, M 3 and T 1)

Singapore leads in all 10 journals above except *J of*

Table 2 Title Classification of Publications according to Morphology of Nanoparticles*

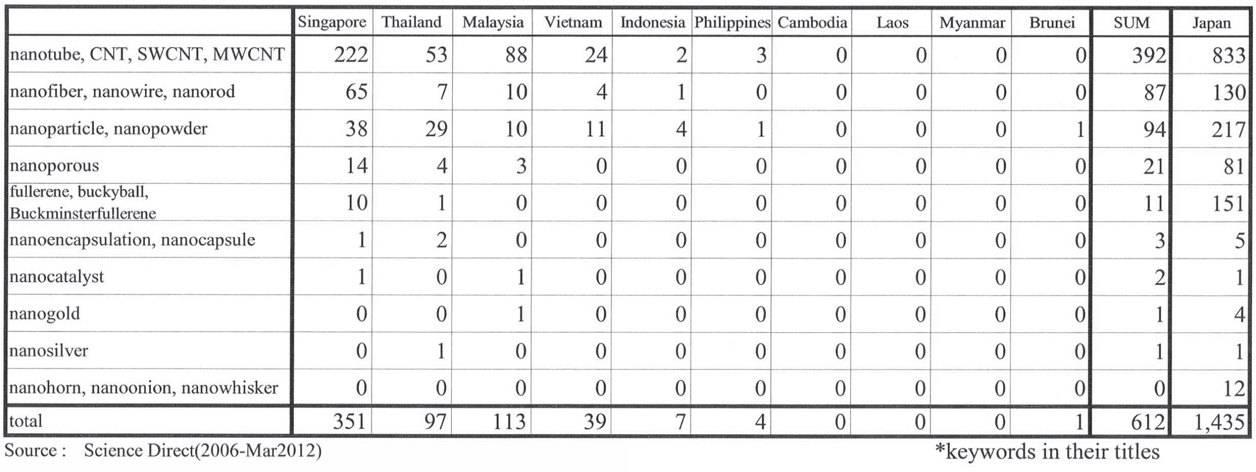

	Singapore	Thailand	Malaysia	Vietnam	Indonesia	Philippines	Cambodia	Laos	Myanmar	Brunei	SUM	Japan
nanotube, CNT, SWCNT, MWCNT	222	53	88	24	2	3	0	0	0	0	392	833
nanofiber, nanowire, nanorod	65	7	10	4	1	0	0	0	0	0	87	130
nanoparticle, nanopowder	38	29	10	11	4	1	0	0	0	1	94	217
nanoporous	14	4	3	0	0	0	0	0	0	0	21	81
fullerene, buckyball, Buckminsterfullerene	10	1	0	0	0	0	0	0	0	0	11	151
nanoencapsulation, nanocapsule	1	2	0	0	0	0	0	0	0	0	3	5
nanocatalyst	1	0	1	0	0	0	0	0	0	0	2	1
nanogold	0	0	1	0	0	0	0	0	0	0	1	4
nanosilver	0	1	0	0	0	0	0	0	0	0	1	1
nanohorn, nanoonion, nanowhisker	0	0	0	0	0	0	0	0	0	0	0	12
total	351	97	113	39	7	4	0	0	0	1	612	1,435

Source : Science Direct(2006-Mar2012) *keywords in their titles

Alloys and Compounds, which is led by Malaysia. Obviously, these statistics confirm that, within ASEAN, the strength of Singapore cover a wide range of nanotechnology and applications, including carbon materials, biosensors, bioelectronics, actuators, hydrogen energy, alloys and pharmaceutics. Malaysia places emphasis on alloys & compounds, carbon materials, applied surface science, and separation technology. Thailand's emphasis is on molecular modeling, carbon materials, and biosensors. When classification is made on the morphology of nanoparticles mentioned in the titles, as shown in **Table 2** the topmost are nanotubes (including CNT, SWCNT, MWCNT) at 392 out of 612 (64.1% of 612) followed by generic nanoparticle/nanopowder at 94 (15.4%) and nanofibers (including nanowire, nanorod) at 87 (14.2%). In short, the top 3 morphologies cover 93.7% with nanoporous being a distant 4th at 21 (3.43%) and fullerene/buckyballs 5th at 11 (1.80%). As expected, nanotubes especially CNT are the most popular morphology for R&D and applications.

Because of space limitation, the authors' personal background and Thailand's lower profile compared to Singapore and Malaysia, the present article will look closer at 2 nanoparticle R&D organizations in Thailand, namely, CEPT (CU) and NANOTEC together with their alliances. The interest in nanotechnology of SCG (Siam Cement Group), a leading Thai industrial conglomerate, will also be briefly introduced.

3. Nanoparticle R&D Activities in Thailand

3.1 Nanoparticle R&D activities in CEPT (CU) and its alliances

Designated a center of excellence by Chulalongkorn University, CEPT (Center of Excellence in Particle Technology) is committed to generating academic and technical outputs in various categories including young generation of high-caliber graduates, research papers, patents and technical services. The present focus of research activities is set on developing and improving alternatives for synthesis and applications of particulate materials and their derivatives in nano-scaled forms. More specifically, synthesis of selected metals and their compounds, such as TiO_2, ZnO, Al_2O_3, ZnS and WO_3, have been investigated using several alternative methods such as gas-phase reaction, solvothermal treatment, sol-gel system and micro-emulsion (Sahu et al. 2011). Similarly, synthesis of carbonaceous materials and their derivatives, including mesoporous and metal-hybridized nanocarbon are carried out using several methods, such as arc-discharge, pyrolysis, solvothermal and RF-gel formulation (Sano et al. 2009, Charinpanitkul et al. 2009a, 2009b, 2009c). In terms of applications, on-going works on photocatalysis, solar concentrator, gas sensing, and pollution removal are conducted in collaboration with alliances in domestic industries and Thai or foreign institutions.

In response to public interest in sustainability, development and regeneration of activated carbon from industrial waste, and production of glucose and its derivatives from agricultural wastes have been explored using specific techniques such as carbonization with pre-treatment, hydrothermal treatment and supercritical fluid process (Petchpradab et al. 2009, Charinpanitkul and Tanthapanichakoon 2011a, Yoshikawa et al. 2007). Innovative ideas on economical systems for particulate collection using spray nozzle and packed bed have been proposed and verified experimentally using actual conditions (Srinives et al. 2010, Charinpanitkul and Tanthapanichakoon 2011b). Progresses of representative works are elaborated as follows.

3.1.1 Nano-scaled metal particles and their derivatives

Research work on nanoscaled metal particles has been focused on synthesis and applications of specific metal oxides and their derivatives, i.e. TiO_2, ZnO, Al_2O_3, WO_3 Cu_2O and ZnS. In CEPT, two alternatives involving either gas-phase or wet-chemistry synthesis are examined for making photocatalyst and sensors (Numpud et al, 2008, Klanwan et al. 2010, Charinpanitkul et al. 2011, Charnhattakorn et al. 2011). Viriyaempikul et al. (2008) reported that titanate nanotubes transformed from TiO_2 nanoparticles would possess higher surface area and short tube-length. Morphology change of the titanates from nanosheet, nanotube and nanowire was affected by an increase in the reaction temperature. The surface area of the samples corresponded well with the amount of hollow titanate nanotube and non-hollow nanowire, whilst the length of titanate nanotube became longer when ultrasonication pretreatment was employed.

For applications, TiO_2, Ni, Co and Fe impregnated on activated carbon were prepared for phenol removal from industrial waste water using three-phase fluidized bed. It was found that the use of Co nanocatalyst with the presence of O_3 led to the best removal condition in which phenol was completely decomposed within 10 min (pseudo-1st order rate constant $k = 0.1944\ min^{-1}$). In contrast, the use of TiO_2 without O_3 resulted in the least decomposition of phenol ($k = 0.0066\ min^{-1}$) (Mungmart et al. 2011). Contributions of adsorption on the porous supporting materials, carbon gel or silica gel, were also examined and deducted from those of the metal catalysts. As a typical example, uniform dispersion of metal nanoparticles in the porous carbon gel is illustrated in **Fig. 1**. At present works are proceeding on new types of hybridized materials which incorporate metal-compound nanoparticles into materials such as carbon in order to gain synergetic effect of their characteristics for applications to chemical sensing, electron-transferring and catalysis.

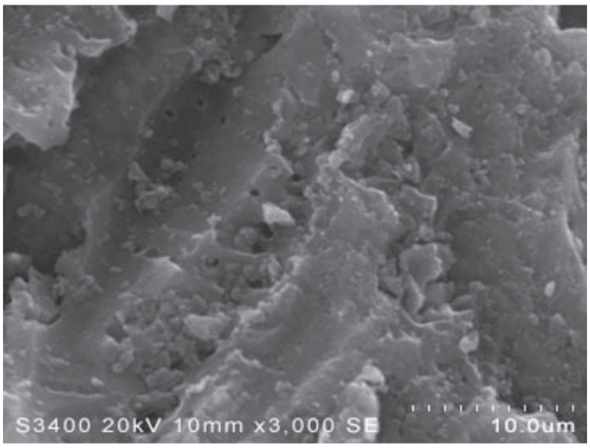

Fig. 1 Typical SEM micrograph of Fe_2O_3 on the surface of carbon gel particle.

3.1.2 Nanocarbonaceous materials synthesis and applications

Nanocarbonaceous materials are potential candidates for numerous applications, such as drug delivery, electron capacitor or molecular separation. Synthesis of multi-walled carbon nanotubes (MWCNTs) and multi-shelled carbon nanocapsules (MSCNCs) has been examined in a simple system of pyrolyzing reactor (Charinpanitkul et al. 2009b). It has been proved that this pyrolysis method could provide a new type of carbon nanoparticles with magnetism due to the presence of iron nanoparticles encapsulated between graphene layers. Schematic diagram for describing the formation of those nanoparticles is shown in **Fig. 2**. Recently, a new method to prepare single-walled carbon nanohorns (SWCNHs), incorporated with Pd or Pt nanoparticles via simple gas-injection arc-in-water, was proposed (Poonjarernsilp et al. 2011). They reported that the size of Pd nanoparticles in a range of 3–6 nm could be controlled by using different sizes of Pd wire inserted into the carbon anode. According to thermogravimetric analyses, the weight fraction of Pd nanoparticles in SWCNHs could be increased by increasing the Pd wire diameter whilst the yield of Pd nanoparticles decreased. SWCNHs hybridized with dispersed Pd nanoparticles exhibited strong anti-oxidation resistance with a highly graphitic structure. In the mean-

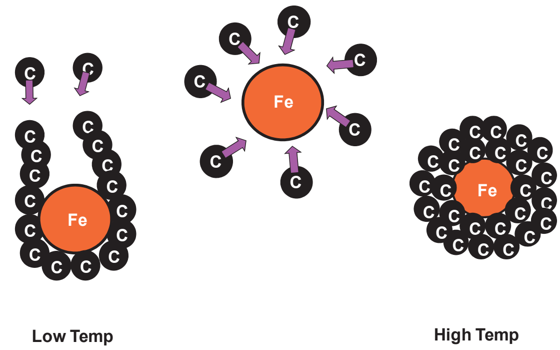

Fig. 2 Schematic of formation mechanism of carbon nanoparticles induced by Fe particles via pyrolysis method.

time, a simple strategy of matching the electrode materials employed for arc discharge in water or liquid nitrogen could also provide hybrid materials of multiwalled carbon nanotubes and Fe or Cu nanoparticles (Charinpanitkul et al. 2009c). These hybrid materials could have potential applications to dye-sensitized solar cells that yield suitably high solar conversion efficiency. In addition, gas sensors made of composite of MWCNT and PMMA have been developed for detecting certain toxic hydrocarbon gases, such as toluene and hexane (Srisurichan et al. 2009). Ice-crystal templating of MWCNTs in macroporous foams by freeze drying was also prepared and tested as gas sensor (Thongprachan et al. 2008).

3.1.3 Utilization of biomaterial for nanoparticle technology

Abundant in Thailand, biomaterials such as curcumin, menthol, and capsaicin as well as certain industrial and household wastes could be used and transformed by supercritical fluid or hydrothermal techniques to obtain nanostructure and other useful forms, such as glucose and their derivatives. For instance, poly(DL-lactic-glycolic acid) or PLGA, which can be employed for drug delivery applications, could be transformed into ultrathin film encapsulating fine particles via rapid expansion of supercritical CO_2 (SCC) (Kongsombut et al. 2008, 2009). Thin film morphology could be controlled by the operating pressure and temperature of polymer dissolving in SCC. Interestingly, supercritical water could be employed for regenerating activated carbon saturated with phenol or pyridine, thereby demonstrating its usefulness to tackle environmental issues of waste reduction (Charinpanitkul and Tanthapanichakoon 2011a). Meanwhile, certain waste materials, such as naphthalene or glycerol, could be transformed by pyrolysis to provide carbon nanoparticles with controlled characteristics as mentioned earlier in section 3.1.2. An alternative to convert biomaterials, such as rubber wood or jatropha seed residue, into glucose or 5-HMF could be achieved by hydrothermal treatment in an autoclave (Petchpradab et al. 2009). Interestingly, solid residues of the hydrothermal process could be a potential source of nanoparticles containing amorphous carbonaceous networks.

3.2 Nanoparticle R&D Activities in NANOTEC and its Alliances

The trends of nanoparticle production of NANOTEC and its alliances have moved toward a facile system which incorporates multicomponents into hybrid or composite nanoparticles with the aim of enhancing performance in specific applications. Metal/metal oxide nanoparticles have been applied to energy and petrochemical, while photocatalysts, metal-doped TiO_2 and ZnO in particular, have extensively been used in textile and environmental fields. The fabrication of composites based on carbon nanotubes shows good performance as electrochemical devices. In addition, organic-based nanoparticles, including chitosan-, gelatin-, and nisin-bonded polymers have been developed for (bio)medical, electronic and food industry.

3.2.1 Metal and metal oxide nanoparticles

Nanoparticles of metal and metal oxides have played a crucial role in various industries such as petrochemical, energy, electronic, and environmental industries. Metal nanoparticles could generally be obtained through the reduction of metal-containing compounds with reducing agents in either gas or liquid phase. Gold nanoparticles provide novel optical and electronic properties while their Ag counterparts are widely employed in a variety of products which require anti-bacterial activity. Metal oxides are extensively used as catalyst supports for metal nanoparticles. In addition, the synthesis and application of photocatalysts, especially ZnO and TiO_2 as well as its modified forms, have actively been studied in recently years to push them toward final products in the market.

The flame spray pyrolysis (FSP) has been generally employed for synthesis of various oxides including alumina and zirconia for catalytic reaction in petrochemical processes. More recently, FSP is developed as one-step synthesis of supported metal catalysts. The flame-made Pt/Al_2O_3 showed an improved turnover frequency in the hydrogenation of ethyl pyruvate compared to conventional porous catalysts. Recent studies show that Pd/SiO_2 synthesized by FSP method exhibited higher hydrogenation activity in the liquid-phase selective hydrogenation of 1-heptyne compared to the ones prepared by conventional impregnation (Mekasuwandumrong et al. 2009). Al_2O_3-supported Pt-based bi- and tri-metallic catalysts were developed for dehydrogenation of propane to propylene (Pisduangdaw et al. 2009, 2011). Stronger metal–support interaction in the flame-made nanoparticles is found to produce highly beneficial effects in such reactions. A typical TEM image of the flame-made nanoparticles is shown in **Fig. 3**. Moreover, the FSP technique has been used for single-step production of unloaded ZnO and loaded Nb/ZnO nanoparticles

(Kruefu et al. 2011). FSP yielded small Nb particles attached to the surface of the supporting ZnO nanoparticles, while they showed a high potential for use as NO_2 sensing material.

One novel approach to disperse metal nanoparticles on oxide supports has been proposed as crystalline phase separation of parent complex oxides during reduction process (Faungnawakij et al. 2009, Shimoda et al. 2010). It has been demonstrated that Cu nanoparticles can be formed on the iron oxide (Fe_3O_4) host from original copper-iron spinel oxide ($CuFe_2O_4$). The size of the copper nanoparticles depends strongly on the reduction temperature, time and reducing species. Beyond that, the reconstruction of the parent spinel phase can be achieved via solid state formation by oxidation at high temperature. This feature leads to ultimate recycle/reuse of the catalyst nanomaterials.

Photocatalysts based on TiO_2 and ZnO have extensively been studied in various applications. Metal doping of ZnO and TiO_2 is a common method to enhance their visible light absorption by narrowing the bandgap energy. It was demonstrated that manganese-doped ZnO photocatalysts synthesized via wet-chemical technique could create tail states within the band gap of ZnO (Ullah and Dutta 2008). The doped photocatalysts can effectively degrade organic contaminants with just visible light irradiation. In addition, solvothermal technique has been employed to synthesize zinc oxide nanoparticles and nanorods (Yiamsawas et al. 2011). It was found that the concentration ratio of sodium hydroxide to zinc acetate has the greatest effect on ZnO nanocrystal growth. Since TiO_2 is well known as an active photocatalyst, the synthesis of Fe(III)-doped TiO_2 by solvothermal method has been done in the presence of isopropyl alcohol using PEG as a template (Wantala et al. 2010). Red shift phenomenon due to substitution of Fe(III) in the TiO_2 crystal lattices was observed, with the improved activity under visible light irradiation. Because a major concern of the use of nanoparticles catalysts in liquid phase processing is catalyst separation from the reaction system, Kangwansupamonkon et al. (2010) have proposed the concept of TiO_2-polymer composite for photocatalytic water treatment. TiO_2/poly[acrylamide-co-(acrylic acid)] composite hydrogel was synthesized by polymerization of TiO_2-containing monomer solution. The composite hydrogel is a good dye adsorbent with self-photodegradability and it can also be easily separated from treated water by simple filtration.

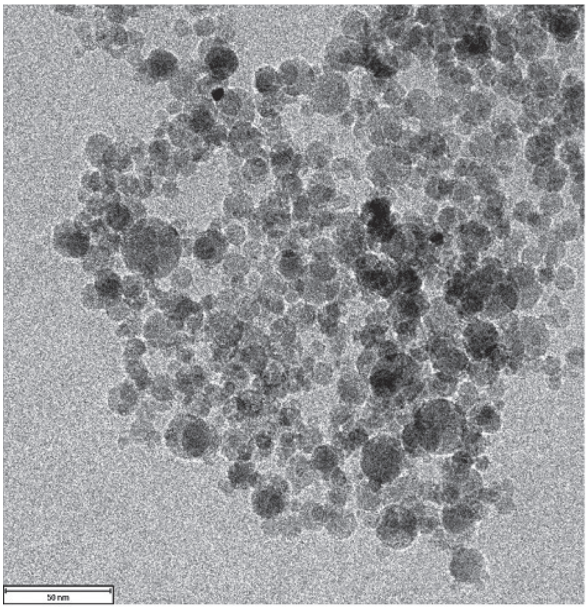

Fig. 3 Typical TEM image of nanoparticles of Pt/Al_2O_3 prepared by flame spray pyrolysis technique.

The potential use of nanosilver-decorated titanium dioxide nanofibers for toxin decomposition with antimicrobial and self-cleaning features was recently proposed and investigated (Srisitthiratkul et al. 2011). The nanofibers were prepared through sol–gel reaction followed by an electrospinning process. Following the Japan Industrial Standard protocol, decompositions of nitrogen oxides (NO_x) and volatile organic compound (VOC) by the TiO_2 nanofibers suggested that they were capable of air treatment. To further enhance their anti-microbial activity, silver nanoparticles were decorated onto the TiO_2 nanofibers via photoreduction of silver ion in a suspension of the nanofibers. Nanostructure of the Ag-TiO_2 fibers was reported and the possibility of using these hybrid nanofibers in environmental and hygienic nanofiltration was proposed, in which the self-cleaning characteristics was expected to facilitate maintenance work.

3.2.2 Carbon nanotubes

Sawatsuk et al. (2009) have developed dye-sensitized solar cells based on TiO_2–MWCNTs composite electrodes. The incorporation of MWCNTs into a TiO_2 active layer contributes to a significant improvement in the energy conversion efficiency of dye-sensitized solar cells. The improvement is correlated with not only increased photocurrent and electrical double layer capacitance but also decreased electrolyte-electrode interfacial resistance and Warburg impedance. A unidirectional-freezing technique for preparation of freeze-dried solid foams of carbon nanotubes has been proposed and the materials were applied to gas diffusion layers of a proton exchange membrane fuel cell (Nakagawa et al. 2011a). Freeze-dried macroporous solid foams were prepared from aqueous suspensions of MWCNTs dispersed with chitosan. It was suggested that the cell performance was closely linked to the interconnected carbon networks formed during the freezing step.

Wisitsoraat et al. (2010) have developed a flow-injection microfluidic device with electrochemical sensor based on functionalized carbon nanotubes for fast cholesterol detection. CNTs working electrode, silver reference and platinum counter electrode layers were fabricated on the chip by sputtering and low-temperature chemical vapor deposition methods. The proposed system is promising for clinical diagnosis of cholesterol with high-speed real-time detection capability, very low sample consumption, high sensitivity, low interference and good stability.

3.2.3 Polymer-based nanoparticles

Prombutara et al. (2012) have produced nisin-loaded solid lipid nanoparticles by high-pressure homogenization at 1500 bars for sustained antimicrobial activity. Nisin is a natural antimicrobial agent that is used as a preservative in heat processed and low pH foods. The antibacterial activity of nisin-loaded solid lipid nanoparticles against Listeria monocytogenes DMST 2871 and Lactobacillus plantarum TISTR 850 was evident for up to 20 and 15 days, respectively, compared to only one and three days, respectively, for free nisin. More recently, a potential use of niosomes for encapsulation of nisin and EDTA nanoparticles was proposed as an alternative approach to nisin encapsulation as good as or better than liposomes (Kopermsub et al. 2011).

Nanoparticles of N,N,N-Trimethyl and chitosan have been developed for the delivery of monoclonal antibodies against hepatocellular carcinoma cells (Vongchan et al. 2011). The chitosan-based nanocomplexes appeared safe and could potentially enhance the half-life of added antibodies. In addition, the core–shell nanoparticles possessing poly(methyl methacrylate) core coated with chitosan (CS), polyethyleneimine (PEI), or chitosan-mixed-polyethyleneimine (CS/PEI) shell were developed using a synthesis method of the emulsifier-free emulsion polymerization triggered by a redox initiating system (Inphonlek et al. 2010). All nanoparticles were spherical in shape with uniform size distribution. The introduction of PEI to CS nanoparticles induced grafting efficiency and percentage comparable with neat CS nanoparticles while it brought about higher colloidal stability of the nanoparticles as evidenced by zeta-potential measurement. The nanoparticles exhibited a promising antibacterial activity against Staphylococcus aureus and Escherichia coli.

Nakagawa et al. (2011b) have studied a formation of unidirectionally frozen poly(epsilon-caprolactone) nanocapsules stabilized by gelatin. The prepared sample had different dispersion characteristics at different positions in the dried bulk sample, and this heterogeneity depended on the freezing protocol. The gel network formation would be advantageous for producing excellent nanocapsule dispersion characteristics after drying. Another synthesis technique of polymer-based nanoparticle is the use of the miniemulsion polymerization technique (Polpanich et al. 2011). With this technique, self-colored nanoparticles containing naphthalene-bisimide derivatives can be synthesized with uniform size distribution. The good colloidal stability of the self-colored nanoparticles has potential application in biomedical areas.

3.3 Industrial applications of particle technology

The Siam Cement Group (SCG) is one of the largest industrial conglomerates in Thailand with leading market positions in each of its core businesses which include, though not limited to, Cement, Chemicals, Construction Materials and Paper. SCG Chemicals (SCGCh) is one of the five core business units of SCG which contributes the highest share to SCG's consolidated revenues in 2011. What follow are some examples of nanoparticle technology applications in SCGCh.

The Research and Development Unit of SCGCh takes on the challenges of employing new technology in various steps of invention and improvement of capabilities. Raising the demand of commodity plastics through novel high-value applications means that new properties must be introduced to common polyolefins like polyethylene and polypropylene. A key development strategy is the application of nanotechnology, including nanoparticle technology. SCGCh has invested resources into research on the use of nanotechnology in various aspects, ranging from synthesis of nanoparticles to improvement of material performance. In recent years, SCGCh has delved into polymer nanocomposites development involving carbon nanomaterials, layered nano-silicates, and novel nano-nucleating agents, which result in improvements to the bulk polyethylene and polypropylene as well as the finished products. Apart from the rather obvious use of nanoparticles to modify polymer matrix, other areas of petrochemical industry can benefit from nanotechnology as well, such as nanoporous support for catalyst system and adsorption media.

SCGCh not only targets development of new products but also aims to build up knowledge in nanotechnology. Recently, SCGCh scientists with collaboration of Chulalongkorn University published a paper on polypropylene/multi-walled carbon nanotubes composites to tackle the issue of scaling up nanocomposite production in the real world. What was found is an interesting regime of operating window with highly predictive manner (Polrut et al. 2011).

Meanwhile, sensitive issues about safety in NPT handling as well as health and environmental impacts cannot be overlooked by industrial companies which would have to fill in the gaps of knowledge. In fact this has been the Achilles' heel of nanotechnology implementation in SCGCh. To deal effectively with these key issues, SCGCh is actively working with regional and world-class universities as well as leading research institutes in pinning down the directions to proceed in the nanotechnology world and in developing new technology, new material system and applications. The aim is to launch nano-enabled products in the near future, thereby creating unique benefits for their customers and maintaining SCGCh's leading position in the market.

4. Conclusions

Singapore is the undisputed leader of nanoparticle technology in ASEAN, followed by Malaysia and Thailand, respectively. Because of Thailand's lower international profile compared to Singapore and Malaysia, the present article is focused at 2 nanoparticle R&D organizations in Thailand, namely, CEPT (CU) and NANOTEC together with their alliances. The interest in nanotechnology of SCG (Siam Cement Group), a leading Thai industrial conglomerate, has also been introduced.

The present focus of research activities of CEPT is set on developing and improving alternatives for synthesis and applications of particulate materials and their derivatives in nano-scaled forms. More specifically, using several alternative methods such as gas-phase reaction, solvothermal treatment, sol-gel system and micro-emulsion, syntheses of selected metals and their compounds such as TiO_2, ZnO, Al_2O_3, ZnS and WO_3 have been investigated. Similarly, synthesis of carbonaceous materials and their derivatives, including mesoporous and metal-hybridized nanocarbon was carried out using several methods, such as arc-discharge, pyrolysis, solvothermal and RF-gel formation. The trends of nanoparticle production of NANOTEC and its alliances have moved toward a facile system which incorporates multicomponents into hybrid or composite nanoparticles with the aim of enhancing performance in specific applications. Metal/metal oxide nanoparticles have been applied to energy and petrochemical, while photocatalysts, metal-doped TiO_2 and ZnO in particular, have extensively been used in textile and environment fields. The fabrication of composites based on carbon nanotubes shows good performance as electrochemical devices. In addition, organic-based nanoparticles, including chitosan-, gelatin-, and nisin-bonded polymers have been developed for (bio)medical, electronic and food industry. The Research and Development Unit of SCG Chemicals (SCGCh) takes on the challenges of employing new technology in various steps of invention and improvement of their capabilities. A key development strategy is the application of nanotechnology, including nanoparticle technology. In recent years, SCGCh has delved into polymer nanocomposites development involving carbon nanomaterials, layered nano-silicates, and novel nano-nucleating agents which result in improvements to the bulk PE and PP as well as the finished products.

References

Charinpanitkul, T., Sano, N., Muthakarn, P., and Tanthapanichakoon, W. (2009a): Enhancing effect of monoolein surfactant on carbon nanoparticle synthesis by arc discharge in liquid, Mater. Res. Bull., 44, 2, pp.324-327.

Charinpanitkul, T., Sano, N., Puengjinda, P., Muthakarn, P., and Tanthapanichakoon, W. (2009b): Possibility of pyrolytic synthesis of carbon nanostructures using naphthalene as carbon source, J. Anal. Appl. Pyrolysis, 86, 2, pp.386-390.

Charinpanitkul, T., Soottitantawat, A., Tonanon, N., and Tanthapanichakoon, W. (2009c): Single-step synthesis of nanocomposite of copper and carbon nanoparticles using arc discharge in liquid nitrogen, Mater. Chem. Phys., 116, 1, pp.125-128.

Charinpanitkul, T., Lorturn, P., Ratismith, W., Viriya-empikul, N., Tumcharern, G., and Wilcox, J. (2011): Hydrothermal synthesis of titanate nanoparticle/carbon nanotube hybridized material for dye sensitized solar cell application, Mater. Res. Bull., 46, 10, pp.1604-1609.

Charinpanitkul, T., and Tanthapanichakoon, W. (2011a): Regeneration of activated carbons saturated with pyridine or phenol using supercritical water oxidation method enhanced with hydrogen peroxide, J. Ind. Eng. Chem., 17, 3, pp.570-574.

Charinpanitkul, T., and Tanthapanichakoon, W. (2011b): Deterministic model of open-space dust removal system using water spray nozzle: Effects of polydispersity of water droplet and dust particle, Sep. Pur. Technol., 77, 3, pp.382-388.

Charnhattakorn, B., Charinpanitkul, T., Sirisuk, A., and Pavarajarn, V. (2011): Controlled synthesis of defects-containing ZnO by the French process modified with pulsed injection and its luminescence properties, Ceram. Inter., 37, 6, pp.2021-2024.

Faungnawakij, K., Kikuchi, R., Fukunaga, T., Eguchi, K. (2009): Stability enhancement in Ni-promoted Cu-Fe spinel catalysts for dimethyl ether steam reforming, J. Phys. Chem. C, 113, pp.18455–18458.

Inphonlek, S., Pimpha, N., Sunintaboon, P. (2010): Synthesis of poly(methyl methacrylate) core/ chitosan-mixed -polyethyleneimine shell nanoparticles and their antibacterial property, Colloids Surf. B: Biointerfaces, 77, pp.219–226.

Kangwansupamonkon, W., Jitbunpot, W., and Kiatkamjornwong, S. (2010): Photocatalytic efficiency of TiO_2/ poly[acrylamide-co-(acrylic acid)] composite for textile dye degradation, Polym. Degrad. Stab., 95, pp.1894-1902.

Klanwan, J., Akrapattangkul, N., Pavarajarn, V., Seto, T., Otani, Y., and Charinpanitkul, T. (2010): Single-step synthesis of MWCNT/ZnO nanocomposite using co-chemical vapor deposition method, Mater. Lett., 64, 1, pp.80-82.

Kongsombut, B., Chen, W., Tsutsumi, A., Tanthapanichakoon, W., and Charinpanitkul, T. (2008): Formation of deagglomerated PLGA Particles and PLGA-coated ultrafine powders by rapid expansion of supercritical solution with ethanol cosolvent, Korean J. Chem. Eng., 25, 4, pp.838-845.

Kongsombut, B., Tsutsumi, A., Suankaew, N., and Charinpanitkul, T. (2009): Encapsulation of SiO_2 and TiO_2 fine powders with PLGA by rapid expansion of supercritical CO_2 incorporated with ethanol cosolvent, Ind. Eng. Chem. Res., 48, 24, pp.11230-11235.

Kopermsub, P., Mayen, V., and Warin, C. (2011): Potential use of niosomes for encapsulation of nisin and EDTA and their antibacterial activity enhancement, Food Res. Int., 44, pp.605–612.

Kruefu, V., Liewhiran, C., Wisitsoraat, A., and Phanichphant, S. (2011): Selectivity of flame-spray-made Nb/ ZnO thick films towards NO_2 gas, Sensors and Actuators B, 156, pp.360–367.

Mekasuwandumrong, O., Somboonthanakij, S., Praserthdam, P., and Panpranot, J. (2009): Preparation of nano-Pd/SiO_2 by one-step flame spray pyrolysis and its hydrogenation activities: comparison to the conventional impregnation method, Ind. Eng. Chem. Res. 48, pp.2819.

Mungmart, M., Kijsirichareonchai, U., Tonanon, N., Prechanont, S., Panpranot, J., Yamamoto, T., Eiadua, A., Sano, N., Tanthapanichakoon, W., and Charinpanitkul, T. (2011): Study on performance of metal catalysts impregnated on porous media for aqueous phenol decomposition within three-phase fluidized-bed reactor, J. Hazard. Mater., 185, pp.606.

Nakagawa, K., Yasumura, Y., Thongprachan, N., and Sano, N. (2011a): Freeze-dried solid foams prepared from carbon nanotube aqueous suspension: application to gas diffusion layers of a proton exchange membrane fuel cell, Chem. Eng. Proc., 50, pp.22-30.

Nakagawa, K., Surassmo, S., Min, S.-G., and Choi, M.-J. (2011b): Dispersibility of freeze-dried poly(epsilon-caprolactone) nanocapsules stabilized by gelatin and the effect of freezing, J. Food Eng., 102, pp.177–18.

Numpud, P., Charinpanitkul, T., and Tanthapanichakoon, W. (2008): Photoinduced hydrophilic property of glass improved by zinc oxide thin films prepared by sol-gel dip coating method, J. Ceram. Soc. Jap., 116, 3, pp.414-417.

Petchpradab, P., Yoshida, T., Charinpanitkul, T., and Matsumura, Y. (2009): Hydrothermal pretreatment of rubber wood for the saccharification process, Ind. Eng. Chem. Res., 48, 9, pp.4587-4591.

Pisduangdaw, S., Panpranot, J., Methastidsook, C., Chaisuk, C., Faungnawakij, K., Praserthdam, P., and Mekasuwandumrong, O. (2009): Characteristics and catalytic properties of Pt–Sn/Al_2O_3 nanoparticles synthesized by one-step flame spray pyrolysis in the dehydrogenation of propane, Appl. Catal. A: Gen., 370, pp.1–6.

Pisduangdaw, S., Panpranot, J., Chaisuk, C., Faungnawakij, K., and Mekasuwandumrong, O. (2011): Flame sprayed tri-metallic Pt–Sn–X/Al_2O_3 catalysts (X = Ce, Zn, and K) for propane dehydration, Catal. Commun., 12, pp.1161–1165.

Polpanich, D., Asawapirom, U., Thiramanas, R., and Piyakulawat, P. (2011): Self-colored nanoparticles containing naphthalene-bisimide derivatives: Synthesis and protein adsorption study, Mater. Chem. Phys., 129, pp.495–500.

Polrut, W., Boonliang, B., Tanthapanichakoon, W., and Damronglerd, S. (2011): Triangle rule for operating windows and scale-up criteria for volume resistivity of pp/carbon nanotubes composites, Int. Polym. Proc., 26, 4, pp.456-459.

Poonjarernsilp, C., Sano, N., Charinpanitkul, T., Mori, H., Kikuchi, T., and Tamon, H. (2011): Single-step synthesis and characterization of single-walled carbon nanohorns hybridized with Pd nanoparticles using N_2 gas-injected arc-in-water method, Carbon, 49, 14, pp.4920-4927.

Prombutara, P., Kulwatthanasal, Y., Supaka, N., Sramala, I., and Chareonpornwattana, S. (2012): Production of nisin-loaded solid lipid nanoparticles for sustained antimicrobial activity, Food Control, 24, pp.184-190.

Sahu M., Suttiponparnit, K., Suvachittanont, S., Charinpanitkul, T., and Biswas, P. (2011): Characterization of doped TiO_2 nanoparticle dispersions, Chem. Eng. Sci., 66, 15, pp.3482-3490.

Sano, N., Yamamoto, T., Shinomiya, H., Endo, A., Eiad-ua, P., Soottitantawat, A., Charinpanitkul, T., Tanthapanichakoon, W., Ohmori, T., and Tamon, H. (2009): Decomposition of phenol in water by ozone oxidation with metal-supported carbongel, J. Chem. Eng. Jap., 42, pp.17-22.

Sawatsuk, T., Chindaduang, A., Sae-kung, C., Pratontep, S., and Tumcharern, G. (2009): Dye-sensitized solar cells based on TiO_2–MWCNTs composite electrodes: Performance improvement and their mechanisms, Diam. Relat. Mater., 18, pp.524–527.

Shimoda, N., Faungnawakij, K., Kikuchi, R., Fukunaga, T., and Eguchi, K. (2010): Catalytic performance enhancement by heat treatment of $CuFe_2O_4$ spinel and γ-alumina composite catalysts for steam reforming of dimethyl ether, Appl. Catal. A: Gen., 365, pp.71-78.

Srinives, S., Charinpanitkul, T., and Tanthapanichakoon, W. (2010): Experimental investigation of time-dependent performance characteristics of fine dust filtration using rice-husk bed, J. Ind. Eng. Chem., 16, 2, pp.224-229.

Srisitthiratkul, C., Pongsorrarith, V., and Intasanta, N. (2011): The potential use of nanosilver-decorated titanium dioxide nanofibers for toxin decomposition with antimicrobial and self-cleaning properties, Appl. Surf. Sci., 257, pp.8850–8856.

Srisurichan, A., Ilcham, A., Soottitantawat, A., Wanna, Y., Sano, N., and Charinpanitkul, T. (2009): Composite of MWCNT/PMMA for gaseous toluene detection, J. Chem. Eng. Jap., 42, pp.s238-241.

Thongprachan, N., Nakagawa, K., Sano, N., Charinpanitkul, T., and Tanthapanichakoon, W. (2008): Preparation of macroporous solid foam from multi-walled carbon nanotubes by freeze-drying technique, Mater. Chem. Phys., 112(1), pp.262-269.

Ullah, R., and Dutta, J. (2008): Photocatalytic degradation of organic dyes with manganese-doped ZnO nanoparticles, J. Hazard. Mater., 156, pp.194–200.

Viriya-empikul, N., Sano, N., Charinpanitkul, T., Kikuchi, T., and Tanthapanichakoon, W. (2008): A step towards length control of titanate nanotubes using hydrothermal reaction with sonication pretreatment, Nanotechnology, 19, pp.35601.

Vongchan, P., Wutti-In, Y., Sajomsang, W., Gonil, P., Kothan, S., and Linhardt R. J. (2011): N,N,N-Trimethyl chitosan nanoparticles for the delivery of monoclonal antibodies against hepatocellular carcinoma cells, Carbohyd. Polym., 85, pp.215–220.

Wantala, K., Laokiat, L.; Khemthong, P., Grisdanurak, N.; and Fukaya, K. (2010): Calcination temperature effect on solvothermal Fe–TiO_2 and its performance under visible light irradiation, J. Taiwan. Inst. Chem. Eng, 41, pp.612–616.

Wisitsoraat, A., Sritongkham, P., Karuwan, C., Phokharatkul, D., Maturos, T., and Tuantranont, A. (2010): Fast cholesterol detection using flow injection microfluidic device with functionalized carbon nanotubes based electrochemical sensor, Biosens. Bioelectron., 26, pp.1514-1520.

Yiamsawas, D., Boonpavanitchakul, K., and Kangwansupamonkon, W. (2011): Optimization of experimental parameters based on the Taguchi robust design for the formation of zinc oxide nanocrystals by solvothermal method, Mater. Res. Bull., 46, pp.639–642.

Yoshikawa, M., Uemura, T., Kan, D., Fukui, T., Charinpanitkul, T., Tanthapanichakoon, W., and Naito, M. (2007): Development of filtration technology for PM2.5 in diesel exhaust, Ceram. Trans., 198, pp.339-346.

Author’s short biography

Wiwut Tanthapanichakoon

Wiwut Tanthapanichakoon is concurrently a professor of chemical engineering (ChE), Graduate School of Science & Engineering, Tokyo Institute of Technology, an adjunct professor of Kyoto Univ. and Distinguished Scholar in Particle Technology, Chulalongkorn University. He received his B.Eng. (ChE) from Kyoto University and PhD (ChE) from University of Texas at Austin. In the recent past, he was Senior Research Advisor, SCG Chemicals Co., Ltd.; founding Executive Director, National Nanotechnology Center (NANOTEC); President, Technology Promotion Assoc. (Thailand-Japan); President, Thai Institute of Chemical Engineering and Applied Chemistry (TIChE); etc. His research interest covers (nano-) particle tech, aerosol engineering, process simulation, heat and mass transfer operations, and energy technology. Wiwut has received numerous research awards and honors: ASEAN Outstanding Engineering Achievements Award 2010; Japan Society for Promotion of Science (JSPS) Fellow; Senior Research Scholar/Team Research Award, Thailand Research Fund (TRF); S&T Award, Thailand Toray Science Foundation; Outstanding Faculty Award in S&T (Univ. Level), Chulalongkorn University. In recognition of his dedication, he was bestowed several Royal Decorations, the highest being the Knight Grand Cordon (Special Class) of the Most Exalted Order of the White Elephant in 2004.

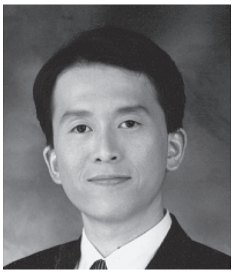

Tawatchai Charinpanitkul

Tawatchai Charinpanitkul is an Associate Professor of Chemical Engineering in Faculty of Engineering, Deputy Director of Energy Research Institute (ERI) and Director of Center of Excellence in Particle Technology (CEPT) affiliated with Chulalongkorn University. He received his Bachelor in Chemical Engineering from Chulalongkorn University in 1986, and Master and Doctor in Chemical System Engineering from University of Tokyo in 1989 and 1992, respectively. His present research interest is focused on Synthesis and Application of Nanomaterials, in particular, Carbonaceous Nanoparticles and Zinc Nanostructure, and Biomass Technology. With his attempt in academic contributions, TCR has published 110 technical journal papers related to the abovementioned research interest. In recognition of his dedication to Chulalongkorn University, he was bestowed several Royal Decorations, the highest being the Knight Grand Cordon (Special Class) of the Most Exalted Order of the White Elephant.

Suracha Udomsak

Dr. Suracha Udomsak received his degree in Chemical Engineering from Chulalongkorn University in 1989. He briefly worked for SCG Building Materials Co., Ltd. before continuing his education in the United States. In 1995, he was awarded Ph.D. degree in Chemical Engineering from Texas A&M University. He re-joined SCG in the technical department of polyethylene and polypropylene production company in SCG Chemicals Co., Ltd. Since then, he had built his successful career in the corporation by holding managing director positions for 3 different subsidiary companies in SCG Chemicals Co., Ltd. Currently, he is the Head of Technology Business for SCG Chemicals Co., Ltd. and the managing director of Texplore Co., Ltd. He is taking the lead of building SCG Chemicals Co., Ltd. towards forefront of technological and innovative business.

Author's short biography

Butra Boonliang

Dr. Butra Boonliang is currently working for SCG Chemicals Co. Ltd., as Technology Intelligence Manager. He obtained his degree in Materials Science and Technology and master degree in Science and Engineering of Materials in The University of Birmingham and was awarded Ph.D. in Manufacturing and Mechanical Engineering with a focus on Micro Engineering and Nanotechnology in 2007. He joined SCG Chemicals Co., Ltd. as a researcher in polymer nanocomposite group. He was then assigned to lead a product development team for fiber, PE wax and master-batch applications and moved to Technology Intelligence Department in 2011. His current responsibility are technical and commercial evaluation of SCG Chemicals' intellectual properties and scouting for emerging technologies with an aim to expand company's portfolio of products and network.

Kajornsak Faungnawakij

Dr. Kajornsak Faungnawakij is a senior researcher and lab-head of Nanomaterials for Energy and Catalysis Laboratory at National Nanotechnology Center, National Science and Technology Development Agency (Thailand). He received his B.Eng. (First-class honor) and D.Eng. in Chemical Engineering from Prince of Songkla University and Chulalongkorn University, respectively. He was a researcher at Japan Science and Technology Agency (JST), and a postdoctoral fellow at Kyoto University (Japan) during 2005-2007. Currently, he has actively worked in research fields of heterogeneous nanocatalysis and biofuels.

The Synthesis and Characterization of Rare-Earth Fluocarbonates[†]

Pradip[1*], **Charles C.H. Li**[2] **and Douglas W. Fuerstenau**[2]
[1] *Tata Research Development and Design Centre, A Division of Tata Consultancy Services*
[2] *Department of Materials Science and Engineering, University of California*

Abstract

A procedure is described for synthesizing cerium fluorcarbonate. This synthetic bastnaesite was characterized through X-Ray diffraction, chemical analysis and thermogravimetric studies. The solubility product of Ce-bastnaesite was determined to be $10^{-10.1}$. *The stability constant pK* $CeHCO_3^{2+}$ *complex was experimentally determined to be 3.04 ± 0.21. Based on the thermodynamic data available in the literature, a speciation diagram has been prepared for the synthetic cerium bastnaesite.*

Keywords: synthesis of rare-earth fluocarbonates, characterization of rare-earth fluocarbonates, bastnaesite, synthesis of cerium bastnaesite, physical and chemical characterization of bastnaesite particles

Introduction

Owing to their unique magnetic and optical properties, the world demand for rare-earths has been steadily increasing in the latter half of the twentieth century and sharply since the 1990s. The discovery of high-temperature superconductivity in mixed oxides involving rare-earths opened up yet another market avenue for them. A recent report prepared by the US Department of Energy highlights the critical role of rare-earth metals in the clean energy economy[1)]. The need to exploit all available rare-earth resources is expected to grow rapidly. Rare-earths occur in nature mainly as salt minerals, most commonly as complex fluocarbonates and phosphates. Bastnaesite, a fluocarbonate of the cerium group of rare-earth metals. $(RE)FCO_3$, was first discovered in 1818 at Bastnas, Sweden[2)]. The mineral contains about 75 percent light rare-earth (RE) oxides distributed as follows: 50.0% cerium, 34.0% lanthanum, 11.0% neodymium, 4.0% praseodymium, 0.5 % samarium, 0.2% gadolinium, 0.1% europium, and 0.2% others. The theoretical composition of bastnaesite ($CeFCO_3$ synthetic or $(Ce,La)FCO_3$ natural) is 74.77% Ce_2O_3, 20.17% CO_3, and 8.73% F. The elemental analysis of natural bastnaesite is generally close to this composition.

Major occurrences of bastnaesite have been reported in several locations, but by far the two largest deposits known are those at Mountain Pass in California and in Inner Mongolia and Kanshu Province, China. The largest single producer of rare-earths was the Molycorp operation at Mountain Pass[3–5)] until low-cost Chinese production caused it to be shut down in the late 1990s. Extensive efforts are underway to reopen the Mountain Pass mine since today 97 percent of the world's production comes from China.

Being a relatively rare mineral, little data are available in the literature about the various physico-chemical properties of bastnaesite. To provide information about pure particles for study of this important source of rare-earth metals, this paper summarizes some of our results on the synthesis and characterization of pure bastnaesite.

Crystal structure of bastnaesite

Bastnaesite belongs to a family of rare-earth/alkaline-earth fluocarbonates (those of the calcium and barium varieties) and is similar in structure to calcium fluorcarbonate. In 1956, Donnay and Donnay[6)] established the following isostructural series of calcium fluocarbonates, with different ratios of $CeFCO_3$ to $CaCO_3$:

[†] Accepted: January 26, 2012
[1] Pune 411013, India
[2] Berkeley, California 94720, USA
[*] Corresponding author:
E-mail: pradip.p@tcs.com
TEL: +91-20-6608-6333 FAX: +91-20-6608-6399

ⓒ 2013 Hosokawa Powder Technology Foundation

Bastnaesite	$CeFCO_3$	$(100\% \ CeFCO_3)$
Parisite	$2CeFCO_3 \cdot CaCO_3$	$(2/3 \ CeFCO_3)$
Rontgenite	$3CeFCO_3 \cdot 2CaCO_3$	$(3/5 \ CeFCO_3)$
Synchisite	$CeFCO_3 \cdot CaCO_3$	$(1/2 \ CeFCO_3)$

Semenov[7] has suggested that additional members of this series with even higher calcium contents might exist:

$2CeFCO_3 \cdot CaCO_3$	$(2/5 \ CeFCO_3)$
$2CeFCO_3 \cdot 2CaCO_3$	$(1/3 \ CeFCO_3)$
Vaterite	$(0\% \ CeFCO_3)$

McConnel[7] later showed that calcite and vaterite are isostructural, vaterite being a special trigonal polymorphous modification of $CaCO_3$ that differs from calcite. The minerals of this group have a characteristic layer structure, in which the layers of Ce and F ions are parallel to the (0001) plane and alternate with the layer of Ca ions. Plane CO_3 triangles are arranged between the Ce-F and Ca layers. Details of the crystal structures of these minerals are available in the excellent paper by Donnay and Donnay[6].

The structural scheme of bastnaesite and related minerals described above was first predicted by Oftedal[6] in 1931 and subsequently confirmed by the Donnays[6]. The structure of bastnaesite is trigonal with $a_o = 7.16A$, $c_o = 9.79A$, with the c_o/a_o ratio being 1.367. Cerium and fluorine ions alternate at the vertices of regular hexagons with carbonate groups interspersed between the Ce-F layers. There are six formula units of $CeFCO_3$ per cell.

Synthesis of Bastnaesite

In our laboratory, we tried to separate some pure bastnaesite crystals from a sample of Mountain Pass ore through physical separation under ultra violet light[5]. However, this was done with only limited success and, therefore, for very precise characterization of this mineral, it was necessary to synthesize pure bastnaesite in the laboratory. Only one previous attempt in this direction was reported in the literature by Jansen et al.[8], who were able to successfully synthesize a few milligrams of bastnaesite in the early 1950's.

We modified the Jansen method in order to synthesize about one gram of bastnaesite in each run. The reaction involved in the synthesis is the following:

Cerium Bastnaesite:

$$Ce_2(CO_3)_3 + 2HF = 2\,CeFCO_3 + CO_2 + H_2O \quad (1) \text{ or}$$

Lanthanum Bastnaesite:

$$La_2(CO_3)_3 \cdot 8\,H_2O + 2HF = 2\,LaFCO_3 + CO_2 + 9H_2O \quad (2)$$

The apparatus used for the synthesis (**Fig. 1**) consisted of a cylindrical container (11 cm × 18 cm) with a capacity of about 1 liter. It was constructed of Monel (resistant to hydrofluoric acid at high temperature), This was surrounded by a heating jacket (Glas-Col Heating Mantle for Griffin type beakers, made up of corrosion-resistant glass cloth with Nichrome heating elements) capable of providing controlled temperatures up to 450 ℃ through a Variac. The container was closed with a Teflon lid, through with a Teflon stirrer and Teflon inlet and outlet tubes (0.6 cm diameter) for CO_2 gas were provided. An alternative method for stirring could be provided by bubbling the CO_2 gas through the solution, with a porous Teflon tube introduced into the solution. The outgoing gases and vapors were condensed through a condenser attached to the lid as shown in the figure and supported by a stand. Bone-dry CO_2 gas was bubbled through the solution so that the reaction was carried out in a CO_2 - saturated solution. Hydrofluoric acid was introduced through a vertical Teflon tube drop by drop over a period of a few minutes so that it was thoroughly mixed with the contents of the container. Basically, the procedure involved dispersing about 1.150 g of cerium carbonate or (1.505 g of lanthanum hydrous carbonate) in 700 cc of preheated distilled

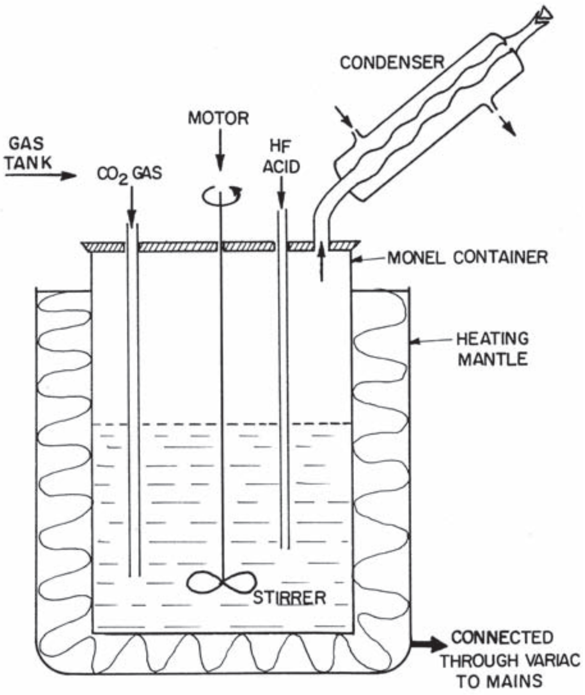

Fig. 1 Schematic drawing of the apparatus used for the laboratory synthesis of bastnaesite in the laboratory.

water. Then 50 cc of 0.1 M HF acid (100 mg of HF) was introduced slowly into the solution, and the reaction was allowed to take place at around 80 – 90 ℃ in a CO_2 atmosphere for about 24 hours. Digestion of this product overnight at this temperature was found sufficient for the reaction to go to completion, after which the product was cooled, filtered, and air dried. Under unfiltered UV light, a characteristic light green color of bastnaesite was visible in the product.

The synthesis of $LaFCO_3$ would essentially involve the same procedure. Bastnaesite of the composition as found in nature (having both La and Ce as major constituents) can also be synthesized starting with the stoichiometric amounts of respective carbonates and hydrofluoric acid as reactants.

It is also important to point out that the limitation of this method for producing larger quantities of bastnaesite is due to the limited capacity (l liter) of the container. Since the solid/liquid ratio was found to affect the purity of the sample, it is impossible to work at higher concentrations.

Characterization of Synthetic Bastnaesite

Chemical Analysis of Synthetic Bastnaesite

Four different batches were selected for analysis and identification purposes. The only differences among these is the amount of cerium carbonate per 700 cc used in the synthesis, batches A and B starting with 0.5753 g, and batch C with 0.4602 g of cerium carbonate. Batch D had several hours of ultrasonic dispersion of the cerium carbonate before the HF was added. The chemical analyses, which were carried out at the Mountain Pass Research Laboratory of Molycorp (Molybdenum Corporation of America) are summarized in **Table 1**. A comparison of the chemical analysis of the synthetic products with the theoretical composition of bastnaesite indicates that the synthetic product is close to pure bastnaesite.

Table 1 Analysis of synthetic cerium bastnaesite and natural mineral samples

Sample	% Re_2O_3	% Ce or RE	% F
Theoretical $CeFCO_3$	74.9	63.95	8.67
Synthetic $CeFCO_3$			
Batch A	70.2	59.9	9.3
Batch B	71.3	60.9	9.0
Batch C	69.96	59.7	8.6
Batch D		63.15	8.83
Natural (Molycorp) bastnaesite crystal $(Ce,La)FCO_3$	69.17	59.04	6.88
Hand picked* (under UV light) Birthday Claims, Mountain Pass sample $(Ce,La)FCO_3$	60.9	51.98	-

*Bastnaesite fluoresces (green color) in UV light (without filter) and so it can easily be hand picked.

Specific Surface of the Synthetic Ce-Bastnaesite Powder

Using the multi-point BET method, the specific surface area of the powder was measured by the adsorption of nitrogen at liquid nitrogen temperature. It was found to be 9.27 m^2/g, giving an average diameter of the particles of 0.14 µm.

X-Ray Diffraction Studies

A Philips diffractometer was used to obtain the x-ray diffraction patterns for the various synthetic samples of bastnaesite. The beam was *Cu Ka* with a Ni filter having a wavelength of 1.5418 Å. **Table 2** compares the values of the

Table 2 X-ray diffraction pattern data for Mountain Pass bastnaesite and for synthesize samples of cerium bastnaesite compared to the synthetic bastnaesite synthesized by Jansen et al.[8)]

Jansen's Synthetic $CeFCO_3$		Natural Bastnaesite $(Ce, La)FCO_3$ (Molycorp)		Synthetic $CeFCO_3$ (this work) Batch A	Batch B	Batch C	Batch D
d, Å	I	d, Å	I	d, Å	d, Å	d, Å	d, Å
4.96	70	4.88		4.874	4.874	4.874	4.901
3.52	100	3.564	70	3.548	3.562	3.562	3.568
2.92	100	2.879	100	2.867	2.876	2.876	2.881
2.46	9	2.445	10	2.442	2.442	2.442	2.446
2.29	2	2.273	3	-	-	-	-
		2.238	3	-	-	-	-
2.09	50	2.057	40	2.049	2.053	2.953	2.050
2.03	50	2.016	40	2.006	2.014	2.014	2.019
1.92	35	1.898	40	1.892	1.895	1.895	1.849
1.81	6	1.783	9	1.778	1.778	1.778	1.784
1.70	18	1.674	21	1.670	1.670	1.670	1.676
1.64	2	1.629	1	-	-	-	-
1.59	13	1.573	15	1.568	1.570	1.573	1.573
1.49	9	1.481	9	1.478	1.482	1.481	1.482
1.46	9	1.439	11	1.435	1.437	1.439	1.439
1.37	4	1.347	7	1.344	1.344	1.344	1.345
1.32	15	1.298	15	1.283	1.296	1.296	1.297
1.29	4	1.277	7	1.274	1.276	1.277	-

d-spacings reported in the literature with those obtained for the synthetic bastnaesite from this work. The values are quite consistent with those of the bastnaesite ($CeFCO_3$) sample synthesized by Jansen et al.[8] and those of the natural bastnaesite from Mountain Pass.

It is also apparent from the data that the methods employed for synthesis did indeed yield bastnaesite mineral particles. The intensities of the peaks (not shown here) obtained with the synthetic bastnaesite samples also compared quite well with the reported literature values.

Thermogravimetric Studies on Bastnaesite

A Perkin-Elmer TGS-2 Thermogravimetric System was used to obtain the weight loss as a function of the temperature of heating. The corresponding first derivative of this curve was also recorded. The heating rate was programmed to be 50 ℃ per minute through a temperature range of 30 to 900 ℃. Since nitrogen was being flushed through the system during heating, the oxygen concentrations must have been minimal. The heating curve as well as its first derivative is plotted in **Fig. 2a** and **b**, respectively. When heated in a nitrogen atmosphere, cerium carbonate exhibits two plateaus with the final weight loss at 900 ℃ asymptotically approaching 30 %, whereas cerium fluocarbonates show an asymptotic weight loss of 20 % at 900 ℃. This total weight loss can be understood in terms of the following reactions in a nitrogen atmosphere.

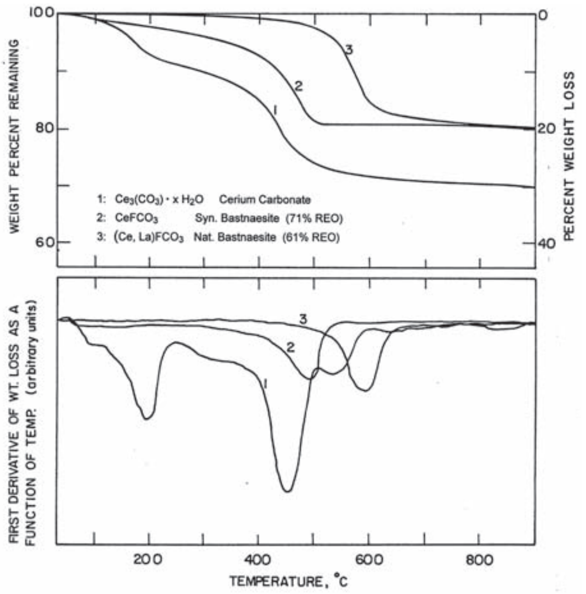

Fig. 2 Thermogravimetric analysis results for cerium carbonate, synthetic bastnaesite and natural bastnaesite (top figure) and the respective differential curves (bottom figure).

i) **Cerium carbonate** $Ce_2(CO_3)_3$ · anhydrous or xH_2O in a nitrogen environment :

$$Ce_2(CO_3)_3 \cdot xH_2O \text{— } N_2 \text{ envir} \longrightarrow Ce_2O_3 + 3CO_2 + xH_2O \cdots (3)$$

460.24 g (anhydrous) 328.24 g

∴ Therefore anhydrous cerium carbonate weight loss = 28.7 %

ii) **Cerium Fluocarbonate** $CeFCO_3$ (synthetic Ce-bastnaesite) in nitrogen atm:

$$3CeFCO_3 \text{ — } N_2 \text{ envir} \longrightarrow Ce_2O_3 + CeF_3 + 3CO_2 \cdots (4)$$

3 × 210.2 g 328.24 g + 197.12 g

∴ Synthetic Ce-bastnaesite weight loss = 20.08 %

iii) **Lanthanum Fluocarbonate** $LaFCO_3$ (synthetic La-bastnaesite) in nitrogen atm:

$$3LaFCO_3 \text{ — } N_2 \text{ envir} \longrightarrow La_2O_3 + LaF_3 + 3CO_2 \cdots (5)$$

653.73 g 521.73 g

∴ Synthetic La-bastnaesite weight loss = 20.2 %

iv) **Natural Bastnaesite** $(Ce,La)FCO_3$ which contains cerium and lanthanum as the majority fluocarbonates, then would be expected to lose about 20 % of its weight upon decomposition, as was observed in this work.

Since the weight loss obtained for synthetic cerium fluocarbonate was very close to this value, the above reaction is very probable.

Note that here the final products of decomposition are the corresponding oxides and fluorides. In an oxygen environment, cerium can also be oxidized to its tetravalent state since CeO_2 is the most stable oxide product. Then the reaction could be

$$2CeFCO_3 \text{ — } O_2 \text{ envir} \longrightarrow 2CeO_2 + F_2 + CO_2 \cdots\cdots (6)$$

No studies on oxidative heating have been reported in the literature. For rare-earth carbonates precipitated from aqueous solutions, Head and Holley, Jr.[9] conducted thermal decomposition studies under several different conditions in vacuum, carbon dioxide and water vapor environments. The decomposition reaction has been postulated as follows:

$$M_2(CO_3)_3 \cdot xH_2O \rightarrow M_2(CO_3)_3 \rightarrow M_2O_2 \cdot CO_3 \rightarrow M_2O_3 \cdot yCO_2 \rightarrow M_2O_3 \cdots\cdots (7)$$

where x varies from compound to compound and the composition $M_2O_3 \cdot yCO_2$ ($y < 1$) is not always observed. The general shape of their curve is consistent with our results except that their cerium carbonate was hydrated (x = 8). The plateau observed around 195 – 200 ℃ in our case is perhaps due to some intermediate in the decomposition of cerium carbonates as postulated by Head and Holley[9].

The decomposition peak for bastnaesite from Mountain Pass was found to occur between 500 to 675℃. Vlasov[7] reported a decomposition peak between 420 and 600 ℃ for a bastnaesite from Mongolia. X-ray analysis of its calcination product also showed a cubic phase with a = 5.555 Å which was in fact a solid solution of lanthanide sesquioxides $CeLaO_{3.5}$.
This is due to the dissociation of the mineral involving the loss of CO_2 and possibly F in an oxygenated environment. Our results also show a shift in the decomposition peak from 600 ℃ for natural bastnaesite to about 500 ℃ in the case of synthetic bastnaesite. With the limited work conducted on this system, it is difficult to explain this shift except to note that these two bastnaesites have different rare-earth compositions and that in the case of natural bastnaesite, small amounts of calcite and barite are also present. The presence of impurities apparently stabilizes the fluocarbonate such that decomposition is delayed by 100 ℃. It is interesting to note that the final products are the same since the final weight losses are identical. Perhaps the enthalpies of the decomposition reactions in the two cases are different.

Solution Chemistry of Synthetic Bastnaesite

Similar to such minerals as apatite, barite and calcite, bastnaesite is a sparingly soluble salt mineral. The soluble species resulting from dissolution of the mineral form ion complexes in the solution as well as at the water-solid interface. Ionic complexes may participate in interfacial reactions and play a significant role in subsequent processing. The synthetic Ce-bastnaesite was therefore subjected to detailed investigation of its solution chemistry.

Thermodynamic Calculations

For all minerals containing carbonate as lattice anions, the solubility and the corresponding solution behavior is primarily controlled by the partial pressure of CO_2. For a system open to the atmosphere, the activity of carbonate species in water will be determined by the aqueous solubility of CO_2 and the mineral. In addition, Ce-bastnaesite ($CeFCO_3$) will contribute Ce^{3+} ions, which will undergo hydrolysis and form a series of hydroxo complexes in solution[10–13]. Similarly, fluoride ions can form such complexes as HF, HF_2, CeF^{2+}. Since fluoride and cerium ions in solution result from the dissolution of bastnaesite, their total concentration will be identical. Based on reported data in the literature, the following charged species are expected to exist in aqueous solution in equilibrium with bastnaesite through the reactions listed in **Table 3**: Ce^{3+}, HCO_3^-, CO_3^{2-}, F^-, $CeOH^{2+}$, $Ce(OH)_2^+$, $Ce(OH)_4^-$, $Ce_3(OH)_5^-$, HF_2^-, CeF^{2+}, $CeHCO_3^{2+}$. Except for the solubility product of $CeFCO_3$, $K_{SO,}$ and the solubility constant of $CeHCO_3^{2+}$, K_{CeHC}, (which were determined experimentally in this work) all the values of equilibrium constants were taken from the published literature.

Determination of K_{so} for Synthetic Ce-Bastnaesite

The solubility product of Ce-bastnaesite is defined as follows:

$$CeFCO_3 = Ce^{3+} + F^- + CO_3^{2-} \quad \cdots\cdots (8)$$

$$K_{SO} = (Ce^{3+})\ (F^-)\ (CO_3^{2-}) \quad \cdots\cdots (9)$$

The total carbonate and fluoride concentrations in solution were measured with the corresponding ion selective electrodes and the cerium concentration was measured by a spectrophotometric technique[14]. One ml of concentrated H_2SO_4 was added to a 10 ml sample solution and heated to fume off SO_3. Water was added and then heated again to thoroughly remove fluoride. The solution was placed into a 25 ml volumetric flask to which 2 ml of 0.1M citric acid and 1 ml of 7% H_2O_2 were added. Next, 6 M NaOH solution was added till the solution reached a slightly basic pH (when a yellow color appeared), The resulting solution was diluted to 25 ml volume and the resultant absorbance was measured with a Bausch and Lomb Spectrophotometer at 390 mm.

Fig. 3 shows the measured total equilibrium concentration of Ce^{3+}, $F^-$and CO_3^{2-} as a function of pH at a constant partial pressure of $10^{-3.5}$ atm. CO_2 in an open system. Based on these solubility data and the thermodynamic data available in the literature for reactions given in **Table 3**, the molar concentrations of various ionic species in solution were computed as a function of pH[19]. The ionic strength of solutions under these conditions was calculated using these results and the corresponding activity coefficients for Ce^{3+}, F^- and CO_3^{2-}ions were computed with the extended Debye-Huckel Law[17–18]. Knowing the activity coefficients and the free ion concentrations, the solubility product of bastnaesite was estimated as a function of ionic strength as plotted in **Fig. 4**. The value of pK_{SO} for Ce-bastnaesite is thus 16.1, on extrapolation to zero ionic strength of the solution.

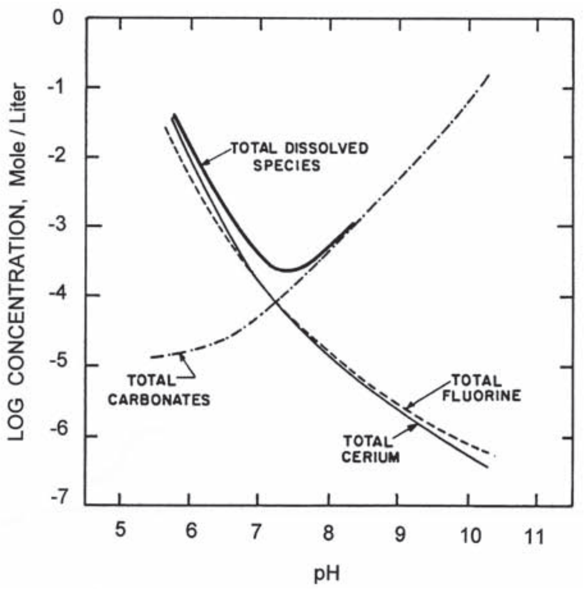

Fig. 3 The pH dependence of total cerium, total fluorine and total carbonate concentrations in aqueous solutions in equilibrium with air.

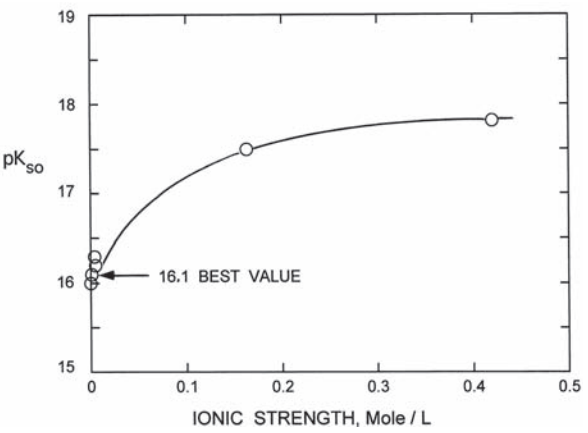

Fig. 4 The solubility product of synthetic cerium bastnaesite in aqueous solutions as a function of ionic strength.

Table 3 Chemical Reactions in the Synthetic Cerium Bastnaesite-Water System Open to the Atmosphere

							Reference
[1]	$CeFCO_3$	=	$Ce^{3+} + F^- + CO_3^{2-}$	K_{SO}	=	$10^{-16.1}$	(this work)
[2]	$HCO_3^- + H_2O$	=	$H_2CO_3 + OH^-$	K_1	=	$10^{-7.65}$	15)
[3]	$CO_3^{2-} + H_2O$	=	$HCO_3^- + OH^-$	K_2	=	$10^{-3.67}$	15)
[4]	$CO_2 + H_2O$	=	H_2CO_3	K_H	=	$10^{-1.47}$	15)
[5]	$Ce^{3+} + OH^-$	=	$CeOH^{2+}$	K_3	=	$10^{5.9}$	10,16)
[6]	$Ce^{3+} + 2OH^-$	=	$Ce(OH)_2^+$	K_4	=	$10^{-2.3}$	10,16)
[7]	$Ce^{3+} + 3OH^-$	=	$Ce(OH)_3^o[aq]$	K_5	=	$10^{-12.0}$	10,16)
[8]	$Ce^{3+} + 3OH^-$	=	$Ce(OH)_3[s]$	K_6	=	$10^{19.7}$	17,18)
[9]	$Ce(OH)_3^o[aq]$	=	$Ce(OH)_3[s]$	K_7	=	$10^{31.8}$	*
[10]	$Ce^{3+} + 4OH^-$	=	$Ce(OH)_4^-$	K_8	=	$10^{-24.0}$	10,16)
[11]	$3Ce^{3+} + 4OH^-$	=	$Ce_3(OH)_5^{4+}$	K_9	=	$10^{-18.8}$	10,16)
[12]	$Ce^{3+} + HCO_3^-$	=	$Ce\,HCO_3^{2+}$	K_{10}	=	$10^{3.4}$	(this work)
[13]	$Ce^{3+} + F^-$	=	CeF^{2+}	K_{11}	=	$10^{3.99}$	13)
[14]	$F^- + H^+$	=	HF	K_{12}	=	$10^{2.91}$	13)
[15]	$2F^- + H^+$	=	HF_2^-	K_{13}	=	$10^{3.48}$	13)

*K_7 is calculated from Reactions [7] and [9].

Determination of the Stability Constant of $CeHCO_3^{2+}$

Titration of H_2CO_3 in aqueous solution in the presence of $Ce(NO_3)_3$ was carried out in order to determine the stability constant of the complex cation $CeHCO_3^{2+}$. For a pure aqueous, air-saturated solution, the pH is defined by the charge balance:

$$[H^+] = [HCO_3^-] + 2[CO_3^{2-}] + [OH^-] .$$

If a metal cation which will form hydroxyl complexes with OH^- or ion-pair complexes with carbonates is added to the solution, the pH value will become lower since the complexing reactions will consume OH^-. Thus by measuring the equilibrium pH values at different additions of $Ce(NO_3)_3$, the concentration of species containing cerium can be calculated from the measured pH and the cerium total concentration based on charge balance equations (14). From this, the stability constant of $CeHCO_3^{2+}$ is simply

$$K_{CeHC} = [CeHCO_3^{2+}] / [Ce^{3+}] [HCO_3^-] \quad \cdots\cdots\cdots (10)$$

For the titration experiment, a weighed amount of $Ce(NO_3)_3$ was introduced into a 100 ml solution of NaOH or HNO_3 of known concentration and the solution was thoroughly stirred under an open-system atmosphere until a stable pH reading was achieved. The pH was determined by a Fisher digital pH/mV meter. The value of K_{CeHC} obtained was 3.40 ± 0.21.

Using the stability constant thus determined with

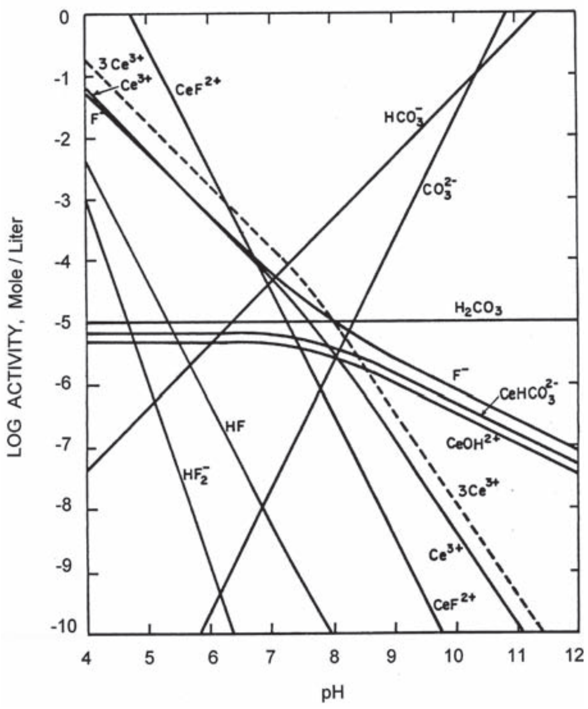

Fig. 5 Equilibria in the synthetic cerium bastnaesite / water system open to the atmosphere at 25 ℃.

Equation 10 and the thermodynamic data given in **Table 3**, the relative concentrations of various solution spcies in equilibrium with synthetic cerium fluocarbonate in a system open to atmosphere at 25 ℃, were computed. The results ace plotted in **Fig. 5**. The main charged species in a solution in equilibrium with synthetic cerium bastnaesite in a system open to atmosphere are Ce^{3+}, CeF^{2+}, HCO_3^-, CO_3^{2-}, F^-, $CeOH^{2+}$, $Ce(OH)_2^+$ and $CeHCO_3^+$ in addition to H^+ and OH^-. As shown in **Fig. 3**, the total species concentration is minimum in the pH range of 7.2 - 7.6.

Summary

A sample of cerium f1uocarbonate ($CeFCO_3$) was synthesized in the laboratory and characterized through X-ray diffraction and chemical analysis. Thermogravimetric studies on the synthetic bastnaesite exhibited a decomposition peak at 500 ℃ as compared to 600 ℃ in the case of natural bastnaesite obtained from Mountain Pass, California. The total weight loss when heated to 900 ℃ was 20 percent, consistent with the decomposition reaction for the mineral.

The solubility product K_{SO} as well as the stability constant K_{CeHC} were experimentally determined through solubility and titration measurements. Using the thermodymamic data available in the literature as well as the constants, a speciation diagram for cerium fluocarbonate has been presented.

References

1） Anon (2011): “Critical Materials Strategy”, US Department of Energy Report on Rare Earth Metals and other Materials in the Clean Energy Program, December 2011, 190 pp. downloaded from internet, (http://energy.gov/sites/prod/files/DOE_CMS2011_FINAL_Full.pdf)

2） Glass, J. J. and Smalley, R. G. (1945): Bastnaesite, The American Mineralogist, Vol.30, pp.601-615.

3） Fuerstenau, D. W. Pradip, Khan, L. A. and Raghavan, S. (1983): “An Alternate Reagent Scheme for the Flotation of Mountain Pass Rare Earth Ore”, XIV International Mineral Processing Congress, Proceedings, Toronto, Canada, pp. IV 6.1 -12.

4） Pradip and Fuerstenau, D. W. (1991): The Role of Inorganic and Organic Reagents in the Flotation Separation of Rare-Earth Ores, International J. Mineral Processing, Vol.32, pp.1-22.

5） Pradip, (1981): “The Surface Properties and Flotation of Rare Earth Minerals,” Ph.D. Thesis, University of California, Berkeley.

6） Donnay, G and Donnay, J.D.H. (1953): The crystallography of Bastanesite, Parisite, Roentgenite and Synchisite, The American Mineralogist, Vol.38, pp.932-963.

7） Vlasov, K. A. (Ed.) (1966): “Mineralogy of Rare Elements,” Vol. II, p. 264.

8） Jansen, G. J., Magin, G. B. Jr. and Levin, B. (1959): Synthesis of Bastnaesite, The American Mineralogist, Vol.44, pp.180-181.

9） Head, E. L. and Holley, C. E. Jr. (1963): “Rare-earth Carbonates,” in Rare Earth Research Proceedings of Third Conference, Gordon & Breach, pp.51-63.

10） Kragten, J. and Decnop-Weever, L. G. (1978): Hydroxide Complexes of Cerium (III), Talanta, Vol.25, pp.147-150.

11） Moeller, T. (1946): Observations on the Rare Earths LV. Hydrolysis Studies upon Yttrium and Cerium Rare Earth (III) Sulfate Solutions at 25 ℃, J. Phys. Chem., Vol.50, No.242, pp.242-250.

12） Stepanov, A. V. and Shuedov, V. P. (1965): Hydroxide Complexes of Lanthanides, Russian J. Inorganic Chem., Vol.10, pp.541-43.

13） Sillen, L. G., Martell, A. E. and Bjerrum, J. (1964): “Stability Constants of Metal-Ion Complexes,” The Chemical Society, London, 754 pp.

14） Vogel, A. I. and Bassett, J. (1978): “A Textbook of Quantitative Inorganic Analysis,” 4th Edition, Longman, UK 555 pp.

15） Garrels, R. M. and Christ, C. L. (1965): “Solutions. Minerals and Equilibria,” Cooper and Company 450 pp.

16） Kragten, J. (1978): “Atlas of Metal Ligand Equilibrium in Aqueous Solutions,” J. Wiley & Sons, 781 pp.

17） Butler, J. N. (1964): “Ionic Equilibria: A Mathematical Approach,” Addison-Wesley Publishing Company, 464 pp.

18） Kelland, J. (1937): Individual Activity Coefficients of Ions In Aqueous Solutions, J. Am. Chem. Soc., Vol.59, pp.1675 -1678.

19） Li, C. (1982): “Solubility and Electrokinetic Behavior of Synthetic Bastnaesite,” M.S. Thesis, University of California, Berkeley.

Author's short biography

Pradip

After graduating from the Indian Institute of Technology in Kanpur, Pradip entered the University of California at Berkeley to continue graduate studies in mineral processing. He obtained his M.S. degree in 1977 and Ph.D. degree in 1981. After serving as Scientific Officer, Ore Dressing Section, at the Bhabha Atomic Research Centre, he joined the Tata Research Design and Development Centre where he currently is Chief Scientist and Head of the Process Innovation Laboratory.

Charles C.H. Li

After graduating from Central South Institute of Mining and Metallurgy in Changsha, Charles Li entered the University of California at Berkeley to pursue graduate studies in mineral processing, and obtained his M.S. degree in 1982 and his Ph.D. degree in 1986. He then joined CRA (now Rio Tinto) in Australia, where he worked as a research engineer on mineral processing problems until his retirement.

Douglas W. Fuerstenau

After receiving his Sc.D. degree at MIT, Dr. Fuerstenau spent a six-year period teaching at MIT and working in industry, after which time he joined the faculty of the University of California. At Berkeley he established an extensive program of teaching and research in mineral processing, applied surface chemistry and particle technology. With his graduate students and post doctoral researchers, he has published a wide range of seminal papers in these fields. He currently is P. Malozemoff Professor Emeritus of Mineral Engineering in the University of California.

A Comparison of Aerosol Performance Using Standardized Entrainment Tubes *vs*. Dry Powder Inhaler Devices[†]

Zhen Xu[1] and Anthony J Hickey[2*]
[1] *Division of Molecular Pharmaceutics, Eshelman School of Pharmacy, University of North Carolina*
[2] *Research Triangle Institute*

Abstract

This paper reviews scientific understandings relevant to the dry powder inhaler (DPI) development including turbulent airflow characteristics in the inhaler, microparticle entrainment and deaggregation within the airflow and device. Using standardized entrainment tubes (SETs) and powder aerosol deaggregation equation (PADE), the aerosol performance profile in a shear stress range defined by SETs can be predicted. However, such predictions are based on the hypothesis that the shear stresses characterized from SETs are readily translatable to those of the DPIs' . Two selected model DPIs (Rotahaler and Aerolizer) with either gelatin or HPMC capsules were used to evaluate the FPF at the DPI shear stresses. The performance result using DPIs was close to the predicted FPF using SETs and PADE method. The application of SETs and PADE method can be used for performance prediction of these DPIs.

Keywords: standardized entrainment tubes, dry powder inhalers, powder aerosol deaggregation equation, inhalation, aerosolization performance, shear stress, fine particle fraction

1. Introduction

There have been significant advances in the development of dry powder inhaler (DPI) products since the first commercial DPI was launched in the late 1940s[1)]. Innovations of both formulations and devices have been made to achieve increased delivery efficiency and reproducibility of therapeutic agents to the target sites. Nevertheless, DPIs are complex delivery systems and slight changes of factors associated with flow profile or formulation may have significant impact on the performance of DPIs. Conventional methods of DPI development are mainly based on trial and error. It is not easy to scientifically interpret the aerosolization process from a static metered powder, by means of aerodynamic interaction with inhaled air, to the respirable particle generation. This is due, at least in part, to the incomplete fundamental understandings of the turbulent fluid dynamics occurring in the DPI devices, the microparticle entrainment in turbulent air condition, and heterogeneous microparticle interactions as a result of fluid forces. Moreover, great differences in DPI devices, formulation designs, and metering mechanisms further contribute to the overall complexity. In sight of these complexities, a set of standardized entrainment tubes (SETs) were designed to cover a range of airflow parameters observed in selected passive DPIs[2)]. SETs have been employed to evaluate a wide variety of formulations[3-7)]. Nevertheless, a fundamental understanding of the airflow and microparticle behavior in the SETs is a prerequisite for performance prediction of DPIs. Establishing the nature of formulation discrimination by SETs with respect to DPIs also requires experimental comparison between SET and

---

[†] Accepted: April 23, 2012
[1] Chapel Hill, NC 27759, USA
[2] 3040 Cornwallis Road, Research Triangle Park, NC 27709, USA
[*] Corresponding author:
E-mail: ahickey@rti.org
TEL: +1-919-541-6771 FAX: +1-919-541-6936

ⓒ 2013 Hosokawa Powder Technology Foundation

DPI.

The first aim of this paper was to briefly discuss current understandings of the fundamental aspects of airflow and microparticle behavior in SETs and DPIs. The paper starts with some basic fluid mechanics knowledge of turbulent pipe flow (Section 2); then it is followed by microparticle entrainment in these turbulent conditions (Section 3) and the interpretation of heterogeneous particle interaction using powder aerosol deaggregation equation (PADE, see Section 4). In addition, the necessity of using SETs was addressed (Section 5). The second aim of this paper was to experimentally compare the aerosol performance of SETs *vs.* DPIs using selected formulations (Section 6). It is proposed that using SETs as device independent screening tools, the aerosol performance of DPIs with defined airflow parameters can be predicted by interpolation from the PADE fitted regression curves.

2. Characteristic Turbulent Pipe Flow

Turbulent airstreams are generally recognized as the major source for particle deaggregation within typical DPI flow rate. However, the detailed nature of turbulent fluid flow and its interaction with the aerosolized particles are still not fully understood.

In typical turbulent flow, large-scale motions are strongly influenced by the boundary conditions, while the small-scale motion is determined by the rate of energy received from the large scales and the fluid viscosity. Eddies carry turbulent kinetic energy distributed over a broad range of scales. Turbulent airflow within a circular pipe consists of three regimes: an inviscid turbulent core, a viscous laminar sublayer, and a buffer layer where transition from turbulent to laminar flow occurs[8]. The velocity vector in turbulent flow varies, but with a mean velocity vector parallel to the wall. Although DPI devices have much more complex flow profiles than circular pipes, the nature of flow inside them can be characterized similarly by several closely related airflow parameters including Reynolds number (*Re*), shear stress (τ_s), pressure drop ($\varDelta P$), and *power*, which in turn, determine the dispersion efficiency of the aerosol formulation.

Among these parameters, *Re* of the device is the ratio of inertial forces to the viscous forces. It is often used for prediction of turbulence (e.g. Re>4000 for fully developed airflow in circular pipe). The value of *Re* to characterize a specific DPI device at defined airflow rate is dependent upon geometry, time scales and initial disturbances[9]. At high *Re*, the random motions of turbulent flow can be treated statistically for the characterization of the turbulent properties, and statistical fields (continuum fluid properties) vary smoothly in position and time.

Shear stress is caused by one sheet of fluid sliding over another. Apparently, it varies within the cross section of a pipe or DPI device and depends on the flow geometry and *Re*. The total shear stress in a pipe is the sum of the viscous stress and the Reynolds stress[10]. The viscous shear stress (τ_s, N/m^2) dominates the wall, causing a velocity gradient. The characterization of turbulent τ_s may be expressed by the energy cascade and Kolmogorov theory. Briefly, the larger scales (eddies) transfer kinetic energy to successively smaller scales until reaching the smallest dissipative scale (Kolmogorov scale), and the energy is dissipated by viscous action into heat. The energy dissipation rate (ε, J/(kg·s) is determined by the transfer of energy from the largest eddies. Based on the conservation of energy, ε can be approximated by relating the root-mean square velocity fluctuation of the nozzle velocity $<u>$ and the nozzle diameter D as[11]:

$$\varepsilon \cong \frac{2\left\langle u\right\rangle^3}{D} \approx \frac{2(0.2u)^3}{D} \tag{1}$$

Relating Kolmogorov scales and dynamic viscosity at high *Re*, the viscous shear stress (τ_s) arising from the turbulent energy transfer can be obtained as[11]:

$$\tau_s = \mu\left(\frac{\varepsilon}{\nu}\right)^{1/2} \tag{2}$$

where μ and ν are the dynamic and kinematic viscosity of the air (μ = 2 × 10^{-5} kg/(m·s) and ν = 1.5 × 10^{-5} m^2/s), respectively.

The kinetic energy dissipation can also cause $\varDelta P$ in a pipe flow or DPI devices. The $\varDelta P$ measured using manometer up- and downstream of a DPI device yields a combined value of both viscous and inviscid contribution[12], but either contribution can also be measured separately[13]. A flow independent parameter, specific resistance (R_D) of the DPI device can be obtained by relating $\varDelta P$ measured and volumetric flow rate Q[12]. The R_D is an intrinsic value that is dependent on the DPI internal geometry and dimension. DPI devices with higher R_D will result in lower volumetric airflow rate due to the capability of patients' maneuver. So optimum R_D exists for the best performance of a specific DPI. The *power* is the rate of work done or inspiratory effort during inhalation, so its value is related to the patient condition and inhalation capability[14].

The airflow parameters (*Re*, τ_s, $\varDelta P$, and *power*) mentioned above are positively correlated in general, and they have close relationship with particle detachment and dispersion. Using conventional or computational fluid dynamics (CFD) technique, the airflow profiles of some DPI devices or different kinds of pneumatic tubes were characterized and correlated with particle aerosolization performance previously[2, 15-17)].

3. Particle Entrainment

Principal forces leading to particle resuspension and entrainment are primarily believed to be turbulence, shear stress, collision, centrifugal, and relative motion[9)]. Two theoretical models, force balance and energy accumulation were developed for particle resuspension in turbulent flows[18)].

When the turbulent airflow entrains through a pipe or DPI device, it exerts aerodynamic forces or moments on the static dry powder to overcome the interparticulate or surface forces. Once fluid forces reach a critical value to balance adhesive forces, particle detachment occurs. For example, the critical diameter for the separation of two identical spheres can be estimated by equating the viscous shear force to the adhesive van der Waals force[9)]. Somehow the aerodynamic lift forces could be smaller than adhesion forces by several orders of magnitude because of rolling and sliding[19-21)]. Once resuspended, the particles move/rotate along the downstream airflow or collide with other particles or walls by momentum transfer. The mechanism of turbulent “burst” within the viscous sublayer has been used to explain particle detachment, but its contribution is controversial[21, 22)].

From another perspective, the flow transfers the turbulent energy into the powder bed. Particles can be resuspended when sufficient energy is accumulated to overcome the adhesion potential resulting in entrainment[23)]. There are several advantages in using the energy accumulation model. It accounts for the resuspension below the critical flow velocity. It also takes into account of the time scale and explains the time dependence of particle resuspension that was observed experimentally. Furthermore, it implies that particle resuspension is analogous to the desorption process that occurs on a molecular level[24)].

4. Heterogeneous Microparticle Interactions

The aerosolization of a powder from DPI is a heterogeneous process with respect to both formulation and airflow condition.

Pharmaceutical powders are inherently heterogeneous, which can be classified in terms of geometric and energetic perspectives. The former includes particle size, size distribution, morphology, surface asperities, meso-/micropores, and particle deformation, and the latter, the energy density distribution caused by surface amorphous content, polymorphic state, and surface impurities[5)]. The heterogeneity feature is also a characteristic of mutual interaction between particles rather than an independent particle.

Solid particles cannot follow fluid motion rigorously due to inertia. Non-spherical particles, surface roughness, particle size distribution, particle concentration are a few factors that could perturb the homogeneity of the turbulence field.

Particle motion associates with a turbulent flow field that has a statistical origin. The heterogeneity described in microparticle dispersion is analogous to that in surface adsorption, which averages local thermodynamic quantities and treats them statistically. In previous studies, standardized entrainment tubes (SETs) were used to comprehensively study the aerosolization performance of carrier-based formulations[3, 4, 6)]. Based on the experiments and fundamental data interpretation, the forces acting at the particle interfaces appear to be analogous to those at the molecular level, and models of molecular surface occupancy, described by an adsorption expression, can be adapted to fit microparticle dissociation, from which a powder aerosol deaggregation equation (PADE) was developed[5)]. Briefly, PADE is a method that directly correlates fine particle fraction (*FPF*) with τ_s using an algebraically equivalent expression to that of surface adsorption. *FPF* is the proportion with respect to the nominal dose (here is the total dose) in a size range considered sufficiently small to enter the lungs. Eqs. 3 and 4 are PADE Langmuir-type nonlinear and linear regression equations, respectively[5)].

$$FPF = \frac{FPF_{\max} k_d \tau_s}{1 + k_d \tau_s} \tag{3}$$

$$\frac{\tau_s}{FPF} = \frac{\tau_s}{FPF_{\max}} + \frac{1}{k_d (FPF_{\max})} \tag{4}$$

where FPF_{max} is the characteristic *FPF* at τ_s approaching invariant region, and further increase of *FPF* would require comminution of the drug or carrier particles, k_d is defined as the deaggregation constant. The advantages of PADE are that the effect of different formulation performance and the heterogeneity can be discussed in terms of theoretical or empirical surface adsorption models and measured experimentally to describe microparticle surface dissociation in a τ_s range, and it is suitable for quick and accurate prediction of the dynamic deaggregation mechanisms for pharmaceutical aerosol formulations having surface energy heterogeneity and lateral interaction forces.

5. SETs vs. DPI Devices

The turbulent airflow profiles within the DPI devices may vary greatly because of short and tortuous internal channels in the device design. Complex designs including internal mesh or grid, compact sizes, formulation enclosure such as capsules, are aimed at enhancing dispersion efficiency and reproducibility, but may also produce complex flow fields. The presence of grid in DPI devices may cause increase or decrease in grid turbulence depending on a variety of factors such as the turbulent flow field, grid type and spacing[25, 26]. The compact sizes of DPI devices are often insufficient for turbulent flow to fully develop. The viscous effects of the airflow are not uniformly spread throughout due to insufficiently developed flow. The use of capsules may also influence the flow field and contribute to additional particle fluidization and deaggregation mechanisms[9, 17]. Consequently, the study of the turbulent flow field and the particle entrainment using DPI device directly is difficult. In addition, the particle entrainment and deaggregation in different DPI devices can vary greatly, due to the different device resistance and dispersion mechanisms. It was suggested that performance comparison between difference DPIs be carried out at a given pressure drop, instead of a fixed airflow rate[27].

Historically, fully developed pipe flow, due to its geometric simplicity, has been extensively studied to increase the experimental and theoretical understanding of wall-bounded turbulence interactions. Likewise, a series of standardized entrainment tubes (SETs) was developed as a standardized method for the DPI formulation evaluation[2, 5]. These SETs have fully developed airflow profile. Their airflow parameters (Re, τ_s, ΔP, and *power*) encompass those of DPI devices[2]. This allows correlation between airflow parameters and formulation performance. Using SETs also eliminates the confounding factors caused by DPI devices and allows focus on formulation effect.

If microparticles are contained within the viscous sublayer of an SET or DPI device, they experience a mean shear flow that produces a combination of translational and rotational motions such as lifting, rolling and sliding contribute to initial particle detachment. Assuming the particle entrainment and deaggregation in an SET or DPI device are governed by these aerodynamic forces within the Kolmogorov scale of turbulence and, τ_s is expressed as Eqs. 1 and 2, the aerosolization performance of both SET and DPI device should be comparable.

6. Experimental

6.1. Material and methods

6.1.1 Formulations

Two micronized pulmonary drugs, disodium cromoglycate (DSCG, Sigma-Aldrich, Inc., St. Louis, MO) and albuterol sulfate (AS, Pfizer Global R&D, Kent, UK) were used. Two carriers, α-lactose monohydrate (Lac) (DMV Fonterra Excipients, Goch, Germany) and D-Mannitol (Mann) (Sigma-Aldrich, Inc., St. Louis, MO) were used. The preparation of carrier-based formulations with drug concentration at 2 %w/w was described previously[3]. They are interactive physical mixtures of DSCG–Lac and AS–Mann. The physico-chemical characterization including morphology (scanning electron microscopy), thermal properties (differential scanning calorimetry), crystallinity (X-ray powder diffraction), and particle size distribution (laser diffraction) of both formulations were reported previously[3, 6].

6.1.2 Devices

A series of seven SETs with their airflow parameters encompassing commercial DPIs were applied. Two commercial DPI devices, Rotahaler® (Glaxo Smith Kline, RTP, NC) and Aerolizer® (Novartis, NJ) were compared with SETs. τ_s values within all the SETs and DPI devices were calculated by applying Kolmogorov turbulent theory (Eqs. 1 and 2) and reported previously[2, 5]. Two types of size 3 hard capsules: the gelatin (Capsugel®, Greenwood, SC) and HPMC capsules (Vcaps® Plus, Greenwood, SC) were used in the DPI devices.

6.1.3 In vitro aerosol performance characterization

The aerosolization performance efficiency represented by *FPF* and emitted dose (*ED*) was generated using a twin-stage liquid impinger (TSLI) at fixed airflow rate of 60 L/min. The TSLI setup has an aerodynamic cutoff diameter of 6.4 μm. *In vitro* aerosolization was performed in triplicate under ambient conditions. Prior to aerosolization, 25 mg of formulation was transferred onto the SET loading area located at the proximal end of the inlet section A solenoid switch was placed between the TSLI and the aspirator to achieve instant actuation for SET experiment. Each actuation was lasted for 10 sec. *FPF* values were correlated with τ_s values using PADE non-linear and linear regression models described in Eqs. 3 and 4. The PADE parameters (FPF_{max} and k_d) and regression statistics were analyzed using SigmaPlot software. (SigmaPlot 2004 Ver 9.01 for Windows, Systat Software, Inc., CA).

Two single dose DPIs (Rotahaler® and Aerolizer®) with either gelatin or HPMC capsules containing 25 mg of formulations were used. The actuation using DPI devices was achieved by twisting (Rotahaler®) or piercing (Aerolizer®) of the individual capsule at steady airflow rate of 60 L/min. The predicted *FPF* values (FPF_{pred}) by interpolation from PADE regression curves were then compared with the *FPF* values obtained experimentally using DPIs. (Paired *t*-test, InStat Ver 3.05 for Windows NT, GraphPad Software, Inc., CA) The *ED* values generated from SETs were compared with those of DPIs.

6.2. Results and discussion

6.2.1 Formulation characterization

Pulmonary drugs (DSCG, AS), carriers (ML, Mann), and dry powder formulations (DSCG-Lac, AS-Mann) were prepared and characterized previously[3,6]. Different drugs and carriers were chosen to represent diversity of the formulation components. Briefly, both DSCG and AS were jet-milled and their particle volume size distribution by laser diffraction was: DSCG (D_{50} = 3.68 μm, *span* = 0.32) and AS (D_{50} = 3.59 μm, *span* = 0.26), respectively. The particle volume size distribution of carriers was: ML (D_{50} = 52.0 μm, *span* ~ 3.10) and Mann (D_{50} = 52.9 μm, *span* = 1.19), respectively. Other physico-chemical characterizations including morphology, thermal properties, and crystallinity were reported previously and will not reiterate[3, 6].

6.2.2 Device characterization

Seven SETs were selected and their τ_s values at airflow rate of 60 L/min were 13.143, 8.742, 4.342, 2.775, 2.199, 1.412, and 0.624 N/m^2, respectively[5].

Rotahaler® and Aerolizer® were chosen because they both are passive DPI devices with relatively simple internal geometry. The airflow conditions and the powder aerosolization within both devices have been well-explored experimentally and theoretically[2, 26, 28-30]. Both Rotahaler® and Aerolizer® products are metered by unit-dose capsule that contains carrier-based formulation. They both have a grid structure perpendicular to the flow vector. Rotahaler® has low specific resistance, R_D = 0.036 cm $H_2O^{0.5}$/(L/min)[2, 12]. Aerolizer has relatively higher specific resistance, R_D = 0.072 cm $H_2O^{0.5}$/(L/min)[31]. The τ_s value of Rotahaler® was measured previously, τ_s = 2.026 N/m^2 [2]. The turbulent energy dissipation rate of Aerolizer® was calculated based on the integral scale strain rate and the rate of turbulence kinetic energy in a computation fluid dynamic study elsewhere[29]. The τ_s value of Aerolizer® was then calculated to be, τ_s = 2.588 N/m^2. (Eq. 2).

6.2.3 Aerosol performance characterization

Using seven SETs, the correlation of *FPF* with SET τ_s by PADE nonlinear (Eq. 3) and linear regression (Eq. 4) analyses are shown in **Fig. 1**A-D, respectively. PADE nonlinear regression statistics of DSCG-Lac yielded FPF_{max} = 46.51%, k_d = 1.19 m^2/N, R^2 = 0.9651, adj R^2 = 0.9593; AS-Mann yielded FPF_{max} = 10.95%, k_d = 0.90 m^2/N, R^2 = 0.9197, adj R^2 = 0.9064 [5]. The PADE linear regression of DSCG-Lac and AS-Mann resulted in R^2 = 0.9909 and 0.9808, respectively. Excellent goodness of fit was observed for both formulation performance evaluations. In previous papers, we stated that FPF_{max} should be an important parameter for evaluating the aerosol formulation[3]. The interpreted data from the slope of linear regression showed the rank order of the formulation performance efficency[3].

From another perspective, the PADE analyses led to the performance evaluation and prediction across the entire τ_s range. The optimum τ_s required for efficient and reproducible aerosolization is close to FPF_{max}. This sets an appropriate criterion for the construction or selection of proper DPI devices for a particular formulation. Assuming *FPF* values reach a plateau when they are equal or greater than 85% of the values of FPF_{max}, the critical τ_s values of DPI devices can be interpolated from the fitted regression curve: τ_s = 4.70 N/m^2 (for DSCG-Lac) and τ_s = 6.37 N/m^2 (for AS-Mann), respectively. At airflow rate 60 L/min, Aerolizer® and Rotahaler® have τ_s = 2.588 and 2.026 N/m^2, respectively. According to the PADE analyses, both devices failed to reach critical τ_s for efficient and reproducible aerosolization of the selected formulations. The FPF_{pred} obtained by interpolation of PADE non-linear curve fitting are shown in **Table 1**. For DSCG-Lac formulation, the FPF_{pred} values were 32.9% (Rotahaler®) and 35.2% (Aerolizer®), respectively. For AS-Mann formulation, the FPF_{pred} values were 7.1% (Rotahaler®) and 7.6% (Aerolizer®), respectively.

6.2.4 Comparative studies

The experimental results of DPI aerosolization per-

Table 1 Predictive Evaluation of Aerosolization Efficiency of DSCG-Lac and AS-Mann Formulations

Formulation	DPI-Capsule	τ_s (N/m^2)	FPF_{pred}(%)*	FPF_{exp}(%)**
DSCG-Lac	Rotahaler®-Gelatin	2.026	32.9	29.6 ± 2.7
	Rotahaler®-HPMC			26.9 ± 6.0
	Aerolizer®-Gelatin	2.588	35.2	37.5 ± 3.7
	Aerolizer®-HPMC			35.2 ± 3.4
AS-Mann	Rotahaler®-Gelatin	2.026	7.1	7.5 ± 2.7
	Rotahaler®-HPMC			9.6 ± 3.0
	Aerolizer®-Gelatin	2.588	7.6	10.8 ± 1.6
	Aerolizer®-HPMC			8.0 ± 1.5

* FPF_{pred}: predicted *FPF* values, obtained by interpolation of PADE non-linear curve fitting.

** FPF_{exp}: FPF obtained experimentally. Mean ± SD, $n = 3$.

formance are show in **Table 1**. When the Aerolizer® was used, DSCG-Lac formulation gave mean *FPF* values of 37.5% (Gelatin) and 35.2% (HPMC), and AS-Mann formulation gave mean *FPF* values of 10.8% (Gelatin) and 8.0% (HPMC), respectively. When Rotahaler® was used, DSCG-Lac formulation gave mean *FPF* values of 29.6% (Gelatin) and 26.9% (HPMC), and AS-Mann formulation gave mean *FPF* values of 7.5% (Gelatin) and 9.6% (HPMC), respectively. *FPF* values generated by Aerolizer® were superior to those by Rotahaler® indicating superior dispersion efficiency of the former. Overall, the results obtained experimentally using DPI devices were very close to the interpolated *FPF* obtained from PADE non-linear fitted curve shown above. The FPF_{pred} values were then compared with mean *FPF* values obtained experimentally using paired *t*-test. The result showed the difference were insignificant ($p > 0.1$) This indicated that using the SETs for aerosol performance studies, the PADE method provided a robust method for the evaluation of aerosol performance of commercial DPI devices, in spite of the differences between SETs and DPI devices mentioned above. No significant difference of *FPF* values was observed when either gelatin or HPMC capsules was used.

It is interesting to observe that *FPF* values generated from DPI devices experimentally can be predicted from the SET data, considering the vast differences in geometry, dimension, grid, capsule, and the corresponding turbulent airflow field and dispersion mechanisms between them. Similar comparable result was demonstrated earlier using Ventolin® formulation and different commercial DPIs[2)]. Particle entrainment and deaggregation mechanisms in SETs are mainly shear force, other mechanisms of dispersion such as collision and momentum transfer may contribute greatly using DPI devices. However, it is reasonable to suggest that particles which can be removed by shear forces may more readily be removed under the influence of collision and momentum transfer, from which it can be inferred that the *FPF* interpolated from the SET data can be used for the performance evaluation of DPI products.

The *FPF* represents the degree of particle deaggregation, whereas the *ED* represents the degree of particle entrainment. The values of *ED* were influenced by both formulation and device. (**Fig. 1** E-1F) For DSCG-Lac formulation, *ED* values using SETs ranged from 64.2% (at $\tau_s = 2.775$ N/m^2, SET-B1) to 86.0% (at $\tau_s = 0.624$ N/m^2, SET-D). This could be explained by the design of expansion region in SETs. The lower shear SET-C, C1 and D had gradual enlargement to facilitate gradual energy loss and central loading platform to maximize airflow velocity, whereas higher shear SET-A, A1, B, B1 did not include such a diffuser for energy recovery. This resulted in relatively higher *ED* in lower shear SETs and lower *ED* in higher shear. For SETs with sudden enlargement, the lower airflow velocity corresponded to the lower *ED* values, indicating that the fluid force could not sustain particle fluidization due to energy loss. For AS-Mann formulation, *ED* values using SETs were similar and ranged from 90.7% (at $\tau_s = 13.143$ N/m^2, SET-A) to 94.8% (at $\tau_s = 2.199$ N/m^2, SET-C). This is likely because of the formulation effect. Carrier ML was milled lactose monohydrate particles with much larger span than that of Mann, which indicated that AS-Mann was much easier to fluidize than DSCG-Lac.

In general, smaller *ED* values were observed using DPI devices than SETs at similar τ_s. Aerolizer® gave higher *ED* values than Rotahaler® for DSCG-Lac formulation. No significant difference of *ED* values was observed when either type of capsules was used.

The differences of dispersion (*FPF*, *ED* values) between SETs and DPIs may be explained from several perspectives including the presence of grid in DPI devices, the compact sizes and complex geometry of DPI devices, and the use of capsule.

The grid may cause increase or decrease in grid turbulence depending on a variety of factors such as the turbulent flow field, grid type and spacing[25, 26)]. Grid may also enhance impaction and effects of viscosity in turbulent flow[25)]. These are the features for the particle deaggregation not presented in SETs. The effect of grid on particle dispersion is sometimes controversial. In one study, *FPF* values generated from performance with grid were similar to those without; indicating mechanical impaction had little effect on particle deaggregation[32)]. While in another

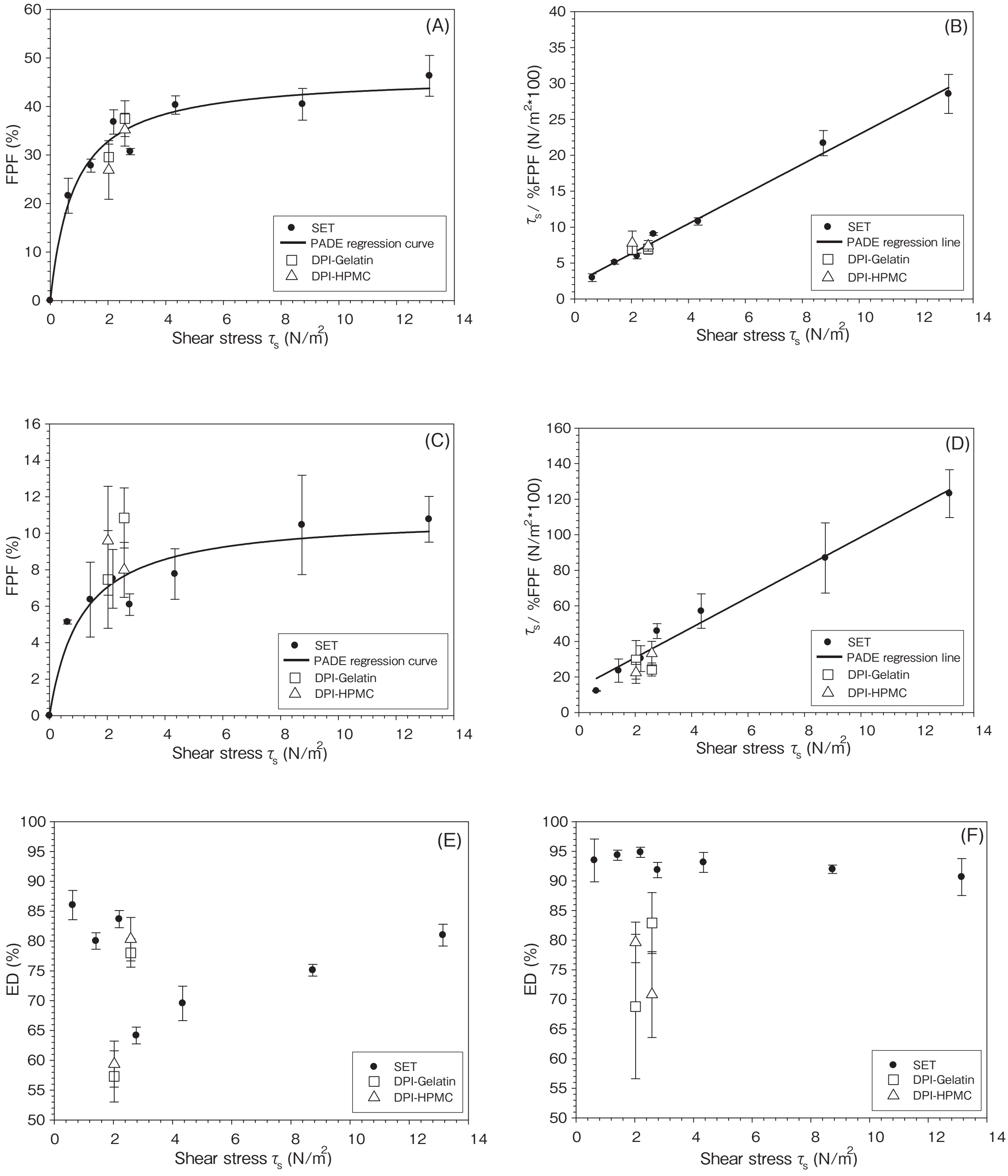

Fig. 1 Aerosolization performance evaluation using PADE Langmuir equivalent analyses (Eqs. 3 and 4). (A) and (B): PADE nonlinear and linear regression analysis (*FPF* – τ_s correlation) for the performance of DSCG-Lac formulation, respectively; (C) and (D): PADE nonlinear and linear regression analysis for the performance of AS-Mann formulation, respectively; (E): *ED* of DSCG-Lac formulation; (F): *ED* of AS-Mann formulation. (*FPF* and *ED*: mean ± SD, n = 3).

study using Aerolizer®, the structure of grid was found to play a vital role in converting high-velocity tangential flow into low-velocity axial flow, thus increasing *FPF* [26].

The turbulent airflow was unlikely to fully develop because of the compact sizes of DPI devices, so the viscous effects of the airflow were not uniformly spread throughout. This led to the fluctuation and higher standard deviation of the *FPF* and *ED* values obtained than typical dispersion data obtained using SETs.

The use of capsules in the DPI devices offered another reason for the difference in *ED* values. The *ED* values obtained using SETs were generally higher than those obtained using DPI devices. The enclosure of powder formulations in the capsules may hinder the powder entrainment and lead to lower *ED*. The mechanisms of entrainment and deaggregation in the Rotahaler® are different from those in the Aerolizer®. The former requires mechanical break of capsules and expose the powder for dispersion, whereas the latter requires capillary fluidization and shear force for powder dispersion[9, 29]. The capillary fluidization may offer additional capsule dispersion, which may result in higher *ED* and *FPF* using Aerolizer®. The use of gelatin or HPMC capsules did not lead to significant difference in *ED* and *FPF*. ($p > 0.1$)

7. Conclusion

This paper describes the important aspects including turbulent airflow and microparticle interactions that are relevant to the DPI performance. A unique PADE method that allows aerosol performance prediction over defined τ_s range was reviewed and utilized in the experimental study.

The aerosol performance study tested the hypothesis that using SETs as device independent screening tools, the aerosol performance of DPIs with defined airflow parameters can be predicted by interpolation from the PADE fitted curves. In addition, the PADE method suggests the critical τ_s required for efficient and reproducible aerosol performance of a formulation. This could be very helpful in the selection of the correct DPI device for the specific formulation to achieve optimum aerosolization.

Undoubtedly, in the final product, different mechanisms of DPI particle separation would be employed. Impaction and momentum transfer mechanisms, for which many devices were designed, have been the focus of considerable research. Nevertheless, it is reasonable to suggest that particles which can be stripped by shear force may more readily be removed under the influence of volume or mass related contributions such as particle-particle and particle-wall collision. The SETs and the PADE method are excellent tools for the formulation optimization in the early stage of DPI development, and the selection of proper DPI device and formulation combination for the whole DPI product development.

A method developed to compare performance of formulations in a manner generally relevant to passive dry powder inhalers should conform to the follow postulates. The method should: 1) Cover the range of airflow performance characteristics for known inhalers (of clinical significance); 2) Discriminate performance differences between a wide range of formulations and; 3) Demonstrate with known formulations adequate prediction of their performance in DPIs.

It should be noted, however, current study covered only a narrow range of τ_s by two DPI devices, further evaluation of DPI devices at different τ_s and the DPIs with principal dispersion mechanisms other than shear flow are necessary to strengthen the hypothesis.

References

1) Clark, A. R. (1995): Medical aerosol inhalers: past, present, and future, Aerosol Sci. Technol., Vol.22, pp.374-391.

2) Louey, M. D., VanOort, M., and Hickey, A. J. (2006): Standardized entrainment tubes for the evaluation of pharmaceutical dry powder dispersion, J. Aerosol Sci., Vol.37, pp.1520-1533.

3) Xu, Z., Mansour, H. M., Mulder, T., McLean, R., Langridge, J., and Hickey, A. J. (2010): Dry powder aerosols generated by standardized entrainment tubes from drug blends with lactose monohydrate: 1. Albuterol sulfate and disodium cromoglycate, J. Pharm. Sci., Vol.99, pp.3398-3414.

4) Xu, Z., Mansour, H. M., Mulder, T., McLean, R., Langridge, J., and Hickey, A. J. (2010): Dry powder aerosols generated by standardized entrainment tubes from drug blends with lactose monohydrate: 2. Ipratropium bromide monohydrate and fluticasone propionate, J. Pharm. Sci., Vol.99, pp.3415-3429.

5) Xu, Z., Mansour, H. M., Mulder, T., McLean, R., Langridge, J., and Hickey, A. J. (2010): Heterogeneous particle deaggregation and its implication for therapeutic aerosol performance, J. Pharm. Sci., Vol.99, pp.3442-3461.

6) Mansour, H. M., Xu, Z., and Hickey, A. J. (2010): Dry powder aerosols generated by standardized entrainment tubes from alternative sugar blends: 3. Trehalose dihydrate and D-mannitol carriers, J. Pharm. Sci., Vol.99, pp.3430-3441.

7) Xu, Z., Mansour, H. M., and Hickey, A. J. (2011): Particle interactions in dry powder inhaler unit processes: a review, J. Adhesion Sci. Technol., Vol.25, pp.451-482.

8) Hickey, A. J. and Ganderton, D. (2010), "Fluid flow", Pharmaceutical Process Engineering, 2nd edition, Informa Healthcare USA, pp.4-30.

9) Dunbar, C. A., Hickey, A. J., and Holzner, P. (1998): Dispersion and characterization of pharmaceutical dry

powder aerosols. KONA Powder and Particle Journal, No.16, pp.7-45.

10) Pope, S. B. (2000): “Wall flows” , Turbulent Flows, Cambridge University Press, Cambridge, UK, p.264-332.

11) Shekunov, B. Y., Feeley, J. C., Chow, A. H., Tong, H. H., and York, P. (2003) Aerosolization behavior of micronized and supercritically-processed powdes, J. Aerosol Sci., Vol.34, pp.553-568.

12) Clark, A. R. and Hollingsworth, A. M. (1993) The relationship between powder inhaler resistance and peak inspiratory conditions in healthy volunteers - implications for in vitro testig, J Aerosol Med., Vol.6, pp.99-110.

13) Mendes, P. J., Pinto, J. F., and Sousa, J. M. M. (2007) A non-dimensional functional relationship for the fine particle fraction produced by dry powder inhales, J. Aerosol Sci., Vol.38, pp.612-624.

14) de Boer, A. H., Winter, H. M. I., and Lerk, C. F. (1996) Inhalation characteristics and their effects on in vitro drug delivery from dry powder inhalers part 1. inhalation characteristics, work of breathing and volunteers' preference in dependence of the inhaler resistane, Int. J. Pharm., Vol.130, pp.231-244.

15) Wong, W., Fletcher, D. F., Traini, D., Chan, H. K., Crapper, J., and Young, P. M. (2010) Particle aerosolisation and break-up in dry powder inhalers 1: evaluation and modelling of venturi effects for agglomerated systes, Pharm. Res., Vol.27, pp.1367-1376.

16) Calvert, G., Ghadiri, M., and Tweedie, R. (2009) Aerodynamic dispersion of cohesive powders: a review of understanding and technoloy, Adv. Powder Tech., Vol.20, pp.4-16.

17) Coates, M. S., Tang, P., Chan, H. K., Fletcher, D. F., and Raper, J. A. (2009): “Characterization of pharmaceutical aerosols and dry powder inhalers for pulmonary drug delivery”, Particulate Systems in Nano- and Biotechnologies”, eds: Sigmund, W., El-Shall, H., Shah, D.O., Moudgil, B.M., CRC Press Taylor & Francis Group, p.193-222.

18) Ziskind, G., Fichman, M., and Gutfinger, C. (1995) Resuspension of particulates from surfaces to turbulent flows - review and analyss, J. Aerosol Sci., Vol.26, pp.613-644.

19) Ziskind, G., Fichman, M., and Gutfinger, C. (1997) Adhesion moment model for estimating particle detachment from a surfae, J. Aerosol Sci., Vol.28, pp.623-634.

20) Wang, H. C. (1990) Effects of inception motion on particle detachment from surfacs, Aerosol Sci. Tech., Vol.13, pp.386-393.

21) Ibrahim, A. H., Dunn, P. F., and Brach, R. M. (2003) Microparticle detachment from surfaces exposed to turbulent air flow: controlled experiments and modelig, J. Aerosol Sci., Vol.34, pp.765-782.

22) Gradon, L. (2009) Resuspension of particles from surfaces: technological, environmental and pharmaceutical aspecs, Adv. Powder Tech., Vol.20, pp.17-28.

23) Reeks, M. W., Reed, J., and Hall, D. (1998) On the resuspension of gas-borne particles in recirculating turbulent flow, J. Phys. D: Appl. Phys., Vol.21, pp.574-589.

24) Wen, H. Y. and Kasper, G. (1989) On the kinetics of particle reentrainment from surfacs, J. Aerosol Sci., Vol.20, pp.483-498.

25) Pope, S. B. (2000): “Free shear flows” , Turbulent Flows, Cambridge University Press, Cambridge, UK, p.158-161.

26) Coates, M. S., Fletcher, D. F., Chan, H. K., and Raper, J. A. (2004) Effect of design on the performance of a dry powder inhaler using computational fluid dynamics. Part 1: Grid structure and mouthpiece lengh, J. Pharm. Sci., Vol.93, pp.2863-2876.

27) Richards, R. and Saunders, M. (1993): Need for a comparative performance standard for dry powder inhalers, Thorax., Vol.48, pp.1186-1187.

28) Chew, N. Y., Bagster, D. F., and Chan, H. K. (2000) Effect of particle size, air flow and inhaler device on the aerosolisation of disodium cromoglycate powdes, Int. J. Pharm., Vol.206, pp.75-83.

29) Coates, M. S., Fletcher, D. F., Chan, H. K., and Raper, J. A. (2005) The role of capsule on the performance of a dry powder inhaler using computational and experimental analyss, Pharm. Res., Vol.22, pp.923-932.

30) Coates, M. S., Chan, H. K., Fletcher, D. F., and Chiou, H. (2007) Influence of mouthpiece geometry on the aerosol delivery performance of a dry powder inhalr, Pharm. Res., Vol.24, pp.1450-1456.

31) Weuthen, T., Roeder, S., Brand, P., Mullinger, B., and Scheuch, G. (2002) In vitro testing of two formoterol dry powder inhalers at different flow rats, J. Aerosol Med., Vol.15, pp.297-303.

32) Voss, A. and Finlay, W. H. (2002) Deagglomeration of dry powder pharmaceutical aerosols, Int. J. Pharm., Vol.248, pp.39-50.

Author's short biography

Zhen Xu

Dr. Zhen Xu obtained his Ph.D. in 2010 in the Eshelman School of Pharmacy, University of North Carolina. His Ph.D. research in Dr. Anthony Hickey's lab focused on dry powder aerosol formulations for the treatment of asthma, with an effort on elucidating the heterogeneous microparticle interactions in the solid-state, and achieving cost-effective formulation screening/prediction. He is currently a postdoctoral fellow in the School of Pharmacy, University of Maryland. His current research focuses on the aerosol device technologies, using valved holding chamber and facemask systems for pediatric pulmonary delivery. He previously received his M.S. degree in Chemistry at Michigan State University.

Anthony J. Hickey

Dr. Hickey is Distinguished RTI Fellow and Program Leader in Inhaled Therapeutics in the Center for Aerosol and Nanomaterials Engineering at the RTI International, Emeritus Professor of Molecular Pharmaceutics of the Eshelman School of Pharmacy, and Adjunct Professor Biomedical Engineering of the School of Medicine, at the University of North Carolina at Chapel Hill. He is a Fellow of the UK Society of Biology, the American Association of Pharmaceutical Scientists, and the American Association for the Advancement of Science. He has edited texts on pharmaceutical inhalation aerosols and co-authored others on Pharmaceutical Process Engineering, Particulate Science and Pharmaco-complexity.

Feasibility of Relationships between Tablet Physical Quality Parameters and Mechanical Properties of Dry Powder Formulation[†]

Anuranjan Pandeya[1*] **and Virendra M. Puri**[2]
[1] *Department of Food Science, The Pennsylvania State University*
[2] *Department of Agricultural and Biological Engineering, The Pennsylvania State University*

Abstract

Compaction is a key unit operation in many particulate industries. Accordingly, this study addresses a research question of considerable importance concerning compact (or tablet) formation, i.e., the feasibility of using mechanical properties of powder formulations in low to medium pressure regime (<10 MPa) as predictors of tablet (i.e., compact) quality parameters. For the feasibility study, mechanical properties, i.e., elastic and elastoplastic, of dry powder formulations at three binder contents were determined using a flexible boundary cubical triaxial tester in low to medium pressure regime. For the same formulations, tablets formed at two pressing pressures (70 and 90 MPa) were tested for four physical quality parameters, i.e., diametral strength, axial penetration strength, indentation hardness, and friability. Some of the key findings were: bulk modulus increased with pressure and binder; shear modulus increased with confining pressure; tablet hardness increased with binder content upto a point and thereafter decreased or remained constant. All the powders' properties related with tablet qualities, i.e., had $R^2 > 0.80$; i.e., demonstrating the feasibility of using powder properties as initial predictors of tablet quality for formulations tested. In particular, the spring-back index, compression index, and bulk modulus were found to be most correlated with tablets' diametral strength, axial penetration strength, indentation hardness, and friability. An elastic energy based hypothesis was proposed to provide a fundamental basis for mechanical properties of powder formulations vs. tablet quality relationships. The positive outcome of this feasibility study suggests that the approach could be used for other similar powder formulations.

Keywords: cubical triaxial tester, mechanical properties, compaction, elastic energy, friability, diametral strength

1. Introduction

Compaction is an important unit operation in many particulate industries, such as, chemical, ceramics, pharmaceuticals, and powdered metal. Compacts or tablets are formed using powder ingredients such as filler, binder(s), lubricant(s), and disintegrant (if needed). These ingredients are blended in desired proportion and compacted. Herein we have used pharmaceutical powder formulations, which include also an active pharmaceutical ingredient (API). This study addresses a research question of considerable importance, i.e., the feasibility of using dry powder formulation properties in low to medium pressure regime (<10 MPa) as predictors of tablet quality parameters. Toward that end, fundamental mechanical properties of powder formulations were determined using a flexible membrane cubical triaxial tester (CTT). Some of these test results have been presented in Pandeya and Puri (2011) and comprehensive results are given in Pandeya (2009). In addition, quality parameters of the tablets formed from the same powder formulations were determined. Various stud-

---

[†] Accepted: May 4, 2012
[1,2] University Park, PA 16802, USA
[*] Corresponding author:
E-mail: Anuranjan.Pandeya@gmail.com
TEL: +1-814-863-9716 FAX: +1-814-863-6132

ⓒ 2013 Hosokawa Powder Technology Foundation

ies have been performed on determining the quality parameters of tablets (Tabor, 2000; Tye et al., 2005; Wu et al., 2005). However, no study could be found that has related the dry powders' fundamental mechanical properties to tablet quality. In accord with the research question, the objective of the study was to determine the feasibility of prediction of the tablet quality parameters based on the mechanical properties of the dry powder formulation at three binder contents in the low to medium pressure regime.

2. Material

The formulation used for the research was composed of Avicel (FMC Biopolymers, Philadelphia, PA), Methocel (Colorcon, PA), Magnesium stearate (Sigma Aldrich, St. Louis MO), Ac-Di-Sol (FMC Biopolymers, Philadelphia, PA), and Acetaminophen (Sigma Aldrich, St. Louis MO) as filler, binder, lubricant, disintegrant and active pharmaceutical ingredient, respectively. The properties of these ingredients are given in **Table 1** Three different levels of methocel (binder): 0 (none), 5, and 10%, were used in powder formulation. The proportion of other four ingredients were maintained at the same level, i.e., Avicel: Acetaminophen: Ac-Di-Sol: Magnesium stearate :0.90:0.05:0.03:0.02 (**Table 2**). Detailed description of all the ingredients used and selection of binder levels are presented in Pandeya (2005) and Pandeya and Puri (2008 and 2011). The drug loading in pharmaceutical formulations varies over the entire spectrum of values (i.e., from 0.1% to 100%) depending upon the type of drug and its application. In our context, the objective was to determine the mechanical properties of a pharmaceutical formulation consisting of major ingredients that are commonly used such as MCC, Methocel, Acetaminophen, Ac-di-sol, and Magnesium stearate, i.e., the study was not targeted to develop an optimum formulation. The powder formulations' mechanical properties where investigated as possible predictors of tablet physical quality metrics.

Table 1 Properties of formulation ingredients

	Parameters		
Ingredients	Bulk density (g/cc)	Particle density* (g/cc)	Median (d50) particle size † (μm)
Avicel PH 102	0.41	1.61	78
Methocel	0.42	1.33	108
Acetaminophen	0.25	1.36	15
Ac-Di-Sol	0.46	1.66	60
Magnesium stearate	0.26	1.13	10

* Measured using Micromeretics Multivolume Helium Pycnometer 1305 (Boynton Beach, FL)

† Measured using the Malvern Instruments Mastersizer (Westborough, MA)

Table 2 Ingredients and their proportions used in pharmaceutical powder formulations

A. Methocel (Binder)	0%	5%	10%
B. Other ingredients	100%	95%	90%
B1. Avicel PH 102	90%	85.5%	81%
B2. Acetaminophen	5%	4.75%	4.5%
B3. Ac-Di-Sol	3%	2.85%	2.7%
B4. Magnesium stearate	2%	1.9%	1.8%

3. Methodology

Hydrostatic triaxial compression (HTC) and conventional triaxial compression (CTC) tests were conducted using a CTT for formulations at different binder content. Tablets at binder contents of 5 and 10% and without binder (i.e., 0%) were formed at pressures of 70 and 90 MPa. Tablets' physical quality parameters (discussed in the following sections) were determined at all three binder contents and both tabletting pressures. The ingredients were stored and tests were conducted in an environment controlled laboratory with temperature setting of 23° C ±1° C and relative humidity setting 35%±5%. Three replications of each test were conducted (Kamath and Puri, 1997; Li and Puri, 1997; Mittal and Puri, 2005).

3.1 Cubical triaxial tester

A medium pressure cubical triaxial tester (**Fig. 1**) developed by Kamath and Puri (1997) and Li and Puri (1997) and modified by Mittal and Puri (2005) was used for the experiments. This CTT is capable of applying pressure on six sides of a cubical sample (powder). The pressure is applied through flexible rubber membranes by pressurized nitrogen gas. The powder sample is contained in a cube-shaped Sample Holding Membrane (SHM) (made out of silicone rubber), which has dimensions of 50.8×50.8×50.8 mm. The SHM is placed in the cubical cavity of the CTT and pressure is applied to the six surfaces of SHM via flexible rubber membranes. Due to the application of pressure, change in the dimensions of the powder sample takes place. The change in the dimensions was recorded using linear motion potentiometers that are in constant contact with pressure application membranes, i.e., all six faces.

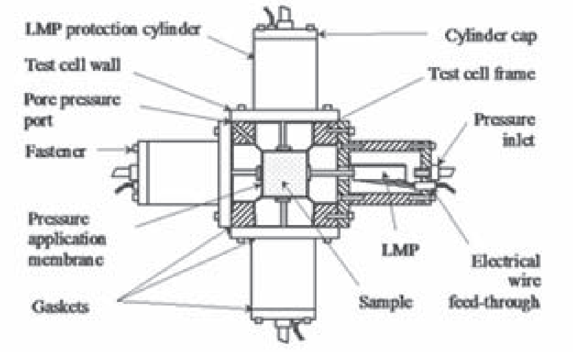

Fig. 1 Cross-sectional view of CTT (Kamath and Puri, 1997) (not to scale).

3.2 Blending

The powders were blended using manual Mini-Inversina (Bioengineering AG, Switzerland) capable of providing 360° motion to the mixture. The mixing was performed at 80 RPM for 5 minutes with a batch size of 400 g. The batch size and mixing time were based on preliminary runs to assess the quality of powder mixture (Pandeya, 2009).

3.3 Hydrostatic triaxial compression (HTC) and conventional triaxial compression (CTC) Tests

In HTC tests, the powder mixture sample was subjected to isotropic loading and the stress state was the same in all three principal directions, i.e. equal pressure is applied on each of the six faces of the cubical sample. Parameters such as bulk modulus, compression index, and spring-back index were determined using the HTC test (Li and Puri, 1997; Mittal and Puri, 2005). All tests were conducted at pressures upto 10 MPa and loading rates of 10 and 20 MPa/min. Since this is the first known feasibility study of using the fundamental mechanical properties of powder formulation as predictors of the tablet quality, two different loading rates were used, i.e., is known that the powders' mechanical behavior can be sensitive to the loading rate. In CTC tests, first the sample was confined by applying same pressure on each face of the cubical sample similar to HTC tests after that deviatoric stress was applied in the top-bottom direction (also the gravity direction). Shear modulus and failure stress were determined using the CTC tests (Li and Puri, 1997; Mittal and Puri, 2005). These tests were conducted at confining pressures of 1, 2, and 3 MPa. Three replications at 0, 5, and 10% binder content were performed at loading rates of 10 and 20 MPa/min. The tests were conducted to produce stress difference of 1 and 2 MPa, which ensured stresses below but in the vicinity of incipient failure of powder specimen. Rationale for selection of these values is discussed in detail (Pandeya, 2009; Pandeya and Puri, 2011).

3.4 Tablet formation

The tablets were formed using a die and punch assembly. A material testing system (MTS 810, Eden Prairie, MN) fitted with a load cell of 100 kN ± 0.1 kN and capable of applying load at varying speeds was used to apply the pressure on the powder through the punch. The tablets were formed at different binder contents of 0, 5, and 10% and compaction pressures of 70 and 90 MPa. Known weight of samples (300 ± 1 mg) was transferred into the die and pressure was applied.

3.5 Determination of tablet quality parameters

Diametral strength, axial compressive strength, indentation hardness, and friability tests were conducted to evaluate the tablet properties. First three tests were conducted using universal testing machine (Instron 4444, Canton, OH); whereas, the fourth (friability) was determined using a friabilator. These are summarized in the following subsections.

Diametral Strength Test: Diametral strength test, also known as tensile strength test, is a most commonly used test to assess the overall mechanical strength of the tablet. The force was applied diametrically at a cross head speed of 12.52 mm/min on the tablet and the crushing force (Fx) was measured. Slow test speed was used to minimize any time-dependent effects. The diametral strength, DS was calculated using the following equation (Tye et. al., 2005):

$DS = 2\,Fx/(\pi\,Dt)$, where D and t are diameter and thickness respectively of the tablet.

Axial Penetration Strength: Axial penetration strength was also conducted at a cross head speed of 12.52 mm/min. In the test, the tablet was compressed axially using a cylindrical probe of 3 mm diameter. The pressure at which the specimen failed was taken as penetration strength of the tablet in compression.

Indentation Hardness: Hardness may be defined as the resistance of a material to local permanent deformation (Kuentz and Leuenberger, 2000). According to Leuenberger and Rohera (1986), hardness is related primarily to the plasticity of the tablet, which is usually measured by the indentation test. They divided the hardness testing technique into two groups: 1) hardness determination by static impression method; and 2) hardness determination by dynamic method.

The first method i.e. hardness determination using static methods being the most widely used, was adopted in this feasibility study. The Brinell hardness number (BHN) is expressed as the ratio of the load to the diameter of the indentation and can be calculated by the following equation:

$$BHN = \frac{2F}{\pi D(D - \sqrt{D^2 - d^2})} = \frac{2F}{\pi Dh}$$

where, F = Indentation Force,
D = diameter of indenter,
d = diameter of indent,
h = depth of indentation.

The indentation hardness was determined by penetration a stainless steel spherical probe upto 0.3 mm at a speed of 0.15 mm/min.

Friability: It is a measure of the tablet's resistance to subsequent process condition and transportation. Friability is measured using a friabilator designed and fabricated in Department's Fabrications Facility (Pandeya, 2009). Riippi et al. (1998) performed the friability test on erythromycin acistrate tablets using a friabilator for 100 rotations. Ameye et al. (2002) performed the friability test on tablets formed using granulated powder formulation. They used Pharma Test-type friabilator at 25 rpm for 4 min (100 rotations). Dedusted tablets were reweighed and percentage loss in weight was measured as friability. Accordingly, for the present research, known weights of dedusted tablets were subjected to a free fall of 152.4 mm for 100 times in a rotating drum (friabilator) at a speed of 26 rpm.

4. Results

4.1 Fundamental mechanical properties of powder formulation

The bulk modulus, compression index, and spring-back index were determined using the HTC test at unloading pressures of 2.5, 5.0, and 10.0 MPa. The shear modulus was determined using the CTC tests at confining pressures of 1, 2, and 3 MPa. These parameters were determined at loading rates of 10 and 20 MPa/min at 0, 5, and 10% binder content. The detailed powder fundamental properties are given in Pandeya and Puri (2011). For completeness; herein, a summary of powder properties: Bulk modulus, Compression index, Spring-back index, and Shear modulus, is presented in the following paragraphs. Rationale for the trends of these properties and corresponding discussion are given in Pandeya and Puri (2011).

Bulk Modulus: Bulk modulus is the measure of the resistance of the material to volumetric change. At 10 MPa/min loading rate, the bulk modulus increased with increase in the isotropic pressure and binder content in all cases. At 20 MPa/min the bulk modulus was maximum at 0% binder (i.e., no binder) followed by those at 10 and 5% binder content.

Compression Index: The compression index, an elastoplastic property, is the measure of compressibility of the material. The compression index value increased with pressure.

Spring-back Index: Spring-back index, an elastic property, is the measure of elastic recovery of the material after the applied pressure has been released. In all cases the spring-back index value increased with pressure. At 10 MPa/min loading rate, the spring-back value decreased with binder content. At 20 MPa/min the spring-back index value was lowest at 0% binder followed by 10 and 5% binder content.

Shear Modulus: The shear modulus is the measure of resistance of the material to deformation in shear loading. The shear modulus increased with increase in the confining pressure in all cases.

4.2 Tablet quality

As mentioned in a preceding section, four physical quality parameters, i.e., diametral strength, axial penetration strength, indentation hardness, and friability were evaluated for the tablets formed at different pressure and binder content. The diameter of the tablets formed were 10 mm with flat surface having average thickness of 3.3 and 3.2 mm in case of 70 and 90 MPa pressure, respectively. These parameters are discussed in the following subsections.

Diametral Strength: Generally, the average diametral strength values were higher for tablets formed at 90 MPa than at 70 MPa compression pressure for all binder contents (**Fig. 2**). The average diametral strength values at 70 MPa were 0.191, 0.345, and 0.330 MPa at 0, 5, and 10% binder, respectively (**Table 3**). These values at 90 MPa compression pressure were 0.323 (69%, percent increase in diametral strength from 70 MPa), 0.386 (12%), and 0.379 MPa (15%). With increase in compaction pressure the void ratio decreased and relative density increased, which resulted in an increase in strength. The diametral strength increased with binder content upto 5%; thereafter, it decreased or remained same when binder content increased from 5 to 10%. This shows that increase in binder after 5% did not affect the diametral strength. Binder addition improved the contact via the hypothesis of filling the void spaces,

Table 3 Diametral strength of tablets made from dry powder formulations at 70 and 90 MPa compression pressures and different binder contents*

Binder content, %	Compression pressure	
	70 MPa	90 MPa
0	0.19 MPa (0.021)	0.32 MPa (0.005)
5	0.35 MPa (0.008)	0.38 MPa (0.008)
10	0.33 MPa (0.030)	0.38 MPa (0.029)

*Standard deviation in parenthesis

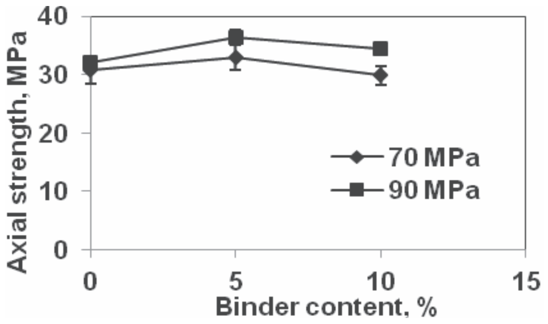

Fig. 2 Diametral strength of tablets.

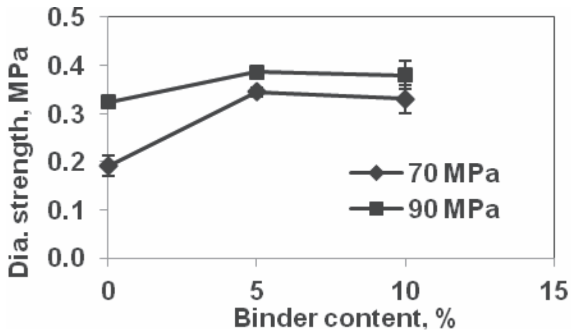

Fig. 3 Axial penetration strength of tablets.

which resulted in increase in strength of the tablets. Beyond 5% binder level, the diametral strength decreased; albeit slightly (not significant, p >0.05). By definition, binder is a softer, high plasticity material compared with the other ingredients. Therefore, beyond a certain level of binder content, the tablet's diametral strength will decrease. For the tested formulations, 5% appears to be the threshold value at which the maximum strength is attained.

Axial Penetration Strength: Axial penetration strength values for tablets formed at 90 MPa were higher than at 70 MPa for all binder contents (**Fig. 3**). The average axial penetration strength values at 70 MPa were 30.8, 32.9, and 29.8 MPa at 0, 5, and 10% binder, respectively (**Table 4**). These values at 90 MPa compression pressure were 32.0 (4%, increase over 70 MPa value), 36.5 (11%), and 34.3 MPa (15%). The axial penetration strength increased with binder content upto 5%; thereafter, it decreased when binder content increased from 5 to 10% similar to the diametral strength. Since axial penetration strength is a measure of failure value similar to the diametral strength, decrease in strength value was measured beyond 5% binder content; i.e., further corroborating that the threshold value at which maximum strength is attained is 5% binder content.

Indentation Hardness: Indentation hardness for tablets formed at 90 MPa were higher than at 70 MPa at all binder contents (**Fig. 4**). The average indentation hardness values at 70 MPa were 1.15, 1.28, and 1.27 MPa at 0, 5, and 10% binder, respectively (**Table 5**). These values at 90 MPa compression pressure were 1.25 (9%, increase over 70 MPa value), 1.38 (8%), and 1.40 MPa (10%). The indentation hardness increased with binder content upto 5%; thereafter, it either decreased slightly or remained nearly the same when binder content was increased from 5 to 10%. Indentation is a measure of surface and top layers' resistance to penetration. It can be hypothesized that as the binder content increases, it helps build bridges between particles, i.e., assisting with the hardness. However, beyond a certain value, i.e., when sufficient bridges have been formed; binder it-

Table 4 Axial penetration strength of tablets made from dry powder formulations at 70 and 90 MPa compression pressures and different binder contents*

Binder content, %	Compression pressure	
	70 MPa	90 MPa
0	30.8 MPa (2.4)	32.0 MPa (1.2)
5	32.9 MPa (2.2)	36.5 MPa (1.3)
10	29.8 MPa (1.6)	34.3 MPa (0.7)

*Standard deviation in parenthesis

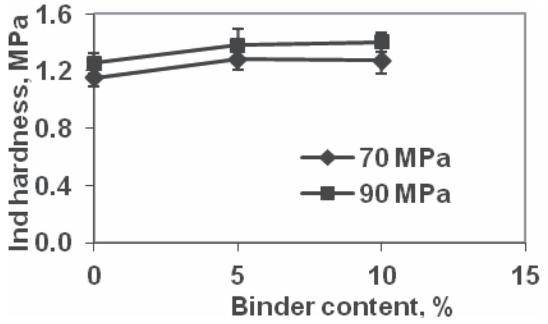

Fig. 4 Indentation hardness of tablets.

self being soft plastic-type material will reduce the resistance to deformation. For the formulations tested, this threshold value appears to be in the vicinity of 5% binder content.

Friability Test: Friability of tablets was higher for forming pressure of 70 MPa compared to 90 MPa for all binder contents (**Fig. 5**). The friability values at 70 MPa were 1.62, 1.31, and 1.48% at 0, 5, and 10% binder, respectively (**Table 6**). These values at 90 MPa compression pressure were 0.92 (43%, decrease over 70 MPa value), 0.79 (40%), and 0.75% (49%). The friability decreased with binder content upto 5%; thereafter, it increased when binder content increased from 5 to 10%. At low binder levels (<5% in this study), addition of binder improved the bonding between the particle and hence the friability decreased. However, as the binder level was increased, although fewer but larger granules were dedusted; which effectively increased the overall friability. In other words, increase in binder level beyond a formulation-specific value can adversely affect both strength and friability. For the specific formulations studied, based on experimental results, the binder level of about 5% produced best values of tablet metrics.

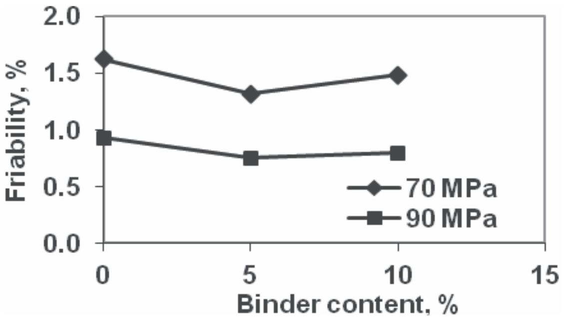

Fig. 5 Friability of tablets.

Table 5 Indentation hardness of tablets made from dry powder formulations at 70 and 90 MPa compression pressure and different binder contents*

Binder content, %	Compression pressure	
	70 MPa	90 MPa
0	1.15 MPa (0.06)	1.25 MPa (0.07)
5	1.28 MPa (0.07)	1.38 MPa (0.11)
10	1.27 MPa (0.09)	1.40 MPa (0.07)

*Standard deviation in parenthesis

Table 6 Friability (%) of tablets made from dry powder formulations at 70 and 90 MPa compression pressures and different binder contents

Binder content, %	Compression pressure	
	70 MPa	90 MPa
0	1.62%	0.92%
5	1.31%	0.75%
10	1.48%	0.79%

4.3 Relationship between tablet quality parameters and powder properties

Relationships based on regression analysis were developed between tablet quality parameters and powder mechanical properties at different binder contents and loading rates. The regression equations between each tablet quality and powder property were developed. Few examples of regression equations for predicting the tablet quality parameters are given in **Table 7** The complete list of equation is given in Pandeya (2009).

Diametral Strength: Compression index, spring-back index, and shear modulus were found most suitable for predicting the diametral strength ($R^2 >$ 0.80), i.e., explains 80% of the variations. All of the six spring-back index values at three different pressures and two loading rates were found to be suitable for predicting with diametral strength of tablets formed at 70 and 90 MPa. Tablets' diametral strength vs. powder formulations' spring back index (determined at 20 MPa/min loading rate; Pandeya and Puri, 2011) at 90 MPa tabletting pressure is presented in **Fig. 6** To explain the relationship between the tablets' diametral strength, axial penetration strength, and indentation hardness with powder formulations' spring-back index, an elastic energy based approach was used. This is given in a later section entitled **Elastic Energy Explanation of Tablet Quality Relationship with Powder Spring-back Index**.

Table 7 Regression equations for predicting the tablet quality parameters

Tablet Quality Parameters	Regression Equations	R^2
Diametral Strength (DS)	$DS_{70} = 14.11\ SI_{10,20} - 0.79^*$	0.99
	$DS_{90} = 5.70\ SI_{10,20} + 0.075$	0.99
Axial Strength (AS)	$AS_{70} = 40.46\ CI_{5,10} - 7.91$	0.93
	$AS_{90} = 247.53\ SI_{5,20} + 17.76$	0.98
Indentation Hardness (IH)	$IH_{70} = -\ 4.90\ SI2._{5,10} + 1.59$	0.99
	$IH_{90} = -\ 9.36\ SI_{10,10} + 2.27$	0.98
Friability (FR)	$FR_{70} = 14.11\ SI_{10,20} - 0.79$	0.99
	$FR_{90} = -\ 15.28\ SI_{10,20} + 1.99$	0.99

BM – Bulk modulus (GPa), CI – Compression index, SI – Spring-back index, SM – Shear modulus.
*$DS_{70} = 14.11\ SI_{10,20} - 0.79$, DS_{70} = Diametral strength at 70 MPa compaction pressure and $SI_{10,20}$ = Spring-back index at 10 MPa pressure and 20 MPa/min loading rate

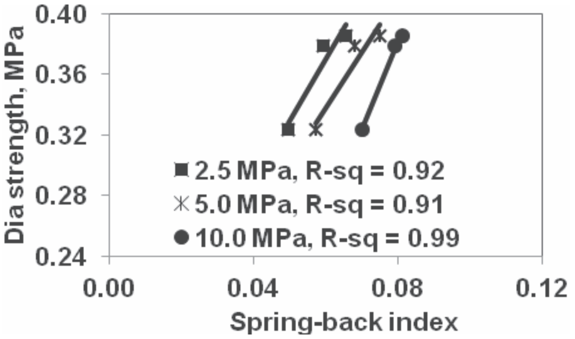

Fig. 6 Relation between tablets' diametral strength and spring-back index (determined at 20 MPa/min loading rate) at different pressures.

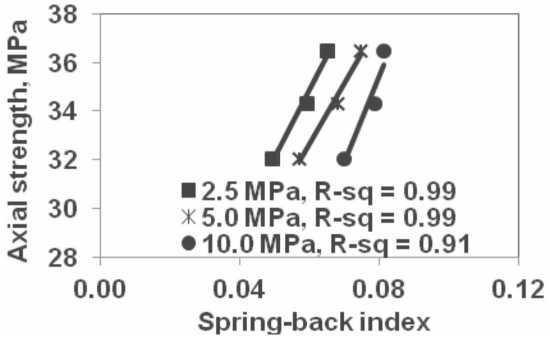

Fig. 7 Relation between tablets' axial penetration strength and spring-back index (determined at 20 MPa/min loading rate) at different pressures.

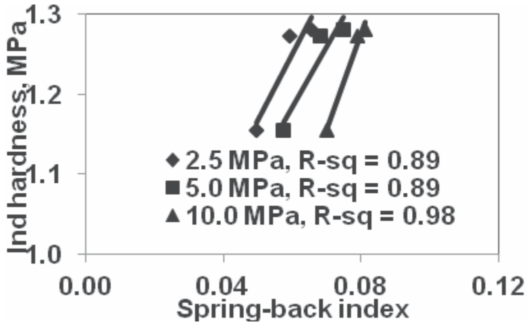

Fig. 8 Relation between tablets' indentation hardness and spring-back index (determined at 20 MPa/min loading rate) at different pressures.

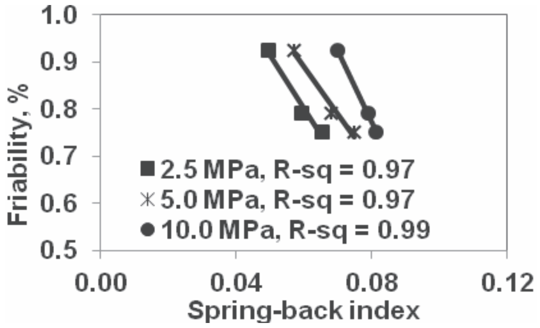

Fig. 9 Relation between tablets' friability and spring-back index (determined at 20 MPa/min loading rate) at different pressures.

Axial Penetration Strength: Compression index, spring-back index, and shear modulus (at 2 MPa stress difference) at higher loading rate had good relationship ($R^2 > 0.80$) with axial penetration strength of tablets formed at 90 MPa. Tablets' axial penetration strength vs. powder formulations' spring back index (determined at 20 MPa/min loading rate) at 90 MPa tabletting pressure is presented in **Fig. 7**.

Indentation Hardness: Compression index, spring-back index, and shear modulus were found most suitable for predicting the indentation hardness. All six values of spring-back index and five values of shear modulus correlated well with indentation hardness of tablet formed at 70 and 90 MPa. Tablets' indentation hardness vs. powder formulations' spring back index (determined at 20 MPa/min loading rate) at 70 MPa tabletting pressure is presented in **Fig. 8**.

Friability: Bulk modulus, compression index, spring-back index, and shear modulus at higher loading rate were found suitable for predicting the friability. Tablets' friability vs. powder formulations' spring back index (determined at 20 MPa/min loading rate) at 90 MPa tabletting pressure is presented in **Fig. 9**.

In summary, all four tablet quality indexes evaluated in this study, namely, diametral strength, axial penetration strength, indentation hardness, and friability, were most correlated with the spring-back index of powder formulations in low to medium pressure regime (<10MPa). Therefore, in the ensuing section, the spring-back index is used as the basis for explaining the tablet quality relationships via the elastic energy approach.

4.4 Elastic energy explanation of tablet quality relationship with powder spring-back index

Spring-back index is the measure of elastic recovery of the powder mass after the pressure is removed. The recovery includes contributions of both the solid particles and inter-particle void spaces. As powder retains some memory of its elastic response in early stages of compaction (<10 MPa herein), this implies that a powder's elastic property could be related to the elastic response of tablet quality metrics. To explain and prove this hypothesis, an energy based approach is proposed and validated. During tablet formation, force or pressure is applied through a punch, which inputs energy into the powder mass. When the compaction force is released, part of the energy is recovered in the form of elastic energy. The overall energy balance for the tablet compaction process can be written as:

$$E_T = E_C + E_E$$

where,

E_T = Total Energy Input

E_C = Energy Used in Compression (Includes Energy utilized in movement and rearrangement of particles, overcoming the friction between the particle and friction between the die wall and particles)

E_E = Elastic Energy Recovered

To establish the energy based approach, tablets were loaded and unloaded similarly as in the case of diametral strength, axial penetration strength, and indentation hardness tests. However, during this study, the force was applied as close as practically feasible to, but below, the failure of the tablet. To ensure the contact of the probe with the tablets, initial force of 2.2 N was applied, before starting the test. Next, force and displacement during both loading as well as unloading were plotted. The area under the curve was used to estimate the energy. The loading and unloading curves for the case of diametral strength, axial penetration strength, and indentation hardness tests are given in **Fig. 10a**, **b**, and **c**, respectively. The elastic energy was calculated by numerical integration to obtain the area under the unloading curve, i.e., shaded area in **Fig. 10a**, **b**, and **c**, respectively. The plots between the diametral strength, axial penetration strength and indentation hardness and their respective elastic energy are given in **Fig. 11a**, **b**, and **c**. Corresponding plots between these tablet qualities and spring-back index values are also shown in **Fig. 11a**, **b**, and **c**, respectively. Spring-back index was used in these relationships since it had the highest R^2 value compared with other measured mechanical properties. From the figures it is clear that with increase in the hardness or strength values, the elastic energy also increased in all cases. The R^2 values for these relationships were greater than 0.84. This

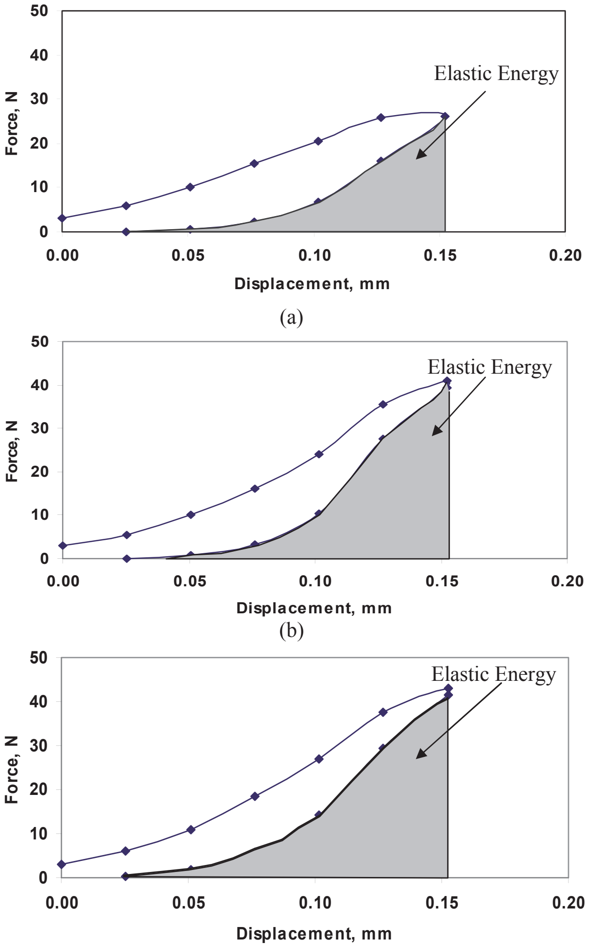

(a)

(b)

(c)

Fig. 10 Force vs. displacement (loading-unloading before failure) plot for tablet formed at 90 MPa using dry formulation in (a) diametral strength test, (b) axial penetration test, and (c) indentation hardness test modes.

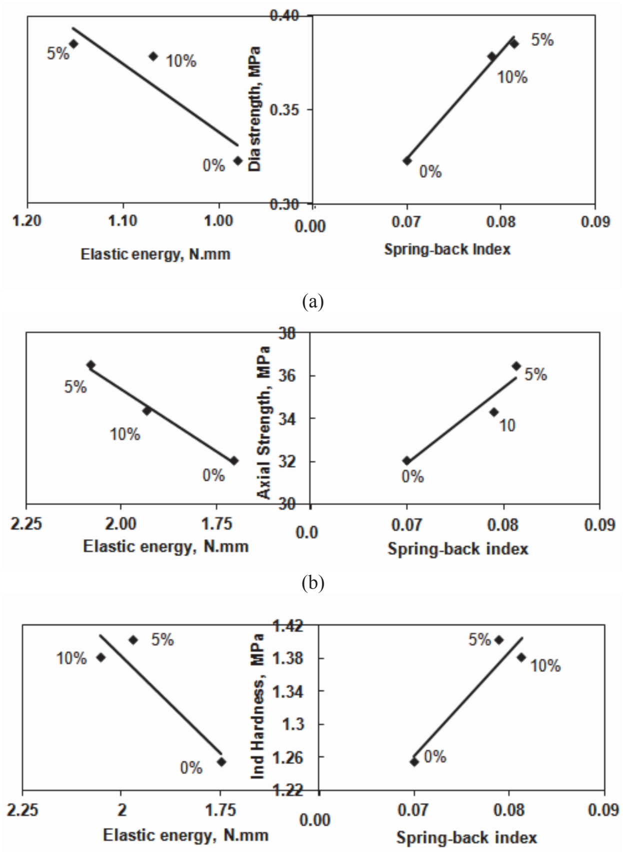

(a)

(b)

(c)

Fig. 11 Plot between elastic energy and spring-back index vs. (a) diametral strength, (b) axial penetration strength, and (c) indentation hardness for tablets formed at 90 MPa using dry powder formulations.

indicated that tablet's elastic energy can be directly related to the tablet's physical properties, i.e., both are related.

An explanation follows for the observed strong relationships between spring-back of powder formulations with the tablet parameters. For an elastic material, energy under identical loading and unloading conditions (i.e., same loading rate and peak strain value in case of strain (displacement) controlled device) must be the same, i.e., elastic energy is the highest. As the inelasticity of material increases, the elastic energy magnitude decreases, i.e., is lower. When the binder content is zero in the formula, i.e., no binder, the bonding as noted in literature is hypothesized to occur between particles welding at points of contacts via melting followed by solidification (German 1994). This leaves only a limited amount of recoverable energy. However, when the binder is added in dry mixture state, it promotes the formation of secondary structures that are larger in size than the primary particles. The secondary structures bond to each other leading to the formation of the tablet. Akin to granulation, these larger, irregularly shaped secondary structures store greater elastic energy (such as during bending and distortion), which is released through rebound during unloading. The elastic energy of tablets formed with 0%, 5%, and 10% binder contents is shown in **Fig. 11a, b**, and **c**. In all cases the elastic energy of 5% and 10% is greater than 0% binder tablets. Furthermore, as the binder content is increased from 5% to 10%, there is an overabundance of binder in the mixture; while the secondary structures are formed as hypothesized, there is excess binder. This excess binder manifests its soft and pliable native characteristics compared with other constituents, i.e., has a portion of energy that goes into the excess binder that is not recovered during unloading. Therefore, there is a decrease in elastic energy, which is true for all three metrics: diametral strength, axial penetration strength, and indentation hardness. In fact, the order of spring-back index value at 0%, 5%, and 10% binder content is consistent with the order of elastic energy. This provides a strong evidence of the feasibility of using elastic response in early stages of compression (<10 MPa) to predict tablet's mechanical quality metrics.

Conclusions

In the present study, the fundamental mechanical properties of powder formulations determined at medium pressure were related with the various physical properties of the tablets. Powder formulations' mechanical properties such as bulk modulus, compression index, spring-back index, shear modulus and failure stress were determined using a cubical triaxial tester. Tablets were formed using the same formulations and their properties such as diametral strength, axial penetration strength, indentation hardness, and friability were determined.

Diametral strength, axial penetration strength and indentation hardness increased with compression pressure. Friability decreased with compression pressure. The diametral strength axial penetration strength and indentation hardness increased with the binder content up to 5% thereafter it decreased or remained same when the binder content increased from 5 to 10%.

Statistical relations were developed between tablets' quality parameters and the powder mechanical properties at different binder contents and loading conditions. Spring-back index and compression index were found most suitable for predicting diametral strength, indentation hardness, and friability for the formulation used in the study. In case of the axial penetration strength, compression index, spring-back index, and shear modulus at higher loading rate had good relation for tablets formed at 90 MPa. An elastic energy-based approach was successfully used to explain the relationship of tablet quality parameters: diametral strength, axial penetration strength and indentation hardness, with spring-back index.

The positive outcome of this feasibility study suggests that the approach of relating mechanical properties of powder formulations in the low to medium pressure range (<10 MPa) vs. tablet physical quality parameters could be used for other similar formulations. Although the study focused only on binder content, the approach could be applied and tested for other ingredients. In closure, the initial results of this research are promising and have the potential for application in industries involved in powder compaction.

References

Ameye, D., Keleb, E., Vervaet,C., Remon, J. P., Adams, E., Massart and D. L. (2002): Scaling-up of a lactose wet granulation process in Mi-Pro high shear mixers, European J. of Pharmceutics and Biopharmaceutics, 17, pp.247 – 251.

German, R. M. (1994): "Powder metallurgy science", 2nd Edition. Princeton, NJ: Metal Powder Industries Federation, 279 p.

Kamath, S. and Puri, V. M. (1997): Measurement of powder flow constitutive model parameters using a cubicle triaxial tester, Powder Technology, 90, pp.59-70.

Kuentz, M. and Leuenberger, H. (2000): A new approach to tablet strength of a binary mixture consisting of well and a poorly compactable substance, European Journal of Pharmaceutics and Biopharmaceutics, 49, pp.151-159.

Li, F. and Puri, V. M. (1997): "Development, testing, and verification of a medium pressure flexible boundary cubical triaxial tester" , ASAE Paper No. 97-4104, American Society of Agricultural Engineers (ASAE), St. Joseph, MI, 12 p.

Leuenberge, H. and Rohere, B. D. (1986): Fundamentals of powder compression. I. The compactibility and compressibility of pharmaceutical powders, Pharmaceutical Research, 3, pp.12 – 22.

Mittal, B. and Puri, V. M. (2005): Rate-dependent elastoviscoplastic constitutive model for industrial powders. Part 1: Parameter quantification, Particulate Science and Technology 23, pp.249-264.

Pandeya, A. (2009): "Relating mechanical properties of dry and granulated pharmaceutical powder formulations with tablet quality parameters" , Ph.D. Dissertation, The Pennsylvania State University, University Park, PA, 313 p.

Pandeya, A. and Puri, V. M. (2008): "Comparison between mechanical properties of dry blended and granulated pharmaceutical powder formulations" , ASABE Technical Paper No. 083540, American Society of Agricultural and Biological Engineers (ASABE), St. Joseph, MI, 22 p.

Pandeya, A. and Puri, V. M. (2011): Rate-dependent mechanical properties of dry blended pharmaceutical powder formulations for tabletting applications, Powder Technology, 207, pp.26-34.

Riippi, M., Antikainen, O., Niskanen, T. and Yliruusi, J. (1998): The effect of compression force on surface structure, crushing strength, friability and disintegration time of erythromycin acistrate tablets, European J. of Pharmceutics and Biopharmaceutics 46, pp.339–345.

Tabor, D. (2000): "The Hardness of metals" , Oxford University Press, London, 175 p.

Tye, C. K., Sun, C. and Amidon, G. E. (2005): Evaluation of the effects of tableting speed on the relationships between compaction pressures, tablet tensile strength, and tablet solid fraction, Journal of Pharmaceutical Sciences, 94, pp.465–472.

Wu, C. Y., Best, S. M., Bentham, A. C., Hancock, B. C. and Bonfield, W. (2005): A simple predictive model for the tensile strength of binary tablets, European Journal of Pharmaceutical Sciences, 25, pp.331-336.

Author's short biography

Anuranjan Pandeya

Anuranjan Pandeya is currently working as a post doctoral scholar at Penn State University. Dr. Pandeya has been involve in research in the area of powder mechanics, particle characterization and size reduction behavior of powders. He worked for industries and research institute prior to joining Ph.D. Dr. Pandeya has co-authored several papers in the area of powder and particulate science. He also presented paper in various national and international professional meetings and gave technical talks to industries and research institutes. The research work reported in the paper is based on the work done during his Ph.D. at Penn State.

Virendra M. Puri

Virendra M. Puri, University Distinguished Professor, has researched in the field of powder science and engineering for over three decades. He served as the Acting Director of the Particulate Materials Center and has co-authored numerous publications. Professor Puri is co-inventor and holder of patents in powder flow, deposition, and compaction and has copyright for multi-purpose computational software on powder processing. He has been invited to serve on Editorial Boards, International Advisory Boards, and Chairpersons of several bulk solids-related publications and professional activities. Professor Puri is Co-Editor-in-Chief of Particulate Science and Technology. He has received several teaching and research awards.

Applications of Engineered Particulate Systems in Agriculture and Food Industry[†]

Aarthi Narayanan[1,2], Parvesh Sharma[1,2] and Brij M. Moudgil[1,2*]
[1] *Department of Materials Science and Engineering, University of Florida*
[2] *Particle Engineering Research Center, University of Florida*

Abstract

The development of nanotechnology for advances in various sectors like health, consumer products has paved way for possible applications in agriculture and food industries. Antimicrobial agents (e.g., silver, titanium dioxide), nano-bio pesticides (hydrophobic silica), smart delivery systems (polymeric nanoparticles) provide promising enhancement or alternatives to the conventional crop protection strategies, which are primarily based on applying chemicals in solid, liquid or suspension forms. Nanotechnology approaches in food industry can impart properties such as resistance to gas penetration, increased tensile strength and enhanced absorption of nutrients leading to novel food packaging and processing materials. Despite these features, the usage of nanotechnology is still limited, owing to the lack of proper toxicity evaluation data. Understanding the risks and taking appropriate measures to mitigate them will significantly enable nanotechnology advances targeting to agriculture and food industries. In this paper, we have reviewed some of the recent research and development efforts that have been carried out in nanotechnology for its potential applications in agrifood sector. More specifically, nanotechnology approaches mediated by particle technology advances are reviewed.

Keywords: nanotechnology, agriculture, food, controlled release, sensors, packaging

1. Introduction

With the global population exceeding 7 billion and an annual growth rate of 1%, there is an increasing demand for food throughout the world. Inflation of food price, climate changes and supply chains are other issues that the agrifood sector faces (ObservatoryNano, 2010). These challenges are the drivers for the farmers and the scientific community to delve into options for maximizing the yield of the crops. Recent report by Food and Agricultural Organization shows that 70% more food needs to be produced by 2050 (FAO, 2009). The major hindrance in accomplishing this goal is the pests and other pathogens that destroy the crops and reduce the resource-use efficiency. For instance, it has been shown that the estimates for potential losses occurring to rice crops due to animal pests and pathogens are 37 and 25 % respectively (Oerke, 2006). Advent of foreign pests is one of the possible reasons for major destruction in the crops with the most recent example being a disease called citrus greening. This disease, which led to a huge loss of $3.6 billion in Florida so far (Hodges and Spreen, 2012) is caused by a bacteria (*Candidatus* Liberibacter asiaticus) and spread by an insect (Asian citrus psyllid), originated in China (USDA, 2007). With devices to diagnose such new pests, farmers will be able to take proactive measures before the onset of the disease. Also, diagnosis of pests and pesticide residues helps the farmers and the food manufacturers to ensure that the product meets the criteria for the quality and safety before despatch (Grunert, 2005). Although analytical methods like gas chromatography and high performance liquid chromatography are available to monitor the

---

[†] Accepted: June 20, 2012

[2] 205 Particle Science and Technology Building,
PO Box 116135, University of Florida, Gainesville, Florida 32611, USA
[*] Corresponding author:
E-mail: bmoudgil@perc.ufl.edu
TEL: +1-352-846-1194 FAX: +1-352-846-1196

ⓒ 2013 Hosokawa Powder Technology Foundation

pesticide residues, there is a need to develop easier, faster, online and accurate methodologies without requiring much sample pretreatment. Biosensors are such devices which can not only detect the pests and the pesticide residues, but are also capable of doing it more accurately and faster than the conventional devices with much smaller sample sizes.

While timely detection of the pests helps in addressing the existing issues partially, a comprehensive solution is achieved only by combining effective diagnosis techniques with efficient crop protection strategies. Usage of pesticides is imperative for any crop treatment; however, the rates at which they are sprayed currently, owing to the evaporation and runoff, leads to accumulation and consequently becomes detrimental to the environment. The adverse effects caused by the pesticide residues calls for an efficient treatment method which can minimize the usage of pesticides and also prolong its efficacy in the crops. Smart delivery systems are modalities which can encapsulate an agrochemical and release it in a controlled manner without compromising the environment. Nanotechnology approaches for crop treatment can lead to effective and efficient solutions. For example, the remote sensing property offered by many biosensors could improve the average farm profits by $31.74/ha (Tenkorang and Lowenberg-DeBoer, 2008) by spatially targeting and channelizing the application of the agrochemical in the field. The importance of nanotechnology extends to food packaging and processing materials. Nanoparticles can enhance the packaging material properties such as resistance to gas and moisture penetration, better tensile strength etc. Additionally, nanotechnology approaches for enhancing the absorption of nutrients into the body can lead to interactive food processing materials.

The following sections highlight some of the pioneering nano-bio based technologies and their applications in the agrifood sector.

2. Agriculture

2.1 Biosensors for diagnosis of pests and pesticide residues

Nano-bio sensors are devices which utilize the principle of biological selectivity along with the processing power of the optoelectronics to analyze target compounds. Biosensors can be used to detect a variety of compounds such as phenols (Munteanu et al., 1998), volatile organic compounds like benzene (Ikariyama et al., 1993) and pesticides (Oroszlan, 1993) besides pathogens (Costello et al., 2000). Typically, biosensors are tagged with enzymes, anti-bodies or any other biologically active systems to impart biorecognition properties to the sensor. The signal generated by these biological systems can be in the form of electric potential/current/resistance, optical properties such as luminiscence, heat or changes in the mass of the reactants or products etc. (**Fig. 1**). The biosensors expected to grow to $16.8 billion market by 2018 (Business Wire, 2012) are also applicable in many other industries like healthcare, environmental, and food processing.

The presence of nanoparticles in a biosensor is expected to improve the overall efficiency of the sensors possibly due to the increased surface for reaction. Typically, the nanoparticles are functionalized by the bioconjugate of the target analyte (Yang et al., 2008). Dye-doped silica, quantum dots (Qdots), and gold are some of the nanoparticles explored for the development of biosensors. Bioconjugated dye doped silica nanoparticles, which is used for the detection of E.coli is shown to be 1000 times more effective in signal amplification than an organic dye. Each silica particle can encapsulate thousands of organic dye molecules and is tagged to a bacterium leading to better signal and enhanced sensitivity (Zhao et al., 2004). Silica matrix is biocompatible, non-toxic and is also optically transparent. In addition, presence of silica shell around the dye is shown to reduce the photodegradation of the dye. However, the major limitation of silica is the lack of inherent spectral properties, which lead to investigation with several other nanoparticles that could address this issue.

Qdots are nanomaterials that possess inherent spectral properties and do not require external fluorophore as in the case of silica particles. This makes Qdots, which have dimensions from 1-10 nm, a strong contender for usage in optical biosensors. The detection of a biomolecule by a Qdot typically depends on the principle of Forster Resonance Energy Transfer (FRET). FRET is an energy transfer between the

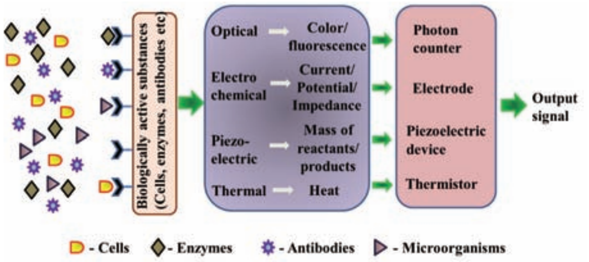

Fig. 1 Components of a biosensor (adapted from Rana et al., 2010).

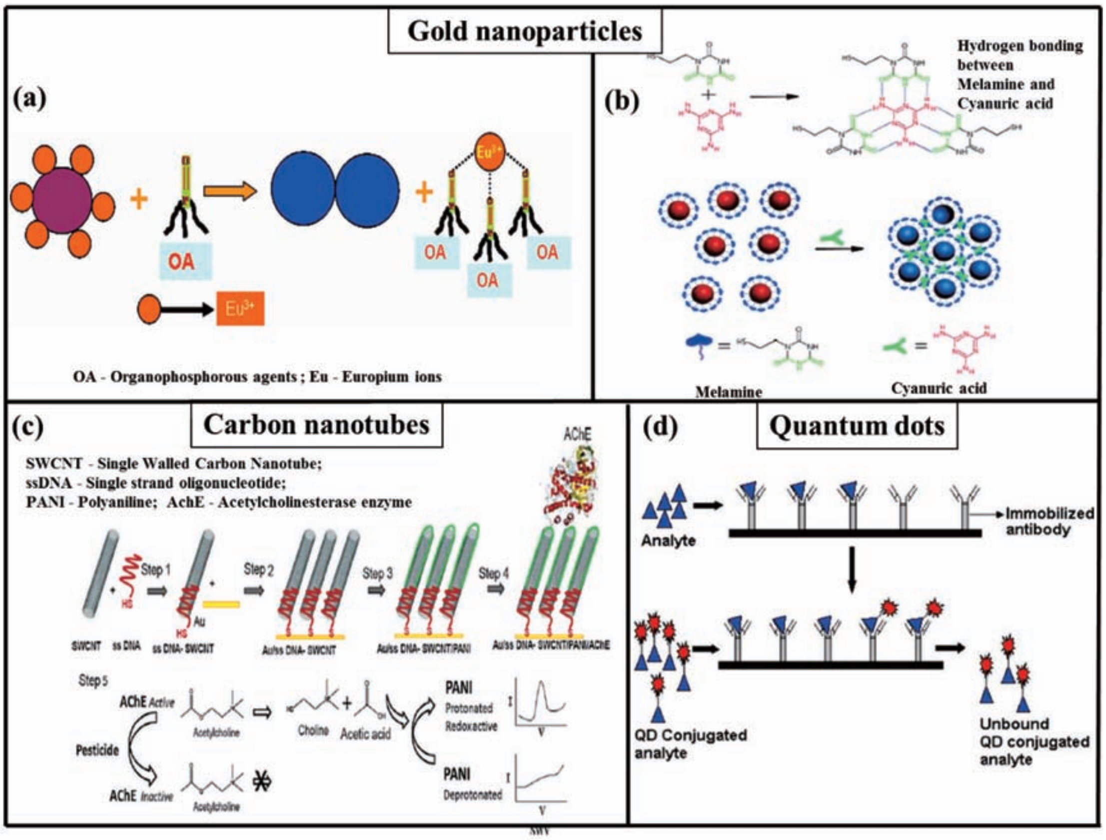

Fig. 2 Schematic of functioning of various biosensors (a) Fluorescence based detection of organophosphorous pesticides using europium tagged gold nanoparticles (Dasary et al., 2008) (b) Colorimetric detection of Melamine in milk using cyanuric acid-gold nanoparticles (Reprinted with permission from (Ai et al., 2009). Copyright (2012) American Chemical Society) (c) Electrochemical detection of pesticides using enzyme activated single walled carbon nanotubes (Viswanathan et al., 2009) (d) Color change of the nanoassembly formed by Qdot nanoprobes and target analyte (Reprinted with permission from (Ho et al., 2005). Copyright (2012) American Chemical Society).

Table 1 Applications of biosensors in the detection of food-borne pathogens and pesticides

Nanoparticle	Target Analyte	Method of detection	Detection limit	Reference
Dye doped silica	E. Coli	Fluorescence	1-400 e.coli/g beef sample	(Zhao et al., 2004)
Molecular imprinted silica nanospheres with Qdots	deltamethrin (pesticide)	Fluorescence	0.16 μg/mL	(Ge et al., 2011)
Gold	Salmonella typhi	Current	98 cfu/mL	(Dungchai et al., 2008)
	Carbofuran and Triazophos	Color	32 μg/L and 4 μg/L	(Guo et al., 2009)
	Salmonella spp	Capacitance	1.0 × 10^2 cfu/mL	(Yang et al., 2009)
	Organophosphorous pesticides	Fluorescence	1 μM	(Dasary et al., 2008)
	Pathogen (Staphylococcal enterotoxin B)	Color	0.01 ng/mL	(Yang et al., 2009)
Carbon nanotubes	Methyl parathion and chlorpyrifos	Current	1 × 10^{-12} M	(Viswanathan et al., 2009)
Zirconium oxide/gold nanocomposite	Parathion	Current	3 ng/mL	(Wang and Li, 2008)
Qdots	Methyl parathion	Fluorescence	0.1-1 ng/mL	(Chouhan et al., 2010)
	E. Coli	Fluorescence	10^4 e. coli/mL	(Mukopadhyay et al., 2009)

donor fluorophore and the acceptor chromophore in which the excitation energy of the donor is transferred to the acceptor nonradiatively. The broad absorption spectra of the Qdots allow it to accept energy nonradiatively from a donor chromophore, a biomolecule and reemit the energy corresponding to their emission spectrum. The narrow emission band, broad absorption spectra and extended photostability render Qdots superior to the conventionally used organic dyes.

Gold nanoparticles, typically 1-100 nm in size, are used both in optical and electrochemical sensors. The optical properties of gold nanoparticles are shown to vary with their size, shape and agglomeration based on Mie scattering theory (Feldheim and Foss, 2002). While small nanoparticles absorb light in the blue-green spectrum (red color), a red shift is observed when the particles get bigger in size (blue or purple in color). The change in the coloration formed due to the aggregation of gold colloids in the presence of a target analyte forms the basis for optical detection of several target analytes. Gold nanoparticles offer several advantages such as less toxicity than their counterparts (e.g. Qdots), lack of photodecomposition, stablility etc. Gold nanoparticles are also used to design a variety of immunoassays for electrochemical sensing of the pesticides and pathogens. For example, Dungchai et al demonstrated amperometric detection of *Salmonella typhi* (*S. typhi*) bacteria using gold nanoparticles (Dungchai et al., 2008).

The polystyrene cell wall was immobilized with monoclonal antibodies and a polyclonal antibody conjugated gold nanoparticle was added to bind to these bacteria. Addition of copper enhanced ascorbic acid enables reduction to Copper(0) and further deposition on the nanoparticles. The Cu(II) released in the nitric acid is measured by anodic stripping voltammetry and the current was found to be linearly dependent on the concentration of *S. typhi*. **Table 1** illustrates several nanomaterials used in biosensors and their applications for detection of various pathogens and pesticide residues.

2.2 Particles for crop protection

Usage of pesticides is imperative in any crop treatment strategy. According to a recent report released by United States Environmental Protection Agency (USEPA), the annual usage of pesticides in United States (US) is 1.1 billion pounds (Grube et al., 2011). Typically, pesticides are applied either by spraying or broadcasting. These methods of application lead to pesticides being lost due to run off, evaporation etc. Encapsulation of these pesticides in nanoparticles facilitates controlled and targeted delivery (smart delivery systems), thus reducing the number of applications required (Jurado-Exposito, 1996). Various modalities have been investigated as potential smart delivery systems (e.g. clay, polymeric particles, and silica capsules). A brief review of some of the particle mediated smart delivery systems is presented below.

2.2.1 Polymeric particles

Encapsulation of agrochemicals such as pesticides, semio-chemicals (attractants and repellents) in polymers are well-studied. Various methodologies, such as solvent extraction, complex coacervation, insitu polymerization etc., are used for the encapsulation of these chemicals in the polymers. The release of the active ingredient from the polymer can be controlled by varying the pore and the particle size of the polymer. There are several mechanisms by which an active ingredient is effectively released into the environment. As illustrated in **Fig. 3**, primarily, the release of the active ingredient is driven by either (a) Diffusion (b) Osmosis or (c) Environment which includes changes in the pH, surrounding solvent, temperature, ions etc. Diffusion occurs when the active ingredient passes through the polymer, either through the pores of the polymer matrix (macroscopic diffusion) or between the polymeric chains (microscopic diffusion) typically driven by the chemical potential or concentration gradient of the active ingredient. The other mechanism for release which is osmosis occurs when the pesticide is present inside an osmotic core surrounded by a semi-permeable membrane. The entrance of water into the core drives the release of the pesticide into the surrounding environment.

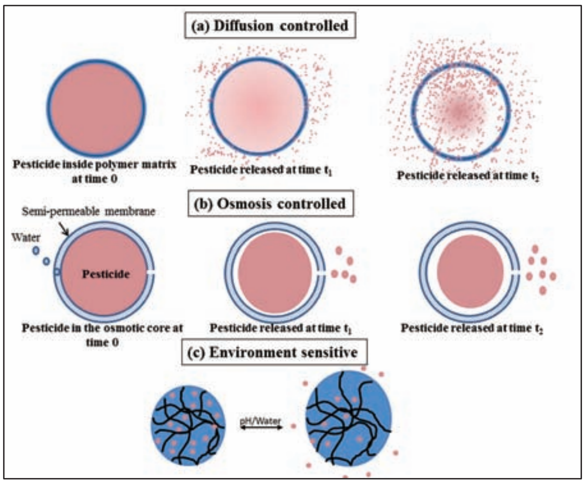

Fig. 3 Schematic of controlled release modalities from a polymer matrix.

Similarly, environment sensitive delivery devices are designed based on the principle that the polymer matrix responds to a change in the surrounding environment like pH, solvent etc., and swells. The swelling of the matrix forces the release of the active ingredient into the environment (e.g. release of active ingredient from a hydrogel). Several polymeric nanoparticles are designed for efficient release of agrochemicals. One of the most widely explored polymeric materials is chitosan. Chitosan is a biodegradable polymer and the derivatives of naturally available chitosan can self-assemble to form nanoparticles. Biodegradability and biocompatibility of such polymers, renders them potentially safe for agrifood applications. For example, chitosan nanomicelles have been studied for the encapsulation and release of bioactive food factors (Zhang et al., 2006). Similarly, the pesticide Bifenthrin was encapsulated in polymers such as Poly (acrylic acid)-b-poly (butyl acrylate), Polyvinyl alcohol (PVOH (Liu et al., 2008).

2.2.2 Clay particles

Kaolin, a white, non-swelling, plate-shaped alumino silicate mineral, is widely used in agriculture as a bio-pesticide and a repellent. The mechanism of this technology is speculated to be the desiccation caused by the inert dust which was first observed by Maxwell (Maxwell, 1937). These clay particles protect plants against various pests and insects (Daniel et al., 2005 ,Eigenbrode et al., 2006 ,Glenn et al., 1999) by masking the visual cues. Another clay that has shown potential in agricultural applications is three layered, swelling clay called Montmorillonite (MMT). While the naturally available MMT clays are hydrophilic, their high cation exchange capacity makes it possible for modification with a cationic surfactant to render them hydrophobic (de Paiva et al., 2008). Encapsulation of various pesticides has been accomplished in both hydrophilic (Mishael et al., 2002) and hydrophobic MMT clays (Celis et al., 2005). By encapsulation, the efficiency of the insecticides diazinon and chlorpyrifos has been shown to improve from 4 weeks in the commercial formulation to as high as 20 weeks using the MMT clay (Choudary et al., 1989). On similar lines, preliminary experiments in our group with MMT clays indicate that the efficiency of insect repellent could be increased from 2 days to few weeks (unpublished results). Given that these clays are abundant and environmentally benign, they provide a greener alternative to the conventional crop protection strategies.

2.2.3 Silica particles

Recent development in the health care industry for encapsulation of various drugs in the mesoporous silica particles (He and Shi, 2011) has paved way for a similar application in agricultural industry. Surface functionalized hydrophobic silica can act as an insecticide by getting adsorbed into the cuticular lipids of insects and causing death of insects by desiccation (Mewis and Ulrichs, 2001). A similar effect was shown recently by Debnath et al against rice weevil *Sitophilus oryzae (Debnath et al., 2011)*. Water soluble pesticide validamycin encapsulated in porous hollow silica nanoparticles (PHSN) with a loading capacity of 36% is shown to last for 800 min as opposed to instantaneous release of free validamycin (Liu et al., 2006). Encapsulation of the pesticides inside the hollow silica spheres has also been shown to protect them from environmental factors such as ultraviolet degradation (Li et al., 2007).

2.2.4 Magnetic nanoparticles

The effective usage of magnetic nanoparticles for imaging and targeted delivery of the drugs has stimulated interest in their application for agricultural purposes. For example, carbon coated iron nanoparticles have been investigated in pumpkin plants which showed signals of varying magnetic strengths in different parts of the plant (Gonzalez-Melendi et al., 2008). The advantages of magnetic nanoparticles lie in the fact that they can be tagged with different substances based upon the application and can be concentrated in a localized area. Ferrofluids are another kind of magnetic material containing a mixture of iron oxides or other ions like Manganese and nickel along with a stabilizer typically a surfactant and carrier liquid. Pintilie et al monitored the catalase activity in Maize as a function of concentration and concluded that the enzyme activity exhibits a maximum before decreasing with further increase in concentration (Pintilie et al., 2004). Similar results were reported in a study conducted in pumpkin plants using magnetic nanoparticles coated with tetramethylammonium hydroxide (TMA-OH) (Zhu et al., 2008). The reason for this trend is speculated to be the oxidative stress generated by the excess iron consequently affecting the process of photosynthesis and metabolism. The highly localized nature of the magnetic nanoparticles will be of interest in studying the local treatment of the plants in greenhouse. Given the inhibitory effects of high concentrations of these particles on the metabolism of the plants, proper selection of the concentration ranges for design of these delivery systems is important.

2.2.5 Nano-Titanium dioxide (TiO_2)

TiO_2 which is a well-known photocatalyst is widely studied for possible enhancement of photosynthesis. For example, Su et. al showed that suitable concentrations of nano-anatase TiO_2 can improve the oxygen evolution in spinach plants (Su et al., 2007), supporting the study performed by Yang et al (Yang et al., 2007). The possible reasons stated for this phenomenon are the increase in light absorbance and energy transfer among the amino acids. Similar results were demonstrated with nano-TiO_2 on wheat plants (Moaveni et al., 2011). Given the importance of photocatalytic activity of TiO_2, various studies have been conducted to improve it. For example, Krishna and coworkers have reported that TiO_2 in combination with water soluble fullerenes has been shown to enhance the degradation of an organic dye indicating an increase in the photocatalytic activity (Krishna et al., 2006). A similar effect was achieved with silver doped TiO_2 nanoparticles (Behnajady et al., 2008). Increased photoactivity is attributed to the scavenging of the photo-generated electrons, which could consequently increase the generation of hydroxyl radicals. Some of the recent patents based on smart delivery systems are listed in **Table 2**.

Table 2 Smart delivery systems for agrochemical delivery – a patent review.

Carrier	Application (Patent number)	Reference
Clays	Pesticides (# 6261997)	(Rubin et al., 2001)
	Anionic herbicides (# 7030062)	(Nir et al., 2006)
	Pesticides (# 0127435)	(VanVoris et al., 2006)
	Fertilizer (Sulfur) (# 6749659)	(Yu et al., 2004)
	Pesticides (# 0215705)	(Cataldo et al., 2010)
Polymers	Pesticides (# 6638994)	(Crooks et al., 2003)
	Fungicide (# 7452546)	(Botts et al., 2008)
	Essential oils (# 0268780)	(Markus et al., 2009)
	Agrochemicals (# 0261043)	(Greiner et al., 2008)
Silica	Pesticides (# 0254082)	(Toledano et al., 2008)
	Pesticides (# 0015236)	(Margadassi et al., 2010)
	Insect repellent (# 0244056)	(Santra, 2011)
	Agrochemicals (# 7537803)	(Wang et al., 2009)

2.2.6 Nanoemulsions

Nanoemulsion can be defined as non-equilibrium colloidal system comprising multiple phases, simplest being oil and water, which is visibly translucent and kinetically stable. The particle size diameter of the nanoemulsion is typically in the region of 20–200 nm (Solans et al., 2005). Nanoemulsions have a wide range of applications in pharmaceutical, skin care and cosmetics industry to name a few. In agricultural applications, nanoemulsions can be used to disperse both hydrophilic and hydrophobic pesticides depending upon the need. By enabling dispersion of hydrophobic pesticides in water, usage of toxic organic solvents can be minimized, in addition to increasing the bioavailability of the active ingredient (Nicolaos et al., 2003). The smaller size of the droplets in the nanoemulsion enables uniform spreading on the plant leaves and also improves internalization in insects (Ebert et al., 1999). Nanoemulsions can be produced by both high energy (mechanical processes) and low energy (addition of surfactants) processes (**Fig. 4**). The surfactants in the emulsion might lower the surface tension and enable better wettability and penetration of the droplets into the leaves (Tadros et al., 2004). Wang and coworkers demonstrated that the nanoemulsion of a water-insoluble model pesticide β -cypermethrin was highly stable and did not form a precipitate when diluted from the concentrated solution (Wang et al., 2007). Similarly, a study on the neem oil nanoemulsions concluded that the larvicidal effect increased with decreasing droplet size (Anjali, et al. 2012). The increased bioavailability of the nanoemulsions could be explained by the higher surface area (smaller size of the droplet), leading to better adsorption of the target entity (McClements

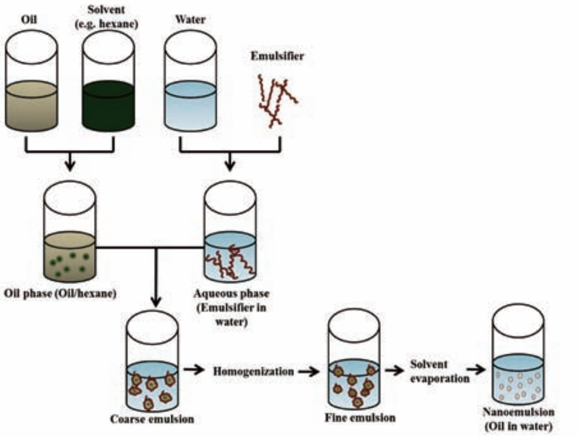

Fig. 4 High energy process of nanoemulsion preparation (adapted from (Troncoso, 2012)).

and Li, 2010). Banner MAXX® (fungicide) and PrimoMAXX® (plant growth regulator) are examples of nanoemulsions in agricultural applications.

3. Food

Food industry finds increasing applications of nanotechnology in areas such as for food safety, processing, novel packaging materials and sensors as illustrated in **Fig. 5**. Examples of nanoparticles that have generated wide interest in this area e.g. nanomposites and nanosensors (packaging) and nanoemulsions and nanocapsules for efficient delivery of nutrients (food processing) are described in following section.

3.1 Food packaging

Improvement in the lifestyle of the people demands for multifunctional food packaging options. Owing to this, there has been a significant effort by the industry to explore smart packaging material. As a result, the market for smart food packaging is estimated to skyrocket to $ 23.5 billion by 2015 (Marketsandmarkets, 2011). This section reviews the set of nanoparticles with great potential for usage in smart food packaging materials.

3.1.1 Nanocomposites

The nanocomposites, expected to be a $3.8 billion annual market by 2015, is the fastest growing market within the polymers. Nanocomposites are typically made of polymers and a nano-additive, which can be nanoclays or any other nano-reinforcement material such as chitosan, cellulose, carbon nanotubes etc. The presence of nano-additives offer advantages such as increased resistance to moisture and gases, and improved tensile strength properties.

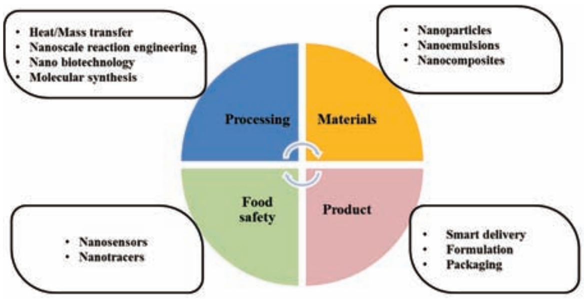

Fig. 5 Applications of Nanotechnology in food sector (adapted from (Weiss, 2006)).

3.1.1.1 Nanoclays

One of the promising materials for smart packaging, nanoclays provide the well-needed resistance to water vapor and gas transmission. This phenomenon has been exploited for packaging of food which is sensitive to moisture, carbon dioxide and oxygen (Lan et al.,2001). Nanoclays are typically montmorillonite clays which are organically modified for enhanced dispersion properties in polymer matrices. When the clay is intercalated into polymers or viceversa, the resulting nanocomposite has better tensile strength and barrier properties (Maul, 2005). The possible interactions between polymer and clay can be either intercalation, which is penetration of polymer into the layers of the clay or exfoliation involving delamination of clay (Adame and Beall, 2009 ,Alexandre et al., 2009 ; as shown in **Fig. 6**). The presence of tortuous path in the nanoclays-polymer composite, which was initially proposed by Nielsen and further studied by other authors (Adame and Beall, 2009 ,Mirzadeh and Kokabi, 2007), is postulated to be the cause of barrier properties. It has been shown that the relative permeability decreases with increase in sheet length because of the increased tortuosity (Bharadwaj, 2001).

Nanocor, a subsidiary of Amcol International Corporation, USA, has developed a nanocomposite called Imperm® that is used as a substitute for glass bottles to store beer and claimed to have a shelf life of around 6 weeks. Oxygen transmission rate (OTR) has been showed to decrease with increased loadings of nanoclays in the composite (Lan et al., 2001). A similar product from Honeywell claims to offer a shelf life of around 26 weeks (Sherman, 2004). Durethan® (Bayer) is another nanoclay product which could reduce the transmission of gases and moisture thus preventing the food from spoilage (McHugh,

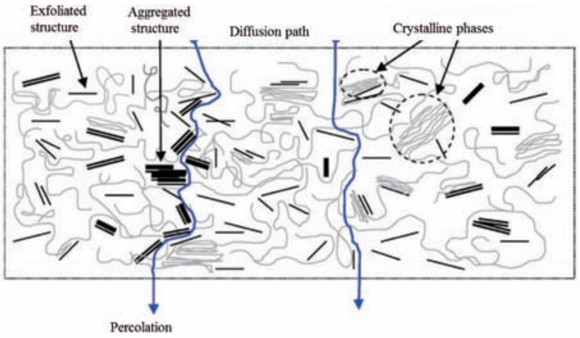

Fig. 6 Illustration of diffusion of water through clay-polymer nanocomposites (Alexandre et al., 2009).

2007).

3.1.1.2 Nanofibres and nanotubes

Nanofibers closely follow nanoclays as an efficient additive in a composite. Cellulose nanofibers (CNFs) are explored for their ability to offer low cost, high tensile materials. These are typically synthesized as nanofibers which are made up of crystalline and amorphous regions. Azeredo et al investigated the effect of nanofibers combined with films made of mango puree (Azeredo et al., 2009) and chitosan (Azeredo et al., 2010). They observed a significant decrease in water vapor transmission rate and increase in young's modulus at 10% addition of CNFs. Similar results were observed with nanofibers in the presence of chitosan films. The improved barrier to water vapor due to the presence of CNFs is attributed to the increased tortuosity as also postulated in case of nanoclay-polymer composites (Sanchez-Garcia and Lagaron, 2010). Apart from CNFs, carbon nanotubes (CNTs) (Kim et al., 2008) and silica nanoparticles are reported to improve the tensile properties of several polymers (Wu et al., 2002 ,Xiong et al., 2008) as summarized in **Table 3**. Xylan is yet another hemicellulose material used for food packaging, which when reinforced with CNF improves the tensile strength and water barrier properties (Saxena et al., 2009).

3.1.2 Metal nanoparticles

The most widely studied metal nanoparticle is silver, principally because of its well-known biocidal activity against a wide range of pathogens including gram-positive, gram-negative bacteria and several fungi (Balazs et al., 2004). Surfaces resistant to bacteria are designed by incorporating silver as silver nanoparticles, silver zeolites or silver ions. While smaller silver nanoparticles have better antimicrobial activity (Baker et al., 2005 ,Panacek et al., 2006) owing to their higher surface to volume ratio, the triangular ones are shown to kill *E.Coli* better than spherical or rod shaped particles (Pal et al., 2007), possibly due to higher atom-density facets. The antimicrobial activity of silver nanoparticles is successfully tested against *E.Coli* (Sondi and Salopek-Sondi, 2004), *E.coli*, *S.aureus* and *P.aeruginosa* (Djokic and Burrell, 1998). The biocidal activity of silver nanoparticles grafted on filter paper against *E.coli* offers promise for food packaging application (Tankhiwale and Bajpai, 2009). Commercial products like Fresh Box from BlueMoonGoods$^{\text{TM}}$ are developed for food storage products based on the antimicrobial properties of silver.

Table 3 Tensile strength properties of various nanocomposites using nanofibres and nanotubes

Nanocomposite (Nanoadditive/ polymer)	Tensile strength of the nanocomposite (MPa)	Percentage increase in tensile strength from pure polymer	Reference
CNT/ polyurethane	21.3	180	(Sahoo et al., 2010)
CNT/ PAN terpolymer	114.8	160	(Ji et al., 2009)
CNT/ Chitosan	73.1	170	(Tang et al., 2008)
CNF/Mango puree films	8.76	214	(Azeredo et al., 2009)
Rice straw nanofiber / Chitosan	193.2	355	(Hassan et al., 2011)
Carbon nanofiber/ epoxy	74.4	110	(Sun et al., 2011)

3.2 Food processing

Nanomaterials exist in the food naturally in the form of proteins, fats etc. Understanding and manipulating such processes lead to smart and interactive food processing materials such as nanocapsules and nanoemulsions. The presence of nanodelivery systems (NDSs) in food could improve the utilization of the nutrients in the body. In this section, we provide insights into some of the NDSs investigated for their usage in food processing.

Nanoencapsulation is the process of packing the materials at nanoscale, typically for controlled delivery purposes. Generally regarded as safe (GRAS) materials and naturally occurring nanoparticles are practiced for delivery of food and other bioactive products. Typically, nanoencapsulation can be carried out by any of the following processes (a) Physical processes (e.g. Spray drying) (b) Physico-chemical processes (e.g. simple and complex coacervation) and (c) Chemical processes (e.g. Interfacial polymerization). Appropriate process for encapsulation is selected depending on the nature of the core material, desired release rate, nature of the substance that has to be encapsulated etc. Examples for nanoencapsulated products include α-lactalbumin, which is a hydrolyzed milk protein as a carrier of nutrients (Bugusu et al., 2009), casein micelles for delivery of sensitive food products (Semo et al., 2007), dextrins for bioactive products and hydrophobically modified starch to encapsulate curcumin (Yu and Huang, 2010). Lipid-based nanoencapsulation can potentially improve the solubility, stability and bioavailability, thus preventing unwanted interactions with other food components. Increase of reactive oxygen species (ROS) such as hydroxyl radical, hydrogen peroxide and superoxide in the body are proven to cause oxidative stress, which in turn can cause pathological disorders such as chronic inflammatory disease and eventually to cancer (Wiseman and Halliwell, 1996). Decrease of this oxidative stress can be accomplished by the presence of anti-oxidants in the body which can inhibit the oxidation by scavenging the ROS. Nanoencapsulation of these anti-oxidants in lipid-based nanocarriers helps in preventing the degradation of food during processing and storage and also helps in reducing the chronic disorders. Nanoliposomes, archaeosomes and nanocochleates are some of the most promising lipid-based carriers for anti-oxidants. Nanocochleates can wrap around micronutrients and has the ability to stabilize and increase the nutritional value of the processed foods (Mannino, 2003). Nanoencapsulated probiotics that could be selectively delivered to certain parts of gastro-intestinal tract might be able to modulate immune responses (Vidhyalakshmi et al., 2009). Examples of nanocapsules in the market include Tip-Top Up bread in Australia which includes fish oil in the capsules (Mazzocchi, 2011), HydraCel, a natural mineral product (≈ 5 nm in size) which reduces the surface tension of drinking water thereby improving the absorption of water and other nutrients in the body (Tonelli, 2011).

Nanoemulsions offer many advantages such as high clarity, decontamination of the food packaging equipment etc. The clarity of the nanoemulsions helps in addition of bioactives and flavors in beverages without compromising the product appearance. Single-layer, double-layer and triple-layer nanoemulsions can be produced using alginate and chitosan polyelectrolytes (Choi et al., 2011). Nanosized self-assembled liquid structures, which are expanded micelles (˜30 nm), are used in the targeted delivery of lycopene, beta-carotene, omega-3 fatty acids, coenzyme Q$_{10}$ (Garti, 2008). It is claimed that canola active oil from Shemen industries, Israel could decrease the cholesterol intake by 14% by nanoencapsulation of fortified phytosterols (Titoria and Groves, 2009).

4. Toxicology of Nanomaterials

Despite the interesting properties, the inconclusive toxicity data on the nanoparticles makes it difficult to achieve unanimous acceptance by consumers. For example, one study concluded that silver nanoparticles when combined with DNA could compromise the replication fidelity (Yang et al., 2009) while Chi et al showed that the silver nanoparticles alone has weak genotoxicity but exhibits significant toxicity when combined with a surfactant such as cetyl pyridinium bromide (Chi et al., 2009). With the increased surface area and other properties such as size, surface chemistry and solubility, the toxicity of the nanomaterials might differ from the bulk material significantly (Gattiand Montanari, 2008; Nel et al., 2006). Also, a study conducted by Bermudez and coworkers indicated that there were significant differences in the pulmonary responses to ultrafine TiO$_2$ nanoparticles between rats, mices and hamsters (Bermudez et al., 2004).This study suggests that the sensitivity nanoparticles may vary from animal to animal, thereby indicating the difficulty in generalizing the bio-effects of nanoparticles.. Although considerable research is being carried out to evaluate the nanoparticles, some concerns such as studying single size nanomaterial, administering high dosage, omitting certain biological parameters need to be addressed (Oberdorster et al., 2007). The biokinetics of certain nanomaterials which possess the ability to bind with proteins or other compounds altering their absorption profile (e.g. chitosan) (Alkhamis et al., 2008) are to be evaluated carefully. From the toxicology results so far, it is imperative that a more structured methodology has to be followed for testing of the nanomaterials. Reports from Food and Agriculture Organization (FAO) and World Health Organization (WHO) suggest that factors such as testing systems, dose metrics and clinical studies need to be considered for assessing nanotoxicology (FAO/WHO, 2010). So far, there is not much data available on the genotoxicity of the nanoparticles (Bouwmeester et al., 2009). The persistence of the nanoparticles in the body might lead to chronic effects, which could cause significant damage to the organs. This makes it important to assess the chronic effects of these particles. The other important factor for the assessment of these particles is the effect of surface area. Typically, dosage

Table 4 Physicochemical and biological indicators to assess nanotoxicology (FAO/WHO, 2010)

Physicochemical indicators	Biological/toxicological indicators
Solubility	Biopersistence
Particle size/size distribution	Bioavailability
Complexity of composition	Biocorona
Surface reactivity	Potential for "Trojan horse" (carriers of contaminants in the body)

of nanoparticles is assessed based on the mass or number. However, studies show that surface area is a much better dose metric than mass, especially when comparing between different types of nanoparticles (Brown et al., 2001 ,Oberdorster et al., 2007). **Table 4** summarizes the FAO/WHO recommended indicators to assess toxicology. Characterization of various particle properties relevant to toxicological assessment are discussed in recent publications (Powers et al., 2006 ,Powers et al., 2007)

5. Concluding Remarks

The integration of novel nanoscale materials such as gold, carbon nanotubes, Qdots into engineered systems has led to applications ranging from highly sensitive biosensors, smart delivery systems for maximizing efficiency and bioavailability in agriculture practices to their role in improving barrier properties of packaging materials, preventing contamination and delivering nutrients effectively in food products. The increased public awareness from the recent pests outbreaks in food and related health implications will necessitate stringent controls and more sensitive methods of detection, prevention and remediation- giving impetus to development of better food and crop protection technologies. Future nanobiotechnology developments would include low cost, portable, real time pathogen detection tools that can be rapidly applied in field settings, food storage and transportation facilities; remediation of pollutants and pathogens; controlling spread of pathogen using nonfouling agents and disinfectants; and more efficient crop protection delivery systems, materials and modalities.

Acknowledgements

The authors acknowledge the partial financial support of the Particle Engineering Research Center (PERC) and the Center for Particulate and Surfactant Systems (CPaSS) at the University of Florida, the National Science Foundation (NSF Grant EEC-94-02989, IIP-0749481) and the CPaSS Industrial Partners. Any opinions, findings, and conclusions or recommendations expressed in this material are those of the author(s) and do not necessarily reflect those of the National Science Foundation.

References

Adame, D., and G.W. Beall.(2009) "Direct measurement of the constrained polymer region in polyamide/clay nanocomposites and the implications for gas diffusion." Applied Clay Science 42:545-552.

Ai, K.L., Y.L. Liu, and L.H. Lu.(2009) "Hydrogen-Bonding Recognition-Induced Color Change of Gold Nanoparticles for Visual Detection of Melamine in Raw Milk and Infant Formula." Journal of the American Chemical Society 131:9496-9497.

Alexandre, B., D. Langevin, P. Mederic, T. Aubry, H. Couderc, Q.T. Nguyen, A. Saiter, and S. Marais.(2009) "Water barrier properties of polyamide 12/montmorillonite nanocomposite membranes: Structure and volume fraction effects." Journal of Membrane Science 328:186-204.

Alkhamis, K.A., M.S. Salem, and M.S. Khanfar.(2008) "The Sorption of Ketotifen Fumarate by Chitosan." Aaps Pharmscitech 9:866-869.

Anjali, C., Sharma, Y., Mukherjee, A. and Chandrasekaran, N. (2012) "Neem oil (Azadirachta indica) nanoemulsion—a potent larvicidal agent against Culex quinquefasciatus. " Pest. Manag. Sci. 68:158–163.

Azeredo, H.M.C., L.H.C. Mattoso, D. Wood, T.G. Williams, R.J. Avena-Bustillos, and T.H. McHugh.(2009) "Nanocomposite Edible Films from Mango Puree Reinforced with Cellulose Nanofibers." Journal of Food Science 74:N31-N35.

Azeredo, H.M.C., L.H.C. Mattoso, R.J. Avena-Bustillos, G. Ceotto, M.L. Munford, D. Wood, and T.H. McHugh. (2010) "Nanocellulose Reinforced Chitosan Composite Films as Affected by Nanofiller Loading and Plasticizer Content." Journal of Food Science 75:N1-N7.

Baker, C., A. Pradhan, L. Pakstis, D.J. Pochan, and S.I. Shah.(2005) "Synthesis and antibacterial properties of silver nanoparticles." Journal of Nanoscience and Nanotechnology 5:244-249.

Balazs, D.J., K. Triandafillu, P. Wood, Y. Chevolot, C. van Delden, H. Harms, C. Hollenstein, and H.J. Mathieu. (2004) "Inhibition of bacterial adhesion on PVC endotracheal tubes by RF-oxygen glow discharge, sodium hydroxide and silver nitrate treatments." Biomaterials 25:2139-2151.

Behnajady, M.A., N. Modirshahla, M. Shokri, and B. Rad. (2008) "Enhancement of photocatalytic activity of TiO(2) nanoparticles by silver doping: Photodeposition versus liquid impregnation methods." Global Nest Journal 10:1-7.

Bermudez, E., J.B. Mangum, B.A. Wong, B. Asgharian, P.M. Hext, D.B. Warheit, and J.I. Everitt.(2004) "Pulmonary responses of mice, rats, and hamsters to subchronic inhalation of ultrafine titanium dioxide particles." Toxicological Sciences 77:347-357.

Bharadwaj, R.K.(2001) "Modeling the barrier properties of polymer-layered silicate nanocomposites." Macromolecules 34:9189-9192.

Botts, F.M., Kohn, F.C. and Miller, M.L.(2008) "Particles containing agricultural active ingredients." US.

Bouwmeester, H., S. Dekkers, M.Y. Noordam, W.I. Hagens, A.S. Bulder, C. de Heer, S.E.C.G. ten Voorde, S.W.P.

Wijnhoven, H.J.P. Marvin, and A.J.A.M. Sips.(2009) “Review of health safety aspects of nanotechnologies in food production.” Regulatory Toxicology and Pharmacology 53:52-62.

Brown, D.M., M.R. Wilson, W. MacNee, V. Stone, and K. Donaldson.(2001) “Size-dependent proinflammatory effects of ultrafine polystyrene particles: A role for surface area and oxidative stress in the enhanced activity of ultrafines.” Toxicology and Applied Pharmacology 175:191-199.

Bugusu, B., C. Mejia, B. Magnuson, and S. Tafazoli.(2009) “Global Regulatory Policies on Food Nanotechnology.” Food Technology 63:24-28.

Businesswire.(2012) “Global Biosensors Market Review by Industry Experts” [Online]. http://www.businesswire.com/news/home/20120316005408/en

Cataldo, D.A., Lipinsky, E.S. and VanVoris, P.(2010) “Use of colloidal clays for sustained release of active ingredients.” US.

Celis, R., G. Facenda, M.C. Hermosin, and J. Cornejo. (2005) “Assessing factors influencing the release of hexazinone from clay-based formulations.” International Journal of Environmental Analytical Chemistry 85:1153-1164.

Chi, Z.X., R.T. Liu, L.Z. Zhao, P.F. Qin, X.R. Pan, F. Sun, and X.P. Hao.(2009) “A new strategy to probe the genotoxicity of silver nanoparticles combined with cetylpyridine bromide.” Spectrochimica Acta Part a-Molecular and Biomolecular Spectroscopy 72:577-581.

Choi, A.J., C.J. Kim, Y.J. Cho, J.K. Hwang, and C.T. Kim. (2011) “Characterization of Capsaicin-Loaded Nanoemulsions Stabilized with Alginate and Chitosan by Self-assembly.” Food and Bioprocess Technology 4:1119-1126.

Choudary, B.M., B.P. Prasad, and M.L. Kantam.(1989) “New Interlamellar Pesticide Metal Montmorillonite Complexes - a Novel Technique for Controlled Release.” Journal of Agricultural and Food Chemistry 37:1422-1425.

Chouhan, R.S., A.C. Vinayaka, and M.S. Thakur.(2010) “Thiol-stabilized luminescent CdTe quantum dot as biological fluorescent probe for sensitive detection of methyl parathion by a fluoroimmunochromatographic technique.” Analytical and Bioanalytical Chemistry 397:1467-1475.

Costello, B.P.J.D., R.J. Ewen, H.E. Gunson, N.M. Ratcliffe, and P.T.N. Spencer-Phillips.(2000) “The development of a sensor system for the early detection of soft rot in stored potato tubers.” Measurement Science & Technology 11:1685-1691.

Crooks, R., Joanicot, M., Prud'Homme, R.K. and Coret, J.(2003) “Aqueous suspension of nanoparticles comprising an agrochemical active ingredient.” US.

Daniel, C., W. Pfammatter, P. Kehrli, and E. Wyss.(2005) “Processed kaolin as an alternative insecticide against the European pear sucker, Cacopsylla pyri (L.).” Journal of Applied Entomology 129:363-367.

Dasary, S.S.R., U.S. Rai, H.T. Yu, Y. Anjaneyulu, M. Dubey, and P.C. Ray.(2008) “Gold nanoparticle based surface enhanced fluorescence for detection of organophosphorus agents.” Chemical Physics Letters 460:187-190.

de Paiva, L.B., A.R. Morales, and F.R.V. Diaz.(2008) “Organoclays: Properties, preparation and applications.” Applied Clay Science 42:8-24.

Debnath, N., S. Das, D. Seth, R. Chandra, S.C. Bhattacharya, and A. Goswami.(2011) “Entomotoxic effect of silica nanoparticles against Sitophilus oryzae (L.).” Journal of Pest Science 84:99-105.

Djokic, S.S., and R.E. Burrell.(1998) “Behavior of silver in physiological solutions.” Journal of the Electrochemical Society 145:1426-1430.

Dungchai, W., W. Siangproh, W. Chaicumpa, P. Tongtawe, and O. Chailapakul.(2008) “Salmonella typhi determination using voltammetric amplification of nanoparticles: A highly sensitive strategy for metalloimmunoassay based on a copper-enhanced gold label.” Talanta 77:727-732.

Ebert, T.A., R.A.J. Taylor, R.A. Downer, and F.R. Hall.(1999) “Deposit structure and efficacy of pesticide application. 1: Interactions between deposit size, toxicant concentration and deposit number.” Pesticide Science 55:783-792.

Eigenbrode, S.D., H.J. Ding, J. Neufeld, and P. Duetting. (2006) “Effects of hydrophilic and hydrophobic kaolin-based particle films on pea aphid (Homoptera : Aphididae) and its entomopathogen Pandora neoaphidis (Entomophthorales : Entomophthoraceae).” Journal of Economic Entomology 99:23-31.

FAO. (2009) State of Food Insecurity in the World 2009 FAO, Rome. (http://www.fao.org/docrep/012/i0876e/i0876e00.htm)

FAO/WHO. (2010) FAO/WHO expert meeting on the application of nanotechnologies in the food and agriculture sectors: potential food safety implications. Food and Agriculture Organization of the United Nations and World Health Organization

Feldheim, D.L., and C.A. Foss. (2002) Metal nanoparticles : synthesis, characterization, and applications Marcel Dekker, New York.

Garti, (ed.) (2008) Delivery and Controlled Release of Bioactives in Foods and Nutraceuticals Woodhead Publishing, Cambridge.

Gatti, M.A.a.M., S. (2008) Nanopathology the health impact of nanoparticles Pan Stanford Publishing Pte.Ltd., Singapore.

Ge, S.G., J.J. Lu, L. Ge, M. Yan, and J.H. Yu.(2011) “Development of a novel deltamethrin sensor based on molecularly imprinted silica nanospheres embedded CdTe quantum dots.” Spectrochimica Acta Part a-Molecular and Biomolecular Spectroscopy 79:1704-1709.

Glenn, D.M., G.J. Puterka, T. Vanderzwet, R.E. Byers, and C. Feldhake.(1999) “Hydrophobic particle films: A new paradigm for suppression of arthropod pests and plant diseases.” Journal of Economic Entomology 92:759-771.

Godfray, H.C.J., J.R. Beddington, I.R. Crute, L. Haddad, D. Lawrence, J.F. Muir, J. Pretty, S. Robinson, S.M. Thomas, and C. Toulmin.(2010) "Food Security: The Challenge of Feeding 9 Billion People." Science 327:812-818.

Gonzalez-Melendi, P., R. Fernandez-Pacheco, M.J. Coronado, E. Corredor, P.S. Testillano, M.C. Risueno, C. Marquina, M.R. Ibarra, D. Rubiales, and A. Perez-De-Luque.(2008) "Nanoparticles as smart treatment-delivery systems in plants: Assessment of different techniques of microscopy for their visualization in plant tissues." Annals of Botany 101:187-195.

Greiner, A., Wendorff, J.H., and Ishaque, M.(2008) "Method for producing nanofibers and mesofibers by the electrospinning of colloidal dispersions." US.

Grube, A., D. Donaldson, T. Kiely, and L. Wu.(2011) "Pesticides Industry Sales and Usage" [Online]. http://www.epa.gov/opp00001/pestsales/07pestsales/market_estimates2007.pdf

Grunert, K.G.(2005) "Food quality and safety: consumer perception and demand." European Review of Agricultural Economics 32:369-391.

Guo, Y.R., S.Y. Liu, W.J. Gui, and G.N. Zhu.(2009) "Gold immunochromatographic assay for simultaneous detection of carbofuran and triazophos in water samples." Analytical Biochemistry 389:32-39.

Hassan, M.M., M. Mueller, D.J. Tartakowska, and M.H. Wagner.(2011) "Mechanical Performance of Hybrid Rice Straw/Sea Weed Polypropylene Composites." Journal of Applied Polymer Science 120:1843-1849.

He, Q.J., and J.L. Shi.(2011) "Mesoporous silica nanoparticle based nano drug delivery systems: synthesis, controlled drug release and delivery, pharmacokinetics and biocompatibility." Journal of Materials Chemistry 21:5845-5855.

Ho, Y.P., M.C. Kung, S. Yang, and T.H. Wang.(2005) "Multiplexed hybridization detection with multicolor colocalization of quantum dot nanoprobes." Nano Letters 5:1693-1697.

Hodges, A.W., and T.H. Spreen. (2012) Economic Impacts of Citrus Greening (HLB) in Florida, 2006/07–2010/11. Food and Resource Economics Department, Florida Cooperative Extension Service, Institute of Food and Agricultural Sciences, University of Florida

Hoppe, P.P., K. Kramer, H. van den Berg, G. Steenge, and T. van Vliet.(2003) "Synthetic and tomato-based lycopene have identical bioavailability in humans." European Journal of Nutrition 42:272-278.

Ikariyama, Y., S. Nishiguchi, E. Kobatake, M. Aizawa, M. Tsuda, and T. Nakazawa.(1993) "Luminescent Biomonitoring of Benzene-Derivatives in the Environment Using Recombinant Escherichia-Coli." Sensors and Actuators B-Chemical 13:169-172.

Ji, J.Y., G. Sui, Y.H. Yu, Y.X. Liu, Y.H. Lin, Z.J. Du, S. Ryu, and X.P. Yang.(2009) "Significant Improvement of Mechanical Properties Observed in Highly Aligned Carbon-Nanotube-Reinforced Nanofibers." Journal of Physical Chemistry C 113:4779-4785.

Jurado-Exposito, M., Castejon-Munoz, M. and Garcıa-Torres, L.(1996) "Broomrape (Orobanche crenata) control with imazethapyr applied to pea (Pisumsativum) seed." Weed Technol 10:774-780.

Kim, J.Y., S. Il Han, and S.P. Hong.(2008) "Effect of modified carbon nanotube on the properties of aromatic polyester nanocomposites." Polymer 49:3335-3345.

Krishna, V., N. Noguchi, B. Koopman, and B. Moudgil.(2006) "Enhancement of titanium dioxide photocatalysis by water-soluble fullerenes." Journal of Colloid and Interface Science 304:166-171.

Lan, T., Cho, J., Liang, Y., Qian, J. and Maul, P. (2001) Applications of Nanomer(R) in nanocomposites: from concept to reality Nanocomposites 2001. Nanocor (R), Chicago, IL, USA.

Li, Z.Z., J.F. Chen, F. Liu, A.Q. Liu, Q. Wang, H.Y. Sun, and L.X. Wen.(2007) "Study of UV-shielding properties of novel porous hollow silica nanoparticle carriers for avermectin." Pest Management Science 63:241-246.

Liu, F., L.X. Wen, Z.Z. Li, W. Yu, H.Y. Sun, and J.F. Chen.(2006) "Porous hollow silica nanoparticles as controlled delivery system for water-soluble pesticide." Materials Research Bulletin 41:2268-2275.

Liu, Y., Z. Tong, and R.K. Prud'homme.(2008) "Stabilized polymeric nanoparticles for controlled and efficient release of bifenthrin." Pest Management Science 64:808-812.

Mannino, D. (2003) New BioGeode(TM) cochleates could make healthy nutrients more available in processed foods

Margadassi, S., Dayan, B., Levi-Ruso.(2010)" Pesticide nanoparticles obtained from microemulsions and nanoemulsions." US.

Marketsandmarkets.(2011) "Global Active, Smart and Intelligent Packaging Market By Products, Applications, Trends and Forecasts (2010-2015)" [Online]. http://www.marketsandmarkets.com/PressReleases/smart-packaging-market.asp

Markus, A., Linder, C., Strongin, P.(2009) "Solid core microcapsular compositions and uses thereof." US.

Maul, P. 2005. Barrier enhancement using additives. Fillers, Pigment and Additives for plastics in packaging applications, Brussels, Belgium.

Maxwell, K.E. (1937) The biology and control of the hairy clinch bug, Blissus hirtux Montd., infesting turf in Long Island. Ph.D. , Cornell University, Ithaca, NY.

Mazzocchi, S.(2011) "5 things you need to know about nanofoods" [Online]. http://www.pbs.org/wnet/need-to-know/five-things/nanofoods/6682/

McClements, D.J., Li, Y.(2010) "Structured emulsion-based delivery systems: controlling the digestion and release of lipophilic food components." Adv Colloid Interface Sci 159:213-228.

McHugh, T. (2007) Food Nanotechnology: Food Packaging Applications.

Mewis, I., and C. Ulrichs.(2001) "Effects of diatomoceous earth on water content of Sitophilus granarius (L.) (Col., Curculionidae) and its possible use in stored product protection." Journal of Applied Entomology-Zeitschrift Fur Angewandte Entomologie 125:351-360.

Mirzadeh, A., and M. Kokabi.(2007) "The effect of composition and draw-down ratio on morphology and oxygen permeability of polypropylene nanocomposite blown films." European Polymer Journal 43:3757-3765.

Mishael, Y.G., T. Undabeytia, O. Rabinovitz, B. Rubin, and S. Nir.(2002) "Slow-release formulations of sulfometuron incorporated in micelles adsorbed on montmorillonite." Journal of Agricultural and Food Chemistry 50:2864-2869.

Moaveni, P., Farahani,H.A. and Maroufi,K.(2011) "Effect of TiO_2 nanoparticles spraying on quality and quantity of wheat (*Triticum Aestium* L.)." Advances in Environmental Biology 5:2211-2213.

Mukopadhyay, B., M. Martins, R. Karamanska, D. Russell, and R.A. Field.(2009) "Bacterial detection using carbohydrate-functionalised CdS quantum dots : a model study exploiting E. coli recognition of mannosides." Tetrahedron Letters 50:886-889.

Munteanu, F.D., A. Lindgren, J. Emneus, L. Gorton, T. Ruzgas, E. Csoregi, A. Ciucu, R.B. van Huystee, I.G. Gazaryan, and L.M. Lagrimini.(1998) "Bioelectrochemical monitoring of phenols and aromatic amines in flow injection using novel plant peroxidases." Analytical Chemistry 70:2596-2600.

Nel, A., T. Xia, L. Madler, and N. Li.(2006) "Toxic potential of materials at the nanolevel." Science 311:622-627.

Nicolaos, G., S. Crauste-Manciet, R. Farinotti, and D. Brossard.(2003) "Improvement of cefpodoxime proxetil oral absorption in rats by an oil-in-water submicron emulsion." International Journal of Pharmaceutics 263:165-171.

Nir, S., Rubin, B., Mishael, Y., Undabeytia, Rabinovitch and Polubesova.(2006) "Controlled release formulations of anionic herbicides." US.

Oberdorster, G., V. Stone, and K. Donaldson.(2007) "Toxicology of nanoparticles: A historical perspective." Nanotoxicology 1:2-25.

ObservatoryNano. 2010 Nanotechnologies for nutrient and biocide delivery in agriculture production.

Oerke, E.C.(2006) "Crop losses to pests." Journal of Agricultural Science 144:31-43.

Orozlan, P.D., G.L., Ehrat,M. and Widmer, H.M.(1993) "Fiber-optic atrazine immunosensor." Sensors and Actuators B-Chemical 11:301.

Pal, S., Y.K. Tak, and J.M. Song.(2007) "Does the antibacterial activity of silver nanoparticles depend on the shape of the nanoparticle? A study of the gram-negative bacterium Escherichia coli." Applied and Environmental Microbiology 73:1712-1720.

Panacek, A., L. Kvitek, R. Prucek, M. Kolar, R. Vecerova, N. Pizurova, V.K. Sharma, T. Nevecna, and R. Zboril.(2006) "Silver colloid nanoparticles: Synthesis, characterization, and their antibacterial activity." Journal of Physical Chemistry B 110:16248-16253.

Pintilie, M., Oprica, L., Surleac, M. , Dragut, I.C. and Creanga, D.E.(2004) "Enzyme activity in plants treated with magnetic liquid." Romanian journal of physics 51:239-244.

Powers, K.W., S.C. Brown, V.B. Krishna, S.C. Wasdo, B.M. Moudgil, and S.M. Roberts.(2006) "Research strategies for safety evaluation of nanomaterials. Part VI. Characterization of nanoscale particles for toxicological evaluation." Toxicological Sciences 90:296-303.

Powers, K.W., M. Palazuelos, B.M. Moudgil, and S.M. Roberts.(2007) "Characterization of the size, shape, and state of dispersion of nanoparticles for toxicological studies." Nanotoxicology 1:42-51.

Rana, J.S., Jindal, J.,Beniwal, V. and Chhokar,V.(2010) "Utility Biosensors for applications in Agriculture – A Review." Journal of American Science 6:353-375.

Rubin, B., El-Nahhal, Y., Nir, S. and Marugulies, L.(2001) "Slow release formulations of pesticides." US.

Sahoo, N.G., Rana, S., Cho, J.W., Li, L., and Chan, S.H.(2010) "Polymer nanocomposites based on functionalized carbon nanotubes." Progress in Polymer Science 35:837–867.

Sanchez-Garcia, M., and J. Lagaron.(2010) "On the use of plant cellulose nanowhiskers to enhance the barrier properties of polylactic acid." Cellulose 17:987-1004.

Santra, S.(2011) "Multifunctinal silica-based compositions and gels, methods of making them, and methods of using them." US.

Saxena, A., T.J. Elder, S. Pan, and A.J. Ragauskas.(2009) "Novel nanocellulosic xylan composite film." Composites Part B-Engineering 40:727-730.

Semo, E., E. Kesselman, D. Danino, and Y.D. Livney.(2007) "Casein micelle as a natural nano-capsular vehicle for nutraceuticals." Food Hydrocolloids 21:936-942.

Sherman, L.M. (2004) Chasing Nanocomposites PlasticsTechnology.

Solans, C., P. Izquierdo, J. Nolla, N. Azemar, and M.J. Garcia-Celma.(2005) "Nano-emulsions." Current Opinion in Colloid & Interface Science 10:102-110.

Sondi, I., and B. Salopek-Sondi.(2004) "Silver nanoparticles as antimicrobial agent: a case study on E-coli as a model for Gram-negative bacteria." Journal of Colloid and Interface Science 275:177-182.

Su, M.Y., X. Wu, C. Liu, C.X. Qu, X.Q. Liu, L. Chen, H. Huang, and F.S. Hong.(2007) "Promotion of energy transfer and oxygen evolution in spinach photosystem II by nano-anatase TiO_2." Biological Trace Element Research 119:183-192.

Sun, L.H., Z. Ounaies, X. Gao, C.A. Whalen, and Z. Yang. (2010) "Preparation, Characterization, and Modeling of Carbon Nanofiber/Epoxy Nanocomposites." Journal of Nanomaterials.

Tadros, T., R. Izquierdo, J. Esquena, and C. Solans.(2004) "Formation and stability of nano-emulsions." Advances in Colloid and Interface Science 108:303-318.

Tang, C.Y., L.X. Xiang, J.X. Su, K. Wang, C.Y. Yang, Q. Zhang, and Q. Fu.(2008) "Largely improved tensile properties of chitosan film via unique synergistic reinforcing effect of carbon nanotube and clay." Journal of Physical Chemistry B 112:3876-3881.

Tankhiwale, R., and S.K. Bajpai. (2009) "Graft copolymerization onto cellulose-based filter paper and its further development as silver nanoparticles loaded antibacterial food-packaging material." Colloids and Surfaces B-Biointerfaces 69:164-168.

Tenkorang, F., and J. Lowenberg-DeBoer. (2008) "On-Farm Profitability of Remote Sensing in Agriculture." Journal of Terrestrial Observation 1.

Titoria, P.a.G., K. (2009) "Nanotechnology for the food industry" [Online]. http://nanomagazine.co.uk/index.php?option=com_content&view=article&id=56:nanotechnology-for-the-food-industry&catid=37:issue-13&Itemid=151

Toledano, O., Binyamin, Bar-Simantov and Seri-Levy. (2008) "Methods for crop protection." US.

Tonelli, R.D. (2011) Neurotech research a new science of spirit.

Troncoso, E., Aguilera, J.M., and McClements, D.J. (2012) "Fabrication, characterization and lipase digestibility of food-grade nanoemulsions." Food Hydrocolloids 27:355-363.

USDA. (2007) Citrus greening:questions and answers. United States Department of Agriculture (USDA)

VanVoris, P., Cataldo, D.A., Lipinsky, E.S. (2006) "Sustained release pest control products and their applications." US.

Vidhyalakshmi, R., R. Bhakyaraj, and R.S. Subhadree. (2009) "Encapsulation "The future of probiotics" - A review." Analytical and Bioanalytical Chemistry 397:1445-1455.

Viswanathan, S., H. Radecka, and J. Radecki. (2009) "Electrochemical biosensor for pesticides based on acetylcholinesterase immobilized on polyaniline deposited on vertically assembled carbon nanotubes wrapped with ssDNA." Biosensors & Bioelectronics 24:2772-2777.

Wang, L.J., X.F. Li, G.Y. Zhang, J.F. Dong, and J. Eastoe. (2007) "Oil-in-water nanoemulsions for pesticide formulations." Journal of Colloid and Interface Science 314:230-235.

Wang, M., and Z.Y. Li. (2008) "Nano-composite ZrO2/Au film electrode for voltammetric detection of parathion." Sensors and Actuators B-Chemical 133:607-612.

Wang, Y., Pfeffer, R. and Dave, R. (2009) "Polymer coating/encapsulation of nanoparticles using a supercritical antisolvent process." US.

Weiss, J., TAKHISTOV,P., MCCLEMENTS, J. (2006) "Functional Materials in Food Nanotechnology."

Wiseman, H., and B. Halliwell. (1996) "Damage to DNA by reactive oxygen and nitrogen species: Role in inflammatory disease and progression to cancer." Biochemical Journal 313:17-29.

Wu, C.L., M.Q. Zhang, M.Z. Rong, and K. Friedrich. (2002) "Tensile performance improvement of low nanoparticles filled-polypropylene composites." Composites Science and Technology 62:1327-1340.

Xiong, M., K. Zhang, and Y.M. Chen. (2008) "ATRP of 3-(triethoxysilyl)propyl methacrylate and preparation of "stable" gelable block copolymers." European Polymer Journal 44:3835-3841.

Yang, F., C. Liu, F.Q. Gao, M.Y. Su, X. Wu, L. Zheng, F.S. Hong, and P. Yang. (2007) "The improvement of spinach growth by nano-anatase TiO_2 treatment is related to nitrogen photoreduction." Biological Trace Element Research 119:77-88.

Yang, H., H.P. Li, and X.P. Jiang. (2008) "Detection of foodborne pathogens using bioconjugated nanomaterials." Microfluidics and Nanofluidics 5:571-583.

Yang, G.J., J.L. Huang, W.J. Meng, M. Shen, and X.A. Jiao. (2009) "A reusable capacitive immunosensor for detection of Salmonella spp. based on grafted ethylene diamine and self-assembled gold nanoparticle monolayers." Analytica Chimica Acta 647:159-166.

Yang, M.H., Y. Kostov, H.A. Bruck, and A. Rasooly. (2009) "Gold nanoparticle-based enhanced chemiluminescence immunosensor for detection of Staphylococcal Enterotoxin B (SEB) in food." International Journal of Food Microbiology 133:265-271.

Yang, W.J., C.C. Shen, Q.L. Ji, H.J. An, J.J. Wang, Q.D. Liu, and Z.Z. Zhang. (2009) "Food storage material silver nanoparticles interfere with DNA replication fidelity and bind with DNA." Nanotechnology 20.

Yu, Z., Hyne, J.B. and Grist, M.E. (2004) "Controlled release rate of fertilizers and methods of making same." US.

Yu, H.L., and Q.R. Huang. (2010) "Enhanced in vitro anticancer activity of curcumin encapsulated in hydrophobically modified starch." Food Chemistry 119:669-674.

Zhang, C., Y. Ding, Q.E. Ping, and L.L. Yu. (2006) "Novel chitosan-derived nanomaterials and their micelle-forming properties." Journal of Agricultural and Food Chemistry 54:8409-8416.

Zhao, X.J., L.R. Hilliard, S.J. Mechery, Y.P. Wang, R.P. Bagwe, S.G. Jin, and W.H. Tan. (2004) "A rapid bioassay for single bacterial cell quantitation using bioconjugated nanoparticles." Proceedings of the National Academy of Sciences of the United States of America 101:15027-15032.

Zhu, H., J. Han, J.Q. Xiao, and Y. Jin. (2008) "Uptake, translocation, and accumulation of manufactured iron oxide nanoparticles by pumpkin plants." Journal of Environmental Monitoring 10:713-717.

Author's short biography

Aarthi Narayanan

Aarthi Narayanan received her B.Tech. in Chemical Engineering from Sri Venkateswara University, India in 2006 and Masters of Science in Environmental Engineering from University of Miami, USA in 2010. She joined Particle Engineering Research Center (PERC) at the University of Florida as a Research Staff in 2011. Her work at PERC is focused on modification of clays and controlled release of agrochemicals.

Parvesh Sharma

Parvesh Sharma received his B.Sc. and M.Sc. in Chemistry from St. Stephen's College, Delhi University. He completed his Ph. D. in the area of analytical coordination Chemistry from Department of Chemistry, Delhi University in 1998. He joined the Chemistry Faculty; St. Stephen's College, Delhi University and taught for 7 years. He is currently working as Research Assistant Scientist in Particle Engineering Research Center at the University of Florida, Gainesville, USA. His areas of interests include development of engineered particulates for medicinal and agricultural applications, non-invasive imaging, multimodal-multifunctional nanoparticles, controlled release formulations, nanotoxicology, and applications of surfactants/polymers in industrial processes.

Brij M. Moudgil

Dr. Brij M. Moudgil is a Distinguished Professor and Alumni Professor of Materials Science and Engineering at the University of Florida. His current research interests are in particulate materials based systems for enhanced performance in bioimaging, nanomedicine, photocatalytic degradation of hazardous microbes, polymer and surfactant adsorption, dispersion and aggregation of fine particles and nanotoxicity.

Dr. Moudgil received his B.E from the Indian Institute of Science, Bangalore, India and his M.S and Eng.Sc.D degrees from Columbia University, New York. He has published more than 400 technical papers and has been awarded 14 patents. He is a member of the U.S National Academy of Engineering.

Mechanochemical Synthesis of Lithium-Niobate-Doped Copper Oxide[†]

Aleksey Alekseevich Gusev*, **Vitaliy Petrovich Isupov and Evgeniy Grigorievich Avvakumov**
[1] *Institute of Solid State Chemistry and Mechanochemistry SB RAS*

Abstract

It is demonstrated by means of XRD, IR spectroscopy, electron microscopy, laser light scattering and measurements of the specific surface area that mechanical activation of a mixture of lithium carbonate, niobium pentoxide and copper oxide in the planetary centrifugal activator AGO-2 involves mixing, dispersion and amorphization of the components, as well as the phase transition of the monoclinic form of niobium (V) oxide into its orthorhombic form. Subsequent mechanical treatment results in the partial formation of a lithium-niobate phase. Thermal treatment of the compacts prepared from mechanically activated powders, at a temperature above 400℃, leads to the appearance of the structure-forming trigonal phase based on $LiNbO_3$*. The data obtained provide evidence that the mechanochemical method is promising for the synthesis of solid solutions based on lithium niobate.*

Keywords: mechanochemical activation, lithium-niobate, modifying additive, sintering, ceramic, piezomaterial

Introduction

The majority of ceramics manufactured in the world are based on lead-containing materials. These materials possess unquestionable advantages but they also have essential disadvantages; one of them is the substantial volatility of lead and its compounds, which causes complications of the technological process for the conservation of the stoichiometry of compounds during ceramics sintering. At the same time, lead is a toxic element, a poison of cumulative action, and it is very hazardous for living organisms. At present therefore, much attention is paid to the development and synthesis of lead-free piezomaterials and piezoelements as the basis for manufacturing measuring devices. These materials include niobates of alkaline metals modified with various additives.

According to the classic technology, the synthesis of the niobates of alkaline metals is generally carried out at a temperature above 750℃ in two stages (each stage lasts for 6 hours) with intermediate grinding, and sintering is carried out at even higher temperatures (>1000℃) for 5 ÷ 6 hours, for example, similarly to 1). The duration of synthesis and its labor-intensive character stimulated the development of new methods for the synthesis of piezoceramic materials; one of these methods is a mechanochemical method[2,3]. Most attention is paid in these works to investigation of the parameters of mechanochemical synthesis affecting the target characteristics of niobates and ceramics based on it. Substantially poorer is the study of the role of mechanical activation in the synthesis. In the present work we study the mechanism of the mechanochemical synthesis of the solid solution based on lithium niobates with copper oxide as the modifying additive. The choice of this system as the subject of investigation is connected with the fact that the materials of this type have a high Curie point (T_C >1200℃), high working temperature – up to 950℃, and low permittivity, which is favorable for the use of these materials in high-temperature high-frequency measuring devices[4,5].

Experimental

Initial reagents for the synthesis of the indicated

[†] Accepted: June 26, 2012

[1] ISSCM SB RAS, Kutateladze str., 18, 630129, Novosibirsk, Russia.
* Corresponding author:
E-mail: gusev@solid.nsc.ru
TEL: +8-383-2170548

ⓒ 2013 Hosokawa Powder Technology Foundation

material were Li_2CO_3 and CuO powders of a quality not less than the pure reagent grade, while the initial Nb_2O_5 was of extra-pure grade. According to the data of XRD, niobium oxide is the monoclinic modification with the space group P2 (no. 3) and lattice parameters close to a = 21.16 Å, b = 3.822 Å, c = 19.350 Å, β = 119.83° (card no. 72-1121). The components' ratio was as follows:

$Li_2CO_3 + Nb_2O_5 + XCuO$

Here X = 0.1, 0.15, 0.2 (2.62; 3.88; and 5.11 mass %, respectively).

A mixture of powdered reagents was placed in provisionally lined cylinders as the weighed portions of 10 g; activation in the planetary-centrifugal mill AGO-2 was carried out[6] with ball acceleration 40 g for 10 and 30 minutes. Steel balls 8 mm in diameter were used for activation, the mass of balls was 200 g. After five minutes of activation in each case, the cylinders were opened, the powder was taken out and mixed, then put back into the cylinders for further mechanical activation.

X-ray diffraction of the initial reagents and the activation products before and after thermal treatment was carried out using a DRON-3 diffractometer ($Cu_{K\alpha}$ radiation, focusing scheme according to Bragg – Brentano).

The specific surface was determined using the gas adsorption method on the basis of argon desorption[7]. The milled iron content was determined by means of atomic adsorption with a Varian 280FS spectrophotometer. Photographs of the powders were taken with the scanning electron microscope TM-1000 made by «HITACHI». The samples were weighed with an UW 220H balance made by SHIMATZU with an accuracy of 0.001 g, the geometric size was determined with the help of a micrometer with an accuracy of 0.001 mm.

Samples were pressed in tablets 10 mm in diameter using a hydraulic press with a pressing force up to 10 t/cm^2.

After pressing, the samples were placed in a crucible filled with aluminum oxide, and heated within the temperature range 400 to 1040℃. The rate of sample heating to 600℃ was 20 degrees per minute; at 600 ℃ and above it was 10 degrees per minute. At all the given temperature points, the samples were heated for 2 hours. Samples were cooled in the furnace after it was switched off.

The IR spectra were recorded with the help of a Tensor 27 spectrometer. The samples for investigation were prepared according to the standard procedure.

Results and Discussion

Processes taking place during mechanical activation of the reagent mixture

Data of XRD and IR Spectroscopy

According to the XRD data (**Fig. 1**), after mechanical activation of the mixture for 10 minutes we observe a decrease in the intensity and broadening of the reflections of all the initial components, and the appearance of the reflections of niobium oxide in the orthorhombic modification. The appearance of the reflections in the orthorhombic modification is evidence of the mechanically stimulated transition of the monoclinic modification into the orthorhombic one with the space group Pbam (no.55)[8]. Mechanochemically stimulated phase transition in niobium oxide was observed previously in 9). It should be stressed that after mechanical activation for 10 min, a mixture with a lower copper oxide content (0.1CuO) exhibits a more substantial phase transition in Nb_2O_5 (monoclinic – orthorhombic) than the mixture containing 0.2CuO. It may be assumed that an increase in the amount of copper oxide is the deterrent for this transition.

A further increase in activation time to 30 minutes causes even more noticeable (almost complete) amorphization of the initial reagents, the disappearance of the reflections characteristic of lithium carbonate and copper oxide, and a further decrease

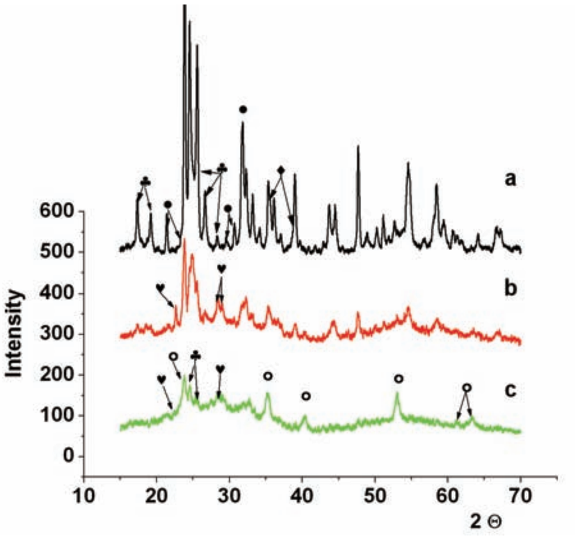

Fig. 1 a) – initial powdered mixture containing 0.2 CuO;
b) – mechanical activation for 10 min
c) – mechanical activation for 30 min
♣ – Nb_2O_5 monoclinic; ♥ – Nb_2O_5 orthorhombic;
● – Li_2CO_3; ◆ – doping additive CuO,
○ – lithium niobate $LiNbO_3$

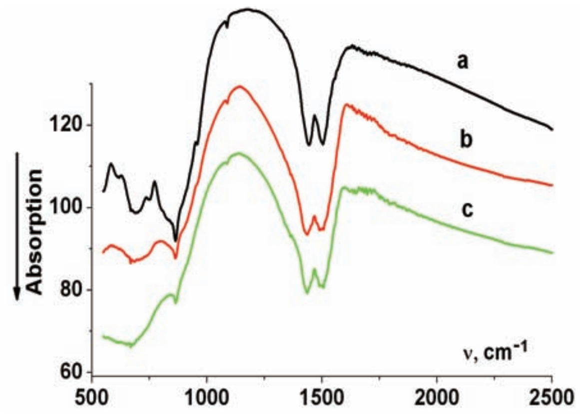

Fig. 2 IR absorption spectra of the samples containing 0.2 CuO:
a) – initial composition; b) – mechanical activation for 10 min;
c) – mechanical activation for 30 min

in the intensity of reflections related to niobium pentoxide, both in the initial monoclinic modification and in the orthorhombic one, formed during mechanochemical treatment. In addition, with an increase in activation time to 30 minutes, we observe the appearance of reflections that are close in their positions to the reflections of lithium niobate (012, 104, 110, 113, 116) of orthorhombic modification (S.G. R3c).

The IR spectra of the reagent mixture (**Fig. 2**) in the region 550-2000 cm^{-1} contain the bands related to lithium carbonate (1505, 1443, 1088, 860 cm^{-1}) and niobium oxide (958, 815, 750, 690, 610 cm^{-1}). Preliminary mechanical activation for 10 minutes causes an asymmetric broadening of the doublet in the region 1500 $cm^{-1,}$ which is assigned to the stretching vibrations of C-O bonds of carbonate ions. Broadening is also observed for other bands of carbonate ions that are present in the spectra: 1088 and 860 cm^{-1}. Activation also causes changes of the bands related to niobium oxide. The disappearance of the bands at 750 and 610 cm^{-1} is observed, as well as broadening of the bands with the maxima at 958, 675 and 820 cm^{-1}.

According to the IR spectroscopic data, an increase in the activation time to 30 minutes leads to further broadening of the doublet at 1500 cm^{-1}; a shoulder is seen to appear on its slope at ~1340 cm^{-1}. A further decrease in the intensities of other bands related to carbonate ion (1088 and 860 cm^{-1}) is observed. Mechanical activation causes further broadening and a decrease in the intensity of niobium oxide band at 825 cm^{-1}. In addition, a broadened band with the maximum at 700 cm^{-1} is observed to appear; it is characteristic of lithium niobate[10,11].

In other words, the data of IR spectroscopy - similarly to the data of XRD - provide evidence that the processes of lithium niobate phase take place. It is interesting to stress that after mechanical activation for 10 min, the powder becomes gray, whereas after activation for 25 min it becomes greenish, and after activation for 30 min the powder becomes light green. These data allow us to assume that activation involves partial interaction of copper oxide with lithium carbonate resulting in formation of the compounds containing copper cations; their coordination sphere includes carbonate ions.

Changes of the disperse state and specific surface of the solid phase during activation

Table 1 shows the results of specific surface measurements and determination of the milled iron content as a result of mechanical activation of the samples. It follows from the data presented in the table that the specific surface of a powder mixture increases to 8.95 m^2/g under the effect of activation.

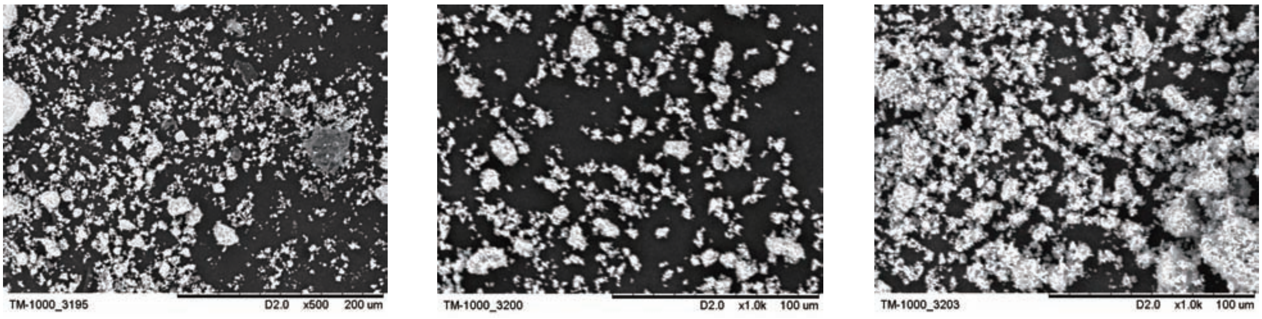

a) b) c)

Fig. 3 Electron microscopic images of the samples containing 0.2 CuO:
a) – Initial powdered mixture; visible are the particles possessing the anisotropic shape. Magnification - 500
b) – Mechanical activation for 10 min; the formation of smaller particles. Magnification - 1000
c) – Mechanical activation for 30 min; the formation of rather large aggregates. Magnification - 1000

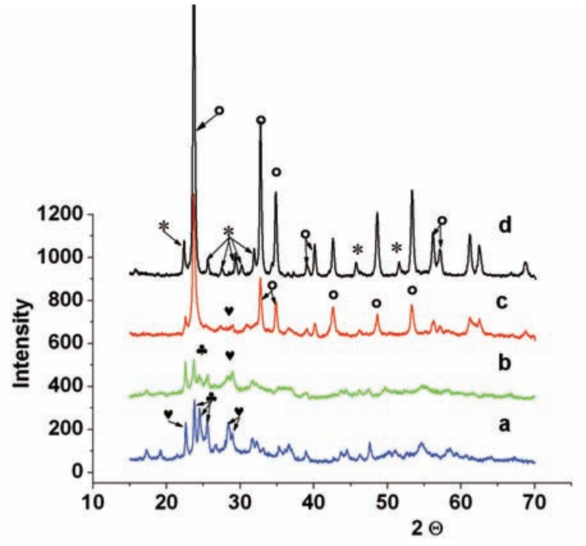

Fig. 4 Diffraction patterns of mechanically activated mixture
a) – 10 minutes, 0.1 CuO and the products of its thermal treatment at
b) – 400℃; c) – 500℃; d) – 600℃.
○ – lithium niobate $LiNbO_3$
∗ – $Cu_2LiNb_5O_{15}$; ♣ – Nb_2O_5 monoclinic;
♥ – Nb_2O_5 orthorhombic

Table 1 Specific surface and milled iron content depending on the time of mechanical activation of the samples

Activation time, min.	0	10	30
Specific surface, m^2/g	1.67	4.71	8.95
Fe content, mass %	0.006	0.013	0.019

The results of electron microscope studies of the samples are shown in **Fig. 3**. One can see in photograph (**Fig. 3a**) that the initial powder contains the particles possessing the anisotropic shape. Activation of this powder for 10 minutes (**Fig. 3b**), along with the formation of smaller particles, causes the formation of agglomerates having the isotropic shape. A further increase in activation time to 30 minutes (**Fig. 3c**) leads to the formation of smaller particles, although at the same time we observe the formation of rather large aggregates. The average size of particles in the mixture, D, determined from the data on the specific surface according to equation $D = 6/\rho S$ (where ρ is the average density of the mixture in g/cm^3, which is close to 3.6; S - is the specific surface in cm^2/g), is 0.3 – 0.4 μm.

Mechanical activation of the mixture therefore causes the formation of aggregates with the size varying from several micrometers to several tens of micrometers, including submicron particles of lithium carbonate, niobium oxide, and copper oxide.

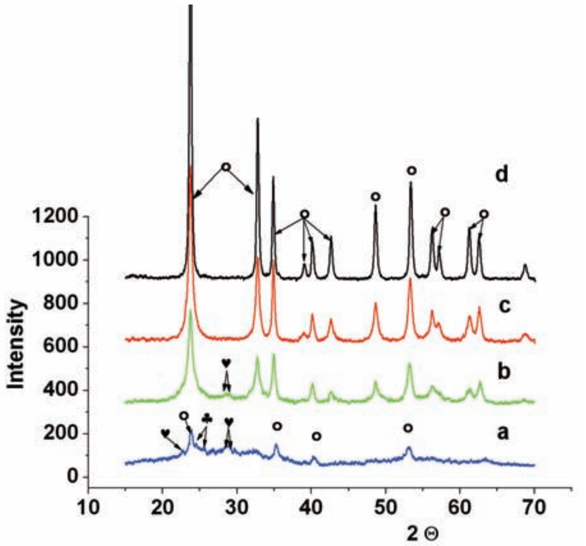

Fig. 5 Diffraction patterns of mechanically activated mixture:
a) – 30 minutes, 0.1 CuO and the products of its thermal treatment at
b) – 400℃; c) – 500℃; d) – 600℃
♣ – Nb_2O_5 monoclinic;
♥ – Nb_2O_5 orthorhombic
○ – solid solution based on lithium niobate $Li_{0.97}NbO_3$.

Thermal treatment of mechanically activated samples

Samples after Activation for 10 minutes, with 0.1 CuO Content

Compact samples in the form of tablets 10 mm in diameter and about 1 mm thick were formed without a plasticizer using a hydraulic press under a pressure force of 10 t/cm^2.

After heating at 400℃ and 500℃, the samples still contain substantial amounts of unreacted niobium oxide phases (**Fig. 4b, c**). After heating at 600℃ (**Fig. 4d**), a two-phase structure is formed; one of the phases is rhombohedral lithium niobate, the second one has tetragonal modification and corresponds to the compound $Cu_2LiNb_5O_{15}$. This phase is conserved for all the studied heating temperature points. Its amount on the surface of the tablets is noticeably larger than inside the tablets. This is confirmed by the fact that after polishing the tablets to a depth of 0.05 mm, this phase is barely pronounced in the X-ray diffraction patterns. For the samples with the high CuO content, and for all the samples with longer activation times, this phase is not formed.

Samples after Activation for 30 minutes

One can see in **Fig. 5** that after activation for

30 min (for any CuO content), the samples exhibit formation of the phase based on lithium niobate, although it is still far from perfect.

The diffraction patterns of the sample obtained after heating at 400℃ contain intense reflections of the new compound along with the weak reflections of unreacted initial components. These reflections coincide with the reflections of lithium niobate having the composition $LiNbO_3$ (**Fig. 5b**).

After heating at 500℃ (**Fig. 5c**), the structure based on the solid solution of lithium niobate having the rhombohedral modification with the space group R3c (no.161) is formed. Its reflections coincide in their positions and intensities with the deflections of compound $Li_{0.97}NbO_3$ with higher accuracy than they do with the composition $LiNbO_3$. The formation of this structure is characteristic of the samples with any copper oxide content. The concentrations of impurities and unreacted phases are comparable with the background level.

The diffraction patterns of the samples annealed at a temperature of 600℃ and above exhibit almost no differences from each other, conserving an almost identical distribution of reflection intensities. Even the traces of initial components are absent from the patterns; the ratios of reflection intensities now coincide better with the data for the solid solution based on lithium niobate having the composition $Li_{0.75}Cu_{0.2}Nb_{1.01}O_3$, rhombohedral, S.G. R3c (no. 161).

It may be concluded from analysis of the diffraction patterns that chemical reactions in the samples stop mainly at the heating temperature in the range of 500℃ to 600℃. Lithium carbonate decomposes into lithium oxide, while carbon dioxide evolves into the atmosphere, which is also confirmed by the mass loss of the samples. For example, the mass loss is about 13% after sintering at 500℃, while the maximal mass change is about 14% (1040℃).

Change in the density of compacted samples during heating

Thermal treatment causes no change to the shape of tablets obtained by pressing mechanically activated mixtures. This allowed us to determine the average density of initial pressed samples and the samples subjected to thermal treatment based on tablet size and mass.

The changes in the average density of samples as a function of the activation time, composition and heating temperature are plotted in **Fig. 6**. The initial density of samples after pressing was averaged over a series of 10 samples; it is 3.29 and 3.35 g/cm^3 for an activation time of 10 and 30 minutes, respectively. One can see that these values differ from each other insignificantly. With an increase in heating temperature, value scattering increases; at 500 – 600℃ scattering is maximal, then decreases. Within this temperature range, the density of the samples at first decreases, due to a decrease in their mass and due to an increase in sample volume. Then, starting from the temperature of 600℃, sample sintering starts; it is accompanied by shrinkage and an increase in average density. Within the temperature range 900 – 1020 ℃ rather strong samples are obtained. One can see in **Fig. 6** that after heating at a temperature above 900℃, the density of samples with different copper content changes depending on the heating temperature. With an increase in heating temperature to above 1040℃, the density of samples decreases and their strength decreases.

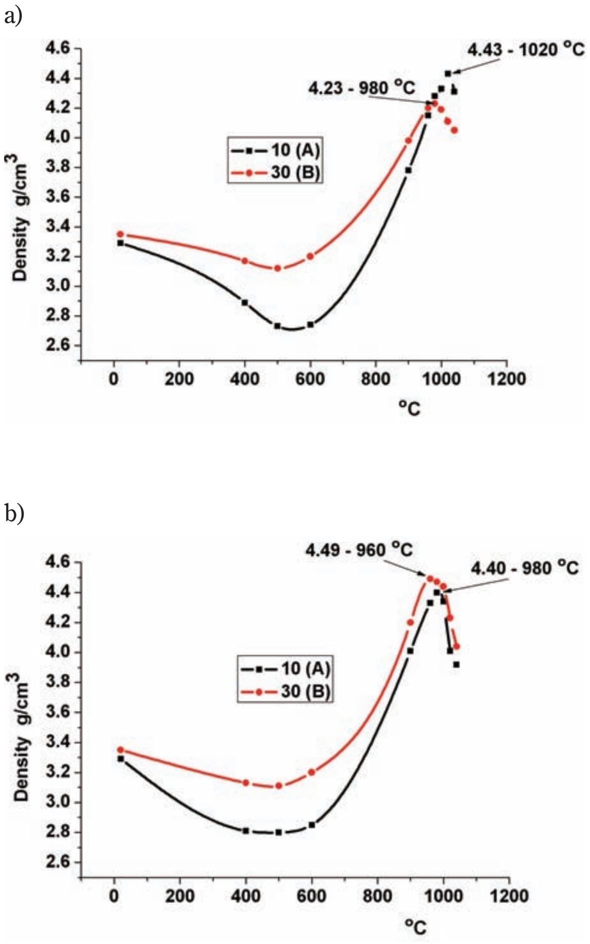

Fig. 6 Dependence of the change to the mean density of samples on the temperature of thermal treatment: A-activation time 10 minutes, B-activation time 30 minutes. Copper oxide content: a) – 0.1 CuO; b) – 0.2 CuO.

Changes of the microstructure of sintered samples

The presented results are related to agglomeration temperatures of 960, 980 and 1000℃. The size of the blocks of coherent scattering (size, nanometer) and their distortion (strain, %), as well as the lattice parameters **a** and **c** for the rhombohedral modification (angstroms) were calculated from the XRD data using PowderCell 2.4 software.

One can see in **Table 2** that an increase in the time of activation of the component mixture from 10 to 30 minutes causes a substantial (by approximately 20-30%) change of the mass loss of samples during subsequent annealing. This character of mass change is independent of the annealing temperature and copper content. These data provide evidence that after longterm mechanical activation, about 30% of initial carbonate ions undergo mechanochemical interaction with the evolution of carbon dioxide in accordance with the equation:

$Li_2CO_3 + Nb_2O_5 = 2LiNbO_3 + CO_2\uparrow$.

Analysis of the data allows us to state, that during the mechanochemical activation of the mixture with copper oxide addition and following thermal treatment, a solid solution of lithium niobate-copper oxide is formed. The lattice parameters and the parameters of microstructure (coherent length and microstrain values) depend on the conditions of the mechanical activation, the temperature of thermal treatment and the copper oxide content.

Thus, for an agglomeration temperature of 1000℃ and an activation time of 30 minutes, the parameter **a** decreases from 5.151 Å to 5.134 Å with an increase in copper content of the solid solution from 0.1% to 0.2%. Similarly, parameter **c** decreases from 13.856 to 13.810 Å. A decrease in parameters **a** and **c** with an increase in copper content of the solid solution can be connected to the fact that copper inclusion in the solid phase causes the substitution of lithium cations by copper with the formation of cation vacancies in the lithium positions according to the reaction:

$Cu^{2+} + Li_{Li} = Cu^{+}_{Li} + V_{Li}^{-} + 2Li^{+}_{s}$

The presence of cation vacancies is likely to cause a decrease in lattice parameters of the solid solution of lithium niobate with an increase in copper content.

After 30 min activation of the initial components, the coherent length in the solid solution for all agglomeration temperatures depends on the copper content: the largest coherent length is observed for a copper content of 0.15%. A similar dependence on the copper content is also observed for microstrain values 9 at temperatures 980 – 1000℃.

Discussion of the obtained crystal chemical data and microstructural parameters exceeds the scope of the present work and requires additional investigation.

Table 2 Some results of the investigation of lithium niobate samples doped with copper oxide

Sintering ℃	CuO	Time activ., min	Size, nm	Strain, %	**a** angstrom	**c** angstrom	Density, g/cm^3	Mass loss, %
960	0.1	10	44	0.1	5.149	13.824	4.15	12.2
	0.1	30	37	0.12	5.139	13.809	4.20	8.2
	0.15	10	32	0.14	5.139	13.814	4.30	13.5
	0.15	30	44	0.03	5.128	13.791	4.37	10
	0.2	10	40	0.09	5.138	13.809	4.33	13.6
	0.2	30	38	0.1	5.138	13.811	4.49	10.7
980	0.1	10	41	0.1	5.151	13.823	4.28	13.1
	0.1	30	41	0.09	5.137	13.815	4.15	11.7
	0.15	10	38	0.11	5.132	13.829	4.34	14.5
	0.15	30	61	0.2	5.134	13.812	4.21	12.2
	0.2	10	41	0.1	5.140	13.820	4.40	13.1
	0.2	30	38	0.1	5.139	13.812	4.47	11.6
1000	0.1	10	45	0.05	5.146	13.809	4.33	13.4
	0.1	30	42	0.1	5.151	13.856	4.19	10.9
	0.15	10	36	0.13	5.142	13.811	4.31	13.1
	0.15	30	61	0.24	5.136	13.830	4.25	11
	0.2	10	44	0.08	5.136	13.817	4.34	13.3
	0.2	30	36	0.2	5.134	13.810	4.44	10.5

Conclusions

Mechanical activation of a mixture of lithium carbonate, niobium oxide and copper oxide is thus accompanied not only by the changes of the dispersity of the initial reagents and their amorphization, but also results in the case of longterm mechanical activation in partial interaction of lithium carbonate with niobium oxide; a lithium niobate matrix is formed. The composites formed during mechanical activation are composed of isometric aggregates of micrometer size containing submicrometer-sized solid particles. The formation of isometric aggregations of particles simplifies the formation of compacts when pressing mechanically activated powders. The large area of contact between the particles of reagents in the compact and the increased reactivity of the reagent are the reasons for the substantial formation of solid solution based on lithium niobate during subsequent heating even at 400℃. An increase in the temperature of thermal treatment causes an increase in the extent of the formation of solid solution and the degree of its crystallization.

References

1) Verbenko, I. A., Razumovskaya, O. N., Shilkina, L. A., Reznichenko, L. A., Andryu-shin, K. P. and Kilessa, V. V. (2009): Deformation, polarization and reversionary properties of lead-free ceramics based on the niobates of alkaline metals, Neorgan. Materialy, V.45, No.7, pp.1-10.
2) Luo, J. H. (2011): Preparation of Lithium Niobate Powders by Mechanochemical Process, Applied Mechanics and Materials, V.121-126, pp.3401-3405.
3) De Figueiredo, R. S., Messai, A., Hernandes, A. C. and Sombra, A. S. B. (1998): Piezoelectric lithium niobate obtained by mechanical alloying, Journal of Material Science Letters, V.17, pp.449-451.
4) Dantsiger, A. Ya., Razumovskaya, O. N., Reznichenko, L. A. and Dudkina, S. I. (1994): “Highly efficient piezoceramic materials. Optimization of search”, Paik Publishers, Rostov-on-Don, Russia.
5) Dantsiger, A. Ya., Razumovskaya, O. N., Reznichenko, L. A., Grineva, L. D., Devlikanova, R. U., Gavrilyachenko, S. V., Dergunova N. V. and Klevtsov A. N. (1994): “Highly efficient piezoceramic materials”, A handbook, Paik Publishers, Rostov-on-Don, Russia.
6) Avvakumov, E. G. (1982): Patent RF No. 975068 B 02 C 17/08.
7) Buyanova, N. E. and Karnaukhov, A. N. (1971): “Determination of specific surface of solids using the chromatographic method of thermal desorption of argon”, Institute of Catalysis SB RAS, Novosibirsk, Russia.
8) The American Society for Testing Materials (2003): “Joint committee on powder diffraction standards”, U.S.A.
9) Avvakumov, E. G. and Razvorotneva, L. I. (1977): Mechanically stimulated phase transitions in niobium and tantalum oxides, Izv. Sibirskogo Otdeleniya Akademii Nauk SSSR. Ser. Khim. Nauk, Issue 4, pp.19-22.
10) Nakamoto, K. (1966): “IR spectra of inorganic and coordination compounds”, Mir, Moscow, Russia.
11) Balicheva, T. G. and Lobaneva, O. A. (1983): “Electron and vibrational spectra of inorganic and coordination compounds”, Publishing House of LSU, Leningrad, Russia.

Author’s short biography

Gusev Aleksey Alekseevich

Research fellow, Laboratory of Intercalationand Mechanochemical Reactions, Institute of Solid State Chemistry and Mechanochemistry, Siberian Branch of the Russian Academy of Sciences. Candidate of Science in Chemistry. Research area: ceramic materials science. Author of 94 publications including 5 monographs and 2 patents for inventions.
Contact information: gusev@solid.nsc.ru, phone 383-170548.

Author’s short biography

Isupov Vitaliy Petrovich

Head of Laboratory of Intercalationand Mechanochemical Reactions,Institute of Solid State Chemistry and Mechanochemistry, Siberian Branch of the Russian Academy of Sciences. Doctor of Science in Chemistry.
Research areas: mechanochemical synthesis of solids, chemistry and technology of lithium compounds, chemistry of intercalation compounds, mechanical activation. Author of 200 publications including 30 patents for inventions.
Contact information: isupov@solid.nsc.ru, phone 383-3363837.

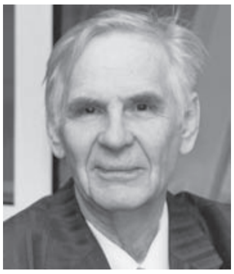

Avvakumov Evgeniy Grigorievich

Chief researcher, Laboratory of Intercalationand Mechanochemical Reactions, Institute of Solid State Chemistry and Mechanochemistry, Siberian Branch of the Russian Academy of Sciences. Doctor of Science in Chemistry, Professor, Laureate of the State Award of Russian Federation in Science and Technology, Full Member of the International Institute for Sintering, Honored Researcher in RF.
Research areas: mechanical activation, mechanochemical synthesis of solids. Author of 5 monographs, 272 research papers, 42 inventions.
Contact information: avvakumov@solid.nsc.ru,
phone 383-3363843.

Nanostructured Media to Improve the Performance of Fibrous Filters[†]

Anna Jackiewicz[1]*, Albert Podgórski[1], Leon Gradoń[1] and Jakub Michalski[2]
[1] *Faculty of Chemical and Process Engineering, Warsaw University of Technology, Warsaw, Poland*
[2] *Faculty of Materials Science, Warsaw University of Technology, Warsaw, Poland*

Abstract

The main objective of this study was to present one of the possibilities of increasing the initial efficiency of aerosol particle removal from the gas stream, i.e. the application of nanofibers in the filter structure. The modified melt-blown technique of producing such thin fibers is hereby presented. During this work, various filter media with fiber diameters from micro- to nanosized made of selected polymers differing in melt flow index were obtained via this method. Their morphology was precisely analysed using high-resolution equipment. The crucial parameters characterizing those fibrous materials were determined: an initial pressure drop across the filters and an initial filtration efficiency. The behavior of clean filters composed of microfibers were compared with the behavior of those made of nanofibers. An attempt was made to decrease the diameter of fibers to the nano range by using different materials for their formation. Collected data of penetration for melt-blown fibrous media were described via experimentally verified realistic models for better simulation of the air filter's performance. Additionally, the obtained results were compared with predictions of the classic filtration theory predominating in the literature on the subject.

Keywords: fibrous filter, filtration efficiency, melt-blown, nanofibers

1. Introduction

In the current state of environmental pollution, especially air and water, effective filtration is becoming increasingly significant. The high-quality filtration materials are also needed in industries applying so-called clean technologies. The requirements for the development and evaluation of such media are becoming more and more stringent. Among all the devices intended to separate small particles from gas streams, fibrous filters are the most widely used. Economically they are the most interesting, since they are both effective and quite simple to operate. By employing fibrous filters, one can remove even very fine particulates from gas with a high efficiency and at a relatively low pressure drop. There is a lot of evidence in the literature showing that fibrous filters can successfully remove nanoparticles from the gas[1,2,3)], and they therefore penetrate new markets, expanding into new branches of industry. Performance of these filtering media, defined through their filtration efficiency, pressure drop and lifetime, strongly depends on their structure - as can be seen from the equation derived on the basis of classic filtration theory. This formula expresses the overall collection efficiency of the filter as follows: $\eta = 1\text{-}\exp[(-4\alpha EL)/(\pi d_F(1-\alpha))]$. Hence one can see that the fiber diameter and the filter porosity determine the quality of the filter.

To produce an optimal filter structure for a given application, it is necessary to have extensive knowledge of the filter's formation, the clean filter's characteristics and of its behavior during loading. Our work was focused on the basic issue, i.e. an improvement of the initial state of the filtration process by increasing the efficiency of aerosol particle removal from the gas stream, at the same time maintaining a relatively low pressure drop. There are a few methods for enhancing a fibrous filter's performance, i.e. by pleating the filter surface to increase the filter-

---

[†] Accepted: July 9, 2012
[1,2] Waryńskiego 1 Street, 00-645 Warsaw, Poland
* Corresponding author:
E-mail: jackiewicz@ichip.pw.edu.pl
TEL: +48-22-234-62-47

ⓒ 2013 Hosokawa Powder Technology Foundation

ing area and to reduce the pressure drop across the filter[4, 5]; by charging fibers (electret filters) - which provides an additional mechanism of aerosol particle capture[6], and by applying nanosized fibers which are very good particle attractors[7,8]. In this paper the latter method has been analysed. The interest in nanostructured media has increased rapidly in the last decade. The specialty filtration applications of nanofibrous media are featured in the work by Barhate and Ramakrishna[9]. Many of them have already been commercialized and some are still in development. The potential of nanofibers in filtration manifested by a high filtration efficiency and dust-holding capacity is the subject of many publications[10,11]. Podgórski et al.[12] confirmed, both theoretically and experimentally, that the most penetrating particle size (MPPS) can be significantly reduced with the use of nanofibrous media. Chronakis[13] presented a review about the active research area of producing ceramic and composite nanofibers with various compositions and properties. Recent trends that can be observed in the works concerning filtration with the use of nanofibers are their surface modification[14, 15] and the study of multilayer systems with a nanolayer[16, 17]. Graham et al.[18] discussed a process for making nanofibers, as well as the benefits, limitations, construction, and performance of filters composed of nano-sized fibers. There are two main techniques for the formation of such thin fibers, i.e. electrospinning and melt-blown. Although electrospinning makes it possible to obtain very thin fibers, it has significant drawbacks such as formation of a huge amount of toxic solvent vapor and a very low production rate. These disadvantages are eliminated in the very stable and controllable advanced melt-blown method developed by Gradoń[19,20], which we use to manufacture our filters. Utilizing this most promising technique and through selection of the appropriate process conditions, the filters of desired structure – for a certain application – i.e. with defined average fiber diameter and desired mean porosity can be obtained. The influence of the process parameters on the properties of the final product can be found in the works by Bresee[21], Gradoń et al.[20] and Ellison et al.[22]. Tan et al.[23] studied an impact of melted polymer viscosity and elasticity on the diameter distribution of melt-blown filters.

Within the framework of this study we tried to use selected polymers differing in melt flow index to produce filaments with increasingly smaller sizes. The structure of the obtained filters, primarily the polydisperse fiber size distribution which is typical for the melt-blown filtering media, was precisely analysed using advanced techniques available in the university's laboratories. This procedure plays a significant role in the investigations of filters, because the nature of the fiber size distribution provides valuable clues about the mechanism of the filtration process. Then, the crucial parameters characterizing tested media were determined: an initial pressure drop across the filters and an initial filtration efficiency. An attempt was made to describe the obtained data. There would be no difficulty if the filters had a homogeneous structure – i.e. are made of identical fibers uniformly distributed in a filter space – which assumes the classic approach. However, melt-blown fibrous filters are non-uniform and this fact strongly affects their performance. Therefore, a new mathematical model was used to approximate the experimental values of penetration through the polydisperse filters. The obtained results were compared with predictions of the classic filtration theory predominating in the literature on the subject.

2. Experimental Protocol

In this section, the method of producing fibrous filtering media as well as the experimental procedure used to characterize their structure and to study their performance are described. All tests performed within this work were conducted in accordance with the “art of measuring”, taking statistics into account.

2.1 Production method for fibrous filters

We developed a modified melt-blown technology which allows us to produce filters composed of fibers with various diameters from micrometer to nanometer in size. The controlled formation of fibers of assumed diameter of the nanosized range is possible due to processing the raw polymer in the extruder, including the reaction with dopants which changes the lengths of the original polymer chains. It results in the reduction of the viscosity of a melted polymer introduced into the fibrillization die.

The melt-blown technology uses only the polymer as the object of the processing. The rate of fiber production with this method is much higher than for the electrospinning process. The melt-blown technique also has an additional advantage over the electrospinning in which a significant amount of the solvent vapor is produced. It requires application of a separation system for solvent recovery. The schematic of the test stand for obtaining filaments by blowing a melted polymer is shown in **Fig. 1**, while some details of the die construction are shown in **Fig. 2(a)**.

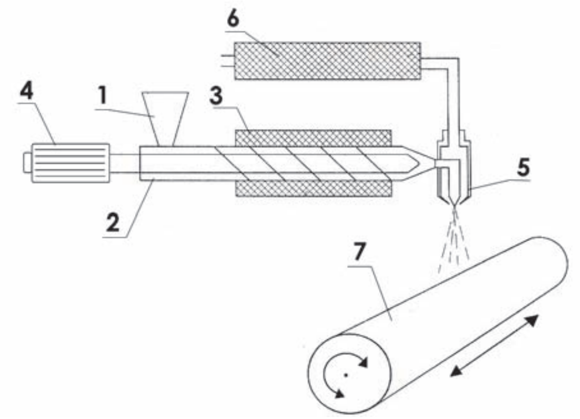

Fig. 1 System for production of melt-blown fibrous materials.

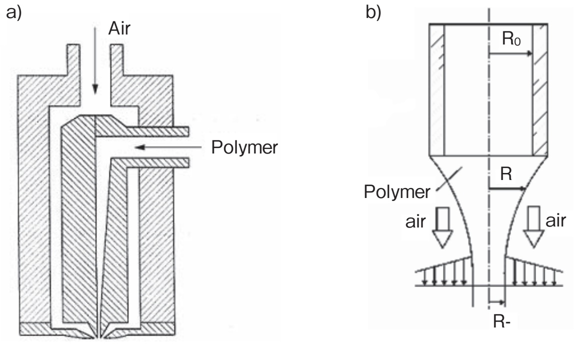

Fig. 2 Diagram showing the die structure a) and single fiber formation b).

Granulated polymer placed in a container 1 falls into the screw of the extruder 2 and is pressed into the die 5. During transportation, the polymer is heated from outside in three steps by an electronic heater 3. The flow rate of melted and homogenized polymer is determined by the rate of screw rotation controlled via an inverter by means of an electronic motor with the gear system 4. The power transmission system is protected from the heating zone by the cooling system. The melted polymer is extruded through the row of the die nozzles. Pressure and temperature of the polymer in the die are measured with the sensing elements. In the die structure, the polymer nozzles are surrounded by the air nozzles. The stream of hot air from compressor and heater 6 flowing along the melted polymer filaments extends them to the desired diameter. The solidified fibers are collected on the mandrel of the fiber receiver 7. This mandrel rotates and moves to and fro to form a proper filter structure defined by the fiber diameter and the local packing density of fibers.

It would be desirable to model the process of single-fiber formation in the melt-blown technology for a better understanding of its principles and for optimization of the operating conditions of fiber manufacture to ultimately obtain the expected filter structure. Let us consider a single hole of the die, **Fig. 2 (b)**, and polymer flowing at volumetric flow rate Q through it. After leaving the hole, a melted fiber of radius R is formed. The basic information describing formation of a thin fiber in the melt-blown technology is derived under the following assumptions: a fiber has a cylindrical shape, a polymer has the same density for melted and solid phases, an axial velocity within a melted fiber is uniform in the fiber cross-section, the polymer is a Newtonian liquid with an Arrhenius type of dependence of viscosity on temperature, the heat capacity of the polymer is constant, the temperature distribution is uniform in the fiber cross-section, the heat conduction in axial direction is negligible.

Taking into account the constancy of the polymer volumetric flow rate, balancing the momentum, and using the stress-strain relations and energy balances, we were able to estimate the influence of the process parameters on the properties of the final product. Theoretical analysis of the single-fiber formation gives us the quantitative information about the radius R of the solidified polymer fiber at the distance x from the nozzle hole of radius R_o for precisely fixed model parameters, i.e. polymer constitutive properties, flow rates and temperatures of polymer and air, and polymer pressure in the die. Using this information, the process parameters for the melt-blown technology were defined.

2.2 Filter media characterization

During this work, the desired melt-blown filter layers were produced for a fixed set of process parameters and were used in the filtration testing procedure. At the beginning, their structure was analysed, because the more we know about the non-uniform nature of the filter material, the better we can predict its performance (filtration efficiency and pressure drop). The following parameters of the tested filters were determined: filter thickness, L, packing density, α, basic weight, q_s. Filter thickness was measured using the precise vernier caliper, and the values of the last two parameters were evaluated by a gravimetric method. Determining the mass of a filter sample, m_F, the surface density was calculated as the ratio of the mass to the filter area, F: $q_s = m_F / F$. The filter porosity, ε, was determined according to the presented formula: $\varepsilon = [1-(m_F/\rho_F \cdot F \cdot L)]*100\%$ and then the filter solidity was computed as: $\alpha = 1 - \varepsilon$.

Because one of the main structural parameters of a melt-blown fibrous filter is the fiber diameter, the procedure of determining the fiber size distribution requires high accuracy and very good equipment, especially if a filter with a significant fraction of nanofibers is considered. The arithmetic mean fiber diameters, d_{Fa}, and observed range of fiber sizes were obtained by analysing images taken under the High-Resolution Scanning Electron Microscope (HRSEM), Hitachi Su-8000, with field emission gun. The flat rectangular specimens of dimensions 10 × 15 mm were cut by laser from different parts of the investigated filters. For each specimen, 16 images were acquired at magnifications varying from 300 to 2000.

On the basis of the literature data[22,24] and structural analysis of our filters, it can be stated that in most cases, the distribution of fiber diameters of melt-blown fibrous filters follows the log-normal one that has the normalized density distribution function described as:

$$g(d_F) = \frac{1}{\sqrt{2\pi} d_F \ln \sigma_{gd_F}} \exp\left[-\frac{\ln^2(d_F/d_{Fg})}{2\ln^2 \sigma_{gd_F}}\right] \qquad (1)$$

and the normalized cumulative log-normal distribution given by:

$$G(d_F) = \frac{1}{2}\left\{1 + \mathrm{erf}\left[\frac{\ln(d_F/d_{Fg})}{\sqrt{2}\ln \sigma_{gd_F}}\right]\right\} \qquad (2)$$

This distribution is characterized by two parameters:
- the geometric mean fiber diameter, d_{Fg}:

$$d_{Fg} = (d_{F1} \times d_{F2} \ldots \times d_{FN_F})^{1/N_F} \qquad (3)$$

where N_F is the number of measured fiber diameters,
- the geometric standard deviation, σ_{gdF}:

$$\ln \sigma_{gd_F} = \sqrt{\frac{\sum\limits_{j=1}^{j=N_F} (\ln d_{Fj} - \ln d_{Fg})^2}{N_F - 1}} \qquad (4)$$

where d_{Fj}, $j=1, \cdots, N_F$.

These parameters were determined by fitting the experimental data of the fiber diameters to the normalized cumulative log-normal function, Eq. 2. Even for a few measured fiber diameters, the applied procedure allows one to find the geometric mean fiber diameter and geometric standard deviation with a high accuracy.

The fact that the fiber diameter distribution of nonwoven filters can be precisely described by a log-normal distribution was utilized by us in mathematical calculations during estimation of the filter penetration (see Section 5).

In the next stage, media were examined with a Palas MFP 2000 test bench to determine the initial pressure drop across the filters and their initial filtration efficiency. Arizona Fine Test Dust ISO 12103-1 (Power Technology Incorporated, USA) was used as the standard test particles in the size range of submicrometers and micrometers. The experiments were performed at an air velocity of 0.2 m/s.

3. Impact of the Filter Morphology on the Filtration Effectiveness

The first task was related to comparison of the experimental data of filtration properties obtained for two filters with different morphology. Their structural parameters are shown in **Table 1**. **Fig. 3** depicts the fiber size distributions of the tested filters together with their precise approximation by the log-normal distribution.

The presented in **Fig. 4** results show the influence of the fiber diameter distribution and porosity of the filter on its effectiveness. It was tested whether the application of thinner fibers in the filter can increase its efficiency and whether simultaneously one has to pay for this with an excessive pressure drop. On the basis of the obtained data it can be seen that Filter 1 with thinner fibers, low basic weight and less packed provides nearly three times higher efficiency than Filter 2 with thicker fibers, higher basic weight and lower porosity. This difference is particularly visible for the most penetrating particles. The increase in pressure drop for the filter with thin filaments in comparison to the pressure drop for the filter with thicker fibers is not so significant. This is the evidence that thinner fibers in a filter have a beneficial effect on the separation efficiency of aerosol particles but they also cause an increase in pressure drop. Therefore, when optimizing the filter structure, two main parameters characterizing the filters, i.e. the filtration efficiency and pressure drop across the filter, must be taken into account.

Table 1 Structural characteristic of the investigated filters

Filter No.	Filter thickness, L [mm]	Filter porosity, ε [%]	Basic weight, q_s [g/m^2]	Arithmetic mean fiber diameter, $d_{Fa} \pm \sigma_{adF}$ [μm]
1	2.05	97.5	39	3.5 ± 1.7
2	1.35	85.0	187	15.4 ± 6.7

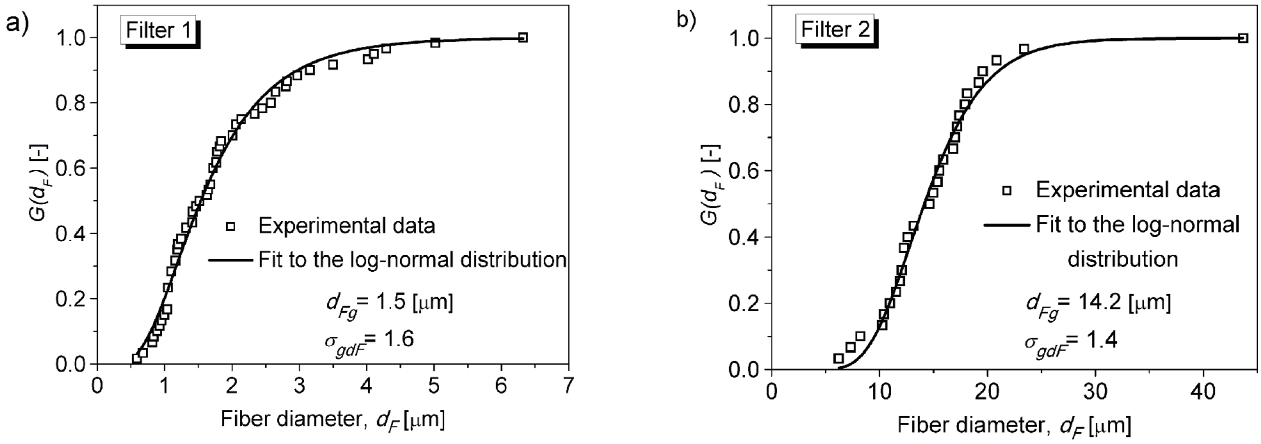

Fig. 3 Fiber size distributions of Filter 1 (a) and Filter 2 (b).

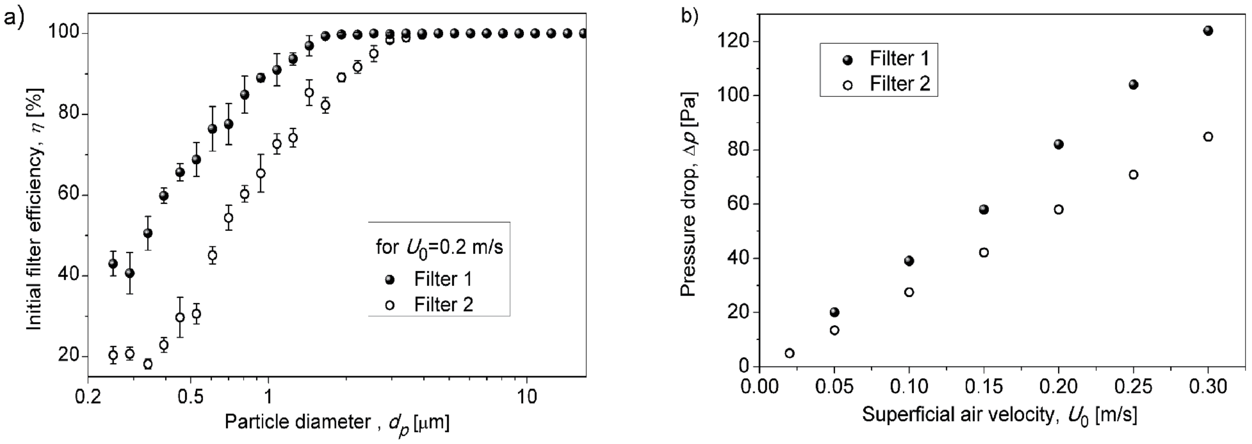

Fig. 4 Initial filter performance: a) filter efficiency vs. particle diameter and b) pressure drop vs. face velocity for Filter 1 and Filter 2.

4. Impact of Material Used to Manufacture Filters for Fiber Diameters

It was proven that the thin fibers in the filter ensure their better quality. A further step in the study was to attempt to reduce the fiber diameter and produce filters with a substantial fraction of nanosized fibers. The investigations of the melt-blown technique for fibrous media production were extended to the case of the polymers with different viscosity, i.e. different values of the melt flow index (MFI). Two kinds of polypropylene were used for the fiber formation, namely Borealis PP504FB with MFI 1200, and Metocene PPM650Y with MFI 1800. The process was carried out using the same structure of the experimental equipment, i.e. the screw of the extruder and construction of the die, only the pressure of the polymer in the die was changed. The filtering media obtained were thoroughly analysed in order to verify the range of fiber diameters formed from the mentioned polymers (see **Table 2**).

Table 2 Characteristic of the filters made of two different polymers

Filter	Filter thickness, L [mm]	Packing density, α [-]	Basis weight, q_s [g/m^2]	Arithmetic mean fiber diameter, $d_{aF} \pm \sigma_{adF}$ [μm]
PP504FB	3.15	0.016	34.5	0.70 ± 0.68
PPM650Y	3.42	0.014	43.3	0.55 ± 0.54

The fiber size distributions presented in **Fig. 5** show the significant influence of the polymer structure, i.e. the polymer chain characteristics, defined through the melt flow index, on the diameters of produced fibers. Metocene PPM650Y with MFI 1800 makes it possible to obtain fibers with the smaller diameters. Therefore, for the lower viscosity of the polymer used to manufacture filters (the greater its MFI), the thinner filaments were made.

In **Fig. 6** the operating parameters at the initial stage of filtration process, determined for those two

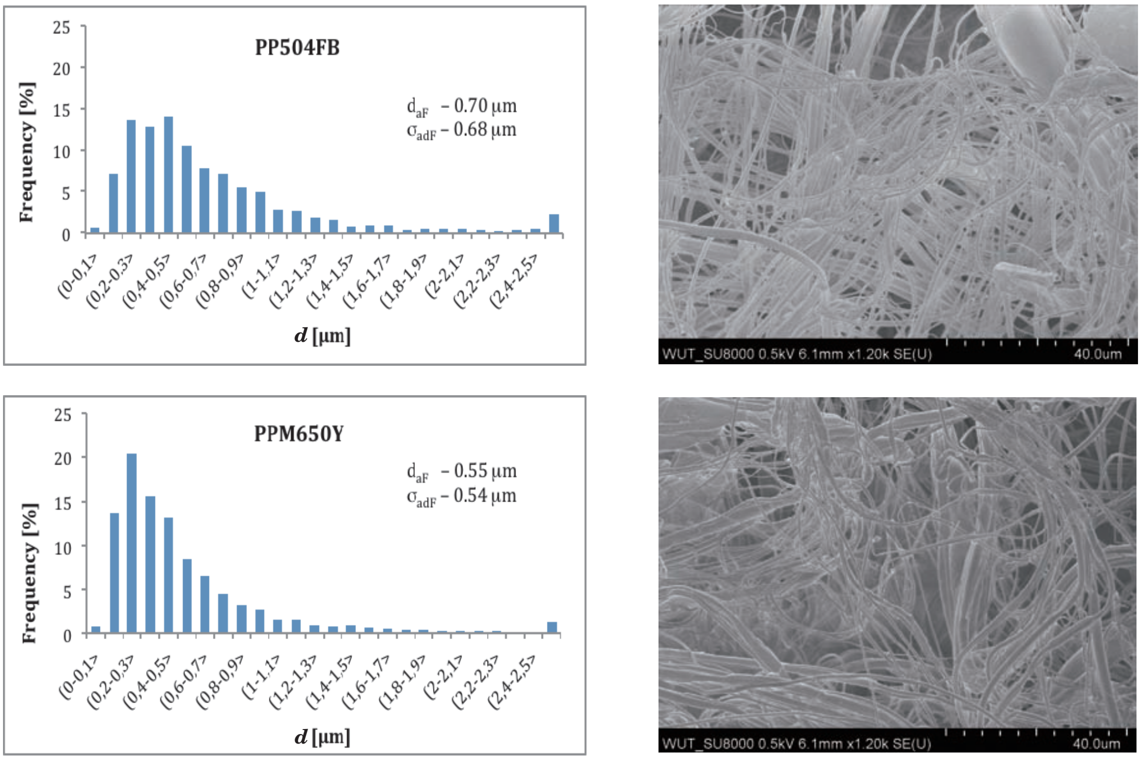

Fig. 5 HRSEM images and fiber diameter distributions of filters made of different polypropylenes: Borealis (Filter PP504FB) and Metocene (Filter PPM650Y).

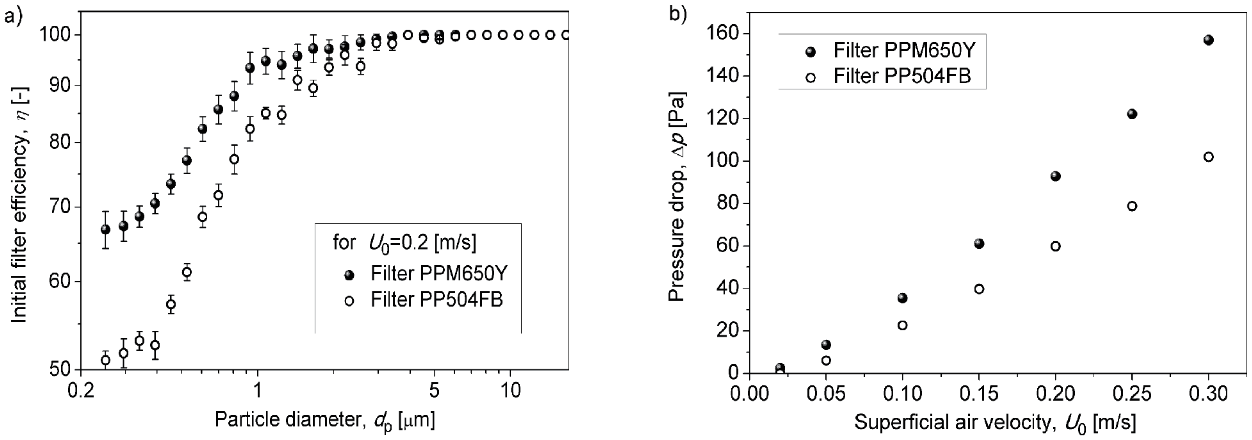

Fig. 6 Initial performance of filters made of various materials : a) filter efficiency and b) pressure drop.

filtering materials made of various polymers, were collated. It turned out that the highest contribution of nanosized fibers in the filter made of Metocene enhanced its effectiveness in comparison with the filter composed of slightly thicker fibers made of Borealis. Filter PPM650Y made of thin fibers displays a greater air-flow resistance, however, the increase compared with Filter PM504FB composed of fibers with larger diameters is not as significant.

5. Theoretical Approach

Aerosol filtration in fibrous filters is a very complex process. A particle's motion during flow is influenced by several stochastic and deterministic forces which act simultaneously, but depending on the particle size and process conditions, one of them may predominate. Moreover, the polydisperse internal structure of these filters creates non-uniform fields of local gas velocity and local particle concentrations in a given filter cross-section, and this is one of the major problems in the theoretical modeling of filtration processes using them. This intricate internal structure, extremely hard to imitate in computer simulations, causes a process of aerosol filtration in fibrous filters that is difficult to describe and which out of necessity must be based on several simplifications. In the literature on the subject, the classic approach used to predict fibrous media performance still prevails. This is without doubt due to its simplicity. It considers filtration at its most elementary level – the collection of an aerosol particle by a single fiber, placed with its axis perpendicular to the air flow. The main assumptions of the classic theory of depth filtration in fibrous filters are: macroscopic homogeneity of the filter; the same efficiency of all fibers; mutual independence of the particular mechanisms of deposition; irreversible removal of a particle upon a contact with a fiber (meaning no rebound of a particle). According to this model, an aerosol particle's penetration, P, through a filter with thickness L and packing density α is expressed as:

$$P = \exp\left[-\frac{4\alpha L}{\pi\,(1-\alpha)}\left(\sum_{m}\frac{E_m(d_F)}{d_F}\right)\right] \tag{5}$$

where $E_m(d_F)$ is the single fiber efficiency due to mth mechanism of deposition calculated additively (i.e., E_D diffusion, E_R interception, E_I inertial impaction, E_{DR} coupling of diffusion and interception), which depends on the fiber diameter, d_F. Equation (5) originates from the balance of the particle's flux deposited in the filter layer with a differential thickness, and such a derivation is included in works by Dorman[25], Brown[26]. The single fiber efficiencies for particular mechanisms can be determined using the correlations that may be found in the literature. Since in this work, particles with diameters in the range of 0.25-17 μm were considered, analysis was limited to the three predominating mechanisms of deposition, i.e. Brownian diffusion, direct interception and inertial impaction. In the absence of an electric charge on fibers and particles, the electrostatic mechanism was omitted. The calculations were performed using the correlations presented below.

$$\text{For diffusion}: E_D = 2.9\left(\frac{1-\alpha}{Ku}\right)^{1/3} Pe^{-2/3} \tag{6}$$

where $Ku = -0.5\ln\alpha - 0.75 - 0.25\alpha^2 + \alpha$ denotes the Kuwabara number, $Pe = U_0 d_F / D$ is the Peclet number, D – the Brownian diffusion coefficient of an aerosol particle, and U_0 – the superficial mean gas velocity. The genesis of creation of Equation (6) is contained in the work by Podgórski et al.[27].

$$\text{For inertial impaction}^{28)}: \quad E_I = \frac{(Stk)J}{2Ku^2} \tag{7}$$

when $NR < 0.4 \rightarrow J = (29.6 - 28\,\alpha^{0.62})NR^2 - 27.5NR^{2.8}$,
when $NR \geq 0.4 \rightarrow J = 2$,

where $Stk = \rho_P d^2{}_P C_C U_0 / 18\,\mu d_F$ is the Stokes number, C_C – the Cunningham slip correction factor, ρ_P – the particle density, μ – the air viscosity, and $NR = d_P/d_F$ signifies the interception parameter.

For direct interception[29]:

$$E_R = \left(\frac{1-\alpha}{Ku}\right)\left(\frac{NR^2}{1+NR}\right) \tag{8}$$

Enhancement of the single fiber efficiency caused by a coupling between diffusion and direct interception, E_{DR}, was also accounted for [30]:

$$E_{DR} = \frac{1.24NR^{2/3}}{(KuPe)^{1/2}} \tag{9}$$

Use of the above-cited formula to calculate the aerosol particle penetration does not give rise to any difficulties for the filter composed of identical fibers uniformly distributed in a filter space. Nevertheless, the real nonwoven filters tend to have relatively wide distributions of fiber diameters, and application of the classic theory outlined above is not explicit. Most authors adapt this model of depth filtration derived for monodisperse media to describe the behavior of polydisperse filters by using a certain equivalent fiber diameter in calculations, e.g. the arithmetic mean diameter determined by image analysis or the equivalent diameter obtained from the pressure drop measurements. Two different filtering media previously characterized were utilized to verify applicability of this common approach for the arithmetic mean fiber diameter.

It can be observed in **Fig. 7** that application of the arithmetic mean fiber diameter failed to precisely describe penetration through polydisperse melt-blown filters composed of both micro- and nanosized fibers. The discrepancies between the experimental data and the predictions of the classic approach were caused by the fact that theoretical calculations had been based on the mean fiber diameter only, whilst the real filters always have a more or less polydisperse distribution of fiber sizes.

In the light of the presented results, it is obvious that in the case of inhomogeneous melt-blown fibrous filters, the classic filtration theory assuming a regular

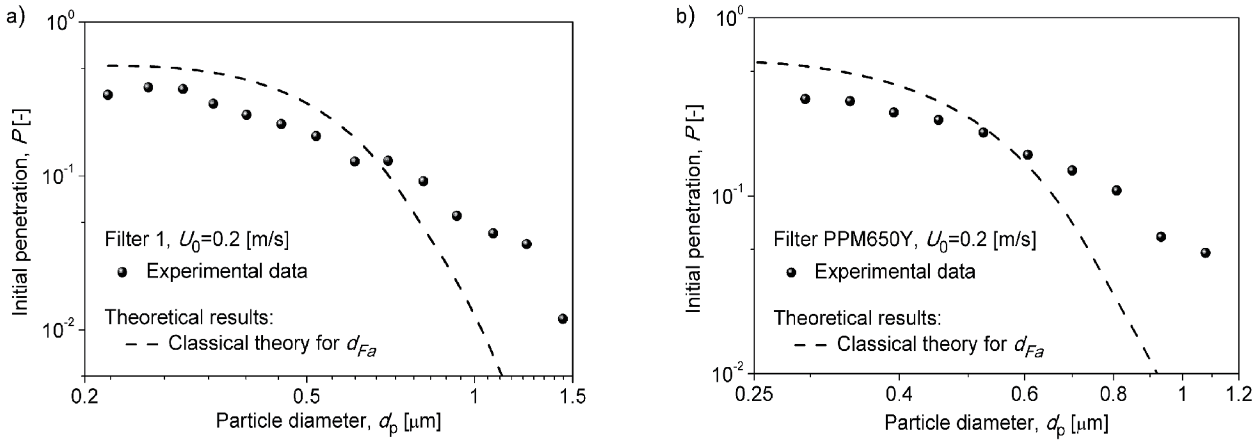

Fig. 7 Comparison of experimental values of the efficiency with results of calculations obtained using the classic theory for: Filter 1 (a) and Filter PPM650Y (b).

array of identical fibers in a filter is an oversimplification. Instead of one mean fiber diameter, the entire fiber diameter distribution should be taken into account, because aerosol penetration through a polydisperse filter depends on it. Therefore, to realistically calculate penetration of aerosol particles through polydisperse filters, theoretically well-founded models were utilized – two limiting models, namely Perfectly Mixed Flow Model (*PMFM*) and Fully Segregated Flow Model (*FSFM*), and the general model called Partially Segregated Flow Model (*PSFM*), which is their linear combination. The proposed models explicitly take one of the main aspects of the filter structure inhomogeneity into consideration, i.e. the entire fiber size distribution. These two limiting models estimate an upper and a lower possible aerosol penetration through a polydisperse filter, while *PSFM* enables determination of the real penetration, which lies somewhere in between Perfectly Mixed Flow Model and Fully Segregated Flow Model. When fibers with different sizes are distributed evenly in a filter space and flow in a filter is well mixed on the mesoscale, Eq. (5) can be simply averaged using the fiber diameter distribution function $g(d_F)$, Eq. (1). This method represents estimation of the lower limit of aerosol penetration through a polydisperse filter and it is called Perfectly Mixed Flow Model (*PMFM*). Such an approach is based on the assumption that the superficial gas velocity is the same for all Kuwabara cells containing various fibers. Thus, aerosol penetration according to *PMFM* is calculated as:

$$P_{PMFM} = \exp\left[\frac{-4\alpha L}{\pi(1-\alpha)}\left(\sum_m \int_0^\infty \frac{E_m(d_F)}{d_F} g(d_F)\mathrm{d}d_F\right)\right] \quad (10)$$

The second extreme model estimating the upper limit of aerosol penetration through a polydisperse filter considers the situation when fibers with different diameters are completely separated from each other. Assuming that the pressure drop per unit filter thickness is the same for all Kuwabara cells with various fibers, the Fully Segregated Flow Model (*FSFM*)[31] was formulated and the penetration according to this model is expressed as:

$$P_{FSFM} = \frac{\int_0^\infty d_F^2 P(d_F) g(d_F)\mathrm{d}d_F}{\int_0^\infty d_F^2 g(d_F)\mathrm{d}d_F} \quad (11)$$

$P(d_F)$ in the above formula denotes penetration calculated using Eq. (5) as for a monodisperse filter with fibers of diameter d_F, and the single fiber deposition efficiencies $E_m(d_F)$ for particular fibers' diameters should be computed for individual superficial gas velocities $U_0(d_F)$, corresponding to various Kuwabara cells with different fibers:

$$U_0(d_F) = \frac{U_0 d_F^2}{\int_0^\infty d_F^2 g(d_F)\mathrm{d}d_F} \quad (12)$$

The actual value of penetration for a specific filter for a given degree of mixing of fibers with different diameters lies between P_{PMFM} and P_{FSFM} and depends on the degree of segregation of the aerosol flow in a filter around the fibers of different sizes. Thus, we formulated the general Partially Segregated Flow Model (*PSFM*), for which the penetration is calculated as a linear combination of penetrations determined from the two limiting models – Eq. (10) and (11):

$$P_{PSFM} = s\,P_{FSFM} + (1\text{-}s)\,P_{PMFM} \quad (13)$$

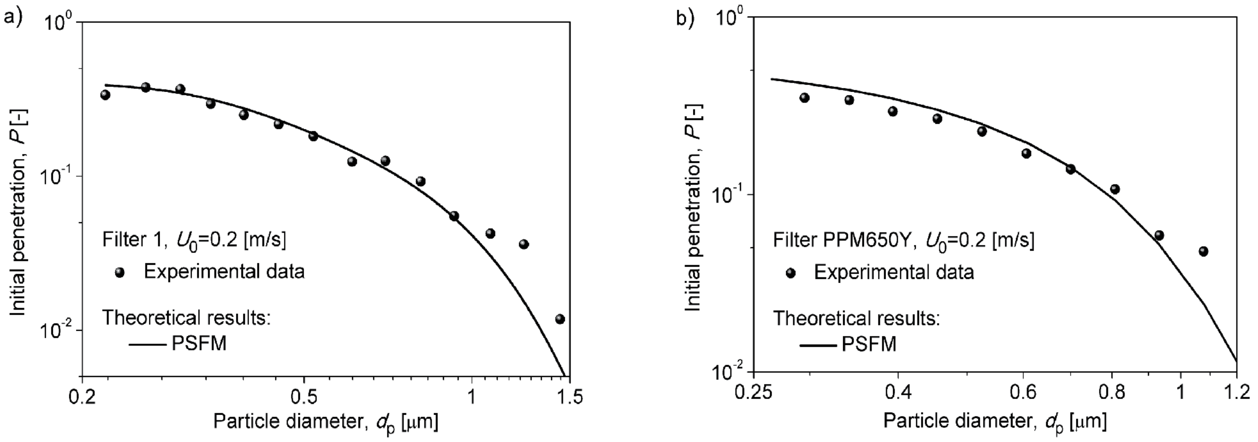

Fig. 8 Partially Segregated Flow Model predictions vs. experimental data of penetration for: Filter 1 (a) and Filter PPM650Y (b).

In Eq. (13) the dimensionless, phenomenological parameter named the flow segregation intensity, s, was introduced. It can vary between zero (for perfect mixing) and one (for full segregation) and must be determined on the basis of experimental penetration data.

The experimental results of submicrometer and micrometer aerosol particle penetration through the same two filters whose data were compared with results of the classic theory, were described by the Partially Segregated Flow Model, see **Fig. 8**. As it can be observed, utilization of the entire fiber size distribution in theoretical calculations, i.e. using the *PSFM*, enables the particle penetration through filters made of both micro- and nanometer sized fibers to be computed much more precisely compared to the common case when only a mean fiber diameter is considered. The latter approach leads to results which diverge tremendously from experimental data and can be either lower or higher than them. The obtained results clearly indicate how strong the effect of the fibers' polydispersity on the filtration of aerosol particles with various sizes can be. Podgórski et al.[27] also successfully applied this model for prediction of the nanoparticles' penetration.

6. Conclusions

In this paper, the way to enhance the dust removal efficiency of fibrous filters by applying nanostructured fibers was presented. We introduced various modifications of the classic melt-blown technique in order to produce fibers with a wide range of sizes. The production parameters have been organized in order to obtain a filter with an assumed structure. Our efforts were particularly directed towards the preparation of media with a high contribution of nanofibers and to identify the role they play during filtration. The analysis of the obtained filter structure made using the highest quality equipment confirmed that we are able to significantly decrease the average fiber diameter to below 1 μm by modulating several processing parameters and by using various materials. It was shown that by designing a filter with nanofibers, one can greatly increase the efficiency of the separation of aerosol particles compared to filters composed of thicker fibers, something which is particularly noticeable in the case of the most penetrating particle size range. An attempt to reduce the fiber diameter using a new polymer with a different melt flow index was successful. Metocene with a higher MFI gives the possibility of obtaining a filter with a higher fraction of fibers less than 1 μm, which improves its effectiveness. Our work also examines the theoretical aspect of filtration in fibrous materials, i.e. contains a description of the obtained penetration via two models: the classic one from the literature and the one proposed by us. The results obtained clearly demonstrate that the classic single fiber theory based on the assumption of a homogeneous filter structure and monodisperse fiber size is incapable of correctly predicting the filter efficiency for real fibrous filters with a high level of polydispersity in fiber sizes. A very good agreement between the experimental data of penetration and the theoretical *PSFM* model was obtained for two different filters composed of micro- and nanosized fibers. It is of great practical importance to be able to precisely calculate filtration efficiency for polydisperse filters made of fibers with various diameters. This work enables us to work out general procedures for designing and optimizing fibrous filters used for different applications.

This work will be extended to the case of the non-steady-state filtration where the dust capacity of the filter will be the challenging parameter for filter structure optimization.

Acknowledgements

This work was partially supported by Cummins Filtration, USA, and by the project from The National Centre for Research and Development EraNet/MNT/NFSM/1/2011.

Nomenclature

C_C	Cunningham slip correction factor, dimensionless
D	coefficient of Brownian diffusion, $m^2 \cdot s^{-1}$
d_F	fiber diameter, m
d_{Fa}	arithmetic mean fiber diameter, m
d_{Fg}	geometric mean fiber diameter, m
d_p	particle diameter, m
E	total single fiber efficiency, dimensionless
E_D	single fiber efficiency due to diffusion, dimensionless
E_{DR}	single fiber efficiency due to diffusion and interception, dimensionless
E_I	single fiber efficiency due to inertial impaction, dimensionless
E_m	single fiber efficiency for m^{th} mechanism of deposition, dimensionless
E_R	single fiber efficiency due to direct interception, dimensionless
F	filter area, m^2
L	filter thickness, m
m_F	mass of a filter sample, kg
N_F	number of measured fiber diameters, dimensionless
NR	interception parameter, dimensionless
P	particle penetration through a filter, dimensionless
Δp	pressure drop across the filter, Pa
q_s	basic weight, $kg \cdot m^{-2}$
R	radius of a fiber, m
R_0	radius of a nozzle hole, m
s	aerosol particles’segregation intensity parameter, dimensionless
U_0	superficial gas velocity, $m \cdot s^{-1}$

Greek

α	filter packing density, dimensionless
ε	filter porosity, dimensionless
η	filter efficiency, dimensionless
μ	gas viscosity, Pa·s
ρ_F	fiber material density, $kg \cdot m^{-3}$
ρ_g	gas density, $kg \cdot m^{-3}$
ρ_p	particle density, $kg \cdot m^{-3}$
σ_{adF}	standard deviation of fiber size distribution, m
σ_{gdF}	geometric standard deviation of fiber size distribution, dimensionless

Dimensionless numbers

Ku	Kuwabara number
Pe	Peclet number
Stk	Stokes number

References

1) Payet, S. et al. (1992): Penetration and pressure-drop of a Hepa filter during loading with submicron liquid particles, Journal of Aerosol Science, Vol.23, pp.723-735.
2) Brown, R. C. and Thorpe, A. (2001): Glass fiber filters with bimodal fiber size distribution, Powder Technology, Vol.118, pp.3-9.
3) Huang, S. H. et al. (2007): Penetration of 4.5 nm to 10 μm aerosol particles through fibrous filters, Journal of Aerosol Science, Vol.38, pp.719-727.
4) Rebaia, M. et al. (2010): Clogging modeling in pleated filters for gas filtration, Chemical Engineering Research and Design, Vol.88, pp.476-486.
5) Cesar, T. and Schroth, T. (2002): The Influence of Pleat Geometry on the Pressure Drop in Deep-pleated Cassette Filters, Filtration and Separation, November 2002, pp.48-54.
6) Chazelet, S., Bemer, D. and Grippari, F. (2011): Effect of the test aerosol charge on the penetration through electret filter, Separation and Purification Technology, Vol.79, pp.352-356.
7) Wang, J., Kim, S. C. and Pui, D. Y. H. (2008): Figure of merit of composite filters with micrometer and nanometer fibers, Aerosol Science and Technology, Vol.42, pp.722-728.
8) Yun, K.M. et al. (2007): Nanoparticle filtration by electrospun polymer fibers, Chemical Engineering Science, Vol.62, pp.4751-4759.
9) Barhate, R. S. and Ramakrishna, S. (2007): Nanofibrous filtering media: Filtration problems and solutions from tiny materials, Journal of Membrane Science, Vol.296, pp.1-8.
10) Barhate, R.S. et al. (2008): Fine chemical processing: The potential of nanofibres in filtration, Filtration and Separation, Vol.45, pp.32-35.
11) Hung, C. and Leung, W. W. (2011): Filtration of nano-aerosol using nanofiber filter under low Peclet number and transitional flow regime, Separation and Purification Technology, Vol.79, pp.34-42.
12) Podgórski, A., Bałazy, A. and Gradoń, L. (2006): Appli-

cation of nanofibers to improve the filtration efficiency of the most penetrating aerosol particles in fibrous filters, Chemical Engineering Science, Vol.61, pp.6804-6815.

13) Chronakis, I. S. (2005): Novel nanocomposites and nanoceramics based on polymer nanofibers using electrospinning process-A review, Journal of Materials Processing Technology, Vol.167, pp.283–293.

14) Karwa, A. and Tatarchuk, B. (2012): Aerosol filtration enhancement using carbon nanostructures synthesized within a sintered nickel microfibrous matrix, Separation and Purification Technology, Vol.87, pp.84-94.

15) Nguyen, T., Chung, O. and Park, J. (2011): Coaxial electrospun poly(lactic acid)/chitosan (core/shell) composite nanofibers and their antibacterial activity, Carbohydrate Polymers, Vol.86, pp.1799-1806.

16) Leung, W. W., Hung, C. and Yuen, P. (2010): Effect of face velocity, nanofiber packing density and thickness on filtration performance of filters with nanofibers coated on a substrate, Separation and Purification Technology, Vol.71, pp.30–37.

17) Zhang, Q. et al. (2010): Improvement in nanofiber filtration by multiple thin layers of nanofiber mats, Journal of Aerosol Science, Vol.41, pp.230-236.

18) Graham, K. et al. (2002): "Polymeric nanofibers in air filtration applications" , Fifteenth Annual Technical Conference & Expo of the American Filtration & Separations Society, Galveston, Texas.

19) Ciach, T. and Gradoń, L. (1996): Highly efficient filtering materials, Journal of Aerosol Science, Vol.27, pp.613-614.

20) Gradoń, L., Podgórski, A. and Bałazy, A. (2005): Filtration of nanoparticles in the nanofibrous filters, FILTECH 2005 Conference and Exhibition, Wiesbaden, Germany. Conference Proceedings, Vol. II, pp.178-183.

21) Bresee, R. R. (2004): Influence of processing conditions on melt blown web structure: Part 1 – DCD, International Nonwovens Journal, Vol.13, pp.49-55.

22) Ellison, C. J. et al. (2007): Melt blown nanofibers: Fiber diameter distributions and onset of fiber breakup, Polymer, Vol.48, pp.3306-3316.

23) Tan, D. H. et al. (2010): Meltblown fibers: Influence of viscosity and elasticity on diameter distribution, Journal of Non-Newtonian Fluid Mechanics, Vol.165, pp.892-900.

24) Kirsch, A. A. and Stechkina, I. B. (1973): Pressure drop and diffusional deposition of aerosol in polydisperse model filter, Journal of Colloid and Interface Science, Vol.43, pp.10-16.

25) Dorman, R. G. (1966): "Filtration. In: Aerosol Science (C. N. Davies, Ed.)" , Academic Press, London, pp.195-222.

26) Brown, R. C. (1993): "Air Filtration: An integrated approach to the theory and applications of fibrous filters" , Pergamon Press, Oxford.

27) Podgórski, A. et al. (2011): Penetration of monodisperse, singly-charged nanoparticles through fibrous filters, Aerosol Science and Technology, Vol.45(2), pp.196-214.

28) Stechkina, I. B. and Fuchs, N. A. (1966): Studies on fibrous aerosol filters – I. Calculation of diffusional deposition of aerosols in fibrous filters, Annals of Occupational Hygiene, Vol.9, pp.59-64.

29) Lee, K. W. and Liu, B. Y. H. (1982): Theoretical study of aerosol filtration by fibrous filter, Aerosol Science and Technology, Vol.1, pp.147-161.

30) Kirsch, A. A. and Stechkina, I. B. (1978): "The theory of aerosol filtration with fibrous filters. In: Shaw, D.T. (Ed.), Fundamentals of Aerosol Science" , Wiley, New York.

31) Podgórski, A. (2009): Estimation of the upper limit of aerosol nanoparticles penetration through inhomogeneous fibrous filters, Journal of Nanoparticle Research, Vol.11, pp.197-207.

Author's short biography

Anna Jackiewicz

Anna Jackiewicz, PhD, MSc, Assistant Professor at the Faculty of Chemical and Process Engineering Warsaw University of Technology, Poland
2004: MSc - Chemical Engineering; 2010: PhD - Chemical Engineering
Scientific interests: filtration, research of filter effectiveness, optimization of filter structure, techniques for aerosol generation.
Author and co-author of over 40 papers published in periodicals and conference proceedings.
Recipient of the awards: Ignacy Łukasiewicz Grant Fund of PGNiG S.A., Fiat award, the presentation of achievements at the exhibition entitled "Maria Skłodowska-Curie in the Service of Science Yesterday and Today" at the European Parliament in Brussels.

Author's short biography

Albert Podgórski

Albert Podgórski (1963-2010), PhD, DSc, Professor at the Faculty of Chemical and Process Engineering Warsaw University of Technology, Poland.
1988: MSc - Chemical Engineering; 1991: PhD - Chemical Engineering; 2003: DSc – Chemical Engineering; 1995-96 - postdoc, Delft University of Technology (The Netherlands); 1992 – research fellow, Lund University of Technology (Sweden); 1999-2002, 2009 - visiting professor, University of Vienna (Austria).
Scientific interests: interfacial phenomena, dynamics of pulmonary surfactants, particle deposition and clearance in the lung, mechanics of aerosol particles including deformable fibers, aerosol filtration, mathematical modeling.
Author and co-author of over 200 scientific papers, 3 patents, 1 book.
Laureate of the scientific awards: Polish Ministry of Science and Education, Rockefeller Foundation.

Leon Gradoń

PhD, DSc, Professor at the Faculty of Chemical and Process Engineering Warsaw University of Technology, Poland.
1969: MSc - Chemical Engineering; 1975: MSc - Mathematics; 1976: PhD - Chemical Engineering; 1978-79 -postdoc, University of Houston (USA); 1985-87 - visiting professor, Buffalo University (USA); 1993-94 - University of Cincinnati (USA); lecturer in European and North American universities.
Scientific interests: filtration, filter production, polymer processing, particle deposition in lungs, controlled drug delivery, functional particle formation.
Author and co-author of over 200 peer-reviewed papers, 60 patents and 3 books.
Recipient of the awards: Smoluchowski, Fulbright, Polish Science Foundation, Japan Society for Promotion of Sciences.

Jakub Michalski

PhD, R&D Manager in Materials Engineers Group Ltd; research position at Faculty of Materials Science, Warsaw University of Technology, Poland.
2001: MSc - Materials Science, 2007: PhD - Materials Science; 2004-2005 - EU Marie Curie Fellowship, Josef Stefan Institute, Slovenia; 2002-2004 - Scholarship of Foundation for Polish Science.
Scientific interests: Materials Science, filtration, investment casting of super alloys, composite materials, nano-composites and robotics.
Author and co-author of 16 papers and 1 patent.

Effects of Particle Size and Morphology on Filtration of Airborne Nanoparticles[†]

Jing Wang
[1] *ETH Zurich, Institute of Environmental Engineering*
[2] *Empa, Analytical Chemistry*

Abstract

The rapid development of nanotechnology brings new challenges to aerosol filtration, which plays a critical role in controlling pollution and protecting the environment and human health. The filtration of airborne nanoparticles is becoming an important issue as they are produced in large quantities from material synthesis and combustion emission. Recent studies indicate that the filtration efficiency increases as the particle size decreases down to 2 – 3 nm. Thus the conventional filters are working well against the nanoparticles. The filtration of non-spherical nanomaterials, such as carbon nanotubes and nanoparticle agglomerates, possesses different filtration characteristics compared to spherical particles. The interception effect for elongated particles is stronger than for spheres with the same mobility, thus higher filtration efficiency is achieved. Modeling results based on the single-fiber theory are compared to experimental data and then used to predict the difference between the filter penetrations for agglomerates and spheres. The effects of the filtration velocity, filter fiber size, solidity and thickness are systematically investigated.

Keywords: filtration, nanoparticles, nanoparticle agglomerates, carbon nanotubes, morphology

1. Introduction

Aerosol filtration is used in diverse applications such as air pollution control, emission reduction, respiratory protection for human, and the processing of hazardous materials. The rising awareness of environmental agencies and the general public for a cleaner environment is forcing many industries to consider a filtration process in their plants. The filtration of airborne nanoparticles is becoming an important issue as they are produced in large quantities from material synthesis and combustion emission. Nanoparticle filtration has received significant attention in the field of occupational health and safety (Wang et al. 2011a). The filter materials and facepiece respirators have been tested using nanoparticles down to single-digit nanometers (Shaffer and Rengasamy 2009). Another important application of nanoparticle filtration is diesel particulate filters. The increasingly stringent regulations regarding engine exhaust emissions are forcing the usage of emission control devices, including the diesel particulate filter (Johnson 2006).

Concerns existed as to whether the conventional filters could be effective against nanoparticles as the thermal rebound of particles may reduce the filtration efficiency. A number of studies of the filtration of nanoparticles down to 2 – 3 nm with spherical or similar shapes have been reported (Ichitsubo et al. 1996, Alonso et al. 1997, Heim et al. 2005). Kim et al. (2007) and Wang et al. (2007) studied the filtration of silver particles in the range of 3 – 20 nm in a variety of filter media including screen filters, standard fiberglass filters and a selection of personal protective equipment filters. The testing results show unambiguously that penetration decreases as the particle size decreases, and no thermal rebound was detected. These results demonstrate that conventional filters can work effectively against nanoparticles as small as 2 – 3 nm, which is very important for nanoparticle manufacturers, filter companies and policy makers.

[†] Accepted: July 27, 2012
[1] 8093 Zurich, Switzerland
[2] 8600 Dübendorf, Switzerland
E-mail: jing.wang@ifu.baug.ethz.ch
TEL: +41-44-633-36-21

© 2013 Hosokawa Powder Technology Foundation

The filtration of nanoparticles smaller than 100 nm is dominated by the diffusion mechanism (Wang et al. 2007), which was modeled based on the single-fiber theory. Penetration of a filter may be computed if one assumes that the filter is composed of uniformly distributed fibers of the same size. Such a model is proven to be accurate for spherical particles and filters with uniform microstructures (Heim et al. 2005, Shin et al. 2008, Wang et al. 2011b,c, Cena et al. 2012). However, the filters comprise fibers of different sizes in various orientations, as commercial fibrous media commonly do, and may display lower efficiency (higher penetration) compared to the model prediction (Wang et al. 2007, Wang et al. 2008 a,b, Kim et al. 2009a, Liu et al. 2011). Such a discrepancy may be due to the inhomogeneity in the microstructure of fibrous filters. Podgorski et al. (2011) developed a model to account for the fiber size distribution in the filters and used the model to explain the observed discrepancy.

Significant research has been performed on the filtration of asbestos and fibrous aerosols. Feigley (1975) modified the classic filtration theory for spherical particles to develop a model for the deposition of fibrous particles in a fibrous filter. Spurny (1986) performed experiments to measure the collection efficiencies of asbestos fibers in Nuclepore and Millipore filters. Gentry et al. (1989) focused on the collection efficiencies of asbestos fibers in Nuclepore filters and considered the collection of fibers in the straight pore theoretically. Gradon et al. (1988) analyzed the transverse and rotary motions of an ellipsoid in the flow near a cylinder and computed the deposition efficiency for the effect of interception, inertia and sedimentation. Cheng et al. (2006), Webber et al. (2007), and Vallero et al. (2009) focused on the measurement of asbestos collection on different filters and occupational safety aspects.

Carbon nanotubes (CNTs) are finding wider applications in structural composites, conductive plastics, semiconductor devices, etc. At the same time, they are raising concerns for negative environmental and health impacts (Kim et al. 2010, Wang and Pui 2012). The studies on the filtration of CNTs in air are scarce. Seto et al. (2010) investigated the filtration of CNTs by fibrous filters. Wang et al. (2011 b, c) reported experimental results for CNT penetration through a screen filter. Both a three-dimensional numerical simulation (Wang et al. 2011b) and single-fiber analysis (Wang et al. 2011c) were performed and compared to the experimental data.

Fu et al. (1990), Lange et al. (1999), Kim et al. (2009a) and Cena et al. (2012) investigated the filtration of nanoparticle agglomerates which are made up of clusters or chains of nanosize spheres referred to as primary particles. In the size range where interception is important, the agglomerate particles showed lower penetration due to their larger interception length compared to spherical particles with the same mobility diameters.

In the present study, we first present the filtration model based on the single-fiber theory. The model is then applied to spherical particles in the nanometer range, and compared to experimental data using filters with uniform and inhomogeneous microstructures. Elongated nanoparticles are then considered with a focus on the different filtration characteristics compared with spherical particles. The model is compared to experimental results for CNTs and nanoparticle agglomerates. The effects of the filtration velocity, filter fiber size, solidity and thickness are systematically investigated using the model.

2. Filtration Model for Fibrous Filters

Mechanisms for particle capture include diffusion, interception, inertial impaction, gravitational settling and electrostatic attraction. Gravitational settling is usually negligible for nanoparticles and electrostatic attraction is insignificant if the nanoparticles are neutralized. The single-fiber efficiency due to diffusion (E_D) may be written as (Kirsch and Stechkina, 1978)

$$E_D = 2.7Pe^{-2/3}, \tag{1}$$

where

$$Pe = \frac{d_f U_0}{D} = d_f U_0 \frac{3\pi\mu}{kTC_c} d_p. \tag{2}$$

In the equations, Pe is the Peclet number, d_f is the fiber diameter in the filter, U_0 is the filtration velocity, D is the particle diffusion coefficient, μ is the air viscosity, k is the Boltzmann constant, T is the temperature, C_c is the slip correction and d_p is the particle diameter. Since the diffusion coefficient can be directly related to the electrical mobility (Wang et al. 2011b), d_p in (2) can be approximated using the mobility diameter of non-spherical particles. The single-fiber efficiency due to the interception (E_R) of spherical particles can be written as (Lee and Liu 1982)

$$E_R = \frac{1+R}{2Ku}\left[2\ln(1+R) - 1 + \alpha + \left(\frac{1}{1+R}\right)^2\left(1-\frac{\alpha}{2}\right) - \frac{\alpha}{2}(1+R)^2\right], \tag{3}$$

where R is the interception parameter

$$R = d_p/d_f\,, \tag{4}$$

$$\text{and } Ku = -0.5\ln\alpha - 0.75 - 0.25\alpha^2 + \alpha\,. \tag{5}$$

In the equations, α is the filter solidity and *Ku* is the Kuwabara hydrodynamic parameter. For non-spherical particles, the choice of d_p in Equation (4) is very important for the calculation results and will be discussed in more detail in the following sections. The efficiency due to inertial impaction (E_I) can be expressed as (Wang and Pui 2009)

$$E_I = \frac{1}{(2Ku)^2}\left[\left(29.6 - 28\alpha^{0.62}\right)R^2 - 27.5R^{2.8}\right]\ \mathrm{Stk}, \tag{6}$$

where *Stk* is the Stokes number. For spherical particles,

$$Stk\ = \frac{\rho_p d_p^2 C_c U_0}{18\mu d_f}, \tag{7}$$

where ρ_p is the particle density. The Stokes number in Equation (7) can also be written as (Kim et al. 2009a)

$$Stk\ = \frac{mC_c(d_m)U_0}{3d_m\mu d_f}, \tag{8}$$

where d_m is the particle mobility diameter and *m* is the particle mass. Equation (8) is used for nanoparticle agglomerates. An additional interaction term, E_{DR}, may be added to the single-fiber efficiency to account for the interception of particles undergoing diffusion. An explicit expression for E_{DR} has been given for spherical particles (Hinds 1999)

$$E_{DR} = \frac{1.24R^{2/3}}{(Ku\cdot Pe)^{1/2}}. \tag{9}$$

The applicability of this expression for elongated particles is not known. Nonetheless, we apply Equation (9) to elongated particles in this study. The definition of *R* in Equation (9) is the same as in Equation (4). The choice of d_p is important for both E_D and E_{DR}, and to a large extent dictates the difference between the filtration results of spherical and elongated particles.

The total single-fiber efficiency is computed as

$$E_T = E_D + E_I + E_R + E_{DR}\,, \tag{10}$$

and penetration of the filter is computed as

$$P = \exp\left(-\frac{4\alpha E_T t}{\pi d_f(1-\alpha)}\right), \tag{11}$$

where *t* is the filter thickness. The pressure drop Δp across the filter is also important to evaluate the filter performance. It may be computed using an expression by Davies (1973)

$$\Delta p = \mu t U_0 f(\alpha)/d_f^2 \text{ with } f(\alpha) = 64\alpha^{1.5}(1+56\alpha^3)$$

$$\text{for } 0.006 < \alpha < 0.3. \tag{12}$$

3. Filtration of Spherical Nanoparticles

The filtration efficiency is determined by measuring the particle number concentrations upstream and downstream of the filter. The number concentration is the most sensitive parameter for nanoparticles and is commonly measured by Condensation Particle Counters (CPCs). Aside from the CPC counting technique, in-situ optical methods have also been used to determine filtration efficiencies (Baumgartner et al. 1993, Schweers et al. 1994, Kasper et al. 2009). The test aerosols in the size range from 15 nm to several hundred nanometers may be generated by atomizing a liquid solution of sodium chloride (Japuntich et al. 2007). The particles generated from an atomizer may not provide concentrations high enough for testing particles below 15 nm. A number of researchers used silver particles generated from an electrical tube furnace as the test aerosols in the size range from 3 nm to 20 nm (Kim et al. 2007, Shin et al. 2008, Rengasamy et al. 2008). The overlapping range from 15 nm to 20 nm can be used to check the consistency of the two methods. Since diffusion is the dominant filtration mechanism for particles well below 100 nm, the particle material barely affects the efficiency.

An example of the test set-up using silver nanoparticles is shown in **Fig. 1**. The silver nanoparticles generated in a furnace first pass through a bipolar neutralizer (Po-210), then through a Nanoparticle Differential Mobility Analyzer (Nano-DMA) to produce monodispersed aerosol particles. The monodispersed particles pass through another Po-210 neutralizer, then enter the filter holder. A pressure gage is used to measure the pressure drop across the filter.

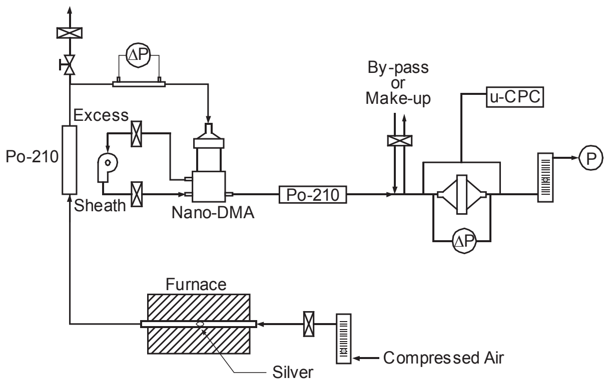

Fig. 1 Set-up for test using silver nanoparticles.

A Condensation Particle Counter measures the number concentration of the aerosol particles upstream and downstream of the filter. Then the penetration is calculated.

Metal screens with a highly regular and uniform microstructure can serve as good model filters. A stainless steel 304 screen (see Scanning Electron Microscopy SEM image in **Fig. 2**) manufactured by McMaster was used. The wire diameter was d_f = 90.31 μm, screen thickness was t = 203.2 μm, and the solidity was α = 0.3105. **Fig. 3** shows the measured penetration as a function of the particle size in the range of 2.5 to 20 nm. The model calculation only included the efficiency due to diffusion E_D since it was the dominant mechanism. The experimental data are in excellent agreement with the theoretical predictions. Experimental studies using screen filters by Heim et al. (2005), Shin et al. (2008), Wang et al. (2011a, b) covered silver and polystyrene latex (PSL) particles from 2.5 to 400 nm, and showed that the filtration model based on the single-fiber theory agreed well with the experimental data.

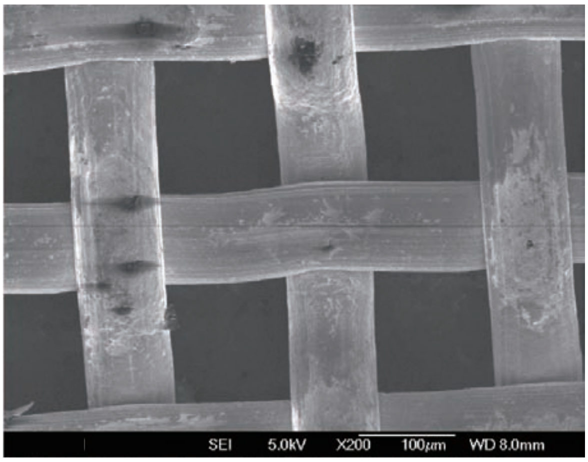

Fig. 2 An SEM image for the stainless steel 304 screen.

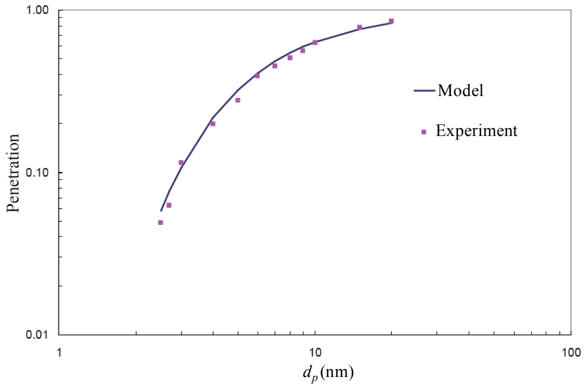

Fig. 3 Penetration vs. particle size d_p measured using the model screen filter.

Kim et al. (2007) and Wang et al. (2007) investigated filtration using standard fiberglass filters, HE1073, HE1021, HF0031 and HF0012 manufactured by Hollingsworth and Vose. HE-type filter media approach the HEPA regime for small aerosol particles; HF-type filter media are more common to standard HVAC systems. The filtration efficiency of these filter media has been tested using the ASTM test method F1215-

Table 1 Characteristic parameters of the four filter media. COV: coefficients of variation

Parameters		HE1073	HE1021	HF0031	HF0012
Thickness (cm)	Average	0.053	0.069	0.074	0.074
	% COV	2.3	4.3	2.3	2.3
Solidity	–	0.05	0.049	0.047	0.039
Effective fiber diameter (μm)	–	1.9	2.9	3.3	4.9
DOP % penetration 0.3 μm at 5.3 cm/s	Average	12.8	39	45.8	79.9
	% COV	2.2	1.7	0.92	1.24
Pressure drop at 5.3 cm/s (mmH$_2$O)	Average	8.4	4.7	3.5	1.3
	% COV	1.48	1.35	1.94	1.47
Fiber density (g/cm^3)	–	2.4	2.4	2.4	2.4

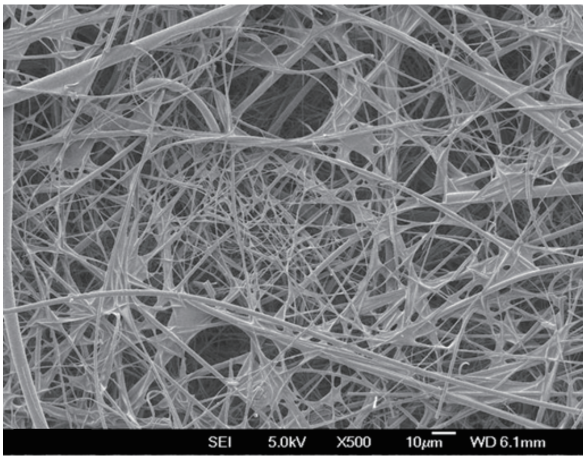

Fig. 4 SEM image of HE 1073 filter.

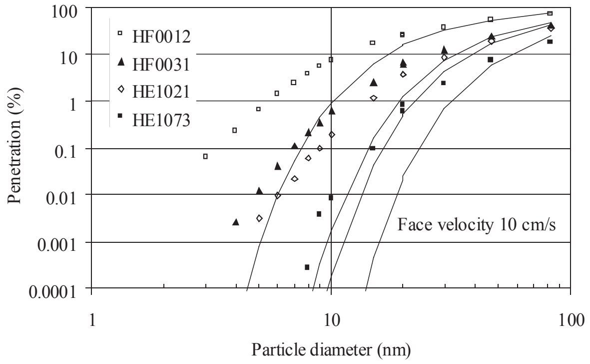

Fig. 5 Penetration vs. particle size. The symbols are experimental results and the solid lines are computed from the model.

89. The results showed low coefficients of variation (COV) and a high degree of reliability. Characteristic parameters for these filter media are given in **Table 1**. The effective fiber diameter was computed based on the pressure drop. An example of SEM pictures for the standard filter media is shown in **Fig. 4**. In **Fig. 5**, the penetration values for the face velocity 10 cm/s from the experiment and model calculation are compared. The penetration computed from the model is in fair agreement with the experimental results when d_p = 30 nm or larger, but substantially smaller than the experimental results when d_p < 30 nm. This discrepancy is attributed to the inhomogeneity and non-uniformity in the microstructures of the standard filter media. The sizes of pores in the fiber network are not uniform. The larger pores may allow very small particles to leak through, which causes the penetration to be higher than expected. Similar discrepancies between the experimental and modeling results were observed in the filtration of nanoparticles by nanofiber filters (Wang et al. 2008 a, b), by solvent-cast membranes (Liu et al. 2011) and by melt-blown fibrous filters (Podgorski et al. 2011). Podgorski and co-workers (Podgorski 2009, Podgorski et al. 2011) developed a partially segregated flow model that accounted for the non-uniformity of the fiber diameters.

The data show clearly that the penetration decreases as the particle size decreases down to 2 - 3 nm. It is therefore confirmed that the diffusion effect is stronger for smaller particles which leads to better filtration efficiency. Thus conventional filters are effective for particles down to 2 – 3 nm. When the particles are even smaller, their thermal speed may be high enough to rebound after contact with filter fibers, thus leading to higher penetration. Kim et al. (2006) investigated the filtration of particles down to 1 nm and reported that thermal rebound was detected for particles below 2 nm. Thermal rebound is dependent on the material properties and more studies are needed to better understand it.

4. Filtration of Elongated Nanoparticles

The filtration of CNTs and nanoparticle agglomerates possesses different characteristics than that of spheres. The airborne nanoparticles are often measured by electrical mobility analyzers, however, their geometric size is more important for the interception mechanism in the filtration process. For spheres, the mobility size and geometric size are the same; for elongated nanoparticles, the relationship is not apparent and depends on the specific morphology. In general, the geometric size of elongated particles is bigger compared to spheres with the same mobility size, thus leading to lower penetration when the interception mechanism is important.

Wang et al. (2011 b, c) measured the penetration of multi-wall CNTs (MWCNTs) through metal screen filters. The CNTs were dispersed into airborne form using a high throughput electrospray (Kim et al. 2010). A DMA was utilized to select CNTs of a certain mobility diameter and deposited on a grid placed inside a Nanometer Aerosol Sampler (NAS, TSI 3089), then samples were analyzed using SEM. A large number of CNTs were measured from the SEM images and the length distribution was fitted into a log-normal distribution. The mean length of the CNTs was then obtained for the corresponding mobility diameter. The results showed that the mean CNT length was 2300 nm, 4300 nm and 6100 nm when the CNT mobility diameter was 200 nm, 300 nm and 400 nm, respectively. The diameter of the CNTs was d_{CNT} = 85 nm in all cases (Wang et al. 2011b, c). Compared to spherical PSL particles, the penetration of CNTs was lower in the mobility size range of 100 – 400 nm (**Fig. 6**). A model calculation was performed and compared to experiments in **Fig. 6**. The agreement for the PSL particles was very good. To obtain good agreement for CNTs, the authors varied the value of d_p in Equation (4). When d_p was 2.4 times the aerodynamic diameter with an orientation angle $\theta \approx 40°$, the model fits the experiment well. The orientation angle θ was the angle between the CNT and the screen wire surface. This value for d_p in the interception calculation was bigger than the mobility size of the CNTs, but smaller than the geometric size. It was

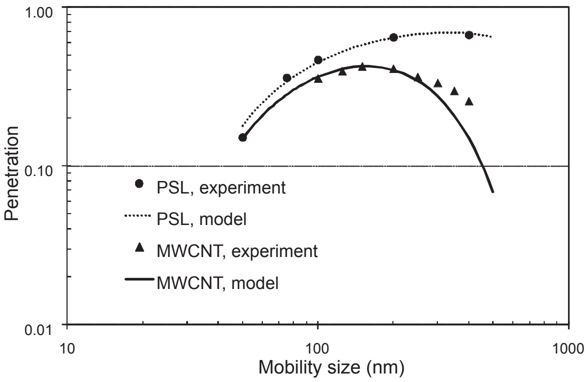

Fig. 6 Penetration as a function of the mobility size for PSL particles and multi-wall CNTs (MWCNTs). The symbols are experimental results and the curves are modeling results.

hypothesized that deformation of the long CNTs in the flow led to a reduced interception length, which happened to be proportional to the aerodynamic diameter.

Kim et al. (2009a) used silver nanoparticles for filtration studies. The two-furnace generation system enabled control of the particle morphology. When the sintering furnace was at room temperature, nanoparticle agglomerates with open structures were obtained; when the sintering furnace was at 600℃, sintered spheres were obtained. SEM image analysis was employed to characterize the morphology of the silver agglomerates, including the primary particle size and the maximum geometric length. The average primary sphere size was 16.2 nm with a standard deviation of 3.1 nm. The maximum geometric length L was correlated to the mobility diameter d_m in a power law

$$L = B d_m^{\gamma}, \tag{13}$$

where $B = 0.603$ and $\gamma = 1.268$ for agglomerates obtained at room temperature. The unit of B serves the purpose of balancing the unit in Equation 13. It is $(lu)^{-0.268}$, where lu is the length unit for L and d_m. A similar correlation between L and d_m was also obtained by Shin et al. (2009). The testing filter was HE 1073 from the Hollingsworth and Vose Company. The test results in **Fig. 7** showed that when the mobility diameter of the particles was small (e.g. 50 nm), the penetration of agglomerates without sintering is similar to that of sintered particles. For the agglomerates with such small sizes, the number of primary spheres in one agglomerate is limited and the morphology is close to the sintered particles. In addition, diffusion is the dominant filtration mechanism for such small particles. The diffusion coefficients of agglomerates and sintered particles are close when they have the same mobility diameter, thus the values of penetration are also similar. When the mobility diameter of the particles is large (e.g. 200 nm), the penetration of agglomerates is considerably lower than that of sintered particles. The interception mechanism plays an important role for the large particles. The agglomerates without sintering have branches and are more likely to be intercepted by the filter fibers, which leads to a lower penetration compared to sintered compact particles.

The modeling results for the silver spheres and agglomerates are plotted in **Fig. 7**. The maximum geometric length L is used as the interception length for the agglomerates in Equation (4). This is plausible since the aspect ratio of the silver agglomerates is about 1.6 – 1.8, and the particle's rotation time is short and less than the time for the particle to pass by filter fibers. The modeling results agree with the experimental ones qualitatively, showing that the spheres and agglomerates have similar penetration at small sizes, and the agglomerate penetration is lower than spheres at large sizes. The penetration predicted by the model is lower than the experimental value for particles of 50 nm and 20 nm. This is similar to the data shown in **Fig. 5**. We believe that inhomogeneity and random orientations of fibers in the filters are important reasons for this discrepancy. The penetration for agglomerates predicted by the model is also lower than the experimental value for particles larger than 200 nm. This may be due to preferential alignment of the longer agglomerates in the flow, thus higher penetration. Overall, the model for fibrous filters cannot accurately predict the penetration, however, it provides a useful tool for analyzing the different filtration efficiencies for spheres and agglomerates.

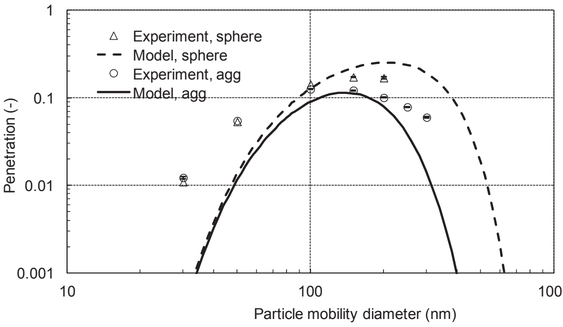

Fig. 7 Silver particle penetration as a function of the mobility size (test filter: HE 1073, face velocity: 5.3 cm/s). The error bars are included but they are smaller than the symbols.

5. Difference Between Spheres and Agglomerates

We use the model to investigate the effects of the filtration velocity, filter fiber size, solidity and thickness on the different penetration values for spheres and agglomerates. We select the silver agglomerates with open structures produced in the two-furnace system as a model agglomerate. Their geometric lengths are characterized by Equation (13). Their fractal dimension was determined to be 2.07 based on the particle mass vs. mobility size measurement (Kim et al. 2009a). The silver agglomerates have a similar morphology to a number of commonly found agglomerates. For example, soot particles from flames often possess a fractal dimension around 1.8 –

1.9 (Samson et al. 1987, Sorensen et al. 1992, Kim et al. 2009b); particles from diesel engine exhaust were found to have open structures (Wang and Pui 2012).

The model calculation is performed using the filtration velocities of 2, 5, 10, 20 and 40 cm/s. The filter parameters of HE 1073 are used in the calculation which include the fiber diameter d_f = 1.9 μm, thickness t = 0.53 mm, and solidity α = 0.05. The calculated penetration values at three filtration velocities are shown in **Fig. 8**. With increasing filtration velocity, the penetration for particles below 200 – 300 nm increases because of the weaker diffusion effect. For particles larger than 300 nm, the trend is reversed because the inertial effect is more important, which increases with the velocity. The difference between the spheres and agglomerates first increases with the particle size, then decreases. The reason is that for very small particles, the dominant diffusion effect is almost the same for spheres and agglomerates with the same mobility size; for particles larger than 400 – 500 nm, the penetration approaches zero for both spheres and agglomerates; in the intermediate size range, the interception mechanism plays an important role and the difference between spheres and agglomerates is apparent. The penetration difference is calculated at each mobility size d_m,

$$\Delta Penetration\ (d_m) = \text{Penetration (sphere, } d_m) - \text{Penetration (agglomerate, } d_m), \qquad (14)$$

then the maximum penetration difference is identified and the corresponding mobility size is referred to as the most differentiating particle size (MDPS). The absolute value of the penetration difference is computed, not the relative value normalized by Penetration (sphere, d_m) or Penetration (agglomerate, d_m). The reason is that the absolute value of the penetration difference is more practical in experiments. For example, if Penetration (sphere, d_m) = 0.01 and Penetration (agglomerate, d_m) = 0.001, the relative difference is large, in filtration experiments, however, it is difficult to accurately measure these close-to-zero penetration values.

The values of the maximum Δ*P*enetration and MDPS at different filtration velocities are listed in **Table 2**. The MDPS is always a bit larger than the most penetrating particle size (MPPS) on the penetration curve for the spheres. At such a particle size, the sphere penetration just starts to decrease from the maximum value and the agglomerate penetration approaches zero because the interception effect is much stronger, thus a large penetration difference is achieved. The value of the maximum Δ*P*enetration first increases with the filtration velocity, reaching the peak value at 10 cm/s, then decreases as the filtration velocity becomes greater. This is because the diffusion and inertial effects are important at low and high filtration velocities, respectively, and interception plays a smaller role. The MDPS decreases with the filtration velocity, from 290 nm at 2 cm/s to 158 nm at 40 cm/s. This trend is the same as the MPPS, which decreases with increasing filtration velocity (Lee and Liu 1980). The results in **Fig. 8** suggest that the lower filtration velocity should be used to differentiate larger spheres and agglomerates, and the higher filtration velocity should be used to differentiate smaller spheres and agglomerates. The optimum filtration velocity depends on the targeted particle size and the filter parameters.

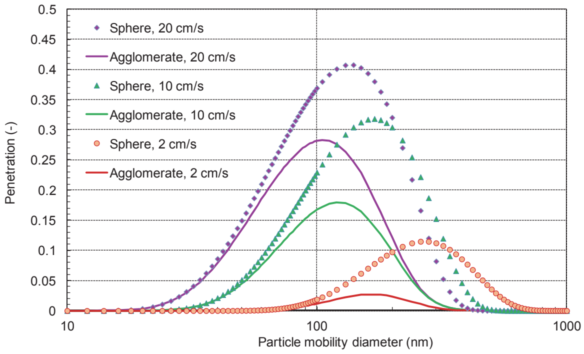

Fig. 8 Penetration values for spherical and agglomerated nanoparticles from model calculations at the filtration velocities of 2, 5, 10, 20 and 40 cm/s.

Table 2 The maximum penetration difference between spheres and agglomerates and the corresponding most differentiating particle size (MDPS) at different filtration velocities

U_0 filtration velocity (cm/s)	2	5	10	20	40
Max Δ*P*enetration	0.108	0.182	0.210	0.201	0.160
MDPS (nm)	290	247	218	189	158

The filtration model here does not consider the possible alignment of elongated particles in the flow field. Preferential orientation and alignment of fibrous particles have been observed in Nuclepore filters (Gallily et al. 1986, Gentry et al. 1989) and in the flow past a circular cylinder (Gradon and Podgorski 1990). The possibility of preferential alignment increases with the velocity and the particle aspect ratio, because the higher shear stress is more likely to overcome the random rotation of the elongated particle. The experimental results shown in **Fig. 7** indicate possible alignment of agglomerates larger than 200 nm in the HE 1073 filter at the filtration velocity of 5.3 cm/s. The possible alignment for elongated particles depends on filter parameters, filtration velocity and particle morphology, and requires further studies. The calculations in this study neglect the alignment effect, thus may overestimate the penetration at high velocities for large particles.

The effect of the filter thickness is evaluated by performing the model calculation for t = 0.265, 0.53 and 1.06 mm. The other filter parameters are the same as HE 1073, including the fiber diameter d_f = 1.9 µm and the solidity α = 0.05. The filtration velocity is set at 10 cm/s, because the largest maximum Δ*P*enetration was observed at 10 cm/s in **Table 2**. Such a calculation represents the case of stacking two layers of HE 1073 or reducing the thickness of HE 1073 to half. The calculated penetration curves are shown in **Fig. 9**. It is clear that the penetration increases as the thickness decreases. The MPPS for the spheres or the agglomerates does not change with the thickness. When t = 1.06 mm, the penetration values for both the spheres and agglomerates are low, thus Δ*P*enetration is small. As t decreases, the maximum penetration increases and larger values of Δ*P*enetration can be found on the right side of MPPS. The data in **Table 3** show that the maximum Δ*P*enetration and MDPS both increase as t decreases.

The penetration of spheres and agglomerates is calculated for filters with fiber sizes of 0.2, 1, 1.9, 5, and 10 µm. The fiber size significantly affects the pressure drop Δp, as shown in Equation (12). In the calculation, the solidity is kept at α = 0.05 and the filter thickness t is varied to keep the pressure drop Δp constant, which is equal to the pressure drop experienced by HE 1073. The thickness is t = 0.006, 0.15, 0.53, 3.67 and 14.68 mm for α = 0.2, 1, 1.9, 5 and 10 µm, respectively. Such an approach is similar to consideration of using the figure of merit (quality factor) to evaluate the filtration performance of different filters (Wang et al. 2008 a, b). The filtration velocity is set at 10 cm/s. Calculated results are shown in **Fig. 10**. The values of the maximum Δ*P*enetration and MDPS for different fiber sizes are listed in **Table 4**.

The results in **Fig. 10** show that the penetration difference for small particles in the range of 50 – 70 nm is significant when the fiber size is 0.2 µm, and is insignificant when the fiber size is larger than 1 µm. This is because interception is important when the particle size is comparable to the fiber size. If the interception parameter R (Equation 5) is too small, the diffusion effect dominates and the penetration difference is hardly observed. For particles larger than 200 nm, the 0.2 µm fibers have very high filtration efficiencies for both spheres and agglomerates, thus the penetration difference is small. The data in **Table 4** demonstrate that both the maximum Δ*P*enetration and MDPS increase with increasing fiber size. It can be concluded that small fibers need to be used to

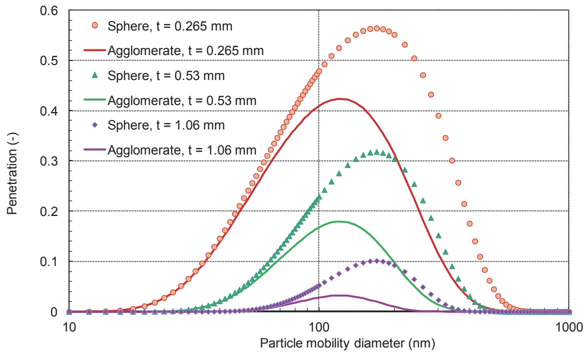

Fig. 9 Penetration values for spherical and agglomerated nanoparticles from model calculations for filter thickness values of 0.265, 0.53 and 1.06 mm.

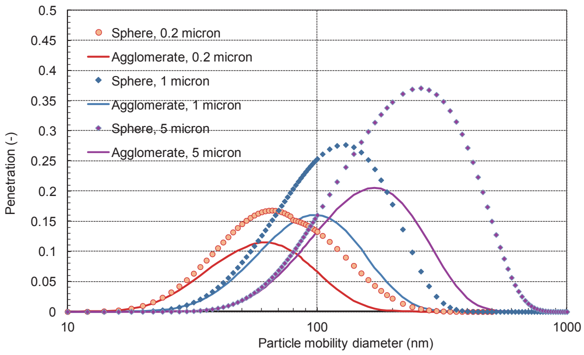

Fig. 10 Penetration values for spherical and agglomerated nanoparticles from model calculations for fiber sizes of 0.2, 1, and 5 µm.

Table 3 The maximum penetration difference between spheres and agglomerates and the corresponding most differentiating particle size (MDPS) at different filter thicknesses

Thickness t (mm)	1.06	0.53	0.265
Max Δ*P*enetration	0.085	0.210	0.288
MDPS (nm)	187	218	267

Table 4 The maximum penetration difference between spheres and agglomerates and the corresponding most differentiating particle size (MDPS) at different fiber sizes

Fiber size d_f (µm)	0.2	1	1.9	5	10
Max Δ*P*enetration	0.069	0.164	0.210	0.276	0.317
MDPS (nm)	111	162	218	336	457

differentiate small spheres and agglomerates; large fibers can be effective for the differentiation of large spheres and agglomerates.

Next, the effect of the solidity is studied by performing the model calculation for α = 0.02, 0.05 and 0.1. The solidity also affects the pressure drop Δp. In the calculation, the fiber size is kept at d_f = 1.9 μm and the filter thickness t is varied to keep the pressure drop Δp constant. The thickness is t = 2.1, 0.53, and 0.18 mm for α = 0.02, 0.05 and 0.1, respectively. The filtration velocity is set at 10 cm/s. The results are shown in **Fig. 11** and **Table 5**. The maximum penetration for the spheres and agglomerates increases with increasing solidity and decreasing filter thickness. The result indicates that the decreasing filter thickness has more impact on the penetration values than the increasing solidity. **Table 5** shows that the maximum Δ*P*enetration slightly increases, and the MDPS and MPPS both slightly decrease with the increasing solidity and decreasing filter thickness.

6. Conclusions

There were serious concerns as to whether the conventional filters could be efficient against exceedingly small particles. Diffusion and interception are important filtration mechanisms for nanoparticles. Diffusion loss is stronger for small particles, therefore the filtration efficiency increases with decreasing particle size in the nanometer range. However, thermal rebound of particles may reduce the filtration efficiency. Recent studies indicate that the filtration efficiency increases as the particle size decreases down to 2 – 3 nm. The possibility of thermal rebound for smaller particles or at elevated temperatures needs further studies.

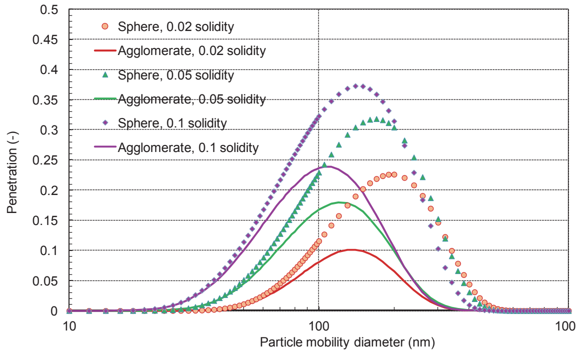

Fig. 11 Penetration values for spherical and agglomerated nanoparticles from model calculations for solidity values of 0.02, 0.05 and 0.1.

Table 5 The maximum penetration difference between spheres and agglomerates and the corresponding most differentiating particle size (MDPS) at different solidity values

Solidity α	0.02	0.05	0.1
Thickness t (mm)	2.1	0.53	0.18
Max Δ*P*enetration	0.174	0.210	0.211
MDPS (nm)	235	218	195

The filtration model based on the single-fiber theory works well for spherical particles in filters with uniform microstructures such as metal screens. However, the model often overestimates the filtration efficiency of the filters composed of fibers of different sizes in various orientations, such as commercial fibrous media. Such a discrepancy may be due to the inhomogeneity in the microstructure of fibrous filters.

Experiments show that filtration efficiency is higher for elongated particles, such as carbon nanotubes and nanoparticle agglomerates, compared to spheres with the same mobility. Analysis using the filtration model demonstrates that the enhanced interception effect is the major reason. Further calculation using the filtration model shows that the penetration difference between spheres and agglomerates is affected by the filtration velocity, filter thickness, fiber size and solidity. The most differentiating particle size (MDPS) decreases as the filtration velocity increases. Thus a lower filtration velocity should be used to differentiate larger spheres and agglomerates, and a higher filtration velocity should be used to differentiate smaller spheres and agglomerates. Small fibers need to be used to differentiate small spheres and agglomerates; large fibers can be effective for the differentiation of large spheres and agglomerates.

There are several limitations for the filtration model used here. The inhomogeneity in the microstructure is not considered, and the preferential alignment of elongated particles is not accounted for. Both could lead to overestimation of the filtration efficiency. Even with these limitations, the model is still a useful tool for qualitative analysis of the filtration process.

Acknowledgements

The authors thank the members of the Center for Filtration Research for their support: 3M, Boeing Commercial Airplanes, Cummins Filtration, Donaldson Co. Inc., Entegris Inc., Hollingsworth & Vose Co., MANN+HUMMEL GmbH, MSP Corp., Samsung Electronics Co. Ltd., Shigematsu Works Co.

Ltd., TSI Inc., and W. L. Gore & Associates Inc. as well as their affiliate member NIOSH.

References

Alonso, M., Kousaka, Y., Hashimoto, T. and Hashimoto, N. (1997): Penetration of Nanometer-Sized Aerosol Particles Through Wire Screen and Laminar Flow Tube, Aerosol Sci. Technol. Vol.27, pp.471-480.

Baumgartner, H., Piesch, C. and Umhauer, H. (1993): High-speed cinematographic recording and numerical simulation of particles depositing on electret fibres. J. Aerosol Science, Vol.24, pp.945-962.

Cena, L. G., Ku, B. K. and Thomas M. Peters (2012): Particle Collection Efficiency for Nylon Mesh Screens. Aerosol Sci. Technol. Vol.46, pp.214-221.

Cheng, Y. S., Holmes T. D. and Fan B. (2006): Evaluation of respirator filters for asbestos fibers. J Occup Environ Hyg. Vol.3,pp.26-35.

Davies, C. N. (1973): "Air filtration" , Academic Press, London.

Feigley, C. E. (1975): A mathematical model for deposition of asbestos in fibrous filter, Clean Air (Heidelberg, Aust.), pp.67-71.

Fu, T. H., Cheng, M. T., and Shaw, D. T. (1990): Filtration of Chain Agglomerate Aerosols by Model Screen Filter, Aerosol Sci. & Technol. Vol.13, pp.151-161.

Gallily, I., Schiby, D., Cohen, A. H., Hollander, W., and Schless, D. (1986): On the Inertial Separation of Nonspherical Aerosol Particles from Laminar Flows. I. The Cylindrical Case, Aerosol Sci. Tech. Vol.5, pp.267-286.

Gentry, G. W., Spurny, K. and Schörmann, D. (1989): Collection efficiency of ultrafine asbestos fibers, experimental and theory, Aerosol Sci. Technol. Vol.9, pp.184-195.

Gradon, L. and Podgorski, A. (1990). Flexible fibrous particle behaviour in the carrier gas flow around cylindrical obstacle, Chem. Eng Sci. Vol.45, pp. 3435-3441.

Gradon, L., Grzybowski, P. and Piłaciński, W. (1988): Analysis of motion and deposition of fibrous particles on a single filter element, Chem. Engng Sci. Vol.43, pp.1253-1259.

Heim, M., Mullins, B., Wild, M., Meyer, J. and Kasper, G. (2005): Filtration efficiency of aerosol particles below 20 Nanometers, Aerosol Sci. Technol., Vol.39, pp.782-789.

Hinds, W. C. (1999): "Aerosol technology: properties, behavior, and measurement of airborne particles", 2nd ed.,Wiley-Interscience,New York, .

Ichitsubo, H., Hashimoto, T., Alonso, M. and Kousaka, Y. (1996): Penetration of ultrafine particles and ion clusters through wire screens, Aerosol Sci. Technol., Vol.24, pp.119-127.

Japuntich, D., Franklin, L., Pui, D., Kuehn, T., Kim, S.C. and Viner, A. S. (2007): A comparison of two nano-sized particle air filtration tests in the diameter range of 10 to 400 nanometers, J. Nanoparticle Research, Vol.9, pp.93-107.

Johnson, T. V. (2006): "Diesel emission control in review", 2006 SAE world congress, Detroit Michigan, USA.

Kasper, G., Schollmeier, S., Meyer, J., and Hoferer, J. (2009): The collection efficiency of a particle-loaded single filter fiber. J. Aerosol Science, Vol.40, pp.993-1009.

Kim, S. C., Chen, D. R., Qi, C., Gelein, R. M., Finkelstein J. N., Elder, A., Bentley, K., Oberdorster, G. and Pui, D. Y. H. (2010): A nanoparticle dispersion method for in vitro and in vivo nanotoxicity study, Nanotoxicology, Vol.4, pp.42-51.

Kim, C. S, Bao, L, Okuyama, K, Shimada, M. and Niinuma, H. (2006): Filtration efficiency of a fibrous filter for nanoparticles, J. Nanoparticle Research, Vol.8, pp.215-221.

Kim, S. C, Wang, J., Shin, W. G., Scheckman, J. and Pui, D. Y. H. (2009b), Structural properties and filter loading characteristics of soot agglomerates, Aerosol Sci. & Technology, Vol.43, pp.1033-1041.

Kim, S. C., Harrington, M. S. and Pui, D. Y. H. (2007): Experimental study of nanoparticles penetration through commercial filter media, J. Nanoparticle Research, Vol.9, pp.117-125.

Kim, S. C., Wang, J., Emery, M., Shin, W. G, Mulholland, G. and Pui, D. Y. H. (2009a): Structural property effect of nanoparticle agglomerates on particle penetration through fibrous filter, Aerosol Sci. Tech, Vol.43, pp.344-355.

Kirsch, A. A. and Stechkina, I. B. (1978): "The theory of aerosol filtration with fibrous filters", in Shaw, D.T. (Ed.), Fundamentals of aerosol science, Wiley, New York.

Lange, R., Fissan, H. and Schmidt-Ott, A. (1999): Predicting the Collection Efficiency of Agglomerates in Fibrous Filter, Particle & Particle Systems Characterization, Vol.16, pp.60- 65.

Lee, K. W. and Liu, B. Y. H. (1980): On the minimum efficiency and most penetrating particle size for fibrous filters. J. Air Poll. Control Assoc., Vol.30, pp.377-381.

Lee, K. W. and Liu, B. Y. H. (1982): Theoretical study of aerosol filtration by fibrous filters. Aerosol Sci. & Technology, Vol.1, pp.147-161.

Liu, J., Pui, D. Y. H., and Wang, J. (2011): Removal of airborne nanoparticles by membrane coated filters, Sci Total Environ, Vol.409, pp.4868-4874.

Podgorski, A. (2009): Estimation of the Upper Limit of Aerosol Nanoparticles Penetration through Inhomogeneous Fibrous Filters, J. Nanopart. Res., Vol.11,pp.197-207.

Podgorski, A., Maißer, A., Szymanski, W. W., Jackiewicz, A. and Gradon, L. (2011): Penetration of Monodisperse, Singly Charged Nanoparticles through Polydisperse Fibrous Filters. Aerosol Science and Technology, Vol.45, pp.215-233.

Rengasamy, S., King, W. P., Eimer, B. C. and Shaffer, R. E. (2008): Filtration Performance of NIOSH-Approved N95 and P100 Filtering Facepiece Respirators Against 4 to 30 Nanometer-Size Nanoparticles, Journal of Occupational and Environmental Hygiene, Vol.5, pp.556-564.

Samson, R. J., Mulholland, G. W., and Gentry, J. W. (1987): Structural analysis of soot agglomerates. Langmuir, Vol.3, pp.272-281.

Schweers, E., Umhauer, H. and Löffler, F. (1994): Experimental investigation of particle collection on single fibers of different configurations, Particles and Particle Systems Characterization, Vol.11, pp.275-283.

Seto, T., Furukawa, T., Otani, Y., Uchida, K. and Endo, S. (2010): Filtration of Multi-Walled Carbon Nanotube Aerosol by Fibrous Filters, Aerosol Sci. & Technology, Vol.44, pp.734-740.

Shaffer, R. E. and Rengasamy, S. (2009): Respiratory protection against airborne nanoparticles: a review, J. Nanoparticle Research, Vol.11, pp.1661-1672.

Shin, W. G., Mulholland, G.W., Kim, S. C. and Pui, D. Y. H. (2008): Experimental study of filtration efficiency of nanoparticles below 20 nm at elevated temperatures, J Aerosol Sci, Vol.39, pp.488-99.

Shin, W. G, Wang, J., Mertler, M., Sachweh, B., Fissan, H. and Pui, D. Y. H. (2009): Structural properties of silver nanoparticle agglomerates based on transmission electron microscopy: relationship to particle mobility analysis, J. Nanopart Res., Vol.11, pp.163-173.

Sorensen, C. M., Cai, J. and Lu, N. (1992): Light-scattering measurements of monomer size, monomers per aggregate, and fractal dimension for soot aggregates in flames, Applied Optics, Vol.31, pp.6547-6557.

Spurny, K. R. (1986): On the filtration of fibrous aerosols. Science of the Total Environment, Vol.52, pp.189-199.

Vallero, D. A., Kominsky, J. R., Beard, M. E. and Crankshaw, O. S. (2009): Efficiency of sampling and analysis of asbestos fibers on filter media: implications for exposure assessment, J Occup Environ Hyg., Vol.6, pp.62-72.

Wang, J, Chen, D. R. and Pui, D. Y. H (2007): Modeling of filtration efficiency of nanoparticles in standard filter media, J. Nanoparticle Research, Vol.9, pp.109-115.

Wang, J. and Pui, D. Y. H. (2009): Filtration of aerosol particles by elliptical fibers: a numerical study, J. Nanoparticle Research, Vol.11, pp.185-196.

Wang, J. and Pui, D. Y. H. (2012): Dispersion and Filtration of Carbon Nanotubes (CNTs) and Measurement of Nanoparticle Agglomerates in Diesel Exhaust, Chem. Eng. Sci., DOI: 10.1016/j.ces.2011.12.045.

Wang, J., Asbach, C., Fissan, H., Hülser, T., Kuhlbusch, T. A. J., Thompson, D. and Pui, D. Y. H. (2011a): How can nanobiotechnology oversight advance science and industry: Examples from Environmental, Health and Safety Studies of Nanoparticles (nano-EHS), J. Nanoparticle Research, Vol.13, pp.1373-1387.

Wang, J., Kim, S. C and Pui, D. Y. H (2011b): Carbon Nanotube Penetration through a Screen Filter: Numerical Modeling and Comparison with Experiments, Aerosol Science & Technology, Vol.45, 443-452.

Wang, J., Kim, S. C. and Pui, D. Y. H. (2011c): Measurement of multi-wall carbon nanotube penetration through a screen filter and single-fiber analysis, J. Nanoparticle Res, Vol.13, pp.4565-4573.

Wang, J., Kim, S. C. and Pui, D. Y. H. (2008a): Investigation of the figure of merit for filters with a single nanofiber layer on a substrate, J. Aerosol Sci. Vol.39, pp.323-334.

Wang, J., Kim, S. C. and Pui, D. Y. H. (2008b): Figure of merit of composite filters with micrometer and nanometer fibers, Aerosol Science & Technology, Vol.42, pp.722-728.

Webber, J. S., Czuhanich, A. G. and Carhart, L. J. (2007): Performance of membrane filters used for TEM analysis of asbestos. J. Occup Environ Hyg., Vol.4, pp.780-789.

Author's short biography

Jing Wang

Jing Wang is an assistant professor at the Institute of Environmental Engineering at ETH Zurich (Swiss Federal Institute of Technology Zurich). He also leads the group Air Quality and Particle Research at Empa (Swiss Federal Laboratories for Materials Science and Technology). Jing Wang obtained his PhD degree from the Department of Aerospace Engineering, University of Minnesota in 2005. He received the ʻBest Dissertationʼ award in physical sciences and engineering from the University of Minnesota in 2006 and the Smulochowski award conferred by the Association for Aerosol Research (Gesellschaft für Aerosolforschung, GAeF) in 2011. His main research interests are nanoparticle transport and emission control, instrumentation for airborne nanoparticle measurement, air and water filtration, and the mechanics of multiphase flow.

Flame Synthesis of Complex Fluoride-Based Nanoparticles as Upconversion Phosphors†

Alexander Stepuk[1], Karl W. Krämer[2] and Wendelin J. Stark[1]*
[1] *Department of Chemistry and Applied Biosciences Institute for Chemical and Bioengineering*
[2] *Department of Chemistry and Biochemistry, University of Bern*

Abstract

Recent improvements in precursor chemistry, reactor geometry and run conditions extend the manufacturing capability of traditional flame aerosol synthesis of oxide nanoparticles to metals, alloys and inorganic complex salts. As an example of a demanding composition, we demonstrate here the one-step flame synthesis of nanoparticles of a 4-element non-oxide phosphor for upconversion applications. The phosphors are characterized in terms of emission capability, phase purity and thermal phase evolution. The preparation of flame-made β*-*$NaYF_4$ *with dopants of Yb, Tm or Yb, Er furthermore illustrates the now available nanoparticle synthesis tool boxes based on modified flame-spray synthesis from our laboratories at ETH Zurich. Since scaling concepts for flame synthesis, including large-scale filtration and powder handling, have become available commercially, the development of industrial applications of complex nanoparticles of metals, alloys or most other thermally stable, inorganic compounds can now be considered a feasible alternative to traditional top-down manufacturing or liquid-intense wet chemistry.*

Keywords: flame pyrolysis, upconversion, sodium yttrium fluoride, rare earth, luminescence, nanoparticles

1. Introduction

Nanoparticle powder technology is a widely applied industrial process for the preparation of advanced functional materials (Hosokawa, 2008). Predesigned and engineered nanostructures attract the interest of research and industry communities. Various methods of synthesis and control of these objects are constantly being developed and appear in high-impact journals, symposia and discussions. Despite a dramatic gap between academic methods for laboratory synthesis and the technological implementation on an industrial scale, various materials based on nanotechnologies are already available from large-scale production. Among the most promising methods are: CVD process for carbon nanotubes (Cassell et al., 1999); emulsion methods for polymeric nanoparticles (Muller et al., 2006) in drug delivery applications (PLGA, (Musyanovych et al., 2008)); sol-gel, e.g. $LiFePO_4$ (Lee et al., 2010); precipitation, e.g. $BaSO_4$, (Adityawarman et al., 2005); and hydrothermal methods (Chen et al., 2009) for various nanoparticles. However, the aforementioned methods are often inapplicable for metastable phases which often possess high functional characteristics.

Gas-phase synthesis stands aside as an independent process to fabricate nanopowders, particularly with aerosol methods. This technique allows a multi-scale and cheap production of nanoparticles. It is a relatively flexible technology by which also metastable phases can be obtained. Flame pyrolysis is currently applied in the large-scale production of SiO_2 and TiO_2 nanoparticles. The method is also promising for the production of nanostructured carbonates, e.g. $CaCO_3$ (Huber et al., 2005) and $SrCO_3$ (Strobel et al., 2006), sulfides, e.g. PbS and ZnS (Athanassiou et al., 2010), highly reactive metals, e.g. Co (Grass and Stark, 2006) and Ni (Jung et al., 2005), alloys, e.g. Cu-Ni (Jung et al., 2003), glasses, e.g. SiO_2–CaO–P_2O_5–Na_2O (Brunner et al., 2006), and halides, e.g. NaCl,

---

† Accepted: September 10, 2012
[1] ETH Zurich 8093 Zurich, Switzerland
[2] 3012 Bern, Switzerland
* Corresponding author:
E-mail: wendelin.stark@chem.ethz.ch
TEL: +41-44-632-0980 FAX: +41-44-633-1571

ⓒ 2013 Hosokawa Powder Technology Foundation

BaF_2, and CaF_2,(Grass and Stark, 2005). An overview of nanoparticles prepared by flame-spray pyrolysis is shown in **Fig. 1**. The established materials, namely spherical oxide nanoparticles, a straightforward product of gas-phase synthesis, stand at the origin of the graph. This group typically includes titanium, silicon, and aluminum oxides. There has been evidence for more complex materials prepared by flame pyrolysis, e.g. $Sr_5(PO_4)_3Cl:Eu^{2+}$ (Kang et al., 2003). A reducing atmosphere helps to step away from oxidic nanoparticles towards metallic compounds. Acetylene-fed flames form carbon shells on the surface of metallic nanoparticles (Grass et al., 2007). Such carbon coatings allow chemical functionalization strategies of the nanoparticle surface to use them in filtration and purification (Rossier et al., 2011), magnetic chemical reagents (Wittmann et al., 2010) and catalysts (Zeltner et al., 2011). Sulfides derived from flame pyrolysis belong to another group of widely applied chalcogenide salts. Recently, Athanassiou et al. successfully prepared doped $ZnS:Mn^{2+}$ nanoparticles (Athanassiou et al., 2010).

Another group of industrially valuable non-oxidic salts are halides. Chlorides and fluorides of alkaline and alkaline-earth metals have been successfully obtained by gas-phase synthesis yielding nanoparticles of various morphologies and structures. Fluorides have unique optical and electronic properties which are widely used in biomaterials and electronic applications, though the need of more complex phosphors requires the preparation of glasses and mixed fluorides.

Recently, upconversion (UC) phosphors based on the rare earth and alkaline-earth materials have been investigated. In a UC process several low energy photons are absorbed, their energy is converted and finally a photon of higher energy is emitted. UC is also known as anti-Stokes emission (Auzel, 2004). It is known for f-elements such as the lanthanide ions Er^{3+} and Tm^{3+}, as well as U^{3+}, and several d-element ions embedded into specific matrices (Auzel, 2004).

Upconversion phosphors such as β-$NaYF_4$: Yb, Tm or Yb, Er are regularly synthesized as bulk microcrystalline materials by high-temperature solid-state synthesis:

$$NaF + (1-x-y)YF_3 + xErF_3 + yYbF_3 \rightarrow NaYF_4 : (xEr^{3+}, yYb^{3+}) \qquad (1)$$

Targeting molecules in biological applications and thin coatings for solar cells imply size limits of the embedded upconversion particles from tens to hundreds of nanometers. For the same purposes, it is preferable to produce upconversion nanoparticles with high luminescence intensity. Few approaches in the production of nanocrystalline UC phosphor materials are known: decomposition of multiprecursors (Yi et al., 2004), co-precipitation (Martin et al., 1999), hydrothermal and solvothermal methods (Zeng et al., 2005). Nonetheless, those methods are limited to predictable crystallite morphology, low production rates and complicated synthesis schemes. Hexagonal sodium yttrium fluoride is one of the most efficient host matrices for NIR-to-visible upconversion phosphors (Sommerdijk, 1973). The upconversion efficiency of sodium yttrium fluoride host matrices is 20 times higher compared to La_2O_3 and 6 times - to $La_2(MoO_4)_3$ crystal matrices (Blasse and Grabmaier, 1994). $NaYF_4$: Yb,Er or Yb,Tm upconversion phos-

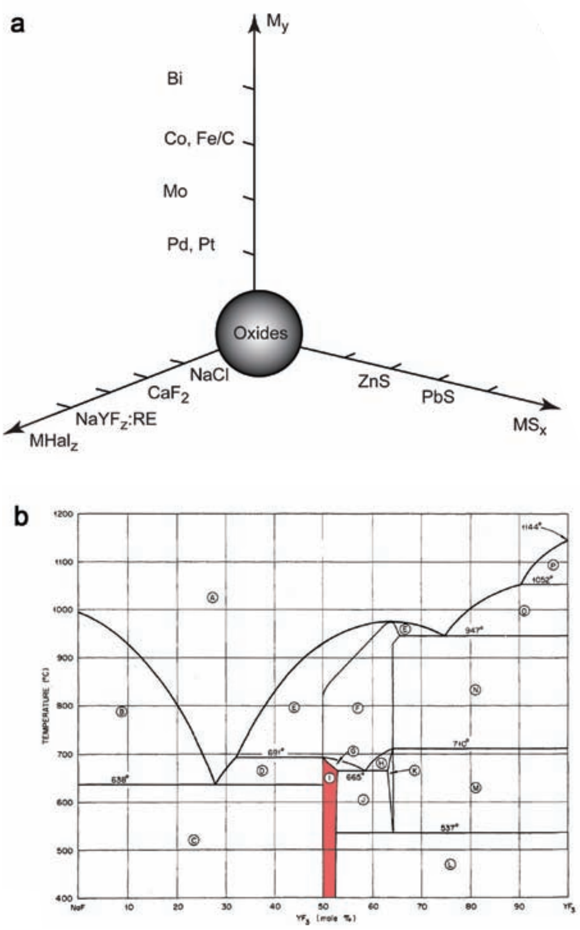

Fig. 1 (a) Schematic representation of various nanostructures currently available by the flame-pyrolysis technique and (b) phase diagram of the NaF-YF_3 system (Thoma et al., 1963). The shaded area marks the hexagonal $NaYF_4$ stability region. Adapted with permission from Thoma et al., 1963. Copyright 1963 American Chemical Society.

phors convert, e.g. continuous-wave 980-nm laser excitation into NIR, visible and UV emissions. Cost-effective diode lasers can be used to obtain UC emissions from transparent nanoparticle solutions (Heer et al., 2004). The prospective applications of such phosphors include bio labels (Wang et al., 2009), solar cells (Richard and Shalav, 2005) and solid-state lasers (Sandrock et al., 1997).

Lim et al. (Lim et al., 2009) successfully produced sub-10-nm polydisperse UC nanophosphors by flame-spray pyrolysis in a one-step continuous synthesis. The host matrix used for their study was cubic Y_2O_3 which is less efficient than hexagonal $NaYF_4$ (Auzel, 2004). Grass et al. (Grass and Stark, 2005) proposed a fluoride doping with rare earth elements by flame synthesis. As a result, it appeared feasible to synthesize upconverting sodium yttrium fluoride nanoparticles doped with Yb-Tm or Yb-Er, although the cubic phase might be obtained instead of the hexagonal phase which shows better UC properties. Due to the limited thermodynamic stability of the hexagonal low-temperature phase, see the phase diagram in **Fig. 1b**, the cubic high-temperature phase of $NaYF_4$ might be obtained from the synthesis as metastable kinetic product.

In the present work, flame pyrolysis is used to prepare nanoparticles of non-oxidic, doped rare earth fluorides. The upconversion emission during excitation with NIR laser and the thermal behavior of the derived phosphors are analyzed. The cubic-to-hexagonal phase transition of $NaYF_4$ will be examined for various syntheses and thermal treatment conditions.

2. Experimental

Preparation of $NaYF_4$: Yb (Tm, Er) nanoparticles

Powders of nano-sized upconversion particles (UCNP, $NaYF_4$: Yb,Tm) were fabricated by flame-spray pyrolysis. Precursors of yttrium, ytterbium, erbium, and thulium were prepared from rare earth acetates $Tm(CH_3CO_2)_3{\cdot}xH_2O$, $Y(CH_3CO_2)_3{\cdot}xH_2O$ (Fluka, 99.90% metal trace), and $Yb(CH_3CO_2)_3{\cdot}xH_2O$ (Acros Organics, 99.90% metal trace) by refluxing them with 2-ethylhexanoic acid (Fluka, puriss.) (Stark et al., 2003, 2004, 2005) and removal of acetic acid, for experimental conditions see **Table 1**. In the case of erbium-doped phosphors, $Er(CH_3CO_2)_3{\cdot}xH_2O$ (Fluka, 99.90% metal trace) was dissolved in 2-ethylhexanoic acid and the solution was directly combusted in the flame. $NaHCO_3$ (Ph Eur, Applichem Co.) was mixed with 2-ethylhexanoic acid to obtain the sodium precursor. Each precursor solution was diluted with xylene (technical grade) to adjust the metal content to 1M and was filtered before combustion.

Table 1 Precursor synthesis conditions

Salt ion	Temperature, ℃	Distillation time, hours	Concentration, wt. %
Y^{3+}	130	6	6.3
Yb^{3+}	110	12	8.32
Tm^{3+}	120	2	0.7

The prepared stoichiometric mixtures of rare earth ethylhexanoates, sodium 2-ethylhexanoate, and fluorobenzene (ABCR-Chemicals, 99%) were combusted to produce $NaYF_4$ nanoparticles, doped with 25 mol.% Yb and 0.3 mol.% Tm, i.e. $NaY_{0.747}Yb_{0.25}Tm_{0.003}F_4$, and 20 mol.% Yb and 2 mol.% Er, i.e. $NaY_{0.78}Yb_{0.2}Er_{0.02}F_4$. The solution was pumped through a 0.4-mm-diameter capillary at rates of 3, 5, 7, and 9 l min^{-1} into fuel flames. Alternatively, the liquid solution was dispersed into an aerosol and burnt in oxygen (99.8%, Pan Gas) at rates of 7, 5, and 3 l min^{-1} with a pressure drop at the capillary tip of 1.5 bar. A steady combustion was achieved by an oxygen (99.8%, Pan Gas) sheath gas flow of 230 l h^{-1} through a concentric sinter metal ring. A Teflon filter was used to collect the prepared particles of UCNP. The particles remained stable at ambient conditions. In the case of the reducing flame pyrolysis, the precursors were burned in a nitrogen-rich atmosphere using a nitrogen (5N, PanGas) glove-box with gas flow (Grass et al., 2007). This flow was circulated by a vacuum pump (Busch, Seco SV1040CV). The oxygen concentration was fixed below 100 ppm (volumetric) for the reducing flame pyrolysis.

Characterization of UC phosphors

The specific surface area was calculated by measuring the nitrogen adsorption at 77 K on a Tristar (Micromeritics Instruments) following the Brunauer–Emmett–Teller (BET) method. Prior to the surface area determination, samples were preheated in vacuum at 150℃ with $p < 0.1$ mbar during 1 hour.

The prepared $NaYF_4$ nanoparticles with Yb-Tm and Yb-Er rare earth dopants were sintered at various temperatures (500 – 800℃) in air or nitrogen flow during 2 or 3 hours at heating rates of 10℃ min^{-1}. A "fast" heating of the $NaYF_4$:Yb, Er upconversion phosphors was achieved by placing the powders directly in an 800℃ preheated furnace.

The relative upconversion luminescence was measured according to the following procedure: Powders of the UC phosphors were filled in glass tubes of 1 mm inner and 1.5 mm outer diameter and then fixed in a sample holder. The powder densities were the same for all samples, as the powders were pressed into the glass tubes with glass tips. The samples were excited by a 980-nm IR laser diode coupled to a 1-mm-diameter fiber. The non-focused laser beam illuminated the sample in a spot of about 1 mm^2 at a distance of 2-3 mm from the surface. The UC emission was collected by a Y-fiber, i.e. parallel to the excitation light, and measured by an Ocean Optics SD1000 spectrometer. The reflected IR laser light was blocked by a filter in front of the spectrometer. The laser power was measured by a power meter. The luminescence spectra were corrected for the spectral response of the detection system. The integrated emission peaks yielded the relative UC efficiencies of the powder samples with a reproducibility of 5%.

The size and shape of the as-prepared upconversion nanoparticles were characterized by transmission electron microscopy (TEM) with a Philips CM30 ST (LaB_6 cathode, operated at 300 kV, point resolution 4 Å). Morphologies were also analyzed by scanning electron microscopy (SEM) with a Zeiss LEO 1530 Gemini. The phase composition was characterized by X-ray diffraction (XRD) patterns recorded with a PANalytical XPert PRO-MPD (CuKα radiation, X'Celerator linear detector system, step size of 0.033°, ambient conditions). The mean crystallite size was estimated from X-ray diffraction patterns by the Scherrer equation.

3. Results and Discussion

Flame-spray powder morphologies and phase analysis

$NaYF_4$: Yb, Tm powders were prepared by flame-spray synthesis. The obtained nanoparticles had diameters of 20-40 nm. The fuel/oxygen flow rates of 3/7, 7/3, and 7/9 L/min resulted in the formation of cubic α-$NaYF_4$ particles, see **Fig. 2a**. Equation (2) shows the reaction scheme,

$$\text{Liquid} \rightarrow \text{NaF} + \text{NaYF}_4 \qquad (2)$$

where liquid corresponds to the melt in the flame before cooling down at the Teflon filter.

The medium 5/5 l min^{-1} feeding rate led to a mixed product with hexagonal(β) and cubic(α) phases of sodium yttrium fluoride, see **Fig. 2a**.

The TEM analysis of this powder revealed the presence of hexagonal particles. The particles have sizes of about 10 nm with agglomerates up to 50 nm, see **Fig. 2b**.

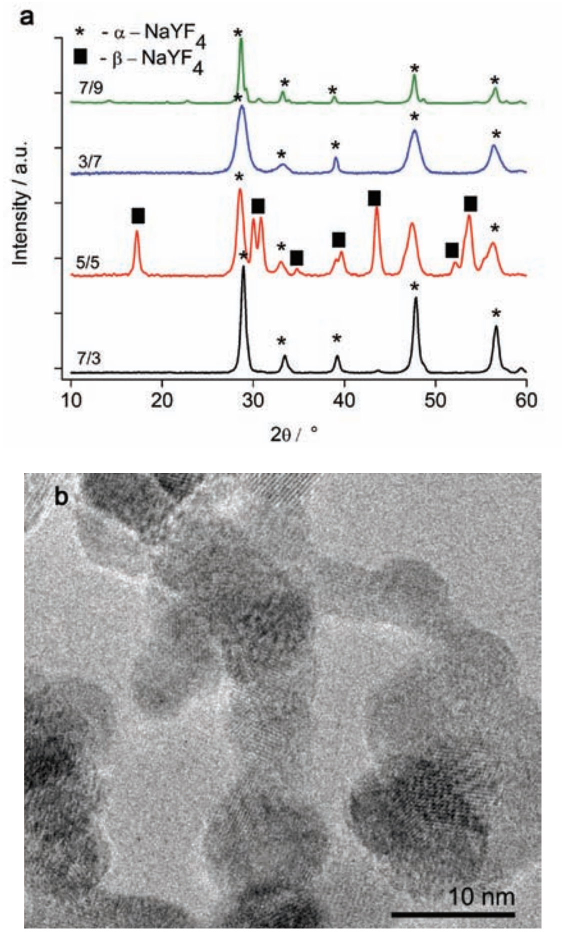

Fig. 2 (a) X-ray diffraction patterns of $NaYF_4$:Yb,Tm nanoparticles from different fuel/oxygen flow rates and (b) Transmission electron microscopy image of hexagonal $NaYF_4$:Yb,Tm nanoparticles obtained from fuel/oxygen flow rates of 5/5 L/min.

By the BET method, specific particle surface areas from 29.5 to 31 m^2 g^{-1} were determined for nanoparticles prepared in oxidic or reduced atmospheres.

The calculated particle diameters according to equation (3) were 47 and 45 nm, respectively,

$$d_{BET} = \frac{6}{\rho \cdot SSA} \qquad (3)$$

where ρ = 4.3 g cm^{-3} is the density of β-$NaYF_4$ (Sobolev, 2000) and SSA is the specific surface area (Sobolev et al., 1963).

The SEM micrographs of flame-sprayed $NaYF_4$: Yb, Tm also demonstrated the homogeneous distribution of nanoparticles without any visible micron-sized agglomerates, see **Fig. 3a**. These particles are stable at room temperature under atmospheric conditions. Images of the as-prepared $NaYF_4$:Yb,Er nanoparticles show agglomerated clusters in the 100-nm range with

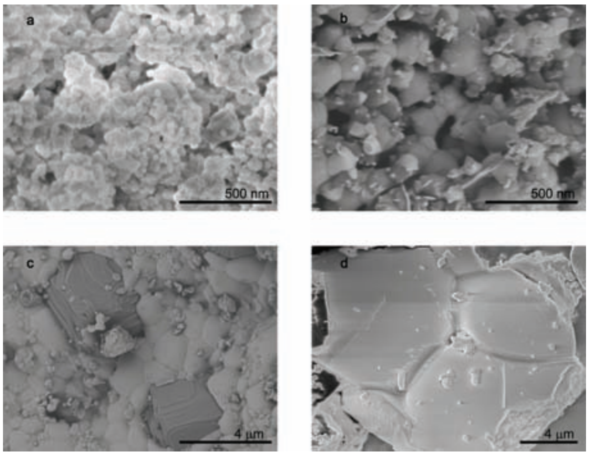

Fig. 3 SEM micrographs of sodium yttrium fluorides prepared by the flame-spray method. (a) and (b) show highly anisotropic hexagonal nanoparticles of $NaYF_4$: Yb, Tm and Yb, Er, respectively. (c) and (d) show images of micron-sized crystallites of $NaYF_4$ and cubic Y_2O_3, respectively, after sintering at 700℃ in ambient atmosphere.

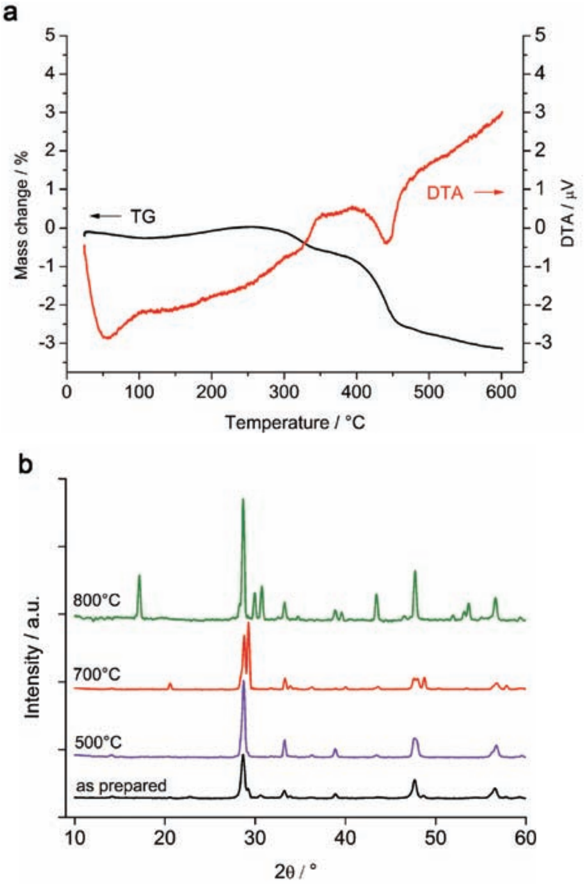

Fig. 4 (a) Differential thermal analysis (DTA) and thermal gravimetric (TG) signals of $NaYF_4$:Yb, Tm nanoparticles and (b) XRD diffraction patterns for different sintering temperatures of $NaYF_4$:Yb, Er. 500℃ and 700℃ sintering was applied at a 10℃ min^{-1} heating rate. For 800℃, a "fast" heating is achieved by placing the powder directly into the preheated furnace.

hexagonal crystallites of less than 50 nm in size, see **Fig. 3b**. It correlates to previously measured BET and TEM particle size estimations. During sintering, the grains grow and micron-sized cubic crystals of Y_2O_3 form, see **Fig. 3c**. The image of a fragment in **Fig. 3d** shows narrow grain boundaries of β-$NaYF_4$ crystals after 3 hours sintering at 700℃ under constant nitrogen flow.

Thermal treatment of UC phosphors

The thermal behavior of the synthesized powders was studied by differential thermal analysis (DTA), see **Fig. 4a**. At low temperatures, the adsorbed water was released from the sample according to a weight loss of 0.3 wt% In addition, the DTA signal indicates a minor exothermal peak at 380℃ It may correspond to the formation of traces of cubic yttrium oxide. At 400-500℃, the TG curve shows a step correlated to an endothermic peak on the DTA curve.

Analysis of the phase composition of upconversion phosphors sintered at 500℃ showed decreasing halfwidths of the Bragg peaks which correspond to an increased size of the crystallites. The $NaYF_4$: Yb, Tm powders were sintered at temperatures from 500℃ to 800℃. The XRD curves up to 700℃ give no hint for a phase transition, see **Fig. 4b**. The sintering at 800℃ shows a partial transition of sodium yttrium fluoride from its cubic to the hexagonal phase. According to the NaF-YF_3 (Thoma et al., 1966) phase diagram, see **Fig. 1b**, the hexagonal β-$NaYF_4$ phase is stable at room temperature whereas the high-temperature cubic α-phase is stable above 691℃. Thus cubic $NaYF_4$ is obtained in the synthesis as a metastable, kinetically stabilized phase. Only at high enough temperatures, close to the α-β phase transition, can the α-phase overcome the activation energy barrier and transform into the β-phase. The '800℃' curve in **Fig. 4b** shows a partial α-β phase transition. The sample temperature had obviously not been 800℃ in this experiment, because then no β-phase would be obtained at all, but it had been high enough to partially activate the transition.

The thermal treatment at 700℃ in an air flow during two hours led to the formation of Y_2O_3. This hydrolysis results in HF gas evolution and leaves Y_2O_3 and NaF behind, cf. equation (4).

$$2\ NaYF_4 + 3\ H_2O \rightarrow 2\ NaF + Y_2O_3 + 6\ HF \qquad (4)$$

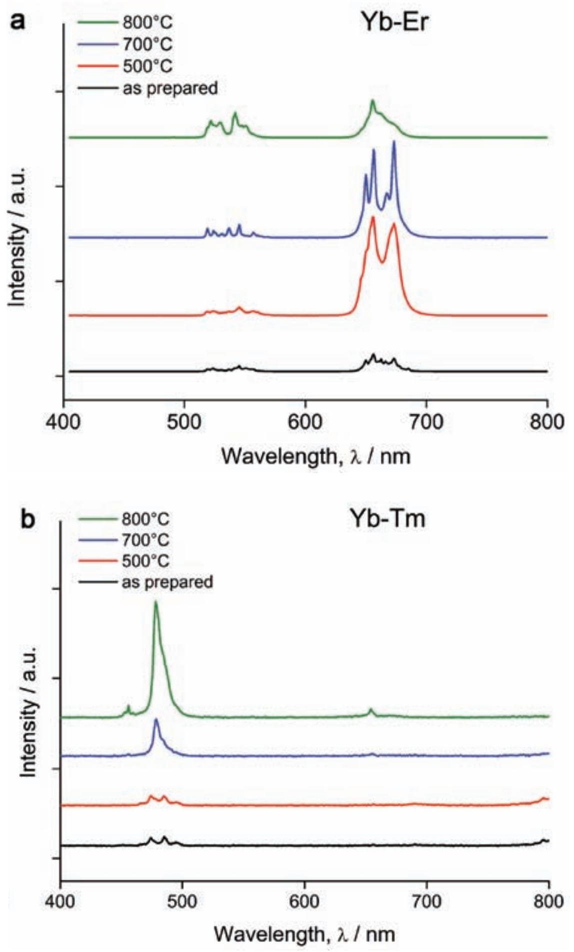

Fig. 5 Upconversion luminescence emission of $NaYF_4$ with Yb-Er (a) and Yb-Tm (b) rare earth dopant couples. The relative peak intensities increase after sintering from 500℃ to 800℃.

In order to transform the cubic phase towards the more favorable hexagonal phase, the powders were sintered in vacuum. The X-ray diffraction patterns of samples treated at 500℃ demonstrate the growth of crystals, see **Fig. 4b**, but no formation of hexagonal $NaYF_4$. Crystallite sizes derived from the Scherrer Equation show a growth from 40 nm to 80 nm. Sobolev et al. (Sobolev et al., 1963) earlier demonstrated that the $NaYF_4$ hexagonal phase undergoes a phase transition into $NaYF_4$ with cubic symmetry at 600℃.

Further examinations of the flame-spray synthesis conditions and thermal treatment modes such as cooling rate are required. Flame pyrolysis allows the synthesis of nanocrystalline upconversion phosphors with a high surface area which show luminescence (**Fig. 5b**, **6a** and **b**).

Thermal behavior and luminescence of $NaYF_4$:Yb, Er

$NaYF_4$:Yb, Er samples were prepared using a 7/9 (L /min) feeding rate. The particles revealed green and red luminescence on excitation with a 980-nm IR laser. After sintering at 500℃ and 700℃, the luminescence intensity increased because the crystallites grew in size. Fast heating, i.e. placing powders into a preheated furnace at 800℃, resulted in rapid formation of hexagonal sodium yttrium fluoride, see **Fig. 4b**. As a result, the green emission intensity increased, see Fig.5a. Phosphors sintered under an inert atmosphere formed oxide phases, which in turn intensified the red emission in the UC luminescence spectrum, see **Fig. 5a**. Yttrium oxide formation in the inert atmosphere is based on phase kinetics and prior built-in oxygen. This embedding happens during flame pyrolysis in an oxygen-containing environment. The formation of micron-size crystallites is observed on the SEM micrographs, see **Fig. 3c**. A slow heating rate of 10℃ min^{-1} yielded a mixture of yttrium oxide and cubic $NaYF_4$; the fast heating leads to hexagonal $NaYF_4$ formation.

The luminescence spectra of upconversion phosphors doped with Yb^{3+} and Tm^{3+} show two characteristic visible emissions upon 980-nm excitation, see **Fig. 5b**. The red emission originates from the $^1G_4 \rightarrow {}^3F_4$ transition. The blue emission consists of the two neighboring transitions of $^1G_4 \rightarrow {}^3H_6$ and $^1D_2 \rightarrow {}^3F_4$. Upconversion luminescence spectra also show emissions in the ultraviolet range ($^1D_2 \rightarrow {}^3H_6$ and $^1I_6 \rightarrow {}^3F_4$). Higher sintering temperatures increase the luminescence intensity because larger crystallites have a smaller surface-to-volume ratio and therefore less defects (Suyver et al., 2006). The Yb^{3+}, Er^{3+}-doped α-$NaYF_4$ shows a significantly higher red ($^4F_{9/2} \rightarrow {}^4I_{15/2}$) than green ($^4S_{3/2} \rightarrow {}^4I_{15/2}$) emission, see **Fig. 5a**. However, for the “fast heating” at 800℃ sample, the green-to-red emission ratio becomes higher because hexagonal β-$NaYF_4$ formed which has a significantly stronger green emission. Photographs of the UC emission of the respective samples are shown in **Fig. 6**.

4. Conclusions

Pre-designed complex nanostructures with characteristic properties are built up by assembling their functional units step by step. In this regard, gas-phase methods have a great potential for industrially realizing some of the promises of nanotechnology. Their scaling potential and access to various types of precursors covers a plethora of nanostructures such as metals, oxides, salts, and complex compounds.

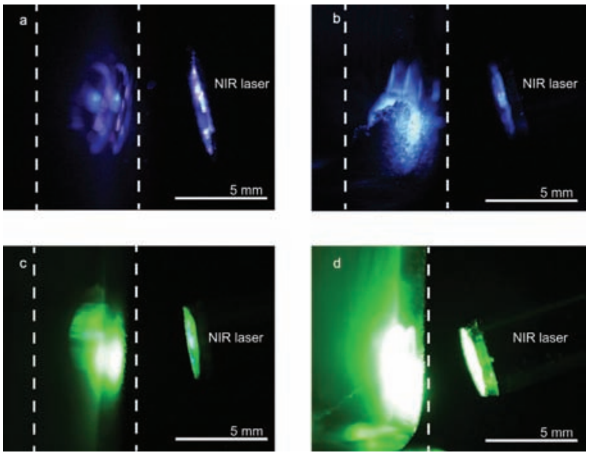

Fig. 6 Photographs of the UC luminescence of Yb^{3+}, Tm^{3+} (a, b) and Yb^{3+}, Er^{3+} (c, d)-doped nanophosphors. The thermal treatment of powders at 800℃ significantly increased the intensity of the visible emissions for the Yb^{3+}, Tm^{3+} (b) and the Yb^{3+}, Er^{3+} (d) phosphors.

In the present work, a successful bottom-up access through a refined flame-spray technique provides access to complex non-oxide particles such as rare-earth-doped sodium yttrium fluorides. The co-doping with Yb-Tm and Yb-Er ion couples leads to blue and green upconversion luminescence, respectively. Particles of less than 50 nm in size were obtained under reducing conditions as cubic $NaYF_4$. It was possible to tune a cubic to hexagonal phase transition by thermal treatment of the nanomaterial. A strongly enhanced UC luminescence intensity was observed for the β-$NaYF_4$. Upconversion luminescence spectra showed a correlation between crystallite size (i.e. low surface area) and luminescence intensity. Oxide impurities reduced the green and increased the red UC emissions in Yb^{3+}, Er^{3+}-doped phosphors.

References

1) Adityawarman, D., Voigt, A., Veit, P. and Sundmacher, K. (2005): Precipitation of $BaSO_4$ nanoparticles in a non-ionic microemulsion: Identification of suitable control parameters, Chem Eng Sci, Vol.60, pp.3373-3381.
2) Athanassiou, E. K., Grass, R. N. and Stark, W. J. (2010): One-step large scale gas phase synthesis of Mn^{2+} doped ZnS nanoparticles in reducing flames, Nanotechnology, Vol.21, 215603, doi:10.1088/0957-4484/21/21/215603 .
3) Auzel, F. (2004): Upconversion and anti-stokes processes with f and d ions in solids, Chem Rev, Vol.104, pp.139-173.
4) Blasse, G. and Grabmaier, B. C. (1994). “Luminescent Materials”, Springer-Verlag, Berlin.
5) Brunner, T. J., Grass, R. N. and Stark, W. J. (2006): Glass and bioglass nanopowders by flame synthesis, Chem Comm, pp.1384-1386.
6) Cassell, A. M., Raymakers, J. A., Kong, J. and Dai, H. J. (1999): Large scale CVD synthesis of single-walled carbon nanotubes, J. Phys Chem B, Vol.103, pp.6484-6492.
7) Chen, L. Y., Shen, Y. M. and Bai, J. F. (2009): Large-scale synthesis of uniform spinel ferrite nanoparticles from hydrothermal decomposition of trinuclear heterometallic oxo-centered acetate clusters, Materials Letters, Vol.63, pp.1099-1101.
8) Grass, R. N. and Stark, W. J. (2005): Flame synthesis of calcium-, strontium-, barium fluoride nanoparticles and sodium chloride, Chem Comm, pp.1767-1769.
9) Grass, R. N. and Stark, W. J. (2006): Gas phase synthesis of fcc-cobalt nanoparticles, J. Mater Chem, Vol.16, pp.1825-1830.
10) Grass, R. N., Athanassiou, E. K. and Stark, W. J. (2007): Magnetische Trennung von organischen Verbindungen durch kovalent funktionalisierte Cobalt-nanopartikel, Angewandte Chemie, Vol.119, pp.4996-4999.
11) Heer, S., Kömpe, K., Güdel, H. U. and Haase, M. (2004): Highly Efficient Multicolour Upconversion Emission in Transparent Colloids of Lanthanide-Doped $NaYF_4$ Nanocrystals, Advanced Materials, Vol.16, pp.2102-2105.
12) Hosokawa, M. (2008), In: “Nanoparticle Technology Handbook”, Hosokawa, M., Nogi, K., Naito, M. and Yokoyama,T., , editors, Amsterdam: Elsevier, pp.v-vi.
13) Huber, M., Stark, W. J., Loher, S., Maciejewski, M., Krumeich, F. and Baiker, A. (2005): Flame synthesis of calcium carbonate nanoparticles, Chem Comm, pp.648-650.
14) Jung, C. H., Lee, H. G., Kim, C. J. and Bhaduri, S. B. (2003): Synthesis of Cu–Ni Alloy Powder Directly from Metal Salts Solution, J. Nanopart Res, Vol.5, pp.383-388.
15) Jung, C. H., Jalota, S. and Bhaduri, S. B. (2005): Quantitative effects of fuel on the synthesis of Ni/NiO particles using a microwave-induced solution combustion synthesis in air atmosphere, Materials Letters, Vol.59, pp.2426-2432.
16) Kang, Y. C., Sohn, J. R., Yoon, H. S., Jung, K. Y. and Park, H. D. (2003): Improved Photoluminescence of $Sr_5(PO_4)_3Cl:Eu^{2+}$ Phosphor Particles Prepared by Flame Spray Pyrolysis, J. Electrochem Soc, Vol.150, pp.H38-H42.
17) Lee, S. B., Jang, I. C., Lim, H. H., Aravindan, V., Kim, H. S. and Lee, Y. S. (2010): Preparation and electrochemical characterization of $LiFePO_4$ nanoparticles with high rate capability by a sol-gel method, J. Alloy Compd, Vol.491, pp.668-672.
18) Lim, S. F., Riehn, R., Tung, C. K., Ryu, W. S., Zhuo, R., Dalland, J. and Austin, R. H. (2009): Upconverting nanophosphors for bioimaging, Nanotechnology,

Vol.20, 405701, doi:10.1088/0957-4484/20/40/405701 .

19) Martin, N., Boutinaud, P., Mahiou, R., Cousseins, J. C. and Bouderbala, M. (1999): Preparation of fluorides at 80 degrees C in the NaF-(Y,Yb,Pr)F-3 system, J. Mater Chem, Vol.9, pp.125-128.

20) Muller, K., Klapper, M. and Mullen, K. (2006): Synthesis of conjugated polymer nanoparticles in non-aqueous emulsions, Macromol Rapid Comm, Vol.27, pp.586-593.

21) Musyanovych, A., Schmitz-Wienke, J., Mailander, V., Walther, P. and Landfester, K. (2008): Preparation of biodegradable polymer nanoparticles by miniemulsion technique and their cell interactions, Macromol Biosci, Vol.8, pp.127-139.

22) Richard, B. S. and Shalav, A. (2005): The role of polymers in the luminescence conversion of sunlight for enhanced solar cell performance, Synth Metals, Vol.154, pp.61-64.

23) Rossier, M., Schaetz, A., Athanassiou, E. K., Grass, R. N. and Stark, W. J. (2011): Reversible As(V) adsorption on magnetic nanoparticles and pH dependent desorption concentrates dilute solutions and realizes true moving bed reactor systems, Chem Eng J., Vol.175, pp.244-250.

24) Sandrock, T., Scheife, H., Heumann, E. and Huber, G. (1997): High-power continuous-wave upconversion fiber laser at room temperature, Opt Lett, Vol.22, pp.808-810.

25) Sobolev, B. P., Mineev, D. A. and Pashutin, V. P. (1963): Low-temperature hexagonal modification of $NaYF_4$ having gagarinite structure, Doklady Akademii Nauk Sssr, Vol.150, pp.791-794.

26) Sobolev, B. P. (2000). Introduction to Materials Science of Multicomponent Metal Fluoride Crystals. In: “Rare Earth Trifluorides”, Barcelona: Inst. D Estudis Catalan’, pp.202-208.

27) Sommerdijk, J. L. (1973): Influence of the host lattice on the infrared-excited blue luminescence of Yb^{3+}, Tm^{3+}-doped compounds, J. Lum, Vol.8, pp.126-130.

28) Stark, W. J., Pratsinis, S. E., Maciejewski, M., Loher, S. F. and Baiker, A. (2005). Flame synthesis of metal salt nanoparticles, in particular calcium and phosphate comprising nanoparticles, Patent WO2005087660.

29) Stark, W.J., Mädler, L., and Pratsinis, S.E. (2004). Metal oxides prepared by flame spray pyrolysis. Patent WO2004005184.

30) Stark, W. J., and Pratsinis, S. E. (2003). Metal delivery system for nanoparticle manufacture, Patent WO2004103900.

31) Strobel, R., Maciejewski, M., Pratsinis, S. E. and Baiker, A. (2006): Unprecedented formation of metastable monoclinic $BaCO_3$ nanoparticles, Thermochimica Acta, Vol.445, pp.23-26.

32) Suyver, J. F., Grimm, J., van Veen, M. K., Biner, D., Kramer, K. W. and Gudel, H. U. (2006): Upconversion spectroscopy and properties of $NaYF_4$ doped with Er (3+), Tm^{3+} and/or Yb^{3+}, J. Lumin, Vol.117, pp.1-12.

33) Thoma, R. E., Hebert, G. M., Insley, H. and Weaver, C. F.(1963): Phase Equilibria in the System Sodium Fluoride-Yttrium Fluoride, Inorg Chem, Vol.2, pp.1005-1012.

34) Wang, G. F., Peng, Q. and Li, Y. D. (2009): Upconversion Luminescence of Monodisperse CaF_2:Yb^{3+}/Er^{3+} Nanocrystals, J. Am Chem Soc, Vol.131, pp.14200-14201.

35) Wittmann, S., Schätz, A., Grass, R. N., Stark, W. J. and Reiser, O. (2010): A Recyclable Nanoparticle-Supported Palladium Catalyst for the Hydroxycarbonylation of Aryl Halides in Water, Angew Chem Int Ed, Vol.49, pp.1867-1870.

36) Yi, G., Lu, H., Zhao, S., Ge, Y., Yang, W., Chen, D. and Guo, L. H. (2004): Synthesis, Characterization, and Biological Application of Size-Controlled Nanocrystalline $NaYF_4$:Yb, Er Infrared-to-Visible Up-Conversion Phosphors, Nano Letters, Vol.4, pp.2191-2196.

37) Zeltner, M., Schatz, A., Hefti, M. L. and Stark, W. J. (2011): Magnetothermally responsive C/Co@PNIPAM-nanoparticles enable preparation of self-separating phase-switching palladium catalysts, J. Mater Chem, Vol.21, pp.2991-2996.

38) Zeng, J. H., Su, J., Li, Z. H., Yan, R. X. and Li, Y. D. (2005): Synthesis and Upconversion Luminescence of Hexagonal-Phase $NaYF_4$:Yb, Er^{3+} Phosphors of Controlled Size and Morphology, Advanced Materials, Vol.17, pp.2119-2123.

Author's short biography

Alex Stepuk

Alex Stepuk received a BSc. in materials science at Moscow State University. He graduated with an MSc of the Materials Science Department at ETH Zurich with a pioneering thesis on the implementation of upconversion phosphors in dental photopolymers. He is currently a PhD candidatein the group of Prof. Wendelin J. Stark at the Department of Chemistry and Applied Biosciences at ETH Zurich. His research interests are interdisciplinary, covering applications of flame-spray-derived nanoparticles in dental materials and orthopedics, materials for energy conversion and polymers in medicine.

Karl W. Krämer

Karl W. Krämer received his chemistry diploma (1988) and his Dr. rer. nat. (1991) from the Justus-Liebig University, Giessen, Germany. He is the group leader of solid state analytics at the Department of Chemistry of the University of Bern, Switzerland. His research focuses on the synthesis of anhydrous metal halides, their crystal growth, and investigation of spectroscopic and magnetic properties. Recent topics are upconversion phosphors, e.g. β -NaYF4:Yb,Er or Yb,Tm, Ce3+-doped scintillators, e.g. LaBr3:Ce, and quantum spin ladders, e.g. [piperidinium]2CuBr4.

Wendelin J. Stark

Wendelin J. Stark received his master'sdegree in chemistry in 2000, followed by a PhD in mechanical engineering in 2002, both from ETH Zurich. In 2004, he founded the Functional Materials Laboratory within the Departments of Chemistry and Applied Bioscience at the ETH Zurich. His research group pursues application-oriented research at the interface of chemistry with materials science and medicine.

Theoretical and Experimental Testing of a Scaling Rule for Predicting Segregation in Differently Sized Silos[†]

Stefan Zigan[*] and Amit Patel
[1] *Department of Mechanical Engineering, University of Greenwich, UK*

Abstract

The generalisation of scientific findings between differently sized silos is a challenge faced across many industries. One obstacle is the scaling of material properties (e.g. particle size), process parameters (e.g. the powder feeding rate) and dimensions (e.g. silo diameter and height) to obtain significant results1). The second issue for a meaningful scaling law is maintaining the dynamic similarity between two differently sized silos. A common phenomenon observed when filling alumina storage silos is called air current segregation (ACS,) and was investigated in detail in Zigan et al.2). This paper is now a continuation, exposing the developed scaling rule to a challenging test by replacing alumina with sand particles and the continuum air with water. Results of the scaling tests show that the proposed dimensionless groups do not capture the complete physics. One reason is that using terminal velocity in the scaling law as a physical parameter to lump in fluid and material properties over-simplifies the problem. Another finding is that the particle dynamics in the water model is somehow different from experiments in the air silo.

Keywords: dimensional analysis, method of least sum squares, segregation, silo, powder flow, air current segregation

1. Introduction

Scaling is important when investigating a physical phenomenon such as ACS which causes severe powder handling problems in industry. Experimental findings have to be scientifically justified to convince industry to change process parameters. One approach is to apply dimensional analysis (DA) by keeping material, process and equipment parameters dynamically and geometrically similar1). Dynamic similarity can be preserved in differently sized silos when particle, process and equipment parameters are scaled according to a scaling rule. The scaling rule presented in Zigan et al.2) (first paper applying the scaling rule) is believed to be able to scale process and equipment parameters between differently sized silos. However, the scaling of material properties such as particle size hampers the use of the DA approach when, for example, scaling to a small size causes a change in the flow behaviour from free flowing to cohesive. The consequences of amending the flow characteristic of powders are changes in the particle dynamics in the silo. To satisfy the scaling law, the material and process parameters have to be adjusted to maintain dynamic similarity between differently sized silos1). This adjustment includes changes of the particle size and the fluid properties. Changing the fluid in which particles settle affects the hydrodynamics of the solid-fluid phase flow. A particle settling in a surrounding fluid will create a disturbance in the fluid. This disturbance creates a convection flow which influences the flow of particles. The particles are separated from each other and settle as single particles in the fluid3). The settling of particles is described by their terminal velocity, and the velocity distribution of the differently sized particles is the most influential parameter for segregation effects4). The settling of particles in a fluid is scientifically well understood even though it is still difficult to predict the particle settling veloc-

---

[†] Accepted: October 2, 2012
[1] Chatham Maritime, Kent ME4 4TB, United Kingdom
[*] Corresponding author:
E-mail: s.zigan@gre.ac.uk
TEL: +44 1634 883450 FAX: +44 1634 883153

ⓒ 2013 Hosokawa Powder Technology Foundation

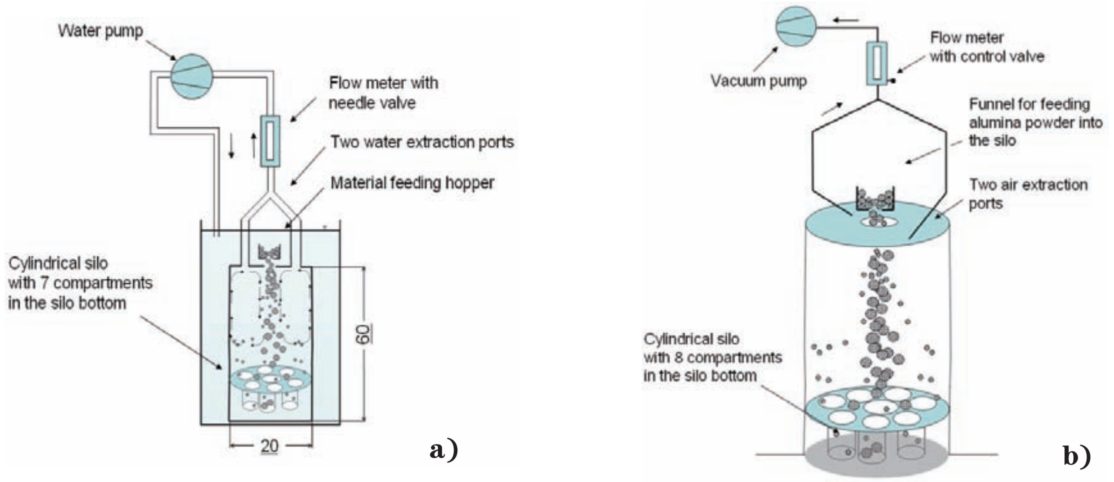

Fig. 1 a) Schematic diagram of the sand-water silo, b) Schematic diagram of the alumina-air silo (units in cm).

ity accurately. The prediction of the particle settling velocity depends on calculating the drag coefficient which is directly linked to the Reynolds number of the settling particle[5]. Hazzab et al.[6] define the drag force *Cd* as:

$$C_d = \frac{(\rho_s - \rho_f)\, gV}{\rho_f\, (V_t/2)\, A} \tag{1}$$

where ρ_s is the density of the particle and ρ_f the density of the fluid, g gravity and V_t is the volume of the particle. *A* is the projected area following the flow, and *Vt* is the terminal velocity. Equation (1) shows that the particle density influences the drag force and consequently the terminal velocity. The density of a bulk of particles can vary when dealing with porous particles such as alumina.

2. Theoretical Model

The calculation of the terminal velocity follows the approach suggested by Turton et al.[7] For convenience, a dimensionless particle diameter defined in equation (2) and a dimensionless terminal velocity defined in equation (3) are calculated to estimate the terminal velocity of a single particle settling in the fluid.

$$\frac{d^*}{d} = \left(\frac{\rho_f\,(\rho_s - \rho_f)\, g}{\mu^2}\right)^{1/3} \tag{2}$$

where d^* is the dimensionless diameter, *d* is the particle diameter of a defined mass fraction and μ is the viscosity.

$$\frac{V_t^*}{V_t} = \left[\frac{\rho_f^2}{\mu\,(\rho_s - \rho_f)\, g}\right]^{1/3} \tag{3}$$

where V_t^* is the dimensionless terminal velocity.

The dimensionless terminal velocity can be calculated using the following empirical relation in equation (4)[7]:

$$\log_{10} V_t^* = -1.64758 + 2.94786 * \log_{10} d^* - 1.09703 * \log_{10} d^{*2} + 0.17129 * \log_{10} d^{*3} \tag{4}$$

The terminal velocity is calculated to scale the material and process parameters between differently sized experiments. The scaling rule proposed by Zigan et al.[2] was applied to predict segregation for different process parameters and silo dimensions. The experimental designs of the air-alumina silo and the sand-water silo are shown in **Fig. 1** The scaling rule is reproduced in equation (5):

$$I_s = f\left(\frac{E}{S}, \frac{R^2 V_t}{S}\right) \tag{5}$$

where *E* is the air extraction rate, *S* the powder feeding rate, *R* is the silo dimension (e.g. radius) and V_t is the terminal particle velocity.

The segregation index as defined in equation (6) includes the particle mass and the particle size distributions over all compartments of the experimental silo as shown in **Fig. 1**:

$$I_s = \left(\sum_i \frac{M_i}{M_L} \times \left[\frac{c_i - c_L}{c_L}\right]^2\right)^{0.5} \tag{6}$$

where c_i is the mass fraction of fines in the single compartment *i*, M_i is the mass of powder in compartment *i*, c_L is the mass fraction of fines over all compartments and M_L is the total mass in all compartments. This paper extends the research work of Zigan et al.[2] and tests the scaling rule in differently sized silos with different materials and process parameters. The comparison of results in differently scaled silos requires an empirical relationship to compare experimental data. The method of least sum squares was selected to correlate experimental data[2].

3. Prediction Model

The development of a theoretical model predicting ACS in silos is useful when process parameters are changing, e.g. variable feeding rate to an industrial storage silo. The prediction model for ACS in silos is based on the method of least sum squares fitting for experimental data. A set of experimental data[2] is correlated and the linear relationship between the dimensionless groups is then plotted in a graph. When plotting the correlated values for two dimensionless groups in a graph, the third dimensionless group should remain unchanged. In the experiments[2], the geometry (e.g. radius of the silo) and material properties (e.g. V_t of the particles) are kept constant. Keeping the ratio of the dimensionless group (E/S) the same as the dimensionless group (R^2V_t/S) requires adjusting the air extraction rate (E) according to the changes of the powder feeding rate (S). The $\log_{10}$ of the dimensionless group (E/S) is plotted vs the $\log_{10}$ of the dimensionless group (I_s) as shown in **Fig. 2**. One of the advantages of choosing a power law formulation for the correlation is that it always results in positive values for I_S.

Data from three different feeding rates (0.05, 0.2 and 1.3 kg/min) and three different air extraction rates (20, 60 and 120 L/min) are correlated to obtain a linear relationship between the two dimensionless groups. For each of the three lines in **Fig. 2**, linear equations such as equation (7) were found by the method of least squares. The values of α_1 and α_2 in equation (7) are constants and are estimated in the next step.

$$\log_{10} I_s = \alpha_1 + \alpha_2 \cdot \log_{10}\left(\frac{E}{S}\right) \tag{7}$$

Since all the trend lines have nearly the same slope in **Fig. 2**, it was decided to use the average value of α_2 from the three lines. The average value obtained for α_2 is 0.024. The values for α_1 were calculated by applying equation (8) and then fitted to the three lines by the method of least squares.

$$\alpha_1 = \log_{10} I_s - \alpha_2 \cdot \log_{10}\left(\frac{E}{S}\right) \tag{8}$$

The resulting values of a1 are then plotted versus the third dimensionless group S/R^2V_t (**Fig. 3**). Finally, values for the constants α_1, α_2 as well as different powder feeding and air extraction rates are computed using equation (9). Equation (9) can be utilised to predict the segregation behaviour of a material when process parameters are altered. Experimental data are taken from Zigan et al.[2] Plotting the third dimensionless group, which includes the geometry of the silo (R) and the material/ fluid properties (V_t), vs the dimensionless group (I_s) provides an indication of how well the theoretical model predicts segregation in the silo (**Fig. 4**). **Fig. 4** shows that the predicted values agree well with the experimental data for high feeding rates. For lower feeding rates, the prediction model does not work very well. This can partly be explained by the characteristic of the particle jet which became more dilute with lower powder feeding rates[2].

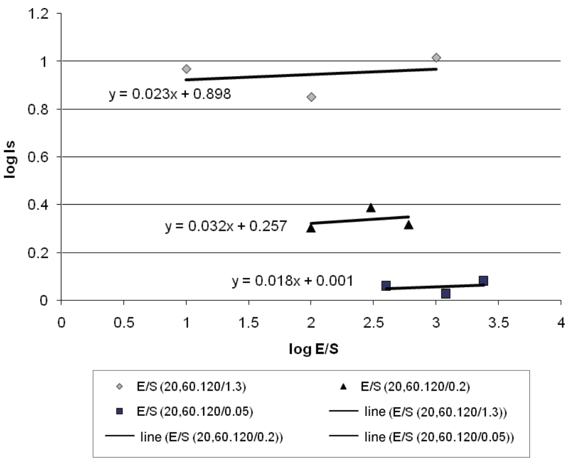

Fig. 2 Effect of different powder feeding and air extraction rates on the segregation index .

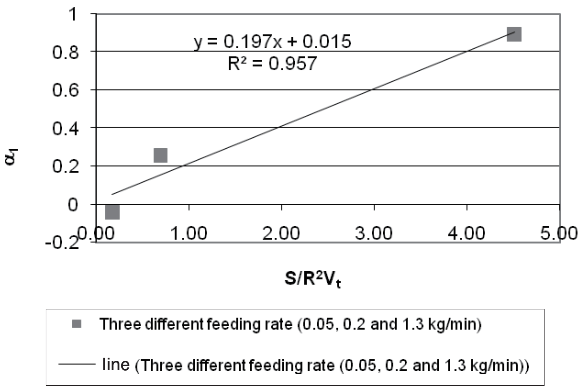

Fig. 3 Correlation of the dimensionless group S/R^2V_t vs α_1 for three different feeding rates (0.05, 0.2 and 1.3 kg/min).

$$\log_{10} I_s = \frac{0.197xS}{R^2 v_t} + 0.015 + 0.024 \cdot \log_{10}\left(\frac{E}{S}\right) \quad (9)$$

The resulting correlation shown in equation (9) can also be applied to predict segregation in differently sized silos and by using **Fig. 4**, the segregation tendency of powders in differently scaled experiments can be compared.

In the next section, the validity of the scaling law presented in equation (5) will be tested. The testing of the scaling law is challenging since material and process parameters have to be scaled according to equation (5) to keep dynamic and geometric similarity.

4. Experimental Model

Two dimensionally similar sets of experimental silos scaled by a factor of two are used to validate the scaling rule. The first experimental apparatus is the air-alumina silo which is set up in the same way as described in Zigan et al.[2] The only difference is that the silo bottom contained only one central compartment and one outer ring with 7 catchments as shown in **Fig. 1**. The cylinder of the larger alumina-air silo has a diameter of 0.4 m and a height of 1.2 m. Two air extraction ports at the top plate are connected to the main vacuum line and extract air from the experimental silo. The set air flow rate is 16 L/min. A total mass of 1000 g alumina is fed centrally into the silo. The funnel in the experiments uses a flow reduction plate with one opening to create a dense particle jet. The alumina is fed at 0.8 kg/min into the silo.

Fig. 1 also shows the set-up of the scaled-down experiment. The air is replaced by water. The water silo is smaller than the air silo by a factor of two. The cylindrical silo is completely submerged in water. All geometric dimensions have to be scaled down from the alumina-air silo to keep dimensional and dynamical similarity between the two experiments. The alumina is replaced by sand. Sand is inert when submerged in water and particles have an almost spherical shape. The density of sand particles is around 2650 kg/m^3 compared to the density of alumina 1500 kg/m^3. In the sand experiment, the silo height is 0.6 m and the silo diameter is 0.2 m. A total mass of 250 g sand is fed into the silo. The mass reduction is necessary because the 7 catchments in the bottom cannot accommodate more material. The mass flow rate into the silo is around 0.2 kg/min. A centrifugal pump extracts water from the silo and pumps it back into the vessel. A needle valve with a flow range of 20 to 270 L/h[1] is used to keep the fluid extraction rate at 4 L/min. After all sand settled at the silo bottom, the water is drained and the sand collected from the seven catchment areas in the silo. Then the sand is dried in an oven. After the sand was completely dry, the particle size and the mass fraction in each compartment was measured.

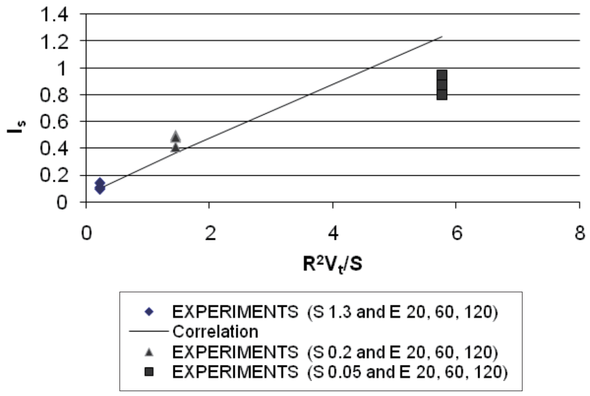

Fig. 4 Segregation index predicted (straight line) compared to experiments with three different powder feeding rates and air extraction rates.

5. Material Properties

Industrial supplied alumina was sieved in eight fractions where the largest particle size was 90 microns. The cumulative mass fraction of alumina is shown in **Fig. 5**. The content of fines was around 20 per cent. The size reduction of the alumina powder did not affect the material flow behaviour. The alumina powder is slightly more cohesive but still free flowing. The fraction of particles larger than 90

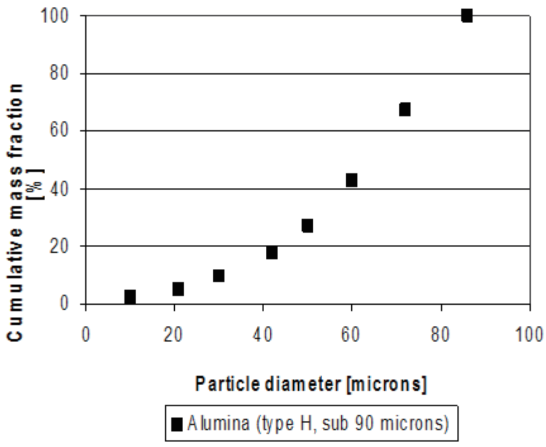

Fig. 5 Alumina fraction less than 90 microns.

---

[1] 1 L/h around 2.7×10^{7} m^3/s

Table 1 Particle fraction of alumina and sand, and the corresponding single particle terminal velocities

Particle size [micron]		Particle mass [g]		Terminal velocity for single particles [m/s]	
Sand	Alumina	Sand	Alumina	Sand	Alumina
90	10	2.3	1.1	0.005	0.005
180	21	2.3	2.1	0.02	0.02
290	30	4.7	4.2	0.04	0.04
480	42	8.1	7.9	0.08	0.08
550	50	9.5	12.1	0.09	0.09
800	60	15.9	19.3	0.13	0.13
1200	72	24.4	30.3	0.19	0.19
2000	90	33.0	45.2	0.28	0.29

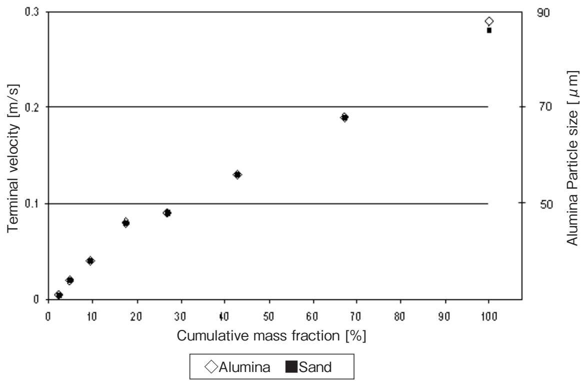

Fig. 6 Mass fraction vs the single particle terminal velocity of alumina and sand particles.

microns was sieved off from the alumina because the corresponding size of the sand particles with the same terminal velocity would otherwise become too large for the experimental set-up.

The mass fraction of sand was kept similar to the mass fraction of alumina and the particle size distribution of the sand particles was estimated using the representative values for the calculated terminal velocities of the alumina fractions in each size interval. Values are presented in **Table 1**. The cumulative mass fraction of the alumina powder was obtained by particle size analysis using the laser diffraction method.

The terminal velocities of sand and alumina were plotted vs the cumulative mass distributions as shown in **Fig. 6**. It can be noticed that there is good agreement of the terminal velocity for the sand and alumina particles in each size interval.

6. Results and Discussion

First, the experiments in the water silo were analysed. It was observed that the particle dynamics in the mixed convection flow was mildly influenced by the fluid extraction at the silo top of the water silo. Further, it could be seen that the particles settled in a dilute particle jet with large gaps between the particles. This observation of the particle jet justified using the single particle settling velocity for calculating the material/fluid properties for the scaled-down experiment. The sand which accumulated in the compartments was analysed. The sieve analysis of the dry sand in the outside compartments showed that around 57 per cent of the total sand mass settled in the outer ring (compartments 1-6). This confirmed the observation that the particle jet carried a large fraction of sand particles to the periphery of the silo. The particle mass in the outer compartment ring varied between 10 and 40 g, and a particle mass of 104 g accumulated in the central compartment (number 7).

The sand particle size distribution in the different compartments and the results from the fines content analysis are shown in **Fig. 7**. The calculated segregation index (equation 6) for the sand-water experiment was 0.45. The water experiment was repeated and a

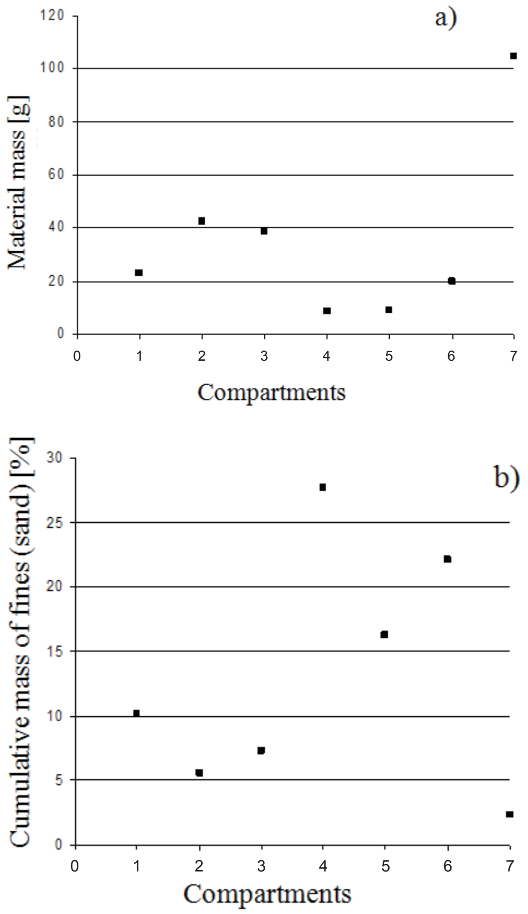

Fig. 7 a) Sand particle mass accumulated in compartments 1 to 6 (outside ring) and 7 (central pot), and b) Mass fraction of fine sand (particles smaller than 480 microns) (feeding rate 0.2 kg/min and water extraction rate 4 L/min).

segregation index of 0.57 obtained.

Next, the alumina from the air experiment was analysed. The analysis of the alumina material in the outside compartment showed that only 3 per cent of the total powder mass accumulated in the periphery of the silo. The total powder mass in the outer compartment ring was around 36 g and the fines content was around 28 per cent as shown in **Fig. 8**. The calculated segregation index for the alumina-air experiment was 0.14. The experiment was repeated twice and segregation indexes of 0.13 and 0.12 were obtained. It was observed during the experiments in the alumina-air silo that the particle jet was dense and the particle dynamics were different to the sand-water experiment.

The difference in the particle jets can be partly explained by the fact that the particle jet in the water experiment broke up right after the sand entered the silo. The settling behaviour of sand in water was affected by the properties of the material and the fluid. However, not all of these properties could be considered in the dimensional analysis.

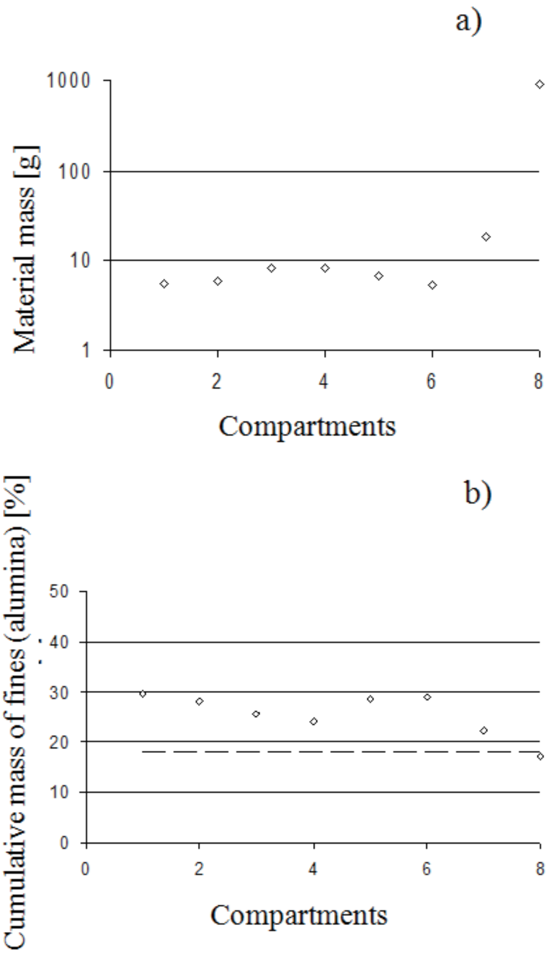

Fig. 8 a) Alumina particle mass accumulated in compartments 1 to 7 (outside ring) and 8 (central ring) (feeding rate 0.8 kg/min and air extraction rate 16 L/min), and b) Mass fraction of fines in compartments 1 to 7 (outside ring) and 8 (central pot).

Fig. 9 indicates that the physics of the particle jet had a strong impact on material segregation. For a dilute particle jet, higher segregation values were obtained. One solution to address the issue of permeability of the particle jet could be the introduction of another dimensionless group. The additional dimensionless group could allow for physical effects caused by varying particle jet densities.

7. Conclusions

The scaling rule presented and tested in this paper was able to provide quantitative information about the change in segregation due to amendments of process parameters such as powder feeding and air extraction rates. Changing material properties was a challenging test for the scaling rule because the sand particle jet showed a different behaviour compared with the alumina jet. To address the difference in the particle jets, a new dimensionless group could be added to the scaling rule. The difference in the particle dynamics caused the accumulation of larger sand particles at the periphery of the silo. Values for the segregation index confirmed this observation. The segregation index could be useful as an optimisation tool to fine-tune process parameters in order to minimise segregation in storage silos.

A correlation was developed to compare segrega-

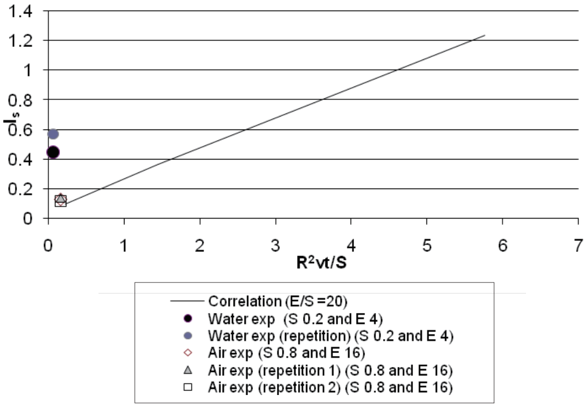

Fig. 9 Predicted segregation index (straight line) compared to experimental data from sand-water experiments (feeding rate 0.2 kg/min and water extraction rate 4 L/min with one repetition) and alumina-air experiments (feeding rate 0.8 kg/min and air extraction rate 16 L/min with two repetitions).

tion of different materials in multiple-scale experiments. The correlation predicted well the segregation index for the alumina-air experiment. For the sand-water experiment, the correlation under-predicted segregation. The correlation could be used in industry to predict segregation when changing process parameters such as the powder feeding rate.

Acknowledgements

I would like to thank Dr. Krystin Zigan for her continuous support as well as Prof. R. B. Thorpe, Prof. U. Tuzun and Prof. G. G. Enstad for their guidance and encouragement, and the great suggestions of many other colleagues from the University of Surrey are much appreciated. I am very grateful for the very useful discussions and the support provided by AOS in Stade, Germany, and Postec/ Tel-Tek, Porsgrunn, Norway.

Notation

ACS	Air current segregation
DA	Dimensional analysis
c_i	Mass % of fines in compartment i
c_L	Mass % of fines averaged over all compartments
E	Air extraction rate, m^3 / s
Is	Segregation index
M_i	Powder mass in compartment i, kg
M_L	Feed powder mass, kg
R	Dimension (radius), m
S	Powder feeding rate, m^3/s
V_t	Terminal particle velocity, m/s

References

1) van der Meer, E. H., Thorpe, R. B. and Davidson, J. F. (1999): Dimensionless groups for practicable similarity of circulating Fluidised beds, Chemical Engineering Science, 54, pp.5369-5376.
2) Zigan, S., Thorpe, R. B., Tuzun, U., Enstad, G., and Battistin, F. (2008): Theoretical and experimental testing of a scaling rule for air current segregation of alumina powder in cylindrical silos, Powder Technology, 183, 1, pp.133-145.
3) Mograbia, E. and Bar-Ziv, E. (2005): Dynamics of a spherical particle in mixed convection flow field, Aerosol Science, 36, pp.387-409.
4) Mitali D., Meikap B. C. and Saha R. K. (2008): Characteristics of axial and radial segregation of single and mixed particle system based on terminal settling velocity in the riser of a circulating fluidized bed, Chemical Engineering Journal, 145, pp.32-43.
5) Zhiyao, S., Tingting, W., Fumin, W. and Ruijie, L. (2008): A simple formula for predicting settling velocity of sediment particles, Water Science and Engineering, 1, pp.37-43.
6) Hazzab, A., Terfous, A. and Ghenaim, A. (2008): Measurement and modelling of the settling velocity of isometric particles, Powder Technology, 184, pp.105-113.
7) Turton, R. and Levenspiel, O. (1986): A short note on the drag correlation for spheres, Powder Technology, 47, 1, pp.83-86.

Author's short biography

Stefan Zigan

After graduating as a chemical engineer, Stefan worked as a process design engineer in the aerospace and car manufacturing industry. He did a PhD in multiphase flows minimising segregation in industrial storage silos. Stefan's research focuses on scaling and understanding flow and flow assurance problems in multiphase flows. He applies modelling techniques such as CFD and DEM as well as experiments to study phenomena in granular materials and fluids. He has a special interest in sustainable energies and energy storage systems (e.g. lithium ion batteries). He is a board member of the non-profit organisation Phalison, which organises knowledge and technology transfers with the Bolivian government to train researchers in Bolivia in lithium technologies and energy storage systems. He is also a member of the scientific board of the Bolivian National Evaporite Deposits Division and the IchemE (PTSIG). Stefan is a lecturer in thermofluids at the University of Greenwich.

Author's short biography

Amit Patel

He graduated in chemical engineering from the Imperial College of London with a further year of study, elevating this to a Master's degree. Amit returned to academia to pursue a doctorate from the University of Greenwich, successfully defending his thesis in November 2011. Amit's current interests lie in the computational modelling of cohesive powder flows. Empirical models are limited to cases where powder, equipment and environment-related variables remain decoupled.

Information Articles

The International Symposium on Nanoparticle Technology in memory of late Mr.Masuo Hosokawa

The International Symposium on Nanoparticle Technology was held in memory of late Mr.Masuo Hosokawa at the Imperial Hotel Osaka, Japan on Tuesday, April 24, 2012. It was organized by Hosokawa Powder Technology Foundation with the Sponsorship of Hosokawa Micron Corporation as one of special events of the Foundation. About 120 people from the industries and academic organizations attended this symposium and had many discussions. On this occasion, the publication of the 2nd edition of the Nanoparticle Technology Handbook was announced and some copies of it were displayed in the conference hall of the symposium.

• Opening speech	Prof.Hiroaki Masuda (Emeritus Prof.of Kyoto Univ.)
Session 1 Chaired by Prof.Yutaka Tsuji (Emeritus Prof.of Osaka Univ.)	
Lecture 1	
• “Particle Advances for Nano and Bio Technology Applications”	Prof.Brij M.Moudgil (Univ.of Florida, USA)
Lecture 2	
• “Manufacture of Functional Ceramic Nanopowders by Thermal Decomposition of Metal-Gel Structures”	Prof.Mojtaba Ghadiri (Univ.of Leeds, UK)
Lecture 3	
• “Trend of Nanoparticle Technology in ASEAN with Emphasis on Thailand”	Prof.Wiwut Tanthapanichakoon, Emeritus Prof.of Chulalongkorn Univ., Thailand, Prof.of Tokyo Institute of Technology, Japan
Session 2 Chaired by Prof.Makio Naito (Osaka Univ.)	
Lecture 4	
• “Process Technologies for Ultrafine Particles - from Research to Production”	Dr.Jürgen Stein (Hosokawa Alpine AG)
Lecture 5	
• “From Bulk Solids Blending into Fine Particle Engineering”	Dr.Peter van der Wel (Hosokawa Mcron BV)
Lecture 6	
• “Creation and Application of Nanoparticles for Advanced Functional Materials”	Dr.Toyokazu Yokoyama (Hosokawa Micron Corporation.)
• Closing speech	Mr.Kiyomi Miyata (President of Hosokawa Micron Corporation)

Closing remarks by Mr.Miyata, President of Hosokawa Micron Corporation

Display of portrait of late Mr.Masuo Hosokawa and the 2nd edition of Nanoparticle Technology Handbook

The 46th Symposium on Powder Technology

Hosokawa Powder Technology Foundation held the 46th Symposium on Powder Technology at Hotel Laforet Tokyo on September 27th, 2012 with the sponsorship of Hosokawa Micron Corporation. The symposium attracted a large attendance of over 140 including 18 academic people. The theme of the symposium was “The Forefront of Application of NanoParticle Technology”. Fruitful discussions took place as usual.

• Opening Address	Prof. Hiroaki Masuda (Kyoto Univ.)
Session 1 Chaired by Prof. Makio Naito (Osaka Univ.)	
Lecture 1	
• “New Approach Towards Establishment of Science for Processing of Ceramics Through Powder Technology”	Keizo Uematsu (Nagaoka University of Technology)
Lecture 2	
• “Role of Nanosized Particles on Ferroelectric/Piezoelectric Devices and Future Prospect”	Yuji Noguchi, (The University of Tokyo)
Session 2 Chaired by Prof. Ko Higashitani (Kyoto Univ.)	
Lecture 3	
• “The Development of Vascular Endothelial Cell Selectivity Nanotechnology Based Drug Delivery System for Less Invasive Nanotherapy”	Kensuke Egashira (Kyushu Univ.)
Lecture 4	
• “NanoComposite Thin Films Using of Functional Nanoparticles and Its Applications”	Miki Egami (JGC Catalysts and Chemicals, Ltd.)
Session 3 Chaired by Kikuo Okuyama (Hiroshima Univ.)	
Lecture 5	
• “Development and Application of Nano-filler / Polymer Composites”	Kazuya Nagata (Asahi Kasei Chemicals Corporation)
Lecture 6	
• “Development Toward to Industrialization of Functional Cosmetics and Medical Devices Based on PLGA Nano Particulate Design and Preparation”	Hiroyuki Tsujimoto (Hosokawa Micron Corporation)
• Closing Address	Yoshio Hosokawa (Hosokawa Micron Corporation)

Opening speech by Prof.Masuda

The KONA Symposium 2012

The KONA Symposium 2012 organized by Hosokawa Powder Technology Foundation was held as one of satellite symposiums of ICCCI 2012 (The Fourth International Conference on The Characterization and Control of Interfaces for High Quality Advanced Materials), which was held at Hotel Nikko Kurashiki, in Okayama, Japan from 2nd to 5th of September, 2012 in the afternoon of its last day. There were 5 lectures given by the authors of papers recently submitted to KONA journal as follows and 40 participants from 10 countries.

• Opening speech	Prof. Jusuke Hidaka (Doshisha Univ.,Japan)
Session 1 Chaired by Prof. Yoshiyuki Shirakawa (Doshisha Univ.,Japan)	
Lecture 1	
• "Aerosol-assisted Tuning of Structural and Morphological Features of Nanoscaled Functional Materials"	Prof. Olivera Milosevic (SASA, Serbia)
Lecture 2	
• "Bio-Inspired Functional Materials Templated from Nature Materials"	Prof. Di Zhang (Shanghai Jiao Tong Univ., P.R.China)
Lecture 3	
• "Structural Joining of Ceramic Nanoparticles: Development of Photonic Crystals for Terahertz Wave Control by Using Micro Stereolithography"	Prof. Soshu Kirihara (JWRI, Osaka Univ., Japan)
Session 2 Chaired by Prof. Makio Naito, JWRI (Osaka Univ., Japan)	
Lecture 4	
• "Designing with Pores-Synthesis and Applications"	Dr. Steven Mullens (VITO, Belgium)
Lecture 5	
• "Creation and Application of Nanoparticles for Advanced Functional Materials"	Dr. Toyokazu Yokoyama (Hosokawa Micron Corp., Japan)
• Closing speech	Dr. Hisao Makino, Central Research Institute of Electric Power Industry (President of the Society of Powder Technology, Japan)

Presentation in the conference room

Display of publications from Hosokawa Powder Technology Foundation

The 18th KONA Award

Dr. keizo Uematsu, Professor of Nagaoka University of Technology (NUT), was selected as the winner of the 18th KONA Award, which is sponsored by Hosokawa Powder Technology Foundation and given to the scientist(s) or group(s) who have achieved distinguished research works in the field of particle science and technology.

Dr. Uematsu received BS(1969) and MS(1971) from Tokyo Institute of Technology(TIT), and Ph.D. in Ceramics(1976) from Massachusetts Institute of Technology. After working as a post-doctoral fellow at MIT, he returned to TIT where he worked for several years as a Research Associate. In 1985 he moved to NUT as an associate professor. He was promoted to the position of full professor in 1991. He served as the director of Library from 2009 to 2011.

He made a great contribution to the particle science and technology through the establishment of processing-structure-property relationship for advanced alumina ceramics. The basis of research was the development of powerful characterization tools for analyzing the packing structures of particles in ceramic green compacts and macro-defects in ceramics in 1990s. They consist of preparation of transparent specimen by the addition of immersion liquid and thinning for green compacts and ceramics, respectively, and the subsequent examination by optical microscopes in the transmission mode. They could identify origins of macro-defects, as well as deformation and cracking of ceramics during manufacturing. Systematic study on ceramic processing successfully showed changes of structures explicitly from raw powders to final ceramics. He could show answers for many important problems in the production of ceramics, leading to the establishment of basis for high reliability and reduction of production costs in ceramics.

On January 25, 2012, Mr. Yoshio Hosokawa, President of the Foundation, handed the 18th KONA Award to Dr. Uematsu at the presentation ceremony held at Hosokawa Micron Corporation in Hirakata.

GENERAL INFORMATION

HISTORY OF THE JOURNAL

In the history of KONA Powder and Particle Journal, two organizations have been playing an important role. The one is the Council of Powder Technology, Japan (CPT) and the other is the Hosokawa Powder Technology Foundation (Hosokawa Foundation). The CPT was established in 1969 by Hosokawa Micron Corporation as a nonprofit organization to enhance the activities of research and development on powder science and technology. The Hosokawa Foundation was established in 1991 as a public-service corporation approved by the Ministry of Education, Culture, Sport, Science and Technology of Japan. The issues from No.1 (1983) to No.12 (1994) of KONA were published by CPT and the issues from No.13 (1995) by the Hosokawa Foundation.

The aim of KONA in the early days was to introduce excellent Japanese papers to the world and thus KONA consisted of papers recommended by some Japanese academic societies and translated from Japanese to English. From the issue of No.8, the CPT changed its editorial policy to internationalize the KONA and to incorporate papers by authors throughout the world in addition to translated papers. In response to this change, three editorial blocks have been organized in the world; Asian-Oceania, American and European. The policy and system have not changed even after the Hosokawa Foundation has taken over from the CPT. From the issue of No.27 (2009), publication of translated papers has been terminated and only original papers have been published. The CPT is active still today and collaborates with the Hosokawa Foundation.

AIMS AND SCOPE

KONA publishes papers in a broad field of powder science and technology, ranging from fundamental principles to practical applications. The papers describing technological experiences and critical reviews of existing knowledge in special areas are also welcome.

The submitted papers are published only when they are judged by the Editor to contribute to the progress of powder science and technology, and approved by any of the three Editorial Committees. The paper submitted to the Editorial Secretariat should not have been previously published.

CATEGORY OF PAPERS

- Invited papers
  Original research and review papers invited by the KONA Editorial Committees.
- Contributed papers
  Original research and review papers submitted to the KONA Editorial Committees, and refereed by the Editors.

SUBMISSON OF PAPERS

Papers should be sent to each KONA Editorial Secretariat.

- Asia/Oceania Editorial Secretariat
  Dr. T. Yokoyama or Dr. L. Cui
  Hosokawa Powder Technology Foundation
  Shodai-Tajika, 1-9, Hirakata, 573-1132 Japan
- Europe/Africa Editorial Secretariat
  Dr. J. Stein or Mrs. N. Winzer
  Hosokawa Alpine AG
  Peter-Dörfler-Straße 13-25
  D - 86199 Augsburg, Germany
- Americas Editorial Secretariat
  Dr. C.C. Huang
  Hosokawa Micron Powder Systems
  10 Chatham Road, Summit NJ 07901 USA

Publication in KONA Powder and Particle Journal is free of charge.

PUBLICATION SCHEDULE

KONA is published annually. The publication date is January 10th.

SUBSCRIPTION

KONA Powder and Particle Journal is distributed free of charge to senior researchers at universities and laboratories as well as to institutions and libraries in the field throughout the world. The publisher is always glad to consider the addition of names of those who want to obtain this journal regularly to the mailing list. Distribution of KONA is made by each Secretariat.

Free electronic publication of KONA Powder and Particle Journal is available in http://www.kona.or.jp

INSTRUCTIONS TO AUTHORS

(1) Manuscript format

- Electric files should be submitted to the Editorial Secretariat by online. Authors' short biography with less than 100 words per person and photograph of all the authors should be attached to the final version.
- The structure of manuscripts should follow the following order; title, authors, affiliations, abstract, keywords, main text, (acknowledgement), (appendix), (nomenclature), references. The items with parentheses are not mandatory. The text should be in single-column format. Figures and tables can be imported into the main text. If figures and table are collated in a separate section at the end of the article, indicate their approximate locations directly in the text. If symbols are defined in a nomenclature section, symbols and units should be listed in alphabetical order with their definition and dimensions in SI units.
- Full postal addresses must be given for all the authors. Indicate the corresponding author by the mark "*" after the name. Telephone and fax numbers and e-mail address should be provided for the corresponding author.
- Abstract should not exceed 200 words.
- The appropriate number of keywords is 5 or 6.
- The maximum pages printed in KONA are supposed to be:
  10 for an original paper and 15 for a review paper.
- Symbols and units should be listed in alphabetical order with their definition and dimensions in SI units.
- The color figures will appear in color on the Web (http://www.kona.or.jp). Because of technical complications which can arise by converting color figures to 'gray scale' (for the printed version), please submit in addition usable black and white versions of all the color illustrations.
- Concerning references, the alphabetical system should be adopted.
  List: References should be arranged first alphabetically and then further sorted chronologically if necessary. More than one reference from the same author(s) in the same year must be identified by the letters "a", "b", "c", etc., placed after the year of publication.
  Examples:
  - Reference to a book:
  Strunk Jr. W., White E.B., The Elements of Style, fourth ed., Longman, New York, 2000.
  - Reference to a chapter in an edited book:
  Mettam G.R., Adams L.B., How to prepare an electronic version of your article, in: Jones B.S., Smith R.Z. (Eds.), Introduction to the Electronic Age, E-Publishing Inc., New York, 2009, pp.281–304.
  - Reference to a journal publication:
  Tsuji Y., Tanaka T., Ishida T., Lagrangian numerical simulation of plug flow of cohesionless particles in a horizontal pipe, Powder Technology, 71 (1992) 239-250.
  Text: All citations in the text should refer to:
  1. Single author: the author's name (without initials, unless there is ambiguity) and the year of publication;
  2. Two authors: both authors' names and the year of publication;
  3. Three or more authors: first author's name followed by "et al." and the year of publication.
  Citations may be made directly (or parenthetically). Groups of references should be listed first alphabetically, then chronologically.
  Examples: "as demonstrated (Allan, 1996a, 1996b, 1999; Allan and Jones, 1995). Kramer et al. (2000) have recently shown ...."

(2) Copyright and permission

- Original papers submitted for publication become immediately the property of the Hosokawa Powder Technology Foundation and remain so unless withdrawn by the author prior to acceptance for publication or unless released by the Editor. The original papers in KONA should not be reproduced nor published in any form without the written permission of the Hosokawa Foundation. Authors are responsible for obtaining permission from the copyright holder to reproduce any figures, tables and photos for which copyright exists.

HOSOKAWA MICRON

New Product

Global standard of Powder Properties Evaluation

Powder Characteristics Tester

with Automatic Tapped Bulk Density Measuring Unit for USP

APPLICATIONS

- ■Quantification of powder characteristics
- ■Quoted in hundreds of research papers.
- ■To evaluate and control the product quality
- ■For all companies related with powder

Quantification of flowability and floodability

FEATURES

■Global standard instrument for quality control
Powder Tester has been widely applied for product control in various industries.

■Equipment to work out Carr’s method for powder characterization
To carry out the procedures proposed by Mr. R.L.Carr, Powder Tester was developed 45 years ago.

■Automatic measurement of tapping density is compliant with U.S. Pharmacopoeia, ASTM and Kawakita procedure.

Packed bulk density

Aerated bulk density

Angle of Repose

Angle of Fall

Cohesion

Uniformity

Angle of Difference

Angle of Spatula

Dispersibility

Compressibility

Contact to... http://www.hosokawamicron.com

Japan : Osaka +81-72-855-2224,Tokyo +81-3-5248-5700
(HOSOKAWA MICRON CORP. World Headquarters)

Our global network

China : +86-21-5306-8031 (Hosokawa Micron (Shanghai) Powder Machinery Co., Ltd.)

Germany : +49-821-59-06-0 (Hosokawa Alpine AG)
+49-7131-9070 (Hosokawa Bepex GmbH)
Korea : +82-2-420-5691 (Hosokawa Micron (Korea) Ltd.)
Netherlands : +31-314-373333 (Hosokawa Micron B.V.)
Russia : +7-812 3326200 (Hosokawa Micron Sankt Petersburg OOO)
U.K. : +44-1928-755-100 (Hosokawa Micron Ltd.)
U.S.A. : +1-908-277-9300 (Hosokawa Micron International Inc.)

HOSOKAWA MICRON

The Hosokawa Micron Group will always be the leading global company covering the mountain range of Powder Technologies. The Group has been a pioneer in the field of powder and particle processing, blown film processing, and confectionary and bakery technologies. We provide R&D, engineering, manufacturing and services in various fields of the world's major industrial markets.

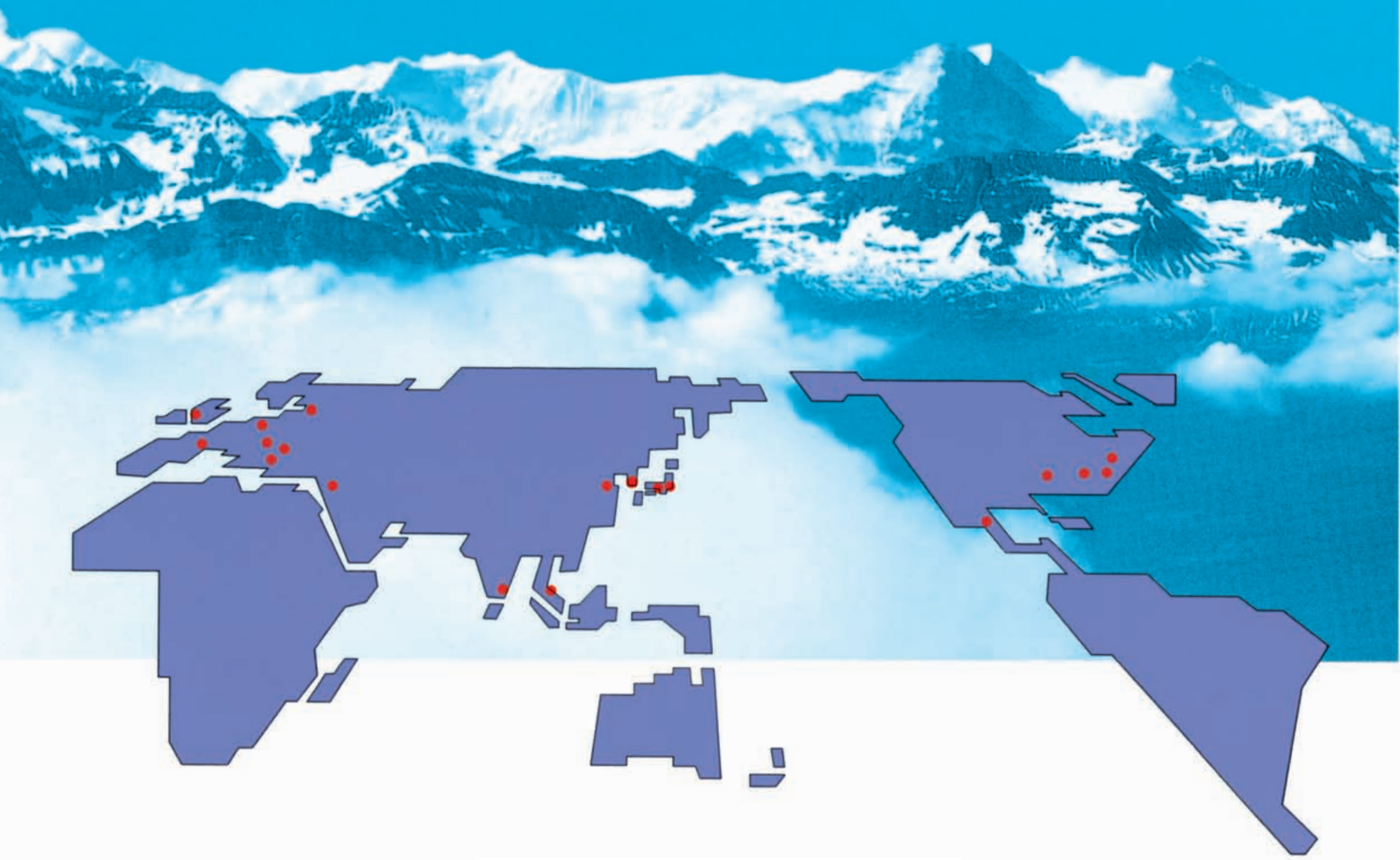

Process Technologies for Tomorrow

HOSOKAWA MICRON

Headquarters Location:
HOSOKAWA MICRON CORPORATION
http://www.hosokawamicron.co.jp